
Optical Spectra of Thermonuclear Supernovae in the Local and Distant Universe

Stéphane Blondin



München 2005

Optical Spectra of Thermonuclear Supernovae in the Local and Distant Universe

Stéphane Blondin

Dissertation
an der Fakultät für Physik
der Ludwig-Maximilians-Universität
München

vorgelegt von
Stéphane Blondin
aus Paris

München, den 11.08.2005

Erstgutachter: Prof. Adalbert Pauldrach

Zweitgutachter: Priv. Doz. Achim Weiss

Tag der mündlichen Prüfung: 07.11.2005

*For my Peruvian queen
and our Franco-Peruvian princess*

Contents

Summary	xvii
Zusammenfassung	xix
1 Introduction	1
1.1 General properties of thermonuclear supernovae	1
1.1.1 The confusing and misleading classification of supernovae	1
1.1.2 Progenitors of Type Ia supernovae	6
1.1.3 Light curves and explosion models of Type Ia supernovae	7
1.2 Type Ia supernovae as distance indicators	11
1.3 Cosmology with Type Ia supernovae	13
1.3.1 Friedmann-Robertson-Walker cosmology	13
1.3.2 Luminosity distances and the accelerating universe	17
1.3.3 Measuring the equation-of-state parameter of “Dark Energy”	23
1.4 Testing for evolution in the SN Ia sample at different redshifts	25
2 Optical spectra of Type Ia supernovae	31
2.1 Modeling Type Ia supernova spectra	31
2.1.1 Velocity field and density/abundance structure in SN Ia ejecta	31
2.1.2 Sources of opacity in SN Ia ejecta	33
2.1.3 Line formation and line profiles in SN Ia spectra	39
2.1.4 A parametrized synthetic SN Ia spectrum	44
2.2 Observational properties of Type Ia supernovae	47
2.2.1 Spectral evolution of SN Ia	47
2.2.2 Homogeneity <i>vs.</i> inhomogeneity in SN Ia spectra	50
2.3 Observations of Type Ia supernovae and data reduction	52
2.3.1 Discovery of a supernova and spectroscopic follow-up	52
2.3.2 Standard approach to reducing supernova spectra	56
2.3.3 A novel method to extract SN spectra	59
3 Extracting clean supernova spectra	69
3.1 Introduction	69
3.2 The algorithm and its implementation	71

3.2.1	Decomposing the SN from its host galaxy	71
3.2.2	Practical implementation for SN and host galaxy	72
3.3	The importance of the slit spread function	73
3.3.1	Measuring the seeing	73
3.3.2	Generating synthetic PSF spectra	74
3.3.3	Impact of the SSF on spectral restoration	77
3.4	The spatial resolution kernel	79
3.5	Testing the algorithm on simulated data	83
3.5.1	Simulated data	83
3.5.2	Simulation steps	86
3.5.3	Simulation results and discussion	92
3.6	Testing the algorithm on real data	92
3.7	Comparison with other methods	94
3.7.1	Standard extraction in IRAF	97
3.7.2	<i>Gaussextract</i> – an iterative Gaussian extractor	98
3.7.3	Statistical approach using \mathcal{SN} -fit	98
3.8	Conclusion	99
4	A tool to determine supernova redshifts	101
4.1	Introduction	101
4.2	Cross-correlation techniques	104
4.2.1	Pre-processing the supernova spectrum	104
4.2.2	Estimation of redshift	109
4.2.3	Estimation of redshift error	114
4.3	Variation of the redshift error with redshift, phase, and spectral range	117
4.4	Accuracy of the cross-correlation method: comparison of SN and host galaxy redshifts	123
4.5	Future developments	127
5	Using line profiles to test the fraternity of Type Ia supernovae at high and low redshifts	133
5.1	Introduction	134
5.2	Measurement techniques	136
5.2.1	Smoothing Supernova Spectra	136
5.2.2	Error Budget	142
5.3	Results	144
5.3.1	Absorption Velocities	148
5.3.2	Emission-Peak Velocities	157
5.3.3	Double-Absorption Features in Ca II λ 3945	162
5.4	Conclusions	166

6	Time-dilation effects in high-redshift Type Ia supernova spectra	183
6.1	Introduction	183
6.2	Determining the phase of a SN Ia <i>via</i> cross-correlation	185
6.3	Testing for time dilation in high- z SN Ia spectra	189
6.3.1	Spectral phases in high- z SN Ia	189
6.3.2	Determining the age factor	191
6.3.3	Time dilation from multi-epoch spectra of SN 2002iy at $z = 0.587$.	192
6.4	Conclusion	195
7	Conclusion	199
A	Spectroscopy of high-redshift supernovae from the ESSENCE project: the first 2 years	203
A.1	Introduction	204
A.2	Target Selection	205
A.3	Observations	207
A.4	Target Identification	207
A.5	Results	210
A.6	Conclusions	230
	Bibliography	264
	Acknowledgements	265
	Curriculum Vitae	267

List of Figures

1.1	SN 1994D in NGC 4526	2
1.2	Classification scheme of supernovae	4
1.3	Supernova spectra of the four major types and subtypes	5
1.4	Cartoon illustrating the progenitor system of a thermonuclear (Type Ia) supernova	8
1.5	Bolometric light curves of Type Ia supernovae	10
1.6	Calibration of <i>BVI</i> magnitudes of SN Ia	12
1.7	Hubble diagram for low-redshift Type Ia supernovae	14
1.8	Hubble diagram for high-redshift Type Ia supernovae	20
1.9	SN Ia likelihood distribution for Ω_Λ vs. Ω_M	21
1.10	SN Ia + 2dF constraints on Ω_Λ and w	24
1.11	Colour evolution in SN Ia	26
1.12	Qualitative comparison of local and high-redshift SN Ia spectra	27
2.1	Density and velocity as a function of the mass for a double-detonation model of a SN Ia	33
2.2	Abundances of stable isotopes as a function of the expansion velocity for a double-detonation model of a SN Ia	34
2.3	Contribution of lines and electron scattering to the total opacity in SN Ia ejecta	36
2.4	Variation of the velocity and radius of total inward-integrated optical depth $\tau_{\text{tot}} = \{0.1, 1\}$ layers with wavelength in SN Ia ejecta	38
2.5	Cartoon illustrating the density/velocity structure in SN Ia envelopes and subsequent line-profile morphology	41
2.6	Comparison of P-Cygni profiles of resonance lines in WR and SN Ia outflows, based on CMFGEN models	43
2.7	Radial and velocity variation of the line source function in WR and SN Ia outflows, based on CMFGEN models	45
2.8	Observed and SYNOW synthetic spectra of SN 1994D near maximum light	48
2.9	Luminosity and spectral evolution of SN 1994D	49
2.10	“Normal” and “peculiar” SN Ia optical spectra around maximum light	51
2.11	Discovery of two Type Ia supernovae using difference imaging	54
2.12	Finder chart for SN 2003jo ($z = 0.524$)	55

2.13	Picture of the VLT UT2 Kueyen telescope and the FORS1 instrument . . .	56
2.14	Cosmic-ray removal in a 2D spectrum	58
2.15	Extraction of a 1D spectrum from a 2D raw image	60
2.16	Wavelength calibration of spectra using a HeNeAr lamp	61
2.17	Flux calibration of spectra using the EG 21 spectrophotometric standard star	62
2.18	Two-channel restoration applied to a 2D spectrum	64
2.19	1D restored VLT ESSENCE SN Ia spectra in the redshift range $0.2 < z \leq 0.4$	65
2.20	1D restored VLT ESSENCE SN Ia spectra in the redshift range $0.4 < z \leq 0.6$	66
2.21	1D restored VLT ESSENCE SN Ia spectra in the redshift range $z > 0.6$. .	67
3.1	FWHM of the cross-dispersion profile of the standard star LTT 7987 . . .	75
3.2	Illustration of SSF synthesis using <i>specpsf</i>	76
3.3	Examples of SSFs used to extract SN 2002go	78
3.4	Impact of the SSF on the restored point source spectrum of SN 2002go . .	80
3.5	Impact of the width of the spatial resolution kernel σ_{kernel} on the background restoration	81
3.6	Restored point source spectra in units of the statistical noise of the input pure galaxy spectrum	82
3.7	Absolute flux-calibrated galaxy and sky spectra used in the <i>specinholucy</i> simulation	85
3.8	Smoothed galaxy spatial profile used in the <i>specinholucy</i> simulation	87
3.9	SN trace position residuals as a function of the SN phase, for different locations of the SN with respect to the galaxy centroid	89
3.10	SN trace FWHM residuals as a function of the SN phase, for different locations of the SN with respect to the galaxy centroid	90
3.11	<i>specinholucy</i> simulation results	93
3.12	Wavelength-averaged spatial residuals in applying <i>specinholucy</i> to real data	96
3.13	Spectral residuals in applying <i>specinholucy</i> to real data	96
3.14	Restored supernova spectra using <i>specinholucy</i> and other methods	97
4.1	Phase distribution of SN Ia spectral templates used in SNID	104
4.2	Preparing a spectrum for cross-correlation using SNID	106
4.3	Example of a SNID SN Ia spectral template	107
4.4	Power spectrum of unfiltered correlation function	108
4.5	Auto- and cross-correlations with SNID	113
4.6	Nugent SN Ia spectral templates used in SNID simulations	116
4.7	SNID redshift residuals <i>vs.</i> r and $rlap$ parameters	118
4.8	Histogram of redshift residuals for $0.1 \leq z \leq 0.9$	119
4.9	Redshift residuals <i>vs.</i> z for phases $-10 \text{ d} \leq t \leq +20 \text{ d}$	120
4.10	Histogram of redshift residuals for different spectral ranges	122
4.11	Redshift residuals <i>vs.</i> t for different spectral ranges	124
4.12	Comparison of supernova and galaxy redshifts	126

4.13	Mean normalized unfiltered correlation functions for SN Ia for which we have a redshift from the host galaxy	128
4.14	Normalized unfiltered correlation functions for SN Ia for which we have a redshift from the host galaxy (<i>cont.</i>)	129
4.15	Normalized unfiltered correlation functions for SN Ia for which we have a redshift from the host galaxy (<i>cont.</i>)	130
4.16	Normalized unfiltered correlation functions for SN Ia for which we have a redshift from the host galaxy (<i>cont.</i>)	131
5.1	Smoothing supernova spectra	138
5.2	P-Cygni profiles of Si II $\lambda 6355$ in local SN Ia	139
5.3	Comparison Gaussian and spline fits to P-Cygni profiles	141
5.4	Absorption velocities for Ca II $\lambda 3945$	149
5.5	Line overlap in SN Ia illustrated using SYNOW	151
5.6	Absorption velocities for Si II $\lambda 6355$	152
5.7	Absorption velocities for S II $\lambda \lambda 5454, 5640$	153
5.8	Illustration of P-Cygni profile formation in SN Ia using CMFGEN	155
5.9	Emission-peak velocities for Ca II $\lambda 3945$	158
5.10	Emission-peak velocities for Si II $\lambda 6355$	159
5.11	Emission-peak velocities for S II $\lambda \lambda 5454, 5640$	160
5.12	Emission-peak velocities for S II $\lambda 5454$ normalized to the S II $\lambda 5640$ absorption velocities	161
5.13	Double-absorption features in Ca II $\lambda 3945$	164
5.14	Absorption velocities for Ca II $\lambda 3945$ in single- and double-absorption features	165
5.15	Time evolution of the ratio of v_{abs} for the blue and red components of the Ca II $\lambda 3945$ absorption feature	166
6.1	Comparison of spectral and light-curve phases for a set of 136 local SN Ia .	186
6.2	Determining the noise in a high- z SN Ia spectrum	188
6.3	Statistical error for spectral phase determinations using SNID	189
6.4	Spectral phase <i>vs.</i> light-curve phase	190
6.5	Variation of the systematic error with phase	191
6.6	Age factor for 29 high- z SN Ia corrected to $\tilde{z} = 0.417$	193
6.7	Multi-epoch spectra of SN 2002iy at $z = 0.587$	194
6.8	Age factor for SN 2002iy at $z = 0.587$	195
A.1	Comparison of redshifts as determined by SNID and from narrow emission or absorption lines in the host-galaxy spectrum	211
A.2	Redshift distribution of definite, spectroscopically identified SN Ia from the first two years of the ESSENCE project	212
A.3	Age distribution (relative to maximum brightness) of definite, spectroscopically identified SN Ia from the first two years of the ESSENCE project . .	213

A.4	Rest-wavelength spectra of SN Ia (or likely SN Ia) from the first two years of the ESSENCE project in order of increasing redshift	215
A.5	Rest-wavelength spectra of ESSENCE SN Ia (<i>cont.</i>)	216
A.6	Rest-wavelength spectra of ESSENCE SN Ia (<i>cont.</i>)	217
A.7	Rest-wavelength spectra of ESSENCE SN Ia (<i>cont.</i>)	218
A.8	Rest-wavelength spectra of ESSENCE SN Ia (<i>cont.</i>)	219
A.9	Rest-wavelength spectra of ESSENCE SN Ia (<i>cont.</i>)	220
A.10	Rest-wavelength spectra of ESSENCE SN Ia (<i>cont.</i>)	221
A.11	Spectra of SN II and one SN Ib/c from the first two years of the ESSENCE project	222
A.12	Spectra of AGNs from the first two years of the ESSENCE project	223
A.13	Spectra of AGNs from the first two years of the ESSENCE project (<i>cont.</i>)	224
A.14	Spectra of four stars from the first two years of the ESSENCE project	225
A.15	Spectra of galaxies from the first two years of the ESSENCE project	226
A.16	Spectra of galaxies from the first two years of the ESSENCE project (<i>cont.</i>)	227
A.17	Spectra of objects whose classification is uncertain from the first two years of the ESSENCE project	228
A.18	Spectra of objects whose classification is uncertain from the first two years of the ESSENCE project (<i>cont.</i>)	229

List of Tables

1.1	Equation-of-state parameters for various energy components	17
2.1	SYNOW model parameters for SN 1994D at -1 d	46
3.1	SSF FWHM data	77
3.2	Distances and flux scaling	83
3.3	SN 1994D data used in the simulation	84
3.4	<i>specinholucy</i> parameters	95
3.5	Supernova observation summary	95
4.1	SN Ia spectral templates for SNID	103
4.2	Characteristic spectral features from Riess et al. [245]	121
4.3	SNID <i>vs.</i> galaxy redshifts	125
5.1	Measurement errors	142
5.2	Characteristic wavelengths of atomic transitions ^a	145
5.3	Local SN Ia data	146
5.4	High- z SN Ia data	147
5.5	CMFGEN model parameters	154
5.6	Absorption velocities in local SN Ia (10^3 km s ⁻¹)	168
5.7	Absorption velocities in ESSENCE high- z SN Ia (10^3 km s ⁻¹)	174
5.8	Emission-peak velocities in local SN Ia (10^3 km s ⁻¹)	176
5.9	Emission-peak velocities in ESSENCE high- z SN Ia (10^3 km s ⁻¹)	181
6.1	Spectral feature ages and time dilation	197
A.1	ESSENCE spectroscopy results: the first two years	231
A.2	ESSENCE spectroscopic targets: the first two years	232

Summary

This thesis is devoted to the study of optical spectra of thermonuclear supernovae, known as “Type Ia” supernovae (SN Ia). These violent stellar explosions, visible across a large fraction of the observable universe, are used to measure distances on cosmological scales. By directly probing the expansion dynamics of the universe, measurements of relative luminosity distances to SN Ia have shown the universal expansion to be accelerating. Such an acceleration can only be explained if the universe is pervaded by a new form of energy with negative pressure – or “Dark Energy”, such as Einstein’s cosmological constant, Λ .

The use of SN Ia as distance indicators requires the use of a purely empirical calibration scheme relating the shape of the SN Ia light curve with its peak luminosity. Although this relation is well verified for SN Ia in the local universe, it lacks convincing theoretical basis. Moreover, in view of the current uncertainties in modeling the explosion mechanisms and inferring the progenitor systems of SN Ia, its extrapolation to higher redshifts could be systematically affected by evolutionary effects, thereby biasing the cosmological results.

Spectroscopy is better suited than photometry to make quantitative comparisons between SN Ia at different redshifts. Large amounts of information are conveyed by spectra on the properties of the ejecta (chemical composition, velocity/density gradients, excitation level); subtle differences, blurred together in photometric measurements, will show up in the spectra. However, comparisons of SN Ia at different redshifts have so far only been qualitative in nature. This thesis presents original results on a quantitative comparison, based on several analysis tools developed and/or tested during the course of the past three years.

The thesis is structured as follows: the first two chapters serve as an introduction to the reader on the cosmological use of SN Ia, and on their optical spectra (theory and observation). Chap. 3 [27] presents a two-dimensional deconvolution method to separate a supernova spectrum from the contaminating background of its host galaxy. This algorithm was used to reduce the SN Ia spectra, taken with the ESO *Very Large Telescope*, presented in Matheson et al. [187] (see Appendix A). In Chap. 4, we discuss the use of a cross-correlation tool to determine the redshift of a SN Ia based on its spectrum alone – i.e., not relying on narrow lines in the spectrum of the host galaxy. The main focus of this thesis is Chap. 5 [26]: using characteristics of line-profile shapes in SN Ia, we provide the first clear quantitative evidence that the high-redshift SN Ia are indeed similar to their local counterparts, providing a confirmation of their use as reliable cosmological distance indicators. Finally, in Chap. 6 we present preliminary results on cosmological time-dilation

effects in high-redshift SN Ia spectra.

Zusammenfassung

Diese Doktorarbeit beschäftigt sich mit dem Studium optischer Spektren thermonuklearer Supernovae, bekannt als “Typ Ia” Supernovae (SN Ia). Diese gewaltigen Sternexplosionen, die über einen grossen Bereich des Universums beobachtet werden können, werden dazu benützt Distanzen auf kosmologischen Skalen zu messen. Relative Leuchtkraftdistanzen zu SN Ia, welche die Expansionsdynamik direkt vermessen, haben gezeigt, dass die universale Ausdehnung beschleunigt ist. Eine solche Beschleunigung kann nur damit erklärt werden, dass das Universum von einer neuen Energieform mit negativem Druck – oder “Dunkler Energie”, wie zum Beispiel Einsteins Kosmologische Konstante, Λ , durchdrungen ist.

Die Benützung von SN Ia als Distanzindikatoren basiert auf einer vollkommen empirischen Eichung, in der die Lichtkurvenform einer SN Ia mit ihrer Leuchtkraft am Maximum korreliert wird. Obwohl diese Beziehung im nahen Universum gut verifiziert werden kann, mangelt es immer noch an einer überzeugenden theoretischen Basis. Berücksichtigt man die momentanen Unsicherheiten bezüglich der Explosionsmodelle und der Vorgängersterne von SN Ia ist eine Extrapolation zu höheren Rotverschiebungen mit möglichen systematischen Entwicklungseffekten befrachtet. Solche Effekte können die kosmologischen Resultate beeinträchtigen.

Spektroskopie ist besser geeignet als Photometrie um einen quantitativen Vergleich zwischen SN Ia bei verschiedenen Rotverschiebung zu ermöglichen. Die Information, die in Spektren zu Verfügung steht, kann benützt werden, um die Eigenschaften der Supernovahülle (chemische Zusammensetzung, Geschwindigkeit- und Dichte-Gradienten, Anregungszustand) zu messen; feine Unterschiede sind in Spektren aufgezeichnet. Vergleiche von Spektren von SN Ia bei unterschiedlichen Rotverschiebungen waren bisher nur von qualitativer Natur. Diese Arbeit präsentiert neue Resultate eines quantitativen Vergleichs. Dazu wurden mehrere neuartige Methoden zur Analyse im Verlaufe der letzten drei Jahre entwickelt und getestet.

Die Doktorarbeit ist folgendermassen gegliedert: die ersten zwei Kapitel dienen als Einleitung zum kosmologischen Gebrauch von SN Ia und deren optischen Spektren (sowohl Theorie als auch Beobachtung). Kapitel 3 [27] stellt eine Methode zur zwei-dimensionalen Trennung von Supernovaspektrum und dem störenden Hintergrund der Muttergalaxie vor. Dieser Algorithmus wurde für die Reduktion der SN Ia Spektren, die mit dem ESO *Very Large Telescope* beobachtet und in Matheson et al. (2005) veröffentlicht wurden (man vergleiche auch Appendix A), verwendet. In Kapitel 4 diskutieren wir den Gebrauch einer Korrelationsmethode zur Bestimmung der Rotverschiebung einer SN Ia aufgrund ihres

Spektrums, i.e. ohne Berücksichtigung der schmalen Spektrallinien der Muttergalaxie. Der Hauptbeitrag dieser Doktorarbeit ist Kapitel 5 [26]: mittels der Charakteristika der Linienprofile von SN Ia konnten wir zum ersten mal deutlich und quantitativ zeigen, dass kein Unterschied zwischen hoch-rotverschobenen und nahen SN Ia besteht. Damit konnten wir die Eigenschaft von SN Ia als gute kosmologische Distanzindikatoren weiter stärken und bestätigen. Zuletzt, in Kapitel 6, werden erste Resultate zur Zeitdilatation in Spektren hoch-rotverschobener SN Ia gezeigt.

Many thanks to Bruno Leibundgut for the German translation.

*Only two things are infinite,
the universe and human stupidity,
and I'm not sure about the former.*

Albert Einstein

Chapter 1

Introduction

Supernovae are amongst the most energetic stellar explosions in the universe. Supernovae that originate from the thermonuclear disruption of a White Dwarf star (known as “Type Ia” supernovae, or SN Ia) have typical energies of $\sim 10^{51}$ erg. Their large luminosities ($4 - 5 \times 10^9 L_\odot$, where L_\odot denotes the luminosity of the sun; see Fig. 1.1) result from photons generated in the decay chain of ^{56}Ni synthesized in the explosion, and make SN Ia visible across a large fraction of the observable universe, when the universe was less than half of its present size. The recognition that the light curves of SN Ia could be used to calibrate their apparent peak luminosity has prompted the use of such events as distance indicators on cosmological scales. This unique property has enabled astronomers to use SN Ia as direct probes of the dynamics of the universal expansion, and led two independent research teams (the High- z Supernova Search Team¹ [244]; the Supernova Cosmology Project² [226]) to conclude that the universe was dominated by a “negative pressure” energy component, causing its expansion to accelerate. Thus, SN Ia have been prime actors in the elaboration of what is known as the “concordance model” of modern cosmology, and the results derived from observations of such events have profound implications for our physical understanding of the universe we live in. SN Ia are also events of astrophysical importance in their own right, with implications for stellar/binary evolution scenarios and chemical enrichment of the universe (SN Ia are the main producers of iron).

In this introductory chapter we give an overview of thermonuclear supernovae and their use in determining cosmological parameters.

1.1 General properties of thermonuclear supernovae

1.1.1 The confusing and misleading classification of supernovae

Minkowski [203] was the first to recognize different types of supernovae, on the basis on the absence (“type I”, or SN I) or presence (“type II”, or SN II) of hydrogen Balmer

¹<http://cfa-www.harvard.edu/cfa/oir/Research/supernova/HighZ.html>

²<http://panisse.lbl.gov/>



Figure 1.1: *Hubble Space Telescope (HST)* image of the Type Ia supernova SN 1994D in its parent galaxy NGC 4526. The supernova is the bright spot on the lower-left corner of the image. SN 1994D is almost as bright (only a factor of three lower in flux) as the entire parent galaxy. (credits: High- z Supernova Search Team [270]; *HST*; NASA).

lines in their optical spectra. SN I were also characterized by a deep absorption trough near 6150 Å, later found to be due to the Si II $\lambda\lambda 6347,6371$ doublet (often denoted “Si II $\lambda 6355$ ”). SN I lacking this feature were referred to as “peculiar” (and denoted SN Ip) by Bertola [21]. Zwicky [324] “refined” this classification scheme by introducing no less than five (labeled I, II, III, IV, V) supernova types, though the types III, IV, and V formed a minority of the SN sample, and were later included amongst SN II. In later years, SN I were further divided into subclasses according to the presence (“Type Ia”, or SN Ia) or absence of the Si II $\lambda 6355$ feature. The latter was subdivided into “Type Ib” (SN Ib [111]) and “Type Ic” (SN Ic) supernovae, based on the presence and absence of He I in their optical spectra, respectively. SN Ib and SN Ic are also characterized by the presence of lines of O I and Na I in their spectra. Whether they form two distinct classes based on their physical properties is still debated [315], and some authors refer to these events as “SN Ib/c”.

The modern classification scheme of supernovae is still based on the presence or absence of lines in their early-time spectra (see, e.g., [316], pp. 1–93; [75]), and is illustrated in Fig. 1.2. Note that “Type II” supernovae (SN II) are divided into the “Type IIL” and “Type IIP” subclasses, according to the shape of their post-maximum *light curve* (linear decline in luminosity for SN IIL; nearly constant luminosity plateau for SN IIP). “Type IIn” correspond to SN II with narrow emission lines in their spectra [269]. Several supernovae (e.g., SN 1987M [79]; SN 1993J [288]) have early-time spectra characteristic of SN II and late-time spectra revealing the presence of He I lines characteristic of SN Ib, and are called “SN I Ib”. Last, SN Ib/c with unusually high explosion energies ($E \gtrsim 10^{52}$ erg), sometimes associated with violent gamma-ray bursts (GRB; e.g., SN 1998bw and GRB 980425 [160, 221]), are often referred to as “hypernovae”.

We show early-time spectra of the main supernova types in Fig. 1.3. The spectra of SN Ia (a) are dominated by lines of singly-ionized, intermediate-mass elements (Mg II, Si II, S II, Ca II), with lines of iron-group elements (Co II, Fe II) blocking most of the flux in the near-UV (see Chap. 2). The hydrogen Balmer series leaves a clear imprint on the spectra of SN II (b), and are easily distinguishable from SN Ia. SN Ib/c ((d) & (c) in Fig. 1.3, respectively), on the other hand, look a lot like SN Ia blueward of ~ 5000 Å, though they lack the weak Si II absorption near 4000 Å. Thus, in high-redshift SN Ia searches, where the rest-frame optical range for redshifts $z \gtrsim 0.4$ excludes the characteristic Si II $\lambda 6355$ feature, complementary information (colour evolution, light curve) is needed to confirm a SN spectrum to be of “Type Ia”. Although SN Ib/c are typically less luminous than SN Ia, at least one example of a luminous SN Ic exists (SN 1992ar [56]), and the “contamination” of SN Ia samples at high redshifts by SN Ib/c will affect the inferred cosmological parameters [126].

To further confuse (amuse?) the reader, we note that some supernovae do not fit the classification scheme above, and are denoted as being “peculiar”. For instance, optical spectra of SN Ia are commonly divided into “normal”, “91T-like” (i.e. resembling the over-luminous SN 1991T), and “91bg-like” (i.e. resembling the sub-luminous SN 1991bg). Even then, some supernovae do not fit any of the above, but are still classified as “Type Ia” (e.g., SN 2000cx [175]; SN 2002cx [174]) [*see next Chapter for more details*]. Moreover, a

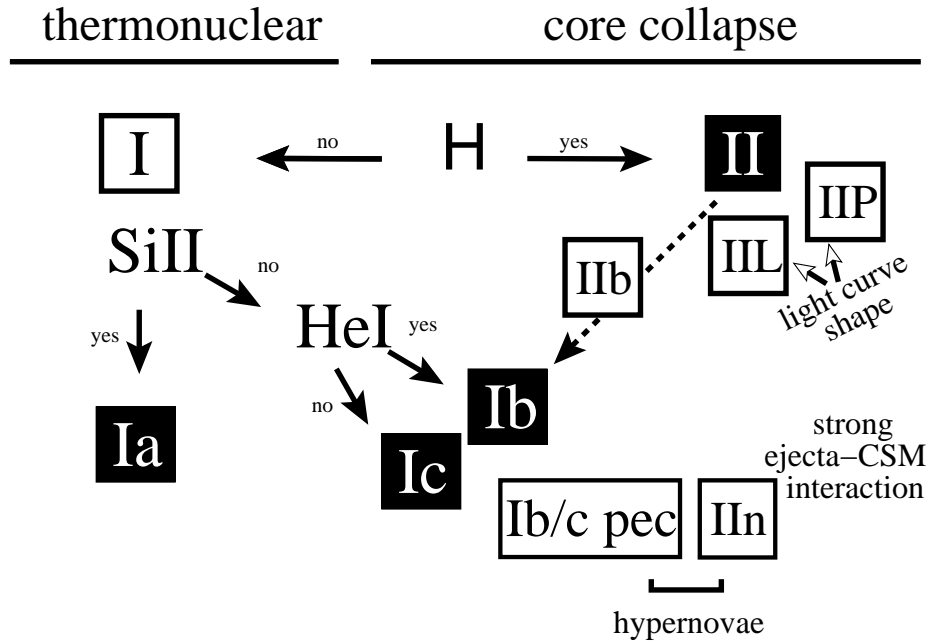


Figure 1.2: The current classification scheme of supernovae is based on the presence or absence of spectral lines in the early-time optical spectra. “Type I” supernovae are characterized by the absence of hydrogen in their spectrum; further Type I subclasses are characterized by the presence of Si II (Type Ia); the absence of Si II and presence of He I (Type Ib); the absence of both Si II and He I (Type Ic). “Type II” supernovae are characterized by the presence of hydrogen in their spectrum; further Type II subclasses include those determined by spectral characteristics (Type IIb: events having an early-time Type II spectrum and a late-time Type Ib spectrum; Type IIIn: events that show narrow emission lines in their spectra), and those determined by post-maximum optical light-curve shapes (Type IIIL: linear post-maximum decline in luminosity; Type IIP: constant post-maximum plateau in luminosity). From a physical standpoint, Type Ia supernovae result from the thermonuclear disruption of a White Dwarf star, whilst all other types result from the core collapse of a massive star. From Turatto [293]; reproduced with permission.

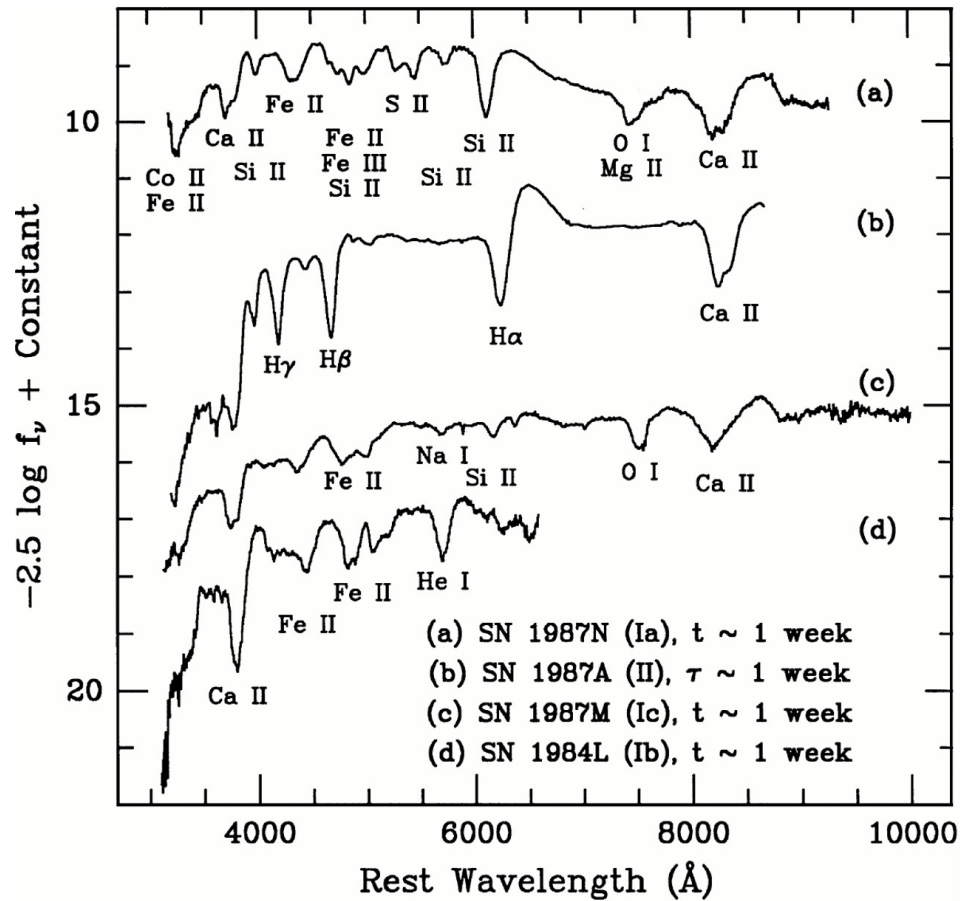


Figure 1.3: Spectra of thermonuclear (“Type Ia”; (a)) and core-collapse (“Type II/Ic/Ib”; (b), (c), and (d), respectively) supernovae, taken at $t \sim 1$ week past B -band maximum. For the Type II SN 1987A, the spectrum is taken at $\tau \sim 1$ week after core-collapse. From Filippenko [75]; reproduced with permission.

definite detection of hydrogen emission in the spectrum of the Type Ia SN 2002ic has been reported by Hamuy et al. [105], where lack of hydrogen was the defining characteristic of the “Type I” supernova class.

The current classification scheme for supernovae, though useful, is confusing and misleading. Confusing because of its complexity, as more objects define specific sub-types (“91T-like”, “91bg-like”, “99aa-like”, in the case of SN Ia); this trend will naturally continue as more supernovae are observed. Misleading due to its elaboration from observational characteristics rather than from physical properties. Thus, although “Type I” supernovae (SN Ia/b/c) are commonly defined by the absence of hydrogen lines in their early-time optical spectra, SN Ia correspond to thermonuclear explosions, whereas all other types (SN Ib/c and SN II) result from the core-collapse in a massive star. However, there are various proposed models for the progenitors of SN Ia, and for the explosion mechanisms, and the inappropriate supernova classification scheme is in part due to these theoretical uncertainties.

1.1.2 Progenitors of Type Ia supernovae

Type Ia supernovae are believed to originate from the thermonuclear disruption of electron-degenerate “White Dwarf³” (WD) stars [131], when they have accreted enough matter from a binary companion to reach the so-called “Chandrasekhar limit” [53, 54] $M_{\text{Ch}} \approx 1.4M_{\odot}$ (see [38, 242, 212, 180] for reviews on possible progenitor scenarios).

The reason for preferring such a compact, evolved object are manifold: light curves show a rapid (~ 20 d) rise in luminosity to maximum [246, 4], and a fast post-maximum decline, hinting at the small size of the progenitor. The lack of hydrogen and helium in their spectra (for possible detection of helium in SN Ia infrared spectra, see [199]), and the appearance of SN Ia in all morphological types of galaxies (including early-type, elliptical galaxies; [44]), hint at the association of SN Ia progenitors with old stellar populations. However, it appears that the less luminous SN Ia preferentially occur in elliptical galaxies, and the more luminous ones in late-type or blue spiral galaxies [108, 110, 39], and could be due to a decrease in the progenitor WD carbon-to-oxygen ratio with lookback time [125, 153, 296], although Röpke and Hillebrandt [240] argue this is unlikely to be the case.

The composition of the exploding White Dwarf is subject to uncertainties, though carbon-oxygen (C/O) WDs are preferred for their allowed range of masses ($0.8 - 1.2M_{\odot}$) and accretion rates ($10^{-8} - 10^{-6}M_{\odot} \text{ yr}^{-1}$), favouring the occurrence of a SN Ia event upon reaching the Chandrasekhar limit [209]. Helium WDs would yield the wrong ejecta composition (He and ^{56}Ni decay products, contrary to observations; see [210]). Oxygen-Neon-Magnesium WDs are expected to lead to an accretion-induced collapse to a Neutron Star⁴, *via* electron-capture, rather than a SN Ia [209, 102].

³White Dwarfs are small ($R_{\text{WD}} \approx R_{\oplus}$, where R_{\oplus} is the Earth’s radius), dense (mean density $\overline{\rho_{\text{WD}}} \approx 10^6 \text{ g cm}^{-3}$) stars of about one solar mass, supported by electron-degenerate gas pressure. They slowly radiate away their residual thermal energy on timescales of ~ 10 Gyr; see [273].

⁴Neutron Stars are small ($R_{\text{NS}} \approx 10 \text{ km}$), dense ($\rho_{\text{NS}} \approx 10^{14} - 10^{16} \text{ g cm}^{-3}$) stars of about one solar mass, supported by neutron-degenerate gas pressure. They were first suggested as the compact remnants

While it is accepted that WD must accrete matter from a binary companion to become unstable, the nature of this “donor” star is still very much debated. Two scenarios are envisaged: (i) the “double-degenerate” scenario results from the merging of two C/O WDs in a close (orbital separation $a \sim 10R_{\odot}$; see [134]) binary system, where the two components are progressively brought together *via* emission of gravitational waves [307, 133]; (ii) the “single-degenerate” scenario in which the WD accretes hydrogen- or helium-rich matter from a non-degenerate subgiant/giant star [317, 208]. The double-degenerate scenario requires a binary WD system in which the total mass exceeds the Chandrasekhar mass, and with short enough orbital periods ($T_{\text{orb}} \lesssim 10$ h; see [134]) for the merger event to occur within the Hubble time. Although such short-period WD binary systems have been detected (e.g., [190]), only two systems has been found with a total mass within 10% of the Chandrasekhar limit [154, 205]. Moreover, the outcome of the merger is still uncertain and collapse to a Neutron Star seems more likely in such a scenario [262, 180], although super-Chandrasekhar explosions could in principle explain the over-luminous SN Ia such as SN 1991T [82]. Last, the recent definite detection of hydrogen ($\text{H}\alpha$) emission in the spectrum of SN 2002ic [105] has brought a fatal blow to the double-degenerate scenario (since it is the signature of interaction with a hydrogen-rich companion star), although Livio and Riess [181] claim that this feature could arise from the interaction of the SN Ia shock wave with material ejected during the AGB⁵ phase of one of the binary WDs.

The favoured progenitor scenario thus appears to be the single-degenerate scenario (Fig. 1.4), although it is still uncertain whether a WD can reach the Chandrasekhar limit by accretion of hydrogen [47]. However, binary systems in which the WD stably accretes hydrogen at a high rate ($\gtrsim 10^{-7}M_{\odot} \text{ yr}^{-1}$) from a subgiant companion have been identified, and are known as Supersoft X-ray Sources (e.g., [297]). The aforementioned detection of hydrogen emission in one SN Ia spectrum also strengthens this scenario.

Thus, despite the existence of a “preferred” progenitor model for SN Ia, several theoretical uncertainties remain that hamper progress in modeling the explosion. In view of the observed diversity of SN Ia (see Sect. 2.2.2, p. 50), it is unclear whether such variations can be accommodated within a single model, or if different progenitor systems need to be invoked for some events.

1.1.3 Light curves and explosion models of Type Ia supernovae

Light curves

With initial radii of $\sim 10^4$ km (corresponding to the White Dwarf radius) and expansion velocities of $\sim 10^4$ km s⁻¹ (as determined from blueshifted absorption features in SN Ia spectra), it is difficult to see how a SN Ia could avoid cooling adiabatically and emit

of core-collapse supernovae by Baade and Zwicky [9].

⁵The final evolutionary stage of stars with initial masses $\lesssim 8M_{\odot}$ is the Asymptotic Giant Branch (AGB). An AGB star consists of a degenerate C/O core surrounded by a very extended convective atmosphere. Mass is lost *via* a dense and dusty outflow at rates of $\sim 10^{-8} - 10^{-4}M_{\odot} \text{ yr}^{-1}$ and expansion velocities of 5 – 30 km s⁻¹

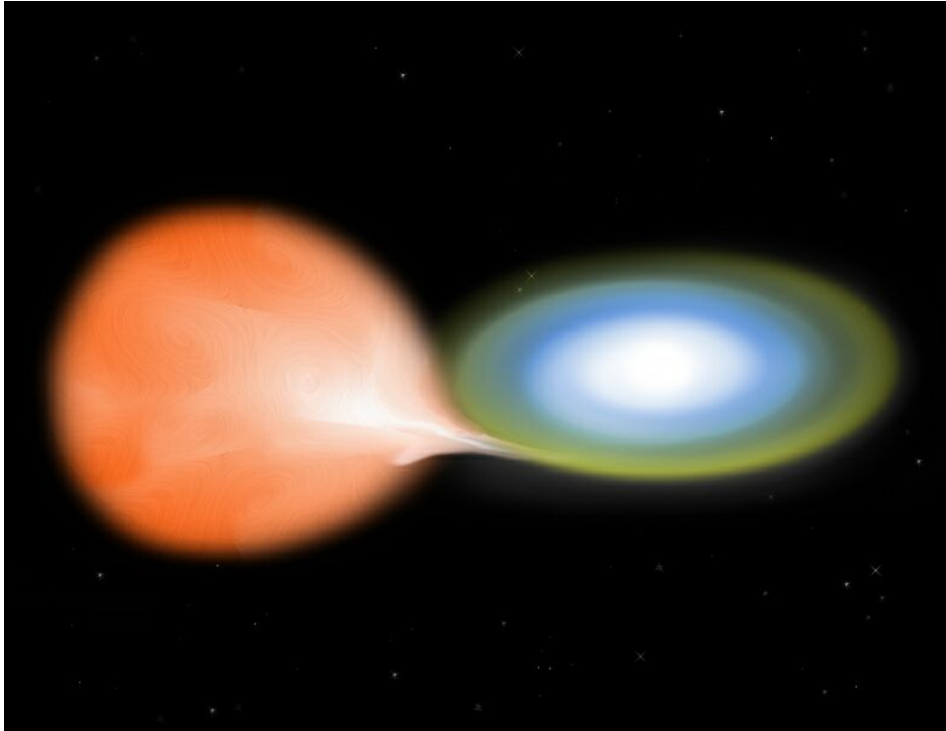


Figure 1.4: Cartoon illustrating the binary progenitor system of a thermonuclear (Type Ia) supernova. An evolved star (here a Red Giant; *left*) and an electron-degenerate White Dwarf (WD) star (*right*) co-rotate in the same gravitational potential. If the two stars are close enough, the Red Giant (“donor star”) can transfer some of its envelope onto the WD star *via* an accretion disk, coplanar with the binary orbit. If the WD star accretes enough material from the donor star such that its total mass reaches the Chandrasekhar limit ($\sim 1.4 M_{\odot}$), the WD star undergoes thermonuclear disruption, resulting in a Type Ia supernova event. (credits: Melissa Weiss; CXC; NASA).

any photons at all. Colgate and McKee [58] solved this embarrassing state of affairs by suggesting that the observed light from SN Ia events was entirely powered by the radioactive decay of ^{56}Ni synthesized during the explosion⁶. Typically $\sim 0.4\text{--}0.8M_{\odot}$ of radioactive ^{56}Ni is synthesized during the explosion [60], and the peak luminosity of the SN Ia event scales with the nickel mass [6, 7, 31]. Subsequent decay to ^{56}Co proceeds *via* electron capture with a half-life of 6.1 d, then through electron capture and β^+ decay to stable ^{56}Fe with a half-life of 77 days. Each of these decays produces γ -ray photons, which down-scatter and diffuse out at longer wavelengths, where the opacity in the ejecta is lower [234]. Thus, radioactive decay of nickel provides the energy input that make SN Ia radiate. Roughly 80% of the radiative flux is emitted at optical and near-infrared wavelengths [286, 287].

We show examples of bolometric (i.e. integrated over several passbands) light curves of SN Ia in Fig. 1.5. The ordinate is in logarithmic units of energy output (erg s^{-1}), whilst the abscissa is a time axis in units of days from bolometric maximum. Although the luminosities vary by a factor of ten at peak, SN Ia light curves share fundamental properties. At the earliest times, the ejecta is so opaque that the radioactive energy input is converted into kinetic energy of the expansion. As the supernova expands, the time for thermalised photons to diffuse out shortens, and the luminosity increases. This, combined with the exponentially decreasing rate of energy input from ^{56}Ni decay, causes a maximum in the light curve [233], at which time the luminosity equals the instantaneous energy deposition rate (under the assumption of constant opacity) – referred to as “Arnett’s rule” [6]. After a rapid post-maximum decline in luminosity, the light curves display an exponential tail after ~ 40 d past maximum. At these phases, the ejecta is optically thin: a large fraction of γ -rays escape conversion to optical photons, and the decline in luminosity is faster than the $^{56}\text{Co}\rightarrow^{56}\text{Fe}$ decay rate (e.g., [170]).

The near-infrared (*IJK*) light curves of SN Ia display a secondary maximum at $\sim 20\text{--}40$ d past maximum light [71], which appear as a shoulder in the *VR* light curves (see Fig. 1.5). Though the mechanisms leading to this secondary maximum are unclear, Pinto and Eastman [234] have suggested that it could be explained by a decrease in the opacity in the outer layers of the SN Ia ejecta. Note that is in not present in the light curves of sub-luminous SN Ia (SN 1991bg and 1999by in Fig. 1.5).

Explosion models

The mechanisms by which SN Ia explode, and in particular the ignition of the burning in the accreting WD, continues to be uncertain, despite more than twenty years of modeling (see [321, 117] for reviews). As for the progenitor systems, two distinct classes of models are proposed for the onset of thermonuclear burning. In one model, carbon is ignited at the WD center, when the latter reaches the Chandrasekhar limit. Variations within this model are associated with the propagation of the burning front: pure detonations (supersonic) have been discarded due to their overproduction of iron-group elements, and excessively high expansion velocities [320]; pure deflagration (subsonic) models, such as the W7 model

⁶The decay process $^{56}\text{Ni}\rightarrow^{56}\text{Co}$ (6.01 days) releases 1.72 MeV of γ -rays per decay; the subsequent decay process, $^{56}\text{Co}\rightarrow^{56}\text{Fe}$ (77 days) releases 3.59 MeV of γ -rays per decay

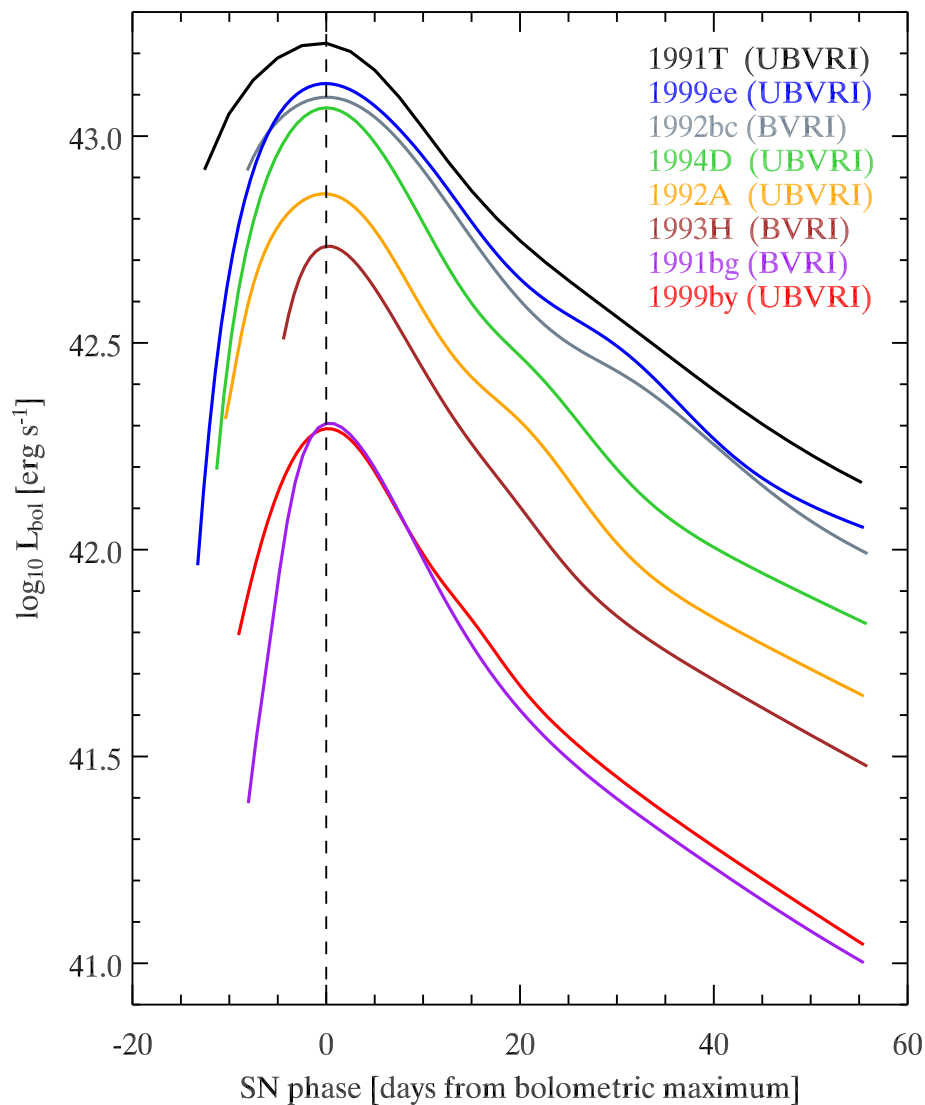


Figure 1.5: Bolometric light curves of Type Ia supernovae [281, 283]. The logarithm of the bolometric luminosity L_{bol} is plotted as a function of the supernova phase. The light curves are colour-coded by supernova name, and we give the filters used to construct each bolometric light curve. Type Ia supernovae are not standard candles: the bolometric luminosity at maximum ($L_{\text{bol,max}}$) of SN Ia spans an order of magnitude. However, the more luminous events tend to have broader light curves, and hence a slower post-maximum decline in luminosity. SN Ia thus appear to be “standardizeable” (*sic*) candles.

of Nomoto et al. [211], have been more successful in reproducing the ejecta composition and expansion velocities as derived from spectral synthesis calculations (e.g., [136, 197]), although the propagation speed of the deflagration wave is parametric. An alternative solution is for the burning front to start as a deflagration and change to a detonation at a given transition density. Such models are referred to as “delayed detonation” (DDT) models [146], and have been shown to reproduce some of the observations [119, 122]. We present some characteristics of a DDT model in Chap. 2.

In a second set of models, applicable to sub-Chandrasekhar mass WDs, helium detonates at the WD surface, near the bottom of the accreted helium layer (see [322, 182]). The resulting inward-propagating pressure wave compresses the C/O core which ignites off-center. Although such models would in principle explain the sub-luminous SN Ia events, the high-velocity ejecta tend to have the wrong composition (He and ^{56}Ni dominate).

Despite all the aforementioned theoretical uncertainties concerning the progenitor systems of SN Ia and their explosion mechanisms, these events are commonly used to determine distances on cosmological scales, through the normalisation of their luminosity at maximum *via* an empirical correlation, presented in the following section.

1.2 Type Ia supernovae as distance indicators

A single glance at the bolometric light curves in Fig. 1.5 is needed to conclude that SN Ia are not “standard candles” (see also [166]). Their bolometric luminosity at maximum varies by a factor of 3(10) when excluding(including) the sub-luminous events. However, Fig. 1.5 also suggests a correlation exists between the shape of the light curve and the peak luminosity, namely that the more luminous events tend to have broader light curves about maximum, and hence display a slower post-maximum decline in luminosity. This correlation was formulated explicitly by Phillips [229], and parametrized using the decline in magnitudes in the B -band between maximum and +15 d past maximum – the $\Delta m_{15}(B)$ parameter. We show plots of the absolute magnitude (assuming a Hubble constant $H_0 = 65 \text{ km s}^{-1} \text{ Mpc}^{-1}$, and determining the distance to the SN Ia from the redshift of the host galaxy) *vs.* the $\Delta m_{15}(B)$ parameter in Fig. 1.6, for the BVI passbands. The correlation is obvious, and commonly referred to as the “Phillips relation” in the literature. The peak magnitudes of SN Ia can be normalized using this relation, and the scatter in the B -band peak magnitudes reduces to ~ 0.13 mag in local SN Ia [218]. Thus, if not standard, SN Ia do appear to be “standardizeable” (*sic*) candles.

The Phillips relation is fundamental to using SN Ia as reliable distance indicators. However, it is purely empirical, and only securely verified for SN Ia in the local universe. The extrapolation of such a relation to SN Ia at higher redshifts might be inaccurate, arising possibly from distinct progenitor properties or yet unknown differences in the explosion mechanism. However, Efstathiou et al. [69] have shown that the low- and high-redshift samples of Perlmutter et al. [226] have the same light-curve width–luminosity relation and consistent peak absolute magnitudes M_B . Höflich et al. [123] have tried to give a theoretical basis to the Phillips relation, invoking a relation between the mass of ^{56}Ni

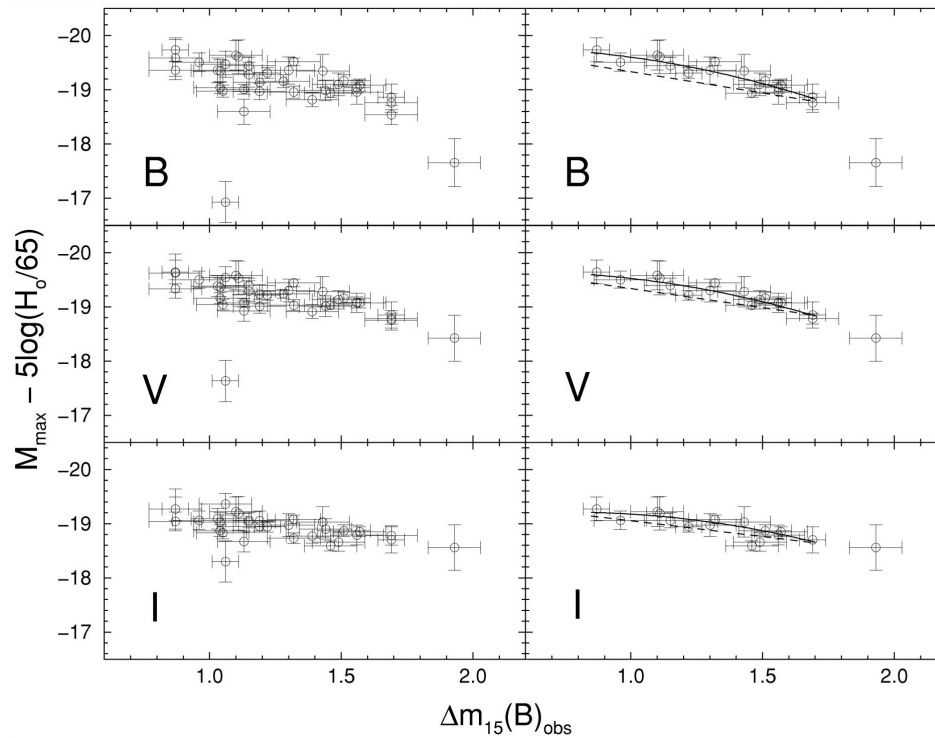


Figure 1.6: **Left:** Absolute BVI magnitudes corrected for Galactic reddening plotted against the $\Delta m_{15}(B)$ decline-rate parameter [229]. This sample comprises 41 SN Ia in the Hubble flow ($z \geq 0.01$) from the Calán/Tololo [106] and CfA [247] supernova searches. **Right:** 23 SN Ia with significant host-galaxy reddening ($E(B - V)_{\text{Avg}} < 0.05$ mag) have been removed from the sample. The linear fits (*dashed lines*) are those of Hamuy et al. [107]. From Phillips et al. [230]; reproduced with permission.

synthesized during the explosion and the resulting temperature of the ejecta; the latter is cooler for little ^{56}Ni produced, leading to a faster recession of the photo-emitting layers in the comoving frame of the ejecta, and hence a faster decline in luminosity. Recently, Krisciunas et al. [158] have noted the absence of relation between luminosity and light-curve shape in the near infrared (JHK bands), opening up exciting prospects for future high- z SN Ia observations in this (rest-frame) passband.

Nevertheless, applying this luminosity correction to local SN Ia yields distances of impressive accuracy, best visualized in the form of a “Hubble diagram” (i.e. a plot of distance *vs.* redshift; Fig. 1.7), after Hubble [132]. The SN Ia used in the Hubble diagram need to be in the “Hubble flow”, such that their redshift is indeed due to the universal expansion and not to peculiar motions of their host galaxies. The ordinate of the plots in Fig. 1.7 is the difference between the apparent and absolute magnitude of a particular SN Ia (its “distance modulus”, see next section). The magnitudes in this plot have been normalized to an absolute magnitude of $M_B = -19.5$ (for $H_0 = 65 \text{ km s}^{-1} \text{ Mpc}^{-1}$). The linear slope (*dashed line*) is the corresponding Hubble law, with a dispersion of corrected SN Ia distance moduli of only $\sim 0.2 \text{ mag}$.

Determinations of H_0 using SN Ia abound in the literature (see [32], and references therein), with values in the range $54 - 67 \text{ km s}^{-1} \text{ Mpc}^{-1}$. Such measurements requires *absolute* distance measurements, and the use of a primary distance indicator to calibrate the SN Ia absolute magnitudes, such as Cepheid variables⁷. To-day, there are thirteen Cepheid-calibrated distances to the hosts of SN Ia [259, 260, 267, 138, 95, 248]. A more recent measurement by Riess et al. [248], using refined Cepheid-calibrated distance to the hosts of two SN Ia, has yielded $H_0 = 73 \pm 4$ (statistical) ± 5 (systematic) $\text{km s}^{-1} \text{ Mpc}^{-1}$, in better agreement with the value found by the Hubble Space Telescope Key Project ($H_0 = 71 \pm 2$ (statistical) ± 6 (systematic) $\text{km s}^{-1} \text{ Mpc}^{-1}$ for SN Ia [85]).

1.3 Cosmology with Type Ia supernovae

In this section we review the arguments that led two independent teams of astronomers, using distance measurements to SN Ia, to the conclusion that the universal expansion is accelerating [244, 226]. An excellent (and enjoyable) historical review of cosmology with Type Ia supernovae is given by Kirshner [148].

1.3.1 Friedmann-Robertson-Walker cosmology

Modern cosmology is based on the assumption that the universe is spatially homogeneous and isotropic on large scales. This assumption, known as the “cosmological principle” (see, e.g., [308], p. 409), implies that there is no preferred location in the universe, from which an observer would have a particular view of the surrounding cosmos. Large redshift surveys of galaxies (such as the CfA redshift survey; [63]), combined with the impressive uniformity

⁷Cepheids are yellow giant/supergiant variable stars whose period of pulsation increases in proportion to their luminosity. It was first discovered empirically by Leavitt and Pickering [163]

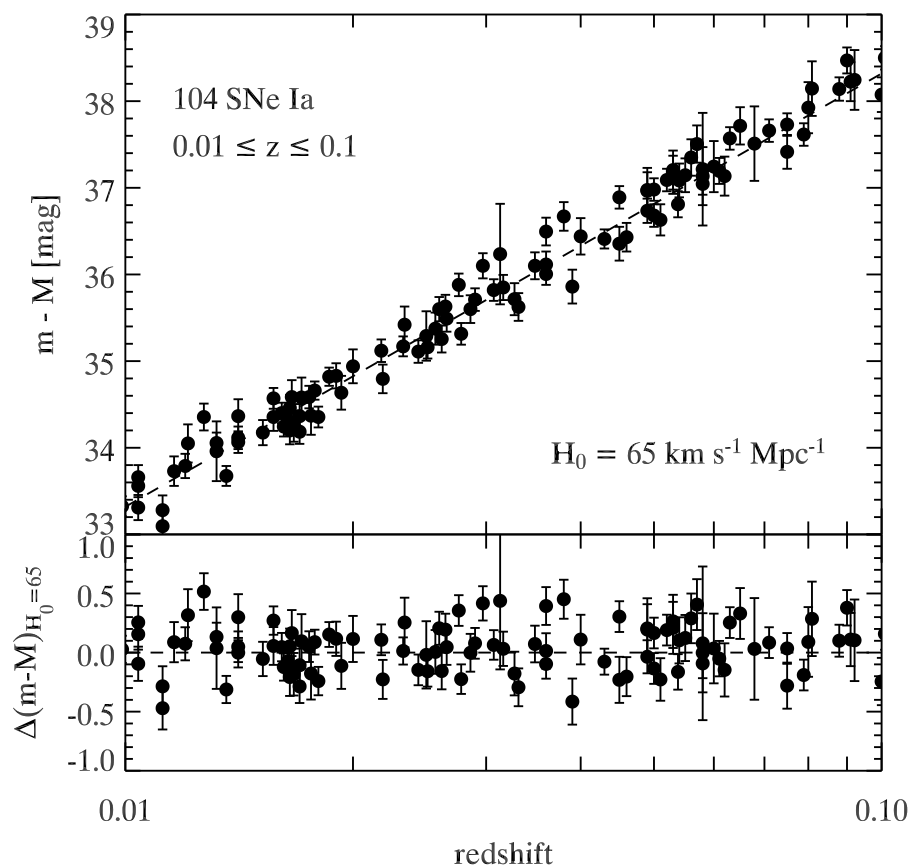


Figure 1.7: **Upper panel:** Hubble diagram for 104 low-redshift ($0.01 \leq z \leq 0.1$) Type Ia supernovae. The ordinate is the distance modulus ($m - M$), where m is the apparent magnitude of the SN Ia, and $M_B = -19.5$ mag its absolute magnitude (for $H_0 = 65 \text{ km s}^{-1} \text{ Mpc}^{-1}$). The dashed line is the Hubble law with $H_0 = 65 \text{ km s}^{-1} \text{ Mpc}^{-1}$. The data are from Tonry et al. [291]. **Lower panel:** Residuals with respect to the Hubble law. The dispersion is only ~ 0.2 mag, confirming the use of SN Ia as reliable distance indicators.

of the Cosmic Microwave Background (as measured, e.g., with the COBE⁸ satellite) have given firm observational basis to this assumption.

H. P. Robertson and A. G. Walker independently derived the only metric consistent with the cosmological principle [254, 255, 303]. In this Robertson-Walker metric, a line element ds is given by:

$$ds^2 = dt^2 - a^2(t)R_0^2 \left[\frac{dr^2}{1 - kr^2} + r^2(d\theta^2 + \sin^2\theta d\phi^2) \right], \quad (1.1)$$

where (r, θ, ϕ) are the usual spherical coordinates, dt is the time coordinate, and $a(t) = R(t)/R_0$ is the dimensionless scale factor, which characterizes the relative size of spatial sections as a function of time. R_0 is the present-day scale factor, such that $a_0 = 1$. k is a curvature parameter which takes the values -1 , 0 , and $+1$ for negatively-curved, flat, and positively-curved spatial sections, respectively.

In such a metric, and assuming that energy-momentum sources can be modeled as perfect fluids with pressure p and density ρ (known as “Weyl’s postulate”), Einstein’s field equations reduce to the two Friedmann equations [89], the first of which is:

$$H^2 \equiv \left(\frac{\dot{a}}{a} \right)^2 = \frac{8\pi G}{3} \rho - \frac{kc^2}{a^2 R_0^2}, \quad (1.2)$$

where G is Newton’s Gravitational constant, c is the speed of light, and \dot{a} denotes the time-derivative of the dimensionless scale factor $a(t)$. $H \equiv (\dot{a}/a)^2$ is the (time-dependent) Hubble parameter; its present-day value, H_0 , is Hubble’s “constant”. The density term ρ is taken to include all possible forms of energy (matter, radiation, and possibly a cosmological constant – see next section). Eqn. 1.2 is fundamental to modern cosmology, as it describes the dynamics of the expansion, encompassed in the evolution of the scale factor with time, as a function of its energy density and geometry.

At any given time, there is a critical value for the energy density, ρ_{crit} , for which the spatial geometry is flat ($k = 0$):

$$\rho_{\text{crit}} \equiv \frac{3H^2}{8\pi G}. \quad (1.3)$$

It is common to express the contribution of a particular energy component X in terms of the critical density, thereby defining a density parameter Ω_X :

$$\Omega_X \equiv \frac{\rho_X}{\rho_{\text{crit}}} = \left(\frac{8\pi G}{3H^2} \right) \rho_X. \quad (1.4)$$

Eqn. 1.2 can then be expressed in terms of the density parameter (see, e.g., [46]):

$$\dot{a}^2 = H_0^2 \left[1 + \Omega_M \left(\frac{1}{a} - 1 \right) + \Omega_\Lambda (a^2 - 1) \right], \quad (1.5)$$

⁸The COsmic Background Explorer (COBE) measured the spectrum of the CMB, best fit by a black-body with a temperature $T = 2.735 \pm 0.06$ K; see [186].

where Ω_M and Ω_Λ are the present-day values of the energy densities of matter and vacuum, respectively, and the total energy density, neglecting radiation, is $\Omega_{\text{tot}} = \Omega_M + \Omega_\Lambda$. Note that H_0 makes no difference to the evolution apart from stretching or compressing the timescale (some authors use the time variable $\tau = H_0 t$ to get rid of the Hubble constant in Eqn. 1.5). The parameters $(\Omega_M, \Omega_\Lambda)$ can be determined with precise *relative* distance measurements only (see next section). The second term on the left hand side of Eqn. 1.2 can be associated with an effective “curvature energy density” (see, e.g., [45], Eqn. 29), so that:

$$\rho_k \equiv -\frac{3kc^2}{8\pi G\rho R_0^2} \left(\frac{1}{a^2}\right) \quad \text{and} \quad \Omega_k = 1 - \Omega_{\text{tot}}. \quad (1.6)$$

The second of Friedmann’s equation is known as the “acceleration equation”, and is obtained by taking the time-derivative of Eqn. 1.2:

$$\frac{\ddot{a}}{a} = -\frac{4\pi G}{3} \left(\rho + \frac{3p}{c^2}\right), \quad (1.7)$$

where we have made use of the energy-conservation equation (see [308], Eqn. 14.2.19 on p. 415):

$$\dot{\rho} + 3\frac{\dot{a}}{a} \left(\rho + \frac{p}{c^2}\right) = 0. \quad (1.8)$$

This last equation tells us that, providing $\rho + p/c^2 > 0$, the energy density of a given component drops ($\dot{\rho} < 0$) as the universe expands ($\dot{a} > 0$), due to the increase in volume (the $3\rho\dot{a}/a$ term), but also because of the work done by the pressure on the surroundings (the $3(p/c^2)\dot{a}/a$ term). This second term is negligible in the present-day universe. However, during the radiation-dominated era in the early universe ($z > z_{\text{eq}} \approx 3500$; from CMB measurements with the *WMAP*⁹ satellite, [278]), this term cannot be neglected as $p = \rho c^2/3$ for radiation.

The acceleration equation (Eqn. 1.7) gives us the rate of change of the scale factor (i.e. of the universal expansion) with time, as a function of the total pressure and energy density contents of the universe. For a universe dominated by pressureless dust ($p = 0$), Eqn. 1.7 implies that $\rho \propto a^{-3}$, a simple statement of conservation of mass. For relativistic particles, such as photons, $p = \rho c^2/3$, and Eqn. 1.7 yields $\rho \propto a^{-4}$. Note that (positive) pressure acts to *decelerate* the expansion, in the same way as density. Thus, pressure does not “drive” the expansion; pressure *gradients* do, and there are no pressure gradients in a homogeneous universe.

Any one of Eqn. 1.2–1.8 can be derived from the other two, and their combination determines the evolution of the expansion of the universe, although more physics is required to describe the relation between pressure and density – i.e. it’s (effective) “equation of state”. The ratio of pressure to density is known as the equation-of-state parameter, and is denoted w :

⁹The *Wilkinson Microwave Anisotropy Probe*; see <http://map.gsfc.nasa.gov/>

Table 1.1: Equation-of-state parameters for various energy components

Energy source	$w = p/\rho c^2$
matter	0
radiation	1/3
strings	-1/3
vacuum	-1

$$w = \frac{p}{\rho c^2}. \quad (1.9)$$

Note that many authors use the convention $c = 1$, and so the equation-of-state parameter reduces to $w = p/\rho$. We summarize the main cosmological sources of energy and their corresponding equation-of-state parameter in Table 1.1. The values given in Table 1.1 assume the equation-of-state parameter to be constant in time. We will briefly comment on cases where this is (possibly) not the case in Sect. 1.3.3.

To understand the negative value of w for the energy of vacuum (e.g., a cosmological constant), we need a relation between the density and the scale factor. One can show that, by plugging Eqn. 1.9 in the energy-momentum conservation equation ($\nabla_\mu T^{\mu\nu} = 0$, where $T^{\mu\nu} = 0$ is the energy-momentum tensor), that the density has a power-law dependence on the scale factor:

$$\rho \propto a^{-3(1+w)}. \quad (1.10)$$

For a cosmological constant (in space *and* in time) Λ , $\rho_\Lambda \propto a^0$, hence $w = -1$. This implies a negative pressure, when $\rho_\Lambda > 0$.

With this in mind, we can now move on to the determination of the cosmological parameters (Ω_M, Ω_Λ) using relative distance measurements to high-redshift SN Ia.

1.3.2 Luminosity distances and the accelerating universe

The luminosity distance

On cosmological scales, there are different ways to measure the distance to an object. A simultaneous ($dt = 0$) measurement of the distance between two objects using a ruler gives the *proper* distance (d_p) between the two objects. Hubble’s law, for instance, applies to proper distances. Placing rulers in between two galaxies is impractical for obvious reasons, and we need to resort to other distance measurements, either using the angular size of the object (the “angular diameter” distance, d_θ) or the flux emitted from that object (the “luminosity” distance, d_L). Note that for *relative* distance measurements (as is the case for SN Ia), the choice of the measurement method has no impact on the result.

The use of SN Ia in cosmology requires the measurement of the luminosity distance to the supernova. This involves a relation between the flux \mathcal{F} and luminosity \mathcal{L} of an object, analogous to the flux-luminosity relation in Euclidean space:

$$d_L = \sqrt{\frac{\mathcal{L}}{4\pi\mathcal{F}}}, \quad (1.11)$$

Taking a radial light ray¹⁰ in the Robertson-Walker metric d_L can be rewritten as an integral equation as a function of redshift z and the density parameters (assuming $\Omega_{\text{tot}} = \Omega_M + \Omega_\Lambda$; see [46]):

$$d_L = \frac{(1+z)c}{H_0\sqrt{|\Omega_k|}} \text{sinn} \left\{ \sqrt{|\Omega_k|} \times \int_0^z \frac{dz'}{\sqrt{\Omega_k(1+z')^2(1+\Omega_M z') - z'(2+z')\Omega_\Lambda}} \right\}, \quad (1.12)$$

where “sinn” a function defined as follows:

$$\text{sinn} = \begin{cases} \sinh & \text{if } \Omega_k > 0 \quad (\text{open universe}) \\ \sin & \text{if } \Omega_k < 0 \quad (\text{closed universe}). \end{cases} \quad (1.13)$$

Note that for flat universe models ($\Omega_k = 0$), Eqn. 1.12 reduces to

$$d_L = \frac{(1+z)c}{H_0} \int_0^z \frac{dz'}{\sqrt{\Omega_k(1+z')^2(1+\Omega_M z') - z'(2+z')\Omega_\Lambda}}. \quad (1.14)$$

Thus, by measuring d_L , and determining z (which is model independent), we can determine the combination $(\Omega_M, \Omega_\Lambda)$.

In astronomy, we do not measure d_L directly; rather, we derive an extinction-corrected *distance modulus* μ_0 , defined to be the difference between the apparent magnitude $m = -2.5 \log \mathcal{F} + \text{constant}$ and the absolute magnitude $M = m - 2.5 \log(d_L/10\text{pc})$ (i.e. the apparent magnitude an object would have at a distance of 10 parsecs – or ~ 33 light years – from the Earth):

$$\mu_0 = m - M = 5 \log d_L + 25, \quad (1.15)$$

where d_L is in units of megaparsecs, and M is the *calibrated* absolute magnitude, using the $\Delta m_{15}(B)$ relation or some other variant (e.g., MLCS – Multicolor Light-Curve Shape [251]; “stretch” [228]).

The accelerating universe

The SN Ia results are best visualized in the form of a Hubble diagram, μ_0 vs. z , plotted in the upper panel of Fig. 1.8, using the latest results of Riess et al. [252]. This figure is the same as Fig. 1.7 for the local SN Ia sample, expect that the redshift range is extended to $z = 1.8$. Note that the redshift axis is plotted in linear units, hence the different shape of the $\mu_0(z)$ relation for $z < 0.1$. Overplotted on the data are the $\mu_0(z)$ curves for different cosmological models, determined from Eqns. 1.12 & 1.15, corresponding to

¹⁰Photons travel on null geodesics in the Robertson-Walker metric, i.e. $ds = 0$; for fixed θ and ϕ , i.e. $(d\theta, d\phi) = (0, 0)$, Eqn. 1.1 then implies $dr/dt = \sqrt{1 - kr^2}/a^2 R_0$

different combinations of $(\Omega_M, \Omega_\Lambda)$. The different cosmological models are indistinguishable at low redshifts ($z \lesssim 0.1$), and only at $z \gtrsim 0.5$ do they clearly separate. However, the local SN Ia are of fundamental importance as they “anchor” the $\mu_0(z)$ at $z = 0$ in the Hubble diagram (remember we are measuring *relative* distances). No cosmological parameters can be inferred without them.

To disentangle the different cosmologies allowed by the SN Ia measurements, it is best to plot the distance modulus residuals with respect to a given cosmological model. The preferred choice for this reference model is a freely coasting, “empty” universe, in which $\Omega_{\text{tot}} = \Omega_M = \Omega_\Lambda = 0$. In such a universe, the Hubble constant would also be constant in time, and $\dot{a} = H_0$ from Eqn. 1.5. The μ_0 residuals with respect to an empty universe, $\Delta(m - M)_{\Omega=0}$, are plotted in the lower panel of Fig. 1.8. Anything above(below) the $\Delta(m - M)_{\Omega=0} = 0$ line corresponds to an accelerated(decelerating) expansion, or $\dot{a} > 0$ ($\dot{a} < 0$). What first appears to be a scatter plot is revealed to single out a cosmological model with $(\Omega_M, \Omega_\Lambda) \approx (0.3, 0.7)$ (see the red data points and corresponding best-fit cosmological model). Note that these values assume a prior on $\Omega_{\text{tot}} = 1$ (i.e. a flat universe, see Eqn. 1.6), as confirmed with great precision by the *WMAP* satellite ($\Omega_{\text{tot}} = 1.02 \pm 0.02$ [20]). Thus, distant SN Ia appear to be dimmer at $z \sim 0.5$ by ~ 0.2 mag, implying that the universe is undergoing a phase of accelerated expansion, requiring the addition of a cosmological constant-like term Λ with negative pressure to the universal energy budget. The results were confirmed independently by two teams of astronomers [244, 226], and have since then be confirmed with increased precision [291, 152, 14].

With Riess et al. [253, 252], relative luminosity distance measurements have been extended to $z > 1$, when the universe was in a *decelerating* phase, due to the domination of matter over Λ at these lookback times (since $\rho_m \propto a^{-3}$ and $\rho_\Lambda \propto a^0$). These new results further strengthen the case for an accelerating universe from SN Ia observations.

To explore the full allowed range of $(\Omega_M, \Omega_\Lambda)$ values (with no priors on Ω_{tot}), we visualize the SN Ia likelihood distribution in the $(\Omega_M, \Omega_\Lambda)$ plane. This is shown in the upper panel of Fig. 1.9, where we have used the data of Tonry et al. [291] corresponding to SN Ia within the Hubble flow ($z > 0.01$) that are not highly extinguished ($A_V < 0.5$ mag). The red (green, blue) contours are the 1σ ($2\sigma, 3\sigma$) probability contours, obtained *via* a standard χ^2 test using model $\mu_0(z)$ curves in the Hubble diagram. The red line corresponds to a flat universe ($\Omega_{\text{tot}} = \Omega_M + \Omega_\Lambda = 1$). The parameter space in the upper-left region of the $(\Omega_M, \Omega_\Lambda)$ plane corresponds to infinite lookback time, or no Big Bang. With such a diagram, it becomes apparent that the SN Ia data only provide a measure of the *combination* of Ω_M and Ω_Λ : the data are highly degenerate along the $0.8\Omega_\Lambda - 0.6\Omega_M$ direction, since the same expansion dynamics can be obtained by varying Ω_M and Ω_Λ in the same direction. Note that the flat universe line is outside the 1σ contour, owing to this degeneracy. As pointed out by Tonry et al. [291] and Leibundgut [165], the SN Ia data favour a dynamical age of the universe $H_0 t_0 \sim 1$ (grey contours in Fig. 1.9), and comfortably excludes flat matter-dominated “Einstein-de Sitter” models ($\Omega_{\text{tot}} = \Omega_M = 1$), which predict $H_0 t_0 = 2/3$. The age of the universe is then consistent with its oldest constituents¹¹.

¹¹ $H_0 = 71 \text{ km s}^{-1} \text{ Mpc}^{-1}$ and $H_0 t_0 = 1$ imply an age of the universe $t_0 \approx 13.6$ Gyr, larger than the

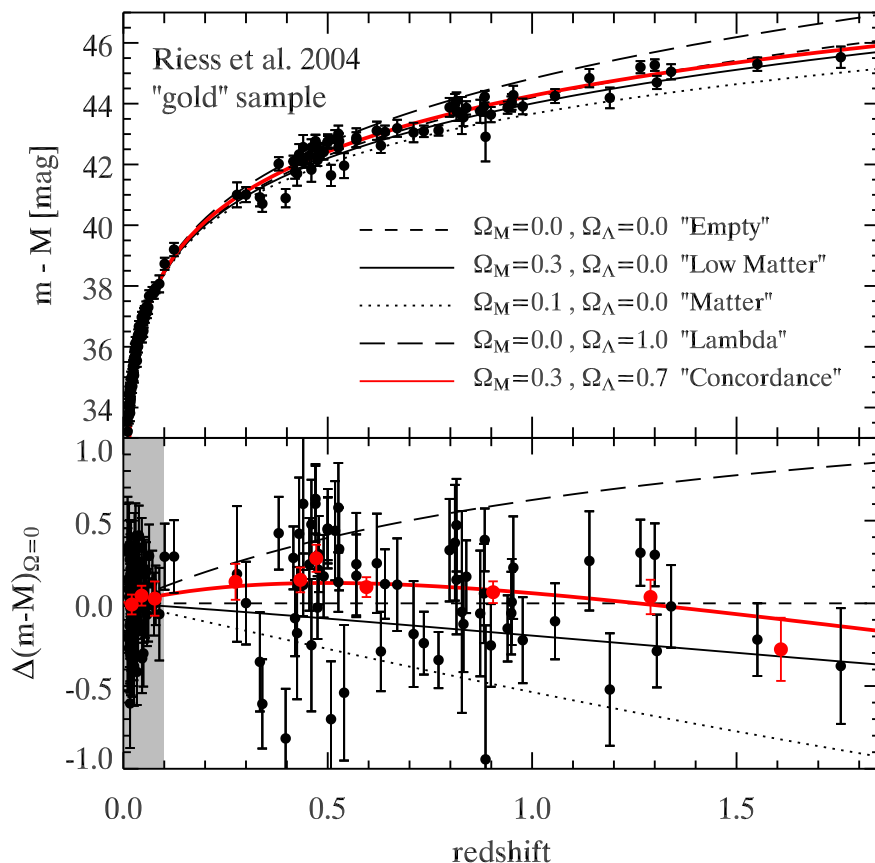


Figure 1.8: **Upper panel:** Hubble diagram for 132 SN Ia from the “gold” sample of Riess et al. [252] with $0.01 < z < 1.8$. Overplotted are cosmological models corresponding to different $(\Omega_M, \Omega_\Lambda)$ combinations. The favoured, “concordance”, model is plotted in red. **Lower panel:** Residuals with respect to an empty universe model ($\Omega_M = 0, \Omega_\Lambda = 0$). The red data points correspond to weighted mean values, highlighting the agreement with the “concordance” model. The grey shaded area corresponds to the redshift range ($0.01 \leq z \leq 0.1$) of the low- z Hubble diagram displayed in Fig. 1.7.

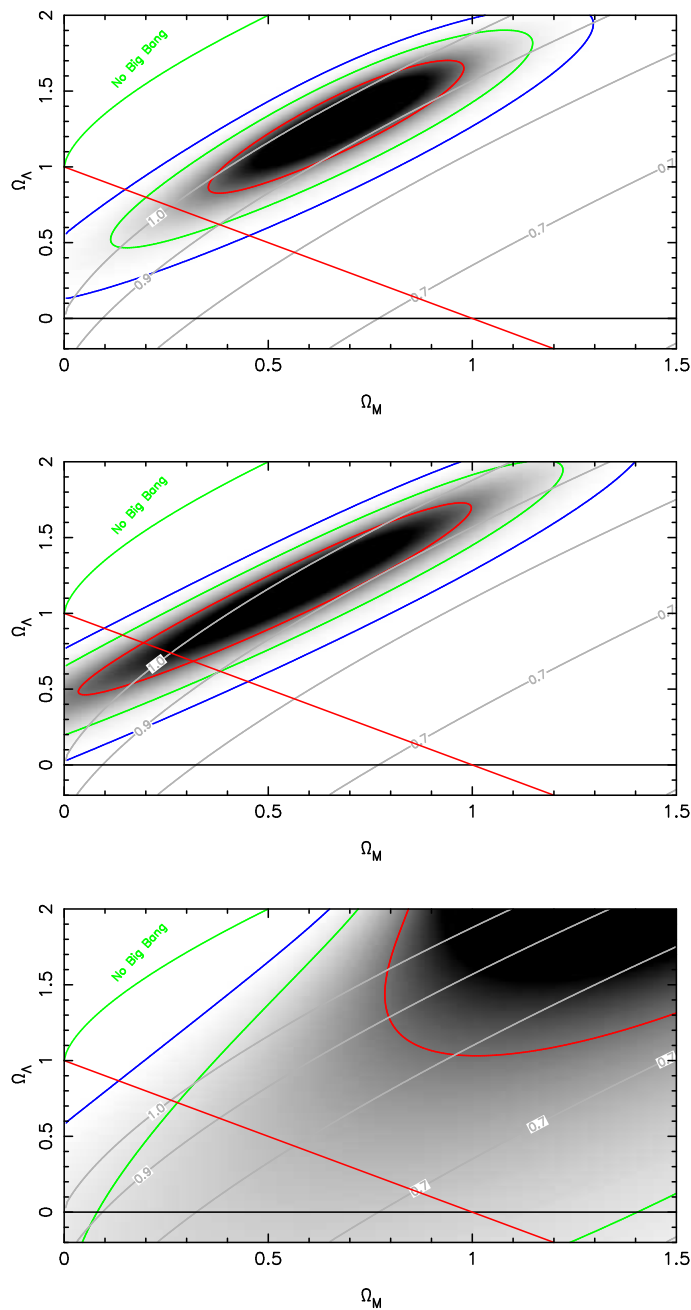


Figure 1.9: **Upper panel:** SN Ia likelihood distribution for Ω_Λ vs. Ω_M . The red (green, blue) ellipses correspond to the 1σ ($2\sigma, 3\sigma$) contours. The input data are from Tonry et al. [291] and include only SN Ia within the Hubble flow ($z < 0.01$) that are not highly extinguished ($A_V < 0.5$ mag). There is a clear degeneracy along $0.8\Omega_\Lambda - 0.6\Omega_M$, and the flat universe model ($\Omega_M + \Omega_\Lambda = 1$, red line) does not lie within the 1σ (68% probability) contour. The grey contours correspond to the dynamical age of the universe, $H_0 t_0$. The SN Ia data favour $H_0 t_0 = [0.9, 1.0]$. **Middle panel:** The three most distant SN Ia ($z > 1$) have been removed (see [25, 167]). **Lower panel:** Only SN Ia in the range $0.2 \leq z \leq 0.8$ have been included.

To determine the values of Ω_M and Ω_Λ individually, one needs to combine the SN Ia results with other data sets. Angular distance measurements (such as the CMB) provide a constraint in the orthogonal direction ($\Omega_{\text{tot}} = \Omega_M + \Omega_\Lambda$), whereas measurements of the matter content in the universe (e.g., from the 2dF galaxy survey, which give $\Omega_m h = 0.20 \pm 0.03$ – where h is the Hubble constant in units of $100 \text{ km s}^{-1} \text{ Mpc}^{-1}$ [224]) provide an independent constraint of Ω_M alone. A combination of any two of these measurements gives the currently preferred cosmological model for the universe: the so-called “concordance model” is a flat universe with $\Omega_M \sim 0.3$ and $\Omega_\Lambda \sim 0.7$. However, Type Ia supernovae *alone* provide the evidence for a strictly positive Ω_Λ ; a null value for Λ is excluded at the 3σ ($> 99.7\%$ confidence) level. We show the result of combining the SN Ia results of Tonry et al. [291] with a prior on Ω_M from the 2dF survey in the left panel of Fig. 1.10.

As previously mentioned, the highest-redshift SN Ia ($z > 1$) greatly reduce the degeneracy in the $(\Omega_M, \Omega_\Lambda)$ plane. In the middle panel of Fig. 1.9, we show the SN Ia likelihood function for the same data sample of Tonry et al. [291], but with the three highest-redshift SN Ia ($z > 1$) removed from the sample. Notice how the degeneracy is enhanced, although this has the side effect of “reconciling” the SN Ia data with a flat universe. The local ($z < 0.1$) SN Ia are required for the overall calibration of the relative distance scale; no cosmology with SN Ia is possible without them (see Fig. 1.9, lower panel).

The cosmological constant problem

The requirement for a cosmological constant to explain away the SN Ia results brought a combination of excitement and perplexity to the astronomy and physics communities. Indeed, the high- z SN Ia surveys were designed to measure the deceleration parameter $q_0 = -(a\ddot{a}/\dot{a}^2)_0$ of the universe, and the initial results of Perlmutter et al. [227] favoured $\Omega_M \approx 1$ with only an upper bound on Ω_Λ . The fact that such a form of “Dark Energy” pervades space and causes the expansion to accelerate poses two fundamental problems to cosmologists and particle physicists: (i) why do we have $\Omega_M \approx \Omega_\Lambda$ *today* and (ii) why is Ω_Λ so small?

The first question is obvious when we consider the variation of both matter and Λ as a function of the scale factor. Since Λ remains constant over time ($\rho_\Lambda \propto a^0$), and the matter density is a strong decreasing function of time ($\rho_m \propto a^{-3}$), the fact that $\Omega_M \approx \Omega_\Lambda$ *today* implies that we are living in a very brief cosmological era. This is uncomfortable in view of the cosmological principle, and an anthropic principle¹² is sometimes invoked to explain this coincidence.

The second problem arises because, although general relativity does not predict a value for Λ , quantum field theory does. For particle physicists, the cosmological constant is a measure of the energy density of vacuum (*not* empty space, but rather the lowest energy

oldest Globular Clusters; see, e.g., [298]

¹²The anthropic principle is a truism which states that the laws of physics are the way they are because, if they were otherwise, we would not even be here to question their validity. Applied, to the cosmological constant, Weinberg [309, 310] argues that the allowed value for Λ on anthropic grounds is close (i.e. small yet non-zero) to the observed value.

state), ρ_{vac} [323]. Assuming ordinary quantum field theory is valid up to the Planck scale ($M_{\text{Pl}} = (8\pi G)^{-1/2} \sim 10^{18}$ GeV), then $\rho_{\Lambda} \sim M_{\text{Pl}}^4 \sim 2 \times 10^{110}$ erg cm $^{-3}$. The observational constraint on Λ is $|\rho_{\Lambda}| \leq 10^{-12}$ GeV $^4 \sim 2 \times 10^{-10}$ erg cm $^{-3}$, i.e. 120 orders of magnitude lower than the theoretical prediction! A ratio of the mass scales (ignoring the fourth power) yields $10^{18}/10^{-12} \equiv 30$ orders of magnitude, still a huge discrepancy.

Thus, the prospect of living in a universe dominated by vacuum energy is both exciting and mind-bothering. In his excellent review on the cosmological constant (from which the discussion in this section was inspired), Carroll [45] refers to the universe we live in as the “preposterous universe”. We next turn to the properties of “Dark Energy” and the constraints that can be placed on its nature.

1.3.3 Measuring the equation-of-state parameter of “Dark Energy”

A cosmological constant with an associated equation-of-state parameter $w = -1$ fits the SN Ia well. In retrospect, it is amusing to note that Einstein first introduced this constant (by adding a $\Lambda/3$ term in Eqns. 1.2 & 1.7) to make the universe static¹³ [70], and is now invoked to explain why the universal expansion is accelerating.

To constrain the nature of the “Dark Energy”, and in particular to check whether it is consistent with a cosmological constant, we need to determine its equation of state. This was attempted for the first time by Garnavich et al. [96] with SN Ia data. Assuming $\Omega_{\text{tot}} = 1$, the luminosity distance (see Eqn. 1.12) can be rewritten in terms of the matter density Ω_M and the equation-of-state parameter of Dark Energy, w :

$$d_L = \frac{(1+z)c}{H_0} \int_0^z \frac{dz'}{\sqrt{(1+z')^3(\Omega_M) + (1-\Omega_M)(1+z)^{3(1+w)}}}. \quad (1.16)$$

Thus, one can construct a likelihood distribution in the (Ω_M, w) plane. Furthermore, by combining the SN Ia data with a prior on Ω_M , one can reduce the high level of degeneracy between these two parameters (see Fig. 1.10, right panel). The recent measurements of Riess et al. [252] lead to $w < -0.5$ at 95% confidence for any value of Ω_M , using the SN Ia data alone. These results are also consistent with $w = -1$. Using a prior on the matter density of $\Omega_M = 0.27 \pm 0.04$, they find $w = -1.02_{-0.19}^{+0.13}$, in good agreement with a cosmological constant.

Alternatives to the cosmological constant have been suggested. These remain speculative in view of the data currently available, and are far beyond the scope of this thesis. We list them here for the sake of completeness. A group of models, dubbed “quintessence”, involves a nearly massless slow-rolling scalar field (see, e.g., [311, 223, 314]). These have

¹³In view of the universal expansion found by Edwin Hubble in 1929, Einstein later recognised his mistake; Gamow [93] reports a conversation with Einstein during which the latter confessed that “the introduction of the cosmological term was the biggest blunder of his life” (although the use of the word “blunder” probably reflects Gamow’s own opinion).

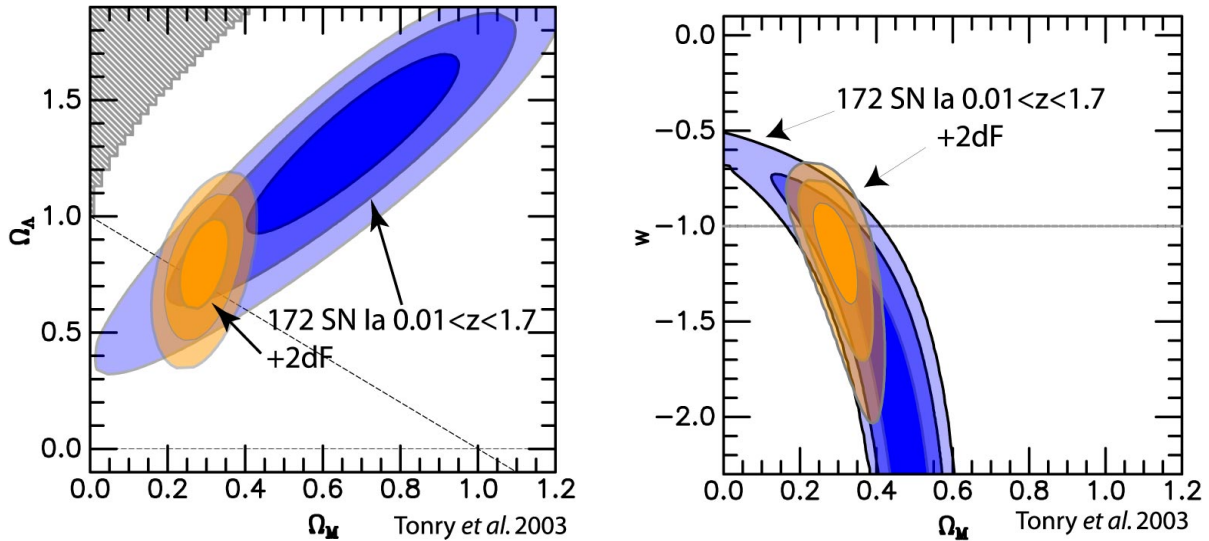


Figure 1.10: Constraints on Ω_Λ (*left panel*) and the equation-of-state parameter w (*right panel*) when the SN Ia data of Tonry et al. [291] are combined with a prior $\Omega_M h = 0.20 \pm 0.03$ from the 2dF survey [224]. Figure courtesy Brian P. Schmidt.

$w < -1/3$ and are dynamic, i.e. their density vary with time (usually tracking the radiation density until matter-radiation equality). Note that a physical lower limit to w is set by the so-called “Dominant Energy Condition” (DEC; see [113]), which requires $w \geq -1$ ¹⁴. However, Caldwell et al. [43] have suggested a form of Dark Energy with $w < -1$, called “Phantom Energy”. Other models, based on “solid” dark matter rather than (nearly) massless particle fields include those based on strings ($w = -1/3$ [299]) and domain walls ($w = -2/3$ [41]).

Currently, there are two projects, ESSENCE¹⁵ and SNLS¹⁶, that aim to constrain the equation-of-state parameter of the Dark Energy to within 10%, using observations of intermediate redshift SN Ia ($0.2 \lesssim z \lesssim 0.8$ for the ESSENCE project). All the high-redshift spectroscopic SN Ia data presented in this thesis have been collected by members of the ESSENCE collaboration.

Although the measurement of w already hits the precision limit of currently-available SN Ia data, some authors have attempted to set constraints on the redshift-variation of w , which then takes the simple parametric form $w(z) = w_0 + w'z$, where $w' \equiv (dw/dz)|_{z=0}$. If $w' = 0$, or $w_0 \neq -1$, then the Dark Energy cannot be a cosmological constant. Using their “gold” sample of SN Ia, Riess et al. [252] have found $w_0 = -1.31^{+0.22}_{-0.28}$ and $w' = 1.48^{+0.81}_{-0.90}$, although the uncertainties in both parameters are strongly correlated.

¹⁴The Dominant Energy Condition implies that $\rho + p \geq 0$ and $|\rho| \geq |p|$

¹⁵Equation of State: SuperNovae trace Cosmic Expansion (ESSENCE), aka “the w project”; see <http://www.ctio.noao.edu/essence/>

¹⁶SuperNova Legacy Survey (SNLS); see <http://www.cfht.hawaii.edu/SNLS/>

1.4 Testing for evolution in the SN Ia sample at different redshifts

Extraordinary claims require extraordinary evidence. This in part describes the attitude of astronomers (starting with those directly working in the field) in view of the cosmological implications of observations of Type Ia supernovae. Great care has been devoted to evaluate the possible sources of systematic error affecting the result. In this section we present a (non-exhaustive) list of such possible systematics:

- **Evolution:** The use of SN Ia as distance indicators relies on a calibration scheme which is only verified for SN Ia in the local universe (Sect. 1.2). The extrapolation of such a calibration scheme to higher redshifts makes the bold assumption that the high-redshift SN Ia are indeed identical to their local counterparts. Possible evidence for colour evolution has been presented in Falco et al. [73] and Leibundgut [165]: the high- z SN Ia are on average bluer than their local counterparts (see Fig. 1.11). Also, the rise times of high- z SN Ia light curves appears to be shorter [246], though the uncertainty is high and it is not clear how this would affect the distance measurements (see [4]). As far as spectroscopy is concerned, studies undertaken thus far are essentially qualitative in nature (see [57, 172]; Fig. 1.12), and reveal no differences between local and high- z SN Ia spectra. We make up for the lack of quantitative spectroscopic comparisons in Chap. 5, where we compare line profiles in local and high- z SN Ia spectra. On the theoretical side, Höflich et al. [125] have shown that a variation of the carbon-to-oxygen ratio in the progenitor White Dwarf star could lead to a difference in peak magnitude of ~ 0.3 mag at intermediate redshifts (although see [240]), thereby mimicking a cosmological constant. All these effects can point to a systematic evolution of SN Ia with redshift, though *all* are expected to have a monotonic evolution with redshift, incompatible with the apparent *brightening* of SN Ia at $z > 1$ (see [252]; Fig. 1.8).
- **Dust:** Reddening by intergalactic dust could explain the apparent dimming of SN Ia at $z \sim 0.5$. In view of the bluer colours of the high- z SN Ia sample (Fig. 1.11), this explanation seems unlikely. However, Aguirre [3, 2] showed that an increase in the average grain dust size would lead to a wavelength-independent, “grey”, effect – and thus go unaccounted in reddening corrections of SN Ia. However, this effect would continuously increase with redshift, and again be unable to explain the apparent brightening in the $z > 1$ SN Ia sample. Parametric dust models, such as “replenishing dust” [101], have been proposed, but they require a dubious amount of fine tuning and are physically inconsistent. More recently, Clements et al. [55] have detected a substantial amount of cold dust in 2/14 host galaxies of high-redshift ($z \sim 0.5$) SN Ia, using radio (sub-millimetre) observations. They suggest a possible evolution in the sub-mm luminosity function from $z = 0$ to $z = 0.5$, or that the sample of high- z SN Ia host galaxies is not representative of the bulk sample of galaxies at that redshift.

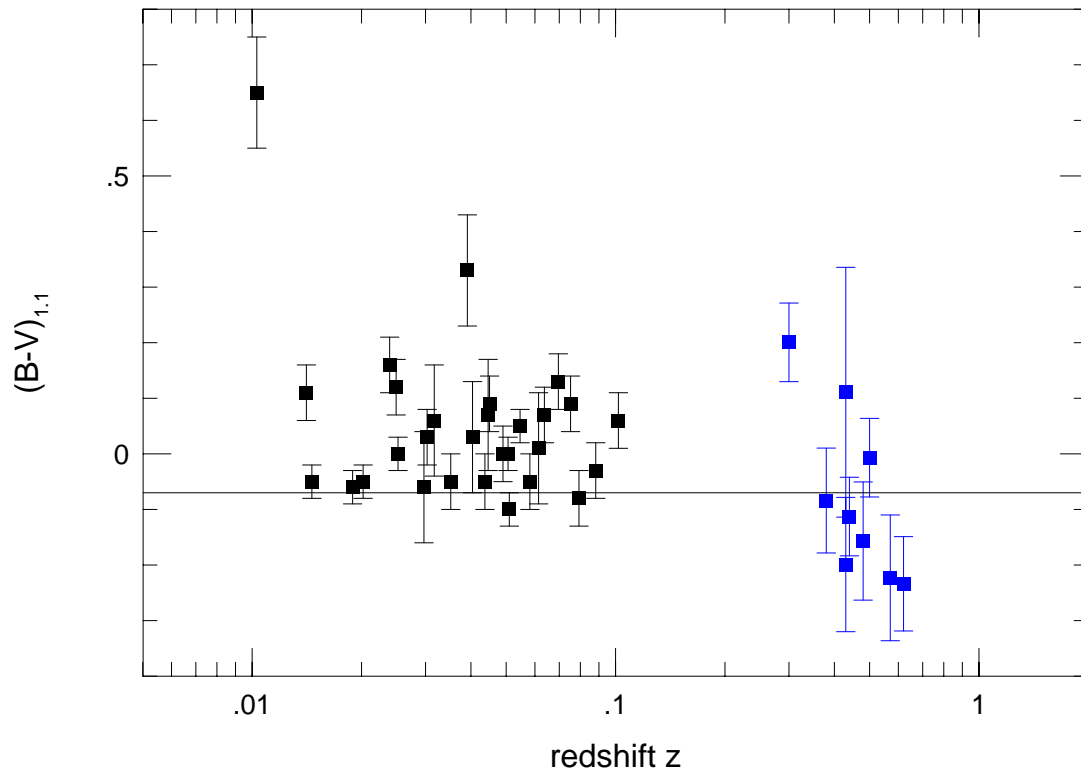


Figure 1.11: $(B - V)$ color as a function of redshift. The low- z ($z \lesssim 0.1$) data are from Phillips et al. [230], whilst the high- z data are from Riess et al. [244]. The horizontal line shows the intrinsic colour of local SN Ia as defined by Phillips et al. [230]. The high- z SN Ia are bluer, on average, than their local counterparts. See Leibundgut [165]; courtesy Bruno Leibundgut.

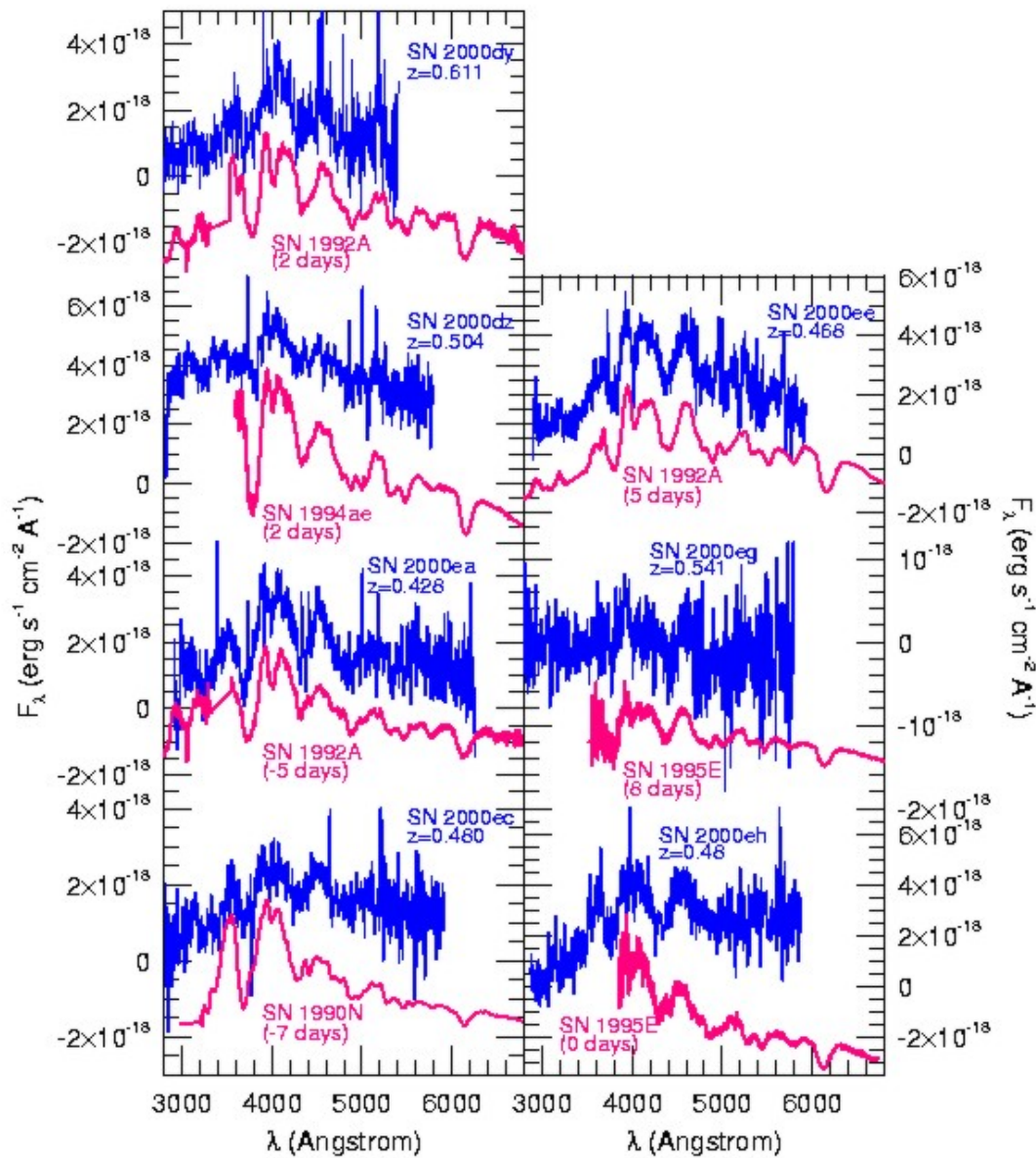


Figure 1.12: Spectra of seven high-redshift Type Ia supernova (*blue*), observed with the VLT, are compared with local SN Ia (*red*) at a similar phase. The distant SN Ia are qualitatively similar to their local counterparts. The local spectra are scaled in flux and an arbitrary offset is added for clarity. Contamination of the spectra with host galaxy light and/or reddening by dust can cause a change in the continuum slope. Figure from Leibundgut and Sollerman [172]; reproduced with permission.

- **Gravitational lensing:** Light traveling from a distant SN Ia to us can be deflected as it passes near massive objects. This effect, known as gravitational lensing, is now commonly used by astronomers (e.g., to infer the mass and geometry of galaxy clusters; see [23] for a review), and can cause an apparent dimming *or brightening* of distant supernovae. In fact, Benítez et al. [19] showed that the farthest known SN Ia, SN 1997ff ($z \sim 0.7$ [250]), is magnified by 0.34 ± 0.12 mag, i.e. a significant fraction of the ~ 1.1 mag apparent brightening reported by Riess et al. [250] for this supernova. In their recent study, Riess et al. [252] find no selection bias introduced by lensing in their “highest- z ” sample, and suggest that the magnification of SN 1997ff was “unusually large”. However, given the small current sample of $z > 1$ SN Ia, an evaluation of the possible impact of gravitational lensing on the measurements is warranted.
- **Contamination by SN Ib/c:** The inclusion of other types of supernovae in the high- z SN Ia sample would introduce a bias in the derived distance moduli, as the normalisation scheme is only applicable to light curves of SN Ia. In a recent study, Homeier [126] has shown that small contamination levels ($\sim 3 - 5\%$) of the SN Ia sample by SN Ib/c would bias the derived cosmological parameters Ω_M and Ω_Λ to higher values. Although SN Ib/c are expected to be dimmer on average than SN Ia, the observation of a SN Ic with a luminosity at peak comparable to a SN Ia has been reported by Clocchiatti et al. [56]. Moreover, for $z \gtrsim 0.4$, the defining Si II $\lambda 6355$ feature of SN Ia is redshifted out of the observed optical range, and one has to rely on a restricted spectral rest-frame range to identify the spectra, where the differences between SN Ia and SN Ic are less obvious. Certainly more work needs to be done here to reliably evaluate the impact of such a contamination on the inferred cosmology.
- **Exotica:** All of the above are astrophysical effects that could possibly mimic a cosmological constant (provided they can account for the apparent brightening of the $z > 1$ SN Ia), and rely on the validity of the underlying Friedmann-Robertson-Walker cosmology. If, on the other hand, the cosmological principle is not valid (e.g., the universe is inhomogeneous on large scales; see [42]), or if the present theory of gravity is wrong on large scales, then the cosmological interpretation of the SN Ia observations would be flawed. Tentative evidence has been presented for a time-variation in the fine structure constant $\alpha = e^2/\hbar c^2$ [306], where e is the electron charge and $\hbar = h/2\pi$ (h being Planck’s constant), and could be explained within the framework of a “Varying Speed of Light” (VSL) theory [15], though the effect would be too small to explain the universal accelerated expansion [165]. More recently, Chand et al. [52] find $\Delta\alpha/\alpha \approx 0$ based on the analysis of Si IV doublets.

Of all the astrophysical sources of systematic error presented in this section, evolution of the SN Ia sample with redshift is the least well constrained, owing to the uncertainties associated with the theoretical modeling of these events (explosion models and progenitor

systems). Observationally, progress on this issue until now has been hampered by poor-quality high-redshift data, and characterized by inherently qualitative comparisons of the local and high- z SN Ia samples. The work presented in this thesis is a first step in remedying this state of affairs, by developing appropriate tools for the analysis of high- z SN Ia spectra. The main success of this thesis is presented in Chap. 5, where we use the higher-quality spectroscopic data of Matheson et al. [187] (see Appendix A) to present a comparative study of optical line-profile morphologies in SN Ia at different redshifts.

*Right now, it's only a notion.
But I think I can get money
to make it into a concept.
And later turn it into an idea.
Woody Allen (Annie Hall)*

Chapter 2

Optical spectra of Type Ia supernovae

Abstract: We present an overview of theoretical and observational properties of optical spectra of Type Ia supernovae. On the theoretical side, we explore the structure of the SN Ia ejecta (density profile, velocity field, abundance stratification) and the formation of spectral lines in such an expanding medium. On the observational side, we describe the evolution of SN Ia around maximum light, and highlight the observed inhomogeneity of the SN Ia class, based on the spectra of several “peculiar” objects. Finally, we briefly discuss the more technical issues relative to supernova observations (discovery, spectroscopic follow-up, and data reduction) and conclude this chapter with the presentation of a novel method to extract supernova spectra, discussed at length in Chap. 3.

2.1 Modeling Type Ia supernova spectra

2.1.1 Velocity field and density/abundance structure in SN Ia ejecta

Shortly after the onset of explosive carbon/oxygen (C/O) thermonuclear burning, the supernova envelope undergoes free (homologous) expansion (see [150], and references therein, in the context of core-collapse supernovae), as the energy input from $^{56}\text{Ni} \rightarrow ^{56}\text{Co} \rightarrow ^{56}\text{Fe}$ radioactive decay ($\approx 2 \times 10^{49}$ erg; see Chap 1, Sect. 1.2) is two orders of magnitude smaller than the kinetic energy of the ejecta ($E_{\text{kin}} \approx 10^{51}$ erg). In the supernova frame, the location of a mass element m is

$$r(m) = v(m) \times (t - t_0) + r(m, t_0), \quad (2.1)$$

where $t = 0$ corresponds to the time of thermonuclear explosion and t_0 is the time at which the homologous expansion sets in ($t_0 \approx 10$ s). The radius of the progenitor White Dwarf (WD) star is $R_{\text{WD}} \equiv r(m, t = 0) \approx 2 \times 10^8$ cm. With an expansion velocity on the order of 10^9 cm s $^{-1}$, the size of the supernova at the onset of homologous expansion

is $r(m, t_0) \approx 10^{10}$ cm. Thus, already a few minutes after explosion ($t \gtrsim 10^2$ s), $r(m, t_0)$ becomes negligible with respect to $v(m) \times (t - t_0)$, and $v(m)$ is constant for all mass elements.

The homologous expansion characterizing SN Ia ejecta is often rephrased in radial (as opposed to mass) coordinates:

$$v(r) = v_0 \left(\frac{r}{R_0} \right), \quad (2.2)$$

where R_0 is the base radius where the luminosity is input, and v_0 the velocity of this layer. Note the resemblance with the Hubble law for the linear expansion of the local universe ($v(r) = H_0 r$). In fact, Eqn. 2.2 is often referred to as the ‘‘Hubble velocity law’’. Eqn. 2.2 simply tells us that that velocity and radial coordinates are equivalent (the same way redshift and distance are equivalent in the local universe), and a mass element can be located within the SN ejecta thanks to its velocity or radius. Thus, from a dynamical point of view, there is no acceleration in the SN Ia outflow (constant $v(m)$); however, there is a steep radial velocity gradient ($dv(r)/dr = v_0/R_0$).

Another consequence of Eqn. 2.2 is that the outflow density profile does not follow a simple inverse-square law, as imposed by mass conservation in, e.g., radiation-driven winds of hot stars [49], but instead results from the disruption of the envelope by the shock wave arising from the explosion. The resulting density profile is steeper, and is best described by a power law [29]:

$$\rho(r) = \rho_0 \left(\frac{R_0}{r} \right)^n, \quad (2.3)$$

where $n = 7$ is found to be a good description of the radial variation of the density in SN Ia ejecta [30]. We will see in Sect. 2.1.3 that the steep density profile and large velocity gradient are essential ingredients governing the escape of radiation from the SN Ia envelope.

We show in Fig. 2.1 (*red line*) the velocity as a function of fractional mass (M/M_* , where M_* is the total mass of the progenitor White Dwarf star), for a double-detonation model (see Chap 1, Sect. 1.1.1) of Höflich et al. [121], in which the burning front changes from a deflagration to a detonation at a transition density $\rho_{\text{tr}} = 25 \times 10^6$ g cm $^{-3}$. The velocity gradient steepens in the outer layers of the ejecta ($M/M_* \gtrsim 0.8$), as the pressure wave resulting from burning in the innermost layers travels through the WD and accelerates matter at large radii.

Also shown in Fig. 2.1 (*blue line*) is the variation of the density (actually ρ/ρ_c , where ρ_c is the central density of the exploding WD star) with fractional mass. In this model, the density varies smoothly with mass, so no dense shell is formed in the ejecta (see, e.g., [145]). However, although the density fall-off with fractional mass is indeed steep for $M/M_* \lesssim 0.2$, the subsequent decline is significantly flatter than a power law, and the density declines slowly with radius in these outer regions.

For this same model, we show the final ($t \rightarrow \infty$) chemical composition as a function of the expansion velocity of the ejecta (or, equivalently, as a function of radius) in Fig. 2.2.

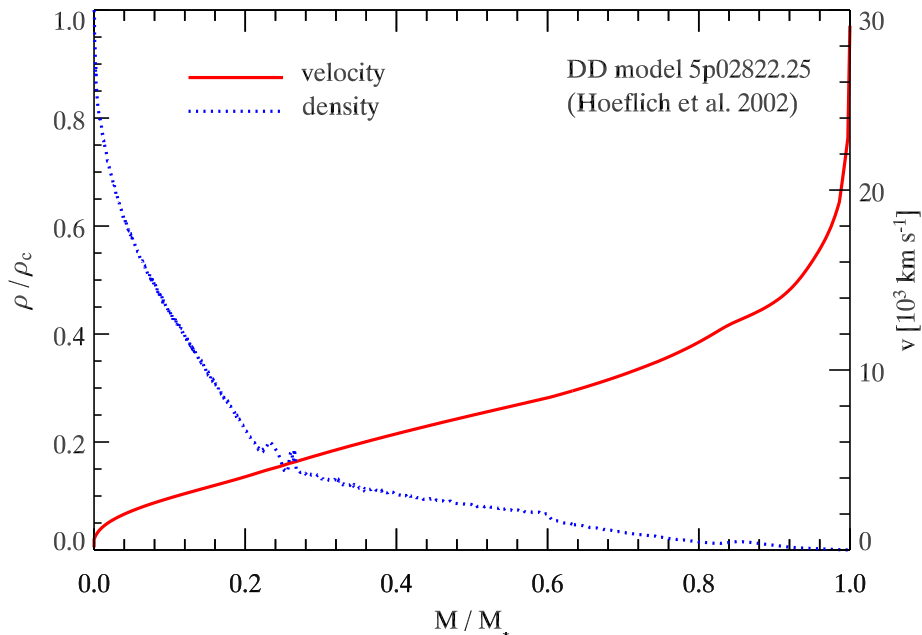


Figure 2.1: Density (blue dotted curves) and velocity (red solid curves) as a function of the mass for a double-detonation model of Höflich et al. [121] with transition density $\rho_{\text{tr}} = 25 \times 10^6 \text{ g cm}^{-3}$. M_* is the total mass of the progenitor White Dwarf star.

Iron-group elements (Fe), resulting from the radioactive decay of $\sim 0.6M_{\odot}$ of ^{56}Ni in this model, are produced in the innermost layers of the ejecta, where the density and temperature remain high for sufficient time during the explosion. Intermediate-mass elements (Mg, Si, S, Ca) are found in the (high-velocity) layers above the iron-rich core, where nuclear statistical equilibrium has had no time to set in [119]. These elements dominate the early spectra of SN Ia [75], and any viable explosion model must be able to reproduce the observed composition/velocity of the ejecta. Some models (including the one presented here) predict a significant amount of unburnt carbon and oxygen in the outer layers of the ejecta. There is no convincing evidence for the presence of such unburnt material in observed SN Ia spectra (although see [83, 191] for the possible detection of carbon in early spectra of SN 1990N). Moreover, the nebular spectra of such SN Ia would be dominated by strong forbidden lines of [O I] [12, 155], never detected before in SN Ia spectra (although see [202] for the possible detection of [O I] $\lambda\lambda 6300, 6394$ in the nebular spectra of SN 1937C).

2.1.2 Sources of opacity in SN Ia ejecta

The total frequency-dependent (specific) opacity $\kappa_{\nu}^{\text{tot}}$ in any stellar atmosphere can be written down as:

$$\kappa_{\nu}^{\text{tot}} = \sigma_e + \kappa_{\nu}^{bf} + \kappa_{\nu}^{ff} + \kappa_{\nu}^{bb}, \quad (2.4)$$

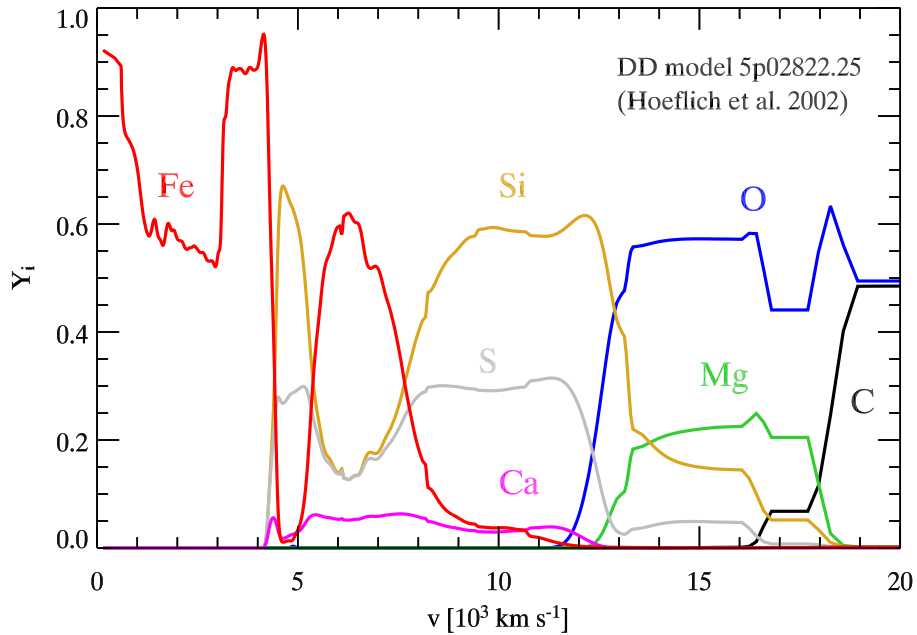


Figure 2.2: Abundances of stable isotopes as a function of the expansion velocity for a double-detonation model of Höflich et al. [121] with transition density $\rho_{\text{tr}} = 25 \times 10^6 \text{ g cm}^{-3}$.

where σ_e , κ_ν^{bf} , κ_ν^{ff} , and κ_ν^{bb} are the Thomson (free electron), bound-free, free-free, and line (bound-bound) opacities, respectively. Note that the Thomson opacity does not depend on frequency, as free electrons simply scatter incoming photons, regardless of their energy. σ_e , κ_ν^{bf} , and κ_ν^{ff} are continuous sources of opacity, so we can define the specific continuum opacity κ_ν^{cont} as

$$\kappa_\nu^{\text{cont}} = \sigma_e + \kappa_\nu^{bf} + \kappa_\nu^{ff}. \quad (2.5)$$

Atomic spectral lines are a discrete source of opacity, and we can define the specific line opacity as

$$\kappa_\nu^{\text{line}} = \kappa_\nu^{bb}, \quad (2.6)$$

such that $\kappa_\nu^{\text{tot}} = \kappa_\nu^{\text{cont}} + \kappa_\nu^{\text{line}}$.

For hydrogen-deficient media (as is the case for SN Ia ejecta), the contribution of κ_ν^{bf} to the total continuous opacity is very much reduced. In typical SN Ia conditions around maximum light (central temperature $T_c > 1.5 \times 10^4 \text{ K}$, density $\rho \lesssim 10^{-12} \text{ g cm}^{-3}$ [233]), the continuum opacity at optical wavelengths is dominated by electron scattering [234], so:

$$\kappa_\nu^{\text{cont}} \approx \sigma_e. \quad (2.7)$$

Although bound-free and free-free sources of opacity are negligible with respect to the total continuous opacity, they nevertheless play an important role in coupling the radiation field with the thermal energy of the gas.

However, the dominating source of opacity in the UV and (although less so) optical ranges is that due to spectral lines (bound-bound transitions). The homologous nature of the SN Ia expansion velocity field, and the resulting steep density gradient, causes each photon to be progressively redshifted with respect to the comoving frame of the SN ejecta, significantly enhancing the probability for a photon to interact with a spectral line [140]. In such an expanding medium, it is convenient to define a frequency-dependent expansion parameter s_ν (see [124], Eqn. 19):

$$s_\nu = (\sigma_e + \kappa_\nu^{bf} + \kappa_\nu^{ff})c\rho \left(\frac{dv}{dr} \right)^{-1}, \quad (2.8)$$

where c is the speed of light, ρ the local density, and dv/dr the local velocity gradient. In this formulation, κ_ν^{bf} and κ_ν^{ff} are assumed to be constant over the photon's mean free path. In what follows, we will use the frequency-independent version of the expansion parameter s_ν , defined as (see [140])

$$s = \sigma_e c \rho \left(\frac{dv}{dr} \right)^{-1}. \quad (2.9)$$

This formulation can then be used to calculate an “expansion opacity” (see [140], Eqn. 4), rigorously re-derived by Blinnikov [24].

The enhancement of line opacity as a function of the frequency-independent expansion parameter s is illustrated in Fig. 2.3 (see [124], their Fig. 1), where we plot the ratio of frequency-dependent opacities $\kappa = \kappa_\nu^{bf} + \kappa_\nu^{ff} + \kappa_\nu^{bb}$ to the total opacity $\kappa_\nu^{\text{tot}} = \kappa + \sigma_e$, as a function of wavelength for iron-rich matter, for $s = 1$ (*left*) and $s = 100$ (*right*), and for three different temperatures: $T = 20,000$ K (*top*), $T = 10,000$ K (*middle*), and $T = 5000$ K (*bottom*). The density is the same for all of these plots, with $\rho = 10^{-12}$ g cm $^{-3}$. Overplotted (*dashed line*) is the normalized Planck function for the corresponding temperature. If there is no opacity enhancement due to lines and/or bound-free and free-free processes, then the ratio $\kappa/(\kappa + \sigma_e) = 0$. If, on the other hand, line opacity is enhanced due to the expansion, or if bound-free and free-free opacities dominate the continuous opacity, then $\kappa/(\kappa + \sigma_e) \rightarrow 1$. As seen from Fig. 2.3, the effects of enhanced line opacity due to the expansion is particularly significant in the UV wavelength range, for a wide range of expansion parameters and temperatures. This process is known as “line-blocking”, and a careful treatment of this effect is important for accurate SN Ia spectral calculations [222, 11]. For $T = 20,000$ K, corresponding to the central temperature of SN Ia ejecta around maximum light, the peak of the Planck function is in the UV ($\sim 2\,500$ Å), where line-blocking by lines of iron-group elements is the greatest. Photons will thus scatter downward in frequency (and outward in radius) till they are sufficiently redshifted with respect to the SN ejecta comoving frame that they are at a frequency where the line optical depth is low enough to permit escape [234].

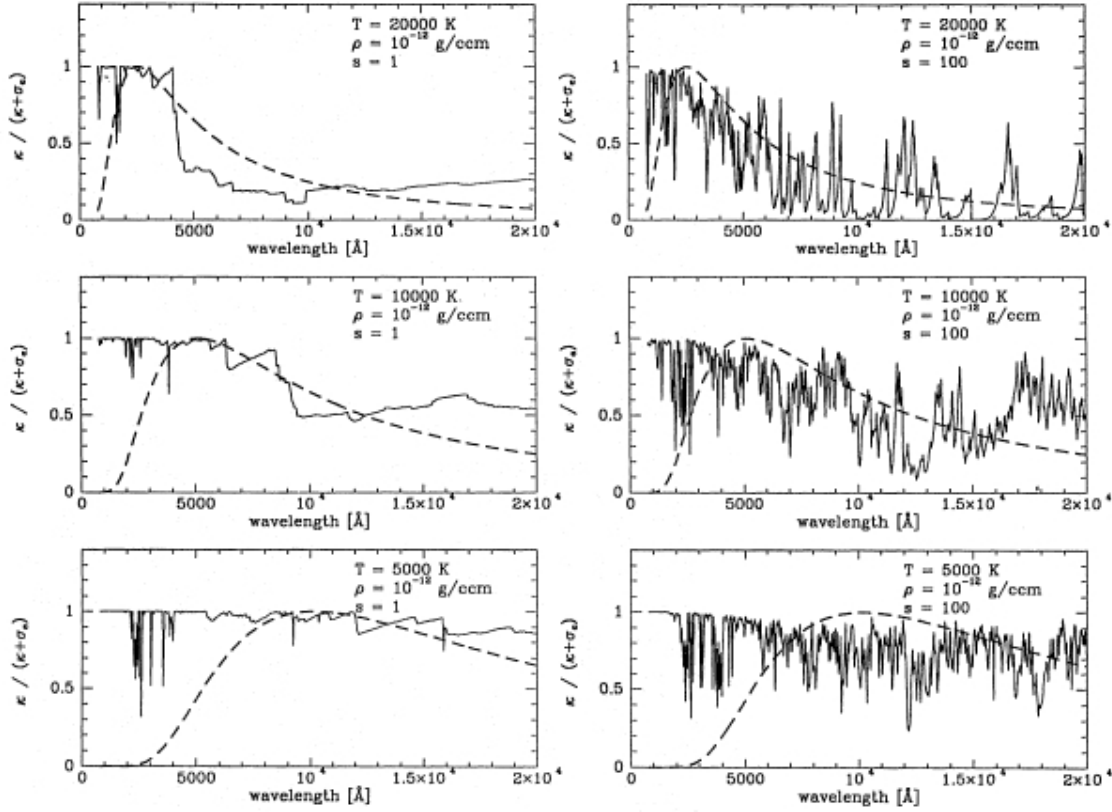


Figure 2.3: Variation of the ratio of the total frequency-dependent opacity $\kappa = \kappa_{\nu}^{bf} + \kappa_{\nu}^{ff} + \kappa_{\nu}^{bb}$ to the total opacity $\kappa_{\nu}^{\text{tot}} = \kappa + \sigma_e$, as a function of wavelength and for iron-rich matter. The plots correspond to two different values of the frequency-independent expansion parameter s (Eqn. 2.9) – $s = 1$ (*left*) and $s = 100$ (*right*), and for three different temperatures: $T = 20,000$ K (*top*), $T = 10,000$ K (*middle*), and $T = 5000$ K (*bottom*). The density is the same for all of these plots, with $\rho = 10^{-12}$ g cm $^{-3}$. Overplotted (*dashed line*) is the normalized Planck function for the corresponding temperature. From Höflich et al. [124]; reproduced with permission.

A consequence of the domination of line opacity in SN Ia spectra is the absence of a well-defined “photosphere”, usually defined as the radius at which the total inward-integrated continuum optical depth (which dominates in most stars) $\tau_{\text{tot}}^{\text{cont}} \sim 2/3$ (see [200], p. 62). In SN Ia ejecta, we cannot ignore the contribution from the line opacity to the total opacity, and the definition of a ‘SN Ia ‘photosphere’ should include τ_{line} in the optical-depth integral. We illustrate the strong wavelength dependence of total (line *and* continuum) inward-integrated optical depth layers in Fig. 2.4, based on results of the M36 models of Höflich [119] applied to SN 1994D. We show this wavelength dependence both in velocity (*left ordinate axis*) and radial (*right ordinate axis*) coordinates, which are equivalent by virtue of the homologous nature of the expansion in SN Ia ejecta (Eqn. 2.2). The results are shown for three epochs, $t_{\text{exp}} = +10$ d (*upper panel*), $t_{\text{exp}} = +16$ d (*middle panel*), and $t_{\text{exp}} = +30$ d (*lower panel*), where $t_{\text{exp}} = t_B + 17$ d is the time *after explosion* (in this particular model) rather than from *B*-band maximum (t_B). In each of these plots, we show the velocity/radial location of the $\tau_{\text{tot}} = 0.1$ (*black line*) and $\tau_{\text{tot}} = 1$ (*red line*) layers, *vs.* wavelength in the (optical) wavelength range 3500–6500 Å. The location of the “photosphere” in this case varies by $\sim 30\%$ at $t_{\text{exp}} = +10$ d, by a factor of 2 at $t_{\text{exp}} = +16$ d, and by a factor of 4 at $t_{\text{exp}} = +30$ d. Already at +30 d past explosion, the optical spectra of SN Ia are dominated by thousands of weak lines of iron-group elements, which greatly affect the opacity structure of the SN ejecta. At the earliest epochs, where the continuum is still optically thick, one can of course resort to the standard definition of the photosphere in terms of continuous opacity sources only (see Chap. 5), although the location of this layer will be different from the region where the photons escape from the ejecta.

Another problem affecting the modeling of SN Ia spectra is the absence of a diffusive inner boundary: even at maximum light, the electron density in the ejecta is too low for collisional destruction of photons to thermalize the radiation field, at least for wavelengths $\lambda \gtrsim 2000$ Å [234]. Thus, even at large optical depths, the radiation field (characterized by its mean intensity J_ν) will be significantly different from a Planck function at the local gas temperature:

$$J_\nu \neq B_\nu(T_{\text{gas}}), \quad (2.10)$$

which prohibits the use of the usual diffusion approximation, applicable to standard stellar atmospheres (see [200], pp. 49–52). Nor is the assumption of local thermodynamic equilibrium (LTE) a valid one for SN Ia, anywhere in the ejecta: the entire supernova must be modeled at once.

Last, before maximum light, the time required for the energy input (at an exponentially-decreasing rate) by the $^{56}\text{Ni} \rightarrow ^{56}\text{Co} \rightarrow ^{56}\text{Fe}$ radioactive decay chain to diffuse outwards in the form of optical photons is $\gtrsim 2$ weeks (roughly corresponding to the rise time of the SN light curve), and so modeling an early SN Ia spectrum at a given phase requires knowledge of the radiation field prior to that phase (see, e.g., [233]). The modeling of optical SN Ia spectra is thus a time-dependent, non-LTE problem.

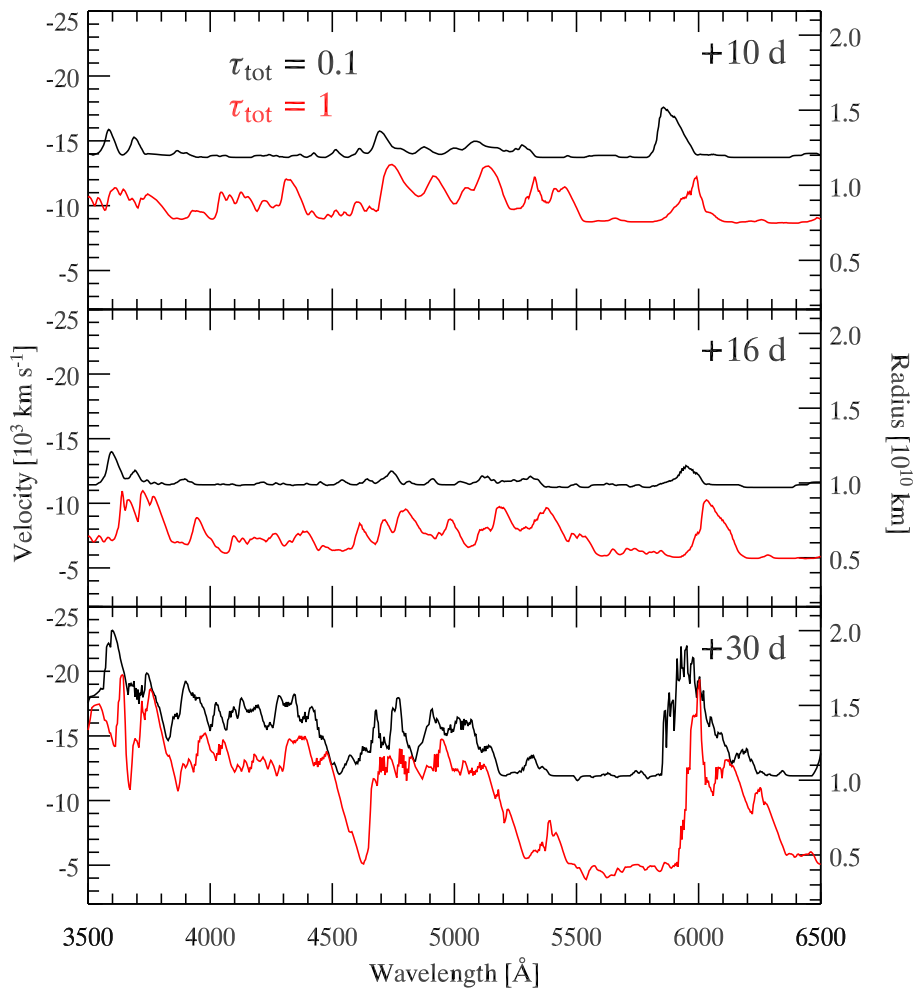


Figure 2.4: Variation of the velocity and radius of total inward-integrated optical depth $\tau_{\text{tot}} = \{0.1, 1\}$ layers with wavelength, for a model of SN 1994D presented by Höflich [119]. Here the quoted phase is $t_{\text{exp}} = \{+10, +16, +30\}$ d, where $t_{\text{exp}} = t_B + 17$ d is the time *after explosion* (in this particular model) rather than from *B-band maximum*. Figure inspired from Fig. 11 of Höflich [119].

2.1.3 Line formation and line profiles in SN Ia spectra

The Sobolev approximation

Spectral lines in SN Ia are mainly formed by resonant scattering of photons in bound-bound transitions (see [135] for a review). Although in practice the line source function (the ratio of its emission to absorption coefficients) may depart significantly from pure resonant scattering, it is a good approximation for qualitative inspection of line formation in SN Ia spectra. As previously mentioned, photons are progressively redshifted with respect to the SN comoving frame till they can resonate with a line at a given frequency. The size of the associated resonance region is determined by the ratio of the intrinsic velocity width of the line (determined by the thermal – and micro-turbulent, if at all relevant – velocity of the SN atmosphere) to the velocity gradient projected along the line of sight. Because of the large expansion velocities in SN Ia, the resonance region is extremely confined, and photons only interact with a line in a small region of the SN atmosphere. In particular, we can assume the line source function to be constant over the resonance region (effectively neglecting the intrinsic line width). Such an approximation, which greatly simplifies the solution to the radiative transfer equation, is known as the “Sobolev approximation” [277, 48, 257].

In the simplest implementation of the Sobolev approximation to supernova spectral synthesis (e.g., the parametrized SYNOW code of Fisher et al. [82]), one assumes a sharp blackbody-emitting photosphere to exist, and lines to form in an expanding atmosphere where continuous sources of opacity are neglected. We have seen that both of these assumptions are inaccurate descriptions of the conditions prevalent in the SN Ia ejecta; however, they are sufficient for our illustrative purposes here, and have been proved extremely useful to associate spectral features in SN Ia spectra with a line of a given ion, a difficult task in such line-dominated spectra (see, e.g., [34]). The supernova is also assumed to be spherically symmetric, which, in view of recent polarization measurements on SN 2001el [304, 142], might also be a simplistic assumption.

P-Cygni profiles in SN Ia

We illustrate such an idealized supernova in Fig. 2.5. The upper panel shows a schematic diagram of the velocity profile and density structure of the SN. The ordinate axis corresponds to the impact parameter p , whilst the abscissa corresponds to the line of sight (depth z), increasing away from the observer – located at $(z, p) = (-\infty, 0)$. Both axes are in units of the photospheric radius, R_{phot} . The opaque photospheric disk is shown as a black disk centered on the origin and of unit radius. The grey shaded region corresponding to $|p| \leq 1$ and $z > 0$ is known as the “occulted region”, and is not visible to the observer. The velocity field is represented by vectors, with $\|\overline{v(r)}\| \propto r$, r being the radial distance from the origin. The magnitude of the *projected* velocity (along the line of sight) is colour-coded using a blue-red scale (in units of the photospheric velocity, v_{phot}) representing the wavelength shift of photons emitted towards the observer at that location. Notice how the homologous nature of the expansion in SN Ia implies that surfaces of constant projected velocity v_z are planes perpendicular to the line of sight:

$$v(r) \propto r \Rightarrow v_z \propto z, \quad (2.11)$$

and thus all photons of a given wavelength corresponding to a particular transition originate from the same z plane.

The density structure is illustrated with iso-density contours. The radial density profile is parametrized as a power law with exponent n , i.e. $\rho(r) = \rho_0(R_0/r)^n$ and $n = 7$. Each successive contour corresponds to a factor 5 decrease in density as we move to larger radii. Surfaces of iso-density are spheres centered on the origin. Thus, an iso-velocity contour (corresponding to photons of a given frequency for a given transition) will encounter a huge range of densities. This characteristic distinguishes supernovae from other expanding outflows (such as Wolf-Rayet stars), and leads to peculiar line-profile morphologies.

In the lower panel of Fig. 2.5, we show the resulting line profile, corresponding here to H α (absent from SN Ia spectra, but present in SN II spectra where the velocity field and density structure are qualitatively similar), computed with SYNOW. The line displays the characteristic ‘‘P-Cygni’’ profile shape (named after the classical P Cygni stars [16]), characterized essentially by absorption on the blue side of, and emission peaking at, the line center (*vertical dashed line*). The flux is per unit frequency (F_ν) and is normalized to the underlying continuum (F_{cont}), assumed to be a blackbody in SYNOW. The deep blueshifted absorption feature results from the scattering of photons with $|p| \leq 1$ out from the line of sight. Since regions with $|p| \leq 1$ and $z < 0$ are occulted, no absorption is seen on the red side of the line center in the resulting profile. The emission comes from the side-lobes of the supernova ($|p| > 1$), and is in principle symmetric about the line center. The observed profile, resulting from a combination of absorption and emission components, is in fact highly skewed to the red, as the strong blue absorption component affects the blue side of the emission profile. Notice how the velocity associated with the location of maximum absorption (v_{abs} , negative by convention for blueshifts) is equal in magnitude to the photospheric velocity ($v_{\text{abs}} = -v_{\text{phot}}$, whereas the velocity associated with the peak of emission (v_{peak}) corresponds to a zero Doppler shift (see Chap. 5 for a discussion of v_{abs} and v_{peak} measurements in SN Ia at different redshifts).

We further illustrate the formation of P-Cygni profiles in SN Ia atmospheres with the non-LTE model atmosphere code CMFGEN [118]: a steady-state, 1D, model that solves the radiative transfer equation in the comoving frame, subject to the constraints of radiative and statistical equilibria. Because CMFGEN is at present not strictly adequate for SN Ia conditions (no chemical stratification; no γ -ray energy deposition; see [66] for details), these results are merely illustrative; nonetheless, they provide a new insight into the sites of optical line and continuum formation, corresponding in this example to a low-luminosity SN Ia (‘‘91bg-like’’; see Sect. 2.2.2) near maximum light. The characteristics of this particular model are presented later on in Chap. 5.

To gain additional insight into line-formation process in SN Ia environments, we compare the formation of resonance lines in SN Ia with that in a nitrogen-rich Wolf-Rayet star (WR), using similar model parameters as other authors (e.g., [118, 114]). Wolf-Rayet stars are hot (several 10^4 K), massive (initial mass $M_i \gtrsim 20 M_\odot$), luminous ($\sim 10^5 - 10^6 L_\odot$)

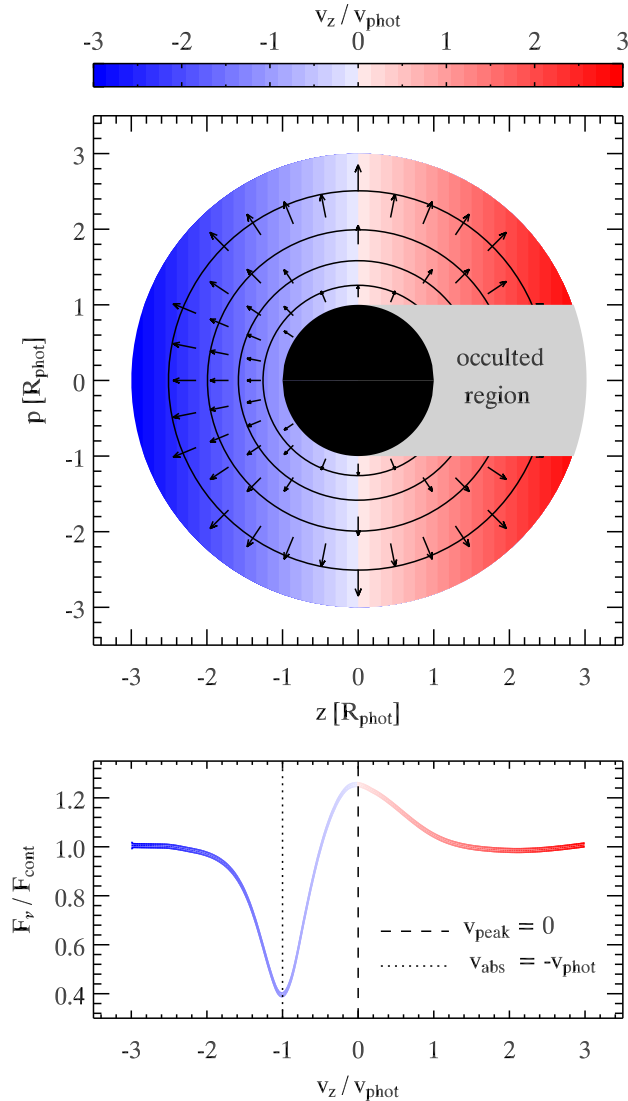


Figure 2.5: Cartoon illustrating the density/velocity structure in SN Ia envelopes and subsequent line-profile morphology. **Upper panel:** Velocity contours (color coded) in units of the photospheric velocity, v_{phot} , in the (z, p) plane. Overplotted (black circles) are logarithmic (base 5) density contours corresponding to a density exponent $n = 7$. Also shown are velocity vectors corresponding to a homologous velocity field ($v(r) \propto r$). The black disk is the photo-disk of the supernova. The observer is located at $(z, p) = (-\infty, 0)$, and hence the “occulted region” corresponds to $-1 \leq p \leq 1$ and $z > 0$. **Lower panel:** Synthetic line profile flux (per unit frequency, F_ν), normalized to the continuum flux F_{cont} , corresponding to the configuration above and computed using the parametrized code SYNOW [82]. The abscissa is now the *projected* velocity, along ($p = 0$), v_p . In this model, the peak of emission is not shifted with respect to the rest wavelength ($v_{\text{peak}} = 0$), and the location of maximum absorption is blueshifted by an amount corresponding to the photospheric velocity ($v_{\text{abs}} = -v_{\text{phot}}$). See text for details.

stars, characterized by broad ($\sim 10^3 \text{ km s}^{-1}$) emission lines in their optical spectra, due to mass loss via sustained stellar winds ($\dot{M} \sim 10^{-5} M_{\odot} \text{ yr}^{-1}$) – see, e.g., [1] for a review. Because the density profile is a lot flatter in WR atmospheres (roughly following a $1/r^2$ law imposed by mass conservation), and the line-formation region is much more extended than in SN Ia, a comparison of line formation in both environments will reveal noticeable differences.

In particular, we want to understand where the line and continuum fluxes originate in the ejecta. We show in Fig. 2.6 (*left panel*) the synthetic line profiles for the resonance C IV $\lambda 1548$ doublet line in a hot hydrogen-free WR model, with asymptotic wind velocity $v_{\infty} = 2000 \text{ km s}^{-1}$. At the bottom of each panel, and following Dessart and Hillier [66, 65], we show gray-scale images in the $(v, p/p_{\text{lim}})$ plane of the flux-like quantity $p \cdot I(p)$, where $v = [(\lambda/\lambda_0) - 1]c$ is the classical Doppler velocity, p is the impact parameter, and $I(p)$ is the specific intensity at p . p_{lim} corresponds to the impact parameter where $p \cdot I(p) = 0$ for $p > p_{\text{lim}}$. In this WR model, $p_{\text{lim}} = 6.8 R_0$, where R_0 is the hydrostatic radius of the WR star. The sum over p of the quantity $p \cdot I(p)$ at v corresponds to the total line flux at v , shown at the top of each panel (*solid line*). This way, for each v , we are able to directly identify the relative contribution to the total flux, at each impact parameter.

Beyond the velocity limits of the line ($\pm v_{\infty}$), we are essentially seeing continuum photons, although some line photons are present (especially on the red side, $v > 0$) due to incoherent electron scattering. The photosphere in this WR model is thus located at $p = p_{\text{lim}}$. Note the large extent of the emission region, which extends to $\sim 7p_{\text{lim}}$ (*not shown*) in this model. Also, emission is roughly symmetric about the line center ($v = 0$), although only extends to $v_{\text{frac}} \sim -0.5v_{\infty}$ on the blue side. The large flux deficit below $v = v_{\text{frac}}$ is not compensated by emission from larger impact parameters, and an absorption profile results in the velocity range $v_{\text{lim}} \lesssim v \lesssim v_{\text{frac}}$. The location of maximum absorption corresponds to $v_{\text{abs}} = -v_{\infty}$, and that of peak emission to $v_{\text{peak}} \approx 0$.

The SN Ia model is shown in the left panel of Fig. 2.6, for the resonance line of Si II $\lambda 6347$, characteristic of SN Ia spectra. In this model, $p_{\text{lim}} = 2.85 R_0$, where R_0 is the base radius of the CMFGEN radial grid where the continuum optical depth $\tau_{\text{cont}} \sim 50$ – a photosphere thus exists in this model configuration, corresponding here to a velocity of $v_{\text{phot}} = 9550 \text{ km s}^{-1}$. Although the resulting profile also has the characteristic P-Cygni shape, there are noticeable differences with respect to the WR model. In particular, both line and continuum originate from the region below p_{lim} ($p/p_{\text{lim}} < 1$), and both become optically thin beyond. Thus, line formation in SN Ia atmospheres is a lot more confined than in WR stars. To quantify the difference in the extent of emission in both the WR and SN Ia models, we compute the ratio of the integral of $p \cdot I(p)$ in the region both below and above p_{lim} . We only consider the extent of the absorption profile, $v_{\text{lim}} < v < 0$, where $v_{\text{lim}} = v_{\text{frac}}$ for the WR case and $v_{\text{lim}} = -16,000 \text{ km s}^{-1}$ for the SN Ia case. This ratio, noted X_{lobe} , will give us the relative fraction of flux emitted at impact parameters $p > p_{\text{lim}}$:

$$X_{\text{lobe}} = \left. \frac{\int_{p_{\text{lim}}}^{\infty} p \cdot I(p) dp}{\int_0^{p_{\text{lim}}} p \cdot I(p) dp} \right|_{v_{\text{lim}} < v < 0}. \quad (2.12)$$

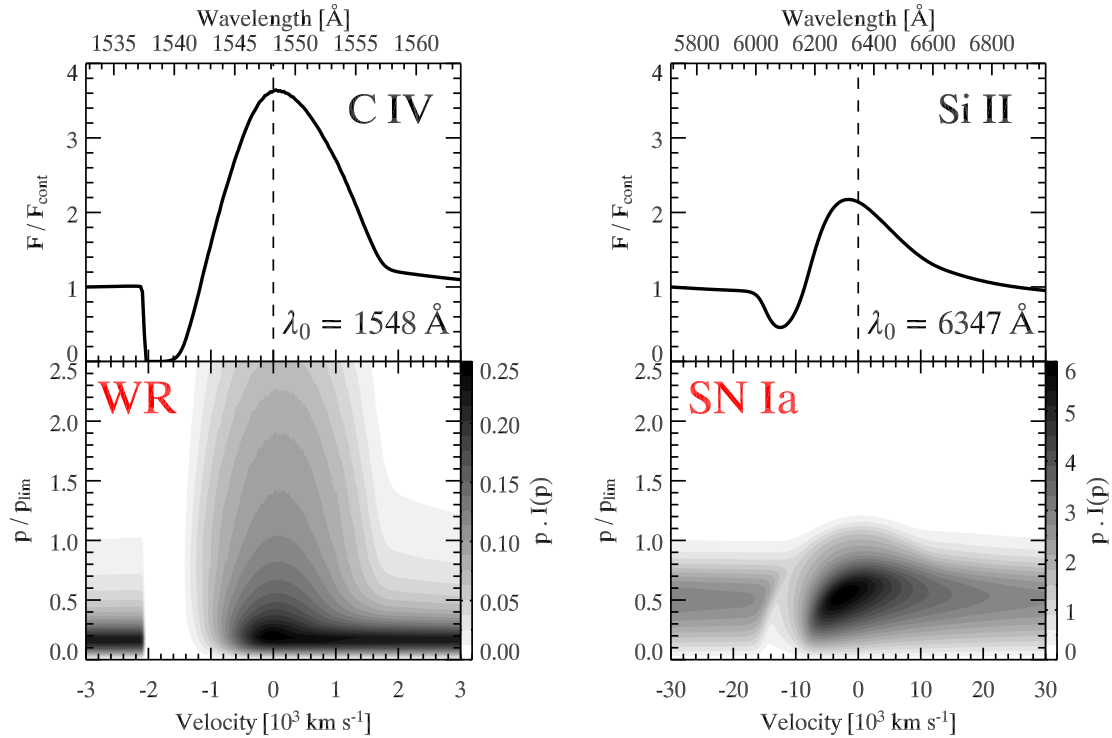


Figure 2.6: Comparison of P-Cygni profiles of the resonance lines C IV $\lambda 1548$ and Si II $\lambda 6347$ in CMFGEN models of a nitrogen-rich Wolf-Rayet (WR) star and a Type Ia supernova, respectively. **Lower panels:** Gray-scale image of the quantity $p \cdot I(p)$ as a function of p/p_{lim} and classical Doppler velocity $v = [(\lambda/\lambda_0) - 1]c$, where p is the impact parameter and $I(p)$ the specific intensity along p (at v). λ_0 is the rest wavelength of the transition and c is the speed of light in vacuum. p_{lim} corresponds to the impact parameter where $p \cdot I(p) = 0$ for $p > p_{\text{lim}}$. For the SN Ia model, $p_{\text{lim}} = 2.85 R_0$, where R_0 is the base radius of the CMFGEN radial grid where the continuum optical depth $\tau_{\text{cont}} \sim 50$ – a photosphere thus exists in this model configuration, corresponding here to a velocity of 9550 km s^{-1} . For the WR model, $p_{\text{lim}} = 6.8 R_0$, where R_0 is the hydrostatic radius of the WR star. The terminal velocity of this model is $v_\infty = 2000 \text{ km s}^{-1}$. **Upper panels:** Line-profile flux obtained by summing $p \cdot I(p)$ over the range of p . The profiles have been normalized to the continuum flux, F_{cont} . See [66, 65] for a detailed and pedagogical explanation of these plots in the context of Type II supernovae.

For the WR model, $X_{\text{lobe}} \sim 0.94$, whilst for the SN Ia model $X_{\text{lobe}} \sim 0.04$, thereby confirming what the eye can make out: emission in the WR model occurs below and beyond p_{lim} in roughly equal fractions, whilst almost all the emission is concentrated at impact parameters $p < p_{\text{lim}}$.

Moreover, the emission in the SN Ia model only appears on the blue side of the profile, resulting in a strongly blueshifted ($v_{\text{peak}} \sim -4000 \text{ km s}^{-1}$) emission peak. The reason for this emission-peak blueshift (explained for the first time by Dessart and Hillier [66], in the context of SN II) is the steep radial density profile in SN Ia ejecta (density exponent $n = 7$ in this particular model). Emission is forced to occur in the inner dense region of the ejecta, enhancing the impact of disk occultation and continuum absorption of red photons.

What ultimately controls the differences in the overall line profile for the WR and SN Ia models is the radial variation of the line source function S_{line} with respect to that of the continuum at a radial optical depth $\tau_{\text{cont}} = 2/3$, noted $S_{\text{cont},\tau=2/3}$. In Fig. 2.7, we plot the ratio $S_{\text{line}}/S_{\text{cont},\tau=2/3}$ for the WR (*upper panels*) and SN Ia (*lower panel*) models, both as a function of the logarithm of the continuum optical depth at the rest-frame wavelength of the transition, $\log(\tau_{\text{cont},\lambda_0})$ (i.e. the radial variation; *left*), and of the velocity (*right*). For the WR model, the line source function drops below the reference continuum source function for $\tau_{\text{cont}} < 2/3$ and $v \gtrsim 1\,200 \text{ km s}^{-1}$. The drop for $v \gtrsim 1\,200 \text{ km s}^{-1}$ is significant, and we expect no emission for $v < -1\,200 \text{ km s}^{-1}$, as seen in Fig. 2.6. The drop beyond $v \gtrsim 1\,500 \text{ km s}^{-1}$ is even greater still, and the flux goes “black” (saturated absorption for $v_{\infty} \lesssim v \lesssim 1\,500 \text{ km s}^{-1}$). For the SN Ia, the line source function drops below the continuum source function for $v \gtrsim 12\,000 \text{ km s}^{-1}$, and emission is reduced for $v < -12\,000 \text{ km s}^{-1}$, as again seen in Fig. 2.6. However, the decline is more gradual as for the WR model, and the line is not saturated in absorption.

Thus, the comparison of line formation mechanisms in the diverse WR and SN Ia environments has revealed fundamental differences in the resulting line profile shapes. The key parameter governing the extent of line formation (and subsequent emission-peak blueshift) in SN Ia is the steep radial density profile, concentrating all emission and absorption processes in the inner regions of the ejecta [66]. We devote Chap. 5 in its entirety to the study of line profiles in SN Ia spectra.

2.1.4 A parametrized synthetic SN Ia spectrum

To end this section on theoretical insights into SN Ia spectral synthesis, and before presenting observed SN Ia spectra in the following section, we present the full synthetic spectral calculation of a SN Ia near maximum light, using the parametrized SYNOW code of Fisher et al. [82]. The theoretical background and model assumptions for this code can be found in Jeffery and Branch [135]. Here, we simply remind the reader that SYNOW assumes a sharp blackbody-emitting photosphere to exist, and lines are formed *via* pure resonant scattering in the Schuster-Schwarzschild approximation (see [200], p. 132) above this photosphere. The model inputs are displayed in Table 2.1. Note that the radial variation of the line optical depth, $\tau(r)$, is input by hand, and is taken here to be an exponential with an e-folding velocity $v_e = 1000 \text{ km s}^{-1}$. Other inputs include: the temperature of the un-

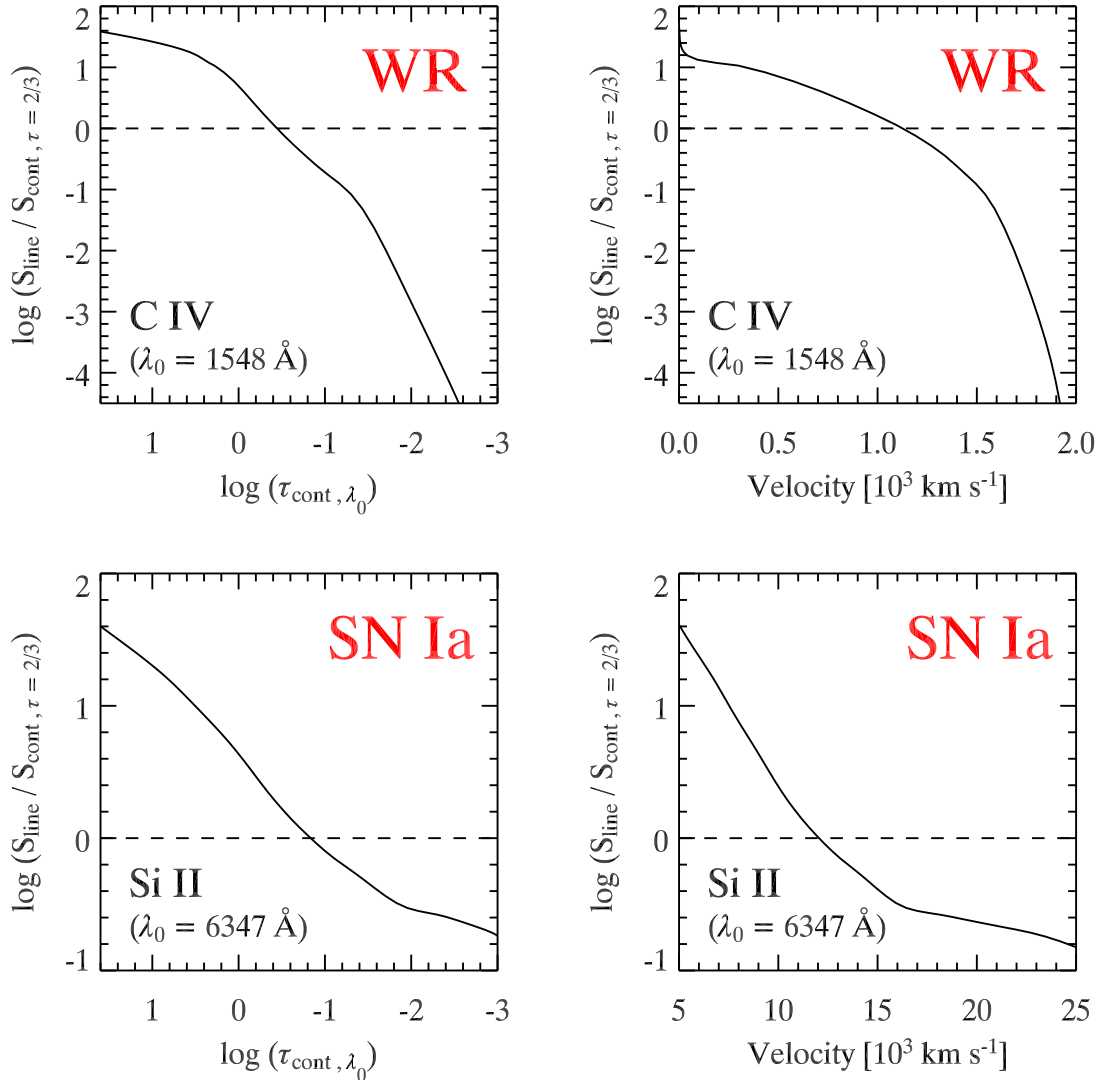


Figure 2.7: Radial and velocity variation of the logarithm of the line source function normalized to the continuum source function at continuum optical depth of two third (*see text for details*). We show the cases corresponding to Fig. 2.6, i.e. for C IV $\lambda 1548$ in the WR model (*upper panels*) and Si II $\lambda 6347$ in the SN Ia model (*lower panels*). See also Fig. 19 of Dessart and Hillier [66] for similar plots in the context of a comparison between WR and SN II models.

Table 2.1: SYNOW model parameters for SN 1994D at -1 d

Model parameter		Parameter value
e-folding velocity, v_e		1000 km s $^{-1}$
temperature of blackbody, T_{BB}		13,000 K
excitation temperature, T_{exc}		10,000 K
photospheric velocity, v_{phot}		11,000 km s $^{-1}$
Ion	τ_0	$[v_{\text{min}}, v_{\text{max}}]$ (10^3 km s $^{-1}$)
O I	0.8	[12, 40]
Na I	0.4	[0, 40]
Mg II	1	[0, 40]
Si II	12	[0, 40]
Si III	1.2	[0, 40]
S II	2	[0, 40]
Ca II	70	[0, 40]
“HV Ca II”	5	[19, 40]
Fe III	0.8	[0, 40]
Co II	0.8	[0, 40]
Ni II	0.8	[0, 40]

derlying blackbody continuum (T_{BB}); the excitation temperature (T_{exc}); the photospheric velocity (v_{phot}); the velocity interval in which a given ion is present ($[v_{\text{min}}, v_{\text{max}}]$). For each ion that is introduced, the optical depth of the corresponding reference line (the one with the largest oscillator strength), τ_0 , is also a fitting parameter, and the optical depths of all other lines corresponding to the ion are calculated assuming Boltzmann excitation at T_{exc} . The atomic data for 42 million lines are from Kurucz [161]. These model parameters are identical to those used by Branch et al. [33] in the SYNOW analysis of SN 1994D.

The assumptions made in the SYNOW code are not applicable to SN Ia ejecta. In particular, the assumption of the existence of a sharp photosphere emitting a blackbody continuum is incorrect for SN Ia (Sect. 2.1.2). Furthermore, some assumptions are physically incoherent: a continuum photosphere exists, yet continuum opacity is ignored in the line-forming region. However, through its ease of installation and use, SYNOW is probably the most popular SN Ia spectral synthesis tool, and has been proved useful in identifying spectral features in SN Ia, associating most of the lines in spectra around maximum light with singly-ionized, intermediate-mass elements.

We show the result of such a synthetic spectrum calculation in Fig. 2.8 (*upper panel*), where we show the observed (*black line*) and synthetic (*red line* – excluding contributions from “high-velocity” Ca II; see later) spectra of SN 1994D at -1 d from B -band maximum. The flux is per unit frequency (F_ν), and the observed spectrum has been corrected for the heliocentric velocity of the host galaxy (NGC 4526; $cz = +448$ km s $^{-1}$ – from NED¹) and for Galactic reddening (using the dust maps of Schlegel et al. [268]). The host galaxy

¹NASA/IPAC Extragalactic Database: <http://nedwww.ipac.caltech.edu/>

reddening for SN 1994D is thought to be negligible ($E(B - V) = 0.00 \pm 0.02$; [230]), and the spectrum has not been de-reddened. The overall fit to the spectrum is satisfactory considering the simplistic assumptions made, although the continuum is too high redward of $\sim 6500 \text{ \AA}$, due to the assumption of a Planckian continuum. At shorter wavelengths ($\lesssim 3400 \text{ \AA}$), the flux is overestimated due to the lack of appropriate treatment of line-blanketing by many weak lines of iron-group elements [222, 11].

Moreover, the fit to the observed spectrum is improved by adding ions in a restricted velocity interval at high ejecta velocities: O I ($12,000 \leq v \leq 40,000 \text{ km s}^{-1}$) and Ca II ($19,000 \leq v \leq 40,000 \text{ km s}^{-1}$) – called “high-velocity” (HV) Ca II by Branch et al. [33]. In the upper panel of Fig. 2.8, both synthetic spectra with (*dash-dotted red line*) and without (*solid red line*) the inclusion of this “HV Ca II” feature are shown. The lower velocity limit for “HV Ca II” is greater than the photospheric velocity of the model, and this velocity is said to be “detached” from the photosphere. Despite the attribution of this feature to Ca II in several local SN Ia spectra (SN 1994D [112]; SN 2001el [304]; SN 2000cx [289]; SN 2003du [97]; SN 1999ee [193]; SN 2002dj, 2003kf, 2002er, 2002bo, 2003cg [192]), more detailed non-LTE calculations attribute the so-called “high-velocity” component of Ca II $\lambda 3945$ to Si II $\lambda 3858$, predicted to dominate past ~ 1 week before maximum [119, 125, 173]. We discuss in more depth the nature of this feature in both local and high-redshift SN Ia spectra in Chap. 5 (Sect. 5.3.3).

In the lower panel of Fig. 2.8, we show the relative contribution of each ion to the overall synthetic spectrum of SN 1994D at -1 d. The flux is normalized to the underlying blackbody continuum (F_{cont}), and the line spectra are offset from one another for the sake of clarity. The deficit in flux caused by the presence of lines of iron-group elements (here Co II and Ni II) is obvious below 3500 \AA . The impact of adding a “detached HV” shell of Ca II is shown in the corresponding line spectrum (*dash-dotted line*). This simple model illustrates well how SN Ia spectra are characterized by overlapping P-Cygni profiles. It is often difficult to say whether a peculiar line profile stems from peculiar line formation processes, or from the contamination of the profile by a line of another ion. This issue of “line overlap” in SN Ia spectra is also discussed at length throughout Chap. 5.

2.2 Observational properties of Type Ia supernovae

2.2.1 Spectral evolution of SN Ia

We have seen in the previous section that spectra of Type Ia supernovae around maximum light are dominated by broad lines with a P-Cygni profile shape, corresponding to singly-ionized, intermediate-mass elements. At later stages ($\gtrsim 2$ weeks past maximum), as the photo-emitting layers recede in the comoving frame of the ejecta, emission lines of iron-group elements (Fe II, Co II) start to dominate the optical spectra, resulting from the decay products of ^{56}Ni synthesized during the explosion. The spectra of SN Ia will reflect the composition of successive layers in the disrupted White Dwarf star, enabling us to probe deeper into the ejecta as time passes.

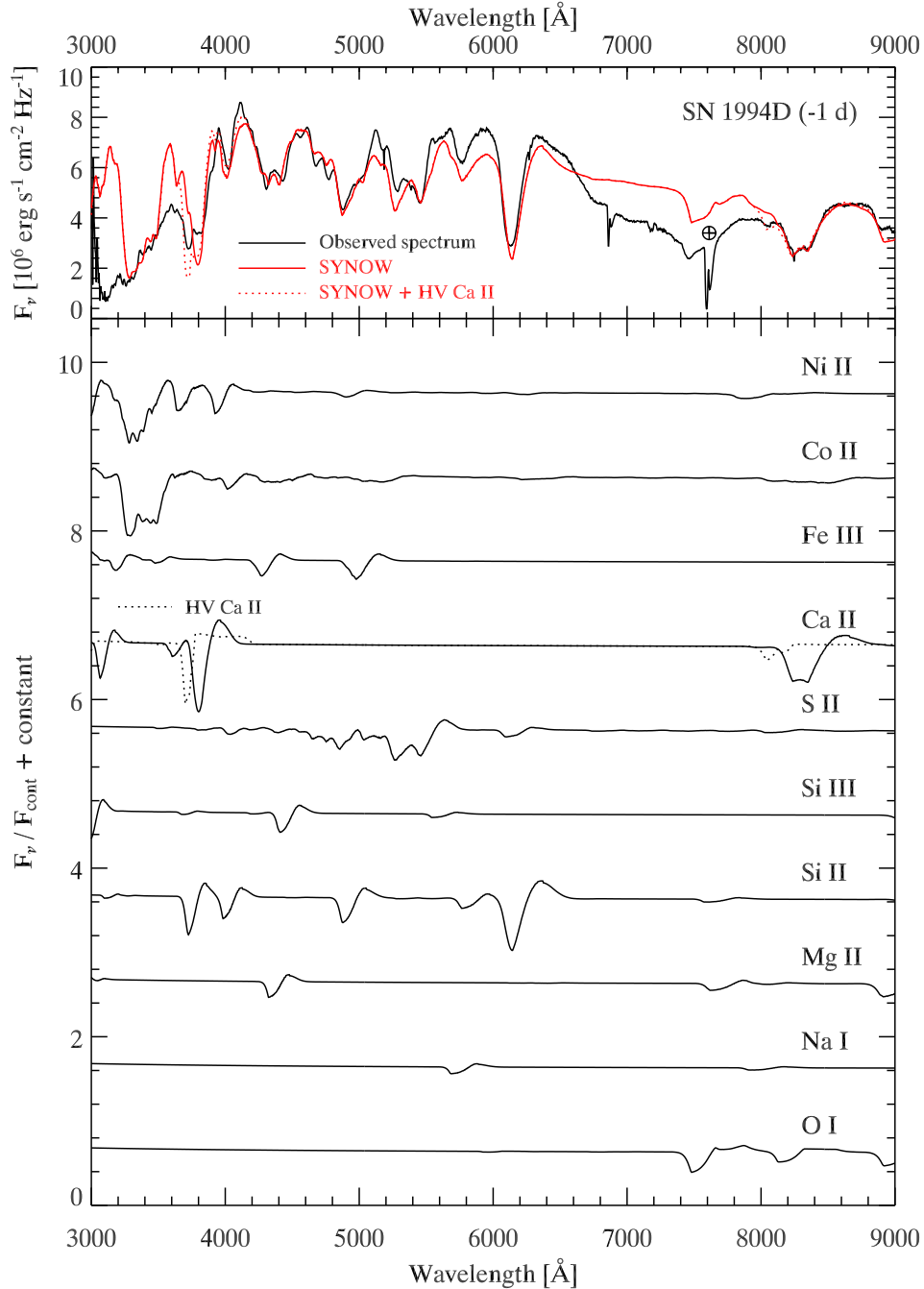


Figure 2.8: Observed and synthetic spectra of SN 1994D at -1 d from B -band maximum. **Upper panel:** Comparison between the observed (*black line*) and synthetic (*solid red line*) spectra of SN 1994D, computed using the parametrized SYNOW code [82] using the same input parameters as Branch et al. [33]. The red dotted line shows the effect of adding a high-velocity shell of Ca II in the SYNOW model. The location of the A-band atmospheric absorption feature is indicated with a telluric symbol. **Lower panel:** Synthetic line spectra for the individual ions used in the SYNOW model, normalized to the continuum synthetic flux (assumed to be a blackbody in SYNOW), in decreasing order of atomic weight (from top to bottom).

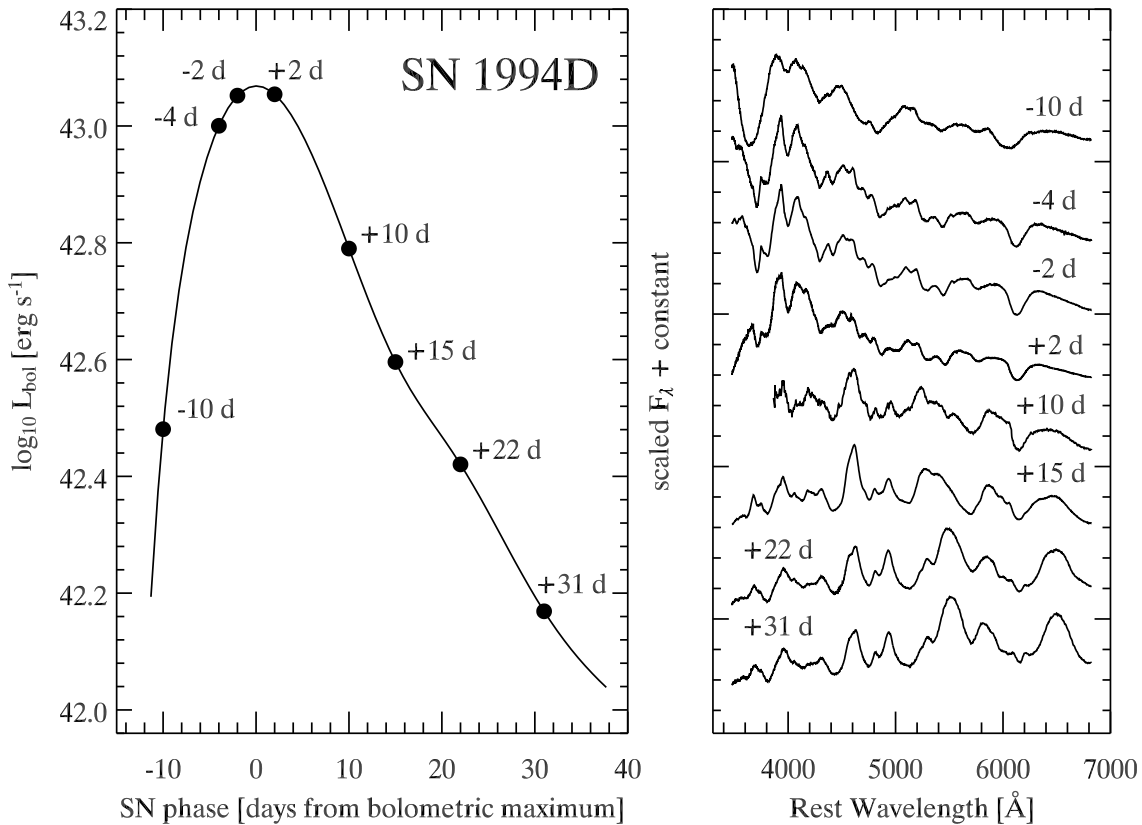


Figure 2.9: **Left panel:** Bolometric light curve of SN 1994D (*UBVRI* filters – see [281]). **Right panel:** Spectral evolution of SN 1994D, at phases marked by a black dot in the light curve. Pre-maximum and maximum spectra of SN Ia are dominated by lines of singly-ionized, intermediate-mass elements (Mg II, Si II, S II, Ca II). At later phases ($\gtrsim +10$ d), lines of iron-group elements (mostly Fe II and Co II) start to dominate the spectra, as the photo-emitting layers recede deep into the WD interior.

In Fig. 2.9, we show the time evolution of the bolometric light curve (*left panel*) and spectra (*right panel*) for SN 1994D [220]. We mark eight phases between -10 d and $+31$ d from bolometric maximum in the light curve, and show the corresponding spectra (increasing in phase from top to bottom) in the right panel, with flux per unit wavelength (F_λ) and arbitrary vertical offsets in between the spectra for clarity. The morphological changes in the spectra around maximum light are significant, and occur on the timescale of days only. We will see in Chap. 6 that the phase of a SN Ia spectrum can in principle be determined without the additional information provided by the light curve, based on the spectral features alone.

It must be noted at this stage that such an evolutionary sequence of SN Ia spectra is not currently available for high-redshift objects. The reason being that surveys of high- z SN Ia are motivated by the cosmological applications of these objects (i.e. luminosity

distance measurements), which require the knowledge of the luminosity at maximum. Since a single spectrum is in principle needed to confirm a supernova as being of Type Ia, and considering the typical exposure times required to obtain a spectrum of such targets at high redshift (~ 1 h per spectrum at an 8–10 m-class telescope; [187], Appendix A), there is little motivation to obtain high signal-to-noise ratio multi-epoch spectra of high- z SN Ia. In fact, such observations would be a valuable tool to test for evolutionary effects in SN Ia spectra as a function of redshift and light-curve properties. Proposals to undertake such observations are currently being made (Richard Ellis, Chris Stubbs, Brian Schmidt; private communication), and will be a worthwhile contribution to the field.

2.2.2 Homogeneity *vs.* inhomogeneity in SN Ia spectra

Despite the apparent homogeneity of the SN Ia class and their successful use as distance indicators (see [40] for an early review), the appearance of peculiar events (both photometrically and spectroscopically) has drawn attention to the diversity amongst SN Ia, and in particular on their use as “standard candles” (see [164] for a review). The appearance of two peculiar events in the same year – the “over-luminous” (by ~ 0.4 mag in the V band) SN 1991T and “sub-luminous” (by ~ 2 mag in the V band) SN 1991bg – has prompted questions concerning the progenitor systems of SN Ia, and in particular whether additional progenitor systems should be invoked to explain the observed differences.

Branch et al. [35] compiled a set of 84 SN Ia spectra, and classified them into “normal”, “1986G-like”, “1991T-like”, and “1991bg-like”. As it turns out, the spectra of SN 1986G and 1991bg share similar characteristics, and can be grouped into a single spectroscopic subtype. In Fig. 2.10, we show spectra of “normal” SN Ia (*left panel*) around maximum light, characterized by strong lines of Ca II, Si II, and other intermediate-mass elements (S II, Mg II). The resemblance is indeed striking. In the right panel of Fig. 2.10, however, we show spectra of “peculiar” SN Ia (from top to bottom: SN 1986G, 1991T, 1991bg, 2000cx, 2002cx), which share little resemblance with “normal” SN Ia spectra.

Spectra of SN 1991T [81, 232, 256, 136, 196] are characterized by the near-absence of Ca II and Si II lines in the early-time spectra, and prominent high-excitation features of Fe III. The Si II, S II, and Ca II features develop during the post-maximum phases, and by a few weeks past maximum the spectra of “1991T-like” objects are comparable to those of “normal” SN Ia. Spectra of SN 1991bg [80, 169, 294, 195], on the other hand, are characterized by the presence of a broad absorption in the range $\sim 4100 - 4400$ Å due to lines of Ti II. The appearance of such a feature in “1991bg-like” spectra was explained by Nugent et al. [215] by a decrease in the “effective temperature” of such sub-luminous events. Conversely, the presence of high-excitation lines of Fe III in the “1991T-like” spectra is explained by an enhanced ejecta temperature in these over-luminous events. Thus, although these events spectroscopically differ from the majority of SN Ia events, they appear to fit a spectral sequence corresponding to a unique SN Ia paradigm. Photometrically, these peculiar objects also reproduced the relation between light-curve width and absolute magnitude at maximum: the light curves of the over-luminous “1991T-like” (under-luminous “1991bg-like”) objects are broad(narrow), with a slow(fast) post-

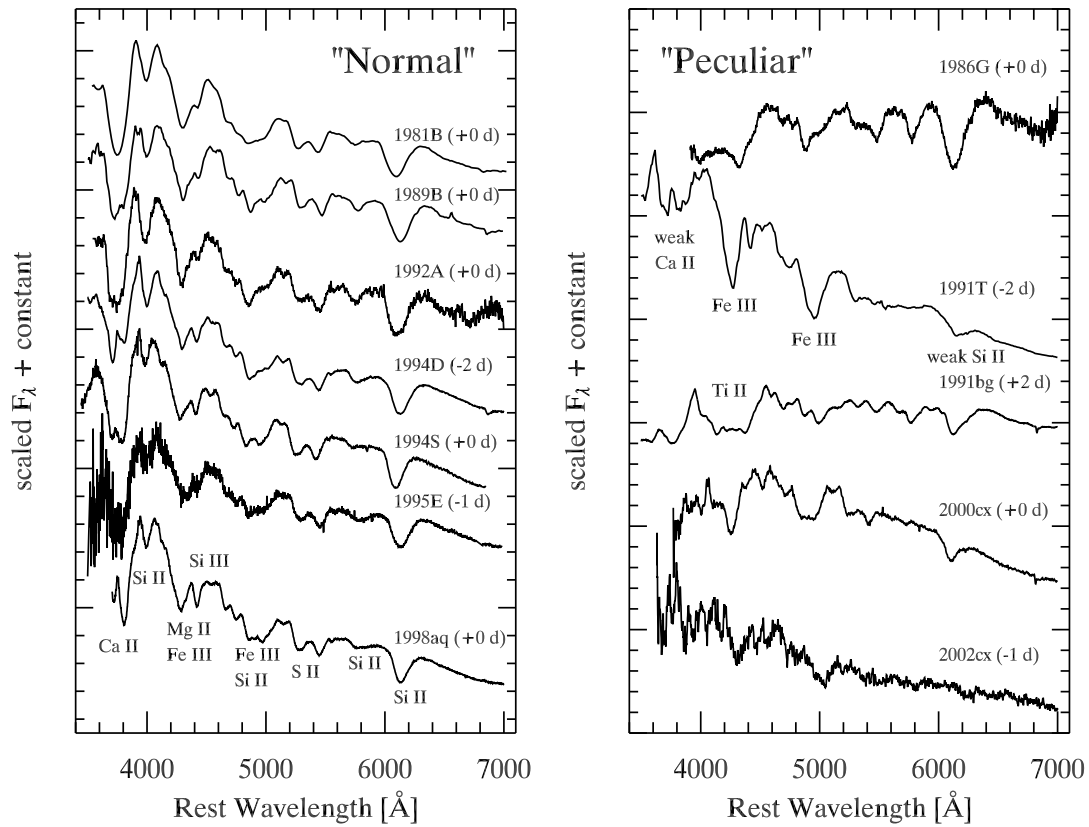


Figure 2.10: **Left panel:** Optical spectra of “normal” SN Ia [35] around maximum light. Their homogeneity is impressive. **Right panel:** Optical spectra of “peculiar” SN Ia around maximum light. There are noticeable differences with the “normal” SN Ia. Thus, the SN Ia class as a whole is not a homogeneous class.

maximum decline.

Recently, several objects classified as supernovae of Type Ia do not fit the above scheme. These are SN 2000cx [175] and SN 2002cx [174]. Spectra of these two supernovae around maximum light are shown at the bottom of Fig.2.10 (*right panel*). While the pre-maximum spectra of SN 2000cx resemble those of SN 1991T, the Si II lines that appear around maximum light remain strong several weeks past maximum. Moreover, the change in the excitation of iron lines is slower. SN 2002cx is even more bizarre, with early-time spectra dominated by lines of iron-group elements (as in the over-luminous SN 1991T), although the luminosity is comparable to the sub-luminous SN 1991bg. Li et al. [174] discuss the validity of the classification of this object as a SN Ia, although conclude in favour of such a classification, on the basis that “[the] photometric and spectral evolution [of SN 2002cx] can be grossly explained within the paradigm of SN Ia observations.”

Overall, one can say that the current classification scheme of supernovae is inappropriate, as spectral sub-types need to be invoked to explain the full range of observed properties. Whereas such “peculiar” objects are commonly found in local SN Ia searches ($\sim 1/3$ of all SN Ia in the sample of Li et al. [176]), they are a lot more rare in high- z SN Ia samples (2/46 “1991T-like” objects in the ESSENCE spectroscopic sample of Matheson et al. [187]; Appendix A). Whether this is due to a selection effect, to the relatively poor quality of high- z SN Ia observations, or to an evolutionary effect in the SN Ia sample needs to be clearly understood, as any systematic bias will affect the inferred cosmological parameters.

2.3 Observations of Type Ia supernovae and data reduction

This Chapter on optical spectra of SN Ia ends on a more technical note with the description of discovery and spectroscopic follow-up of high-redshift SN Ia, as well as a brief overview of the standard spectral data reduction procedure. The section ends with the presentation of a novel method to extract supernova spectra, discussed at length in the next chapter (Chap. 3).

2.3.1 Discovery of a supernova and spectroscopic follow-up

Finding a supernova at high-redshifts is no easy task. At $z \sim 0.5$, the peak apparent magnitude of a “normal” SN Ia in the R -band is $m_R \gtrsim 22$ mag, while this drops to $m_R \gtrsim 23$ mag at $z \sim 0.7$ (see [291], Table 7). Thus, although high- z SN Ia surveys are limited by the magnitude of the faintest objects, it is the exposure times in a given filter that will constrain the redshift distribution of the sample. For the ESSENCE project, which aims to discover ~ 200 SN Ia in the redshift range $0.2 \leq z \leq 0.8$ in the course of five years (see Chap. 1), Miknaitis et al. [201] found that relatively short exposure times in R (~ 200 s with the Mosaic II camera on the 4 m Blanco telescope at the Cerro-Tololo

Inter-American Observatory²) was the best compromise between availability of telescope resources and photometric signal-to-noise ratio.

The technique used to discover distant supernovae is fairly basic: one images the same region of the sky repeatedly over several weeks, and subtracts an older image (or a combination thereof), known as the “template image”, from the more recent one (potentially the “discovery” image). Any positive residuals in the difference image will be the signature of a photometric variation in the new image. Residuals that do not have a recognizable point spread function, and that are thus not point-like sources, are immediately discarded by the observer. These are often due to poor subtractions, diffraction spikes in bright stars, or cosmic rays. To determine whether the object is a supernova of Type Ia, one has to continue monitoring the photometric evolution of the variable object, and make sure the light curve shape, magnitude, (and colour, when images in at least two filters are taken) are compatible with that of SN Ia in the local universe. In Fig. 2.11, we show the template (*left*), discovery (*middle*), and difference (*right*) images for two transient events monitored by the ESSENCE project, later spectroscopically confirmed to be supernovae of Type Ia. Although images are systematically taken in two filters (R and I), we show in Fig. 2.11 the R -band images, corresponding to exposure times of 200 s.

To maximise the efficiency with which SN Ia are discovered, the ESSENCE project has selected ~ 25 fields in which transient events are discovered and followed-up photometrically. These fields are monitored every four days during the search period (October – December each year), such that new supernovae are discovered in fields where previously discovered supernovae are being monitored – a technique known as a “rolling search” (see Smith et al., in prep, for more details on the ESSENCE observing strategy). This way, new SN Ia are continuously discovered, and well-sampled light curves are elaborated. One can then determine the magnitude of the SN Ia at maximum light, and derive the corresponding distance modulus (see Chap. 1).

Even with photometric constraints on the nature of a transient event (light curve, magnitude, colour), one needs a spectrum to confirm the event to be a supernova of Type Ia. Despite the great care that is taken to select the subset of transient events that are most likely to be SN Ia (based on the photometric properties), after a spectrum is taken several objects turn out to be variable events of another nature (Active Galactic Nuclei, variable stars, Type II/Ib/Ic supernovae – see [187]; Appendix A). In Fig. 2.12, we show the finder chart for the ESSENCE object d033.waa6_10, later confirmed by a spectrum to be a supernova of Type Ia at $z = 0.524$. Such finder charts are used by observers at telescopes used for the spectroscopic follow-up to locate the target of interest.

The ESSENCE project uses several large-aperture ground-based telescopes for the spectroscopic follow-up of their targets: Keck (10 m; Mauna Kea, Hawaii); Very Large Telescope (VLT, 8 m; Cerro Paranal, Chile); Gemini North & South (8 m; Mauna Kea, Hawaii [*Gemini North*] and Cerro Pachón, Chile [*Gemini South*]); Magellan Baade & Clay (6.5 m; Las Campanas Observatory, Chile). In Fig. 2.13, we show a picture (*left panel*) of one of the four Very Large Telescopes, and of the FOCal Reducer/low dispersion Spectrograph

²CTIO - see <http://www.ctio.noao.edu/>

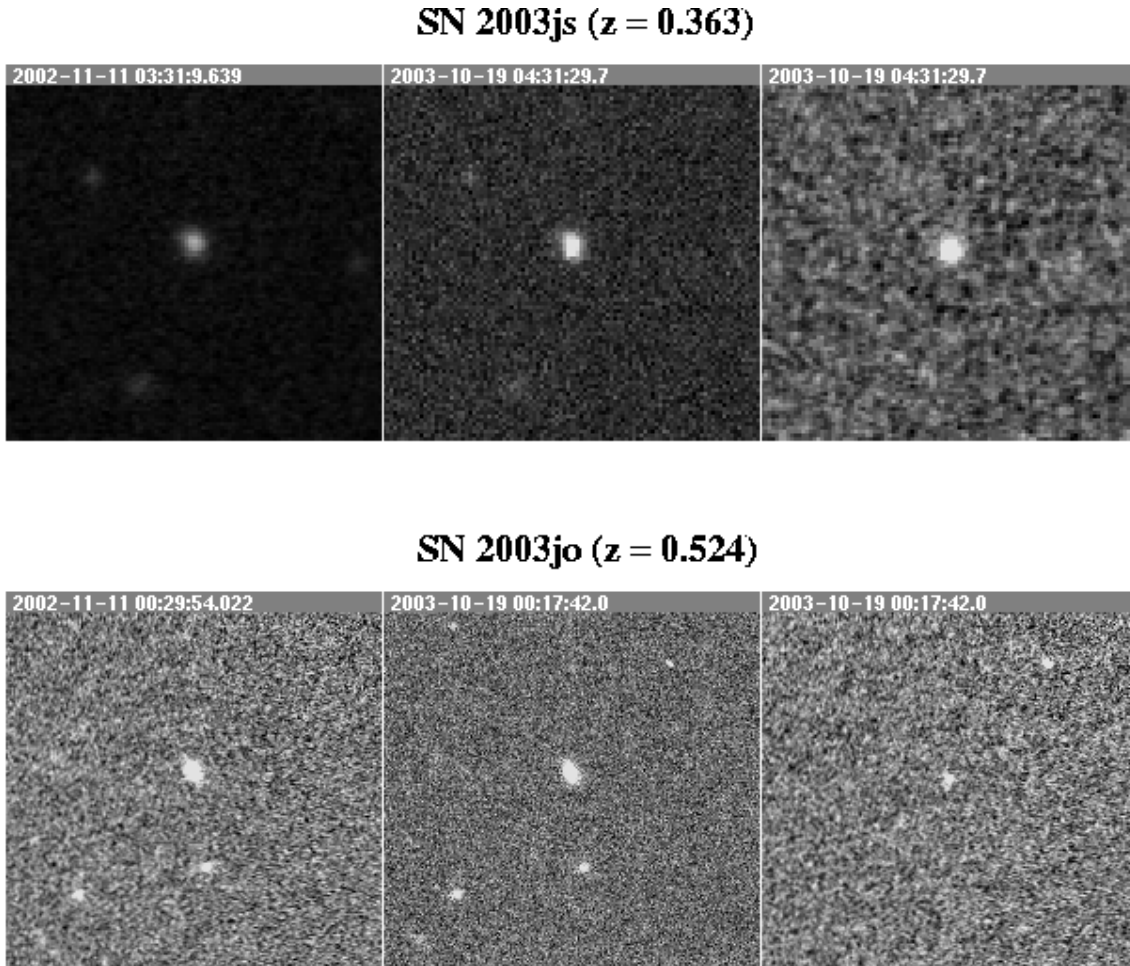


Figure 2.11: Discovery of two transient events from the ESSENCE project using difference imaging (SN 2003js, $z = 0.363$, *upper panel*; SN 2003jo, $z = 0.524$, *lower panel*). For each supernova, we show the template image (taken on 11 Nov 2002; *left*), the discovery image (taken on 19 Oct 2003; *middle*), and the difference between the discovery and template images (*right*), revealing the transient event as a positive residual signal. Both transient events were later confirmed to be SN Ia using spectra obtained with VLT+FORS1. Images courtesy ESSENCE project (see <http://www.ctio.noao.edu/essence/sne/sn2003.html>).

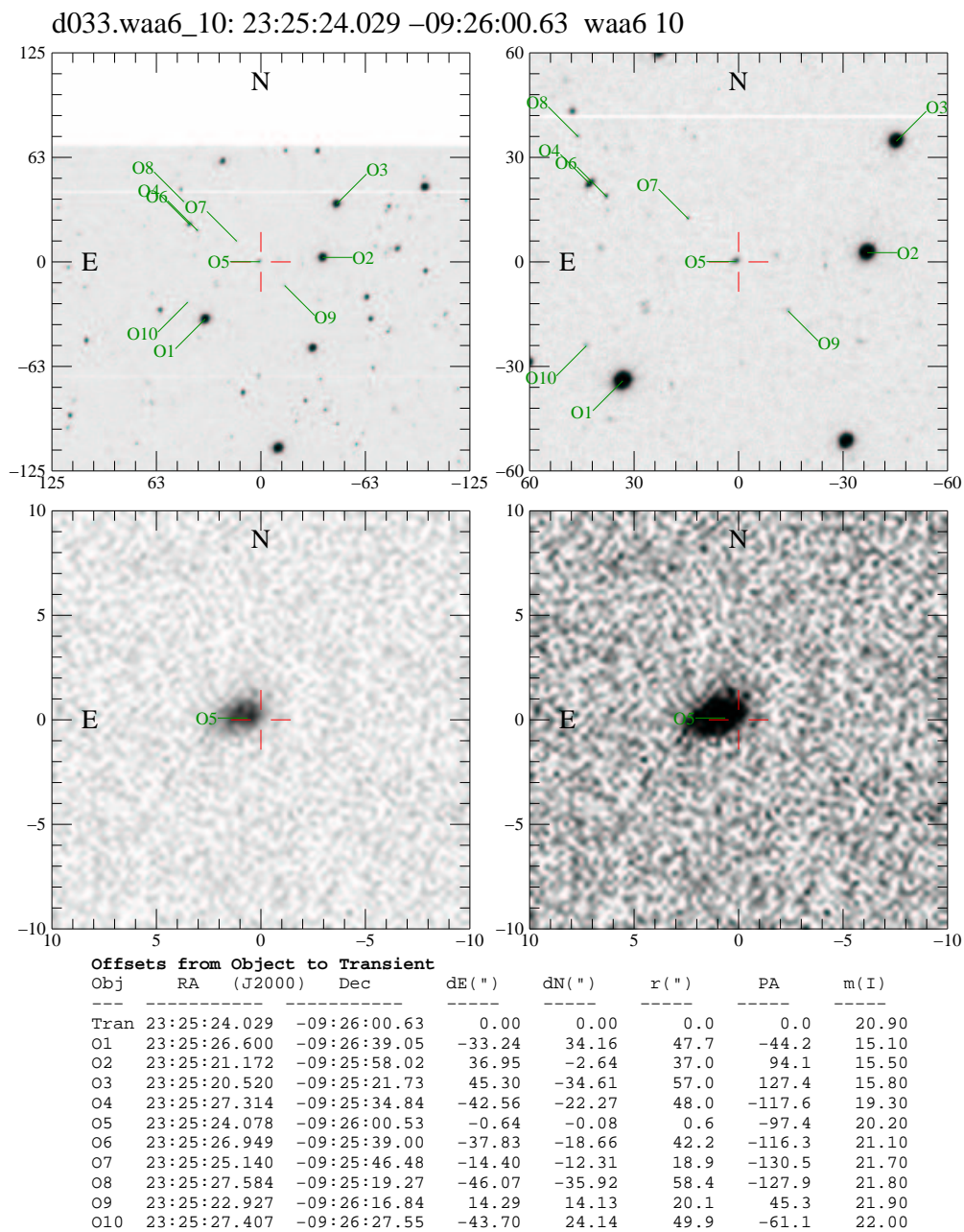


Figure 2.12: Finder chart for the ESSENCE object d033.waa6_10, later confirmed by VLT+FORs1 spectra to be a supernova of Type Ia at $z = 0.524$. The transient event is marked by a red target cross in each of the four panels (which progressively zoom in – from top to bottom and left to right – onto the transient object). Reference targets are also marked in green to facilitate the identification of the transient target whilst at the telescope. Finder charts for all ESSENCE supernovae are publicly available on the ESSENCE web page (<http://www.ctio.noao.edu/essence/>).

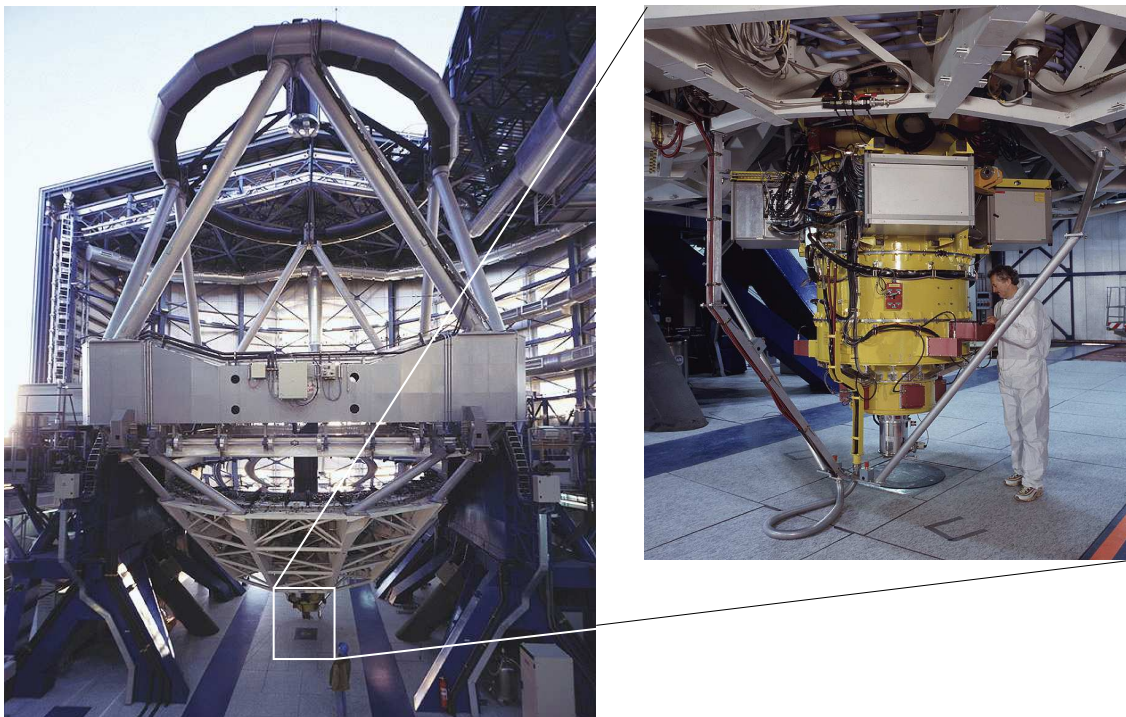


Figure 2.13: **Left:** Very Large Telescope (VLT) Unit Telescope 2 (UT2; “Kueyen”) at the European Southern Observatory (ESO) Paranal observatory in Chile. **Right:** FOcal Reducer/low dispersion Spectrograph (FORS) 1 mounted at the Cassegrain focus of the telescope (now UT1 “Antu”). (credits: European Southern Observatory; see <http://www.eso.org/outreach/gallery/vlt/>).

(FORS) 1 (*right panel*) used to take spectra of several ESSENCE SN Ia.

2.3.2 Standard approach to reducing supernova spectra

The following sections describe the reduction of CCD images and extraction/calibration of spectra taken with the VLT+FORS1 (see [25]). The wavelength coverage of the spectra ($\sim 4500 - 8500 \text{ \AA}$ for a 300V grism with an OG435 filter) was chosen so as to include most of the defining spectroscopic characteristics of SN Ia – namely S II, Si II, and Ca II H&K – up to redshifts of $z \sim 0.8$. The FORS1 instrument was chosen for its optimal sensitivity. Long-slit spectroscopy (LSS) mode was chosen since we are essentially following a single object at a time, excepting the cases where a spectrum of the host galaxy can be obtained. In this case one also obtains spatial information, namely the position of the supernova with respect to the galaxy. The $1''$ slit is usually positioned so as to include one bright object in the field for reference.

The reader should keep in mind the standard character of this reduction procedure, which is essentially the same for any long-slit spectroscopy observation. Most of the data are extracted using the optimal algorithm of Horne [129], implemented in many standard

software packages (e.g., IRAF³ or MIDAS⁴). A novel method based upon Richardson-Lucy restoration (Chap. 3 [27]) is employed to extract the VLT spectra presented in Sect. 2.3.3.

From raw to extracted: a brief overview of spectral reduction steps

Despite being the most efficient light detectors available to astronomers (quantum efficiencies, or QE \gtrsim 90% – cf. 3% for photographic plates), modern CCDs are still prone to additive effects that need to be removed via the appropriate calibration frames. The output signal has added a pedestal level of several hundred ADUs (Analogue to Digital Units), which can be removed using data in the overscan region of the chip, typically the first and last few columns on the chip in the case of FORS1. This bias level needs to be determined for each frame individually since it is not stabilized and can vary slightly due to differences in temperature and telescope position. Any residual variation in the bias level can be removed by making use of frames obtained with zero integration time – known as “bias frames”.

The CCD images are then flat-fielded. Since variations in sensitivity are multiplicative across the chip, one needs to divide by the pixel-to-pixel gain variations, as well as the larger-scale spatial variations in the case of long-slit spectroscopy. This is done by taking large-count exposures of a uniformly illuminated surface (known as a “flat-field” image), typically a uniformly illuminated screen.

In a CCD, radioactive decays in the material of the camera can penetrate the CCD detector and cause huge variations in counts from one pixel to the next. These sharp noise spikes are misleadingly referred to as “cosmic rays” in the astronomer’s jargon. One can remove this effect by linearly interpolating across pixels that show a significant difference in the number of detected counts with respect to their neighbours, or by comparing several frames of the same object and discarding any high signal that does not appear on all frames. We detect and remove cosmic rays in the VLT+FORs1 data using the algorithm of Pych [239]. The result of applying this algorithm to a raw 2D spectrum is shown in Fig. 2.14. The upper panel shows the input spectrum, whilst the middle and lower panels show the output spectrum and the cosmic rays detected by the algorithm, respectively.

Emission lines ([O I], OH, Na I_D) from the night sky will show up as bright lines in the spatial direction, and are the dominant source of noise in optical ground-based spectra. They can be removed using a polynomial fit to the 2D spectra in the spatial direction, although bright saturated sky lines will leave an imprint in the extracted 1D spectrum, and should not be confused with emission lines from the host galaxy.

Once these preliminary reduction steps have been applied to the raw 2D spectrum, one can then extract a 1D spectrum (in ADUs *vs.* dispersion coordinate) by summing up the spectral trace in the spatial direction. These steps are illustrated in Fig. 2.15, where we

³IRAF is distributed by the National Optical Astronomy Observatories, operated by the Association of Universities for Research in Astronomy, Inc., under contract to the National Science Foundation of the United States.

⁴ESO-MIDAS is a registered trademark of the European Southern Observatory; see <http://www.eso.org/projects/esomidas/>.

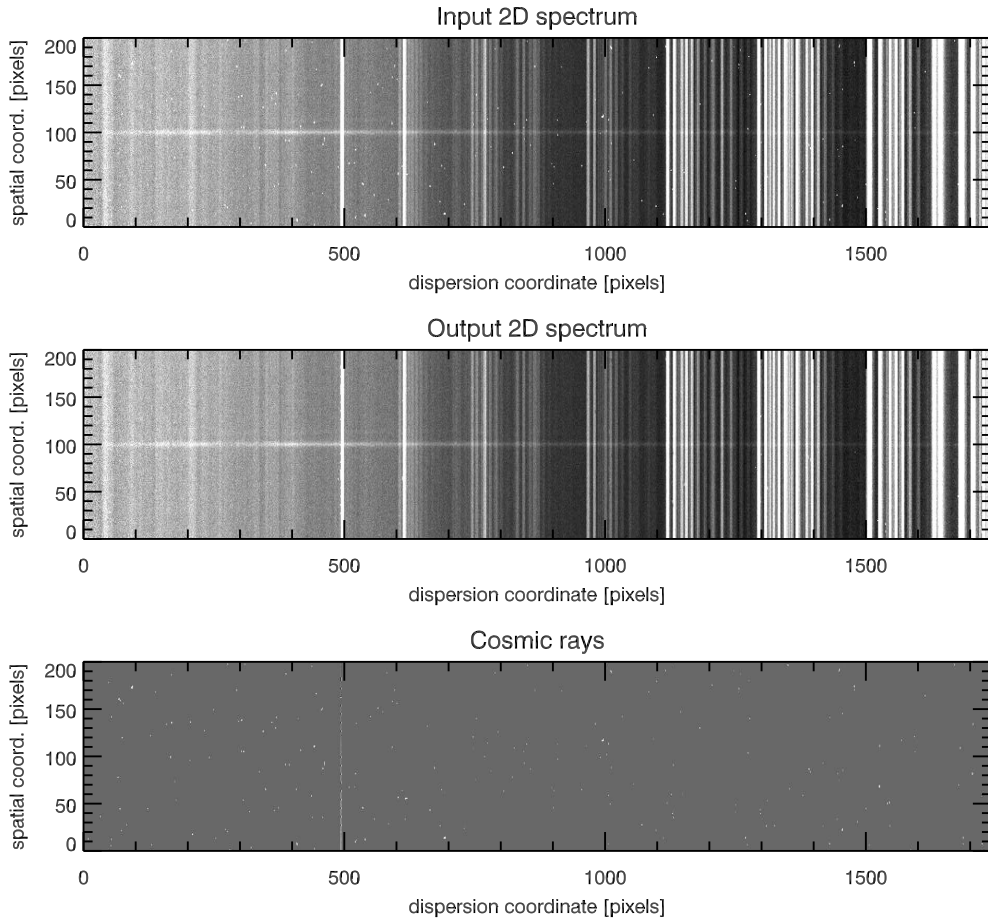


Figure 2.14: Cosmic-ray removal in a two-dimensional spectrum, using the algorithm of Pych [239]. We show the input (*upper panel*) and output (*middle panel*) spectra, as well as the cosmic rays detected by the algorithm and removed from the input image (*lower panel*). Note how the saturated sky line at dispersion coordinate ~ 500 pixels has been detected as a “cosmic ray” by the algorithm.

show the input “raw” 2D spectrum (*upper panel*), the reduced (bias corrected, flat-fielded, cosmic ray-cleaned, background-subtracted) 2D spectrum (*middle panel*), and finally the extracted 1D spectrum (*lower panel*). Final reduction steps include wavelength and flux calibration of the 1D spectrum, and are described below.

Wavelength calibration

To convert the dispersion coordinate from pixels to wavelength, we use a calibration arc lamp – a Copper, Helium, Neon and Argon (CuHeNeAr) lamp for FORS1 observations. Taking a spectrum of this lamp produces a series of narrow emission lines that can be identified and compared with a line list, which in turn allows for the wavelength calibration of the extracted 1D spectrum. In Fig. 2.16 we show the spectrum of such an arc lamp (here a HeNeAr lamp), with identification of the most prominent emission lines. The correspondence between pixel and wavelength coordinate can accurately be derived from such spectra, with typical RMS uncertainties $\lesssim 0.5 \text{ \AA}$.

Flux calibration

For most astronomical purposes it is necessary to determine the *absolute* flux incident on the detector as a function of wavelength. To do this one takes a spectrum of a well-known spectroscopic standard star (for which the spectral energy distribution is well determined), and correlates the number of counts with the independently determined flux from that object. The outcome of this exercise is a sensitivity function that is subsequently used to flux calibrate the out-coming spectra. We show a 1D spectrum of the spectrophotometric standard star EG 21 [109], as observed with the VLT+FORs1, in the upper panel of Fig. 2.17 (*red line*). A sensitivity function (here in units of $2.5 \times \log_{10} [\text{counts s}^{-1} \text{ \AA}^{-1}] / [\text{erg s}^{-1} \text{ cm}^{-2} \text{ \AA}^{-1}]$; *lower panel*) is calculated based on the comparison of this spectrum with the accurately tabulated synthetic fluxes (*upper panel, black line*) by Hamuy et al. [109]. Dividing the extracted 1D spectrum by the sensitivity function (after appropriate scaling for the exposure time) will produce a 1D spectrum calibrated in flux, per unit wavelength in this case.

Finally, the wavelength and flux calibrated 1D spectra can be corrected for extinction by dust grains in our Galaxy (using the dust maps of Schlegel et al. [268]) and in the supernova host galaxy (using the reddening $E(B - V)$ value determined from a fit to the SN light curve), and corrected for the heliocentric velocity of the supernova (which consists in scaling the wavelength axis by a factor $(1 + z)^{-1}$).

2.3.3 A novel method to extract SN spectra

An alternative to the algorithm of Horne [129] for extracting 1D spectra has been suggested by Lucy and Walsh [185] and applied to supernova spectra by Blondin et al. [27] (Chap. 3). The algorithm is based on the Richardson-Lucy iterative restoration method [243, 183], and implemented in the IRAF code *specinholucy* [185]. This new technique enables us to

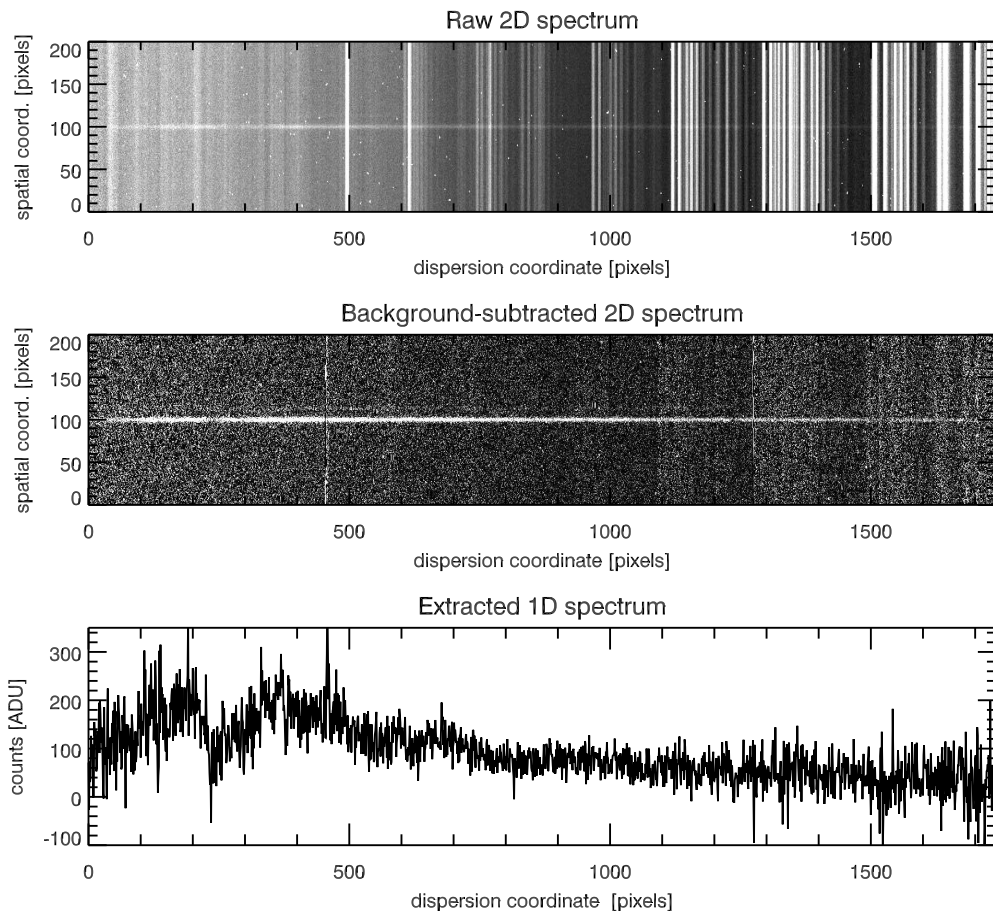


Figure 2.15: Extraction of a 1D spectrum from a 2D raw image, obtained with the VLT+FORs1 during the 2002 ESSENCE campaign [25]. **Upper panel:** Raw two-dimensional spectrum as detected by the FORs1 CCD. The abscissa corresponds to the dispersion axis (wavelength increasing to the right, whilst the spatial axis is on the ordinate). The faint trace at spatial coordinate ~ 100 pixels is the spectrum we want to extract. The vertical lines correspond to emission ([O I], OH, Na I δ), from the night sky (see [219]). **Middle panel:** The raw 2D image has now been flat-fielded and corrected for bias (see text for details). Cosmic rays have also been removed using the algorithm of Pych [239] (see Fig. 2.14). The background (sky emission lines) has been removed, revealing the spectral trace. **Lower panel:** The spectral trace in the middle panel has been collapsed in the spatial direction over a ~ 10 pixel-wide extraction window centered on the trace. The ordinate is in units of ADU (Analogue to Digital Unit), which correspond to the number of photo-electrons generated in the CCD within a gain factor ($1.47 \text{ e}^-/\text{ADU}$ here). The spectrum is that of Type Ia supernova SN 2002jw ($z = 0.356$; see [187], Appendix A).

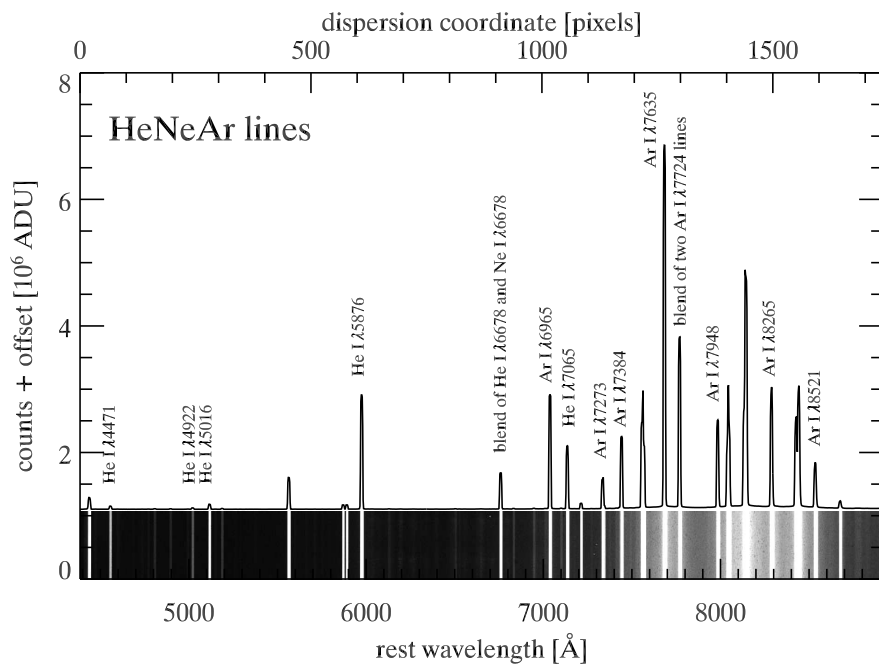


Figure 2.16: Wavelength calibration of spectra using a helium-neon-argon (HeNeAr) lamp. The 2D spectrum is shown as a band in the lower part of the plot. Lines are identified from a HeNeAr line list and a dispersion solution is computed using the dispersion coordinate in pixels. The HeNeAr 1D spectrum has been vertically offset by 1.1×10^6 ADU for clarity.

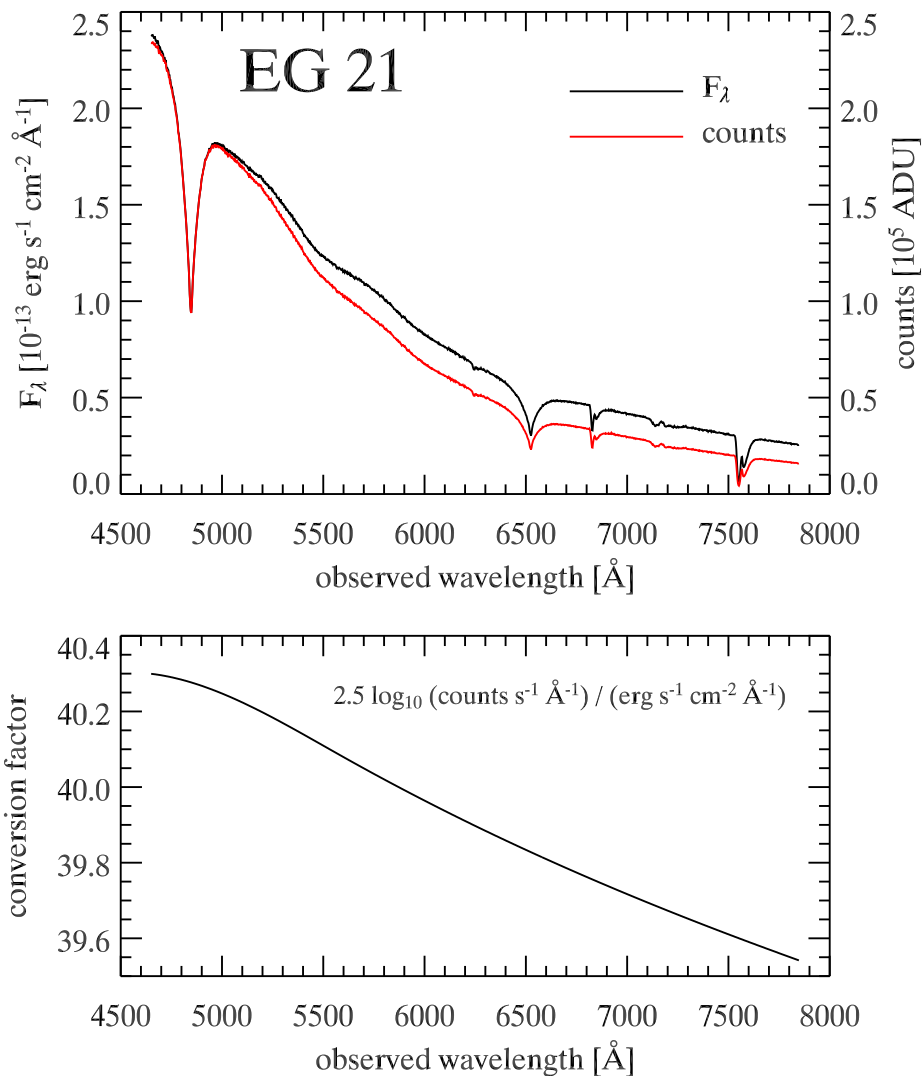


Figure 2.17: Flux calibration of spectra using the EG 21 spectrophotometric standard star [109]. A sensitivity function (here in units of $2.5 \times \log_{10} [\text{counts s}^{-1} \text{ \AA}^{-1}] / [\text{erg s}^{-1} \text{ cm}^{-2} \text{ \AA}^{-1}]$; *lower panel*) is calculated based on the comparison of an extracted spectrum of EG 21 in counts *vs.* wavelength (*upper panel, black line*) with the accurately tabulated synthetic fluxes (*upper panel, red line*) by Hamuy et al. [109].

extract the spectrum of a supernova from that of the contaminating background of its host galaxy (“two-channel” restoration).

In the top panel of Fig. 2.18, we show a reduced, wavelength calibrated, 2D spectrum, that will serve as an input to the *specinholucy* code. The middle panel shows the restored 2D spectrum of the background, revealing the spectrum of the supernova host galaxy. The lower panel shows a plot of the restored 1D spectrum. The spectrum is a lot “cleaner” than the optimally-extracted version of this same spectrum, shown in the lower panel of Fig. 2.15.

All the VLT SN Ia spectra presented by Matheson et al. [187] (Appendix A) were reduced using this two-channel restoration algorithm. For completeness, we show these 21 SN Ia spectra in Figs. 2.19–2.21, in increasing redshift (from top to bottom in each of the plots). The 1D restored spectra are plotted as black lines, and a low-redshift SN Ia spectrum is overplotted (*red line*) for comparison.

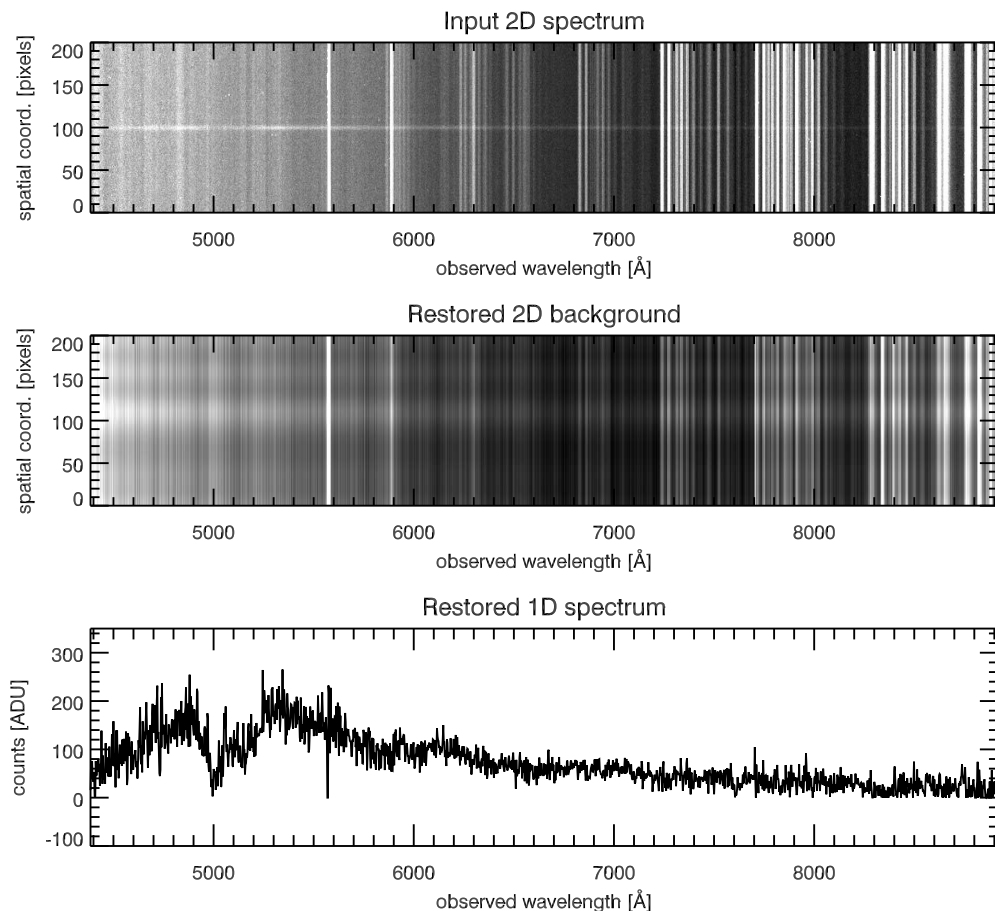


Figure 2.18: Two-channel restoration of a 2D spectrum employing the Richardson-Lucy iterative restoration method [243, 183], and implemented in the IRAF code *specinholucy* [185]. This new technique enables us to extract the spectrum of a supernova from that of the contaminating background of its host galaxy (see [27]). **Upper panel:** Input two-dimensional spectrum, corresponding to a bias corrected, flat-fielded, cosmic-ray cleaned, and wavelength-calibrated version of the raw 2D spectrum in Fig. 2.15 (*upper panel*). **Middle panel:** Restored two-dimensional background spectrum. The broad trace centered on spatial coordinate ~ 100 pixels is the underlying host-galaxy spectrum. **Lower panel:** Restored one-dimensional spectrum using *specinholucy*. The quality of the spectrum is enhanced with respect to more traditional spectral extraction methods (cf. Fig. 2.15, *lower panel*).

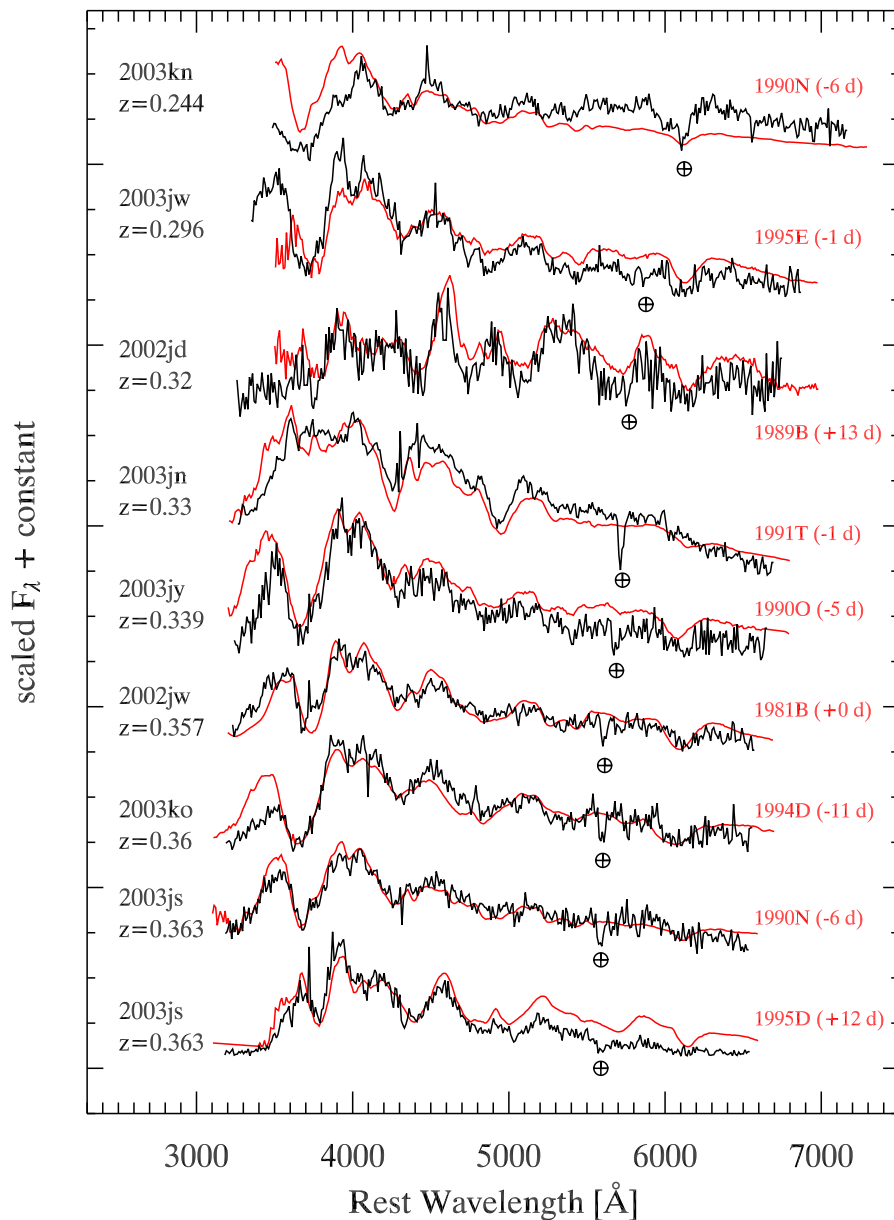


Figure 2.19: Rest-wavelength spectra of high-redshift ($0.2 < z \leq 0.4$) Type Ia supernovae (black line) taken with VLT+FORS1 for the ESSENCE 2002-2003 campaigns. All the spectra were reduced using the two-channel restoration method of Lucy and Walsh [185] and applied to supernova spectra by Blondin et al. [27], so as to reduce contamination by host-galaxy light (see also Fig. 2.18). The spectra have *not* been de-reddened. Each high-redshift spectrum is overplotted (red line) by a low-redshift SN Ia for comparison. The low-redshift SN Ia used for comparison corresponds to the best-fit local template spectrum as determined by our cross-correlation algorithm (SNID; Blondin et al., in prep – see Chap. 4). In addition, each spectrum is labeled with the IAU identification number and the deduced redshift ([187]; Appendix A). The de-redshifted location of the A-band atmospheric absorption feature is indicated with a telluric symbol. The flux scale is F_λ with arbitrary additive offsets between the spectra.

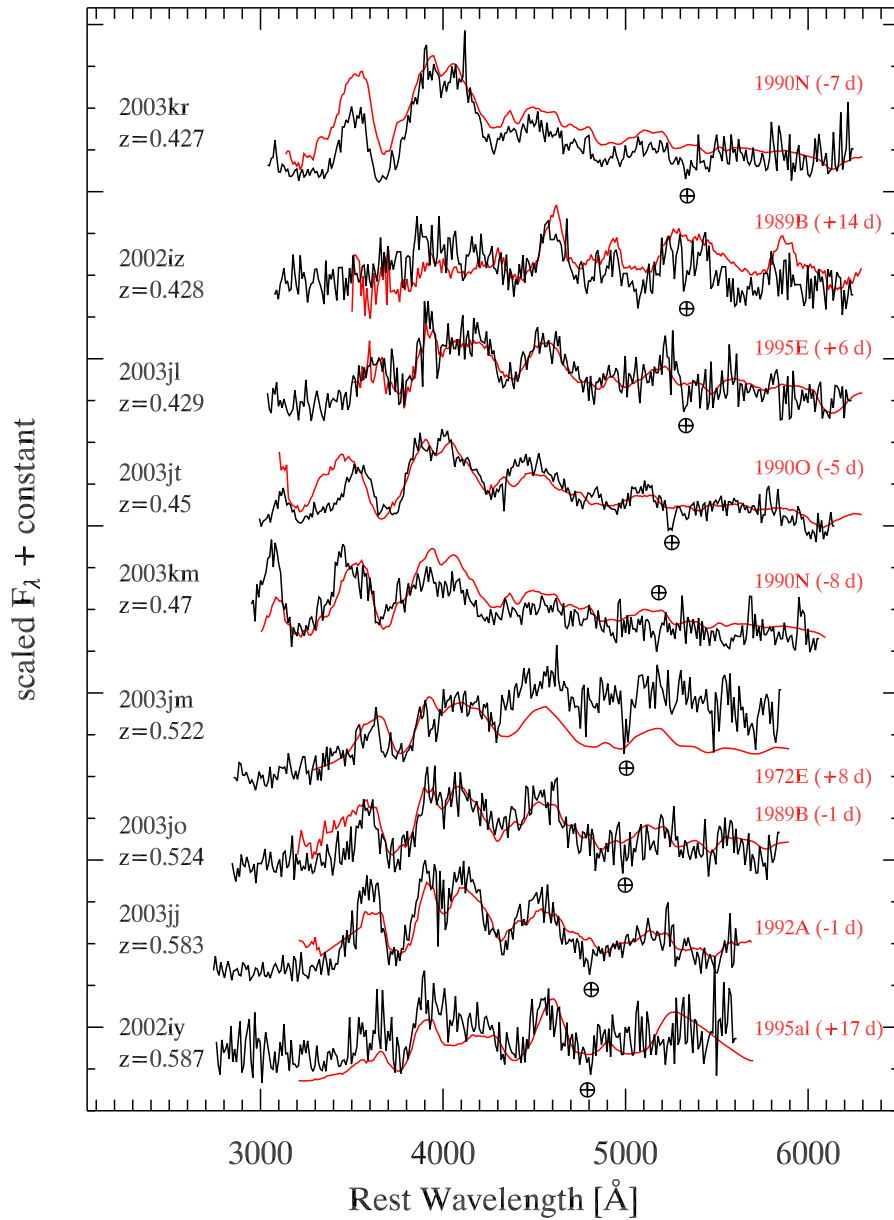


Figure 2.20: Rest-wavelength spectra of high-redshift ($0.4 < z \leq 0.6$) Type Ia supernovae (black line) taken with VLT+FORIS1 for the ESSENCE 2002-2003 campaigns. See Fig. 2.19 for details.

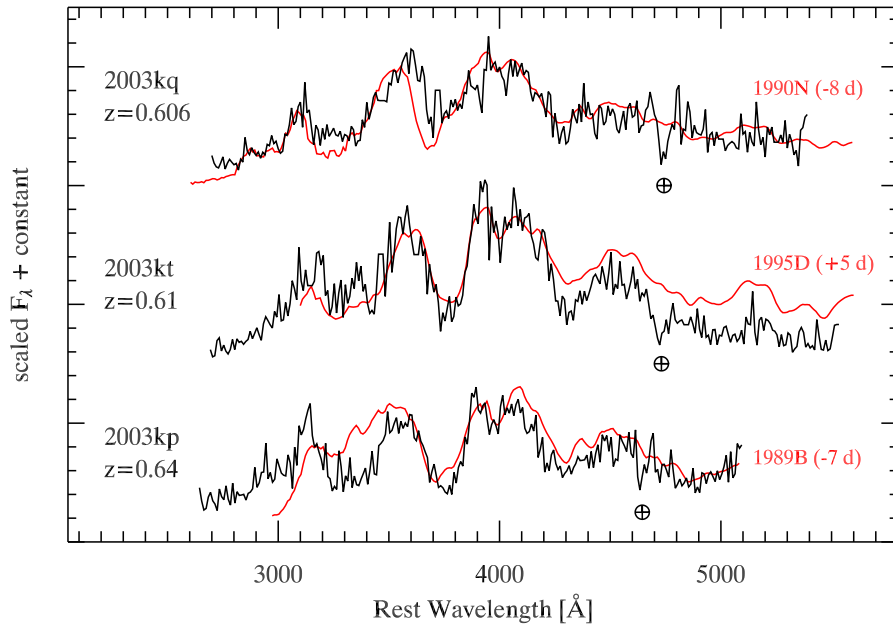


Figure 2.21: Rest-wavelength spectra of high-redshift ($z > 0.6$) Type Ia supernovae (*black line*) taken with VLT+FORs1 for the ESSENCE 2002-2003 campaigns. See Fig. 2.19 for details.

*For filth and elde, also may I thee,
Be greate wardens upon chastity.
Geoffrey Chaucer (The Wife of Bath and her Tale)*

Chapter 3

Extracting clean supernova spectra

Towards a quantitative analysis of high-redshift Type Ia supernova spectra

Stéphane Blondin, Jeremy R. Walsh, Bruno Leibundgut, and Grégory Sainton
Astronomy & Astrophysics, **431**, 757 (2005)

Abstract: We use a new technique to extract the spectrum of a supernova from that of the contaminating background of its host galaxy, and apply it to the specific case of high-redshift Type Ia supernova (SN Ia) spectroscopy. The algorithm is based on a two-channel iterative technique employing the Richardson-Lucy restoration method and is implemented in the IRAF code *specinholucy*. We run the code both on simulated (SN Ia at $z = 0.5$ embedded in a bright host galaxy) and observed (SN Ia at various phases up to $z = 0.236$) data taken with VLT+FORS1 and show the advantages of using such a deconvolution technique in comparison with less elaborate methods. This paper is motivated by the need for optimal supernova spectroscopic data reduction in order to make meaningful comparisons between the low and high-redshift SN Ia samples. This may reveal subtle evolutionary and systematic effects that could depend on redshift, and bias the cosmological results derived from comparisons of local and high- z SN Ia in recent years. We describe the various aspects of the extraction in some detail as guidelines for the first-time user and present an optimal observing strategy for successful implementation of this method in future high- z SN Ia spectroscopic follow-up programmes.

3.1 Introduction

The initial claim made by two independent teams – the High-Z Supernova Search Team [270] and the Supernova Cosmology Project [226] – that the apparent dimming of Type Ia supernovae (SN Ia) at redshifts of $z \approx 0.5$ implies a present accelerating expansion of the universe [244, 226], and its subsequent confirmation with improved precision [291, 152, 14], have prompted an increased interest in these astrophysical events. On the theoretical side,

much effort and computing time has been devoted to multi-dimensional modelling of the explosion in order to provide physical input parameters for spectral synthesis calculations (see [117] for a review). On the observational side several teams are currently using SN Ia both to probe the decelerating expansion at higher ($z \gtrsim 1$) redshifts – the Hubble Higher- z Supernova Search [253] – and to measure second order effects (the equation-of-state parameter $\omega = p/\rho c^2$) at intermediate ($0.2 \lesssim z \lesssim 0.8$) redshifts – such as ESSENCE [201, 187] and the CFHT SuperNova Legacy Survey, or SNLS [217].

However, the physical parameters governing the SN Ia explosion mechanism are today not fully understood and the empirical parametrization of the entire SN Ia class – the so-called “Phillips relation” (see [229]) – has no physical basis. The aforementioned observational programmes will detect several hundreds of high- z SN Ia, at which stage the statistical errors in the sample will have reached the systematic error floor. The cosmological effect detected via observations of Type Ia supernovae is indeed a subtle one (see [165] for a review) and the field is limited by the systematic errors involved in such measurements and their possible evolution with redshift.

Spectroscopy is an ideal way to probe these potential evolutionary effects through systematic comparison of high- z SN Ia spectra with local templates. This requires the extraction of clean SN Ia spectra devoid of background contamination, mainly by the host galaxy and sky lines (for ground-based observations). For high signal-to-noise (hereafter S/N) cases, when the supernova is bright with respect to its immediate underlying background, standard extraction software will in general work well. However, when the supernova is faint compared to the background, e.g. at late phases, heavily superposed on its host galaxy or simply at a high redshift, a more elaborate technique is required to ensure that we are not extracting non-SN flux.

The purpose of this paper is to test such a method that has been implemented in the IRAF¹ code *specinholucy* [185]. It is based on a two-channel restoration algorithm that restores a point spread function (PSF)-like component in a 2D image and an underlying extended background *separately*. It is of wide astronomical use and has already been successfully applied to the restoration of point-source spectra in highly inhomogeneous backgrounds (see [185]), such as is often the case for high- z SN Ia embedded in their host galaxy. The fact that the entire 2D spectrum of the background (with or without the inclusion of the restored point source spectrum) is restored in such an algorithm means that we have a firm hold on potential systematic errors associated with the restoration. This is done by simply comparing the residuals in the restored 2D spectrum with the statistical noise limit of the input 2D spectrum (the square root of the number of photoelectrons). Should these residuals fall below this limit then we can consider the restoration to be successful. This is a clear advantage over traditional spectral extraction routines where no secure hold on systematic errors is possible. Furthermore, the very nature of the algorithm presented in this paper implies that all non PSF-like components in the input

¹IRAF is distributed by the National Optical Astronomy Observatories, operated by the Association of Universities for Research in Astronomy, Inc., under contract to the National Science Foundation of the United States.

2D spectrum are automatically allocated to the background channel. We are making no *a priori* assumptions on the nature of the contaminating extended background component and only rely on the point-like nature of the supernova’s spatial profile.

In Sect. 3.2 we present the algorithm and its application to the case of supernovae embedded in their host galaxy. We dedicate Sects. 3.3 and 3.4 to the specific issues of the PSF spectrum – or slit spread function (SSF) – used to restore the point source and of the spatial resolution kernel used to discriminate between the point source and the underlying extended background, respectively, as they are of crucial importance to the proper functioning of *specinholucy*. In Sects. 3.5 and 3.6 we test the algorithm on simulated and observed data, respectively. Section 3.7 serves the purpose of comparing our technique to alternative spectral extraction methods, and we further discuss the advantages of using our approach alongside an optimal observing strategy for its successful implementation in Sect. 3.8.

The need for comparisons between the high- z and the local SN Ia spectra in order to make quantitative statements on their potential differences requires the use of such an elaborate two-channel deconvolution technique. The code *specinholucy* enables a truly quantitative analysis of high- z SN Ia spectra and opens the path for meaningful detections of potential evolutionary signatures in their spectra.

3.2 The algorithm and its implementation

3.2.1 Decomposing the SN from its host galaxy

Lucy and Walsh [185] – subsequently LW03 – have described two iterative techniques for decomposing a long-slit spectrum into spectra of designated point sources and an underlying background. The methods are based on a two-channel restoration [128, 184] using the Richardson-Lucy [243, 183] iterative restoration. The essence of this technique is to treat the point source(s) and the extended background as two channels for restoration. It must be emphasized at the outset that this restoration occurs purely in the spatial direction and no implied spectral restoration is undertaken. Thus, for instance, residuals from fringing corrections should not be relevant unless the fringes are tilted with respect to the dispersion axis, in which case an additional inhomogeneous component would be added to the background. The first channel contains the point source(s) which are restored to delta functions using an appropriate PSF. For a spectrum the PSF must be specified as a function of wavelength; this is simply the aforementioned SSF in Lucy and Walsh [185]. In order to iteratively restore the extended component, it is necessary to impose a limiting resolution, larger than that set by the PSF, in order to prevent the second channel from modelling the point sources as peaks in the extended component. The resolution limit for the background is set by defining the restored background to be the convolution of a non-negative auxiliary function with a wavelength-independent resolution kernel R . Then no feature whose width is less than R can appear in the restored background. If the width of R is greater than the PSF, then the convolution of the model of the extended background

ψ with the PSF cannot fit a point source, which must therefore be modelled by the first channel.

Two methods are described in LW03: one for a homogeneous background (i.e. the spectrum of the background is homogeneous - does not vary with position); the second, more general, case allows the spectrum of the background to vary as a function of position along the slit - termed the inhomogeneous background case. In the case of a galaxy including an SN the inhomogeneous case is appropriate. The observed spectrum $\phi(\lambda, y)$, where λ is the dispersion direction and y the cross-dispersion direction, can then be modelled as:

$$\phi(\lambda, y) = \int F(\lambda, \eta)P(\lambda, y - \eta)d\eta + f_{\text{SN}}(\lambda)P(\lambda, y - y_{\text{SN}}), \quad (3.1)$$

where η is the independent variable for the spatial dimension (cross dispersion direction). The first term represents the spectrum of the background and the second represents the spectrum of the SN. In this study it is $f_{\text{SN}}(\lambda)$, the spectrum of the SN, which is the desired output product. $P(\lambda, y - \eta)$ is the SSF, i.e. a PSF as a function of wavelength. The restored background, ψ , is a convolution of a non-negative auxiliary function $\chi(\lambda, \zeta)$ and the non-negative normalized resolution kernel centred at $\eta = \zeta$, $R(\eta - \zeta)$:

$$F(\lambda, \eta) = \int \chi(\lambda, \zeta)R(\eta - \zeta)d\zeta, \quad (3.2)$$

which is convolved with the SSF to match the observed extended component. R is specified as a Gaussian function of sigma σ_{kernel} .

The unknowns f_{SN} and χ are determined by iterative improvement of the fit of ϕ to the observed spectrum, using the R-L algorithm to improve both the point source spectrum and the background until convergence is reached. The iteration steps are described in detail in LW03. There are two convergence criteria: the fractional change in the spectrum per R-L iteration summed for all wavelengths; the fractional change in χ per iteration summed over all wavelengths and cross-dispersion range. In practice, depending on the particular details of the spectrum, one of these criteria may converge much faster than the other, though both must be met for the code to converge.

3.2.2 Practical implementation for SN and host galaxy

The situation of an SN observed in a host galaxy is an ideal use of the inhomogeneous case (see LW03 for some other examples). This is the simplest application since there is ideally one point source and a structurally well-resolved galaxy. When the SN is in the outer regions of an early-type galaxy, then the sophistication of the technique is probably not essential and more traditional methods, such as a linear or polynomial fit to the background and extraction, with or without weighting, of the point source, are adequate. However, when the SN is near the centre of a galaxy, or the galaxy does not have a smooth radial profile, or there is line emission in the galaxy host (e.g. for late-type galaxies), then the simple methods fail and a dedicated extraction or a restoration approach is mandatory. In Sect. 3.7 we compare the technique presented here with other less advanced methods.

The inhomogeneous case is implemented in the IRAF code *specinholucy*, which is available in the ST-ECF layered package *specres*. In addition to the input long-slit 2D spectrum, there are two important input parameters: the SSF, which obviously must match as well as possible the cross-dispersion profile as a function of wavelength for the SN observation, and the position of the SN on the slit. The inhomogeneous decomposition technique needs the position of the point source that is to be extracted from the extended background (i.e. the host galaxy). Errors in this position will result in mixing of the two channels in the output-restored spectrum so that for example the background is excavated asymmetrically around the point source. However, this requirement is not as limiting as it sounds since one of the outputs is a 2D restored version of the input 2D long-slit spectrum (including both the SN and the host galaxy) which can be directly compared with the latter spectrum, and a mismatch of the position shows up as a higher frequency component than the resolution kernel in the neighbourhood of the designated SN. The primary output is the spectrum of the SN, which is strictly 1D. If an error image is available for the input long-slit spectrum, it can be supplied to produce Monte Carlo error estimates for the restored output spectra (point source and extended background).

3.3 The importance of the slit spread function

LW03 discuss some of the difficulties with using an empirical SSF. For ground-based data a spectrum of a bright standard star is ideal, but this must be taken in identical conditions to those of the SN spectrum. In practice this is almost impossible to achieve. Even a star on the slit of the same observation as the SN cannot be guaranteed to provide an ideal SSF, since the star may not be centred on the slit as the SN is centered and instrumental optical aberrations can produce off-axis distortions of the spatial profile of a point source. A simple task, *spepsf*, is provided for constructing model SSFs in the *specres* package. A number of PSFs (viz stellar images) are provided as input at specified wavelengths; these are sampled by a slit of specified size (relative to the PSFs) and the signal within a slit is integrated across the slit width as a function of offset position (cross-dispersion). The set of point sources are then spline-interpolated in the dispersion direction to provide the 2D spectrum of the point source, the SSF. For an observation with no accompanying SSF, a considerable amount of trial-and-error is required to choose the seeing of a set of model PSFs in order to provide a high quality restoration, and thus successful extraction of the SN spectrum. In the low signal-to-noise cases, it will be the major source of uncertainty in the SN spectrum (see Sect. 3.5.3). However, all methods that rely on provision of a PSF (in imaging) or an SSF (in spectroscopy) are subject to this difficulty; it usually provides the fundamental limit on the uncertainty of the restoration.

3.3.1 Measuring the seeing

To successfully extract the point source spectrum from the extended background component one needs in principle to know the width of the point-source spatial profile at each

dispersion coordinate – i.e. the FWHM-wavelength relation for that object. In practice, however, we often cannot do this because of poor S/N (this is especially the case in high- z SN Ia spectroscopy) and so we rely on average quantities, such as the mean seeing during the observation. One can then imagine reconstructing a more reliable description of the seeing (θ) variation along the dispersion direction (λ) using for instance the following seeing-wavelength relation [272]:

$$\left. \begin{array}{l} \theta = \lambda/r_0 \\ r_0 \propto \lambda^{6/5} \end{array} \right\} \Rightarrow \theta \propto \lambda^{-0.2}, \quad (3.3)$$

where r_0 is the so-called Fried parameter, which describes the quality of a wave that has propagated through atmospheric turbulence [87, 88].

However, a specific telescope and instrument combination can introduce systematic errors due to instrumental spatial distortions which are not taken into account in the above relation. Fig. 3.1 shows that one should not rely on measurements by external seeing monitors on observatory sites – such as the Differential Image Motion Monitor (DIMM) on the ESO-Paranal site, which measures the image quality via a differential centroiding method [265, 264]. Although precise, these measurements are inadequate for our purpose since the DIMM probes a region of sky significantly different from that where the telescope is pointing (see [219], his Fig. 17). Moreover the optical train is different and the observation wavelength is restricted to 5000 Å. Even varying the exponent in the above seeing-wavelength relation does not make it possible to accurately reproduce the FWHM profile of a bright standard star (Fig. 3.1). We will see in Sect. 3.5.3 that errors of $\gtrsim 15\%$ in the determination of the FWHM of the point source can lead to significant errors in the restored point source flux. One possible alternative is to construct a *synthetic* SSF based on the wavelength-dependent FWHM characteristics of the point source spectrum to be extracted. This has the prime advantage of extracting the point source with a PSF spectrum that has been subject to the *same* seeing variations. To do so one can either use the SN spectrum itself or carefully align the slit to include a bright single star as well as the object of interest.

3.3.2 Generating synthetic PSF spectra

The IRAF-implemented code *specpsf* is illustrated in Fig. 3.2. A standard star is used to determine the corresponding FWHM-wavelength relation, from which Gaussian PSF images are generated every 50 Å. The resulting stellar images are run through *specpsf* and the profile of the corresponding output PSF spectrum (or SSF) is compared with that of the input standard star. The errors fall below 0.1% over the whole wavelength range. We also show a polynomial fit to the data, since in practice the scatter is significantly larger for low S/N point sources, and such a fit to the data is more representative of the actual seeing variations in the dispersion direction. Here the residuals are as high as $\sim 2\%$ in the red region of the spectrum (mainly due to an increase of sky brightness in this spectral range), still an order of magnitude below the lower threshold where errors on the FWHM start to matter (see below).

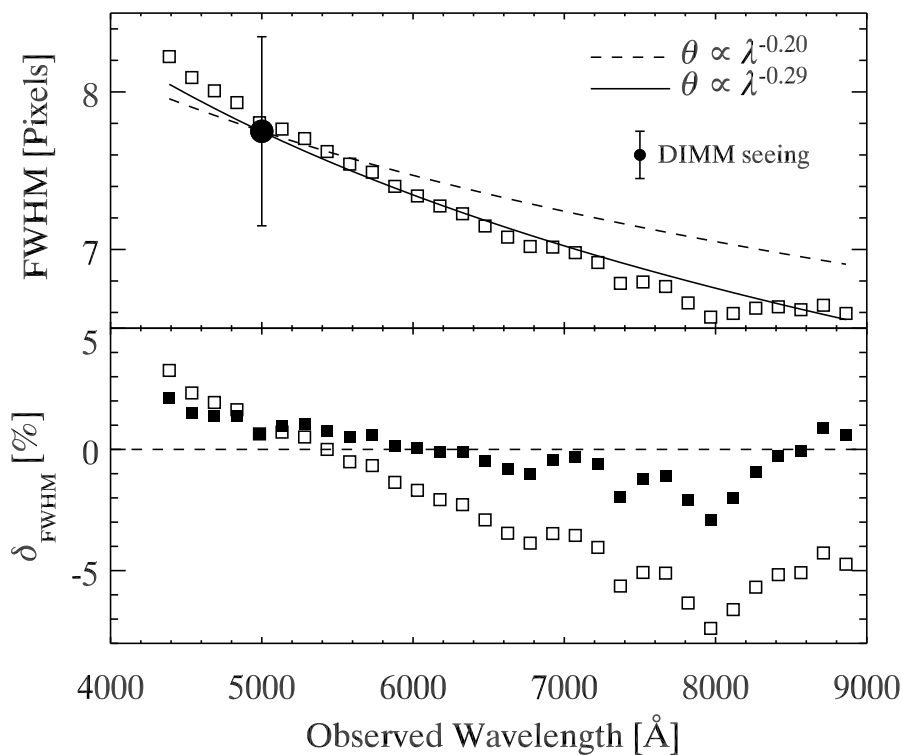


Figure 3.1: **Top panel:** FWHM of the cross-dispersion profile of the standard star LTT 7987 taken with VLT+FORs1 on UT 11 October 2002. The single data point with an error bar shows the mean seeing as measured by the DIMM station – namely $1.55 \pm 0.12''$ (the pixel scale of FORs1 is $0.2'' \text{ pix}^{-1}$) at 5000 \AA . Overplotted is the FWHM-wavelength relation fixed at the DIMM data point, both for the predicted exponent (-0.20) and our best-fit value (-0.29). **Lower panel:** Fractional residuals with respect to the $\theta \propto \lambda^{-l}$ relation, for $l = 0.20$ (open squares) and $l = 0.29$ (filled squares).

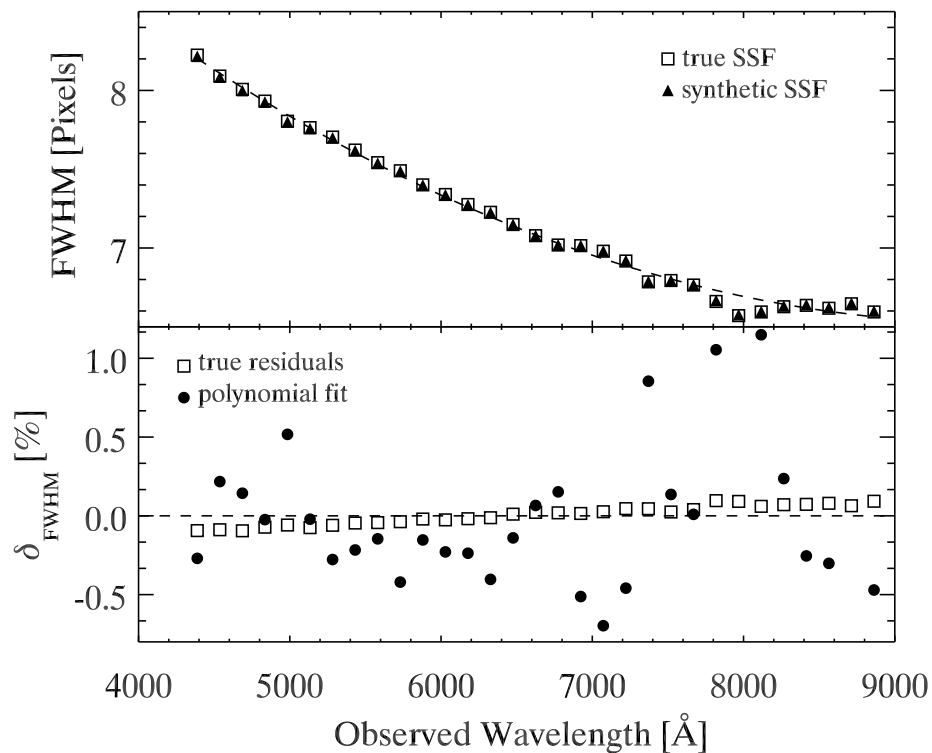


Figure 3.2: Illustration of SSF synthesis using *specpsf*. The input spectrum is the same as in Fig. 3.1. **Top panel:** FWHM of LTT 7987 (open squares) and of the synthetic SSF (filled triangles). The dashed line shows a polynomial fit to the synthetic SSF. **Lower panel:** Residual plots of the FWHM of the synthesized SSF (open squares) and polynomial fit to the synthetic SSF (filled circles) with respect to the input SSF.

Table 3.1: SSF FWHM data

SSF	pixels ^a	arcseconds ^a
SN 2002go	$3.83_{3.48}^{4.74} \pm 0.41$	$0.77_{0.70}^{0.95} \pm 0.08$
star on slit	$4.71_{4.18}^{5.44} \pm 0.39$	$0.94_{0.84}^{1.10} \pm 0.08$
standard star	$4.17_{3.93}^{4.64} \pm 0.23$	$0.83_{0.79}^{0.93} \pm 0.05$

(a) the quoted values are read as $\langle \text{mean} \rangle_{\text{min}}^{\text{max}} \pm 1\sigma$ error

3.3.3 Impact of the SSF on spectral restoration

The astronomer wishing to extract point source spectra using *specinholucy* has various options for the SSF. In low S/N cases like the ones we describe in this paper the choice of the SSF is by far the most limiting factor and will have a severe impact on the quality of the restoration.

We illustrate the impact of the SSF choice on the restoration of SN 2002go, a Type Ia supernova at $z = 0.236$ (IAUC 7994) slightly offset from the center of its host galaxy (see also Sect. 3.6). We consider three options for the SSF: (1) a synthetic SSF based on FWHM measurements of SN 2002go itself, (2) a PSF star that happened by chance to be on the same slit as SN 2002go and (3) a VLT+FORs1 standard star for which the FWHM-wavelength relation was the closest we could find to that of SN 2002go. The resulting cross-dispersion profiles are shown in Fig. 3.3, and the corresponding mean seeing values are shown in Table 3.1. Note that the quoted mean values are not representative of the wavelength-dependent nature of the seeing, and one should produce plots such as those shown in Fig. 3.3 to appreciate the differences between the SSFs. Despite having been observed on the same location of the CCD chip, the SN and the standard star were not observed on the same night and were thus subject to different seeing conditions. The difference is also a function of wavelength, hinting at possible instrumental effects on the spatial profile. These same comments apply to standard stars having been observed on the same night as the object of interest, and we discourage the potential user of this method from using standard stars for the SSF.

More interesting, perhaps, are the quasi-systematic differences in the profiles of the SN and the PSF star that was accidentally placed on the same slit. The SN and PSF star should be subject to identical seeing variations, but the reconstructed profiles differ by as much as $\sim 30\%$, or $0.2''$. There could be several reasons for this: (a) the observation is not made at the parallactic angle, and so the dispersion direction is not along the slit; (b) the star spectrum is located at a different location on the CCD chip where the spatial distortion differs; (c) the star is not centred on the slit and we are not measuring its true PSF profile. FORs1 is equipped with a longitudinal atmospheric dispersion compensator (LADC) which has an accuracy $\lesssim 0.1''$ (0.5 pix) over the considered wavelength range [8], and so (a) should not be relevant. FORs1 is linear at the $< 0.4\%$ level (see the FORs1+2 User Manual²) and distortions associated with the instrument's optics should not affect the

²<http://www.eso.org/instruments/fors1/>

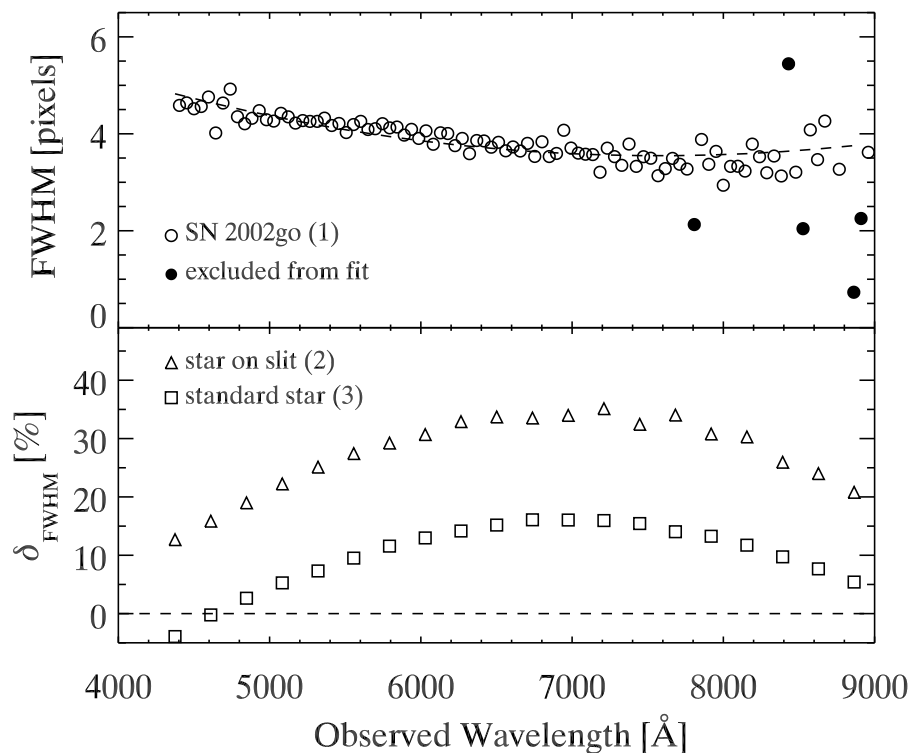


Figure 3.3: Examples of SSFs used to extract SN 2002go: (1) the supernova itself; (2) a bright PSF star that happened to be on the same slit; (3) the closest FORS1 standard star to match the supernova profile. **Top panel:** The dashed line is a polynomial fit to the SN profile, from which low S/N points affected by the increase in sky background have been excluded. **Lower panel:** Fractional differences in the SSF FWHM with respect to the polynomial fit.

whole spectral range at this level, so (b) should not matter either. This leaves (c) as the probable explanation for this difference, which is significant enough to be a major source of error in the restoration.

The impact of these various SSFs on the restored SN flux is shown in Fig. 3.4. We view the solid curve as the most accurate restoration, and one sees that using the other two (wider) SSFs means we are also restoring part of the extended background component (sky and host galaxy) in the point source spectrum. In the case of the star that was by chance located on the same slit the $\sim 20\%$ difference in the FWHM results in an error in the restored SN flux that can be as high as 100-150%! We see from the two inlays in Fig. 3.4 that the slope of the pseudo-continuum around strong SN Ia spectral features (Ca II H&K and Si II) changes significantly due to contamination of the underlying background spectrum, and so the very definition of “line strength” in this case is very ambiguous. The fact that the FWHM of the point source varies with wavelength will cause variable contributions of the background to the restored spectrum, and will affect the determination of line ratios of distantly spaced lines, if the PSF vector is not determined properly. Thus, the extraction has a significant impact on empirical correlations based on such measurements, as the errors made at this stage will add to those associated with the subsequent calibration in flux. Examples of such correlations are given by Nugent et al. [215] and are used to determine distances to SN Ia by Riess et al. [249].

One might ask how one can decide which SSF to choose to restore a particular point source spectrum and if it is possible to *a posteriori* tell whether the chosen SSF was indeed the appropriate one. Indeed, through restoring the complete 2D background spectrum *specinholucy* enables us to check the accuracy of the restoration at each pixel of the input 2D frame, or simply in the spatial (cross-dispersion) direction by comparing the collapsed spatial profiles of the input and restored 2D spectra. This is illustrated using real data in Fig. 3.12.

3.4 The spatial resolution kernel

The choice of the width of the resolution kernel for the background resides with the user. It is implemented as a Gaussian of user-chosen sigma σ_{kernel} in the *specinholucy* code. It is difficult to give a general guide to its choice. Obviously it should be wider than the equivalent maximum Gaussian sigma of the SSF $\sigma_{\text{SSF,max}}$ in the cross-dispersion direction. The sigma of the kernel has to be tuned and is strongly dependent on the nature of the extended source and more specifically on the extended background component in the vicinity of the point source. Comparison of the restored background with the input spectrum will quickly show if narrow features in the extended background, above the noise, have failed to be modelled through choice of too wide a kernel width (see Fig. 3.5, left column). If the kernel width is too narrow then the point source will be partially modelled as a peak in the background channel and the fluxes in our restored point source spectrum will be underestimated (Fig. 3.5, right column). The optimal width for the spatial resolution kernel corresponds to a compromise between the lower spatial frequency of the extended

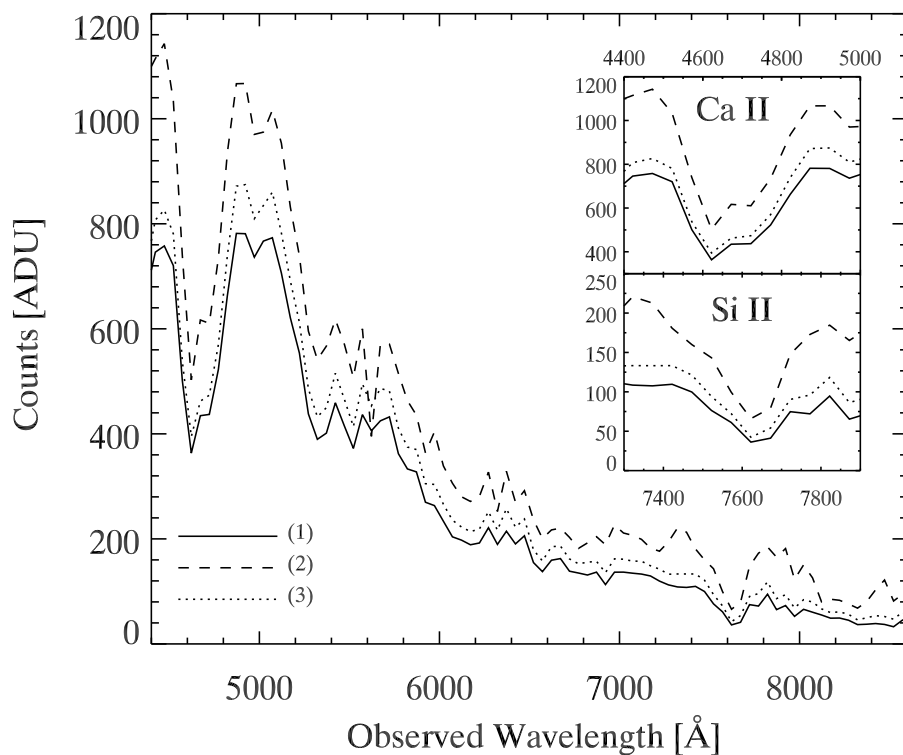


Figure 3.4: Impact of the SSF on the restored point source spectrum of SN 2002go. Refer to Fig. 3.3 for the meaning of the line annotations (1), (2) and (3), noting that (1) corresponds to the polynomial fit to the SN 2002go profile. The two inlays zoom in on the blueshifted Ca II H&K and Si II features, both prominent in SN Ia spectra, and highlight the impact of non-optimal spectral extractions on empirical correlations involving line strengths (see text).

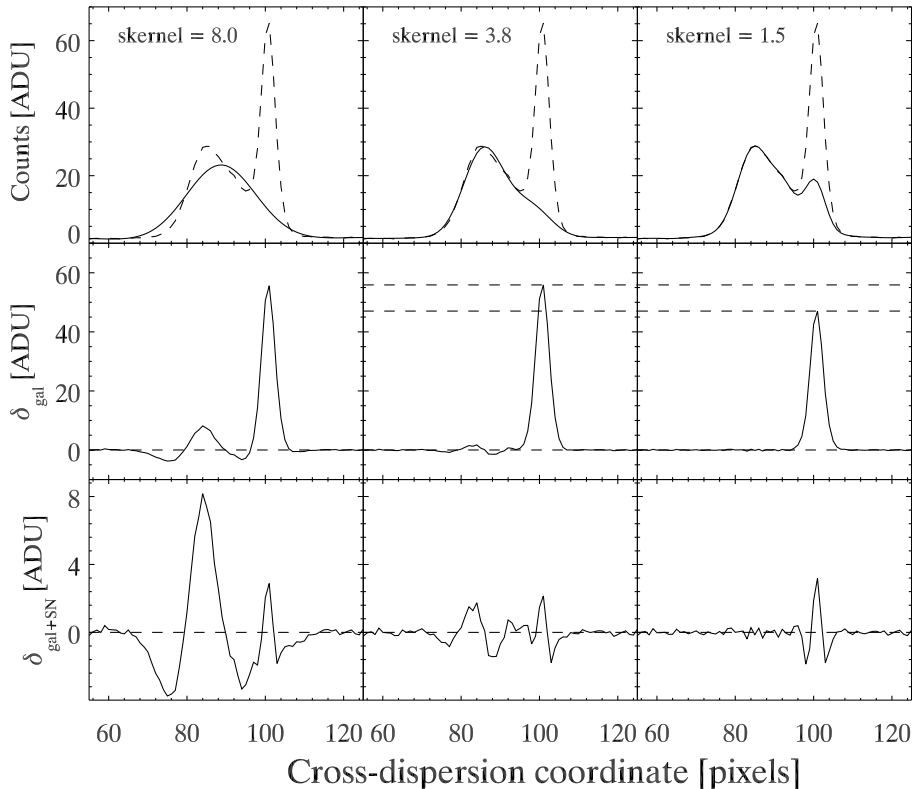


Figure 3.5: Impact of the width of the spatial resolution kernel σ_{kernel} on the background restoration. **Top panel:** Input average (dashed line) and restored background (solid line) cross-dispersion profiles. **Middle panel:** Residuals of the previous plot, revealing the point source channel (i.e. the supernova itself). **Lower panel:** Spatial residuals of the input and restored 2D frames. Negative (positive) values in the residual plots mean we are over (under)-restoring the flux at that location.

background cross-dispersion profile and the higher spatial frequency of the point source cross-dispersion profile. A decent first guess would be $\sigma_{\text{kernel}} \approx 2-3\overline{\sigma_{\text{SSF}}}$. In Fig. 3.5 (middle column) we have used $\sigma_{\text{kernel}} \approx 2.3\overline{\sigma_{\text{SSF}}} > \sigma_{\text{SSF,max}}$. From Fig. 3.5 we further note that, if one can clearly see the impact of a wide kernel on the spatial residuals $\delta_{\text{gal+SN}}$, discriminating between the narrow and optimal kernel widths – respectively 1.5 and 3.8 – is not obvious *a priori*. The optimal kernel width in Fig. 3.5 was chosen such as to maximise the counts in the point source channel, or δ_{gal} , whilst keeping the spatial residuals $\delta_{\text{gal+SN}}$ below the statistical noise limit of the input 2D frame.

One important test is to ensure we are not capable of restoring a PSF-like spectrum from a pure extended source. This is particularly relevant to high- z SN Ia spectroscopy since in many cases one is only able to extract a spectrum of the supernova host galaxy whereas one is convinced of having obtained a combined spectrum including the SN. Then the currently widespread technique of subtracting a galaxy template from this “combined” (and noisy) spectrum can sometimes reveal SN-like features where no supernova is present!

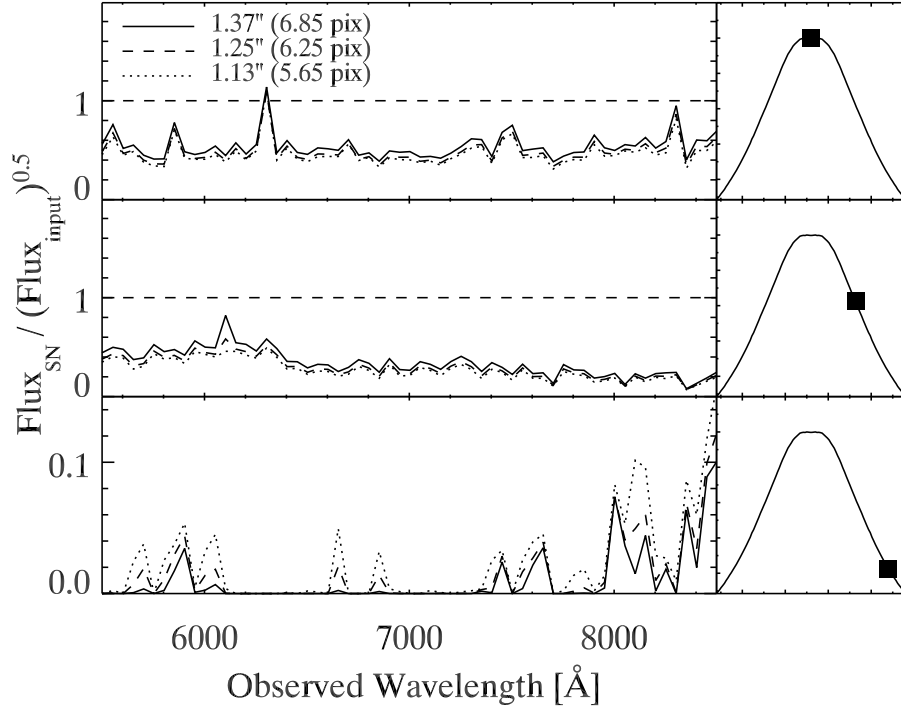


Figure 3.6: Restored point source spectra in units of the statistical noise of the input pure galaxy spectrum. The different plots correspond to different positions of the point source to extract, marked by a filled square in the galaxy spatial profiles shown in the right column. The different lines correspond to different seeing conditions. The horizontal dashed line marks the limit below which no point source was detected in the background. Note the change of scale in the lower plot, where no flux at all is restored in many bandpasses. The peak above the dashed line in the uppermost plot is due to bad cosmic ray removal.

This is illustrated later on in Sect. 3.7.3 where we compare the *specinholucy* output with that of a statistical algorithm (\mathcal{SN} -fit) which decomposes a 1D spectrum into its SN and galaxy components using a galaxy spectral template (see also Fig. 3.14).

Here we have used the uncontaminated galaxy spectrum of the host of SN 2002bo (see Sect. 3.6), obtained by constructing a mirror image of the portion of the galaxy profile devoid of supernova signal. We try to extract a point source component from this pure galaxy spectrum at different locations of the galaxy trace, including the centroid, using for this purpose three different SSFs of widths corresponding to the mean and extrema of the seeing values measured by the DIMM station for this observation. We then compare the restored point source flux with the statistical noise limit of the input 2D spectrum at the position of the point source. Should this ratio fall below one this means that no point source was detected. We see from Fig. 3.6 that in all cases the restored spectrum is inconsistent with that of a PSF-like object over the whole spectral range.

Table 3.2: Distances and flux scaling

galaxy	d (Mpc)	Reference	factor ^a
NGC 4526	13	Drenkhahn and Richtler [67]	1.5×10^{-5}
NGC 6181	34	Sil'chenko et al. [275]	1.1×10^{-4}

(a) Factor used to scale down the flux, computed as $(d/d_{L,z=0.5})^2 \times (1+z)^{-1}$.

3.5 Testing the algorithm on simulated data

In this Sect. we present tests of the algorithm on simulated data, namely 2D spectra of a Type Ia supernova (SN Ia) at $z = 0.5$ embedded in a late-type galaxy. We have chosen to reproduce a situation where a one hour-long exposure is taken at the ESO Very Large Telescope VLT-UT1 (8.2m) using the FOcal Reducer Spectrograph (FORS1) in Long-Slit Spectroscopy (LSS) mode. The grism corresponds to 300V, and the slit width is 1". The reason behind choosing these specific settings is that they correspond to those used for the real data on which the algorithm will be tested further in Sect. 3.6. In what follows we assume a $(\Omega_M, \Omega_\Lambda, h) = (0.3, 0.7, 0.72)$ cosmology (where $h = \frac{H_0}{100 \text{ km s}^{-1} \text{ Mpc}^{-1}}$ is the dimensionless Hubble constant), and so the luminosity distance corresponding to $z = 0.5$ is $d_{L,z=0.5} \sim 2.72 \text{ Gpc}$. The factors used to scale down the fluxes as the SN and galaxy are artificially redshifted to $z = 0.5$ are listed in Table 3.2. The additional factor of $(1+z)$ comes from the fact that we are integrating the flux over a finite bandpass, where the wavelength axis has been diluted by that same factor.

3.5.1 Simulated data

The simulated 2D spectra are a combination of a 2D supernova spectrum and a 2D background spectrum, itself consisting of a galaxy and a sky spectrum. We vary the phase of the SN, i.e. the brightness and the input spectrum, and its position within the galaxy from 0.75 to 1.75, in units of FWHM of the galaxy trace. Random Poisson noise is added to the image using the gain and read noise characteristics of FORS1 so as to degrade the overall S/N of the image and thereby reproduce plausible observing conditions.

Supernova spectrum

The 2D supernova spectra are synthesized using the 1D, flux-calibrated spectra of the Type Ia supernova SN 1994D in NGC 4526 ($cz = 448 \text{ km s}^{-1}$) as obtained from the SUSPECT database³. Where spectral coverage at a given phase was lacking (i.e. at -6d , $+0\text{d}$, $+6\text{d}$, $+8\text{d}$ and $+14\text{d}$), approximate synthetic spectra were obtained from the two observed spectra closest in phase using the *UBVRI* photometry published by Patat et al. [220]. The same technique was applied to observed spectra whose wavelength range did not extend below 3650 \AA in the blue (at -8d and $+10\text{d}$), so as to make sure to cover the Ca II H&K

³<http://bruford.nhn.ou.edu/~suspect/>.

Table 3.3: SN 1994D data used in the simulation

phase ^a	date ^b	m_B ^c	$m_{R,z=0.5}$ ^d	counts ^e
-10	11/03/94	13.26	24.86	13.5
-8	13/03/94	12.67	24.27	22.7
-6	...	12.26	23.86	30.7
-4	17/03/94	11.99	23.59	37.4
-2	19/03/94	11.86	23.46	39.5
+0	...	11.84 [†]	23.44	51.6
+2	23/03/94	11.89	23.49	48.4
+4	25/03/94	11.99	23.59	34.8
+6	...	12.13	23.73	31.3
+8	...	12.33	23.93	27.9
+10	31/03/94	12.55 [†]	24.15	21.5
+12	02/04/94	12.80	24.40	15.0
+14	...	13.10	24.70	12.7

(a) SN phase in rest-frame days from B -band maximum.

(b) UT date of spectroscopic observation. Absence of date means the spectrum is synthetic.

(c) B -band magnitude taken from Table 1 of Patat et al. [220]. Data marked with [†] results from a polynomial fit to the B -band light curve.

(d) the R -band at $z = 0.5$ is close to rest-frame B -band, and so

$$m_R(z = 0.5) \approx m_B - 2.5 \log \left(\frac{d_{L,SN}}{d_{L,gal}} \right)^2 \approx m_B + 11.60.$$

(e) mean total counts in the whole SN profile in ADUs per pixel along the dispersion axis.

(3934 Å, 3968 Å) absorption trough blueshifted to ~ 3750 Å, prominent in SN Ia optical spectra (see [75] for a review). Each spectrum is then redshifted to $z = 0.5$ and rebinned to the pixel scale of FORS1 equipped with a 300V grism and a 1" slit (~ 2.66 Å pix⁻¹). The flux (in units of erg s⁻¹ cm⁻² Å⁻¹) is scaled down to take into account the change in luminosity distance as the source is artificially placed at $z = 0.5$ – assuming SN 1994D to be at the same distance as its host galaxy – and is converted to counts (ADU) using a FORS1 sensitivity function. At this stage we have a 1D supernova spectrum in ADUs as a function of wavelength, corresponding to a one-hour integration on FORS1. Finally, a 2D supernova spectrum is synthesized by replicating this 1D spectrum along the lines of a 2D image array (i.e. along the dispersion axis) and multiplying each image column by a 1D Gaussian profile normalised to unity of FWHM corresponding to 1" seeing. Note that the flux vector is normalised to an airmass of 1, and no scaling was applied to account for observations (usually) made at higher airmasses.

The supernova data used in this simulation are summarised in Table 3.3. The quoted R -band magnitudes are only approximate and are affected by systematic effects because of the lack of any k -correction. For comparison the mean number of counts (in ADUs) per pixel is 105.7 and 19.8 for galaxy and sky (including sky lines), respectively.

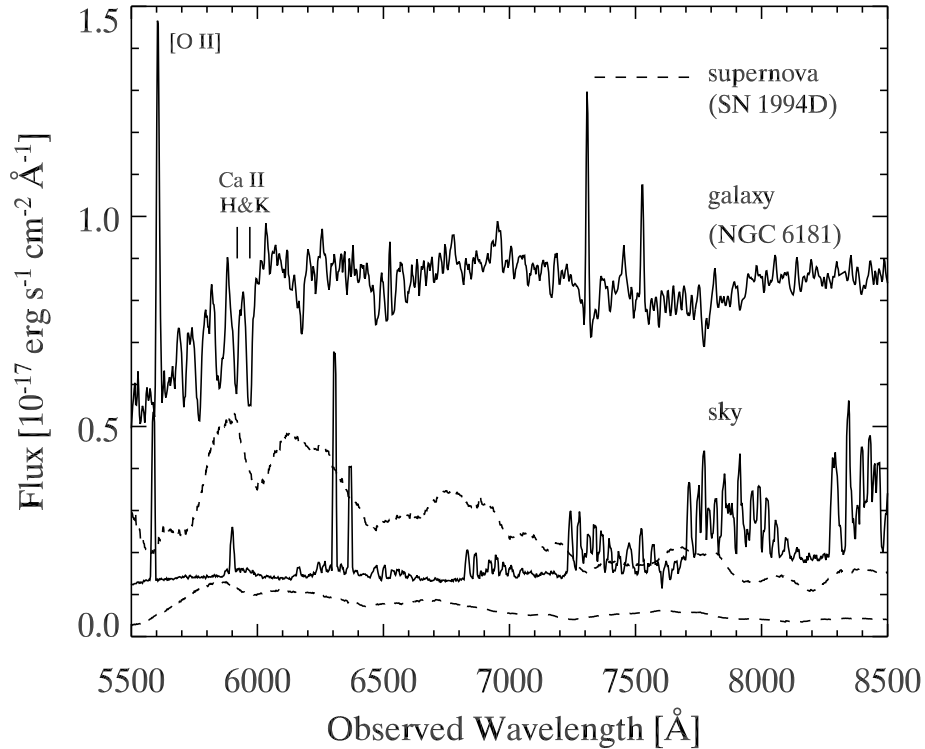


Figure 3.7: Absolute flux-calibrated galaxy and sky spectra used in the simulation. The spectra are shown in observed wavelength at $z = 0.5$, and without shot noise for sake of clarity. The prominent [O II] emission and the Ca II H&K absorption in NGC 6181 are labelled accordingly. Overplotted (dashed lines) are the spectra of SN 1994D at maximum intensity (top) and ten days before maximum (bottom).

Background spectrum

For the galaxy spectrum we choose to artificially place SN 1994D in NGC 6181, an SC galaxy part of Kennicutt’s spectrophotometric atlas of galaxies [143]. The reason behind this is the prominent [O II] emission at 3727 \AA present in its spectrum (see Fig. 3.7), which could then serve as an diagnostic tool for probing the efficiency of our algorithm in restoring a clean point source spectrum. If successful, the restored 1D spectrum of the point source should be devoid of [O II] flux residuals.

The spectrum of NGC 6181 was redshifted to $z = 0.5$ and rebinned to the pixel scale of FORS1 using the same procedure as for the supernova spectrum. The flux was scaled down to take into account the change in luminosity distance, and converted to counts (again in ADUs) using the same sensitivity function as for the supernova. The resulting galaxy has a magnitude $m_{\text{gal}} \sim 21.5$ in a redshifted B -band filter (very roughly corresponding to the R -band at $z = 0.5$) i.e. more than an order of magnitude brighter than when the supernova is at its faintest (see Table 3.3).

Next, a galaxy spatial luminosity profile was constructed based on a standard bulge+disk model. The bulge component is usually described analytically using the so-called $r^{1/4}$ law and the disk component follows an exponential decline with distance r from the nucleus [64, 86]. One can derive a global analytical form of the surface brightness profile $\Sigma_S(r)$ of spiral galaxies, as a function of the effective radius r_e of the bulge only. In doing so we assume a bulge-to-total luminosity ratio $B/T = 0.4$ [241] and a ratio between the effective radii of the bulge and disk components $r_{b,e}/r_{d,e} = 0.5$ [144, 241]:

$$\begin{aligned}\Sigma_S(r) &= \Sigma_b(r) + \Sigma_d(r) \\ &= 0.76931 \Sigma_{S,e} \exp\left(-7.6692 \left[\left(\frac{1.6617r}{r_e}\right)^{1/4} - 1\right]\right) \\ &\quad + 2.9343 \Sigma_{S,e} \exp\left(-\frac{1.3945r}{r_e}\right),\end{aligned}\tag{3.4}$$

where $\Sigma_b(r)$ and $\Sigma_d(r)$ are the surface brightness profiles of the bulge and disk components, respectively, and $\Sigma_{S,e}(r)$ is the surface brightness at the effective radius r_e .

The angular size of NGC 6181 is $2.5' \times 1.1'$ (NASA/IPAC Extragalactic Database⁴), which corresponds to $4.5'' \times 2.2''$ at $z = 0.5$, and in turn to 22.5×11 pixels on a FORS1 image. Assuming the slit was placed along the major axis of NGC 6181 the effective radius of the disk r_e is 22.5 pixels. The derived luminosity profile is then normalised to unity and is multiplied into each column of the 2D galaxy image array. Each column is further convolved with a Gaussian profile of FWHM corresponding to $1''$ seeing to reproduce similar observing conditions as for the supernova. The resulting spatial profile $I_{\text{gal}}(r)$ is shown in Fig. 3.8. Notice how at these redshifts the core spatial profile of galaxies is entirely seeing-dominated, and one must rely on the broad extended wings of the profile to differentiate between a galaxy and a point source.

The sky 2D spectrum (the second background component for ground-based observations) is generated by uniformly replicating an observed 1D sky spectrum with the required settings (300V grism, 1'' slit) along lines of an image array, and scaled to the required exposure time (3600s in our case). It is thus by construction perfectly flat and monochromatic in the spatial direction. We do not have to worry about spatial distortions of sky lines, and sky background removal in the input 2D spectrum is rendered trivial.

3.5.2 Simulation steps

We now move on to outlining the steps made in carrying out the simulation. Far from being redundant these are the same steps that one should in principle go through when applying this technique to real data. They include determining the position (and slope) of the supernova spectral trace, its FWHM as a function of wavelength, synthesizing a corresponding SSF and running the *specinholucy* code with the optimal settings. For the

⁴<http://nedwww.ipac.caltech.edu/>

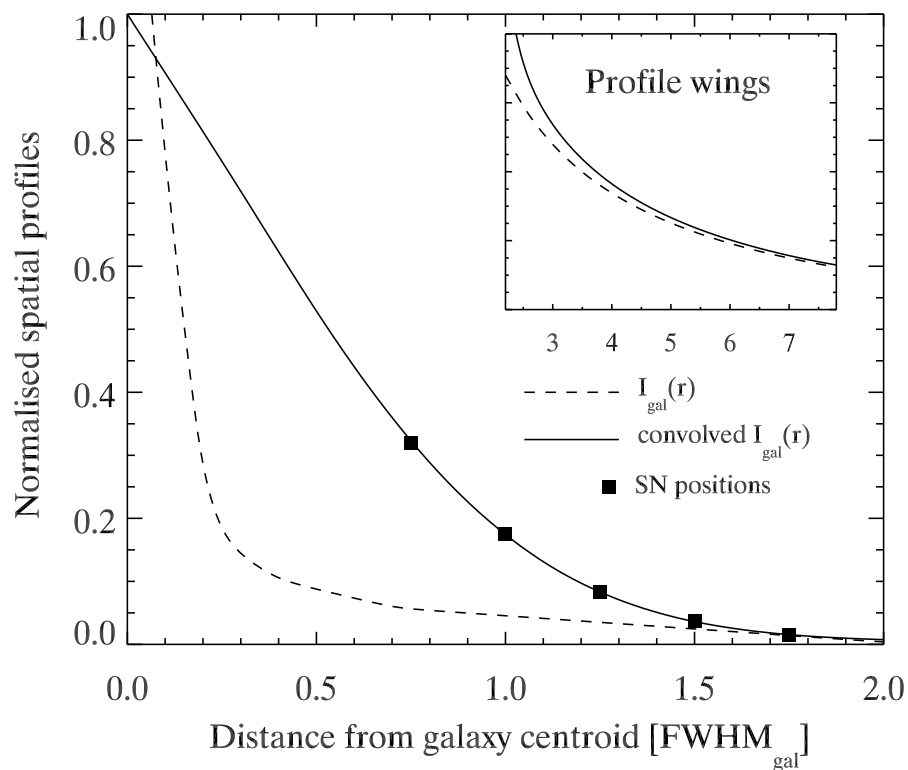


Figure 3.8: Smoothed galaxy spatial profile used in the simulation, resulting from the convolution of a standard spiral galaxy luminosity profile and a $1''$ seeing Gaussian kernel. The abscissa is in units of FWHM of the convolved galaxy profile ($\cong 3.06$ pix). The effective radius r_e in these units is at ~ 7.36 . Filled squares indicate the position of the SN used in this simulation, namely 0.75, 1.00, 1.25, 1.50 and 1.75.

purpose of this simulation and for ease in computing statistics these steps have been made automatic, though we strongly advise to make them highly interactive when dealing with real data.

SN trace position and slope

One of the inputs to the *specinholucy* routine is a position table containing the $(x, y, \text{slope pix}^{-1})$ of the supernova spectral trace. Since in the case of high- z SN Ia we are limited in S/N we cannot simply give an approximate position and rely on cross-correlations with the SSF to determine a more accurate one. Here we must input the *exact* SN trace position to which the SSF profiles will be shifted. The results of our simulation (see Sect. 3.5.3) show the impact of positional accuracy on the point source restoration.

To some extent one should base the method used to determine the trace position on the characteristics of the instrument used for the observation. In the case of FORS1 we know from observations of standard stars that the position of a point source does not vary by more than one pixel across the whole CCD chip. Thus, a $\sim 1\text{pix}$ accuracy can almost routinely be achieved by summing up each of the spatial channels and finding the maximum intensity (other than the galaxy) in a given cross-dispersion region. Clearly this will be problematic for cases where the SN is close to the centroid of the galaxy trace or when its phase is far from maximum (-10d or $+14\text{d}$). Alternatively one can try to fit the background around the SN trace and subtract this fit from the overall profile. The residuals can then be fit with a Gaussian profile and the trace position is taken to be the profile centre.

The result of this operation is a relation between SN trace position and dispersion coordinate x , which is fit linearly so as to determine the trace position and slope. We now have our input $(x, y, \text{slope pix}^{-1})$ table necessary to run *specinholucy*. A plot of the error made in determining the trace position using this approach is shown in Fig. 3.9. The position is best determined when the signal-to-noise ratio is high, namely when the contrast is high between the SN and the underlying background, as expected.

SN trace FWHM and SSF synthesis

To construct a synthetic SSF we need to know the FWHM of the SN trace as a function of the dispersion coordinate. We proceed in a way analogous to determining the SN trace position, except we are now interested in the width of the Gaussian fit to the residual signal left over after sky and galaxy subtraction rather than the Gaussian centre. A similar relation between FWHM_{SN} and dispersion coordinate is established and a table of $(\text{FWHM}_{\text{SN}}, \text{wavelength})$ values is elaborated and serves as input for the SSF synthesis using *specpsf*. A plot of the error made in determining the trace FWHM using this approach is shown in Fig. 3.10. Again, the FWHM is better determined for cases with a higher SN flux relative to the galaxy background.

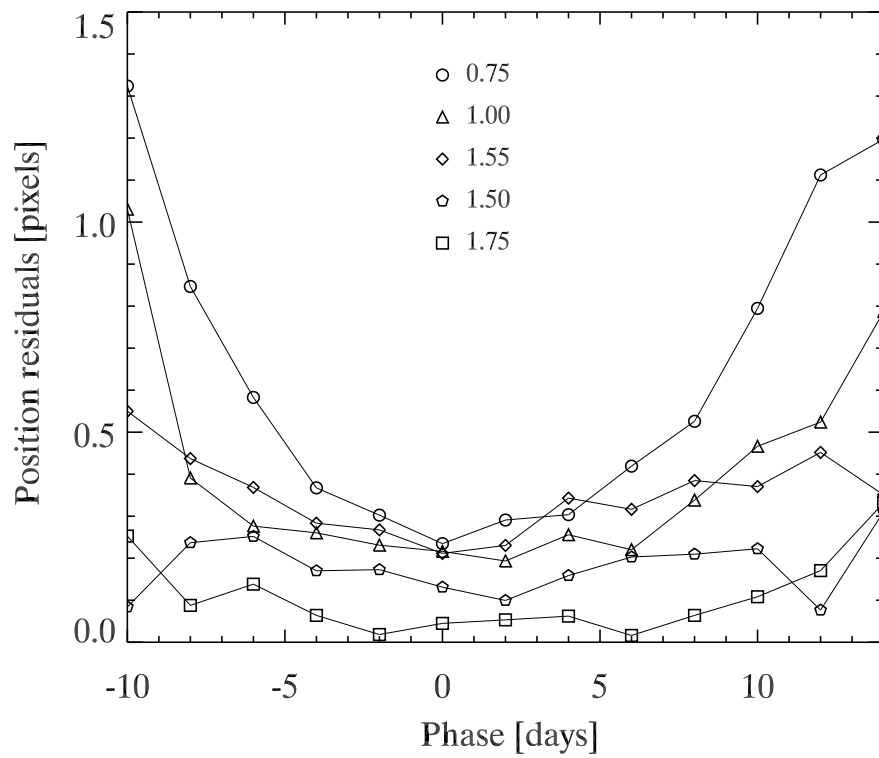


Figure 3.9: SN trace position residuals as a function of the SN phase, for different locations of the SN with respect to the galaxy centroid. Each curve corresponds to a specific SN position, given in units of FWHM_{gal} .

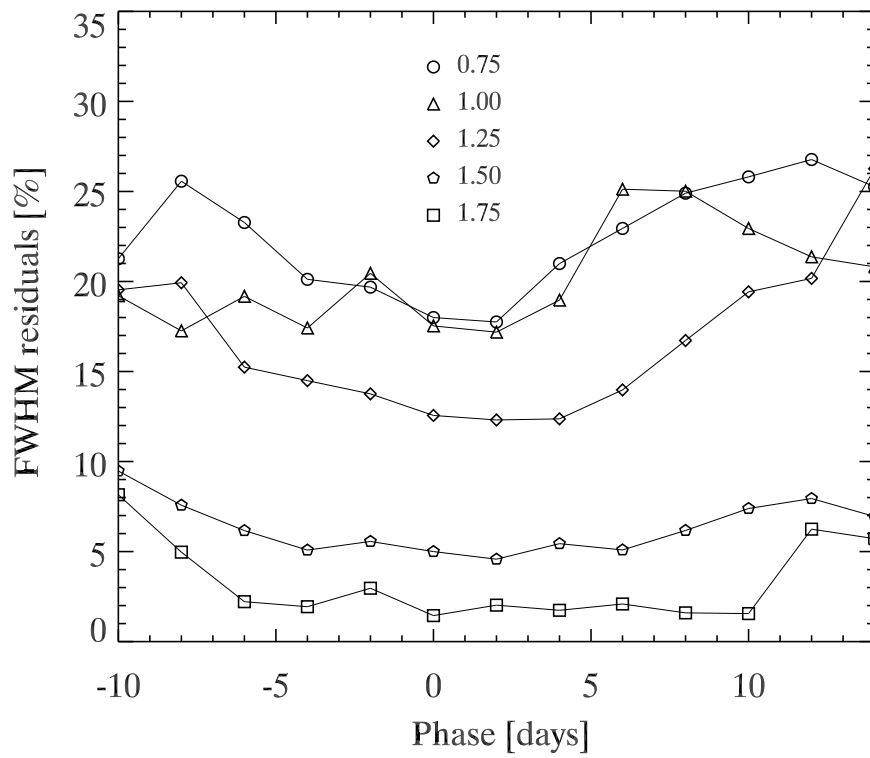


Figure 3.10: SN trace FWHM residuals as a function of the SN phase, for different locations of the SN with respect to the galaxy centroid. The curves and plotting symbols have the same meaning as in Fig. 3.9.

Running *specinholucy*

Once we have determined the position (and slope) of the SN trace and synthesized an SSF spectrum using its FWHM-wavelength dependency, we can run *specinholucy* on the input sky-subtracted 2D spectrum. We refer the reader to Lucy and Walsh [185] and to the IRAF help pages for the *specinholucy* task for a more complete description of the input parameters. A centroid fitting is used to determine the SSF peak at each column, and no subsampling (in the spatial direction) is performed since the resulting PSF profile is not oversampled with respect to the input 2D spectrum. A cubic spline is used as the interpolation method to shift the SSF to the position of the point source – which is defined *exactly* in the input position table. Note that no input statistical image to determine the statistical error at each pixel is used in these simulations.

The only input parameter made to vary from one run to the other is the width σ_{kernel} of the Gaussian used for the spatial resolution kernel. We see from Fig. 3.8 that the galaxy spatial profile is entirely seeing-dominated, meaning that the widths of the SN and galaxy traces are comparable at each wavelength. This in turn implies that the spatial frequency of the galaxy profile will vary hugely when varying the SN position from 0.75 to 1.75 FWHM_{gal} . To avoid confusion in the point/extended source discrimination we must use a narrow (wide) spatial resolution kernel when the SN is close to (far from) the galaxy centroid, where the spatial frequency is high (low). The input values for the smoothing kernel were chosen such as to minimise the mean flux residuals in restoring all phases of the SN spectrum at a given position. For all runs the convergence criteria for the SN and background spectra per R-L iteration (see Sect. 3.2) were set to 0.1% and 1%, respectively.

Two runs (A & B) were executed: in run A we use the SN position and FWHM as determined using the method outlined in Sects. 3.5.2 and 3.5.2, whilst in run B we use the known values of the SN trace position and FWHM to synthesize the SSF and restore the SN spectrum. This enables us to investigate the joint impact of the errors in the SN position and FWHM on the accuracy of the SN spectral restoration (see Sect. 3.5.3).

Statistical calculation

To evaluate the efficiency of the method we compare the (known) input SN spectrum with its restored version. More specifically we compute the ratio of the flux residuals with the statistical variation in the input 2D spectrum. Should this ratio fall below one this means that we are statistical noise-limited and cannot improve on the restoration.

In this simulation we compare the flux residuals both over the whole observed spectral range (5500 Å–8500 Å) and around the region of host galaxy [O II] 3727 Å emission. This region is simply defined in wavelength space (in Å) as $3727(1+z) \pm \text{FWHM}_{[\text{O II}]}(1+z)$, where $\text{FWHM}_{[\text{O II}]}$ is the width of the [O II] line in the input non-redshifted spectrum of NGC 6181 and $z = 0.5$ is the redshift of the simulation. For both cases the flux residual δF is evaluated at each pixel according to:

$$\delta F = \frac{|F_{\text{SN},i} - F_{\text{SN},r}|}{\sqrt{F_{\text{SN},i} + F_{\text{gal},i} + F_{\text{sky},i}}}, \quad (3.5)$$

where $F_{\text{SN},i}$ and $F_{\text{SN},r}$ are the input and restored SN fluxes, respectively. $F_{\text{gal},i}$ and $F_{\text{sky},i}$ are the galaxy and sky fluxes at the location of the SN, defined as an interval centred on the exact SN trace position and of width the FWHM of the SN trace. It is important to compute the statistical noise as that in the *total* signal at the position of the supernova (i.e. including the underlying background) and not just in the SN signal itself. If $\delta F \leq 1$ one can in principle consider the SN restoration to have converged.

3.5.3 Simulation results and discussion

The simulation results are summarised in Fig. 3.11. Both runs A and B (see Sect. 3.5.2) are shown in order to evaluate the impact of the error made in the determination of the SN trace position and FWHM on the restoration of the supernova spectrum.

These plots clearly show that the limiting factor of this two-channel restoration technique (as for any other spectral extraction method) is the contrast between the point source and the underlying background. The overall flux is systematically restored to the statistical noise limit when the supernova is at its brightest stages ($-5\text{d} \lesssim \text{phase} \lesssim +5\text{d}$), irrespective of its position with respect to the centroid of the galaxy trace. In this phase regime the error in the SN trace position and FWHM is also at its lowest (see Figs. 3.9 and 3.10) and has little impact on the quality of the restoration – as shown by the dashed lines in Fig. 3.11. This is not always the case for the $[\text{o}2]$ flux residuals, where the added background noise due to the presence of this emission line affects the restoration (cf. at positions 0.75 and 1.00, in units of FWHM_{gal}).

One sees the dramatic impact of the error made in the SN trace position and FWHM at low S/N, namely when the SN is outside the $-5\text{d} \lesssim \text{phase} \lesssim +5\text{d}$ range and close to the centroid of the galaxy (at positions of 0.75, 1.00 and 1.25). For errors in the position $\gtrsim 0.3$ pix and $\text{FWHM}_{\text{SN}} \gtrsim 15\%$, the restoration fails to reach the statistical noise limit. These are the main sources of systematic error in the restoration method and great care should be taken when determining the SN trace position and FWHM when applying it to real data.

3.6 Testing the algorithm on real data

In this Sect. we apply this restoration technique to real supernova data. An outline of the steps involved (determination of the SN trace position and FWHM; SSF synthesis; running of *specinholucy*) has already been given in Sect. 3.5.2. We simply provide the input parameters that were used to run the code (see Table 3.4). All the data were collected by the authors via the ESO observing programme 170.A-0519 and are available through

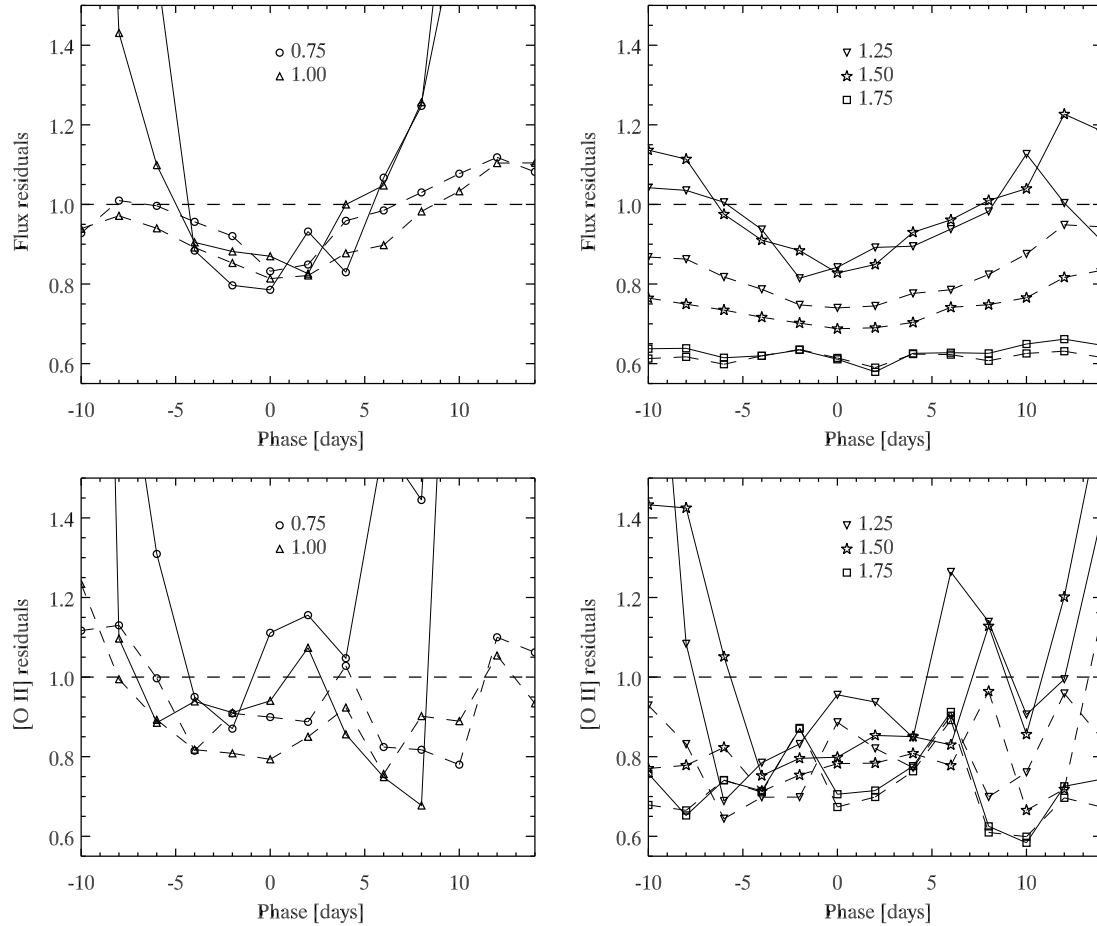


Figure 3.11: **Top panel:** Flux residuals δF as a function of the SN phase for different positions of the SN with respect to the centroid of the galaxy trace, given in units of FWHM_{gal} . $\delta F \leq 1$ means the SN spectrum has been restored to the statistical noise limit. The solid and dashed lines correspond to runs A and B, respectively (see Sect. 3.5.2). **Lower panel:** [O II] flux residuals as a function of phase for different SN positions.

the ESO Science Archive Facility⁵. The observations were made with VLT+FORs1 in Long Slit Spectroscopy (LSS) mode with a 300V grism and a 1'' slit. The results of the two-channel restoration are shown in Figs. 3.12 and 3.13, whilst the individual objects are presented in Table 3.5. On average ~ 150 iterations were needed to reach convergence for the restoration of the point source spectra, corresponding to ~ 2 minutes on a 2.4 GHz Pentium 4 processor.

There is one important distinction to be made in the calculation of the flux residuals here as opposed to that made for the simulation in Sect. 3.5.2. For observed cases we do not know how the total flux F_{tot} separates into the individual components F_{SN} , F_{gal} and F_{sky} , and so our evaluation of the accuracy of the restoration is restricted to the calculation of the mean *total* flux residuals δF_{tot} :

$$\delta F_{\text{tot}} = \frac{|F_{\text{tot},i} - F_{\text{tot},r}|}{\sqrt{F_{\text{tot},i}}}. \quad (3.6)$$

This is not as limiting as it may seem since we are again able to quantitatively evaluate our combination of σ_{kernel} and σ_{SSF} through maximising the counts in the point source channel whilst ensuring that $\delta F_{\text{tot}} < 1$ (cf. Sect. 3.4).

Fig. 3.12 illustrates what has been said about an *a posteriori* check of the adequacy of both the SSF and the spatial resolution kernel. In all cases we not only fit the SN trace but also the underlying background such that the flux residuals $\delta F_{\text{tot}} \leq 1$. For the case of SN 2002bo a secondary point source (indicated by an arrow) in its vicinity had to be included in the input position table – and hence allocated to the point source channel – for the restoration to succeed.

Fig. 3.13 on the other hand shows the flux residuals in the dispersion direction, and one can immediately appreciate the successful allocation of (extended) atmospheric absorption features and sky emission lines to the background channel. Moreover one can immediately pick out the spectral regions affected by systematic errors in the restoration ($\delta F_{\text{tot}} > 1$) and only use those where $\delta F_{\text{tot}} \leq 1$ for analysis. The (spectral) residuals in this case were evaluated in the dispersion direction by evaluating the *spatial* residuals in a region centred on the SN position and of extent $3\sigma_{\text{SSF}}$. This ensures that we are only including the point source and its immediately underlying background.

3.7 Comparison with other methods

We choose to compare our method with alternative techniques, namely a standard extraction using IRAF, an iterative Gaussian extractor and a statistical decomposition of a 1D flux-calibrated spectrum into SN and galaxy contributions. The reason for including the latter (1D) approach is to highlight the need for the SN-galaxy separation to occur at the earliest stages of the reduction process, and not as part of a post-processing chain of data analysis. The results are summarised in Fig. 3.14. Note that algorithms similar to ours do

⁵<http://archive.eso.org/>

Table 3.4: *specinholucy* parameters

SN ^a	σ_{kernel} [pixels]	FWHM		SN+bg ^c	SN/bg ^d
		DIMM	SSF		
2002bo_1	4.0	6.25	6.93	63.6	4.8
2002bo_2	4.0	7.95	6.57	62.5	4.6
2002gr	2.2	5.85	3.46	9.0	1.4
2002go	3.5	5.75	3.97	5.2	2.1

(a) IAU designation. Note that two spectra were taken of SN 2002bo.

(b) mean FWHM in pixels of the Gaussian seeing corresponding to the DIMM station measurement or to the SSF used to extract the spectrum.

(c) mean number of counts (ADU) in the dispersion direction of the input 2D spectrum at the location of the SN.

(d) ratio of the integrated SN flux and that of the underlying background. One can calculate the mean signal-to-noise per pixel using $\text{SNR pix}^{-1} = \text{SN/bg} + 1$.

Table 3.5: Supernova observation summary

SN ^a	Archive id. ^b	UT date	z^c	phase ^d
2002bo	2002bo	06 Dec 2002	0.0042	+258
2002gr	sloan9	11 Oct 2002	0.091	+14 [†]
2002go	sloan5	11 Oct 2002	0.236	+2 [†]

(a) IAU designation.

(b) target name for search in the ESO archive.

(c) redshift determined from nebular lines in the host galaxy.

(d) SN phase in rest-frame days from B -band maximum. Phases marked with [†] have been determined from cross-correlations with local SN Ia templates using the SuperNova IDentification (SNID) code (Blondin et al., in prep).

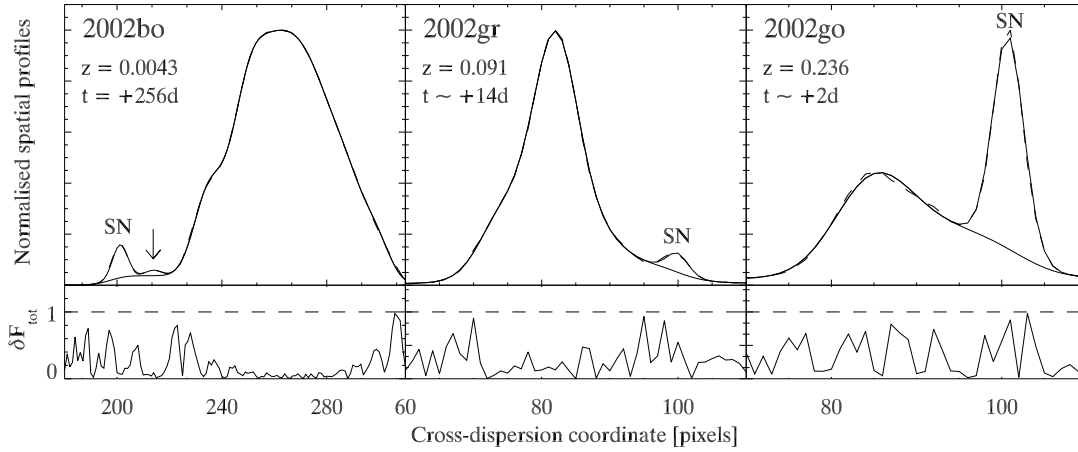


Figure 3.12: **Top panel:** Normalised average spatial profiles of the input (dashed line) and restored (solid line) 2D background spectra. Two runs of *specinholucy* were executed, one including the point source in the restored 2D background spectrum and the other excluding it, so as to appreciate how well the background underneath the SN was fit. **Lower panel:** Wavelength-averaged spatial residuals in units of the statistical noise of the input 2D spectrum. For all cases we have $\delta F_{\text{tot}} \leq 1$, meaning the combined SN+background spatial profile is restored to the statistical noise limit over the whole spatial range.

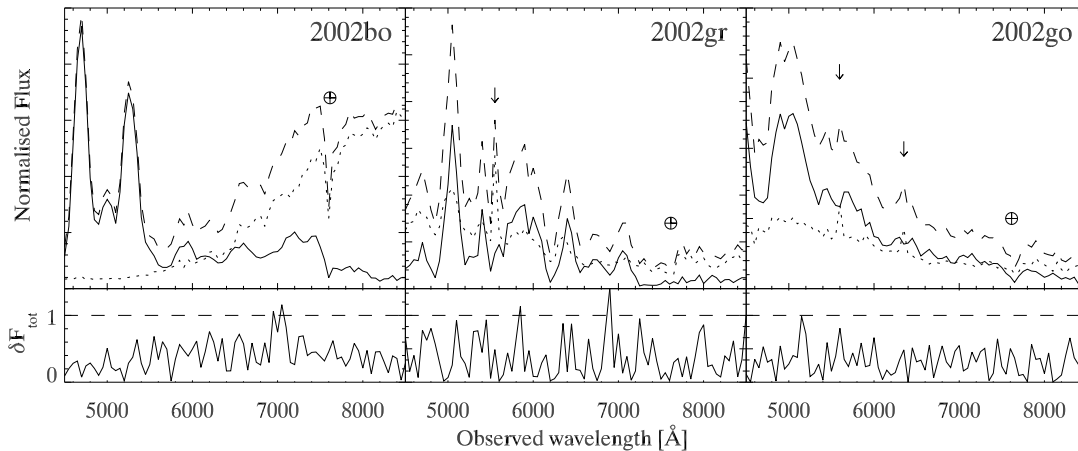


Figure 3.13: **Top panel:** Normalised restored point source spectra (solid line) and underlying background, both including (dashed line) and excluding (dotted line) the point source. The spectra have been normalised to the integral of the underlying background flux. The symbol \oplus denotes the atmospheric A-band ($\sim 7600\text{-}7630$ Å), whilst arrows indicate strong sky emission lines. **Lower panel:** Spectral residuals in units of the statistical noise of the input 2D spectrum.

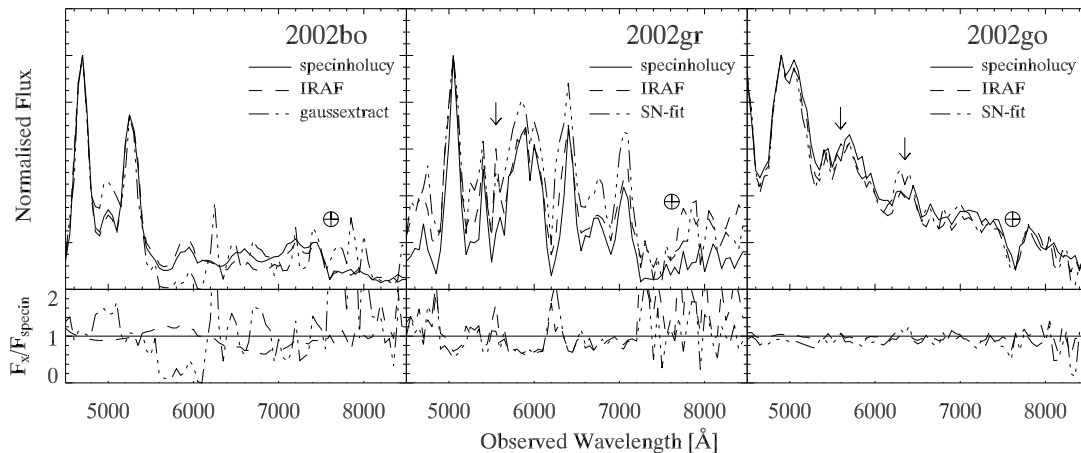


Figure 3.14: **Top panel:** Restored supernova spectra using *specinholucy* (solid line) and other methods presented in Sect. 3.7. The spectra are normalised to the maximum flux value of the *specinholucy* output. Due to the specificities of *SN-fit* – namely the restriction of the local SN template spectra to epochs $-20\text{d} < t < +20\text{d}$, we restrict its application to SN 2002gr and 2002go (we plot the solution corresponding to the smallest χ^2 – see text.), for which we have not plotted the *gaussextract* output for the sake of clarity. The symbol \oplus and arrows have the same meaning as in Fig. 3.13. **Lower panel:** Ratios of the various spectra to the *specinholucy* output. We have deliberately restricted the y-axis range to $[0,2]$ to be able to visualise small $\sim 20\%$ differences in the SN flux.

exist (though unlike ours they are not publicly available), and should these be of interest to the reader we refer him/her to Lucy and Walsh [185], Sect. 6.

3.7.1 Standard extraction in IRAF

For most purposes IRAF and similar reduction software are sufficient for extracting a high S/N supernova spectral trace. The extraction can be further optimised by e.g. tracing the point source signal along the dispersion direction or variance-weighting the output flux. However, the hold on *systematic* errors is null and one tends to evaluate the resulting spectrum on purely qualitative grounds. In the case of high- z SN Ia spectroscopy the extraction of the SN spectrum is often considered successful when the cross-correlation with a local SN Ia template spectrum is maximal. This clearly bypasses the specificity of the high- z spectrum and affects the search for systematic spectral differences between high- z SN Ia spectra and their local counterparts.

Of equal concern is the arbitrary definition of the SN “background” in IRAF. One specifies a set of spatial coordinates in the vicinity of the SN trace to be fit by some user-defined polynomial ... and essentially hopes for the best! In particular one has to find a compromise between the varying width of the SN cross-dispersion profile (i.e. its FWHM-wavelength relation) and the varying structure of the underlying background. Cases such as

that encountered for SN 2002bo – namely the contamination of the close SN background by a secondary point source – are extremely delicate to handle in a coherent way with standard spectral reduction packages and lead in this case to $\gtrsim 40\%$ errors in the SN flux. Other errors in the extraction using IRAF are due to the varying spectrum of the underlying background, to strong sky emission lines and to the overall increase in sky noise at long wavelengths. The extracted spectrum of SN 2002go for instance is clearly affected by sky residuals, and more specifically the Si II feature (6355 Å) blueshifted to ~ 6150 Å and characteristic of Type Ia supernovae lies in the same region as the atmospheric A-band at $z = 0.236$, and is clearly contaminated by it. Any measure of line strengths and ratios in this region will thus also be affected, leading to significant errors in empirical correlations based on such measurements, e.g. the “Nugent relation” (see [215] and Sect. 3.3.3 in this paper). In cases where the signal-to-noise ratio is low (cf. SN 2002gr) there is obvious contamination from the underlying background in the SN spectrum, leading to significant errors; in fact, in many bandpasses no SN flux is output at all, where *specinholucy* is able to restore the SN contribution over the whole wavelength range.

3.7.2 *Gaussextract* – an iterative Gaussian extractor

In applying *specinholucy* to the restoration of supernova spectra we need to degrade the resolution of the background channel to discriminate between the SN and its underlying background. To illustrate the advantages of using a two-channel restoration we have written a software (*gaussextract*) that iteratively extracts the point source spectrum using the *same* synthetic SSF as for the *specinholucy* run. As in *specinholucy*, each dispersion channel is treated independently and the process is iterated till some minimal fractional change in the restored SN flux is achieved. For the sake of comparison with *specinholucy*, *gaussextract* runs the same convergence criteria for the point source flux. The difference here is that the SN and underlying background are jointly extracted in the same channel, leading to significant contamination by sky lines and host galaxy in the output SN spectrum (cf. SN 2002bo in Fig.3.14).

3.7.3 Statistical approach using \mathcal{SN} -fit

\mathcal{SN} -fit is a software package developed by Grégory Sainton (see [261]) to rapidly identify the supernova type and redshift in the SuperNova Legacy Survey (SNLS). The goal is to quickly identify candidates from their spectrum, for which the SN phase and the fraction of host galaxy light can be estimated. The algorithm is based on a χ^2 fitting of the observed (and reduced) 1D spectrum to known template spectra. More specifically the observed spectrum is compared with a model made of a fraction α of SN (\mathcal{S}) and a fraction β of galaxy (\mathcal{G}). The following model spectra \mathcal{M} are built :

$$\mathcal{M}(\lambda_{\text{rest}})(z, \alpha, \beta) = \alpha \mathcal{S}(\lambda_{\text{rest}}(1+z)) + \begin{cases} \beta \mathcal{G}(\lambda_{\text{rest}}(1+z)) & \text{(a)} \\ \beta \mathcal{G}(\lambda_{\text{obs}}), & \text{(b)} \end{cases} \quad (3.7)$$

where λ_{rest} and λ_{obs} are the rest-frame and observed wavelength, respectively. (a) corresponds to the case where a local galaxy template spectrum is redshifted to fit the observed spectrum, whereas (b) makes use of the observed SN host galaxy itself. The χ^2 is made robust against aberrant points (remaining sky lines, mostly). The fit is done for every galaxy-supernova pair and the results are sorted in ascending χ^2 . One is therefore able to evaluate how significant the best result is with respect to other SN-galaxy combinations, and in turn how confident one should be about the output supernova type, redshift and epoch.

It should be noted that, contrary to the other methods presented in this Sect., \mathcal{SN} -fit is a *post*-processing tool and thus cannot be required to correct for systematic errors made in the reduction process (most likely using standard software packages such as IRAF or MIDAS⁶), such as improper removal of sky lines. These errors will propagate in the \mathcal{SN} -fit result, as seen in the output spectrum of SN 2002go where the Si II feature is also affected by the atmospheric A-band. SN 2002gr on the other hand illustrates the limits of using a χ^2 minimisation technique to separate the SN from the underlying background in low signal-to-noise cases.

The advantages of this purely statistical approach is that no *a priori* assumption is made about the underlying background. The host galaxy contamination is removed using a galaxy template or better still the SN host galaxy itself. The determination of the supernova type and redshift is greatly improved upon and the enhanced accuracy of this approach is discussed by Sainon [261]. The disadvantage is that we are limited by the database of local SN, and any spectral peculiarities will not be independently accounted for, if they are not reproduced in local SN spectra. Also, the fact that in both cases we use the observed SN host galaxy itself as a template to decompose the extracted SN trace into a supernova and a galaxy component – case (b) in the above system of equations – illustrates what we were implying in Sect. 3.4 about the propagation of supernova “features” in the final SN spectrum through the inherent imperfections of the galaxy template removal approach.

3.8 Conclusion

We have presented the advantages of using a more elaborate spectral extraction algorithm for obtaining supernova spectra devoid of background contamination, and hence make possible a truly quantitative analysis of high- z Type Ia supernova spectra. This will allow us in the future to set constraints on potential evolutionary effects that could affect SN Ia as function of redshift. Not only are we able to extract the PSF-like components of an input spectrum, we can also restore the entire 2D spectrum and hence get a hold on systematic errors linked with the restoration process. We thus have a quantitative way of judging whether the extracted SN spectrum is optimal for subsequent analysis and whether we are

⁶ESO-MIDAS is a registered trademark of the European Southern Observatory; see <http://www.eso.org/projects/esomidas/>.

not mistakenly “seeing” SN-like features in a pure galaxy spectrum, as is sometimes the case in low S/N high- z SN Ia spectra.

However, there are some caveats mainly associated to the complexity of *specinholucy*. Errors associated with the use of an inappropriate SSF for restoring the point-source channel or a mis-evaluation of the width of the spatial resolution kernel necessary for the point-source/extended background discrimination will strongly affect the restoration (see Sect. 3.3). Through restoration of the 2D background spectrum one is however able to produce diagnostic plots to critically evaluate the error in each case and repeat the restoration with different settings (see Fig. 3.5).

Note that a valuable by-product of this novel technique is the acquisition of a host galaxy spectrum with no contamination from the supernova flux! Galaxies at $z \sim 0.5$ are at most a few arcseconds in size and one can essentially obtain integrated spectra of high- z SN host galaxies by centering a slit on both the SN and its host. This in turn makes it possible to study of properties of high- z SN Ia host galaxies and compare them with integrated spectra of local SN Ia hosts [285, 318, 92].

Thus, *specinholucy* provides the high- z supernova community with a reliable tool to obtain clean SN Ia spectra and in turn to derive accurate physical quantities associated with the ejecta. Two of the authors (Stéphane Blondin and Bruno Leibundgut) are part of the ESSENCE project, and Grégory Sainton is part of the SNLS collaboration. Both teams recognise the need for a quantitative analysis of their results in order to constrain potential systematic effects that could distort the cosmological results derived from observations of high- z SN Ia. We have shown *specinholucy* to be the ideal tool for this purpose. In fact, the VLT data taken for the ESSENCE project will be shown in their restored form via *specinholucy* by Matheson et al. [187].

Many thanks to John Moustakas for providing the zero-point for the spectrum of NGC 6181 and to Mattia Vaccari for deriving the galaxy luminosity profile used in the simulation. We further would like to thank the anonymous referee for many detailed and useful comments on the original manuscript.

But lo! Men have become the tools of their tools.
Henry David Thoreau

Chapter 4

A tool to determine supernova redshifts

Abstract: We present an algorithm used by members of the ESSENCE Team to identify the type of supernova spectra and determine their redshift. This algorithm, based on the correlation techniques of Tonry and Davis [290], is implemented in the SuperNova IDentification code (SNID; Blondin et al., in prep). We show that an appropriate use of this code can enable to determine whether a noisy spectrum is indeed that of a Type Ia supernova. Furthermore, by comparing the correlation redshifts obtained using SNID with those determined from narrow emission/absorption lines in the host galaxy, we show that accurate redshifts (with a typical error $\sigma_z \lesssim 0.01$) can be determined for SN Ia for which a spectrum of the host galaxy is unavailable.

4.1 Introduction

A fundamental part of using Type Ia supernovae (SN Ia) as cosmological probes is to determine their redshift. It is the comparison of the supernova redshift with its luminosity distance d_L that enables a joint determination of the $(\Omega_M, \Omega_\Lambda)$ cosmological parameters (see Chap. 1). Computing d_L also requires *a priori* knowledge of the SN redshift (see Eqn. 1.12 in Chap. 1), although Barris and Tonry [13] have presented a method to obtain redshift-independent distances to high- z SN Ia.

There are essentially two ways to determine the redshift of a SN Ia, both requiring a spectrum: (1) the redshift can be determined from narrow emission/absorption lines in the host galaxy spectrum; (2) the redshift can be estimated *via* cross-correlating the high- z SN Ia spectrum with zero-redshift local templates. The first method yields a more accurate redshift estimate, as the error is governed by the galaxy velocity dispersion (which does not exceed $\sim 300 \text{ km s}^{-1}$, or 0.001 in redshift – see Sect. 4.4), though the implicit assumption is that the galaxy superimposed on the supernova is indeed the latter’s host. A recent example of such a confusion is given by Blakeslee et al. [22]. Using grism spectra taken with the Advanced Camera for Surveys (ACS) on board the Hubble Space Telescope

(*HST*), Blakeslee et al. [22] showed that the host galaxy of SN 2002dd [292], a Type Ia supernova at $z \approx 0.95$, was in fact a faint galaxy projected onto a brighter galaxy at a lower redshift ($z_{\text{gal}} = 0.79$). Moreover, most high- z SN Ia host galaxy spectra only have a single prominent emission line in their optical spectra, almost always assumed to be [O II] $\lambda 3727$. One can justify this assumption on the account that a faint galaxy barely detectable with 8–10 m-class telescopes is “bound” to be at a high redshift, shifting [O II] $\lambda 3727$ in the middle of the optical range; moreover, if the emission was due to a higher rest-frame wavelength line, e.g. H α $\lambda 6563$, then other prominent lines ([O III] $\lambda\lambda 4959, 5007$, [N II] $\lambda 6583$, [S II] $\lambda\lambda 6717, 6731$) should also be visible in the spectra. Thus, in principle, a reliable galaxy redshift should rely on more than one emission/absorption feature.

Moreover, sometimes the SN host galaxy is too faint for a spectrum to be obtained, or the resulting spectrum has too low a S/N ratio for a redshift to be determined. Also, galaxies with no recent or ongoing star formation will lack prominent emission lines, and the galaxy redshift has to be determined from absorption lines (typically Ca II H&K), which have lower signal than the galaxy continuum. Even when a reliable galaxy redshift can be determined, an agreement with a correlation SN redshift is highly desirable (see Sect. 4.4). The second method (cross-correlation) has typical associated errors of ~ 0.01 in redshift (see Sect. 4.2.3), although it is not subject to the possible projection effects of the first method.

In this chapter we present such a cross-correlation tool, based on the algorithm presented by Tonry and Davis [290], and originally applied to galaxy spectra. Here, we present the specific application of this algorithm to the estimation of supernova redshifts based on cross-correlations with high S/N local SN templates shifted to zero redshifts (Sect. 4.2). The algorithm is implemented in the SuperNova IDentification (SNID; Blondin et al., in prep) code, developed for determining redshifts to high-redshift SN Ia, and actively used by members of the ESSENCE team ([187]; Appendix A).

The phase distribution of the local templates is plotted in Fig. 4.1. Only templates corresponding to Type Ia supernovae are shown, although we also have a comparatively low number of Type Ib/c and Type II supernova template spectra, as well as galaxies from the Kennicutt atlas [143] and M (flare) stars. The 224 SN Ia spectral templates also include objects whose spectra at a given phase and/or spectral evolution is non-standard: SN 1986G, 1991T, 1991bg, 1997br, 1997cn, 1999by. The data used to build the histograms of Fig. 4.1 are listed in Table 4.1. In the last column of Table 4.1 we also list the database from which these templates were drawn, namely the CfA spectral database or the SUSPECT¹ database.

In all that follows, we implicitly assume that the input supernova spectrum is that of a Type Ia supernova. Of course, a good correlation with a local SN Ia spectral template means that the input spectrum has a high probability of being a SN Ia at the redshift output by SNID; however, as of the current version we have no way of quantifying this probability in SNID. In particular, we have no way of quantifying the probability that the input spectrum is *not* that of another supernova type. The current SNID database is

¹The Online SUPernova SPECTrum Archive; <http://suspect.nhn.ou.edu/~suspect/index1.html>

Table 4.1: SN Ia spectral templates for SNID

SN	Phases ^a	Database
1981B	+0, +6, +17, +20, +24	CfA
1989B	-6, +0, +4, +6, +[8-10], +[12-15], +18	CfA
1990N	-[14-13], -[8-6], +5, +8, +15, +[17-18]	CfA + SUSPECT
1990O	-[7-5], +0, +[19-20]	CfA
1992A	-5, +0, +3, +[5-7], +9, +12, +16, +17	CfA
1993ac	+6	CfA
1994D	-[11-2], +[2-3], +[10-13], +15, +17, +19, +22, +24, +29	SUSPECT
1994M	+ [3-5], +8, +13	CfA
1994S	-3, +0, +2	CfA
1994ae	-1, +[0-5], +[8-10], +29	CfA
1995D	+ [3-5], +7, +9, +11, +[14-15]	CfA
1995E	-[3-1], +1, +8	CfA
1995al	+17, +26	CfA
1995bd	+12, +16, +21	CfA
1996C	+8	CfA
1996X	-[3-1], +[0-3], +7, +8(2), +9, +13, +22, +24	CfA + SUSPECT
1996Z	+6	CfA
1998aq	-[9-8], +[0-7]	SUSPECT
1998bu	-[3-1], +[9-14], +[28-30]	CfA
1999ee	-9, -7, -2, +0, +2, +7, +11, +16, +19, +22, +27	SUSPECT
Spectroscopically peculiar SN Ia		
1986G	-[5-1], +[0-3], +5	CfA
1991T	-11, -[9-5], -2, +[8-11], +[14-22], +26	CfA
1991bg	+ [1-2], +3(2), +[15-16], +19, +26, +29	CfA + SUSPECT
1997br	-[9-6], -4, +8, +18, +24	SUSPECT
1997cn	+4	SUSPECT
1999by	-[-2], +8, +11, +25, +29	SUSPECT

^a SN phase in rounded days from *B*-band maximum. Consecutive phases are listed in between square brackets, and phases for which we have to spectra of a given supernova are denoted by (2).

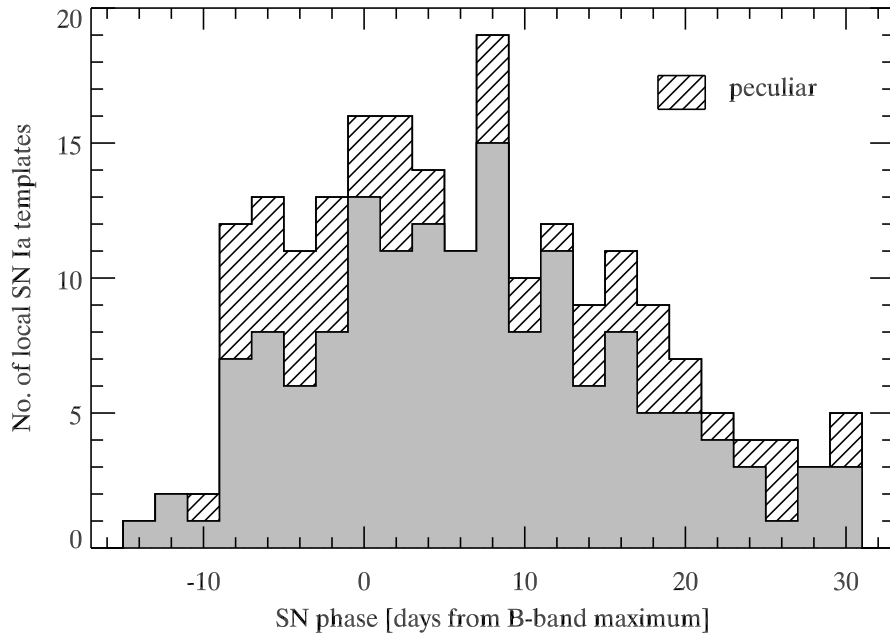


Figure 4.1: Phase distribution of the 224 SN Ia spectral templates used in SNID. The hashed area corresponds to 71 spectra of “peculiar” objects: SN 1986G, 1991T, 1991bg, 1997br, 1997cn, 1999by.

heavily biased towards SN Ia spectra (there are ~ 10 times more SN Ia templates than of supernova of other types), and a poor correlation with, e.g., a Type Ic supernova does not necessarily imply that the input spectrum is not a supernova of that type. We will come back to this issue in Sect. 4.5.

4.2 Cross-correlation techniques

The correlation method presented in this section is extensively discussed by Tonry and Davis [290], where it is exclusively applied to galaxy spectra. We reproduce part of this discussion here to highlight the specificity of determining supernova (as opposed to galaxy) redshifts.

4.2.1 Pre-processing the supernova spectrum

The correlation technique is in principle fairly straightforward. One correlates a supernova spectrum $s(n)$ whose redshift is to be found with a template spectrum $t(n)$ at zero redshift, and determine which $(1+z)$ wavelength scaling, where z is the redshift of $s(n)$, is required to maximize the cross-correlation $c(n) = s(n) \star t(n)$, where \star denotes the cross-correlation product.

In practice, however, it is convenient to bin the spectra linearly with $\ln \lambda$, where λ is the wavelength. Supposing the spectra are discretely sampled into N bins, labelled by bin number n , the relation between n and wavelength λ_n is then:

$$n = A \ln \lambda_n + B. \quad (4.1)$$

The spectra are assumed to be periodic with period N for purposes of discrete Fourier transforms and derived correlation functions. Scaling the wavelength axis of $t(n)$ by a factor $(1+z)$ is then equivalent to adding a $\ln(1+z)$ shift to the logarithmic wavelength axis of $t(n)$, i.e. a (velocity) redshift corresponds to a uniform linear shift. Suppose we want to bin $s(n)$ and $t(n)$ into N bins in the range $[\lambda_0, \lambda_1]$; the size of a logarithmic wavelength bin is simply:

$$d\lambda_{\log} = \frac{\ln(\lambda_1/\lambda_0)}{N}, \quad (4.2)$$

and each logarithmic wavelength element $\lambda_{\log,n}$ is given by:

$$\lambda_{\log,n} = \lambda_0 e^{n \times d\lambda_{\log}}, \quad (4.3)$$

assuming n runs from 0 to N .

We show the result of mapping the input supernova spectrum onto a logarithmic wavelength axis with $(\lambda_0, \lambda_1, N) = (2500 \text{ \AA}, 10,000 \text{ \AA}, 1024)$ in the left panels of Fig. 4.2. In panel (a), we plot the input spectrum in F_λ flux units *vs.* λ , and in panel (b) we plot a portion of this spectrum in the same flux units, but binned onto the logarithmic wavelength axis. Here, the size of a logarithmic wavelength bin is $d\lambda_{\log} = \ln(10,000/2500)/1024 \approx 0.0014$, according to Eqn. 4.2. So a shift by one bin in $\ln \lambda$ space corresponds to a redshift of ~ 0.0014 , or a velocity shift of $\sim 400 \text{ km s}^{-1}$.

The next step in preparing the spectrum for correlation analysis is continuum subtraction [290]. This effectively removes any intrinsic colour information in the input and template spectra, and ensures the correlation is not affected by reddening uncertainties or instrumental distortions. For galaxy spectra, the continuum is well defined and is easily subtracted using a fourth-order least-squares polynomial fit. This minimizes discontinuities between each end of the spectrum, which would cause artificial peaks in the correlation function. Further discontinuities are removed by apodizing the spectra with a cosine bell ($\sim 5\%$ at either end). For Type Ia supernova spectra, however, the continuum is ill-defined (and is optically thin by maximum light; see Chap. 2). Removing a 13-point cubic spline fit to the spectrum is akin to subtracting a *pseudo* continuum from the supernova spectrum. This effectively discards any spectral colour information, and the correlation only relies on the *relative* shape of spectral features in the input and template spectra. The result of subtracting a *pseudo* continuum from the input spectrum is shown in panel (c) of Fig. 4.2. We show the full suite of spectra for a local SN Ia spectral template (SN 1992A [149]) shifted to zero redshift in Fig. 4.3. The phase of a given spectrum is indicated in days from B -band maximum.

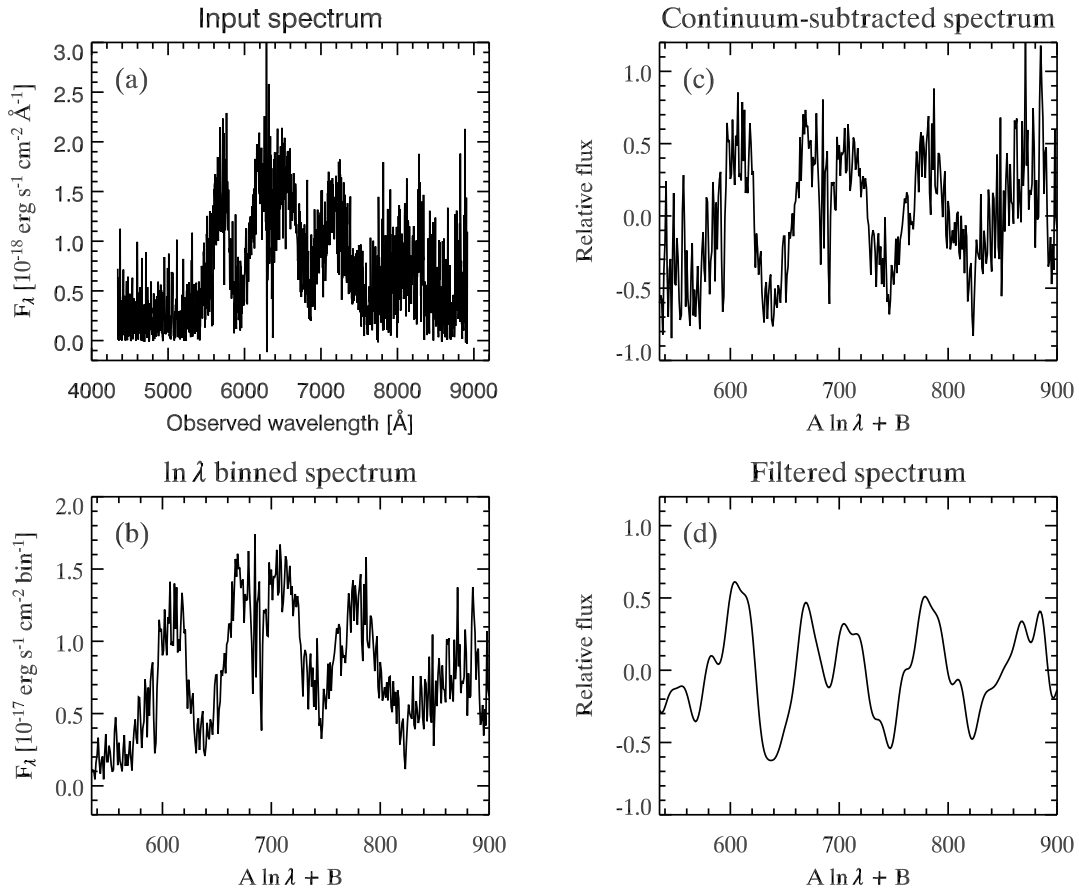


Figure 4.2: (a) Spectrum of the Type Ia supernova SN 2003jj ($z = 0.583$); (b) The result of mapping the spectrum to $\ln \lambda$ coordinates, with $(\lambda_0, \lambda_1, N) = (2500 \text{ \AA}, 10,000 \text{ \AA}, 1024)$ (see text for details); (c) A 13-point spline has been subtracted and the result apodized with a cosine bell; (d) A bandpass filter with $(k_1, k_2, k_3, k_4) = (5, 10, 50, 75)$ has been applied to the spectrum. The same filter will be applied to the correlation function, so as to remove correlation peaks resulting from noisy spectral features ($k > k_4$) and from large-scale variations remaining after the spline subtraction ($k < k_1$) (see also [290], their Fig. 2).

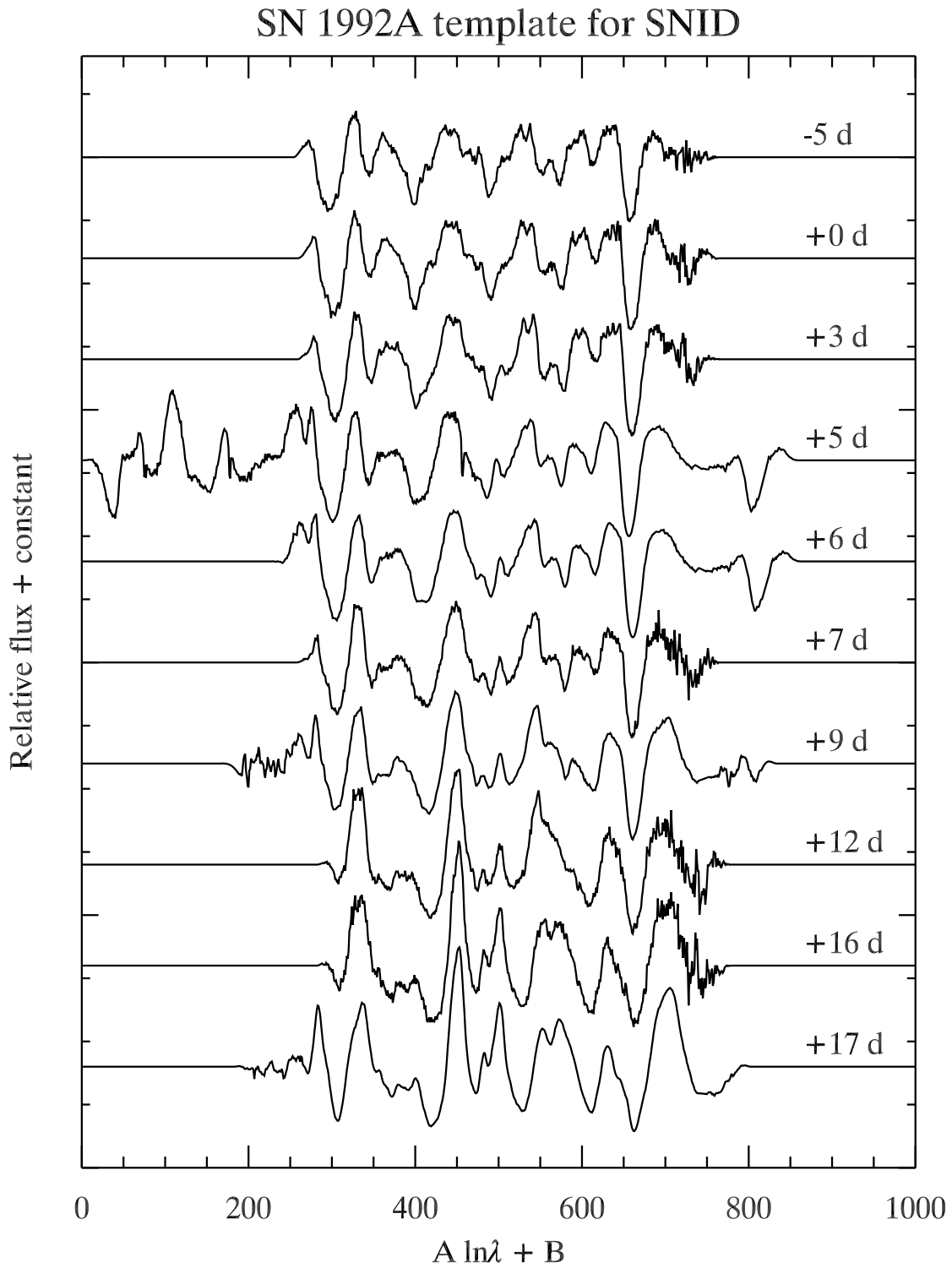


Figure 4.3: Example of a SNID SN Ia spectral template (SN 1992A [149]). The spectra are binned onto a logarithmic wavelength scale, and a pseudo-continuum is subtracted via a spline fit. The labels indicate the phase of the spectrum, in days from B -band maximum.

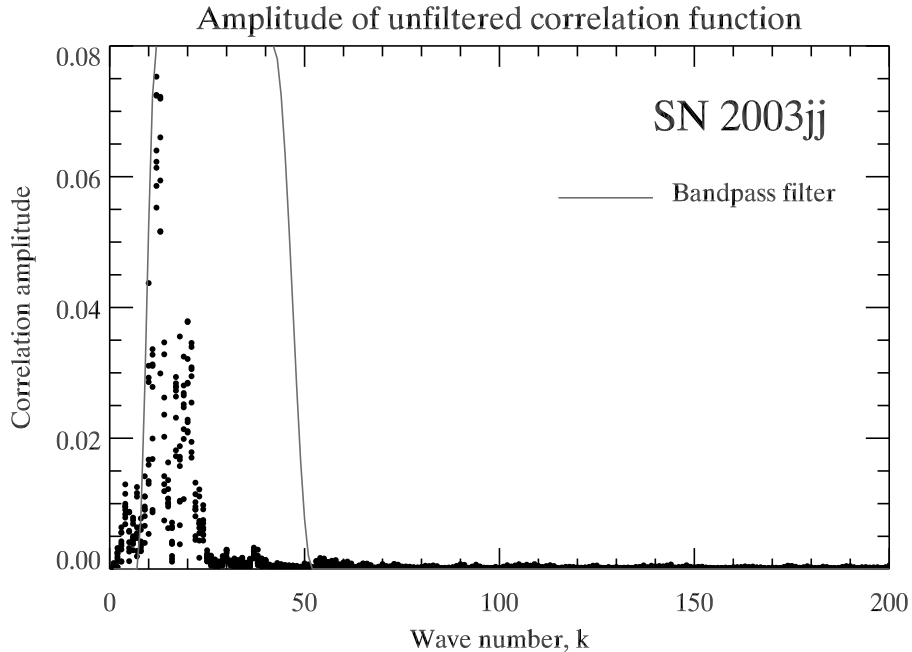


Figure 4.4: Amplitude of the Fourier transform of the unfiltered correlation function of SN 2003jj (Fig. 4.2) with the nine best-fit spectral templates found by SNID. Most of the correlation power is concentrated at low wave numbers ($k < 50$), thereby justifying our use of a bandpass filter.

In the original Tonry and Davis [290] paper, a bandpass filter is applied to the (galaxy) spectrum before the cross-correlation proceeds. This removes low-frequency residuals left over from the pseudo-continuum subtraction and high-frequency noise components. In SNID, however, a bandpass filter is applied at a later stage, directly to the correlation function (see next Sect.). Supernova lines have typical widths of $\sim 100 - 150 \text{ \AA}$, due to the large ($\sim 10,000 \text{ km s}^{-1}$) expansion velocities of the ejecta (see Chap. 2). The mean size of a logarithmic wavelength bin with $(\lambda_0, \lambda_1, N) = (2500 \text{ \AA}, 10,000 \text{ \AA}, 1024)$ is $\sim 7.2 \text{ \AA}$, so a typical SN line will have a width of $w_{\text{SN}} \sim 13.7 - 20.5 \log$ wavelength bins. In Fourier space, most of the information will be at wave numbers $k = (N/2\pi) \times w_{\text{SN}} \approx 8 - 12$. Since SN spectra consist of overlapping spectral lines, a typical SN feature may have a lower width ($\lesssim 50 \text{ \AA}$). This translates to $k \sim 24$, so most information is at wave numbers less than 24 and almost everything above wave number $k \sim 50$ is noise. Also, low wave numbers ($k \lesssim 5$) contain information about the low-frequency residuals from continuum subtraction. In Fig. 4.4 we show the amplitude of the Fourier transform of the unfiltered correlation function of the Type Ia SN 2003jj (Fig. 4.2) with the nine best-fit zero-redshift templates, as a function of wavenumber. As expected, most of the correlation power is at wave numbers $k \sim 10 - 20$, and virtually no information is contained in wave numbers $k > 30$.

So the Fourier transform of the $c(n)$ correlation function is multiplied by a *real* bandpass

function (so that no phase shifts are introduced) which starts rising from 0 at $k_1 = 5$, reaches 1 at $k_2 = 10$, starts falling from 1 at $k_3 = 40$, and reaches 0 again at $k_4 = 50$. An example of such a bandpass filter is overplotted in Fig. 4.4 (*grey line*). The result of applying this filter to a supernova spectrum is shown in panel (d) of Fig. 4.2. Note how most of the sharp noisy features have been removed from the input spectrum.

Obviously the exact choices for (k_1, k_2, k_3, k_4) depend on the size of each k bin (which corresponds to a certain $\ln \lambda$ and therefore a certain $\ln(1+z)$), and on the spectral distribution of a supernova spectrum (which depends on the velocity broadening). In the current version of SNID, the choices of wave numbers used for filtering are left to the user. A future version will optimize the bandpass filter used for a given input/template spectra combination, taking into account the adopted $\ln \lambda$ grid used and the spectral characteristics of both supernovae.

4.2.2 Estimation of redshift

Cross-correlation formalism

Correlations in SNID occurs in Fourier space, since algorithms such as the Fast Fourier Transform (FFT) reduce the number of computations needed for N points from $2N^2$ to $2 \log_2 N$, i.e. a factor of $\sim 10^5$ for $N = 1024$.

In what follows, we assume the supernova spectrum whose redshift is to be determined and the zero-redshift template spectrum to be binned in $\ln \lambda$, *pseudo*-continuum subtracted and apodized (see previous section). Let $S(k)$ and $T(k)$ be the discrete Fourier transforms of the supernova and template spectra, $s(n)$ and $t(n)$, respectively, defined by

$$S(k) = \sum_{n=0}^{N-1} s(n) e^{-2\pi i n k / N} \quad (4.4)$$

$$T(k) = \sum_{n=0}^{N-1} t(n) e^{-2\pi i n k / N}. \quad (4.5)$$

Let σ_s and σ_t be the root-mean-square (RMS) of the supernova and template spectrum, respectively:

$$\sigma_s^2 = \frac{1}{N} \sum_{n=0}^{N-1} s(n)^2 \quad (4.6)$$

$$\sigma_t^2 = \frac{1}{N} \sum_{n=0}^{N-1} t(n)^2. \quad (4.7)$$

The *normalized* correlation function $c(n)$ is defined as

$$c_{\text{norm}}(n) = s(n) \star t(n) = \frac{1}{N\sigma_s\sigma_t} \sum_{n=0}^{N-1} s(m)t(m-n), \quad (4.8)$$

such that if the supernova spectrum is the same as the template spectrum, but shifted by δ log wavelength bins – i.e. $s(n) = t(n - \delta)$, then $c_{\text{norm}}(n) = 1$ at $n = \delta$. The Fourier transform of the correlation function is

$$C_{\text{norm}}(k) = \frac{1}{N\sigma_s\sigma_t} S(k)\overline{T(k)}, \quad (4.9)$$

where $\overline{T(k)}$ denotes the complex conjugate of $T(k)$.

We then multiply $C_{\text{norm}}(k)$ by our real bandpass filter function $B(k_1, k_2, k_3, k_4)$, and inverse-Fourier transform the result. The real part of the outcome is the filtered correlation function $c_{\text{filt}}(n)$:

$$C_{\text{norm}}(k) \longrightarrow C_{\text{filt}}(k) = C_{\text{norm}}(k) \times B(k_1, k_2, k_3, k_4) \quad (4.10)$$

$$c_{\text{norm}}(n) = \sum_{k=0}^{N-1} C_{\text{filt}}(k) e^{2\pi ink/N} \quad (4.11)$$

$$c_{\text{filt}}(n) = \Re[c_{\text{norm}}(n)]. \quad (4.12)$$

Examples of such filtered normalized correlation functions are shown in the middle panel of Fig. 4.5 (we will shortly describe Fig. 4.5 at length when discussing the correlation parameter, r). One can see that, in general, $c_{\text{filt}}(n)$ has many peaks in redshift space. The true redshift is most likely the one corresponding to the highest peak in $c_{\text{filt}}(n)$, although in poor signal-to-noise ratio (S/N) cases some peaks can distort or surpass the true redshift peak (see the middle plot in the right column of Fig. 4.5). In practice, one selects all the peaks in $c_{\text{filt}}(n)$ one by one, and performs a fit with a smooth function (here a fourth-order polynomial) to determine the peak height and position, h and δ , respectively. We compute a correlation parameter (r , discussed below) for each correlation peak, and estimate the most likely redshift.

Cross-correlation r -value

One can consider $c_{\text{filt}}(n)$ to be the sum of an auto-correlation of a template spectrum $t(n)$ with a shifted template spectrum $t(n - \delta)$ and of random function $a(n)$ that can distort the correlation peak. Namely,

$$c_{\text{filt}}(n) \equiv t \star t(n - \delta) + a(n). \quad (4.13)$$

The first term on the right-hand side of Eqn. 4.13 is supposed to give a correlation peak of height $h = 1$ at the exact redshift (corresponding to a shift δ in log wavelength units), whilst the second part can distort the peak. Since $t \star t(n - \delta)$ is symmetric about $n = \delta$,

the antisymmetric part of $c_{\text{filt}}(n)$ about $n = \delta$ equals the antisymmetric part of $a(n)$ about $n = \delta$:

$$\frac{1}{2}[c(n + \delta) - c(-n + \delta)] = \frac{1}{2}[a(n + \delta) - a(-n + \delta)]. \quad (4.14)$$

A mismatch between input and template spectra can in principle produce noise that is symmetric about $n = \delta$, though one can assume that the amplitude of the symmetric part of $a(n)$ will have roughly the same amplitude as its antisymmetric part. Moreover, we assume that the symmetric and antisymmetric parts of $a(n)$ are uncorrelated, in which case the RMS of $a(n)$, σ_a , is $\sqrt{2}$ times the RMS of its antisymmetric component. From Eqn. 4.14, it follows that:

$$\sigma_a^2 \approx \frac{1}{N} \frac{1}{2} \sum_{n=0}^{N-1} [c(n + \delta) - c(-n + \delta)]^2. \quad (4.15)$$

For each correlation peak in $c_{\text{filt}}(n)$, one can define a correlation parameter r_p as the ratio of the height of the correlation peak h_p to the average peak height in $a(n)$:

$$r_p = \frac{h_p}{\sqrt{2}\sigma_a}. \quad (4.16)$$

Thus, r_p will be small ($r_p < 3$) for a spurious correlation peak, and large for a significant peak, since $h_p \rightarrow 1$ and $\sigma_a \rightarrow 0$.

By correlating the input spectrum with each of the available template spectra (see Sect. 4.4), one can determine the distribution of peak centre δ_p vs. r_p -value, in which each δ_p is replicated w times according to the following weighting scheme:

$$\begin{aligned} w &= 5 & \text{for } r_p > 6 \\ w &= 3 & \text{for } r_p > 5 \\ w &= 1 & \text{for } r_p > 4 \\ w &= 0 & \text{for } r_p \leq 4. \end{aligned}$$

The peak position δ which is most likely to correspond to the actual shift between input and template spectra is taken to be the median δ_p value. The redshift output by SNID is then simply

$$z = e^{\delta \times d\lambda_{\log}} - 1, \quad (4.17)$$

where $d\lambda_{\log}$ is the logarithmic wavelength bin given in Eqn. 4.2.

In Fig. 4.5 we show examples of cross-correlations and redshift estimates using SNID in the case of: an auto-correlation (*left*); a good correlation (*middle*); a poor correlation (*right*). Let us first turn to the auto-correlation of SN 1994D [220] at -2 d. In the upper plot, we show a spectrum of SN 1994D shifted to zero redshift prepared for cross-correlation in SNID (binned in log wavelength; *pseudo*-continuum subtracted and

apodized). In the middle plot, we show the resulting normalized unfiltered auto-correlation function SN 1994D*SN 1994D, in the redshift interval $0 \leq z \leq 1$. Since the spectrum of SN 1994D is shifted to zero redshift, the correlation function reaches unity at $z = 0$. Note how the auto-correlation function is very different from a delta function centered on $z = 0$, has many correlation peaks separated by ~ 0.1 in redshift, characteristic of the overall width of a typical SN Ia spectral P-Cygni profile (several 100 Ångstroms). The dominant correlation peak also has an intrinsic width corresponding to the redshift uncertainty in SNID modulated by the S/N ratio of the input spectrum. The lower plot shows the same correlation function, this time centered on the correlation redshift (and actual redshift of the input spectrum), $z = 0$. Note how the auto-correlation is symmetric about $z = 0$, as expected for an auto-correlation. We show the antisymmetric component of the correlation function in red (zero everywhere). Since $\sigma_a = 0$ for an auto-correlation, $r = h/(\sqrt{2}\sigma_a) \rightarrow \infty$.

The middle panel of Fig. 4.5 shows the same plots for a correlation of an ESSENCE high-redshift SN Ia (SN 2003jj at $z = 0.583$ [187]; Appendix A) with a local SN Ia spectral template (SN 1989B) shifted to zero redshift. In the upper plot, we show the de-redshifted spectrum of SN 2003jj (*black*) and that of SN 1989B (*red*). The visual comparison of the two spectra is satisfactory. The normalized unfiltered correlation function in the middle plot confirms this first evaluation of the quality of the spectral-template match. There are many broad peaks every ~ 0.2 in redshift, though the dominating correlation peak is easily identifiable. The correlation redshift in this case (indicated by a vertical dotted line) is $z = 0.583$, which corresponds to the redshift of the parent galaxy (see also Sect. 4.4). The lower plot reveals the antisymmetric component of the correlation function about $z = 0.583$; the corresponding correlation r value is 13.6, indicative of a reliable correlation redshift.

The lower-right panel of Fig. 4.5 displays the case of a poor correlation. The input supernova spectrum is SN 2003ku ([187]; Appendix A) and the local spectral template (shifted to zero redshift) is SN 1994S at maximum light (+0 d). The visual comparison of the two spectra is not satisfactory, and the corresponding normalized unfiltered correlation function has many peaks of approximately the same height. The peak chosen by SNID is the highest one at $z = 0.785$. The antisymmetric component of the correlation function is a lot more structured than in the previous case, and the corresponding r value is low. This high-redshift supernova was classified as “Ia?” by Matheson et al. [187]. This last example illustrates how SNID can also be used to remove supernovae of a different spectroscopic type from a sample of high- z Type Ia supernovae.

Revision of redshift estimate

An important step in the determination of the supernova redshift using SNID is the revision of the initial estimate taking into account the overlap in $\ln \lambda$ space between the input spectrum and each of the template spectra used in the correlation. In practice, the template spectra are trimmed to match the wavelength range of the input spectrum at the redshift corresponding to the initial estimate. For an input spectrum with wavelength range $[\lambda_0, \lambda_1]$,

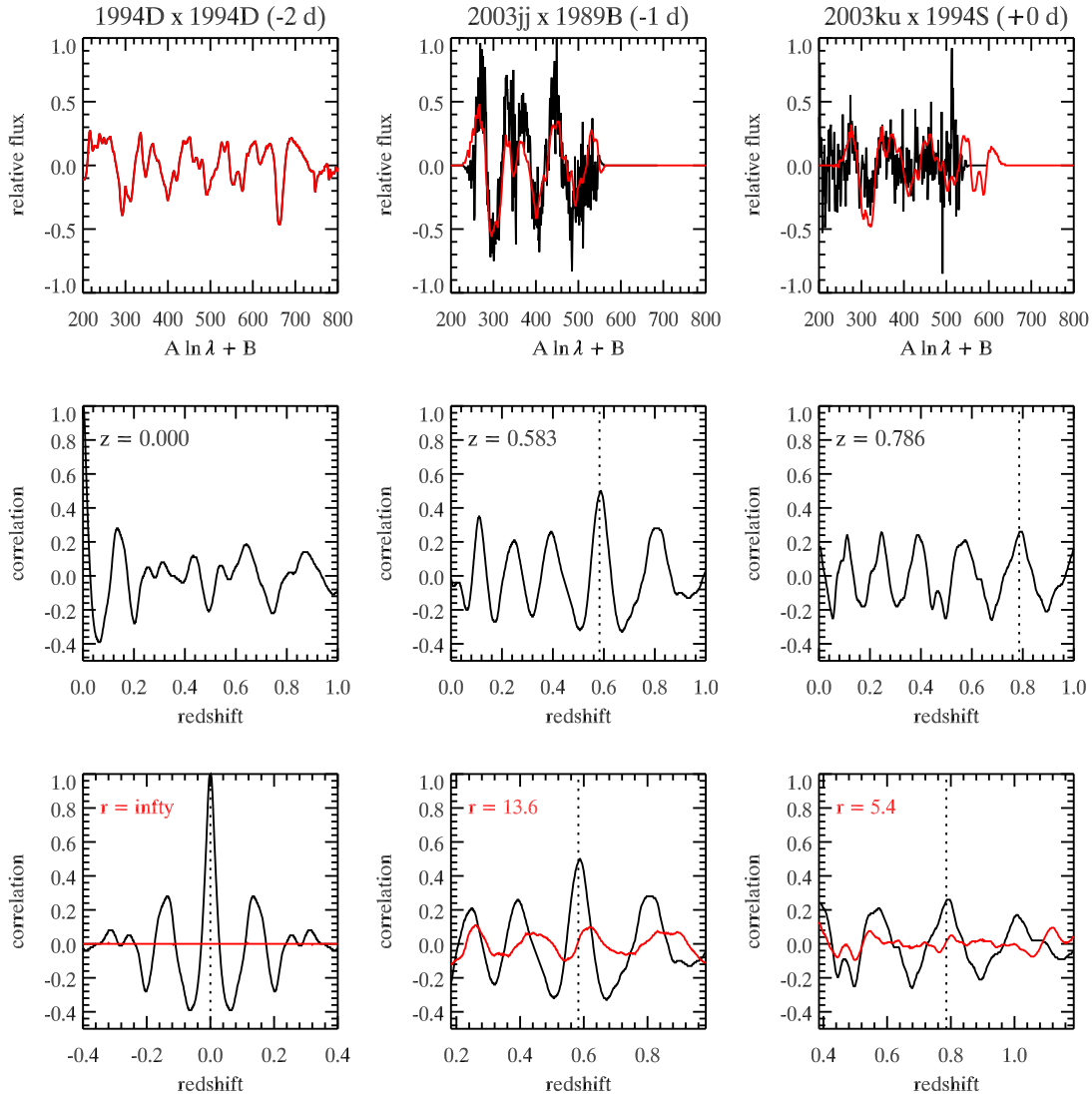


Figure 4.5: **Upper plots:** (from left to right) Continuum-subtracted spectra of SN 1994D at -2 d; SN 2003jj (*black*; $z = 0.583$) and SN 1989B at -1 d (*red*); SN 2003ku (*black*; $z = 0.786$?) and SN 1994S at $+0$ d (*red*), in $\ln \lambda$ coordinates. SN 2003jj and 2003ku have been shifted to zero redshift. **Middle plots:** (from left to right) Auto-correlation function of SN 1994D at -2 d and cross-correlation functions of SN 2003jj and 2003ku, in the range $0 \leq z \leq 1$. We indicate the redshift corresponding to the highest correlation peak. **Lower plots:** (from left to right) Auto-correlation function of SN 1994D at -2 d and cross-correlation functions of SN 2003jj and 2003ku, centered on the redshift corresponding to the highest correlation peak. Also plotted (*red line*) is the antisymmetric component of the correlation function. We compute a correlation coefficient $r = h/\sqrt{2}\sigma_a$, where h is the height of the correlation peak and σ_a is the RMS of the antisymmetric component. For an auto-correlation, $h = 1$ and $\sigma_a = 0$ (*left plot*), hence $r \rightarrow \infty$.

the maximum overlap in $\ln \lambda$ space between it and each template spectrum is

$$\text{lap}_{\max} = \ln \left(\frac{\lambda_1}{\lambda_0} \right). \quad (4.18)$$

For a spectrum in the range $4000 - 9000 \text{ \AA}$, $\text{lap}_{\max} \sim 0.8$.

The overlap value (lap) conveys important absolute information about the quality of the correlation, complementary to the correlation parameter r . Supposing a typical SN Ia spectral feature has a full width at half-maximum (FWHM) of $\lambda_{\text{FWHM}} \sim 400 \text{ \AA}$ at $\lambda \sim 5000 \text{ \AA}$, $\ln(5400/5000) \sim 0.08$, and so any correlation with $\text{lap} = 0.08$ is meaningless: *any* feature will match any other at practically any redshift. Only when a correlation has an associated lap value that is several times $\ln(\lambda_{\text{FWHM}}/\lambda)$ can we rely on the redshift output by SNID. The minimum lap value to consider can be fixed by the user and its default value is $\text{lap}_{\min} = 0.35$.

4.2.3 Estimation of redshift error

Lacking in the current version of SNID is an error model for the output redshift. One can take the correlation parameter r to be equivalent to a number of σ of statistical significance (i.e. $r = 5$ is a 5σ correlation; John Tonry, private communication), though there is no formal proof of this. Better still is to use a combination of r and the overlap between input spectrum and template, $\text{rlap} = r \times \text{lap}$, though again there is no formal proof of the relation between rlap and redshift error.

Moreover, the user has the possibility to impose various restrictions on the parameter space explored by SNID for the correlation, such as (we indicate in parentheses the default values): redshift ($-0.01 \leq z \leq 1.2$); supernova phase ($-15 \text{ d} < t < +30 \text{ d}$, in days from B -band maximum); wavelength range of input spectrum; minimum r value allowed ($r_{\min} = 3.5$); minimum overlap allowed ($\text{lap}_{\min} = 0.35$); redshift range for the final estimate ($z_i \pm 0.02$, where z_i is the initial redshift estimate). Moreover, the use of a bandpass filter means that some Fourier components will be weighted according to the values of the wave numbers used for filtering (k_1, k_2, k_3, k_4), whilst some others (those with $k < k_1$ or $k > k_4$) will be discarded from the correlation completely. Also, the fourth-order polynomial fit to the peaks in the filtered correlation function will be affected more by some Fourier components than others.

All these parameters will bias the correlation redshift somewhat, and it will be important in the near future to take their impact into account in the elaboration of an error estimator for SNID. In the meantime, we have elaborated a Monte-Carlo (MC) simulation to investigate the meanings of the r and rlap parameters in terms of redshift error.

Presentation of the simulation

In this simulation (and others that follow) we use a set of SN Ia spectral templates constructed by Peter Nugent [214]. These templates are elaborated from a combination of

observed and synthetic spectra. Most of the data used are publicly available *via* the SUSPECT database. The Nugent templates span the entire wavelength range from 1000 Å to 2.5 microns, and cover all phases (one spectrum per day) from -20 d to $+70$ d from maximum B -band luminosity. Synthetic spectra were used when there was insufficient data at a given phase to cover the desired wavelength range. These templates are well suited for such simulations, as they form a uniform and representative set of SN Ia spectra. On what follows we only use the so-called “Branch-normal” (*sic*) set of Nugent templates.

The Monte-Carlo simulation is set up as follows: a spectrum is picked at random in the phase range $-10 \text{ d} \leq t \leq +20 \text{ d}$, and redshifted to a random redshift in the range $0.1 \leq z \leq 0.9$. We then add random Poisson noise convolved with a (non-redshifted) fiducial sky spectrum (to reproduce ground-based observing conditions), to match S/N ratios between ~ 2 and ~ 15 per 5 Å bin, with a bias to high(low) S/N ratio at the lowest(highest) end of our redshift range. This roughly corresponds to one-hour integration at an 8 m class telescope, typical for high-redshift SN Ia spectroscopy. Each MC spectrum is then run through SNID, with the following restrictions on the correlation parameter space: $-0.01 \leq z \leq 1.2$ (allowed redshift range); $-15 \text{ d} \leq t \leq +30 \text{ d}$ (allowed spectral phase range, in days from B -band maximum); $4000 \text{ Å} \leq \lambda \leq 9000 \text{ Å}$ (observed wavelength range to consider in the correlation). No restrictions are imposed on the minimum r or lap values for SNID to consider in determining a correlation redshift. Degrading the S/N ratio of a give spectrum will effectively decrease the r correlation parameter, whilst increasing the supernova redshift (whilst maintaining the observed wavelength range to 4000–9000 Å) will decrease the lap (and hence the rlap) parameter. This way, we are able to explore the variation of the redshift difference between the actual and correlation redshift for a range of r and rlap values. A total of 100,000 SN Ia spectra at different redshifts and phases were generated in this Monte-Carlo realization.

In Fig. 4.6 we show a subset of SN Ia templates used in the simulation, at phases (from top to bottom) -10 d, -5 d, $+0$ d, $+5$ d, $+10$ d, $+15$ d and $+20$ d. In the upper part of this plot we use colour-coded horizontal bars to show the rest-frame wavelength range corresponding to the redshifted observed 4000–9000 Å wavelength range used in the simulation. The overlap between each of the horizontal bars with the zero-redshift black bar gives a measure of the overlap in wavelength between the input spectrum and the SNID spectral templates, and hence a qualitative feel for the variation of the lap parameter with redshift.

Simulation results

The outcome of the Monte-Carlo realization are displayed in Fig. 4.7. The upper panels show the redshift residuals Δz as a function of the r (*left*) and rlap (*right*) correlation parameters, respectively. The scatter in Δz reduces significantly for higher r and rlap values, as expected. Note that for our restricted wavelength range 4000–9000 Å, $\text{lap}_{\text{max}} \sim 0.8$, such that $\text{rlap} < r$, for all r . The mean redshift residual is approximately zero ($\overline{\Delta z} \ll 10^{-3}$) for all r and rlap values, indicating no systematic error in the determination of correlation redshifts using SNID.

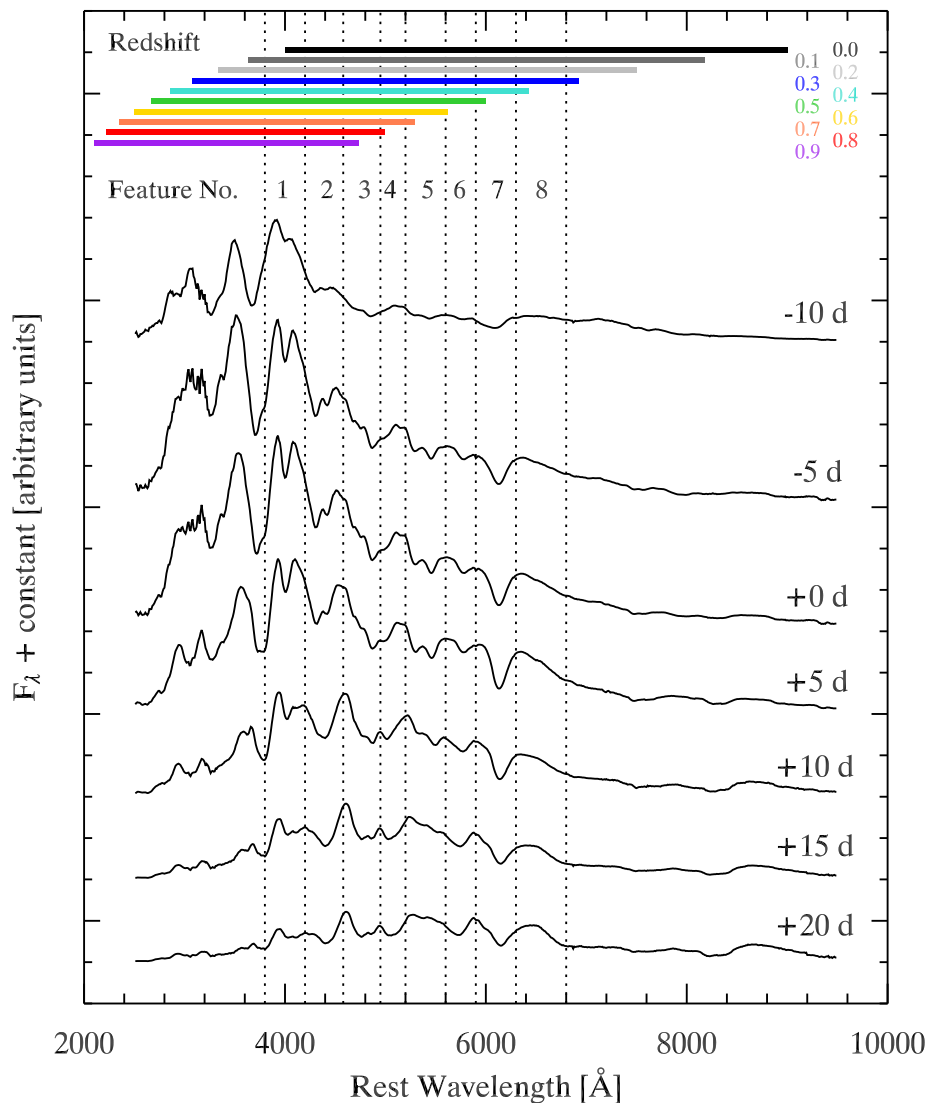


Figure 4.6: Peter Nugent's spectral templates [214] at phases $t = \{-10, -5, +0, +5, +10, +15, +20\}$ days from B -band maximum (27 April 2005 version downloaded from http://supernova.lbl.gov/~nugent/nugent_templates.html). The coloured lines indicate rest-frame wavelength ranges corresponding to the redshifted *observed* wavelength range $4000 - 9000 \text{ \AA}$ ($z = 0.0$; *black line*), for the redshifts $0.1 \leq z \leq 0.9$ used in the SNID simulation. The vertical dashed lines give the wavelength ranges corresponding to the spectral features listed in Table 4.2.

4.3 Variation of the redshift error with redshift, phase, and spectral range 117

The lower panels of Fig. 4.7 show the standard deviation in Δz for points that correspond to r (*left*) and rlap (*right*) values greater than a given cutoff value (r_{cut} and rlap_{cut} , respectively), as a function of this cutoff value. For a redshift error $\sigma_z \lesssim 0.01$, we need to consider correlations with $r > 10$ or $\text{rlap} > 5$. In most cases, we will assume a SNID redshift to be reliable when $\text{rlap} > 5$ for a given correlation; the redshift “error” σ_z will be calculated as the standard deviation of all correlations with $\text{rlap} > 5$ (see, e.g., [187]; Appendix A).

In what follows we will explore in more detail the variation of the SNID redshift error as a function of redshift, supernova phase, and spectral range.

4.3 Variation of the redshift error with redshift, phase, and spectral range

Using the output of the Monte-Carlo realization presented in the previous section, we show histograms of the redshift residuals Δz for correlations with $\text{rlap} > 5$, as a function of redshift, in Fig. 4.8. Only redshift residuals for Nugent templates at maximum light ($t = +0$ d) are shown here. Until $z = 0.7$, the histogram of Δz peaks at $\Delta z \sim 0$, confirming the lack of systematic errors in the redshift determination. The widths of the Δz distributions increases with redshift, due to the decreasing overlap between input spectrum and template. At redshifts $z > 0.7$, the maximum overlap is $\text{lap}_{\text{max}} < 0.3$, and the redshift error blows up.

We next investigate the change in the $\Delta z(z)$ distributions as a function of supernova phase. In Fig. 4.9 we show the evolution of the centre and width of the Δz distributions as a function of redshift, for seven spectral phases separated by 5 d in the range $-10 \text{ d} \leq t \leq +20 \text{ d}$. For phases in the range $-5 \text{ d} \leq t \leq +5 \text{ d}$, the redshift residuals are centered on $\Delta z = 0$. At $t = -10 \text{ d}$, the scatter in Δz is high and the distribution of redshift residuals is biased to lower redshifts ($\Delta z < 0$). This is due to the lack of SNID spectral templates at $t \sim -10 \text{ d}$ (see Fig. 4.1), and the redshift is determined by correlations with templates at a later (rest-frame) phase, where the velocities associated with SN Ia spectral features are lower (by several 1000 km s^{-1} ; see Chap. 5). For phases between $+10 \text{ d}$ and $+20 \text{ d}$, the scatter in Δz centroids is low, however there is a systematic offset of $\sim +0.005$ in redshift. Although there are more templates at these phases than at -10 d (hence the lower scatter), the bias to lower phases is nevertheless present, and a bias to higher redshifts results, due to the larger expansion velocities of the supernova ejecta.

Last, we turn to the specific SN Ia spectral features that SNID “locks” onto when determining the best-guess correlation redshift. In the current version of SNID, all wavelengths are given equal weight in the correlation, which is clearly inappropriate since some wavebands will be more defining (i.e. characteristic of SN Ia spectra) than others. Table 4.2 lists the features we consider here, used by Riess et al. [245] in determining the “spectral-feature age” (SFA) of a given high-redshift spectrum (see also Chap. 6).

We then rerun the Monte-Carlo simulation, adding an extra loop in which we succes-

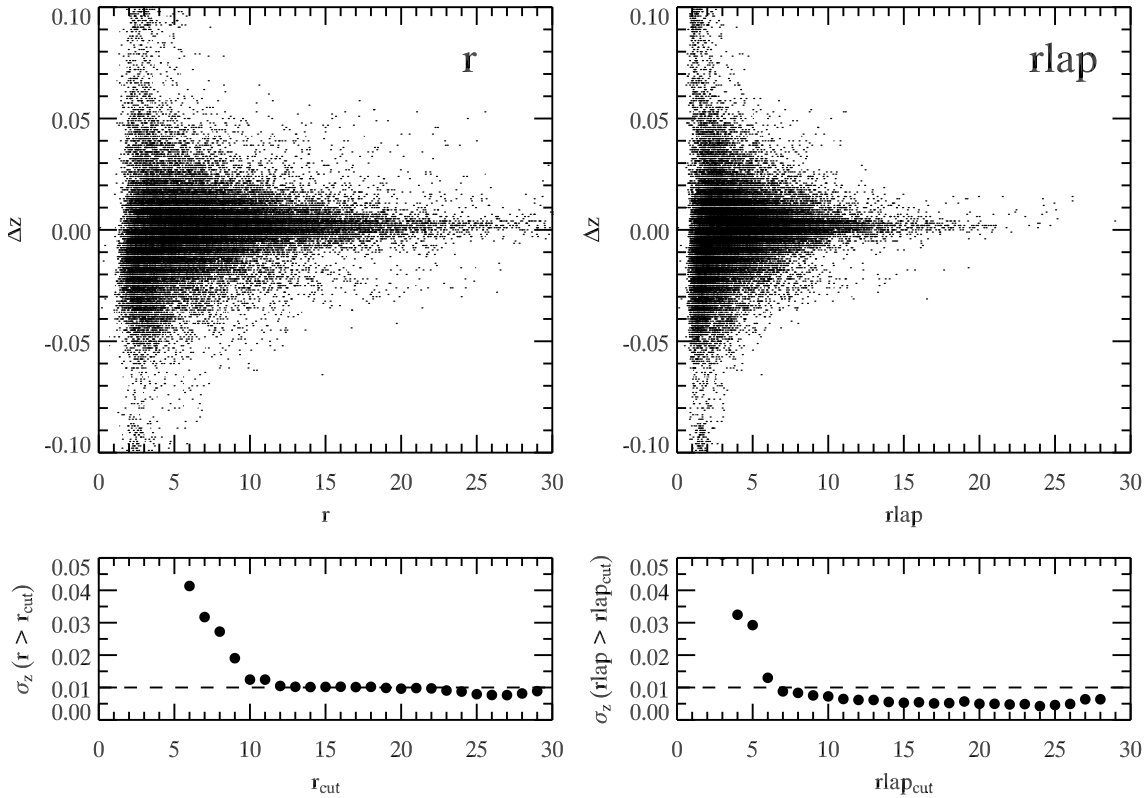


Figure 4.7: **Left panel:** (*Upper panel*) Redshift residuals *vs.* the correlation coefficient r in SNID, from a simulation using Peter Nugent’s SN Ia spectral templates (see Fig. 4.6) as input spectra. There is no systematic error in the correlation redshift output by SNID. (*Lower panel*) Standard deviation of redshift residuals for $r > r_{\text{cut}}$ as a function of the cutoff value r_{cut} . For an error in redshift $\sigma_z \lesssim 0.01$, we require $r > 10$. **Right panel:** Same plots as in the left panel for the $rlap$ ($r \times lap$) parameter, where lap is the overlap in $\ln \lambda$ between the input spectrum and template spectrum. The maximum lap value for spectra in the (observed) wavelength range $4000 - 9000 \text{ \AA}$ is $lap_{\text{max}} \sim 0.8$ (*see text*), hence $rlap < lap$, for all r . For an error in redshift $\sigma_z \lesssim 0.01$, we require $rlap > 5$.

4.3 Variation of the redshift error with redshift, phase, and spectral range 119

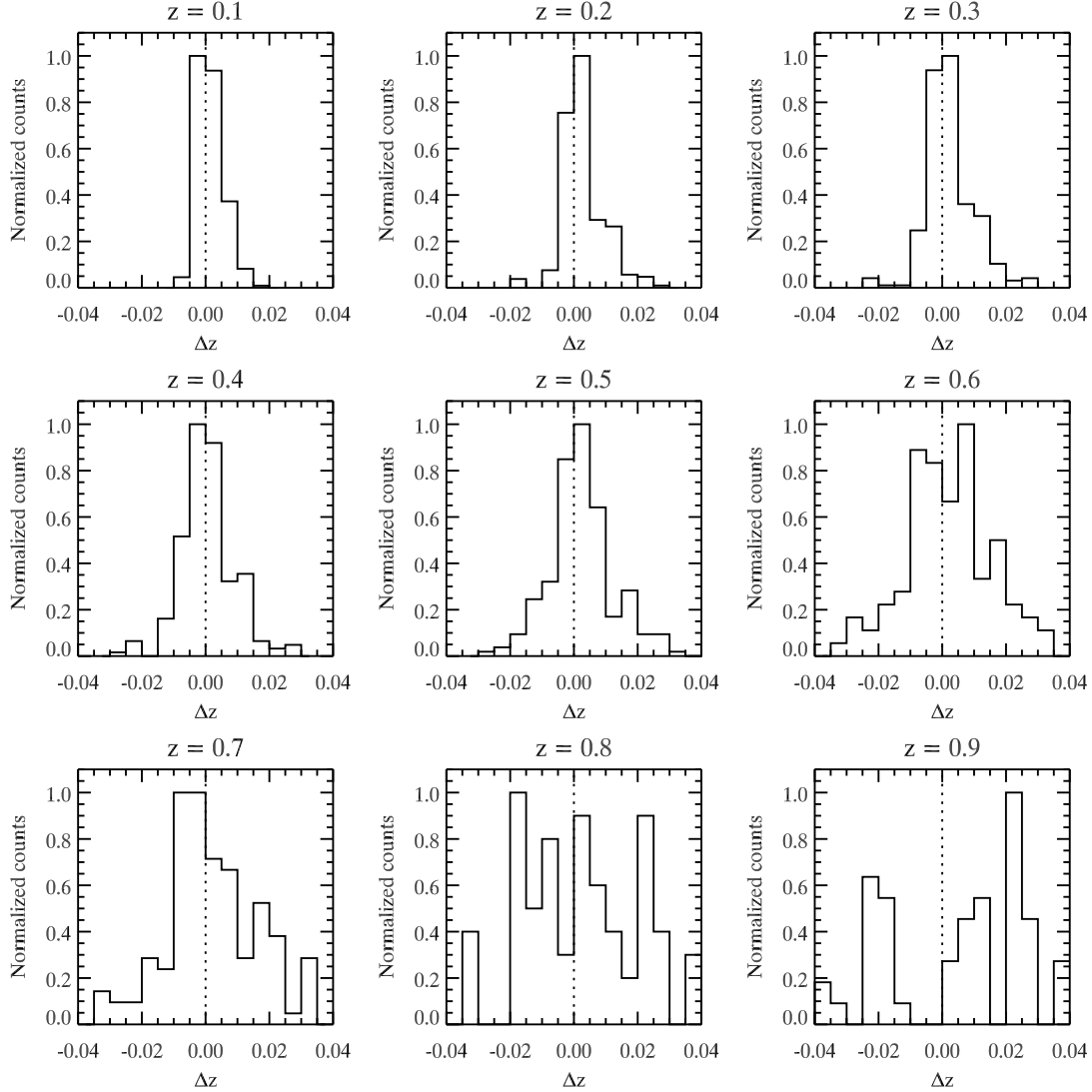


Figure 4.8: Normalized distribution of redshift residuals in our simulation, at redshifts $0.1 \leq z \leq 0.9$, for cross-correlations with SNID that have $\text{rlap} > 5$. Only the Nugent templates for SN Ia at maximum ($t = +0$ d) are used. Up until $z = 0.7$, the distributions of redshift residuals are well centered on $\Delta z = 0$, though their widths increase steadily beyond $z = 0.4$, due to the lesser overlap in rest-frame wavelength between the input and template spectra. At $z = 0.8(0.9)$, an observed wavelength range of $4000 - 9000 \text{ \AA}$ translates to a rest-frame wavelength range of $\sim 2200 - 5000 \text{ \AA}$ ($\sim 2100 - 4700 \text{ \AA}$), at which stage the overlap with local templates is minimal $\text{lap}_{\text{max}} < 0.2$, and the error in redshift blows up.

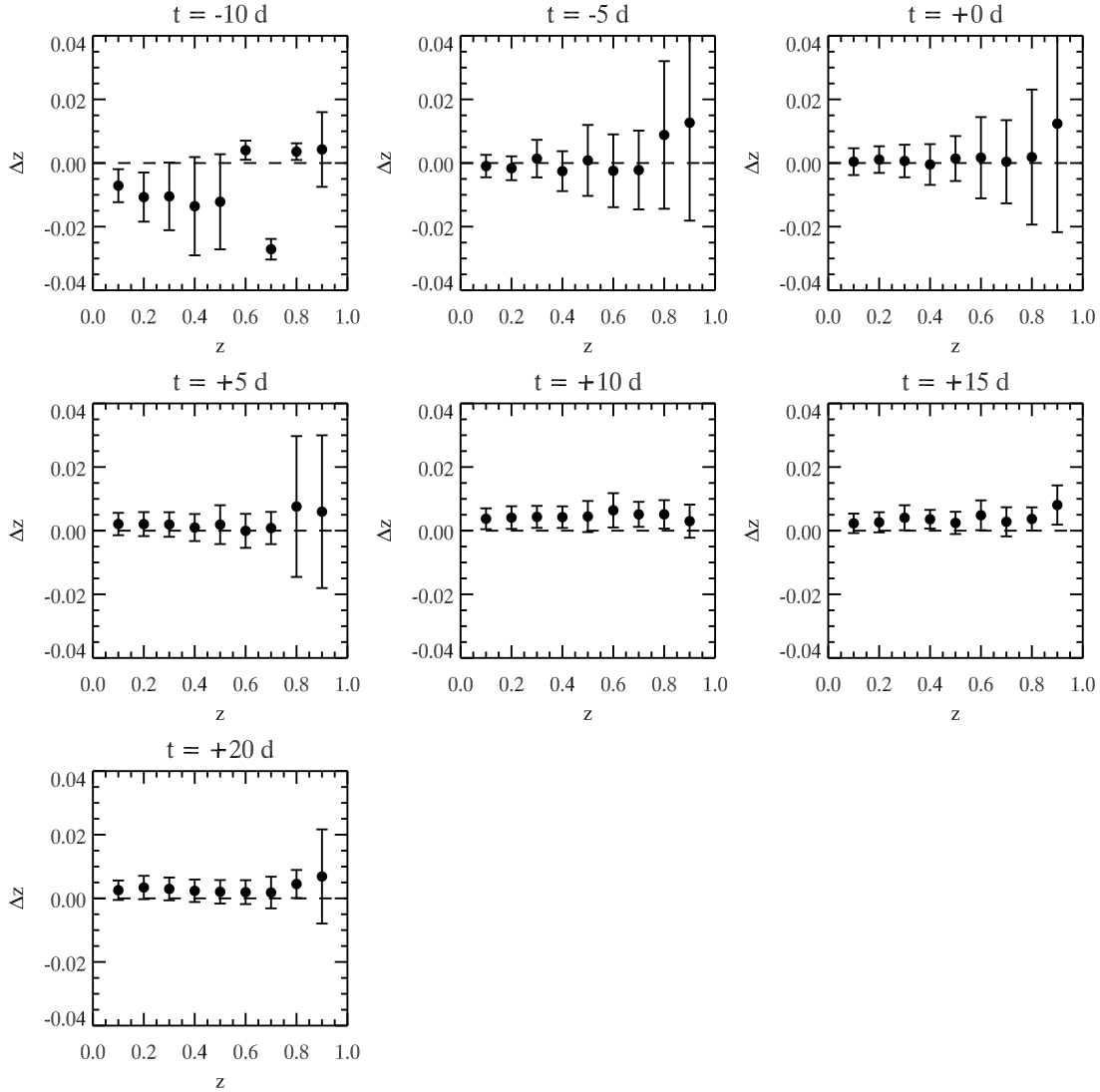


Figure 4.9: Redshift residuals as a function of redshift for different supernova phases in our simulation, for cross-correlations with SNID that have $\text{rlap} > 5$. The points indicate the centre of the corresponding redshift residuals distribution (see Fig. 4.8), and the error bars correspond to the 1σ Gaussian width of the distribution. For phases $-5 \text{ d} \leq t \leq +5 \text{ d}$, the residuals are centered on $\Delta z = 0$ out to $z = 0.7$. We are lacking spectral templates at $t \sim -10 \text{ d}$, and larger errors result. For $t \geq +10 \text{ d}$, redshifts are systematically overestimated by $\lesssim +0.005$, due to the bias to lower spectral template phases, where the blueshifts associated with the dominant features of SN Ia are greater (*see text for details*).

4.3 Variation of the redshift error with redshift, phase, and spectral range 121

Table 4.2: Characteristic spectral features from Riess et al. [245]

Feature No.	Elements	Wavelength range [Å]
1	Si II, Ca II	3800–4200
2	Mg II, Fe II	4200–4580
3	Fe IIa	4580–4950
4	Fe IIb	4950–5200
5	S II	5200–5600
6	Si II, Na I	5600–5900
7	Si II	5900–6300
8	Fe IIc	6300–6800

sively remove one of the eight features listed in Table 4.2 from the input spectrum before running through SNID. We only run the simulation for $z = 0.3$, to ensure that all the features are within the observed wavelength range of the simulation (4000–9000 Å). Also, only correlations with $\text{rlap} > 5$ are considered, to minimize the impact of poor correlations. The resulting distribution of redshift residuals are shown in Fig. 4.10, corresponding to templates with $t = +0$ d. The first histogram (*top left*) shows the Δz distribution when all the features are present. The distribution is well centered on $\Delta z = 0$, with a longer tail for positive residuals. The overall shape of the distribution is well preserved when the following features are removed from the input spectra: “Mg II, Fe II” (4200–4580 Å); “Fe IIa” (4580–4950 Å); “Fe IIb” (4950–5200 Å); “S II” (5200–5600 Å); “Si II, Na I” (5600–5900 Å); “Fe IIc” (6300–6800 Å). Thus, for a SN Ia spectrum around maximum light, these features do not seem to provide any useful information for a correlation redshift to be determined. On the other hand, when we remove the “Si II, Ca II” (3800–4200 Å) feature from the input spectra, the resulting Δz distribution appears bi-modal, with a peak at $\Delta z = 0$ and another at $\Delta z = -0.01$. Also, excluding the “Si II” (5900–6300 Å) feature shifts the Δz distribution slightly to positive residuals, though the effect is not significant.

We investigate how removal of spectral features affects the Δz distributions, this time as a function of supernova phase, in Fig. 4.11. Each of the points represents the center of the corresponding redshift residual distribution, whilst the error bars indicate the 1σ width of the distributions. At $t = -10$ d, the redshift is systematically biased to lower values $\Delta z \sim -0.01$, except when the “Si II” (5900–6300 Å) feature is removed from the input spectrum. Although the Si II $\lambda 6355$ feature is the defining characteristic of SN Ia spectra, it causes a systematic ~ -0.01 redshift error. Thus, removing this feature from the input spectrum at early phases seems to minimize the bias of the correlation to templates at greater phases (due to the shape of the template phase distribution; Fig. 4.1). It could also be that the Nugent spectral template at -10 d has a Si II $\lambda 6355$ feature that extends to higher blueshifts than the SN Ia spectral templates in our database. Around maximum, however, the “Si II” feature is needed to reliably constrain the redshift of the supernova spectrum: a bias to higher redshifts ($\Delta z > 0$; i.e. a bias to lower phases) results when this feature is removed from the input spectrum at these phases. The “Si II, Ca II” (3800–

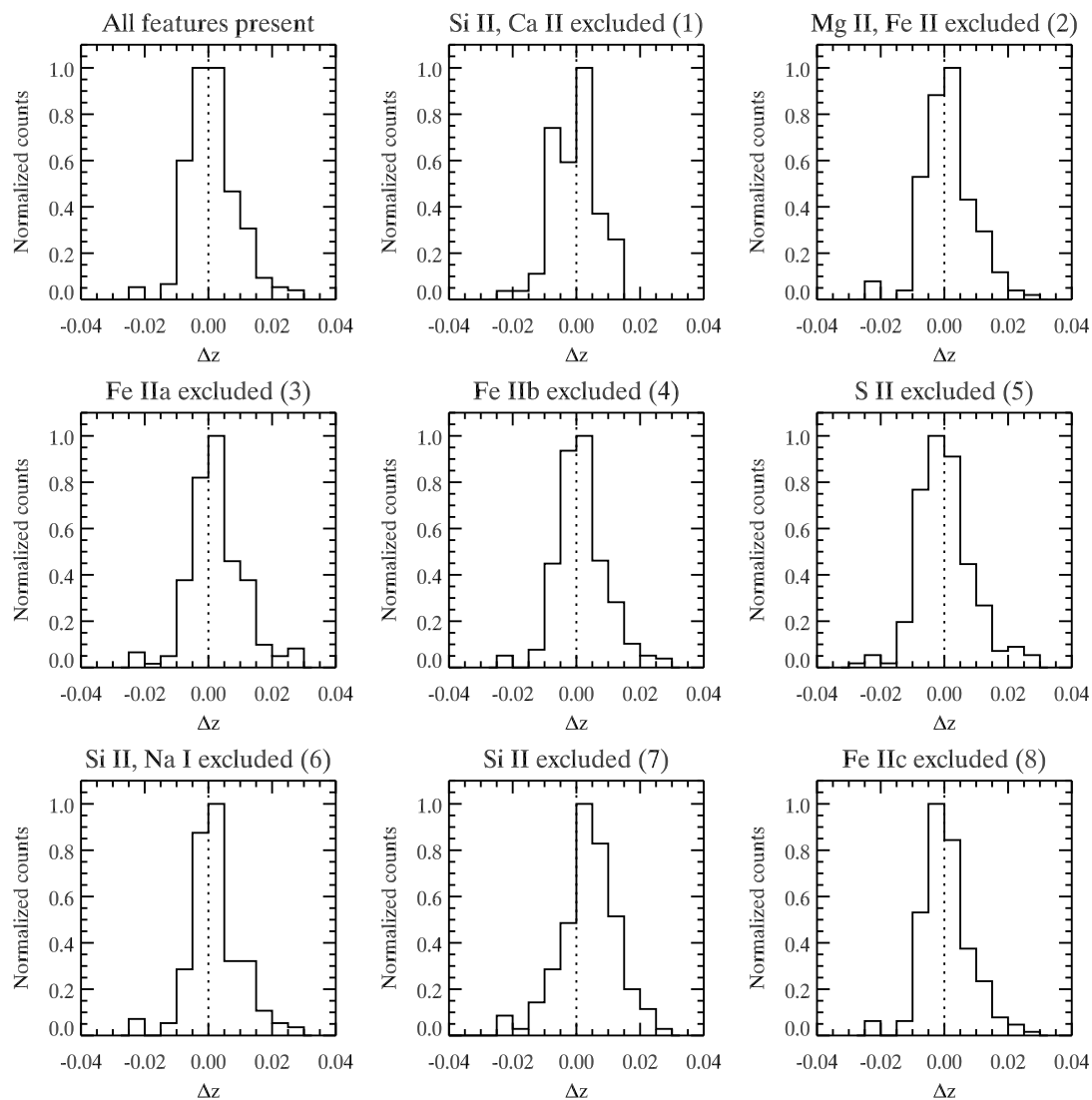


Figure 4.10: Normalized distribution of redshift residuals for a simulated $z = 0.3$ SN Ia spectrum at maximum light (+0 d): when all spectral features in the range $3800 - 6800 \text{ \AA}$ are included (*top left plot*); when a specific feature of Table 4.2 is removed from the spectrum (*all other plots*). Only cross-correlations with SNID that have $\text{rlap} > 5$ are included. The synthetic spectrum used is a Nugent template at +0 d.

4200 Å) feature is also important for determining a reliable correlation redshift at phases $> +10$ d.

Thus, it is clear that a phase-dependent wavelength weighting is necessary to enhance the accuracy of the SNID correlation redshifts. In particular, the “Si II, Ca II” (3800–4200 Å) and “Si II” (5900–6300 Å) features play a crucial role in ensuring an accurate redshift is determined at post-maximum phases. Since the “Si II” feature is redshifted out of the optical wavelength at redshifts $z \gtrsim 0.4$, the correlation redshifts of post-maximum, $z \gtrsim 0.4$ SN Ia spectra will be systematically biased to slightly higher redshifts.

4.4 Accuracy of the cross-correlation method: comparison of SN and host galaxy redshifts

In this section, we test the accuracy of correlation redshifts using SNID by comparing the SNID redshift with that obtained from narrow emission/absorption lines in the parent galaxy. Galaxy redshifts z_{gal} are typically accurate to < 0.001 , due to velocity dispersion of their light-emitting component ($\sim 100 \text{ km s}^{-1}$ and $\sim 200 \text{ km s}^{-1}$ in early- and late-type galaxies, respectively [198]). This velocity dispersion translates into an error in the supernova redshift determined using z_{gal} , since the supernova event may have occurred in a region where its velocity (in the galaxy rest frame) is different from the mean value. However, z_{gal} nevertheless gives a more accurate determination of the SN redshift than SNID (which has typical redshift errors of ~ 0.01 for $\text{rlap} > 5$), so a comparison of the two gives a valuable indication on the accuracy of the SNID redshifts, determined from real data rather than from Monte-Carlo simulations.

We have chosen high-redshift SN Ia spectra taken by members of the ESSENCE team ([187]; Appendix A), for which a redshift of the host galaxy could be obtained. This amounts to 33 SN Ia spectra in the redshift range $0.164 \leq z \leq 0.606$, listed in Table 4.3. The error on the SNID redshift is computed as the standard deviation of correlation redshifts with $\text{rlap} > 5$, to which we add a 0.01 error in quadrature to account for potential effects on the cross-correlation related to unusual velocity features in the spectra.

The results of this comparison are shown in Fig. 4.12. It is essentially the same as Fig. 1 of Matheson et al. [187] – cf. Appendix A, though the SNID spectral database has now been refined to trim noisy ends of template spectra, and correct for slight errors in the shift to zero-velocity of some spectra. The upper panel of Fig. 4.12 is a plot of the supernova redshift determined *via* cross-correlations using SNID, versus that determined from narrow lines in the host galaxy spectrum. The dispersion about the one-to-one correspondence of the redshifts is excellent, with $\sigma_z \sim 0.009$ over the whole redshift range. This is in good agreement with the 0.01 redshift error we found for correlations with $\text{rlap} > 5$ from Monte-Carlo simulations. The lower panel of Fig. 4.12 shows a plot of the redshift residuals as a function of the galaxy redshift. The mean residual is $\sim 10^{-4} \ll \sigma_z$, which shows that there are no systematic effects in using SNID to determine the SN redshift.

In Figs. 4.13–4.16 we show the mean normalized unfiltered correlation functions for the

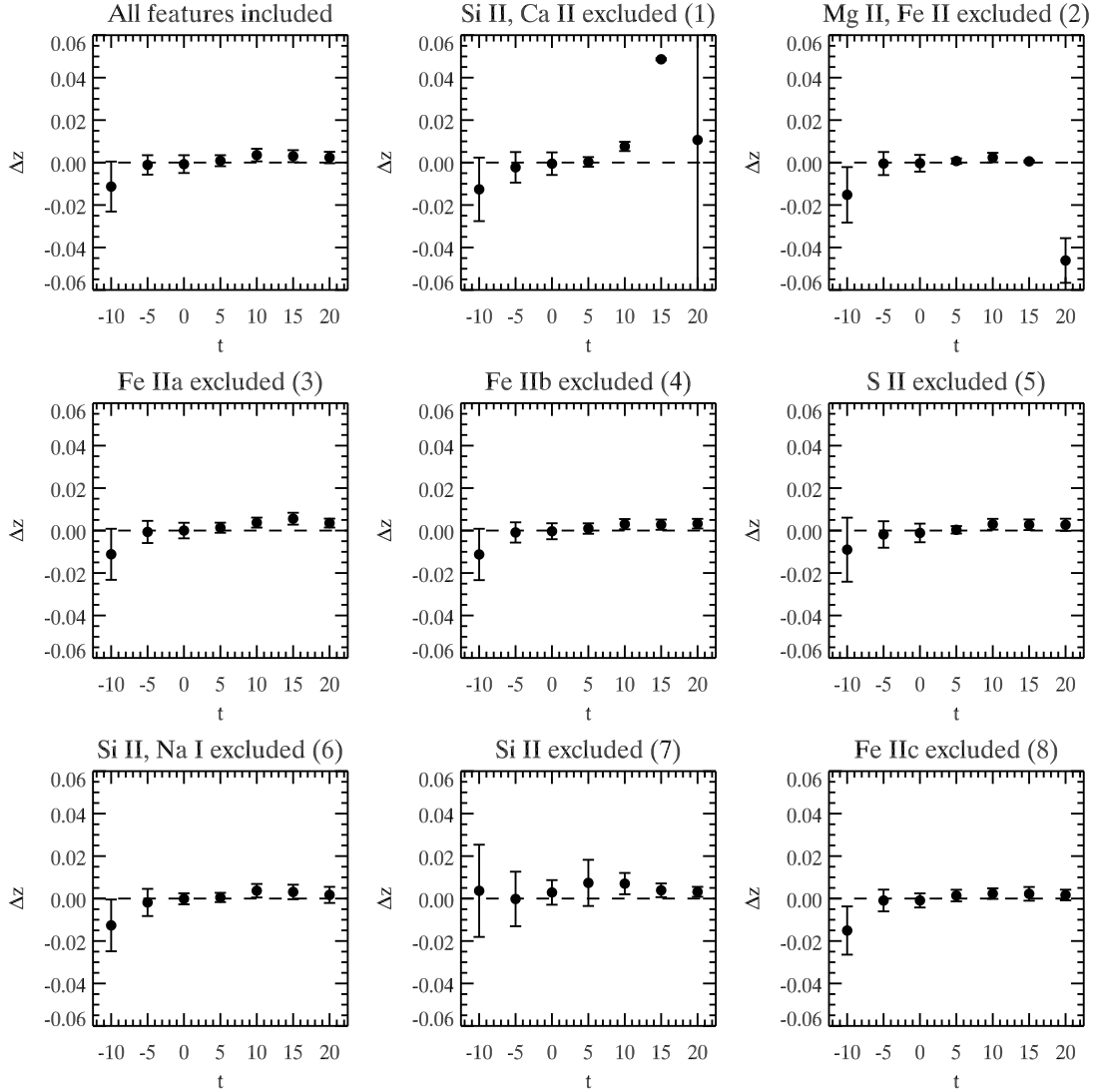


Figure 4.11: Redshift residuals as a function of SN phase for a simulated $z = 0.3$ SN Ia spectrum at maximum light (+0 d): when all spectral features in the range $3800 - 6800 \text{ \AA}$ are included (*top left plot*); when a specific feature of Table 4.2 is removed from the spectrum (*all other plots*). The points indicate the centre of the corresponding redshift residuals distribution (see, e.g., Fig. 4.10), and the error bars correspond to the 1σ Gaussian width of the distribution. Only cross-correlations with SNID that have $\text{rlap} > 5$ are included.

Table 4.3: SNID *vs.* galaxy redshifts

IAU ID	ESSENCE ID	z_{gal}^a	z_{SN}^b	$\sigma_{z_{\text{SN}}}^c$
2002iv ^d	b004	0.231	0.225	0.011
2002iy	b010a	0.587	0.603	0.012
2002iy	b010b	0.587	0.588	0.012
2002iy	b010c	0.587	0.597	0.011
2002iy	b010d	0.587	0.588	0.012
2002iz	b013a	0.428	0.422	0.012
2002iz	b013b	0.428	0.428	0.011
2002ju	c012a	0.348	0.347	0.011
2002ju	c012b	0.348	0.374	0.013
2002jw	c015a	0.357	0.354	0.013
2002jw	c015b	0.357	0.374	0.012
...	c023	0.399	0.402	0.011
2003jj	d058	0.583	0.578	0.012
2003jl	d089	0.429	0.433	0.012
2003jm	d084	0.522	0.517	0.012
2003jo	d033	0.524	0.528	0.011
2003jr	d087	0.340	0.344	0.011
2003js	d093a	0.363	0.370	0.013
2003js	d093b	0.363	0.359	0.011
2003jv	d085	0.405	0.400	0.011
2003jw	d117	0.296	0.294	0.012
2003jy	d149	0.339	0.336	0.012
2003kk	e020	0.164	0.162	0.012
2003kl	e029a	0.335	0.328	0.012
2003kl	e029b	0.335	0.329	0.012
2003kn	e132	0.244	0.230	0.012
2003ko	e136	0.360	0.350	0.012
2003kq	e140	0.606	0.618	0.016
2003kr	e148	0.427	0.418	0.014
2003li	f244	0.544	0.542	0.011
2003lj	f235	0.417	0.420	0.011
2003ll	f216	0.596	0.597	0.013
2003lm	f096	0.408	0.411	0.013

^a Redshift as determined from narrow emission/absorption lines in the host galaxy spectrum.

^b Redshift as determined from cross-correlations with local SN Ia spectral templates using SNID.

^c Error in the SNID redshift, calculated as the RMS of cross-correlation redshifts with $r \times \text{lap} > 5$ (*see text for details*), to which we add a 0.01 error in quadrature to account for potential effects on the cross-correlation related to unusual velocity features in the spectra.

^d SN 2002iv is similar to the “peculiar” SN 1991T at similar phases. In determining the redshift of SN 2002iv, we exclusively use the SN 1991T template shifted to zero redshift.

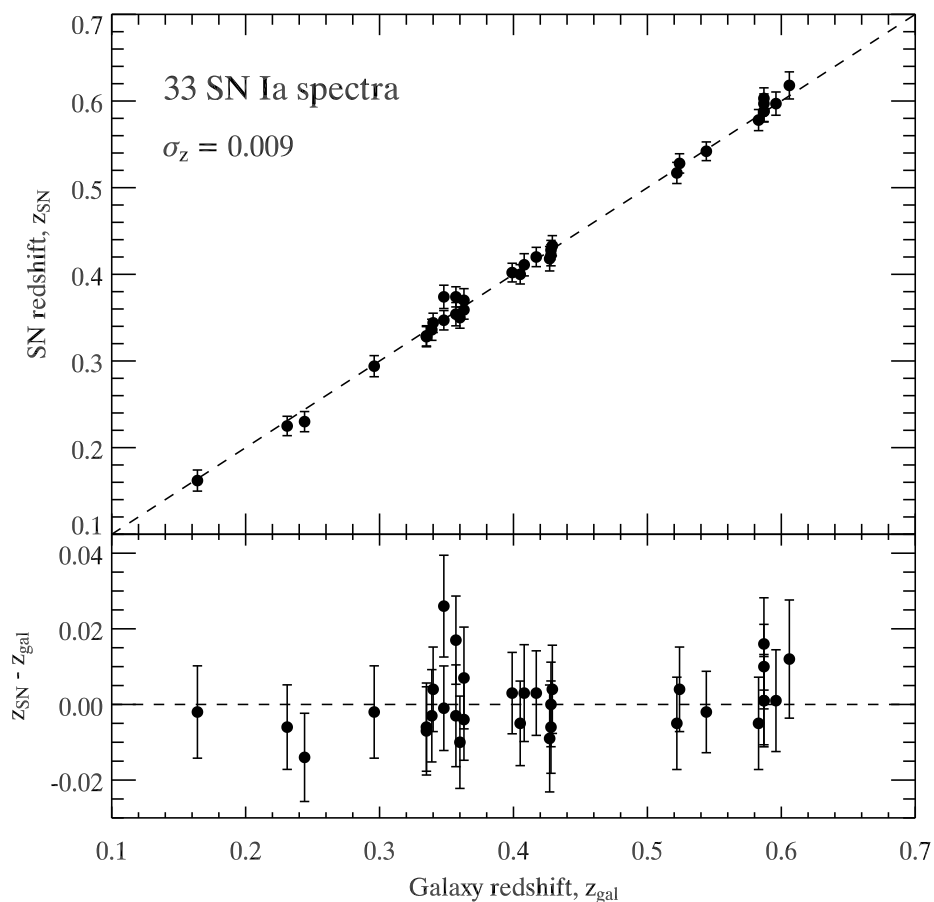


Figure 4.12: **Upper panel:** Comparison of redshifts determined from cross-correlations with SN Ia spectral templates using SNID and from narrow emission/absorption lines in the host galaxy spectrum. The dispersion about the ($z_{\text{SN}} = z_{\text{gal}}$) line is $\sigma_z = 0.009$, and hence the agreement between supernova and galaxy redshift is excellent. **Lower panel:** Redshift residuals *vs.* galaxy redshift. The mean residual is $\sim 10^{-4} \ll \sigma_z$, which shows that there are no systematic effects in using SNID to determine the SN redshift.

SN Ia spectra listed in Table 4.3. Only correlations with $\text{rlap} > 5$ are used to compute the mean correlation function. In each of the plots, the vertical dotted line indicates the galaxy redshift, z_{gal} . For three spectra (b013b, Fig. 4.15; b010a and e140, Fig. 4.16), the correlation peak chosen by SNID to determine the redshift is not the one corresponding to the highest correlation amplitude. For b013b (SN 2002iz; $z_{\text{gal}} = 0.428$), the highest correlation peak at $z \sim 0.65$ corresponds to a lower lap value, and the antisymmetric component of the correlation function about that redshift is higher. For b010a (SN 2002iy; $z_{\text{gal}} = 0.587$) and e140 (SN 2003kq; $z_{\text{gal}} = 0.606$), the highest correlation peaks are at $z \sim 0.4$ – i.e. at *higher* lap values. However, after applying the bandpass filter to both these correlation functions, the antisymmetric component about $z \sim 0.4$ is a factor ~ 1.5 higher than about the galaxy redshift, which is the reason why these peaks were preferred over the obvious choice.

4.5 Future developments

We have shown SNID to be a useful tool to accurately estimate the redshifts of high- z SN Ia spectra. Both simulations using semi-empirical templates (Sect. 4.2.3), and the comparison of high- z SN Ia correlation redshifts with host galaxy redshifts (Sect. 4.4), yield redshift errors of ~ 0.01 , with no systematic offsets. However, a few features need improving/implementing:

- **Error model:** The redshift error in SNID is calculated as the standard deviation of redshifts whose correlation has $\text{rlap} > 5$. In a future version, the redshift error will be calculated as the width of a given correlation peak modulated by the S/N ratio of the input and template spectra.
- **Bayesian analysis:** With the current version of SNID, we can only say that a given high-redshift spectrum is *likely* to be that of a Type Ia supernova at the correlation redshift, though we have no means of quantifying this likelihood. A future version of SNID should take into account the various user-input options (e.g.: redshift range, phase range, wavelength range) and output a probability density function in redshift space, also taking into account the supernova type. This will ensure the high- z SN Ia samples are not contaminated by supernovae of other types (in particular, SN Ic [56, 126])
- **Phase determination:** In principle, SNID can also be used to constrain the phase of a given supernova spectrum (see Chap. 6). This can enable us to test for cosmological time-dilation effects in multi-epoch high- z SN Ia spectra (by comparing the elapsed time between observations with the rest-frame phases of the SN spectra), as well as set further constraints on the type of a supernova spectrum. Currently, errors on phase determination using SNID are $\sigma_t \sim 3$ d, and here again there is room for improvement.

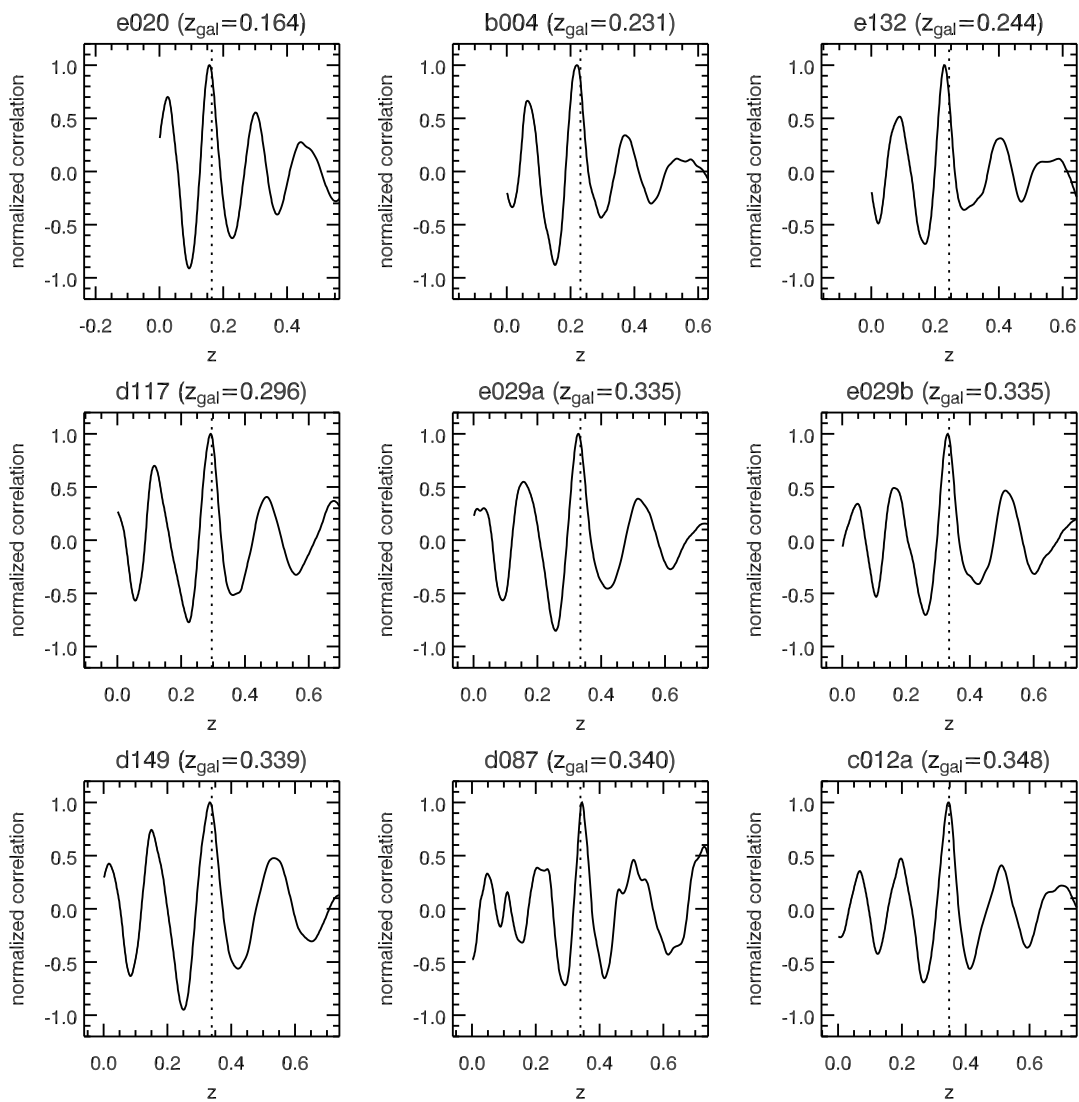


Figure 4.13: Mean normalized unfiltered correlation functions for SN Ia for which we have a redshift from the host galaxy (z_{gal} ; see Fig. 4.12). Only correlations with $\text{rlap} > 5$ are included. The vertical dotted line indicates the galaxy redshift. The correlation function is then bandpass filtered, and trimmed to match the best-guess (median) redshift.

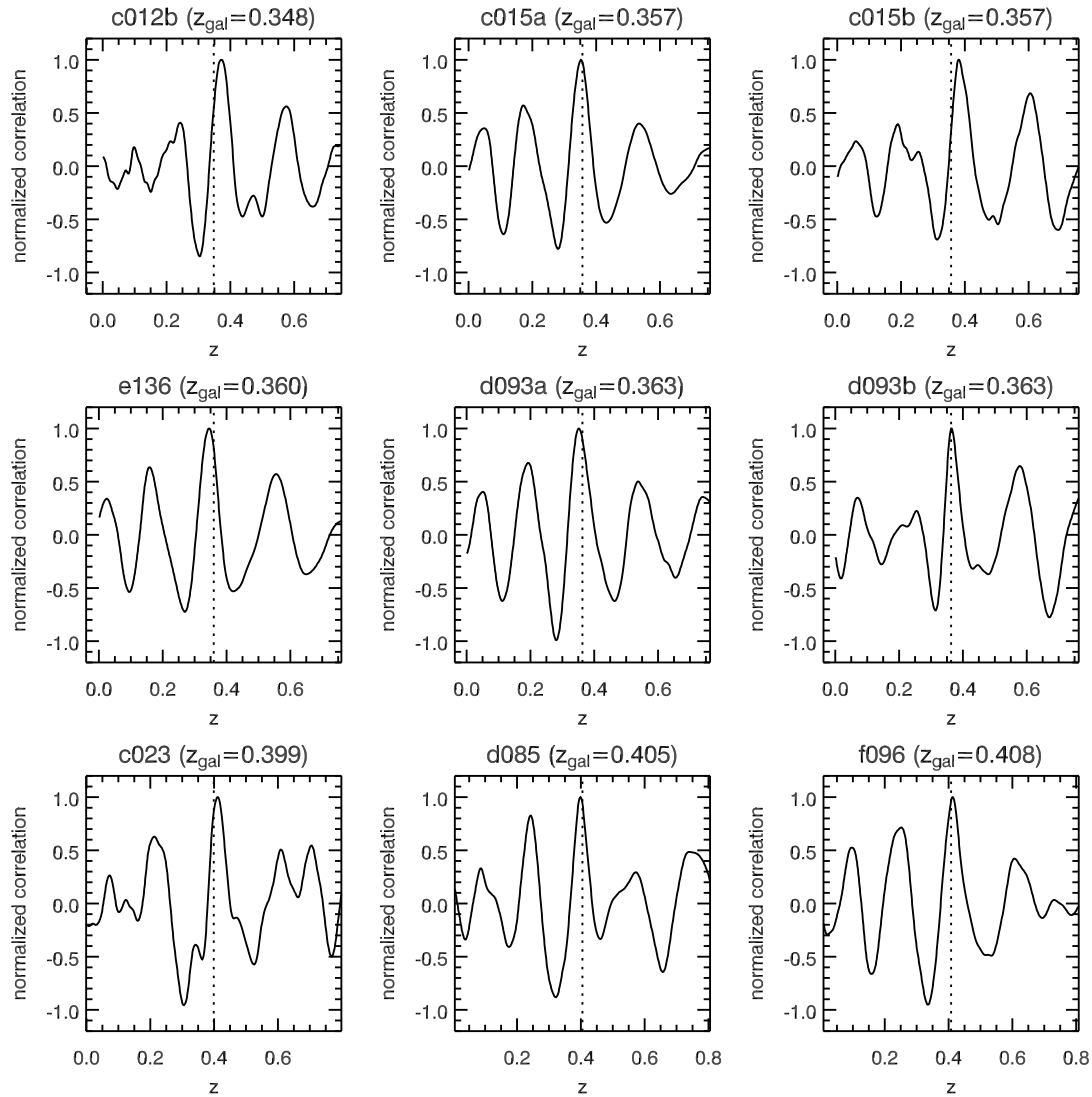


Figure 4.14: See Fig. 4.13.

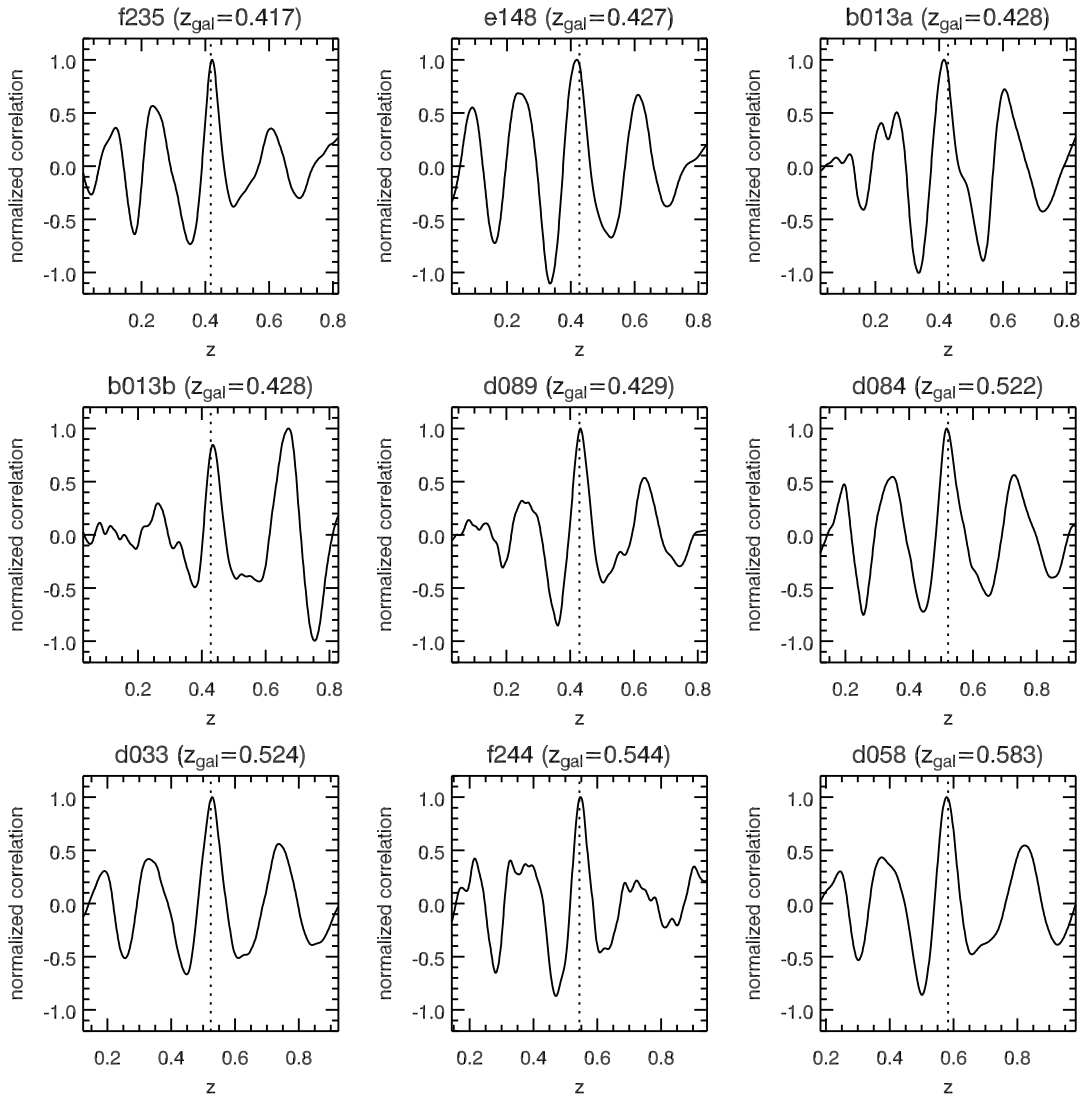


Figure 4.15: See Fig. 4.13.

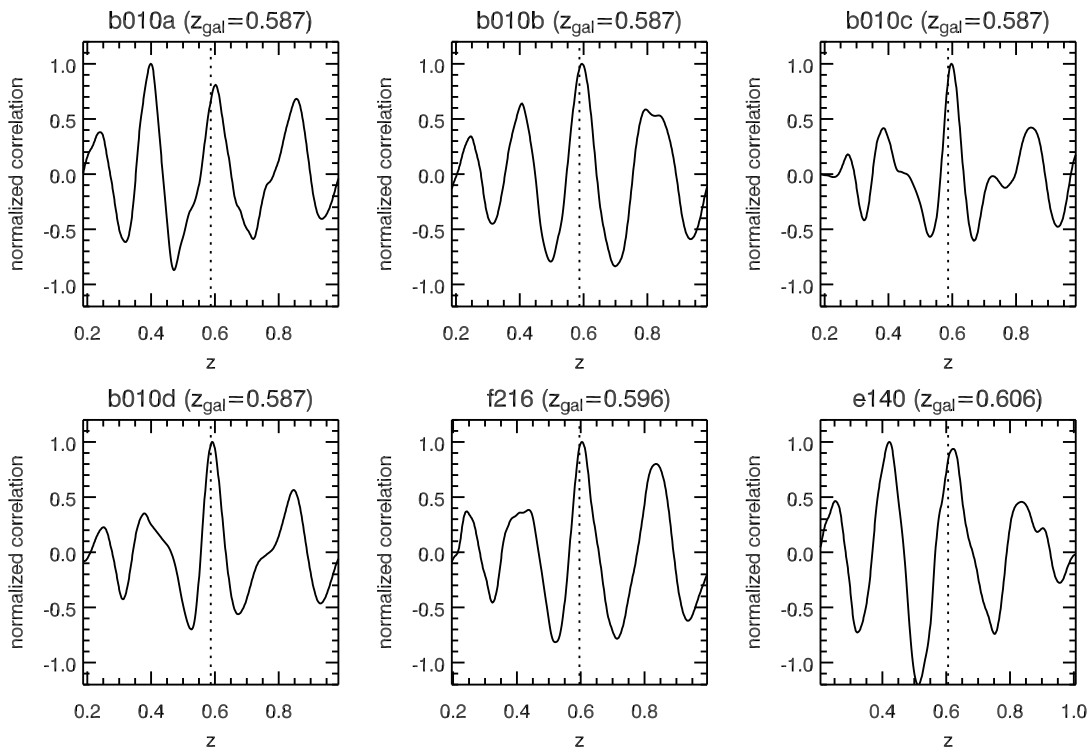


Figure 4.16: See Fig. 4.13.

- **Refined spectral database:** SNID was developed to estimate SN Ia redshifts, and the bias of the current spectral database towards SN Ia spectra reflects this initial aim. It is necessary to populate the spectral templates of other supernova types, in particular the SN Ic sample that is the most likely contaminant of high- z SN Ia samples. Moreover, a set of templates with accurate rest-frame phases, and extending to the near-UV range (corresponding to the observed B -band for $z \gtrsim 0.5$) supernovae, is highly desirable.
- **Wavelength and inverse-variance weighting:** We have seen in Sect. 4.3 that the correlation redshift is more affected by some SN Ia spectral features than others, and that this effect is also highly phase-dependent. Thus, a wavelength weighting scheme should be implemented in SNID. Along the same lines, one would like to use the noise (variance) spectrum of the supernova to give more relative weight to spectral regions less affected by sky noise (or noise of any type for that matter). Such an inverse-variance weighting procedure has already been applied by Saunders et al. [266] to galaxy spectra of the 2dF [59] and 6dF [139] galaxy surveys. In fact, Saunders et al. [266] state that the correlation redshift obtained with this improvement is more reliable than the emission-line galaxy redshift. There is hope for similar improvements to be made in the determination of SN Ia redshifts.
- **Automation of bandpass filter setup:** The choice of the appropriate wave numbers to use for the bandpass filter should be automated, and optimized for each supernova/template combination. This way, one would take into account the variation of the Fourier spectra from supernova to supernova, and the variation with phase for a given supernova template.
- **Web interface:** Any tool useful to a specific high- z SN Ia project is useful to other similar projects. To help make SNID a standard in the high- z SN Ia community, a web-based interface would greatly help. One can imagine an online SN identifier tool with redshift/phase estimation, used by observers in real-time whilst observing at the telescope. This would be particularly useful considering the amount of telescope time needed to obtain a decent high-redshift SN Ia spectrum [201, 187].

This is a non-exhaustive list of possible improvements to make SNID “excellent” instead of simply “good”, which offer many exciting research prospects in the near future. One can hope that, after such improvements, the correlation redshift will be more accurate than the galaxy redshift. With a prior on phase (when a well-sampled light-curve is available) and on redshift (when a galaxy spectrum is available), the correlation redshift will also gain in precision – an important requirement if one is to measure the equation-of-state parameter of Dark Energy. Ultimately, one would like the various ongoing high- z SN Ia searches to merge their analysis tools, providing various standard packages for the field of SN observational cosmology. The future of SNID is set along those lines.

*Exhaustion is the shortest way to equality and fraternity,
and liberty is added eventually by sleep.*

Friedrich Nietzsche

Chapter 5

Using line profiles to test the fraternity of Type Ia supernovae at high and low redshifts

Stéphane Blondin, Luc Dessart, Bruno Leibundgut, David Branch, Peter Höflich,
John L. Tonry, Thomas Matheson, Ryan J. Foley, Ryan Chornock, Alexei V. Filippenko,
Jesper Sollerman, Jason Spyromilio, Robert P. Kirshner, W. Michael Wood-Vasey,
Alejandro Clocchiatti, Claudio Aguilera, Brian Barris, Andrew C. Becker, Peter Challis,
Ricardo Covarrubias, Tamara Davis, Peter Garnavich, Malcolm Hicken, Saurabh Jha,
Kevin Krisciunas, Weidong Li, Anthony Miceli, Gajus Miknaitis, Giuliano Pignata,
Jose Luis Prieto, Armin Rest, Adam G. Riess, Maria Elena Salvo, Brian P. Schmidt,
R. Chris Smith, Christopher W. Stubbs, and Nicholas B. Suntzeff

Accepted for publication in *The Astronomical Journal* on 4th October 2005
(astro-ph/0510089)

Abstract: Using archival data of low-redshift ($z < 0.01$; CfA and SUSPECT databases) Type Ia supernovae (SN Ia) and recent observations of high-redshift ($0.16 < z < 0.64$ [187]) SN Ia, we study the “uniformity” of the spectroscopic properties of nearby and distant SN Ia. We find no difference in the measures we describe here. In this paper, we base our analysis solely on line-profile morphology, focusing on measurements of the velocity location of maximum absorption (v_{abs}) and peak emission (v_{peak}). Our measurement technique makes it easier to compare low and high signal-to-noise ratio observations. We also quantify the associated sources of error, assessing the effect of line blending with assistance from the parametrized code SYNOW [82]. We find that the evolution of v_{abs} and v_{peak} for our sample lines (Ca II $\lambda 3945$, Si II $\lambda 6355$, and S II $\lambda\lambda 5454, 5640$) is similar for both the low- and high-redshift samples. We find that v_{abs} for the weak S II $\lambda\lambda 5454, 5640$ lines, and v_{peak} for S II $\lambda 5454$, can be used to identify fast-declining [$\Delta m_{15}(B) > 1.7$] SN Ia, which are also subluminous. In addition, we give the first direct evidence in two high- z SN Ia spectra of a double-absorption feature in Ca II $\lambda 3945$, an event also observed, though infrequently, in low-redshift SN Ia spectra (6/22 SN Ia in our local sample). Moreover,

echoing the recent studies of Dessart and Hillier [66, 65] in the context of Type II supernovae (SN II), we see similar P-Cygni line profiles in our large sample of SN Ia spectra. First, the magnitude of the velocity location at maximum profile absorption may underestimate that at the continuum photosphere, as observed for example in the optically thinner line S II $\lambda 5640$. Second, we report for the first time the unambiguous and systematic intrinsic blueshift of peak emission of optical P-Cygni line profiles in Type Ia spectra, by as much as 8000 km s^{-1} . All the high- z SN Ia analyzed in this paper were discovered and followed up by the ESSENCE collaboration, and are now publicly available.

5.1 Introduction

Type Ia supernovae (SN Ia) have been the subject of intense theoretical modeling and dedicated observational campaigns in recent years. The implications of relative luminosity distance measurements for low-redshift and high-redshift SN Ia, namely the requirement for an additional negative pressure term in Einstein’s field equations (“dark energy”), are extraordinary for cosmologists and particle physicists alike ([244, 226]; see [76, 77] for recent reviews). These results have not only been confirmed at moderate redshifts [291, 152, 14], but also at higher ($z > 1$) redshifts where the universal expansion is in a decelerating phase [252]. Currently, two ongoing projects are aiming to measure the equation-of-state parameter of the dark energy: the ESSENCE (Equation of State: SuperNovae trace Cosmic Expansion [201, 156, 187]) and SNLS (SuperNova Legacy Survey [238]) projects.

A non-uniformity in the SN Ia properties at different redshifts might influence the resulting inferred cosmological models, motivating a precise assessment of potential differences. For example, the use of SN Ia as distance indicators requires an empirical relation between light-curve width and maximum luminosity [229], verified for nearby SN Ia. The extrapolation of such a relation to SN Ia at higher redshifts might be inaccurate, arising possibly from distinct progenitor properties or yet unknown differences in the explosion mechanism (see [117, 165, 120] for reviews).

Such evolutionary effects, however, would also need to explain the apparent brightening of SN Ia at $z \gtrsim 1$ [252]. Recently, Krisciunas et al. [158] have noted the absence of a relation between luminosity and light-curve shape in the near infrared (JHK bands), opening up exciting prospects for future high- z SN Ia observations in this (rest-frame) passband. In the meantime, it is worthwhile to look for potential differences between SN Ia at different redshifts, based on their light-curve properties.

Spectroscopy is better suited than photometry to make quantitative comparisons between local and high- z SN Ia. Large amounts of information are conveyed by spectra on the properties of the ejecta (chemical composition, velocity/density gradients, excitation level); subtle differences, blurred together in photometric measurements, will show up in the spectra. So far, comparisons of SN Ia at different redshifts have only been qualitative in nature [57, 172], although preliminary results on a quantitative analysis have been presented by Lidman [178]. The ESSENCE spectra published by Matheson et al. [187] clearly show that a significant fraction of the high- z data is of sufficient quality for such

comparisons, made possible through the public availability of many local SN Ia data *via* the SUSPECT database¹. The high- z data, presented by Matheson et al. [187], are now publicly available².

The optical spectra of SN Ia near maximum light are dominated by resonance lines of singly ionized, intermediate-mass elements, Doppler-broadened due to the large expansion velocities in SN Ia envelopes; see Filippenko [75] for an observational review. Optically thick lines forming in such fast-expanding ejecta have a P-Cygni profile shape, characterized essentially by absorption on the blue side of, and emission peaking at the line center (see, e.g., [151]). Although these two components always appear qualitatively similar in P-Cygni profiles associated with optically thick outflows, there are significant differences, which may become relevant if one seeks an accurate association with, say, the velocity at the photosphere – defined here as the outflow location where the inward integrated *continuum* optical depth is $2/3$ – of the SN ejecta [150] or the asymptotic velocity of a radiatively driven hot star wind [237].

Recently, Dessart and Hillier [66, 65] performed detailed analyses of line-profile formation in SN II spectra, using hydrogen Balmer lines and Fe II $\lambda 5169$ diagnostics. Although first identified by Branch [29], Dessart and Hillier [65] explained the origin of the possible underestimate, with optically thinner lines, of the photospheric velocity with the use of v_{abs} . They also explained [66] the origin of the significant blueshift of P-Cygni profile emission compared to the rest wavelength of the corresponding line: for SN 1987A on the 24th of February 1987, this blueshift is on the order of 7000 km s^{-1} , equivalent to a very sizeable 150 \AA (see, e.g., [66]).

Both effects result from the fast declining density distribution in SN II, with $n \approx 10$ for a power law given by $\rho(r) = \rho_0(R_0/r)^n$, r being the radius and R_0 (ρ_0) some reference radius (density). Although the density drop-off in SN Ia is estimated to be smaller (see, e.g., [119]), with $n \approx 7$, this is still large enough for the above two effects to occur. Such velocity shifts are not trivial: they represent key observables to constrain the density distribution and the sites of line formation (and interpret, for example, line-polarization measurements), the magnitude of disk-occultation and continuum optical-depth effects, and the ubiquitous but modulated influence of line overlap. The velocity locations corresponding to maximum absorption and peak emission are thus carriers of important information on the SN ejecta; they are, moreover, convenient and well-defined observables, and can thus be used to objectively compare SN Ia at different redshifts. The present paper is the result of such an investigation, using 229 spectra of local ($z < 0.05$) and 48 of high- z ($0.16 < z < 0.64$) SN Ia, at phases between -2 weeks to $+3$ weeks from maximum light.

To minimize the higher bias in our measurements, introduced primarily by the signal-to-noise ratio (S/N) obtained for the faint, high-redshift SN Ia, we develop a spectral-smoothing technique, which uses the expected large widths of observed SN Ia spectral features. We give a detailed account of our measurement technique and associated error

¹SUSPECT: SUPernova SPECTrum Archive, <http://nhn.ou.edu/~suspect/>

²<http://www.noao.edu/noao/staff/matheson/spectra.html>; the VLT spectra are also publicly available *via* the ESO archive: http://archive.eso.org/archive/public_datasets.html

model in Sect. 2. The results of these measurements are presented in Sect. 3, with individual discussion of v_{abs} and v_{peak} for Ca II $\lambda 3945$, Si II $\lambda 6355$, and S II $\lambda\lambda 5454, 5640$. We discuss the wide range of v_{abs} values found for the different lines; the large magnitude of v_{peak} for the optically thinner lines S II $\lambda\lambda 5454, 5640$; and the detection, for the first time, of double-absorption features in Ca II $\lambda 3945$ in high- z SN Ia spectra. We provide insights into the nature of the above measurements by illustrating, following Dessart and Hillier [66, 65], some aspects of line and continuum formation in SN Ia spectra; namely, we explain the origin of the blueshift of peak emission and the relation of the absorption velocity to the photospheric and expansion velocities. In Sect. 4, we present our conclusions.

5.2 Measurement techniques

Any comparison between low- z and high- z SN Ia spectra suffers from the significantly degraded signal quality for the latter, due to the limited integration time available per spectrum when undertaking large SN Ia surveys [187]. To minimize this bias, we have developed a smoothing technique, presented in detail in the following section.

5.2.1 Smoothing Supernova Spectra

We apply a filter (suggested by John Tonry) to both local and high- z SN Ia spectra, to measure the absorption and emission-peak velocities in a consistent manner. This filter takes into account the wavelength-dependent nature of the noise in optical ground-based spectra, and is based on the fact that supernova spectral features are intrinsically broadened due to the large expansion velocity in the corresponding line-formation region. Assuming this broadening to have typical values of $\sim 1000\text{--}3000 \text{ km s}^{-1}$, one can write down a “smoothing factor” $d\lambda/\lambda$ as (c is the speed of light in vacuum)

$$\Delta v_{\text{line}} \approx 0.003 - 0.01c \implies \frac{d\lambda}{\lambda} \approx 0.003 - 0.01. \quad (5.1)$$

For such a spectrum, a well-suited filter is a Gaussian of the same width, σ_{g} . This assumes the S/N of the spectrum to be uniform over the whole wavelength range, which is clearly not the case for ground-based observations in which sky emission lines increase the noise in the red part of the spectrum. Thus, we instead adopt an inverse-variance weighted Gaussian filter.

Let \vec{F}_{SN} and \vec{F}_{var} be the 1D, flux-calibrated supernova spectrum and its corresponding variance spectrum (usually the variance of the optimally extracted spectrum; see [129]). Both spectra share the same wavelength axis, $\vec{\lambda}$. At each wavelength element λ_i , construct a Gaussian \vec{G}_i of width

$$\sigma_{\text{g},i} = \lambda_i \frac{d\lambda}{\lambda}. \quad (5.2)$$

We thus have

$$\vec{G}_i = \begin{pmatrix} G_{i,1} \\ G_{i,2} \\ \vdots \\ G_{i,N_i} \end{pmatrix} = \frac{1}{\sqrt{2\pi}} \exp \left[-\frac{1}{\sigma_{g,i}} \begin{pmatrix} \lambda_1 - \lambda_i \\ \lambda_2 - \lambda_i \\ \vdots \\ \lambda_{N_i} - \lambda_i \end{pmatrix} \right]^2 \quad (5.3)$$

where N_i is the number of wavelength elements of a subset of $\vec{\lambda}$, centered on λ_i . The inverse-variance weighted Gaussian is then

$$\vec{W}_i = \begin{pmatrix} W_{i,1} \\ W_{i,2} \\ \vdots \\ W_{i,N_i} \end{pmatrix} = \begin{pmatrix} G_{i,1}/F_{\text{var},1} \\ G_{i,2}/F_{\text{var},2} \\ \vdots \\ G_{i,N_i}/F_{\text{var},N_i} \end{pmatrix} \quad (5.4)$$

and the corresponding smoothed flux at λ_i is therefore

$$F_{\text{TS},i} = \frac{\sum_j W_{i,j} F_{\text{SN},j}}{\sum_j W_{i,j}}. \quad (5.5)$$

By repeating this process for each wavelength element λ_i , we obtain the smoothed supernova spectrum \vec{F}_{TS} .

We show the result of applying this spectral smoothing algorithm with $d\lambda/\lambda = 0.005$ in Fig. 5.1. The upper spectrum is that of SN 2003jy ($z = 0.339$), plotted in rest wavelength. The spectrum just below is the smoothed version, showing how most of the high-frequency noise has been removed, while the lower-frequency SN spectral features have been preserved. In this paper, we use the same smoothing factor $d\lambda/\lambda = 0.005$ in applying this smoothing technique to both the local and high- z SN Ia spectra.

We show examples of smoothed spectra of several local SN Ia at different phases (and with different S/N) in Fig. 5.2, where we concentrate on the Si II $\lambda 6355$ feature, plotted in velocity space (assuming $\lambda_0 = 6355 \text{ \AA}$ and using the relativistic Doppler formula). We also show (down arrows) the location of maximum absorption and emission peak, measured with our smoothing technique and corresponding to v_{abs} and v_{peak} . We see that line profiles in SN Ia come in many shapes and sizes, from the well-defined absorption trough of SN 1992A at -5 d to the flat-bottomed one of SN 1990N at -13 d, which extends over $\gtrsim 5000 \text{ km s}^{-1}$ (perhaps due to contamination from C II $\lambda 6580$; see [83, 191]). The emission-peak region is often less well defined than the absorption trough [135], and is more affected by contamination by emission from iron-group elements at late phases ($\gtrsim 2$ weeks past maximum brightness). Our spectral smoothing technique does a fine job in reproducing the broad features in SN Ia spectra, both for low-S/N spectra and for contaminated line profiles.

For some spectra we do not have a corresponding variance spectrum at our disposal, either because these variance spectra are not archived in the spectral databases (this is

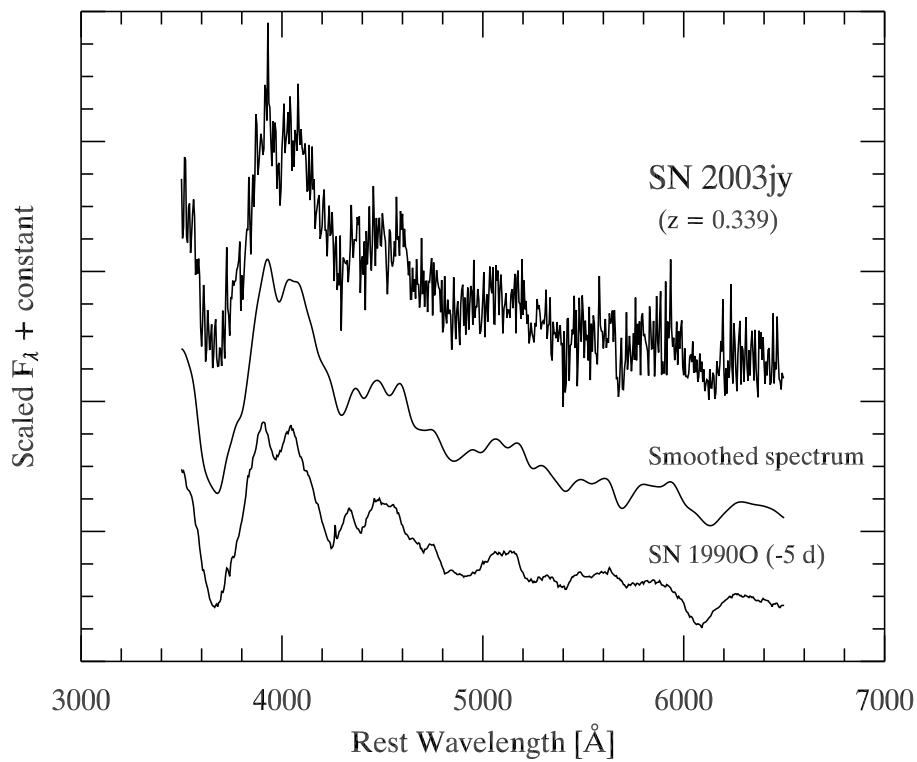


Figure 5.1: (*From top to bottom*) A high- z SN Ia spectrum (SN 2003jy; $z = 0.339$), its smoothed version (with $d\lambda/\lambda = 0.005$), and a local zero-redshift template (SN 1990O at -5 d), plotted for comparison with the smoothed spectrum.

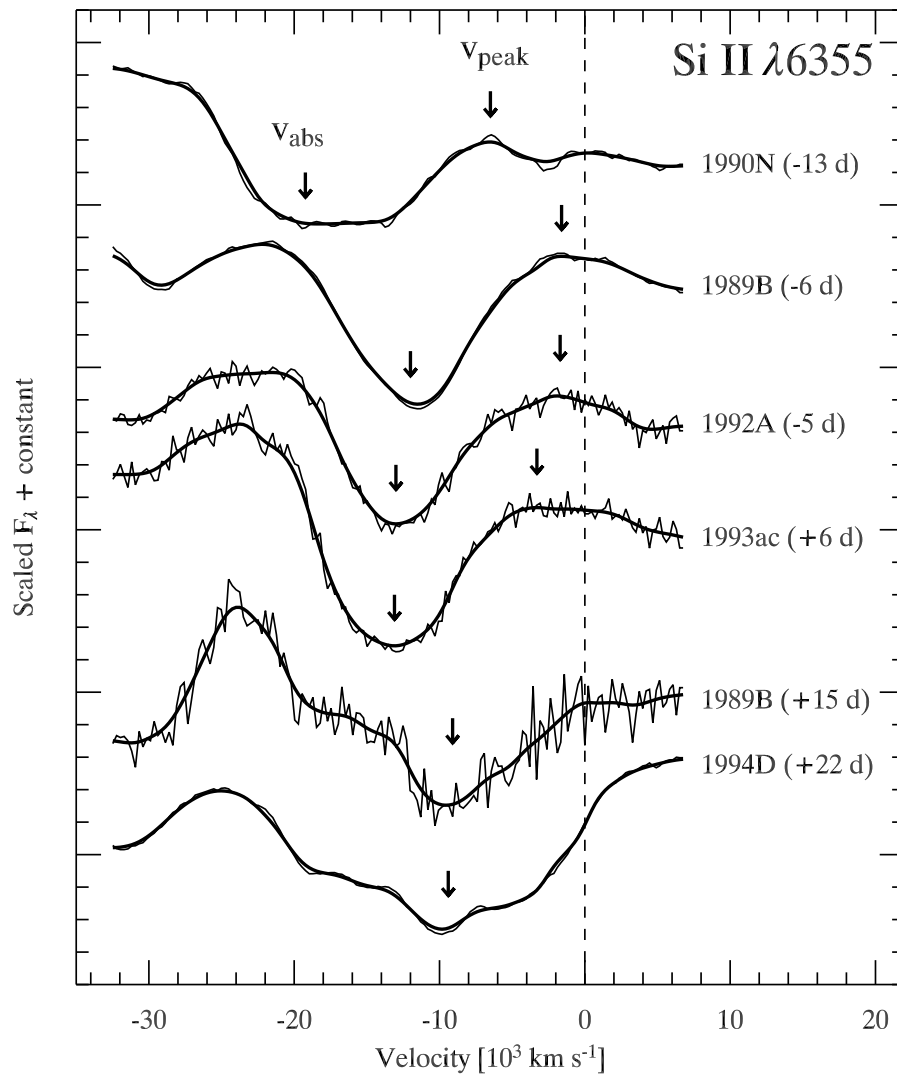


Figure 5.2: P-Cygni profiles of Si II $\lambda 6355$ in local SN Ia. Overplotted on the spectra are their smoothed version (thick black line, see Sect. 5.2.1). The arrows indicate the measured maximum absorption and emission peak, used to determine v_{abs} and v_{peak} . Contamination of the sides of the Si II absorption profile by strengthening emission from iron-group elements is apparent at late phases ($\gtrsim 2$ weeks), and prevents us from measuring the emission-peak velocity.

the case for many local SN Ia spectra), or because the pipeline used to reduce the spectra did not generate the variance spectra (as was the case for spectra taken with Keck+LRIS, at the time of data reduction). For these spectra we use a fiducial sky spectrum taken with the same telescope/instrument combination in place of a variance spectrum. This is adequate since our smoothing technique relies on the relative variance only, and we expect sky emission to be the dominant source of noise in our optical ground-based spectra.

We then spline interpolate the smoothed spectrum $\overrightarrow{F}_{\text{TS}}$ onto a 0.1 Å resolution grid, and determine the wavelengths of maximum absorption (λ_{abs}) and emission peak (λ_{peak}). The absorption and emission-peak velocities are then calculated using the relativistic Doppler formula,

$$v_{\text{Doppler,rel}} = c \left\{ \frac{[(\Delta\lambda/\lambda_0) + 1]^2 - 1}{[(\Delta\lambda/\lambda_0) + 1]^2 + 1} \right\}, \quad (5.6)$$

where $\Delta\lambda = \lambda_{\text{abs}} - \lambda_0$ or $\Delta\lambda = \lambda_{\text{peak}} - \lambda_0$ when inferring v_{abs} and v_{peak} , respectively, and λ_0 is the rest-frame wavelength of the corresponding transition.

This approach has the advantage over using a Gaussian fit to the overall absorption/emission profiles, since it makes no assumption on their shape (in particular, whether the absorption/emission profiles are symmetric or not). Moreover, fitting a function to the whole $\sim 100 - 200$ Å-wide profiles would enhance the impact of line overlap on the fit. In Fig. 5.3 we show velocity residuals as a function of S/N, when using a Gaussian fit to the absorption profile, and when spline interpolating a spectrum smoothed using our algorithm. Here the “noise” is defined as the root-mean-square (RMS) deviation between the input spectrum $\overrightarrow{F}_{\text{SN}}$ and the filtered spectrum $\overrightarrow{F}_{\text{TS}}$, with $d\lambda/\lambda = 0.005$:

$$\text{S/N} = \frac{|\overrightarrow{F}_{\text{SN}}|}{\sqrt{(1/N_\lambda) \sum_{j=0}^{N_\lambda-1} (|\overrightarrow{F}_{\text{SN},j}| - |\overrightarrow{F}_{\text{TS},j}|)^2}}, \quad (5.7)$$

where N_λ is the number of elements in $\overrightarrow{\lambda}$. We find this to be an accurate description of the actual mean S/N, which then enables us to evaluate the mean S/N of spectra for which we do not have the corresponding variance spectrum.

Each of the points of Fig. 5.3 corresponds to a fit to the absorption profile of Si II $\lambda 6355$ in SN 1989B at -6 d (S/N ≈ 70 in that spectral region), for which we have added increasing random Poisson noise weighted by a fiducial sky spectrum, to reproduce signal-to-noise ratios in the range 2–40. In this case, we are making a systematic error of $\sim +400$ km s $^{-1}$ when using a Gaussian, while this uncertainty drops to $\lesssim 100$ km s $^{-1}$ for the spline interpolation method. The latter method is more sensitive to the S/N, namely the drop in precision with decreasing S/N is more significant for the spline ($\sigma_{\text{spline}} \approx 320$ km s $^{-1}$) than for the Gaussian ($\sigma_{\text{gauss}} \approx 130$ km s $^{-1}$). We use such simulations to evaluate the error due to a spectrum’s S/N on our inferred values of v_{abs} and v_{peak} (see next Sect.). All the measurements in this paper make use of the spline-interpolation method.

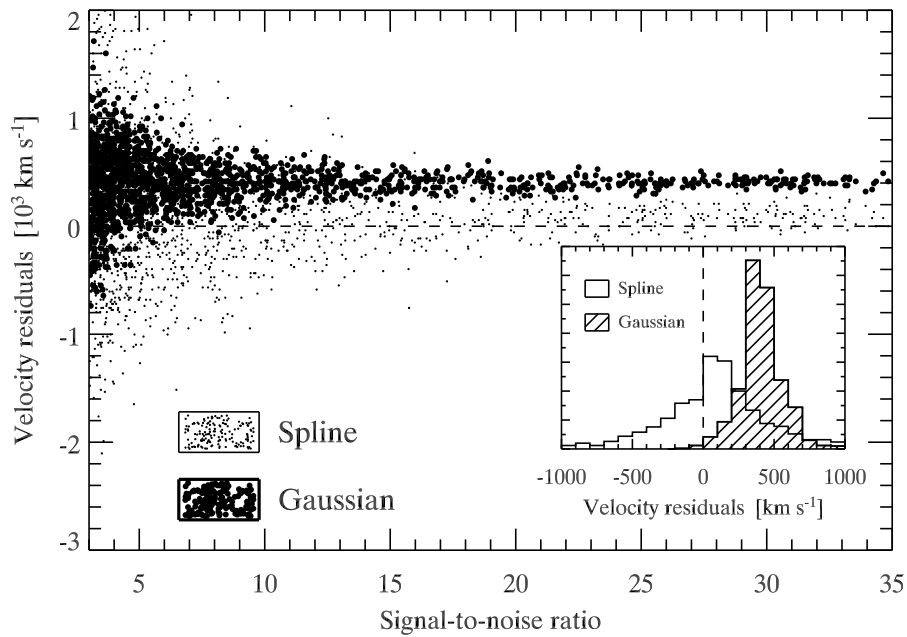


Figure 5.3: Velocity residuals when fitting the minimum of the P-Cygni profile of Si II $\lambda 6355$ in 1989B at -6 d with a Gaussian (*black dots*), or when determining the minimum from a spline interpolation of an inverse-variance weighted Gaussian spectrum (*small points*). The original S/N ratio of the spectrum is ~ 70 . Each of the points corresponds to the original spectrum to which we have added random Poisson noise weighted by a fiducial sky spectrum.

Table 5.1: Measurement errors

Error source	Error size [km s ⁻¹]
<i>Errors related to SN Ia spectral properties:</i>	
Line blending/contamination	Not included
Contamination from host galaxy	Not included
<i>Errors related to the measurement:</i>	
Skewed profile	~ 1000
Signal-to-noise ratio	~ [200, 500, 700, 1200] for S/N ≈ [20, 10, 5, 2] per 5 Å bin
<i>Other errors:</i>	
Redshift uncertainty	~ [200, 3000] for galaxy and SN redshift, respectively
Reddening uncertainty $\sigma_{E(B-V)}$	$\lesssim 100$ for $\sigma_{E(B-V)} \lesssim 0.5$ mag
Use of classical Doppler formula	~ [200, 400, 600] for $v \approx [10, 15, 20] \times 10^3$ km s ⁻¹

5.2.2 Error Budget

In this section we give a detailed account of the various sources of systematic error. We give estimates of these errors in Table 5.1. The elaboration of an error model is an important part of the comparison of v_{abs} and v_{peak} amongst local SN Ia, and between the local and high- z SN Ia. Several authors presenting measurements of v_{abs} in local SN Ia either do not give their error model [17] or do not report errors at all [220].

Note that we do not include errors related to line blending, as this would require detailed modeling of every individual spectrum. We discuss the issue of line blending when presenting our results in Sect. 3.

Errors Related to the Measurement

The smoothing and spline-interpolation technique we use to measure the absorption and emission-peak velocities minimizes the impact of inherently asymmetric profiles. However, in some cases we are unable to rely entirely on this method. This occurs when (i) the profile is highly skewed over a wavelength scale $\Delta\lambda/\lambda < d\lambda/\lambda$ ($d\lambda/\lambda = 0.005$ here); (ii) the feature is too weak, yet a minimum is clearly identifiable; (iii) the absorption profile has a flat minimum (e.g., Si II $\lambda 6355$ in SN 1990N at early phases; Fig. 5.2); (iv) there is a sharp feature which affects the smoothing technique (galaxy line, cosmic ray, noise spike). For (i) and (ii) we resort to a smaller smoothing factor ($0.001 \leq d\lambda/\lambda \leq 0.003$). For (iii), we report the velocity corresponding to the blue edge (i.e., the optically thinner part) of the absorption profile, and associate a lower error bar corresponding to the velocity difference between the blue and red edges of the profile. For (iv), we simply use a linear interpolation over the sharp feature when its width is less than $(d\lambda/\lambda)\lambda_{\text{abs}}$ (for v_{abs} measurements) or $(d\lambda/\lambda)\lambda_{\text{peak}}$ (for v_{peak} measurements).

The S/N of the input spectrum will limit the accuracy of the measurement. For every local SN Ia spectrum in our database, we progressively degrade the S/N of the spectrum by adding random Poisson noise weighted by a fiducial sky spectrum (see previous Sect.), and

construct plots of velocity residuals *vs.* S/N (as in Fig. 5.3) for each of the four spectral features studied here. Most of the local SN Ia spectra used in this study have $S/N > 10$ (per 5 Å bin), and the associated error is $\lesssim 500 \text{ km s}^{-1}$ (Table 5.1), whereas for many of the high- z spectra, the error due to poor S/N can be $> 1000 \text{ km s}^{-1}$.

Further Errors

Further errors affecting measurements of v_{abs} and v_{peak} include the following.

1. *Redshift of parent galaxy:* All the supernova spectra have been corrected for the heliocentric velocity of their host galaxy, z_{gal} . This measurement is affected not only by the galaxy’s internal velocity dispersion ($\sim [200, 100] \text{ km s}^{-1}$ for [early,late]-type galaxies [198]), but also by the position of the SN within the galaxy. An illustration of this is SN 1994D in NGC 4526 for which the NASA/IPAC Extragalactic Database (NED) gives $cz = +448 \text{ km s}^{-1}$ but King et al. [147] measure $cz = +880 \text{ km s}^{-1}$, *at the supernova position*. We have therefore added a $\sigma_{cz,\text{gal}} \approx 200 \text{ km s}^{-1}$ error in quadrature to the total error to account for this effect. Note that for some of the high- z SN Ia the redshift has been determined *via* cross-correlation with local SN Ia spectral templates, with a typical error $\sigma_{z,\text{SN}} \approx 0.01 \equiv 3000 \text{ km s}^{-1}$ [187]. Thus, for these high- z SN the major source of error is due to redshift. Note that such an error leads to a global shift in velocity, and is different in nature from effects such as line overlap which are difficult to assess and vary from line to line.
2. *Reddening:* All of the local and high- z SN Ia spectra have been corrected for both host galaxy and Galactic [268] reddening. For the local SN Ia, we use the host-galaxy reddenings of Phillips et al. [230] (see Table 5.3). For the high- z SN Ia, we use the reddening values derived from fitting the light curves using the algorithm of Prieto et al. [236]. An error in the reddening correction applied to a spectrum can affect the overall continuum slope and in turn bias v_{abs} to higher(lower) values, if the reddening is under(over)-estimated. We have run a simulation to evaluate the errors associated with reddening mis-estimates. They are $\lesssim 50 \text{ km s}^{-1}$ for $\sigma_{E(B-V)} \lesssim 0.3 \text{ mag}$. Since the reddening is typically known down to $\sim 0.1 \text{ mag}$ in local and high- z SN Ia (see Tables 5.3 & 5.4), we ignore this error.
3. *Host-galaxy contamination:* We do not include errors related to contamination of SN Ia spectra by host-galaxy light. The S/N of most local SN Ia spectra is such that the line shapes are expected to be little affected by host-galaxy contamination. For the high- z data, we cannot make this assumption. Nor do we have a reliable way of evaluating the amount of galaxy light present in our spectra, and we ignore this error. All the VLT spectra analyzed here and presented by Matheson et al. [187] were extracted using a 2D deconvolution technique employing the Richardson-Lucy restoration method, minimizing the contamination from the host galaxy [27]. However, we see no systematic effect between the VLT spectra and those from other telescopes.

We further assume the wavelength calibration to be accurate to within $\pm 0.5 \text{ \AA}$, which corresponds to errors $< 50 \text{ km s}^{-1}$ (not included in the error budget).

We note that, since absorption velocities in the SN Ia ejecta can reach $\sim 30,000 \text{ km s}^{-1}$ (i.e., $0.1c$), relativistic corrections to the classical Doppler formula become noticeable ($\sim 1500 \text{ km s}^{-1}$). Different authors may or may not apply the relativistic Doppler formula in their determination of absorption velocities, and systematic differences can result from a blind comparison of different measurements. All the velocities calculated here make use of the relativistic Doppler formula.

An error in the SN phase is of a different nature as it is not a direct error on a velocity measurement, but rather an indirect one affecting the correlation of v_{abs} and v_{peak} measurements with SN phase. The typical error in the time of rest-frame B -band maximum is $\lesssim 1$ day (Table 5.3). This error will of course directly propagate as an error in the phase of the supernova spectrum. For the local SN Ia, we use an updated version of the multi-color light-curve shape (MLCS) method of Riess et al. [251], MLCS2k2 ([137]; Jha et al., in prep), to determine the time of B -band maximum. We could use the MLCS2k2 1σ error on HJD_{max} as the 1σ error on the SN phase, but the MLCS2k2 templates are sampled only once per day, introducing sampling errors on the order of ~ 0.5 day. For the local SN Ia we add a fiducial ± 0.5 day error in quadrature to the MLCS2k2 error in HJD_{max} , while for the high- z ones we use the 1σ error output by the light-curve fitting routine of Prieto et al. [236].

5.3 Results

In this section, using the above method, we present absorption (Sect. 5.3.1) and emission-peak (Sect. 5.3.2) velocity measurements for the Ca II $\lambda 3945$, Si II $\lambda 6355$, and S II $\lambda \lambda 5454, 5640$ line profiles (Table 5.2). These lines do not have the same observed profile shape, presumably because they form differently, and have the potential to reveal distinct aspects of the SN outflow. Note that here, these measurements are sometimes compared with the velocity at the photosphere; let us stress again that throughout this paper, we refer to the photosphere as the outflow location where the inward integrated *continuum* optical depth is $2/3$ – no account is made of line opacity in this definition.

Our sample comprises 30 local SN Ia with phases between -14 d and $+30$ d from B -band maximum (Table 5.3), and 37 high- z ($0.16 < z < 0.64$) SN Ia with (rest-frame) phases between -12 d and $+19$ d from (rest-frame) B -band maximum (Table 5.4; see [187]). We thus performed measurements for a total of 229 local and 48 high- z spectra. Emission-peak velocity measurements, more affected by line contamination (see [135]), are only quoted for 178 local and 39 high- z spectra. In Tables 5.6–5.9, we present the relativistic Doppler velocities v_{abs} and v_{peak} corresponding to the above four line diagnostics, using for each the rest-frame wavelength given in Table 5.2. For the doublet lines of Ca II and Si II this corresponds to the gf -weighted mean wavelength, where g and f are the statistical weight and oscillator strength of the transition, respectively. For the two S II features we instead use the wavelength of the highest $\log(gf)$ transition, due to the large number of transitions

Table 5.2: Characteristic wavelengths of atomic transitions^a

Ion	Multiplet designation	λ [Å]	$\log(gf)$	λ_{gf} [Å]	λ_{used} [Å] ^b
Ca II	4s ² S–4p ² P ⁰	3933.66, 3968.47	0.134, –0.166	3945.28	3945
S II ^c	4s ⁴ P–4p ⁴ D ⁰	5432.80, 5453.86	0.311, 0.557	5442.69	5454
S II ^d	3d ⁴ F–4p ⁴ D ⁰ , 4s ² P–4p ² D ⁰	5606.15, 5639.98	0.156, 0.330	5638.12	5640
Si II	4s ² S–4p ² P ⁰	6347.11, 6371.37	0.297, –0.003	6355.21	6355

^a From Kurucz and Bell [162].

^b Assumed rest-frame wavelength for the transition of the given ion; for Ca II and Si II this is simply the gf -weighted mean wavelength of the two strongest transitions, while for S II this is the wavelength corresponding to the strongest transition.

^c There are five transitions corresponding to S II in the range $5400 \text{ \AA} < \lambda < 5500 \text{ \AA}$; we list the two corresponding to the largest gf values. Note that the value for λ_{gf} corresponds to the gf -weighted mean of these five transitions.

^d There are eight transitions corresponding to S II in the range $5600 \text{ \AA} < \lambda < 5700 \text{ \AA}$; we list the two corresponding to the largest gf values. Note that the value for λ_{gf} corresponds to the gf -weighted mean of these eight transitions.

involved (see Sect. 5.3.1).

Table 5.3: Local SN Ia data

SN (1)	Host galaxy (2)	cz (3)	$E(B - V)$ (4)	M_B (5)	$\Delta m_{15}(B)$ (6)	HJD _{max} (7)	Phases (8)	Ref. (9)
1981B	NGC 4536	1808	0.11 (0.03)	-19.616 (0.038)	1.10 (0.07)	44670.95 (0.73)	+0,+6,+17,+20,+24	(1)
1986G	NGC 5128	547	0.50 (0.05)	-18.273 (0.113)	1.73 (0.07)	46561.36 (0.24)	[5-1],[0-3],+5	(2-3)
1989B	NGC 3627 (M166)	727	0.34 (0.04)	-19.537 (0.064)	1.31 (0.07)	47564.32 (0.59)	+6,+0,+4,+6,+[8-9],+10,[12-15],+18	(4-7)
1990N	NGC 4639	1010	0.09 (0.03)	-19.704 (0.022)	1.07 (0.05)	48081.89 (0.17)	[14-13],[8-6],+5,+8,+[17-18]	(8)
1990Q	MCG +03-44-3	9193	0.02 (0.03)	-19.657 (0.037)	0.96 (0.10)	48076.13 (1.02)	[7-5],+0,[20-21]	(9)
1991IT	NGC 4527	1736	0.14 (0.05)	-19.694 (0.015)	0.94 (0.05)	48374.03 (0.14)	[8-11],[14-17],+26	(10-12)
1991lb	NGC 4374 (M184)	1060	0.03 (0.05)	-17.600 (0.098)	1.93 (0.10)	48603.12 (0.31)	[1-3],[15-16],+19,+26	(13-15)
1992A	NGC 1380	1877	0.00 (0.02)	-19.148 (0.062)	1.47 (0.05)	48640.63 (0.19)	+5,+0,+3,[5-7],+9,+12,+16,+17	(16)
1993ac	Anon.	14791 ^a	0.12 (0.04)	-19.599 (0.071)	1.19 (0.10)	49269.70 (1.19)	+6	...
1994D	NGC 4526	448	0.00 (0.02)	-19.452 (0.030)	1.32 (0.05)	49432.47 (0.10)	[1-2],[2-3],[10-13],+15,+17,+19,+22,+24,+29	(17-19)
1994M	NGC 4493	6943	0.08 (0.03)	-19.345 (0.076)	1.44 (0.10)	49473.61 (0.90)	[3-5],+8,+13	(9)
1994S	NGC 4495	4550	0.00 (0.03)	-19.617 (0.046)	1.10 (0.10)	49518.28 (0.50)	+0,+2,+5	(9)
1994T	Anon.	10399 ^a	0.09 (0.04)	-18.778 (0.148)	1.39 (0.10)	49514.54 (0.52)	+3,+5,+8	...
1994ae	NGC 3370	1279	0.12 (0.03)	-19.679 (0.019)	0.86 (0.05)	49684.65 (0.15)	-1,+[0-5],[8-10],+29	...
1995D	NGC 2962	1966	0.04 (0.02)	-19.676 (0.021)	0.99 (0.05)	49768.60 (0.44)	[3-5],+7,+9,+11,[14-15]	(20)
1995E	NGC 2441	3470	0.74 (0.03)	-19.558 (0.041)	1.06 (0.05)	49774.67 (0.54)	[3-1],+1,+8	...
1995al	NGC 3021	1541	0.15 (0.03)	-19.722 (0.015)	0.83 (0.05)	50028.95 (0.44)	+17,+26	...
1995bd	UGC 3151	4377	0.15 (0.06)	-19.703 (0.024)	0.84 (0.05)	50086.31 (0.24)	+12,+16,+21	...
1996C	MCG +08-25-47	8094	0.09 (0.03)	-19.630 (0.033)	0.97 (0.10)	50128.42 (0.90)	+8	...
1996X	NGC 5061	2065	0.01 (0.02)	-19.490 (0.038)	1.25 (0.05)	50190.85 (0.33)	[3-1],[0-3],[7-9],[13,+22,+24	(21-22)
1996Z	NGC 2935	2271	0.33 (0.04)	-19.482 (0.167)	1.22 (0.10)	50215.25 (1.45)	+6	...
1997br	ESO 576-40	2080	0.24 (0.10) ^b	-19.731 (0.013)	1.00 (0.15) ^b	50559.26 (0.23)	[9-6],-4,+8,+18,+24	(23)
1997cn	NGC 5490	4855	0.00 (...) ^c	-17.656 (0.095)	1.86 (...) ^c	50586.64 (0.78)	+4	(24)
1998aq	NGC 5584	1638	0.08 (...) ^d	-19.604 (0.023)	1.15 (0.05) ^e	50930.80 (0.13)	[9-8],[0-7]	(25-26)
1998bu	NGC 3368 (M196)	897	0.33 (0.03)	-19.572 (0.026)	1.01 (0.05)	50952.40 (0.23)	[3-1],[9-14],[28-30]	(27-28)
1999aa	NGC 2565	4330	0.00 (...) ^f	-19.726 (0.012)	0.75 (0.02) ^f	51231.97 (0.15)	[9-1],+1,[15-18],[27,30]	(29-30)
1999by	NGC 2841	638	0.00 (...) ^g	-17.719 (0.061)	1.90 (0.05) ^g	51309.50 (0.14)	[5-3],+8,+11,+25,+29	(31-33)
1999ee	IC 5179	3422	0.28 (0.04) ^h	-19.688 (0.015)	0.94 (0.06) ^h	51469.29 (0.14)	-9,-7,-2,+0,+2,+7,+11,+16,+19,+22,+27	(34-35)
2000cx	NGC 524	2379	0.00 (...) ⁱ	-19.484 (0.021)	0.93 (0.04) ⁱ	51752.40 (0.13)	[2-1],[0-1],+6,+7(2),+9,+11,+14,+19,+22	(36)
2002bo	NGC 3190	1271	0.43 (0.10) ^j	-19.595 (0.027)	1.13 (0.05) ^j	52356.89 (0.14)	-11,-[9-8],[6-5],[4-1],+0,+6,+29	(37)

REFERENCES – (1) Branch et al. [37]; (2) Frogel et al. [90]; (3) Phillips et al. [231]; (4) Bolte et al. [28]; (5) Barbon et al. [10]; (6) Wells et al. [313] (7) Wells and Lee [312] (erratum in Wells et al. [313]); (8) Leibundgut et al. [168]; (9) Gomez et al. [100]; (10) Filippenko et al. [80]; (11) Ruiz-Lapuente et al. [256]; (12) Phillips et al. [232] (13) Filippenko et al. [81]; (14) Leibundgut et al. [169]; (15) Turatto et al. [294]; (16) Kirshner et al. [149]; (17) Höflich [119]; (18) Patat et al. [220]; (19) Meikle et al. [199]; (20) Sadakane et al. [258]; (21) Wang et al. [305]; (22) Salvo et al. [263]; (23) Li et al. [177]; (24) Turatto et al. [295]; (25) Vinkó et al. [301]; (26) Branch et al. [36]; (27) Jha et al. [138]; (28) Hernandez et al. [115]; (29) Li et al. [176]; (30) Garavini et al. [94]; (31) Vinkó et al. [300]; (32) Howell et al. [130]; (33) Garnavich et al. [95]; (34) Hamuy et al. [103]; (35) Hamuy et al. [104] (erratum on Hamuy et al. [103]); (36) Li et al. [175] (37) Benetti et al. [18].

Column headings: (1) IAU designation. (2) Name of SN host galaxy; “Anon.” (“Anonymous”) means the galaxy has no official designation. (3) Heliocentric radial velocity of host galaxy as quoted in the NASA/IPAC Extragalactic Database (NED); we assume an error of 300 km s⁻¹ in the galaxy redshift; units: km s⁻¹. (4) Average host-galaxy reddening as quoted in Table 2, column (7) of Phillips et al. [230]; units: mag. (5) Absolute B -band magnitude at maximum, derived from an MLC2k2 fit to the rest-frame B -band light curves ([137]; Jha et al., in prep); units: mag. (6) Decline in magnitudes in the rest-frame B -band between maximum and +15 days, as quoted in Table 2, column (2) of Phillips et al. (1999). (7) Actually Heliocentric Julian Date - 2,440,000 of B -band maximum; derived from an MLC2k2 fit to the rest-frame B -band light curves. The 1σ uncertainties are given in between brackets. (8) Rest-frame phase in days from B -band maximum, rounded to closest whole day; adjacent phases are listed in between square brackets; a “(2)” indicates that two spectra correspond to a same rounded phase. (9) Reference of refereed articles presenting optical spectroscopic data in the range $-15 \leq$ phase $\leq +30$ [days from B -band maximum], as found on the NASA ADS server (see “References” below); “...” indicates that no references were found for a given supernova.

^a From [247], Table 3.
^b From [177]; the host galaxy $E(B - V)$ was determined from the total $E(B - V)$ quoted by Li et al. [177] and a Galactic reddening of 0.11 mag, as derived using the dust IR emission maps of Schlegel et al. [268].
^c From [295].
^d From [260]. (Note: this value assumes the supernova experiences the same reddening as the Cepheids in NGC 5584; see [260] for a thorough discussion of this issue).
^e From [246].
^f From [157].
^g From [95]; see this same paper for a long discussion on the low/null reddening in the host galaxy.
^h From [282].
ⁱ From [175].
^j From [18]; consult this article and [159] for an extensive discussion on the abnormally high $E(B - V)$ value obtained for SN 2002bo.

Table 5.4: High- z SN Ia data

IAU name	z^a	$E(B - V)^b$	$\Delta m_{15}(B)^b$	MJD_{\max}^b	Phases ^c
2002iy	0.587	0.01 (0.03)	0.93 (0.10)	52592.75 (1.34)	+14
2002iz	0.428	0.14 (0.08)	1.17 (0.05)	52587.80 (1.56)	-1, +19
2002ja	0.33	0.19 (0.08)	0.94 (0.09)	52585.42 (1.97)	+2
2002jb	0.25	0.12 (0.10)	1.10 (0.03)	52596.01 (0.67)	-7
2002jc	0.52	0.00 (0.02)	1.47 (0.04)	52596.27 (0.52)	-6, +11
2002jd	0.32	0.00 (0.05)	0.84 (0.04)	52593.29 (0.56)	-3, +16, +18
2002jq	0.49	0.06 (0.11)	1.48 (0.07)	52603.47 (0.02)	+6
2002js	0.54	0.00 (0.03)	1.03 (0.07)	52600.21 (1.19)	+7
2002jt	0.56	0.00 (0.07)	0.83 (0.01)	52615.42 (1.34)	+3
2002jw	0.357	0.08 (0.05)	1.00 (0.08)	52618.35 (0.76)	-2, +19
2003ji	0.21	0.00 (0.04)	0.84 (0.05)	52921.14 (1.79)	+19
2003jj	0.583	0.25 (0.10)	0.84 (0.11)	52946.83 (1.33)	-2
2003jl	0.429	0.15 (0.05)	0.92 (0.04)	52931.72 (0.66)	+8
2003jm	0.522	0.05 (0.06)	0.84 (0.08)	52933.97 (1.72)	+5
2003jo	0.524	0.00 (0.07)	0.84 (0.13)	52935.81 (1.81)	+3
2003jq	0.16	0.30 (0.03)	0.83 (0.01)	52935.25 (0.36)	+1
2003jr	0.340	0.18 (0.05)	0.83 (0.05)	52920.76 (1.44)	+17
2003js	0.363	0.00 (0.01)	0.99 (0.03)	52948.38 (0.40)	-5, +13
2003jt	0.45	0.12 (0.05)	0.83 (0.08)	52936.84 (1.03)	+3
2003ju	0.20	0.06 (0.06)	1.29 (0.01)	52948.44 (0.37)	-8, +18
2003jv	0.405	0.14 (0.07)	0.83 (0.10)	52942.48 (1.01)	-2
2003jw	0.296	0.08 (0.10)	1.69 (0.01)	52949.85 (0.48)	-6
2003jy	0.339	0.03 (0.04)	1.05 (0.04)	52956.13 (0.53)	-10
2003kk	0.164	0.20 (0.05)	1.02 (0.03)	52966.29 (0.39)	-4
2003kl	0.335	0.23 (0.11)	1.47 (0.08)	52965.52 (1.46)	-3, +0
2003km	0.47	0.02 (0.03)	0.94 (0.04)	52981.10 (0.46)	-12, -11
2003kn	0.244	0.15 (0.07)	1.47 (0.03)	52974.01 (0.46)	-7
2003ko	0.360	0.20 (0.05)	1.21 (0.06)	52968.25 (0.88)	-2
2003kp	0.64	0.02 (0.05)	1.29 (0.05)	52963.14 (1.48)	+1
2003kq	0.61	0.09 (0.05)	0.88 (0.07)	52969.64 (1.31)	-3
2003kr	0.427	0.09 (0.03)	1.17 (0.05)	52976.71 (0.48)	-8
2003kt	0.61	0.02 (0.05)	1.23 (0.07)	52959.82 (1.75)	+4
2003le	0.56	0.07 (0.08)	0.83 (0.02)	52995.50 (1.56)	-1
2003lf	0.41	0.09 (0.04)	1.40 (0.07)	52990.69 (0.57)	+2, +3
2003li	0.544	0.05 (0.05)	1.06 (0.04)	52984.95 (1.23)	+5
2003lj	0.417	0.27 (0.09)	1.11 (0.07)	52989.60 (1.60)	+3
2003lm	0.408	0.11 (0.05)	1.47 (0.05)	52992.14 (0.91)	+2
2003ln	0.63	0.02 (0.04)	0.85 (0.18)	52987.80 (1.23)	+4

^a For redshifts determined from narrow lines in the host galaxy (quoted with three decimal places), we assume an error of 0.001; for those determined *via* cross-correlations with local SN Ia spectra templates [187], we assume an error of 0.01.

^b Light-curve parameters (and 1σ errors) output by the fitting routine of Prieto et al. [236]. $E(B - V)$ values correspond to host-galaxy extinction only.

^c Rest-frame phase in days from rest-frame B -band maximum, rounded to closest whole day.

To facilitate the visual inspection of figures, we show the temporal evolution of v_{abs} (Figs. 5.4, 5.6, and 5.7) and v_{peak} (Figs. 5.9–5.12) for all spectra by grouping data points according to the decline-rate parameter $\Delta m_{15}(B)$ (the decline in B -band magnitudes between maximum and +15 d [229, 230]) of the corresponding SN Ia. Following this selection criterion, our sample of local (high- z) SN Ia has 10 (17) objects with $\Delta m_{15}(B) < 1.0$, 17 (20) with $1.0 \leq \Delta m_{15}(B) \leq 1.7$, and 3 (0) with $\Delta m_{15}(B) > 1.7$; the lack of $\Delta m_{15}(B) > 1.7$ SN Ia in our high- z sample could be due to a selection effect [201, 156]. Note that when computing the decline rate $\Delta m_{15}(B)$ of high- z SN Ia, time dilation is accounted for by scaling the time axis by a factor $(1+z)^{-1}$ [171, 99].

5.3.1 Absorption Velocities

All *spectroscopic* velocity measurements reported in this paper are negative, and thus correspond to blueshifts; to avoid any confusion, we apply the standard rules of arithmetic and say, e.g., that a v_{abs} measurement *increases* from $-25,000 \text{ km s}^{-1}$ to $-15,000 \text{ km s}^{-1}$, while the simplistic interpretation of such a variation suggests that the corresponding location of maximum absorption *decreases* from outflow *kinematic* velocities of $25,000 \text{ km s}^{-1}$ down to $15,000 \text{ km s}^{-1}$ — see Sect. 5.3.1.

Presentation of v_{abs} Measurements

In the top panel of Fig. 5.4, we show v_{abs} measurements for the local SN Ia sample for the Ca II $\lambda 3945$ feature, as a function of phase and ordered according to their decline rate: $\Delta m_{15}(B) < 1.0$ (“slow-decliners,” *downward-pointing triangles*), $1.0 < \Delta m_{15}(B) < 1.7$ (*circles*), and $\Delta m_{15}(B) > 1.7$ (“fast-decliners,” *upward-pointing triangles*). For the few objects showing a double-absorption Ca II feature (tagged “blue” and “red” according to wavelength; see Sect. 5.3.3 and Table 5.6), we plot only the redder component. We invert the ordinate (v_{abs}) axis for consistency with previously published measurements, which usually associate the absorption blueshifts with positive velocities.

The absorption velocities for Ca II $\lambda 3945$ reveal two v_{abs} sequences at pre-maximum phases: one sequence shows a steady increase in v_{abs} from a minimum of $\gtrsim -25,000 \text{ km s}^{-1}$ at the earliest observed phases ($\lesssim -10 \text{ d}$) to $\sim -15,000 \text{ km s}^{-1}$ at B -band maximum, after which the evolution is more gradual or even constant. A second sequence is located at less negative v_{abs} ($v_{\text{abs}} \gtrsim -15,000 \text{ km s}^{-1}$) and remains almost constant around $\sim 12,000 \text{ km s}^{-1}$. This sequence corresponds to red Ca II absorption components that have a blue counterpart, and the resulting contamination biases the measurements to higher v_{abs} (see Sect. 5.3.3). The scatter in v_{abs} decreases with SN phase, irrespective of decline rate, from $\sim \pm 7000 \text{ km s}^{-1}$ at -10 d to $\lesssim \pm 3000 \text{ km s}^{-1}$ at $+20\text{--}30 \text{ d}$. The fast-decliners overlap significantly with the other SN Ia, and thus cannot be used to discriminate between subluminous and overluminous objects, contrary to claims made by Lidman [178]. Within the $\Delta m_{15}(B) < 1.0$ sample, two objects (SN 1990O and 1999ee) form a v_{abs} sequence at more negative velocities, suggesting higher explosion kinetic energies. The other 8 slow-declining SN Ia cannot be distinguished from those with $\Delta m_{15}(B) \geq 1.0$, at all phases.

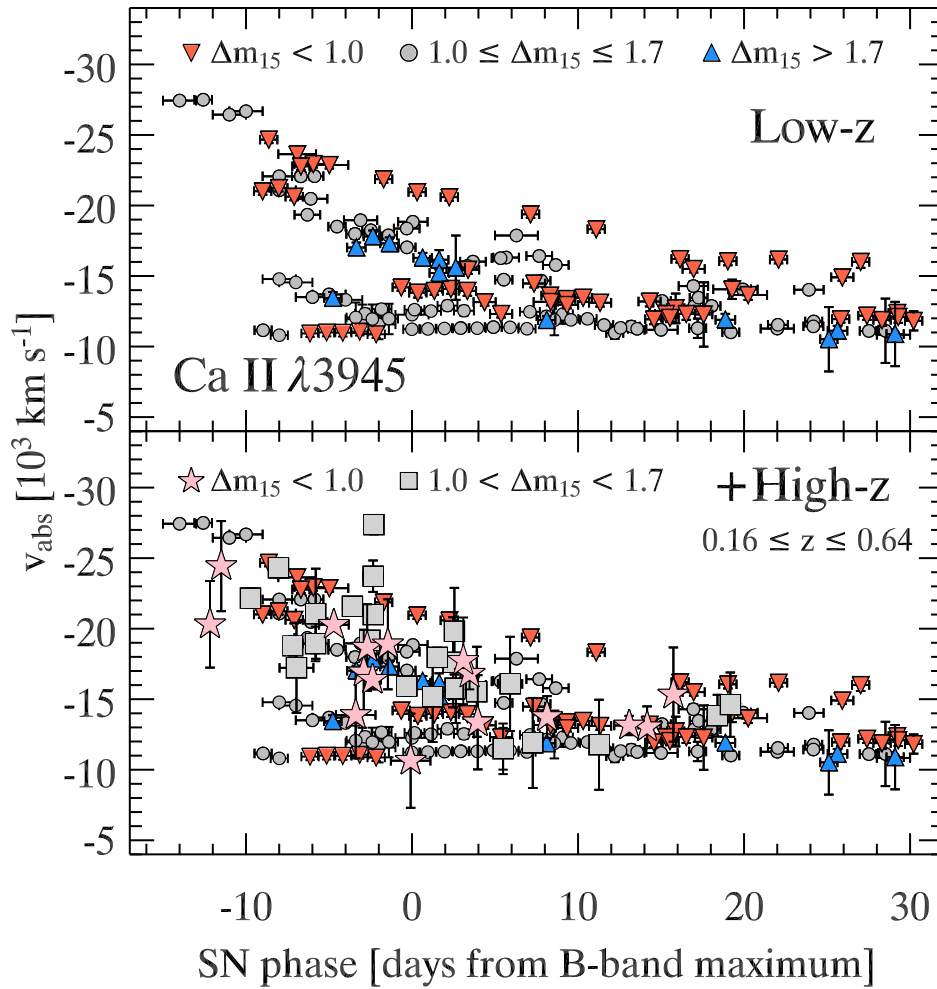


Figure 5.4: *Upper panel:* Absorption velocities for Ca II $\lambda 3945$ in local SN Ia, for three different $\Delta m_{15}(B)$ ranges. If a double-absorption is present, only the redder component is plotted. *Lower panel:* The high- z data are overplotted.

In the lower panel of Fig. 5.4, we overplot the v_{abs} measurements for our sample of high- z ($0.16 < z < 0.64$) SN Ia. The time evolution of v_{abs} for Ca II $\lambda 3945$ in our high- z sample is similar to that for the local SN Ia: a steady increase from $\gtrsim -25,000 \text{ km s}^{-1}$ at very early phases ($\lesssim -10 \text{ d}$) to $\sim -15,000 \text{ km s}^{-1}$ at maximum, and a more gradual post-maximum increase. Again, the slow-declining high- z SN Ia cannot be distinguished.

Because this Ca II feature is a few hundred Ångstroms wide, it likely overlaps with other lines. To illustrate and assess the magnitude of such a line overlap, we show in the top panel of Fig. 5.5 synthetic SYNOW spectra for SN 1994D at -10 d , -1 d , and $+10 \text{ d}$ from B -band maximum ([33]; *solid line*), as well as the relative contribution from Ca II (*dotted line*), S II (*dashed line*), and Si II (*long-dashed line*). (All spectra are normalized to the adopted blackbody continuum energy distribution.) We see that the strong Ca II $\lambda 3945$ absorption feature (including the blue absorption, see Sect. 5.3.3) is contaminated at all phases, predominantly by Si II $\lambda 3858$ (gf -weighted mean rest-frame wavelength). However, it is only around and past maximum that the v_{abs} measurement is affected by the Si II $\lambda 3858$ absorption: at maximum ($+10 \text{ d}$), v_{abs} is biased to less (more) negative values. Despite this corrupting effect, the Ca II $\lambda 3945$ line is the major contributor to the wide absorption trough seen at $\sim 3750 \text{ Å}$, for all phases $\lesssim 2$ weeks from B -band maximum.

In Fig. 5.6 (top panel), we reproduce Fig. 5.4 for Si II $\lambda 6355$, showing in the top panel the v_{abs} measurements for the local SN Ia sample. The v_{abs} evolution for this feature is comparable to that for Ca II $\lambda 3945$, though values are at all phases less negative, by $\sim 5000 \text{ km s}^{-1}$ (see also Fig. 5.5 and Sect. 5.3.1). The fast-declining SN Ia form, on average, a sequence of less negative v_{abs} , at post-maximum phases, but this sequence separates only at $t \gtrsim +20 \text{ d}$ from the $1.0 \leq \Delta m_{15}(B) \leq 1.7$ objects. The higher scatter in the slow-declining SN Ia causes an overlap with the fast-declining ones at all phases. We are lacking data at $t \gtrsim +20 \text{ d}$ to make a clear distinction between the slowest and fastest decliners of our sample. At these late phases, however, the optical spectra of SN Ia are dominated by lines of iron-group elements (mainly Co II and Fe II), and the Si II $\lambda 6355$ feature suffers from increasing line blending. Note that the Si II $\lambda 6355$ absorption profile is sometimes unusually flat and extended (see, e.g., SN 1990N at -14 d and -13 d with $v_{\text{abs}} \sim -20,000 \text{ km s}^{-1}$; also see SN 2001el [189]), perhaps due to contamination from C II $\lambda 6580$ forming in a high-velocity shell ([83]; see also [191]). The high- z sample (Fig. 5.7, lower panel) reveals similar properties. Note that Si II $\lambda 6355$ falls outside the optical spectral range for $z \gtrsim 0.4$; the highest redshift at which we were able to measure v_{abs} for this feature was $z = 0.428$.

We now turn to the weakest lines in our study, the S II $\lambda \lambda 5454, 5640$ features, for which we show the time-evolution of v_{abs} in Fig. 5.7. Compared to Ca II $\lambda 3945$ and Si II $\lambda 6355$, v_{abs} -values for the S II lines are less negative at all phases (always greater than $-13,000 \text{ km s}^{-1}$ for $\lambda 5454$ and $-15,000 \text{ km s}^{-1}$ for $\lambda 5640$), with a nearly constant and smaller increase with phase. These optically thinner lines are increasingly contaminated by those of iron-group elements at $t \gtrsim 2$ weeks, becoming unnoticeable at later phases – this explains the lack of data at late phases in Fig. 5.7. Three of the $1.0 \leq \Delta m_{15}(B) \leq 1.7$ points for S II $\lambda 5640$ at $t \sim -10 \text{ d}$, associated with SN 2002bo [18], lie at more negative velocities ($< -13,000 \text{ km s}^{-1}$) than the bulk of our sample. Several points at phases between maximum and $+10 \text{ d}$, associated with SN 1994M [100], also have more negative

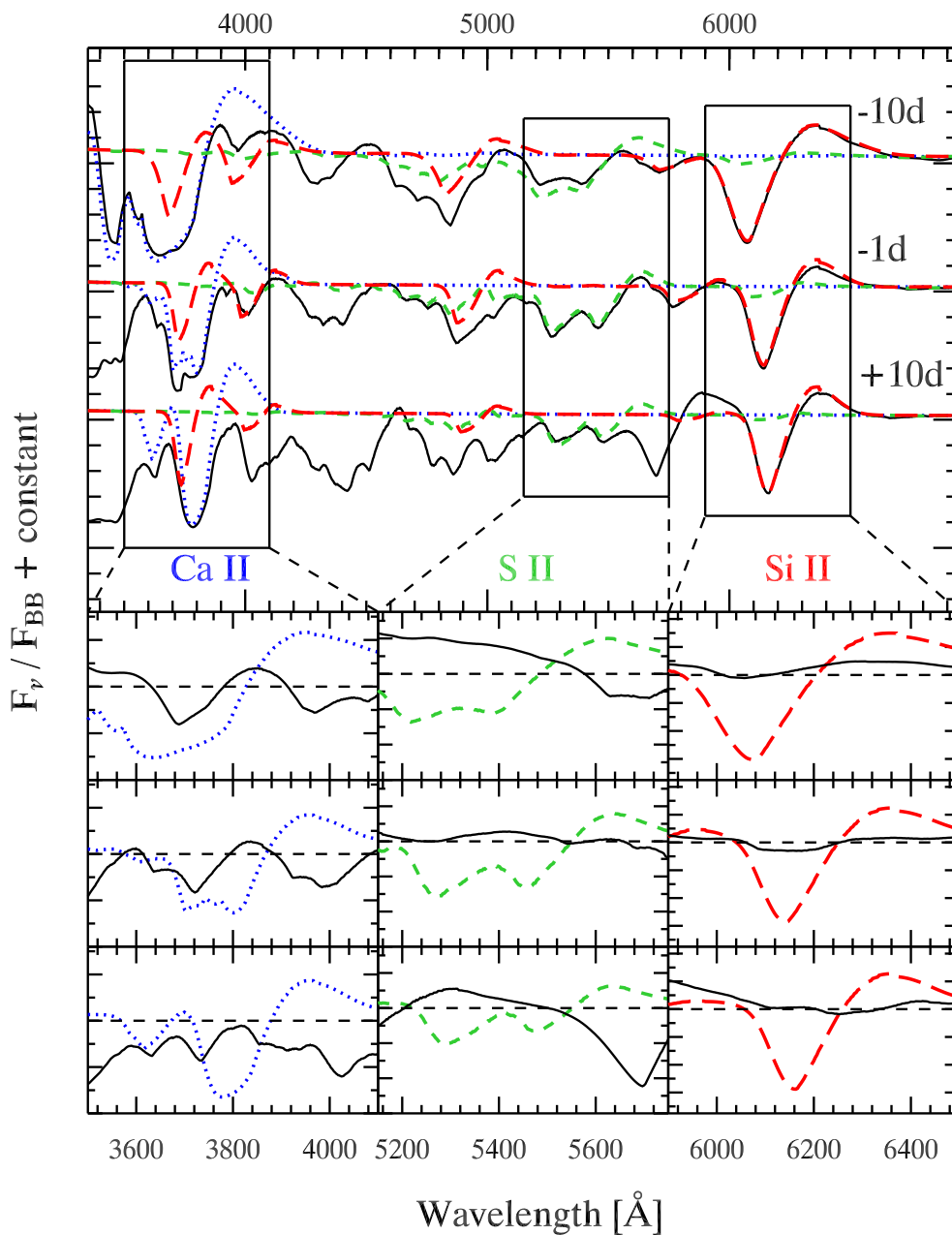


Figure 5.5: *Top panel:* SYNOW models of SN 1994D at -10 d, -1 d, and $+10$ d (*solid line*), along with the contributions from Ca II (*dotted lines*), S II (*dashed line*), and Si II (*long-dashed line*). *Lower panels:* Close-up of the Ca II $\lambda 3945$ (*left*), S II $\lambda\lambda 5454, 5640$ (*middle*), and Si II $\lambda 6355$ (*right*) features. The linestyle coding is the same as for the top panel, except that now the solid line corresponds to the contribution from all *other* ions. The fluxes (per unit frequency, F_ν) are normalized to the underlying blackbody continuum (F_{BB}). Unlike Branch et al. [33], we have not included (weak) contributions from C II in the -10 d spectrum.

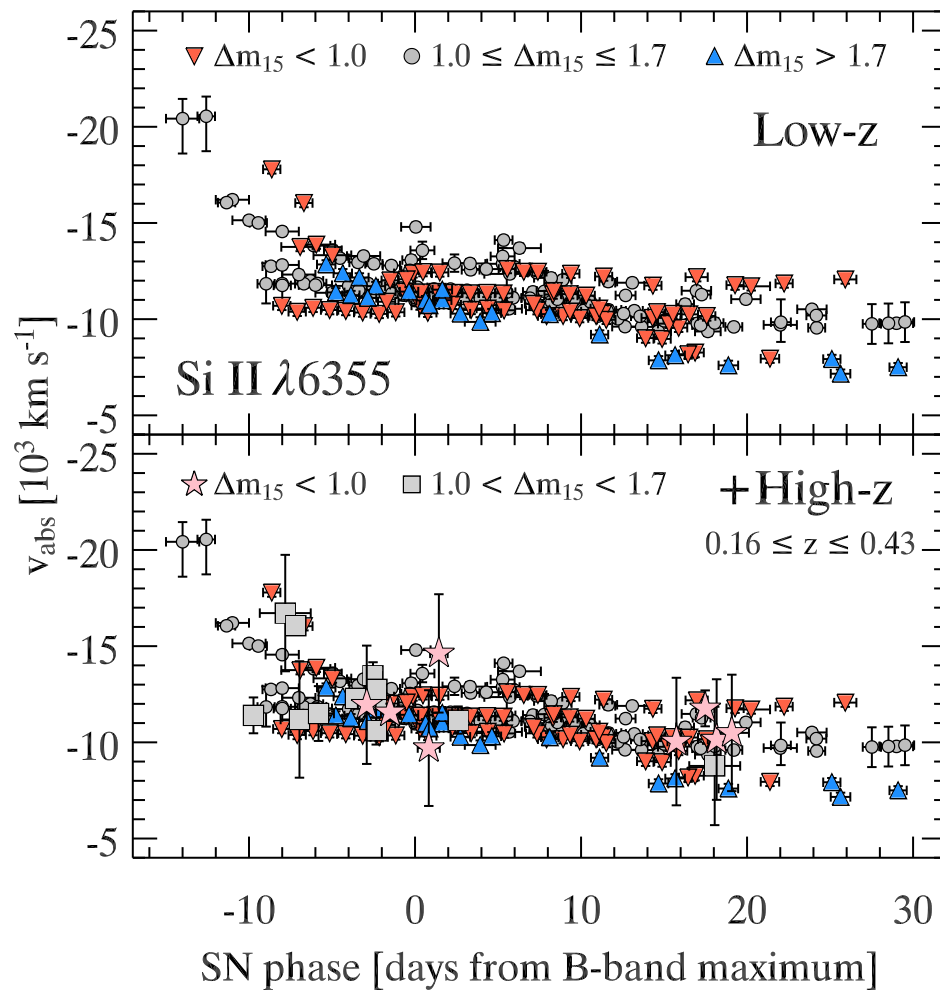


Figure 5.6: *Upper panel:* Absorption velocities for Si II $\lambda 6355$ in local SN Ia, for three different $\Delta m_{15}(B)$ ranges. *Lower panel:* The high- z data are overplotted.

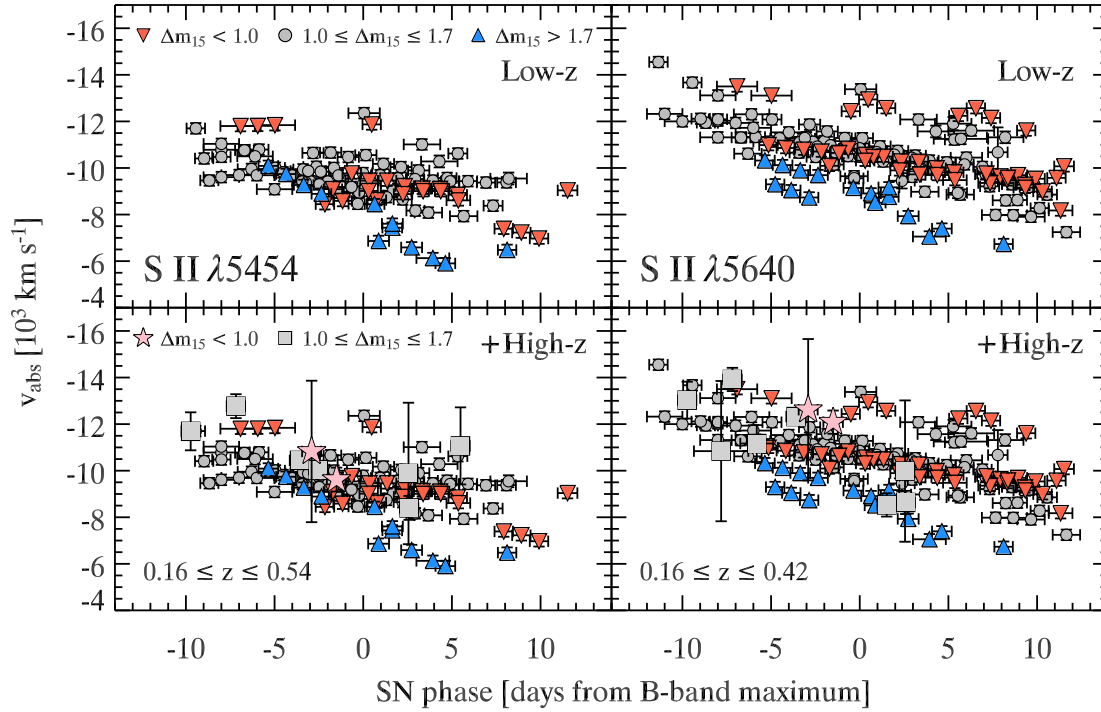


Figure 5.7: *Upper panels:* Absorption velocities for S II $\lambda 5454$ (*left*) and S II $\lambda 5640$ (*right*) in local SN Ia, for three different $\Delta m_{15}(B)$ ranges. *Lower panels:* The high- z data are overplotted.

velocities than the rest of our sample data. This may result from line blending, although our SYNOW investigation (see Fig. 5.5, middle panels) suggests this overlap to be weak or absent.

Alternatively, the S II v_{abs} measurements might be influenced by the overlap between the 13 individual S II features in the range 5300–5700 Å (Kurucz & Bell 1995). For example, distinct intrinsic excitation temperatures and formation mechanisms for one transition could cause its optical depth to vary differently from that of others and thus modulate, at selected phases, the observed location of maximum absorption in the total profile. Note that the Ca II $\lambda 3945$ and Si II $\lambda 6355$ features are the result of transitions corresponding to a single multiplet, and will not be affected by this issue.

Interestingly, fast decliners at positive phase show the least negative S II $\lambda 5454$ – $\lambda 5640$ v_{abs} values with a lower limit of ~ -8000 km s $^{-1}$, combined with the most pronounced v_{abs} gradient with phase amongst the different $\Delta m_{15}(B)$ subgroups. Provided the phase is known accurately, these two S II features can be used to discriminate between fast- and slow-decliners at post-maximum phases.

Table 5.5: CMFGEN model parameters

Model parameter	Parameter value
Radius, R_0	4×10^4 cm ($\sim 5750R_\odot$)
Luminosity, L_0	$8 \times 10^8 L_\odot$
Density, ρ_0	2×10^{-11} g cm $^{-3}$
Density gradient, n	7 [in $\rho(r) = \rho_0(R_0/r)^n$]
Turbulent velocity, v_{turb}	90 km s $^{-1}$
Element	Mass fraction
C	0.12
O	0.63
Mg	0.1
Si	0.1
S	0.05
Ca	0.0001
Fe	0.0014
Ni	0.001

Interpretation of v_{abs} measurements

We now investigate the causes of the variations in line profile shapes and v_{abs} values for our optical diagnostics. We base our discussion on synthetic line profiles computed with CMFGEN [118], a steady-state, one-dimensional, non-local thermodynamic equilibrium (non-LTE) model atmosphere code that solves the radiative transfer equation in the co-moving frame, subject to the constraints of radiative and statistical equilibria. Because CMFGEN is at present not strictly adequate for SN Ia conditions (no chemical stratification; no γ -ray energy deposition; see [66] for details), these results are merely illustrative; nonetheless, they provide a new insight into the sites of optical-line and continuum formation, corresponding in this example to a low-luminosity SN Ia (“SN 1991bg-like”) near maximum light.

The SN Ia conditions are epitomized here by the absence of hydrogen and helium in the outflow, and thus the dominance of metal species. Their mass fractions, alongside basic model parameters, are listed in Table 5.5. Note that the continuum optical depth at the base radius R_0 is ~ 50 .

We show in Fig. 5.8 the synthetic line profiles for Ca II $\lambda 3934$ (*left*), Si II $\lambda 6347$ (*center*), and S II $\lambda 5432$ (*right*), computed under such model assumptions. At the bottom of each panel, and following Dessart and Hillier [66, 65], we show gray-scale images in the (v, p) plane of the flux-like quantity $p \cdot I(p)$, where $v = [(\lambda/\lambda_0) - 1]c$ is the classical Doppler velocity, p is the impact parameter in units of R_0 , and $I(p)$ is the specific intensity at p . The photosphere (corresponding to $\tau_{\text{cont}} = 2/3$) is shown as a solid thick line. The sum over p of the quantity $p \cdot I(p)$ at v corresponds to the total line flux at v , shown at the top of each panel (solid line). Note that for each line, we select a single transition to avoid the corrupting effect of line overlap, stemming from other transitions of the same or different

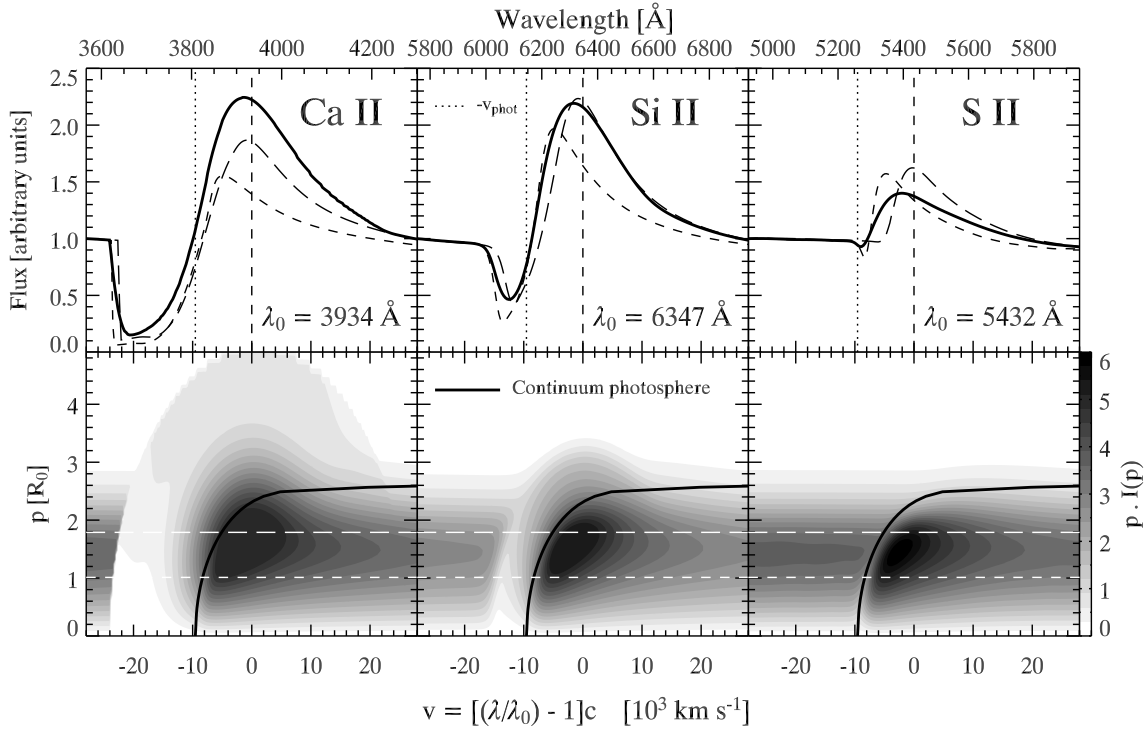


Figure 5.8: P-Cygni profiles of Ca II $\lambda 3934$, S II $\lambda 5432$, and Si II $\lambda 6347$ in a CMFGEN model of a low-luminosity SN Ia near maximum brightness, with density exponent $n = 7$, revealing the sites at the origin of synthetic line profile flux, and the resultant blueshift of the P-Cygni profile emission peak. *Lower panels:* Gray-scale image of the quantity $p \cdot I(p)$ as a function of p and classical Doppler velocity $v = [(\lambda/\lambda_0) - 1]c$, where p is the impact parameter and $I(p)$ the specific intensity along p (at v). R_0 is the base radius of the CMFGEN radial grid where the continuum optical depth $\tau_{\text{cont}} \approx 50$ – a photosphere thus exists in this model configuration, corresponding here to a velocity of 9550 km s^{-1} . λ_0 is the rest wavelength of the transition and c is the speed of light in vacuum. The overplotted thick black curve gives the line-of-sight velocity location where the integrated continuum optical depth at 5500 Å, along z and at a given p , equals $2/3$. The dotted white lines are for $p = [1, 1.8]$. *Upper panels:* (*solid curve*) Line profile flux obtained by summing $p \cdot I(p)$ over the range of p ; (*broken curves*) line profile flux along $p = [1, 1.8]$. The vertical dotted line corresponds to the (continuum) photospheric velocity. The profiles have been normalized to the flux at the inferior boundary of the plotted velocity range, where the line optical depth is zero. See [66, 65] for a detailed and pedagogical explanation of these plots in the context of Type II supernovae.

species.

Let us first focus on the absorption trough, controlling the resulting v_{abs} , of such synthetic line profiles. For Ca II $\lambda 3934$, we see that the trough is nearly saturated with essentially no residual flux down to $\sim -22,000 \text{ km s}^{-1}$, while Si II $\lambda 6347$ shows a maximum absorption at a less negative velocity of $-12,000 \text{ km s}^{-1}$; S II $\lambda 5432$ is the weakest line of all three, with a very modest absorption and extent, located at $\sim -9500 \text{ km s}^{-1}$.

We thus reproduce here the general trend shown in Figs. 5.4-5.7 and presented in the previous section: absorption velocities for Ca II $\lambda 3945$ are more negative by several 1000 km s^{-1} at any given phase than those for S II $\lambda\lambda 5454, 5640$ and Si II $\lambda 6355$, because it remains optically thick out to larger radii (i.e., lower densities and higher expansion velocities). Indeed, this feature is the result of a blend of Ca II K (3933.66 \AA) and H (3968.47 \AA) transitions, both corresponding to the same $4s^2S-4p^2P^0$ multiplet, linking the ground state and low-lying upper levels (just 3 eV above the ground state). Despite the low $\log(gf)$ -value of the transition and the considerably lower calcium abundance compared to silicon and sulphur in our model (by a factor of 1000 and 500, respectively), the high Ca II ground-state population in this parameter space translates into a very large line optical depth ($\tau_{\text{line}} \propto \kappa_{\text{line}} \rho_{\text{ion}}$). The sample Si II and S II lines result, however, from higher-level transitions, less populated, which translate into systematically lower optical depths and less negative v_{abs} -values, the more so for the S II lines. Also, at a given phase, the maximum absorption is further to the blue in S II $\lambda 5640$ than in S II $\lambda 5454$, which likely results from differences in the atomic properties of each transition.

Despite the assumed *homogeneity and smooth density distribution* of the CMFGEN model, a scatter in v_{abs} between line diagnostics is not only present but also large and comparable to the observed scatter; inferring the presence, at a given phase, of chemical stratification in the SN outflow thus requires careful analysis, with a detailed and accurate account of all line optical depth effects [280]. This argues for caution in the interpretation of v_{abs} measurements, since one sees the numerous competing effects arising from differences in the atomic-transition properties, chemical abundances, density, and velocity distribution; additional corrupting effects such as line overlap are discussed later in this paper.

In Fig. 5.8, we also see that $|v_{\text{abs}}|$ underestimates the velocity of the photosphere for the weak, optically thinner S II $\lambda 5432$ line. The physical origin of this effect is given by Dessart and Hillier [65], and stems from the steep density gradient in supernova atmospheres [$\rho(r) \propto r^{-n}$]: iso-velocity curves are at constant v (depth z in the (p, z) plane) but the density varies as $1/r^n$. Thus, at fixed z , the density drops fast for increasing p , at the same time reducing the probability of line scattering and/or absorption. In practice, the location of maximum absorption along a ray shifts to larger depths (z closer to zero) for increasing p , showing overall the same curvature as seen for the photosphere (see overplotted curve). Along a p -ray with impact parameter p , the location of maximum absorption is always exterior to the photosphere along that ray (the line opacity comes on top of the default continuum opacity), but shifts toward line center for increasing p . As a consequence, the total line profile, which results from the contribution at all impact parameters, shows a maximum absorption at a velocity v_{abs} , the magnitude of which can be higher *or* lower than the photospheric value v_{phot} . This offset between $|v_{\text{abs}}|$ and v_{phot} is determined primarily by

the magnitude of the line optical depth. As we move from Ca II $\lambda 3934$ to Si II $\lambda 6347$ and S II $\lambda 5432$, the line optical depth decreases and the corresponding absorption velocity is closer to zero.

Note that the comparison with the photospheric velocity of the SN Ia outflow is not necessarily meaningful. First, electron scattering, which provides the dominant source of continuum opacity in ionized hydrogen-free and helium-free outflows, corresponds to a small mass absorption coefficient due to the high mean molecular weight of the outflow ($\kappa_e \lesssim 0.05 \text{ cm}^2 \text{ g}^{-1}$, a factor at least ten times smaller than in hot-star outflows). Second, the outflow density decreases with the cube of the time, following the homologous expansion of the SN Ia, so that the outflow becomes optically thin in the continuum after about 10 days past explosion; the concept of a photosphere then becomes meaningless. The alternative definition (not adopted here) of the photosphere as the location where the total (line and continuum) inward integrated optical depth is $2/3$ changes this conception somewhat: the ubiquitous presence of lines makes the photospheric radius (and velocity) highly dependent on wavelength, and thus non-unique and ambiguous (see [124, 279, 119, 234]).

5.3.2 Emission-Peak Velocities

Large negative v_{peak} values are common in optical line profiles of Type II SN spectra, explained for the first time by Dessart & Hillier (2005a); the root cause is the strong SN outflow density gradient, and because such a property is common to both SN Ia and SN II, such peak-emission blueshifts are also expected in SN Ia line profiles. Using the same approach as before for v_{abs} , we present in Sect. 5.3.2 the first census of v_{peak} measurements, using our large sample of local and high- z SN Ia spectra. We then comment on these results in Sect. 5.3.2, using the CMFGEN model presented in the previous section.

Presentation of v_{peak} Measurements

Keeping the same structure as for previous figures displaying v_{abs} measurements, we show in Fig. 5.9 the phase-dependent v_{peak} measurements for the Ca II $\lambda 3945$ feature in local SN Ia (upper panel) and all sampled SN Ia (lower panel), separating objects according to their decline-rate parameter, $\Delta m_{15}(B)$. As for SN II, all v_{peak} measurements for Ca II $\lambda 3945$ at $\lesssim +20$ d are *negative*; that is, the peak emission is blueshifted with respect to the rest wavelength of the line, increasing with phase from $\sim -6000 \text{ km s}^{-1}$ (at -10 d) up to -1000 km s^{-1} ($+20$ d). The scatter is, however, significant. Moreover, at any phase, near-zero values are found. As previously for v_{abs} measurements, Si II $\lambda 3858$ modifies the Ca II intrinsic line profile shape but now introduces, at all phases, a blueshift of the emission peak of the 3945 \AA feature (Fig. 5.5, left panels), likely influencing the scatter and the magnitude of v_{peak} values (see next section). A few points at $\gtrsim +25$ d (corresponding to the spectroscopically peculiar SN 1999aa [176]) show a counterexample to the above trend, with $v_{\text{peak}} > 0$. At these phases, however, Ca II $\lambda 3945$ is increasingly contaminated from lines of iron-group elements, and the measurements of v_{peak} at these phases are highly

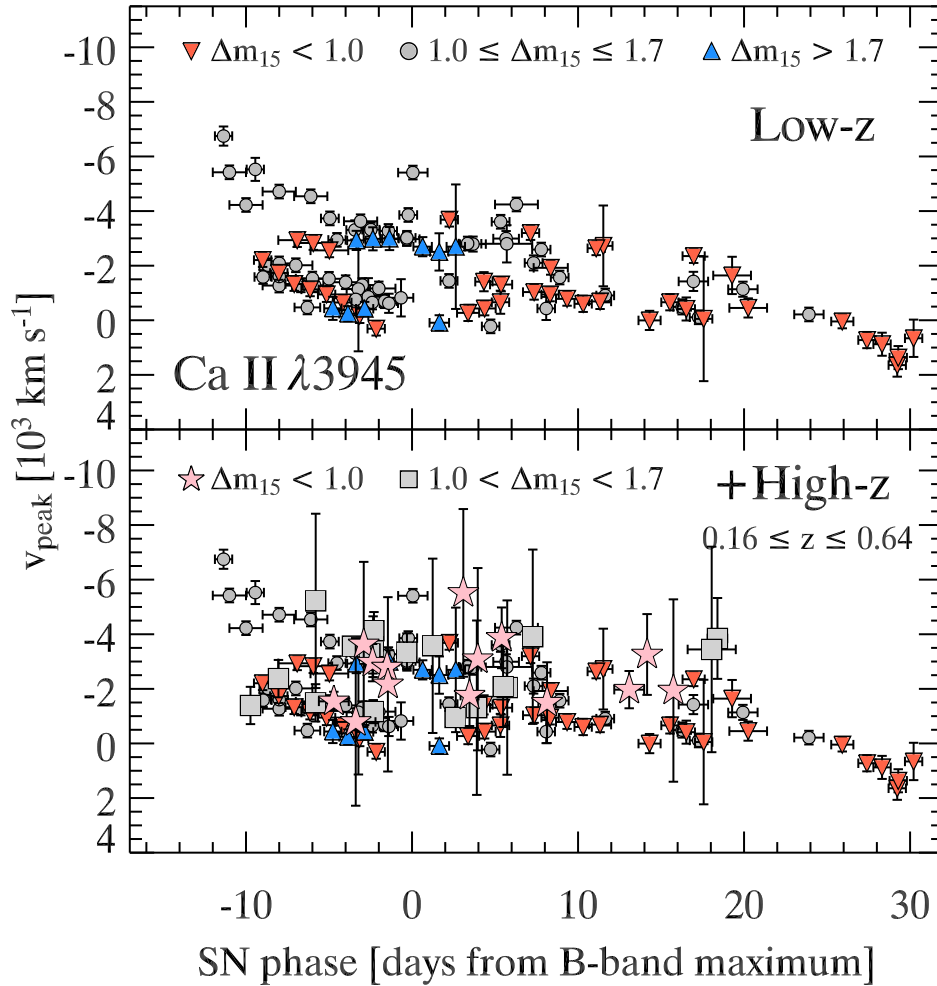


Figure 5.9: *Upper panel:* Emission-peak velocities for Ca II $\lambda 3945$ in local SN Ia, for three different $\Delta m_{15}(B)$ ranges. *Lower panel:* The high- z data are overplotted.

uncertain. Note that v_{peak} measurements for the high- z sample are consistent with the trend in the local sample, both qualitatively and quantitatively (Fig. 5.9, lower panel).

A similar pattern is also found for Si II $\lambda 6355$, both for local and high- z SN Ia (Fig. 5.10), although the measurement errors for the latter are $\sim 1000 \text{ km s}^{-1}$. Unlike for the Ca II feature, these measurements are free of sizeable line overlap (see previous section), and therefore represent a genuine intrinsic blueshift of peak emission of Si II $\lambda 6355$. Note that v_{peak} for the slow-declining (overluminous) SN Ia is slightly more negative (by $\sim 1000 \text{ km s}^{-1}$), on average, than for the fast-declining (underluminous) objects. Since the magnitude of the emission-peak blueshift scales with the expansion velocity of the ejecta (see end of the section), this dependence supports the idea that slow-declining SN Ia correspond to higher kinetic energy explosions [194, 164]. The two points with $v_{\text{peak}} < -6000 \text{ km s}^{-1}$ at $t < -10 \text{ d}$ correspond to SN 1990N, for which the v_{abs} measurements at

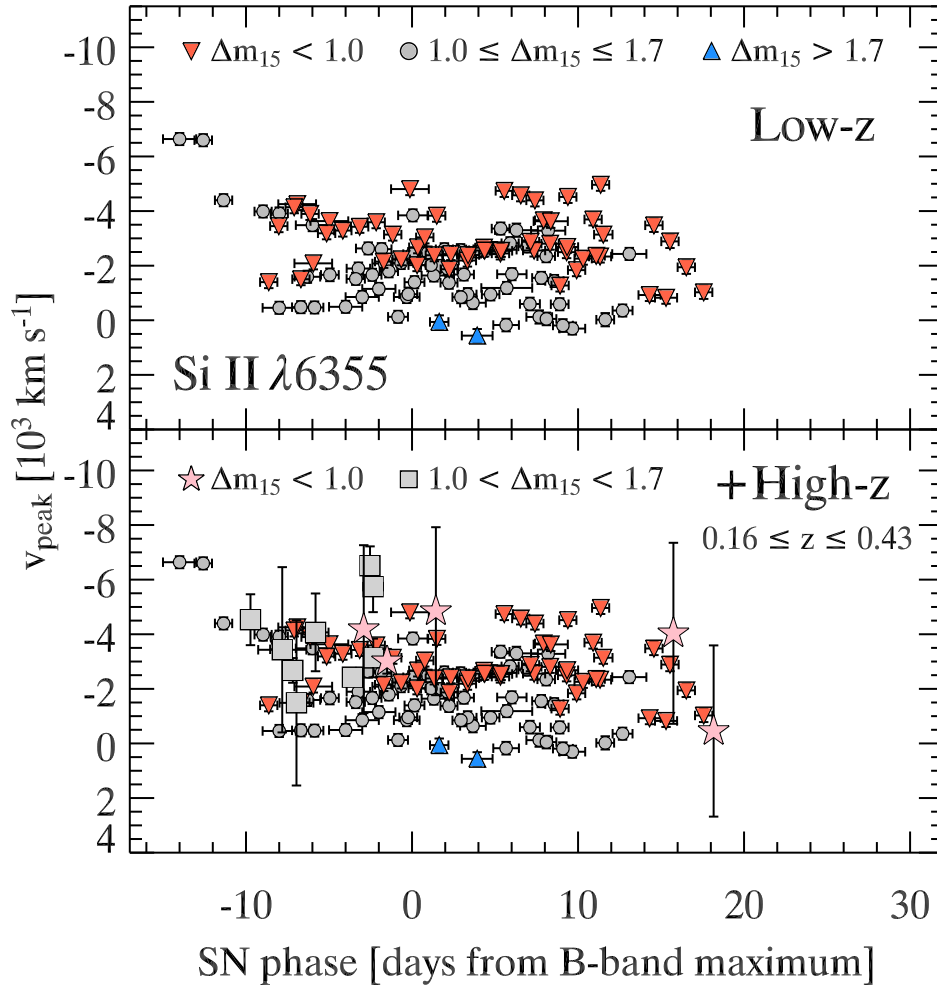


Figure 5.10: Same as Fig. 5.9 for Si II $\lambda 6355$.

these phases are also more negative (Fig. 5.6).

We finally turn in Fig. 5.11 to the v_{peak} measurements for the S II $\lambda 5454$, 5640 features. We first start with the right panels, which show that the S II $\lambda 5640$ data points, both for the local and high- z samples, follow a similar pattern of increasing values with phase as for the Ca II and Si II features, with velocity shifts always negative but now reaching down to -8500 km s^{-1} at $\sim -10 \text{ d}$. We associate the large scatter of data points to contamination by Si II $\lambda 5972$ at pre-maximum phases, and Na I D $\lambda 5892$ at post-maximum phases. Note that for the high- z sample, a $\sim 3000 \text{ km s}^{-1}$ uncertainty is introduced when the SN redshift is determined *via* cross-correlation with local SN Ia spectral templates (see Table 5.1). For S II $\lambda 5454$ (left panel), we find, on average, a steady increase of v_{peak} with phase, from -8500 km s^{-1} at -10 d to -4000 km s^{-1} at $+10 \text{ d}$, but with a clear dichotomy according to $\Delta m_{15}(B)$ parameter: fast-decliners show systematically faster-increasing and less-negative values, related to the modest expansion velocity of their outflows and the

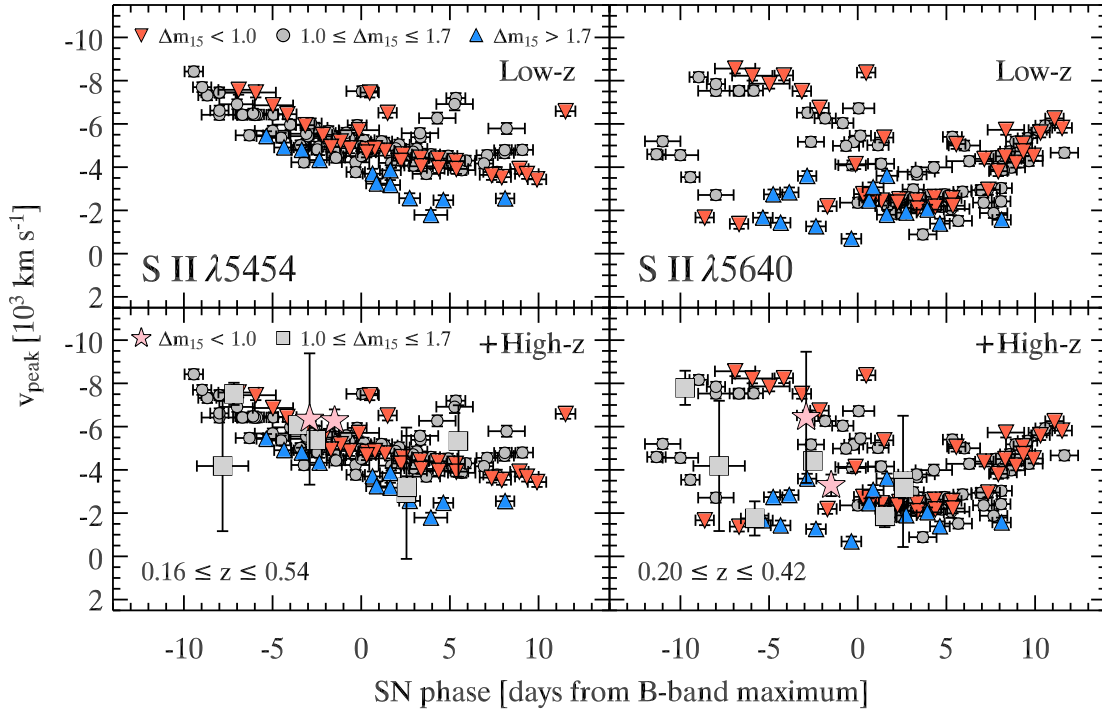


Figure 5.11: *Upper panels:* Emission-peak velocities for S II $\lambda 5454$ (*left*) and S II $\lambda 5640$ (*right*) in local SN Ia, for three different $\Delta m_{15}(B)$ ranges. *Lower panels:* The high- z data are overplotted.

larger (comoving) recession velocity of the photo-emitting layers in the SN ejecta. The low scatter of data points, due to the absence of sizeable line overlap, makes this distinction clear and suggests that, as before from v_{abs} measurements, the blueshift of peak emission at post-maximum phases can now also be used to isolate fast-declining SN Ia, provided the SN phase is accurately known.

To conclude this section on the v_{peak} measurements, we show in Fig. 5.12 the values for S II $\lambda 5454$, but this time normalized to $v_{\text{abs},5640}$ at the same phase, a quantity that closely matches, at early times, the photospheric velocity of the flow (Fig. 5.8). For both local and high- z SN Ia, this ratio covers the 0.2–0.7 range, and thus represents a significant shift of a line profile, comparable to the shift identified in the measurement of the absorption velocity. The time evolution of $v_{\text{peak}}/v_{\text{abs}}$ is also flatter than the corresponding v_{peak} sequence of Fig. 5.11 (left panels), suggesting that the magnitude of emission blueshift is a good tracer of the expansion velocity (see Sect. 5.3.2).

Physical Origin of the Emission-Peak Blueshift

To investigate the origin of the observed blueshift of peak emission, let us go back to the left panel of Fig. 5.8 and study the sites of emission in the Ca II $\lambda 3934$ line. As in the

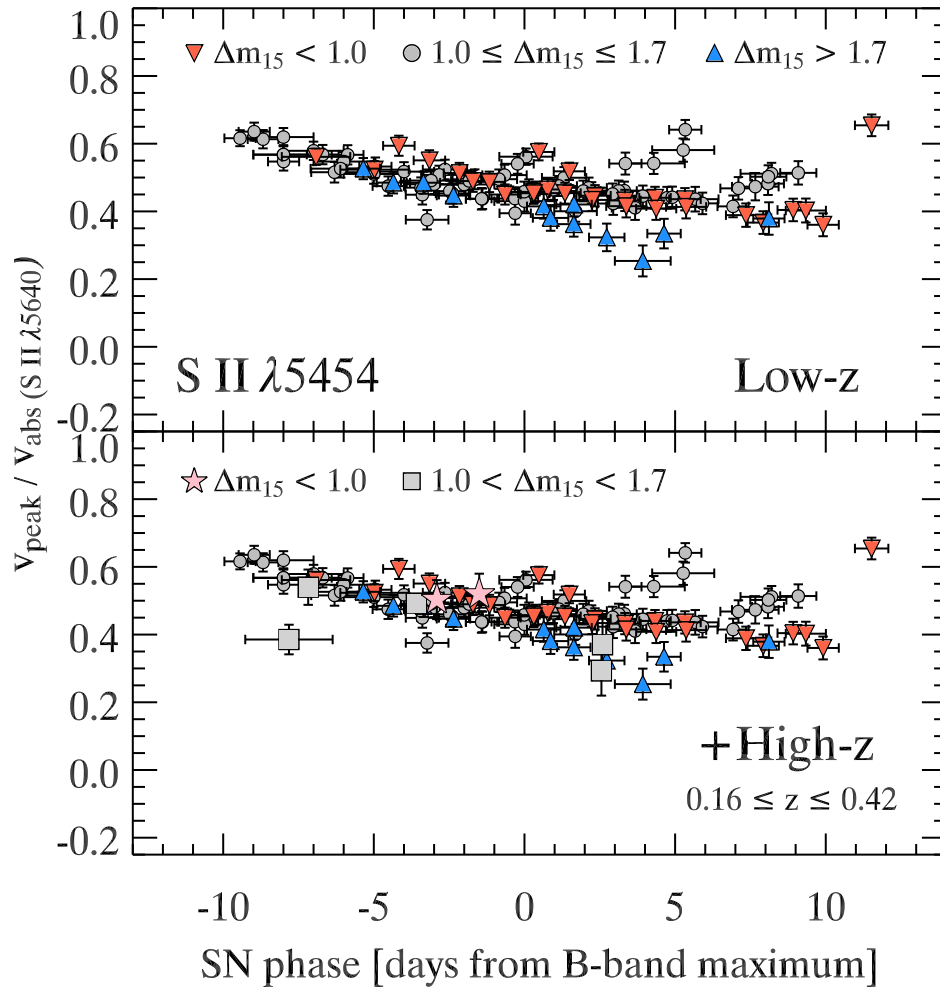


Figure 5.12: *Upper panel:* Emission-peak velocities for S II $\lambda 5454$ normalized to the S II $\lambda 5640$ absorption velocities. *Lower panel:* The high- z data are overplotted.

standard cartoon of P-Cygni profile formation, one can view a significant amount of flux arising from the side lobes, corresponding to regions with $p > p_{\text{lim}} \approx 3R_0$ – this defines the spatial extent of the photodisk. Despite the weaker emission at such distances from the “photosphere,” the total contribution is quite large because it involves a large and optically thin emitting volume. Contrary to such a heuristic P-Cygni profile formation, a significant amount of emission arises also from the region with $p < p_{\text{lim}}$; this more restricted volume is also affected by continuum optical depth effects since it resides partly within the photosphere (represented by the solid dark line). Although this latter emission source appears in the blue side of the profile, the larger contribution from the lobes leads to a symmetric emission peak.

However, moving to the optically thinner Si II $\lambda 6355$ line (middle panel), we now see that the relative (symmetric) emission contribution from the lobe is lower compared to that arising from within the limbs of the photodisk, leading to a more pronounced blueshift of peak emission. This situation becomes even more extreme in the case of S II $\lambda 5432$ (right panel), whereby no side-lobe emission is present: the resulting P-Cygni profile shows a strongly blueshifted centroid, corresponding to a sizeable fraction of the velocity at maximum absorption. For this very optically thin line, disk occultation and continuum optical depth effects are severe.

These synthetic line profiles are computed by accounting solely for the opacity of the chosen line (plus all sources of continuum opacity); thus, they lift any ambiguity brought upon by line overlap. In view of these results, the large and scattered observed (negative) v_{peak} measurements for Ca II $\lambda 3945$ are likely caused by line overlap, the most likely candidate being Si II $\lambda 3858$. However, the measured and sizeable blueshifts for the Si II and S II lines are indeed expected theoretically; CMFGEN computations also predict the larger blueshift velocity (more negative v_{peak}) for the optically thinner S II lines, compared to either Si II or Ca II diagnostics.

Interestingly, Kasen et al. [141] argued that such blueshifted emission must stem from peculiar effects, for example of a non-LTE nature, rather than from modulations of the line source function or optical depth. It now seems that their combined assumptions of a sharp photosphere, the neglect of continuum opacity, and a pure scattering source function enforce the symmetry of P-Cygni profile emission; here, CMFGEN demonstrates that such assumptions may be invalid for a number of lines, particularly at epochs where the ejecta are optically thick in the continuum.

5.3.3 Double-Absorption Features in Ca II $\lambda 3945$

Double-absorption features in Ca II are frequently observed in local SN Ia, usually in the near-infrared lines at $\lambda 8498$, $\lambda 8542$, and $\lambda 8662$ (see, e.g., [97, 192, 189]). Gerardy et al. [97] suggest the interaction of a circumstellar shell within the progenitor system, but Kasen et al. [142] proposed a departure from sphericity in the explosion, inferred from polarization measurements of SN 2001el [304]. Gerardy et al. [97] also discuss the possibility of detecting such double-absorption Ca II absorption features in the $\lambda 3945$ doublet; alternatively, such identification could be influenced by the overlap of the bluer component with Si II $\lambda 3858$

(see Fig. 5.5), predicted to dominate past ~ 1 week before maximum [119, 125, 173]. The association of the blue component in Ca II $\lambda 3945$ with high-velocity Ca II absorption is uncertain, and we therefore prefer referring to the *observed* blue/red, in place of the *interpreted* high-velocity/low-velocity components as commonly used in the literature.

Here, line-profile measurements on Ca II $\lambda 3945$ reveal possible double-absorption features for 6 (out of 22) local SN Ia, and, for the first time, for 2 (out of 34) high- z SN Ia (Table 5.4), SN 2003kn (at -7 d, $z = 0.244$) and SN 2003jt (at $+3$ d, $z = 0.45$). In Fig. 5.13, we show a time sequence of the Ca II $\lambda 3945$ region for a subset of the local and high- z SN Ia samples, identifying the blue and red absorption components, and showing the good correspondence between profile shapes.

In Fig. 5.14 (upper panel), we show the evolution of v_{abs} for single- and double-absorption features in Ca II $\lambda 3945$, selecting objects with $1.0 \leq \Delta m_{15}(B) \leq 1.7$: the value of the blue (red) component v_{blue} (v_{red}) is systematically more (less) negative than single-absorption v_{abs} values at the same phase, perhaps caused by overlap with Si II $\lambda 3858$. The blue and red data points for the high- z object (SN 2003kn) are consistent with the local SN Ia sample, although significantly shifted to more negative velocities and closer together (~ 7000 rather than $\sim 10,000$ km s $^{-1}$); more observations are needed to draw any conclusion. In the lower panel of Fig. 5.14, we show data points for objects with $\Delta m_{15}(B) < 1.0$. Only one (SN 1999aa) out of 10 local slow-declining SN Ia shows such a double-absorption Ca II feature; one high- z fast-declining SN Ia (SN 2003jt) out of 17 (Fig. 5.13) also clearly displays this feature.

Contrary to the $1.0 \leq \Delta m_{15}(B) \leq 1.7$ objects, the blue component of Ca II $\lambda 3945$ double absorptions in SN 1999aa does not correspond to a more negative v_{abs} than for the single absorptions. The red component, however, lies at significantly less negative v_{abs} ($\sim 10,000$ km s $^{-1}$ greater than v_{abs} for the single-absorption features at similar phases). The ~ -5000 km s $^{-1}$ vertical offset for SN 2003jt (Fig. 5.13) is clearly seen, although we are lacking local SN Ia with Ca II $\lambda 3945$ double-absorption features at these phases. Slow decliners are often associated with more luminous events (though not necessarily; see Table 5.3), which result from more energetic explosions [194, 164]. It would be worthwhile to study this spectral range in a large sample of local slow-declining SN Ia, to link the presence/absence of this feature with the kinematics of the explosion. We note the absence of Ca II $\lambda 3945$ double absorption in our sample of fast-declining SN Ia (4 SN Ia with $\Delta m_{15}(B) > 1.7$).

Finally, selecting the five local SN Ia of our sample (SN 1994D, 1996X, 1998aq, and 1998bu) having the best temporal coverage, we show in Fig. 5.15 the evolution of the ratio $v_{\text{blue}}/v_{\text{red}}$. The non-unity as well as the linear decline (except for SN 1994D) of $v_{\text{blue}}/v_{\text{red}}$ over ~ 2 weeks seems difficult to reconcile with the presence of an inhomogeneity, expected to leave a more transient imprint.

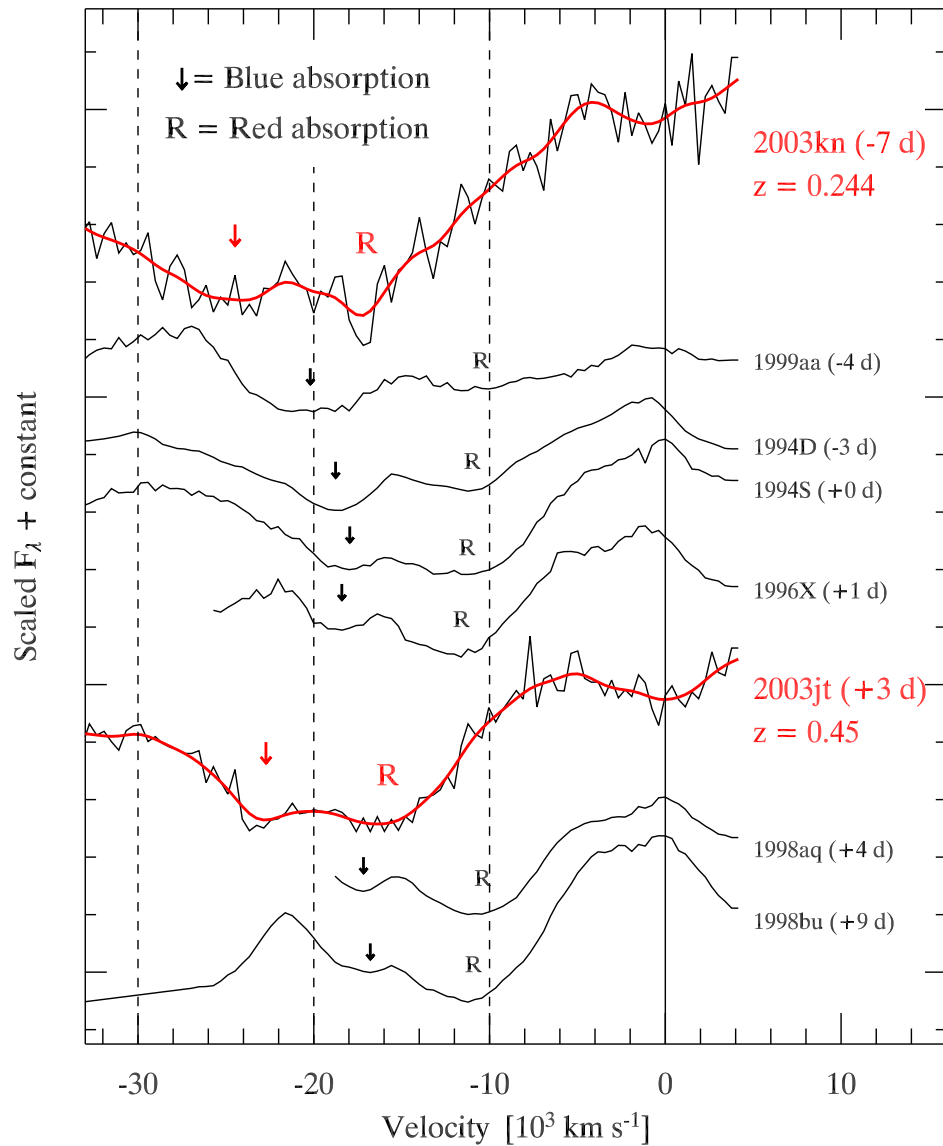


Figure 5.13: Double-absorption features in Ca II $\lambda 3945$. Two of our high- z SN Ia also show a double-absorption feature. The thick line overplotted on these spectra corresponds to their smoothed version (see Sect. 5.2.1). Note the apparent $\sim -5000 \text{ km s}^{-1}$ offset of the SN 2003jt spectrum with respect to local SN Ia at similar phases, probably due to an error in the SN redshift (determined *via* cross-correlations with local SN Ia spectra; see [187])

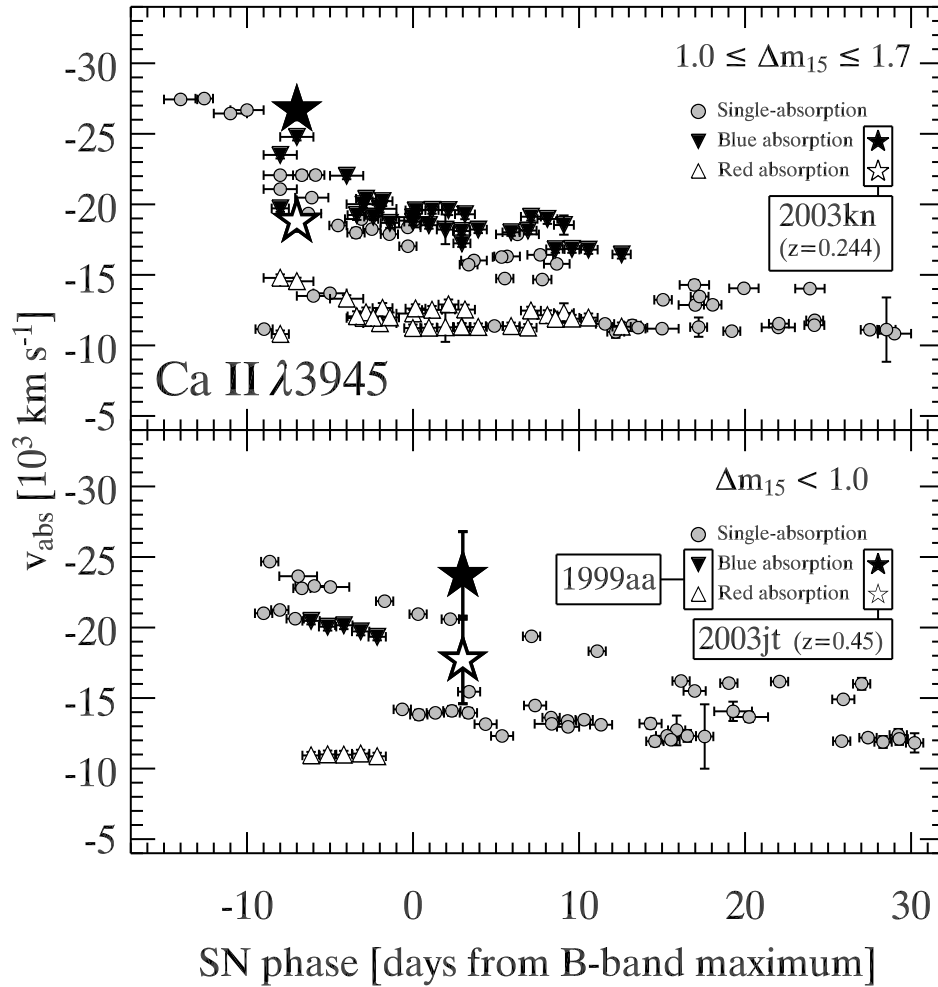


Figure 5.14: Absorption velocities for $\text{Ca II } \lambda 3945$ in single- and double-absorption features (blue and red components), for objects with $1.0 \leq \Delta m_{15}(B) \leq 1.7$ (upper panel) and $\Delta m_{15}(B) < 1.0$ (lower panel). Also shown are v_{blue} and v_{red} absorption velocities for SN 2003kn ($z = 0.244$) and SN 2003jt ($z = 0.45$).

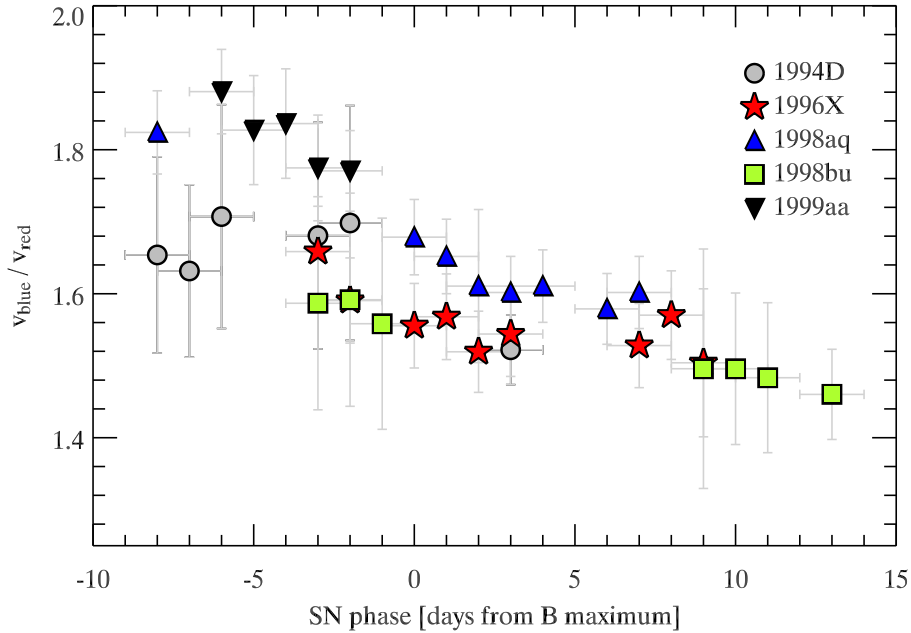


Figure 5.15: Time evolution of the ratio of v_{abs} for the blue and red components of the Ca II $\lambda 3945$ absorption feature, in five local SN Ia.

5.4 Conclusions

No major systematic differences in the spectral evolution of absorption and emission-peak velocities of several prominent lines can be seen between local and high- z SN Ia spectra.

We present a robust measurement technique (Sect. 5.2.1), which is applied to both local and high- z SN Ia spectra. We also elaborate a reliable, if limited, error model (errors due to blending of spectral features cannot be reliably included). We use a spectral-smoothing algorithm which takes into account the Doppler broadening of SN Ia spectral features due to the large velocities in the ejecta, as well as the wavelength-dependent noise affecting ground-based spectra. Our line-profile fitting reduces the impact of line overlap, since it relies on a smaller wavelength interval, and allows for asymmetric line profiles. The source code is available *via* the ESSENCE web page³, both as an IDL function and a Fortran script. All the results of our measurements are displayed in Tables 5.6–5.9.

We find both the magnitude and time evolution of v_{abs} for SN Ia with different decline-rate parameters $\Delta m_{15}(B)$ to be consistent out to $z = 0.64$. As expected, strong lines have more negative absorption velocities, and weaker lines are better tracers of the decline-rate parameter, since they form over less extended regions. In fact, the S II $\lambda\lambda 5454, 5640$ features can be used as diagnostic tools to separate fast-declining SN Ia [$\Delta m_{15}(B) > 1.7$] from the rest, given a reliable phase. The lack of fast-declining SN Ia in our high- z

³<http://www.ctio.noao.edu/essence/>

sample prevents us from assessing the validity of such a diagnostic at high redshifts. Most probably the magnitude selection in ESSENCE prevents us from finding the intrinsically less luminous, fast-declining SN Ia at higher redshift [156].

For the first time, we present a census of peak emission velocities, found, up to 20 d past maximum B -band light, to be systematically negative. Such a blueshifted emission peak for the three studied lines is present in all SN Ia of our local and high- z samples, irrespective of their decline-rate parameter. We measure v_{peak} associated with this blueshift and find it to be a significant fraction of v_{abs} for the S II $\lambda 5454$ feature. We show that v_{peak} for the S II $\lambda 5454$ feature can also be used to distinguish SN Ia with $\Delta m_{15}(B) > 1.7$ at post-maximum phases, again given a reliable SN phase. Using CMFGEN models [118], we illustrate the line-profile formation mechanisms in SN Ia and show that this blueshifted emission stems from the steep density distribution prevalent in supernova atmospheres [66].

We report the detection of double-absorption Ca II $\lambda 3945$ features in several local SN Ia, and for the first time confirm its detection in two high- z SN Ia ($z = 0.244$ and $z = 0.45$, Fig. 5.13). The association of the blue component of this double absorption with Ca II is still under debate, and could be due to contamination by Si II $\lambda 3858$ [97].

The present investigation has not only shown the importance of such quantitative studies in assessing systematic differences between local and high- z SN Ia, but also makes a strong case for the need for higher quality SN Ia spectral data at high redshifts. From the first high- z spectrum of an SN Ia ever obtained (at $z = 0.31$; [213]), previous and ongoing high- z SN Ia surveys have gathered sufficient data for detailed quantitative comparisons to be made between the two samples. To make the assertion of no evolution in the SN Ia sample with redshift, one would need a few high-quality SN Ia spectra, preferably with a ~ 5 d sampling in rest-frame phase (i.e. a ~ 1 week sampling at $z \approx 0.5$). This could ideally be done with the *Hubble Space Telescope*, but could also be attempted with ground-based 8–10-m-class telescopes [187]. Since the redshift uncertainty is the dominant source of error for our high- z measurements (when the redshift is determined from the SN itself), it is important for future studies of absorption and emission-peak velocities in SN Ia to obtain a spectrum of the host galaxy along with that of the supernova.

The ESSENCE high- z SN Ia spectra analyzed in this paper, and initially presented by Matheson et al. [187], are now publicly available.

The ESSENCE project is supported primarily by grants AST-0206329 and AST-0443378 from the U.S. National Science Foundation. S. B. would like to thank Nando Patat and Paolo Mazzali for useful discussions on SN Ia spectral features and spectral synthesis. Darin Casebeer’s help in installing and running SYNOW is also greatly appreciated. S. B. acknowledges support from the International Max-Planck Research School (IMPRS) on Astrophysics *via* a graduate fellowship. A.V.F. is grateful for the support of NSF grant AST-0307894, and for a Miller Research Professorship at UC Berkeley during which part of this work was completed.

5. Using line profiles to test the fraternity of Type Ia supernovae at high and low redshifts

168

Table 5.6: Absorption velocities in local SN Ia (10^3 km s^{-1})

Phase ^a	Ca II $\lambda 3945^b$		S II $\lambda 5454$	S II $\lambda 5640$	Si II $\lambda 6355$
	Blue absorption	Red/Single absorption			
1981B					
+0	...	-18.8 ± 0.3	-12.4 ± 0.2	-13.4 ± 0.2	-14.8 ± 0.2
+6	...†	...†	...†	-10.4 ± 0.2	-12.7 ± 0.2
+17	...	-14.3 ± 0.4	-11.5 ± 0.2
+20	...	-14.0 ± 0.3	-11.0 ± 0.2
+24	...	-14.0 ± 0.3	-10.5 ± 0.2
1986G					
-5	...†	...†	-10.1 ± 0.2	-10.3 ± 0.2	-12.8 ± 0.2
-4	...†	...†	-9.7 ± 0.2	-10.1 ± 0.2	-12.4 ± 0.2
-3	...	-17.0 ± 0.4	-9.3 ± 0.2	-9.9 ± 0.2	-12.2 ± 0.2
-2	...	-17.8 ± 0.4	-8.9 ± 0.2	-9.7 ± 0.2	-11.7 ± 0.2
-1	...	-17.3 ± 0.4	...†	...†	...†
+0	-9.1 ± 0.2	-11.4 ± 0.2
+1	...	-16.3 ± 0.4	-8.4 ± 0.2	-8.9 ± 0.2	-11.0 ± 0.2
+2	...	-16.2 ± 0.7	-7.4 ± 0.2	-8.8 ± 0.2	-11.0 ± 0.2
+3	...	-15.6 ± 2.3	...†	...†	...†
+5	...†	...†	-5.9 ± 0.2	-7.4 ± 0.2	-10.3 ± 0.2
1989B					
-6	...	-19.3 ± 0.3	-10.0 ± 0.2	-10.6 ± 0.2	-12.0 ± 0.2
+0	...	-18.4 ± 0.3	-9.0 ± 0.2	-9.6 ± 0.2	-11.3 ± 0.2
+4	...	-16.0 ± 0.3	-8.1 ± 0.2	-9.0 ± 0.2	-11.2 ± 0.2
+6	...	-16.3 ± 0.3	-7.9 ± 0.2	-8.9 ± 0.2	-10.5 ± 0.2
+8	...	-16.4 ± 0.3	...	-8.0 ± 0.2	-10.7 ± 0.2
+9	...	-15.8 ± 0.3	...	-8.0 ± 0.2	-10.5 ± 0.2
+10	-7.9 ± 0.2	-10.6 ± 0.2
+12	-7.2 ± 0.2	-10.5 ± 0.2
+13	-9.6 ± 0.2
+14	-9.6 ± 0.2
+15	-9.4 ± 0.3
+18	-9.4 ± 0.2
1990N					
-14	...	-27.4 ± 0.3	$-20.4^{+1.8}_{-1.0}$
-13	...	-27.5 ± 0.3	$-20.5^{+1.8}_{-1.0}$
-8	...	-22.1 ± 0.3	-10.8 ± 0.2	-11.3 ± 0.2	-11.8 ± 0.2
-7	...	-22.1 ± 0.3	-10.8 ± 0.2	-11.3 ± 0.2	-11.8 ± 0.2
-6	...	-22.1 ± 0.3	-10.8 ± 0.2	-11.3 ± 0.2	-11.9 ± 0.2
+5	-9.6 ± 0.2	-10.0 ± 0.2	-11.0 ± 0.2
+8	-9.4 ± 0.2	-9.6 ± 0.2	-10.8 ± 0.2
+15	...	-13.2 ± 0.3	-10.0 ± 0.2
+17	...	-12.9 ± 0.3	-9.8 ± 0.3
+18	...	-12.9 ± 0.3	-9.8 ± 0.3
1990O					
-7	...	-23.6 ± 0.3	-11.8 ± 0.2	-13.5 ± 0.2	-13.8 ± 0.2
-6	...	-22.9 ± 0.3	-11.8 ± 0.2	...	-13.9 ± 0.2
-5	...	-22.9 ± 0.3	-11.8 ± 0.2	-13.1 ± 0.2	-13.3 ± 0.2
+0	-12.4 ± 0.2
+19	...	-14.1 ± 0.7

+20	...	-13.7 ± 0.4	-11.7 ± 0.2
1991T					
+8	...†	...†	-7.4 ± 0.2	-9.6 ± 0.2	-10.2 ± 0.2
+9	...†	...†	-7.2 ± 0.2	-9.7 ± 0.2	-10.2 ± 0.2
+10	...†	...†	-7.0 ± 0.2	-9.5 ± 0.2	-10.1 ± 0.2
+11	...†	...†	-10.2 ± 0.2
+14	...†	...†	-9.0 ± 0.2
+15	...†	...†	-9.0 ± 0.2
+16	...	$-12.7^{+1.1}_{-1.0}$	-9.6 ± 0.2
+17	...†	...†	-8.3 ± 0.2
+26	...	-11.9 ± 0.3
1991bg					
+1	...†	...†	-6.9 ± 0.2	-8.5 ± 0.2	-10.7 ± 0.2
+2	...	-15.2 ± 0.3	-7.6 ± 0.2	-9.2 ± 0.2	-11.5 ± 0.2
+3	-6.6 ± 0.2	-7.9 ± 0.2	-10.3 ± 0.2
+15	-7.9 ± 0.2
+16	...†	...†	...†	...	-8.1 ± 0.2
+19	...	-11.9 ± 0.4	-7.6 ± 0.2
+26	...	-11.1 ± 0.4	-7.2 ± 0.2
1992A					
-5	-10.0 ± 0.2	-12.1 ± 0.2	-13.6 ± 0.2
+0	-8.9 ± 0.2	-11.0 ± 0.2	-13.1 ± 0.2
+3	...	-15.7 ± 0.3	-9.1 ± 0.2	-10.0 ± 0.2	-12.6 ± 0.2
+5	...	-16.3 ± 0.3	-10.6 ± 0.2	-11.2 ± 0.2	-14.1 ± 0.2
+7	-8.4 ± 0.2	-9.2 ± 0.2	-12.4 ± 0.2
+9	-8.6 ± 0.2	-12.0 ± 0.2
+12	-12.0 ± 0.2
+16	-10.8 ± 0.2
+17	...	-13.5 ± 0.3	-11.3 ± 0.2
1993ac					
+6	...	-17.9 ± 0.3	...	-11.6 ± 0.2	-13.7 ± 0.2
1994D ^c					
-11	...	-26.4 ± 0.3	...	-12.3 ± 0.2	-16.2 ± 0.2
-10	...	-26.7 ± 0.3	...	-12.0 ± 0.2	-15.1 ± 0.2
-9	...†	...†	-9.5 ± 0.2	-11.9 ± 0.2	-12.7 ± 0.2
-8	-23.5 ± 0.3	-14.8 ± 0.3	-9.6 ± 0.2	-12.0 ± 0.2	-12.8 ± 0.2
-7	-24.8 ± 0.3	-14.5 ± 0.3	-9.7 ± 0.2	-11.9 ± 0.2	-12.3 ± 0.2
-6	...	-13.5 ± 0.3	-9.7 ± 0.2	-11.7 ± 0.2	-11.8 ± 0.2
-5	...	-13.7 ± 0.3	-9.1 ± 0.2	-11.1 ± 0.2	-11.4 ± 0.2
-4	-22.0 ± 0.3	-13.3 ± 0.3	-9.7 ± 0.2	-11.5 ± 0.2	-11.7 ± 0.2
-3	-20.0 ± 0.3	$-11.9^{+1.1}_{-1.0}$	-9.4 ± 0.2	-11.3 ± 0.2	-11.5 ± 0.2
-2	-19.7 ± 0.3	$-11.6^{+1.1}_{-1.0}$	-9.4 ± 0.2	-11.2 ± 0.2	-11.4 ± 0.2
+2	-8.6 ± 0.2	-10.2 ± 0.2	-11.1 ± 0.2
+3	-17.2 ± 0.3	-11.3 ± 0.3	-8.2 ± 0.2	-9.6 ± 0.2	-10.9 ± 0.2
+10	...†	...†	...	-8.3 ± 0.2	-10.4 ± 0.2
+11	-10.2 ± 0.2
+12	...	-11.0 ± 0.4	-10.0 ± 0.2
+13	...	-11.4 ± 0.4	-10.4 ± 0.2
+15	...	-11.2 ± 0.3	-9.9 ± 0.2
+17	...	-11.3 ± 0.7	-9.7 ± 0.2
+19	...	-11.0 ± 0.3	-9.6 ± 0.2

5. Using line profiles to test the fraternity of Type Ia supernovae at high and low redshifts

170

+22	...	-11.3 ± 0.3	-9.7 ± 0.2
+24	...	-11.8 ± 0.3	-9.5 ± 0.2
+29	...	-10.8 ± 0.3	-9.8 ± 0.2
1994M					
+3	... [†]	... [†]	-11.0 ± 0.2	-12.1 ± 0.2	-12.9 ± 0.2
+4	... [†]	... [†]	-10.3 ± 0.3	-11.6 ± 0.3	-12.6 ± 0.3
+5	-11.9 ± 0.3	-12.9 ± 0.3
+8	-9.5 ± 0.3	-11.3 ± 0.3	-12.1 ± 0.2
+13	-11.9 ± 0.2
1994S					
-3	... [†]	... [†]	-9.4 ± 0.2	-11.3 ± 0.2	-11.5 ± 0.2
+0	-19.1 ± 0.3	-12.3 ± 0.3	-9.3 ± 0.2	-10.5 ± 0.2	-11.0 ± 0.2
+2	... [†]	... [†]	-9.0 ± 0.2	-10.5 ± 0.2	-11.2 ± 0.2
1994T					
+0	-13.6 ± 0.5
+2	-9.4 ± 0.3	-12.9 ± 0.5
+5	-13.3 ± 0.5
1994ae					
-1	...	-14.2 ± 0.3	-9.8 ± 0.2	-10.8 ± 0.2	-11.4 ± 0.2
+0	...	-13.8 ± 0.4	-9.5 ± 0.2	-10.6 ± 0.2	-11.4 ± 0.2
+1	...	-13.9 ± 0.3	-9.5 ± 0.2	-10.5 ± 0.2	-11.4 ± 0.2
+2	...	-14.1 ± 0.4	-9.2 ± 0.2	-10.3 ± 0.2	-11.4 ± 0.2
+3	...	-13.9 ± 0.4	-9.1 ± 0.2	-10.3 ± 0.2	-11.3 ± 0.2
+4	-9.1 ± 0.2	-10.0 ± 0.2	-11.4 ± 0.2
+5	-8.8 ± 0.2	-9.8 ± 0.2	-11.3 ± 0.2
+8	...	-13.6 ± 0.3	...	-9.5 ± 0.2	-11.3 ± 0.2
+9	...	-13.4 ± 0.3	...	-9.3 ± 0.2	-11.3 ± 0.2
+10	...	-13.5 ± 0.3	...	-9.0 ± 0.2	-11.2 ± 0.2
+29	...	-12.4 ± 0.4
1995D					
+3	...	-15.4 ± 0.3	-9.0 ± 0.2	-9.7 ± 0.2	-10.5 ± 0.2
+4	...	-13.2 ± 0.3	-9.0 ± 0.2	-9.7 ± 0.2	-10.6 ± 0.2
+5	...	-12.3 ± 0.3	-8.6 ± 0.2	-9.5 ± 0.2	-10.5 ± 0.2
+7	...	-14.5 ± 0.3	...	-9.4 ± 0.2	-10.5 ± 0.2
+9	...	-13.0 ± 0.3	...	-9.2 ± 0.2	-10.4 ± 0.2
+11	...	-13.1 ± 0.3	...	-8.2 ± 0.2	-10.3 ± 0.2
+14	...	-13.2 ± 0.4	-10.1 ± 0.2
+15	...	-12.3 ± 0.3	-9.8 ± 0.2
1995E					
-3	-10.1 ± 0.2	-11.1 ± 0.2	-11.5 ± 0.2
-2	-10.0 ± 0.2	-11.0 ± 0.2	-11.3 ± 0.2
-1	-9.2 ± 0.2	-10.5 ± 0.2	-11.2 ± 0.2
+1	-8.7 ± 0.2	-10.3 ± 0.2	-11.3 ± 0.2
+8	-8.6 ± 0.2	-10.9 ± 0.2
1995al					
+17	...	-15.5 ± 0.3	-12.2 ± 0.2
+26	...	-14.9 ± 0.3	-12.1 ± 0.2
1995bd					
+12	-9.0 ± 0.2	-10.1 ± 0.2	-10.0 ± 0.2
+16	-8.2 ± 0.2

+21	-7.9 ± 0.2
1996C					
+8	...	-13.2 ± 0.3	...	-9.6 ± 0.2	-11.5 ± 0.2
1996X					
-3	-20.4 ± 0.4	-12.3 ± 0.4	-10.6 ± 0.2	-11.9 ± 0.2	-11.9 ± 0.2
-2	-20.2 ± 0.4	-12.7 ± 0.4	-10.7 ± 0.2	-11.6 ± 0.2	-11.7 ± 0.2
-1	-10.5 ± 0.2	-11.3 ± 0.2	-11.6 ± 0.2
+0	-19.6 ± 0.3	-12.6 ± 0.3	-10.6 ± 0.2	-11.3 ± 0.2	-11.7 ± 0.2
+1	-19.6 ± 0.3	-12.5 ± 0.3	-10.2 ± 0.2	-10.9 ± 0.2	-11.6 ± 0.2
+2	-19.6 ± 0.4	-12.9 ± 0.4	-10.0 ± 0.2	-10.7 ± 0.2	-11.6 ± 0.2
+3	-19.3 ± 0.4	-12.5 ± 0.4	-9.9 ± 0.2	-10.5 ± 0.2	-11.5 ± 0.2
+7	-19.1 ± 0.3	-12.5 ± 0.3	...	-9.7 ± 0.2	-11.4 ± 0.2
+8	-19.0 ± 0.4	-12.1 ± 0.4	...	-9.5 ± 0.2	-11.3 ± 0.2
+9	-18.5 ± 0.7	-12.3 ± 0.7	...	-9.3 ± 0.2	-11.3 ± 0.2
+13	... [†]	... [†]	-11.2 ± 0.2
+22	...	-11.5 ± 0.3	$-9.8^{+1.0}_{-1.2}$
+24	...	-11.4 ± 0.3	-10.2 ± 0.2
1996Z					
+6	-11.2 ± 0.2	-12.4 ± 0.2
1997br					
+8	...	-14.7 ± 0.3	...	$-10.7^{+1.0}_{-1.1}$	$-11.4^{+1.0}_{-1.1}$
1997cn					
+4	-6.1 ± 0.2	-7.1 ± 0.2	-9.9 ± 0.2
1998aq					
-9	...	-11.2 ± 0.3	-10.4 ± 0.2	-12.1 ± 0.2	$-11.8^{+1.0}_{-1.1}$
-8	-19.7 ± 0.3	-10.8 ± 0.3	-10.5 ± 0.2	-12.1 ± 0.2	$-11.8^{+1.0}_{-1.1}$
+0	-18.8 ± 0.3	-11.2 ± 0.3	-9.8 ± 0.2	-10.8 ± 0.2	-11.1 ± 0.2
+1	-18.5 ± 0.3	-11.2 ± 0.3	-9.7 ± 0.2	-10.7 ± 0.2	-11.1 ± 0.2
+2	$-18.2^{+1.0}_{-1.1}$	-11.3 ± 0.3	-9.6 ± 0.2	-10.6 ± 0.2	-11.1 ± 0.2
+3	-18.1 ± 0.3	-11.3 ± 0.3	-9.5 ± 0.2	-10.4 ± 0.2	-11.1 ± 0.2
+4	-18.2 ± 0.3	-11.3 ± 0.3	-9.5 ± 0.2	-10.3 ± 0.2	-11.1 ± 0.2
+5	...	-11.4 ± 0.3	-9.4 ± 0.2	-10.2 ± 0.2	-11.1 ± 0.2
+6	-18.0 ± 0.3	-11.4 ± 0.3	-9.4 ± 0.2	-10.2 ± 0.2	-11.1 ± 0.2
+7	-18.1 ± 0.3	-11.3 ± 0.3	-9.4 ± 0.2	-10.0 ± 0.2	-11.1 ± 0.2
1998bu					
-3	-19.2 ± 0.4	-12.1 ± 1.1	-9.9 ± 0.2	-11.1 ± 0.2	-11.5 ± 0.2
-2	-19.1 ± 0.3	$-12.0^{+1.1}_{-1.0}$	-9.8 ± 0.2	-10.9 ± 0.2	-11.4 ± 0.2
-1	-18.7 ± 0.4	-12.0 ± 1.1	-9.7 ± 0.2	-10.7 ± 0.2	-11.3 ± 0.2
+9	-16.8 ± 0.3	$-11.9^{+1.1}_{-1.0}$...	-9.3 ± 0.2	-11.0 ± 0.2
+10	-16.8 ± 0.3	-11.9 ± 0.3	...	-9.2 ± 0.2	-11.0 ± 0.2
+11	-16.8 ± 0.3	-12.0 ± 0.3	...	-8.9 ± 0.2	-10.9 ± 0.2
+12	...	-11.5 ± 0.3	-10.4 ± 0.2
+13	-16.5 ± 0.3	-11.3 ± 0.3	-10.3 ± 0.2
+14	...	-11.3 ± 0.3	-10.1 ± 0.2
+28	...	-11.1 ± 0.3	-9.8 ± 1.0
+29	...	-11.1 ± 2.3	-9.8 ± 1.0
+30	-9.9 ± 1.0
1999aa					
-9	...	-21.0 ± 0.3
-8	...	-21.2 ± 0.3	-10.7 ± 0.2

5. Using line profiles to test the fraternity of Type Ia supernovae at high and low redshifts

172

-7	...	-20.6 ± 0.3	-10.4 ± 0.2
-6	-20.5 ± 0.3	-10.9 ± 0.3	-10.6 ± 0.2
-5	-20.1 ± 0.3	-11.0 ± 0.3	...	-11.0 ± 0.2	-10.5 ± 0.2
-4	-20.2 ± 0.3	-11.0 ± 0.3	...	-10.9 ± 0.2	-10.4 ± 0.2
-3	-19.7 ± 0.3	-11.1 ± 0.3	...	-10.8 ± 0.2	-10.3 ± 0.2
-2	-19.3 ± 0.3	-10.9 ± 0.3	-8.4 ± 0.2	-10.7 ± 0.2	-10.3 ± 0.2
-1	-8.6 ± 0.2	-10.6 ± 0.2	-10.4 ± 0.2
+1	-8.6 ± 0.2	-10.5 ± 0.2	-10.3 ± 0.2
+15	...	-11.9 ± 0.4	-10.4 ± 0.2
+16	...	-12.0 ± 0.3	-10.3 ± 0.2
+17	...	-12.3 ± 0.4	-10.3 ± 0.2
+18	...	-12.3 ± 2.3	-10.2 ± 0.2
+27	...	-12.2 ± 0.3
+28	...	-11.9 ± 0.4
+29	...	-12.1 ± 0.4
+30	...	-11.8 ± 0.7
1999by					
-5	...	-13.4 ± 0.4	...	-9.3 ± 0.2	-11.4 ± 0.2
-4	-9.0 ± 0.2	-11.2 ± 0.2
-3	-8.7 ± 0.2	-11.1 ± 0.2
+8	...	-11.9 ± 0.3	-6.5 ± 0.2	-6.7 ± 0.2	-10.3 ± 0.2
+11	...†	...†	-9.2 ± 0.2
+25	...	-10.5 ± 2.3	-7.9 ± 0.2
+29	...	-10.9 ± 2.3	-7.5 ± 0.2
1999ee					
-9	...	-24.7 ± 0.3	-17.8 ± 0.2
-7	...	-22.8 ± 0.3	-16.0 ± 0.2
-2	...	-21.9 ± 0.3	-9.1 ± 0.2	-10.1 ± 0.2	-10.9 ± 0.2
+0	...	-20.9 ± 0.3	-9.0 ± 0.2	-10.3 ± 0.2	-10.7 ± 0.2
+2	...	-20.6 ± 0.3	-8.9 ± 0.2	-9.9 ± 0.2	-10.8 ± 0.2
+7	...	-19.4 ± 0.3	...	-9.8 ± 0.2	-10.8 ± 0.2
+11	...	-18.3 ± 0.3	...	-9.6 ± 0.2	-10.6 ± 0.2
+16	...	-16.2 ± 0.3
+19	...	-16.1 ± 0.3
+22	...	-16.2 ± 0.3
+27	...	-16.0 ± 0.4
2000cx					
-1	...†	...†	-12.0 ± 0.2
-1	...†	...†	...	-12.4 ± 0.2	-12.1 ± 0.2
+0	...†	...†	-11.9 ± 0.2	-12.9 ± 0.2	-12.5 ± 0.2
+1	-12.6 ± 0.2	-12.4 ± 0.2
+6	-12.2 ± 0.2	-12.6 ± 0.2
+7	-12.6 ± 0.2	-12.5 ± 0.2
+7	...†	...†	...	-12.2 ± 0.2	-12.5 ± 0.2
+9	...†	...†	...	-11.6 ± 0.2	-12.4 ± 0.2
+11	...†	...†	-12.2 ± 0.2
+14	...†	...†	-11.7 ± 0.2
+19	...†	...†	-11.8 ± 0.2
+22	...†	...†	-11.9 ± 0.2
2002bo					
-11	-14.6 ± 0.2	-16.1 ± 0.2

-9	-11.7 ± 0.2	-13.7 ± 0.2	-15.0 ± 0.2
-8	...	-21.1 ± 0.3	-11.0 ± 0.2	-13.1 ± 0.2	-14.6 ± 0.2
-6	...	-20.5 ± 0.3	-10.5 ± 0.2	-12.3 ± 0.2	-13.8 ± 0.2
-5	...	-18.5 ± 0.3	-9.8 ± 0.2	-11.3 ± 0.2	-13.2 ± 0.2
-3	...	-18.0 ± 0.4	-9.4 ± 0.2	-10.7 ± 0.2	-12.9 ± 0.2
-3	...	-19.0 ± 0.3	-9.9 ± 0.2	-11.3 ± 0.2	-13.3 ± 0.2
-2	...	-18.2 ± 0.3	-9.3 ± 0.2	-10.5 ± 0.2	-12.9 ± 0.2
-1	...	-17.9 ± 0.3	-8.9 ± 0.2	-10.1 ± 0.2	-12.8 ± 0.2
+0	...	-17.0 ± 0.3	-8.5 ± 0.2	-9.6 ± 0.2	-12.5 ± 0.2
+6	...	-14.7 ± 0.3	...	-8.9 ± 0.2	$-11.4 \begin{smallmatrix} +1.0 \\ -1.1 \end{smallmatrix}$

† Insufficient wavelength coverage.

^a Rest-frame days from *B*-band maximum, rounded to closest whole day.

^b v_{abs} measurements for Ca II $\lambda 3945$ are separated into “blue” and “red” components (when a double absorption is present). Both “red” and single-absorption velocities are reported in the same column.

^c For SN 1994D there is evidence for several “blue” Ca II components (see [112], their Fig. 3). In the “blue” column we report the absorption velocity corresponding to the bluest component.

5. Using line profiles to test the fraternity of Type Ia supernovae at high and low redshifts

174

Table 5.7: Absorption velocities in ESSENCE high- z SN Ia
(10^3 km s^{-1})

IAU name	Phase ^a	Ca II $\lambda 3945^b$		S II $\lambda 5454$	S II $\lambda 5640$	Si II $\lambda 6355$
		Blue absorption	Red/Single absorption			
2002iy [‡]	+14	...	-13.0 ± 1.5
2002iz	-2	...	-23.7 ± 1.1	-12.2 ± 0.9
2002iz [‡]	+18	...	-13.8 ± 1.5
2002ja	+1	-14.6 ± 3.1
2002jb	-7	...	-17.2 ± 3.2	-11.2 ± 3.0
2002jc	-6	...	-21.1 ± 3.2
2002jc	+11	...	-11.8 ± 3.2 [†]
2002jd	-3	...	-16.9 ± 3.0	-10.8 ± 3.0	-12.6 ± 3.0	-12.0 ± 3.1
2002jd [‡]	+16	...	-15.3 ± 3.3	-10.0 ± 3.3
2002jd	+18	... [†]	... [†]	-10.1 ± 3.1
2002jq	+6	...	-16.1 ± 3.3
2002js	+7	...	-11.9 ± 3.2 [†]
2002jt	-3	...	-13.9 ± 3.1 [†]
2002jt	+0	...	-10.6 ± 3.3 [†]
2002jw [‡]	-2	...	-21.0 ± 0.4	-10.6 ± 0.7
2002jw	+19	...	-14.6 ± 2.3
2003ji	+19	... [†]	... [†]	-10.5 ± 3.0
2003jj [‡]	-2	...	-16.4 ± 0.7
2003jl [‡]	+8	...	-13.7 ± 1.5
2003jo [‡]	+3	...	-16.8 ± 1.1
2003jq	+1	-9.7 ± 3.0
2003jr	+17	... [†]	... [†]	-11.8 ± 0.9
2003js [‡]	-5	...	-20.3 ± 0.4
2003js [‡]	+13	...	-13.1 ± 0.7
2003jt [‡]	+3	-23.7 ± 3.1	-17.7 ± 3.1
2003ju	-8	... [†]	... [†]	...	-10.8 ± 3.0	-16.7 ± 3.0
2003ju	+18	-8.8 ± 3.1
2003jv	-2	-9.6 ± 0.5	-12.1 ± 0.5	-11.6 ± 0.5
2003jw [‡]	-6	...	-18.9 ± 0.7	...	-11.2 ± 0.8	-11.5 ± 1.4
2003jy [‡]	-10	...	-22.2 ± 0.7	-11.7 ± 0.8	-13.0 ± 0.8	-11.4 ± 0.9
2003kk	-4	...	-21.6 ± 0.3	-10.4 ± 0.2	-12.3 ± 0.2	-12.3 ± 0.2
2003kl	-3	...	-19.2 ± 0.4	-10.0 ± 0.3	...	-13.5 ± 0.7
2003kl	+0	...	-15.9 ± 0.7
2003km	-12	...	-20.3 ± 3.1 [†]
2003km [‡]	-11	...	-24.4 ± 3.2
2003kn [‡]	-7	-26.7 ± 0.7	-18.8 ± 0.7	-12.8 ± 0.5	-13.9 ± 0.5	-16.1 ± 0.5
2003ko [‡]	-2	...	-27.4 ± 0.7	-12.8 ± 0.7
2003kp [‡]	+1	...	-15.2 ± 3.2
2003kq [‡]	-3	...	-18.7 ± 3.1
2003kr [‡]	-8	...	-24.3 ± 0.7
2003kt [‡]	+4	...	-15.5 ± 3.2
2003le	-1	...	-18.9 ± 3.2 [†]
2003lf	+3	...	-19.8 ± 3.1	-9.9 ± 3.0	-10.0 ± 3.0	... [†]
2003lf	+2	...	-17.6 ± 3.2
2003li	+5	...	-11.5 ± 1.5	-11.1 ± 1.7 [†]
2003lj	+3	...	-15.8 ± 0.3	-8.4 ± 0.5	-8.6 ± 0.5	-11.2 ± 0.7

2003lm	+2	...	-18.0 ± 0.7	...	-8.5 ± 0.5	...
2003ln	+4	...	-13.4 ± 3.3 [†]

[†] Insufficient wavelength coverage.

[‡] VLT spectra reduced with the 2D restoration method of Blondin et al. [27].

^a Rest-frame days from *B*-band maximum, rounded to closest whole day.

^b v_{abs} measurements for Ca II $\lambda 3945$ are separated into “blue” and “red” components (when a double absorption is present). Both “red” and single-absorption velocities are reported in the same column.

5. Using line profiles to test the fraternity of Type Ia supernovae at high and low redshifts

Table 5.8: Emission-peak velocities in local SN Ia (10^3 km s^{-1})

Phase ^a	Ca II λ 3945	S II λ 5454	S II λ 5640	Si II λ 6355
1981B				
+0	-5.4 ± 0.3	-7.5 ± 0.2	-6.7 ± 0.2	-3.8 ± 0.2
+6	... [†]	... [†]	-5.0 ± 0.2	-1.7 ± 0.2
+17	-1.4 ± 0.4
+20	-1.1 ± 0.3
+24	-0.2 ± 0.3
1986G				
-5	... [†]	-5.4 ± 0.2	-1.7 ± 0.2	...
-4	... [†]	-4.9 ± 0.2	-1.4 ± 0.2	...
-3	-2.9 ± 0.4	-4.8 ± 0.2
-2	-3.0 ± 0.4	-4.3 ± 0.2	-1.3 ± 0.2	...
-1	-3.0 ± 0.4	... [†]	... [†]	... [†]
+0	-0.7 ± 0.2	...
+1	-2.7 ± 0.4	-3.7 ± 0.2	-2.5 ± 0.2	...
+2	-2.5 ± 0.7	-3.2 ± 0.2	-1.8 ± 0.2	0.1 ± 0.2
+3	-2.7 ± 2.3	... [†]	... [†]	... [†]
+5	... [†]	-2.5 ± 0.2	-1.4 ± 0.2	...
1989B				
-6	-0.5 ± 0.3	-5.5 ± 0.2	...	-1.6 ± 0.2
+0	-3.0 ± 0.3	-4.2 ± 0.2	-4.1 ± 0.2	-0.9 ± 0.2
+4	-2.8 ± 0.3	-3.7 ± 0.2	-0.9 ± 0.2	-0.6 ± 0.2
+6	-3.0 ± 0.3	-3.9 ± 0.2	-1.5 ± 0.2	0.2 ± 0.2
+8	...	-3.8 ± 0.2	-1.9 ± 0.2	-0.1 ± 0.2
+9	-4.0 ± 0.2	...
+10	-4.3 ± 0.2	0.3 ± 0.2
+12	-4.7 ± 0.2	...
1990N				
-14	-6.6 ± 0.2
-13	-6.6 ± 0.2
-8	-1.3 ± 0.3	-6.4 ± 0.2	-7.5 ± 0.2	-0.5 ± 0.2
-7	-1.3 ± 0.3	-6.4 ± 0.2	-7.5 ± 0.2	-0.5 ± 0.2
-6	-1.3 ± 0.3	-6.4 ± 0.2	-7.5 ± 0.2	-0.5 ± 0.2
+5	0.2 ± 0.3	-4.4 ± 0.2	-2.2 ± 0.2	-0.9 ± 0.2
+8	-0.4 ± 0.4	-4.6 ± 0.2	-2.4 ± 0.2	-2.3 ± 0.2
1990O				
-7	-2.9 ± 0.3	-7.6 ± 0.2	-8.6 ± 0.2	-4.3 ± 0.2
-6	-2.8 ± 0.3	-7.5 ± 0.2	-8.2 ± 0.2	-2.1 ± 0.2
-5	-2.6 ± 0.3	-6.9 ± 0.2	-7.9 ± 0.2	-3.6 ± 0.2
+0	...	-5.7 ± 0.2	-4.1 ± 0.2	-4.8 ± 0.2
+19	-1.6 ± 0.7
+20	-0.5 ± 0.4
1991T				
+8	... [†]	-3.5 ± 0.2	-3.8 ± 0.2	-3.7 ± 0.2
+9	... [†]	-3.9 ± 0.2	-4.2 ± 0.2	-1.3 ± 0.2
+10	... [†]	-3.4 ± 0.2	-4.5 ± 0.2	-1.8 ± 0.2
+11	... [†]	-3.7 ± 0.2
1991bg				
+1	... [†]	-3.2 ± 0.2	-3.1 ± 0.2	...

+2	0.1 ± 0.3	-3.9 ± 0.2	-3.6 ± 0.2	...
+3	...	-2.6 ± 0.2	-1.9 ± 0.2	...
1992A				
-5	-3.7 ± 0.3	-6.4 ± 0.2	...	-1.7 ± 0.2
+0	-3.9 ± 0.3	-5.9 ± 0.2	-5.2 ± 0.2	-1.0 ± 0.2
+3	-2.8 ± 0.3	-5.4 ± 0.2	-3.7 ± 0.2	-0.9 ± 0.2
+5	-3.6 ± 0.3	-7.2 ± 0.2	-5.4 ± 0.2	-3.4 ± 0.2
+7	-2.1 ± 0.3	...	-2.9 ± 0.2	...
+9	-1.6 ± 0.3	...	-5.2 ± 0.2	-0.6 ± 0.2
+12	-0.9 ± 0.3	-0.0 ± 0.2
+16	-0.5 ± 0.3
+17	-0.1 ± 0.3
1993ac				
+6	-4.2 ± 0.3	...	-4.3 ± 0.2	-3.3 ± 0.2
1994D				
-11	-5.4 ± 0.3	...	-5.2 ± 0.2	...
-10	-4.2 ± 0.3	...	-4.6 ± 0.2	...
-9	-2.0 ± 0.3	-7.3 ± 0.2
-8	-2.1 ± 0.3	-7.5 ± 0.2
-7	-2.0 ± 0.3	-6.9 ± 0.2
-6	-1.5 ± 0.3	-6.4 ± 0.2	...	-3.5 ± 0.2
-5	-1.5 ± 0.3	-5.7 ± 0.2
-4	-1.4 ± 0.3	-6.0 ± 0.2	...	-0.5 ± 0.2
-3	-1.3 ± 0.3	-5.4 ± 0.2	...	-0.9 ± 0.2
-2	-1.2 ± 0.3	-5.3 ± 0.2	...	-1.1 ± 0.2
+2	-1.4 ± 0.3	-4.6 ± 0.2	-2.4 ± 0.2	-1.4 ± 0.2
+3	...	-4.1 ± 0.2	-2.2 ± 0.2	-0.8 ± 0.2
+10	... [†]	...	-5.7 ± 0.2	...
1994M				
+3	... [†]	-5.6 ± 0.2	-3.8 ± 0.2	-2.4 ± 0.2
+4	... [†]	-6.3 ± 0.3	-4.0 ± 0.3	-2.6 ± 0.3
+5	...	-6.9 ± 0.3	-2.1 ± 0.3	-2.6 ± 0.3
+8	...	-5.8 ± 0.3	-4.4 ± 0.3	-3.3 ± 0.2
+13	-2.4 ± 0.2
1994S				
-3	-1.1 ± 2.3	-4.2 ± 0.2	...	-1.9 ± 0.2
+0	...	-4.5 ± 0.2	-2.4 ± 0.2	-2.3 ± 0.2
+2	... [†]	-4.2 ± 0.2	-2.2 ± 0.2	-2.0 ± 0.2
1994ae				
-1	...	-4.9 ± 0.2	...	-2.2 ± 0.2
+0	...	-4.8 ± 0.2	...	-2.7 ± 0.2
+1	...	-4.8 ± 0.2	-2.5 ± 0.2	-2.4 ± 0.2
+2	...	-4.6 ± 0.2	-2.5 ± 0.2	-2.4 ± 0.2
+3	...	-4.4 ± 0.2	-2.5 ± 0.2	-2.2 ± 0.2
+4	-1.4 ± 0.4	-4.4 ± 0.2	-2.6 ± 0.2	-2.7 ± 0.2
+5	-0.7 ± 0.4	-4.3 ± 0.2	-2.6 ± 0.2	-2.4 ± 0.2
+8	-0.9 ± 0.3	...	-4.5 ± 0.2	-2.8 ± 0.2
+9	-5.1 ± 0.2	-2.5 ± 0.2
+10	-0.6 ± 0.3	...	-5.6 ± 0.2	-2.3 ± 0.2
+29	1.6 ± 0.4

5. Using line profiles to test the fraternity of Type Ia supernovae at high and low redshifts

178

1995D				
+3	-0.3 ± 0.3	-4.0 ± 0.2	-2.1 ± 0.2	-2.4 ± 0.2
+4	-0.4 ± 0.3	-4.0 ± 0.2	-2.2 ± 0.2	-2.6 ± 0.2
+5	-1.3 ± 0.3	-3.9 ± 0.2	-2.2 ± 0.2	-2.5 ± 0.2
+7	-1.0 ± 0.3	-3.6 ± 0.2	-3.0 ± 0.2	-2.6 ± 0.2
+9	-0.8 ± 0.3	-3.7 ± 0.2	-4.7 ± 0.2	-2.7 ± 0.2
+11	-0.7 ± 0.3	-2.3 ± 0.2
+14	0.0 ± 0.4	-0.9 ± 0.2
+15	-0.8 ± 0.2
1995E				
-3	-0.9 ± 0.7	-5.8 ± 0.2	-5.2 ± 0.2	-2.6 ± 0.2
-2	-0.7 ± 0.3	-5.4 ± 0.2	...	-2.1 ± 0.2
-1	-0.8 ± 0.7	-5.3 ± 0.2	-5.0 ± 0.2	-2.1 ± 0.2
+1	...	-5.1 ± 0.2	-4.2 ± 0.2	-1.6 ± 0.2
+8	-3.9 ± 0.2	...
1995al				
+17	-2.4 ± 0.3
+26	0.0 ± 0.3
1995bd				
+12	-2.7 ± 1.5	-6.6 ± 0.2	-5.8 ± 0.2	-3.1 ± 0.2
1996C				
+8	-1.9 ± 0.3	...	-5.7 ± 0.2	-3.6 ± 0.2
1996X				
-3	...	-6.0 ± 0.2	-6.5 ± 0.2	...
-2	...	-5.7 ± 0.2	-6.3 ± 0.2	-2.6 ± 0.2
-1	...	-5.6 ± 0.2	-6.0 ± 0.2	-0.1 ± 0.2
+0	...	-5.3 ± 0.2	-5.5 ± 0.2	-1.4 ± 0.2
+1	...	-5.2 ± 0.2	-5.0 ± 0.2	-2.0 ± 0.2
+2	...	-5.0 ± 0.2	-1.8 ± 0.2	-1.9 ± 0.2
+3	...	-4.9 ± 0.2	-3.0 ± 0.2	-1.7 ± 0.2
+7	...	-4.6 ± 0.2	-2.4 ± 0.2	-0.6 ± 0.2
+8	...	-4.8 ± 0.2	-3.0 ± 0.2	-0.1 ± 0.2
+9	...	-4.8 ± 0.2	-4.7 ± 0.2	0.2 ± 0.2
+13	... [†]	-0.4 ± 0.2
1996Z				
+6	-2.8 ± 0.7	-1.2 ± 0.2
1997br				
+8	-2.6 ± 0.3	...	-4.5 ± 0.2	-1.6 ± 0.2
1997cn				
+4	...	-1.8 ± 0.2	-2.0 ± 0.2	0.6 ± 0.2
1998aq				
-9	-1.6 ± 0.3	-7.7 ± 0.2	-8.2 ± 0.2	-4.0 ± 0.2
-8	-1.6 ± 0.3	-6.6 ± 0.2	-7.8 ± 0.2	-3.9 ± 0.2
+0	...	-5.0 ± 0.2	...	-2.4 ± 0.2
+1	...	-5.0 ± 0.2	...	-2.5 ± 0.2
+2	...	-4.9 ± 0.2	-2.5 ± 0.2	-2.6 ± 0.2
+3	...	-4.7 ± 0.2	-2.6 ± 0.2	-2.6 ± 0.2
+4	...	-4.6 ± 0.2	-2.7 ± 0.2	-2.5 ± 0.2
+5	...	-4.5 ± 0.2	-2.7 ± 0.2	-2.6 ± 0.2
+6	...	-4.3 ± 0.2	-2.9 ± 0.2	-2.8 ± 0.2

+7	...	-4.2 ± 0.2	-2.9 ± 0.2	-2.7 ± 0.2
1998bu				
-3	-0.8 ± 0.4	-5.0 ± 0.2	...	-1.5 ± 0.2
-2	-0.7 ± 0.3	-4.9 ± 0.2	...	-1.7 ± 0.2
-1	-0.6 ± 0.4	-4.7 ± 0.2	...	-1.8 ± 0.2
+9	-4.7 ± 0.2	-1.4 ± 0.2
+10	-5.3 ± 0.2	...
+11	-5.9 ± 0.2	...
1999aa				
-9	-2.2 ± 0.3
-8	-1.7 ± 0.3	-3.4 ± 0.2
-7	-1.3 ± 0.3	-4.1 ± 0.2
-6	-1.1 ± 0.3	-3.9 ± 0.2
-5	-0.9 ± 0.3	-3.2 ± 0.2
-4	-0.7 ± 0.3	-6.4 ± 0.2	-8.2 ± 0.2	-3.3 ± 0.2
-3	-0.2 ± 0.3	-5.9 ± 0.2	-7.5 ± 0.2	-3.4 ± 0.2
-2	0.3 ± 0.3	-5.5 ± 0.2	-6.7 ± 0.2	-3.6 ± 0.2
-1	...	-5.2 ± 0.2	...	-3.1 ± 0.2
+1	...	-4.9 ± 0.2	-2.6 ± 0.2	-3.0 ± 0.2
+15	-3.5 ± 0.2
+16	-0.7 ± 0.3	-2.9 ± 0.2
+17	-0.4 ± 0.4	-1.9 ± 0.2
+18	-0.1 ± 2.3	-1.0 ± 0.2
+27	0.7 ± 0.3
+28	0.9 ± 0.4
+29	1.4 ± 0.4
+30	0.7 ± 0.7
1999by				
-5	-0.4 ± 0.4	...	-2.7 ± 0.2	...
-4	-0.2 ± 0.3	...	-2.8 ± 0.2	...
-3	-0.4 ± 0.3	...	-3.6 ± 0.2	...
+8	...	-2.6 ± 0.2	-1.6 ± 0.2	...
1999ee				
-9	-1.7 ± 0.2	-1.4 ± 0.2
-7	-1.4 ± 0.2	-1.5 ± 0.2
-2	...	-4.9 ± 0.2	-2.2 ± 0.2	-2.2 ± 0.2
+0	...	-4.7 ± 0.2	-2.8 ± 0.2	-2.0 ± 0.2
+2	-3.7 ± 0.3	-4.3 ± 0.2	-2.4 ± 0.2	-1.9 ± 0.2
+7	-3.2 ± 0.3	...	-4.4 ± 0.2	-2.9 ± 0.2
+11	-2.6 ± 0.3	...	-6.3 ± 0.2	-2.4 ± 0.2
2000cx				
+0	... [†]	-7.5 ± 0.2	-8.4 ± 0.2	...
+1	...	-6.5 ± 0.2	-5.4 ± 0.2	-3.8 ± 0.2
+6	-5.1 ± 0.2	-4.7 ± 0.2
+7	... [†]	-4.6 ± 0.2
+7	... [†]	-4.4 ± 0.2
+9	... [†]	-4.5 ± 0.2
+11	... [†]	-5.0 ± 0.2
2002bo				
-11	-6.7 ± 0.4	...	-4.6 ± 0.2	-4.4 ± 0.2
-9	-5.5 ± 0.4	-8.4 ± 0.2	-3.5 ± 0.2	...

5. Using line profiles to test the fraternity of Type Ia supernovae at high and low redshifts

-8	-4.7 ± 0.3	-7.5 ± 0.2	-2.7 ± 0.2	...
-6	-4.5 ± 0.3	-6.5 ± 0.2
-5	-2.9 ± 0.3	-5.4 ± 0.2
-3	-3.3 ± 0.4	-5.0 ± 0.2
-3	-3.6 ± 0.3	-5.5 ± 0.2
-2	-3.3 ± 0.3	-4.8 ± 0.2
-1	-3.3 ± 0.3	-4.4 ± 0.2
+0	-3.0 ± 0.3	-3.8 ± 0.2

† Insufficient wavelength coverage.

^a Rest-frame days from *B*-band maximum, rounded to closest whole day.

Table 5.9: Emission-peak velocities in ESSENCE high- z SN Ia
(10^3 km s^{-1})

IAU name	Phase ^a	Ca II λ 3945	S II λ 5454	S II λ 5640	Si II λ 6355
2002iy [‡]	+14	-3.3 ± 1.5
2002iz	-2	-3.5 ± 1.1	-5.7 ± 0.9
2002iz [‡]	+18	-3.8 ± 1.5
2002ja	+1	-4.8 ± 3.1
2002jb	-7	-1.5 ± 3.0
2002jc	-6	-5.2 ± 3.2
2002jd	-3	-3.6 ± 3.0	-6.4 ± 3.0	-6.4 ± 3.0	-4.2 ± 3.1
2002jd [‡]	+16	-1.9 ± 3.3	-4.0 ± 3.3
2002jd	+18	... [†]	-0.5 ± 3.1
2002js	+7	-3.9 ± 3.2
2002jt	-3	-0.8 ± 3.1
2002jw [‡]	-2	-1.2 ± 0.4	-3.1 ± 0.7
2003jj [‡]	-2	-3.0 ± 0.7
2003jl [‡]	+8	-1.5 ± 1.5
2003jm	+5	-3.9 ± 1.1
2003jo [‡]	+3	-1.8 ± 1.1
2003js [‡]	-5	-1.5 ± 0.4
2003js [‡]	+13	-2.0 ± 0.7
2003jt [‡]	+3	-5.5 ± 3.1
2003ju	-8	... [†]	-4.2 ± 3.0	-4.2 ± 3.0	-3.4 ± 3.0
2003ju	+18	-3.4 ± 3.8
2003jv	-2	-2.8 ± 0.3	-6.3 ± 0.5	-3.3 ± 0.5	-3.0 ± 0.5
2003jw [‡]	-6	-1.5 ± 0.7	...	-1.8 ± 0.8	-4.1 ± 1.4
2003jy [‡]	-10	-1.4 ± 0.7	...	-7.8 ± 0.8	-4.5 ± 0.9
2003kk	-4	-3.6 ± 0.3	-6.1 ± 0.2	...	-2.4 ± 0.2
2003kl	-3	-3.3 ± 0.4	-5.4 ± 0.3	-4.4 ± 0.3	-6.5 ± 0.7
2003kl	+0	-3.4 ± 0.7
2003kn [‡]	-7	...	-7.5 ± 0.5	...	-2.7 ± 0.5
2003ko [‡]	-2	-4.1 ± 0.7
2003kp [‡]	+1	-3.6 ± 3.2
2003kr [‡]	-8	-2.4 ± 0.7
2003kt [‡]	+4	-1.3 ± 3.2
2003le	-1	-2.2 ± 3.2 [†]
2003lf	+3	...	-2.9 ± 3.0	-3.5 ± 3.0	... [†]
2003lh	+6	-2.0 ± 3.2
2003li	+5	-2.1 ± 1.5	-5.3 ± 1.7 [†]
2003lj	+3	-1.0 ± 0.3	-3.2 ± 0.5	-3.2 ± 0.5	...
2003lm	+2	-1.8 ± 0.5	...
2003ln	+4	-3.1 ± 3.3 [†]

[†] Insufficient wavelength coverage.

[‡] VLT spectra reduced with the 2D restoration method of Blondin et al. [27].

^a Rest-frame days from B -band maximum, rounded to closest whole day.

*Blessed is he who expects nothing,
for he shall never be disappointed.*

Jonathan Swift

Chapter 6

Time-dilation effects in high-redshift Type Ia supernova spectra

Abstract: We present a cross-correlation method to determine the phase of a Type Ia supernova (SN Ia) based on its spectrum *alone*. The comparison with the light-curve phases yields a satisfactory result, with a dispersion of ~ 3 days in the range $-15 \leq t \leq +30$ d, in days from B -band maximum. Using this method, we determine the rest-frame spectral phases for 29 high-redshift SN Ia spectra ($0.20 \leq z \leq 0.64$), and find them to be inconsistent with the null hypothesis of no time dilation at a confidence level ($> 90\%$), thereby discarding alternative explanations to the cosmological nature of redshifts, such as tired-light or variable-mass theories. However, we are off by $\sim 1.6\sigma$ from the $(1+z)$ time-dilation factor expected from cosmological expansion. Using spectra of SN 2002iy ($z = 0.587$) at three different phases, we show a higher level of consistency with the expected $(1+z)$ factor, although are still off by $\sim 0.8\sigma$. We discuss the sources of systematic error affecting our measurements, and argue that more accurate results will be obtained with future access to large databases of well-sampled SN Ia spectra.

6.1 Introduction

In an expanding universe, a clock will appear to run slow by a factor $(1+z)$, where z is the cosmological redshift of the clock (see, e.g., [308], pp. 415–418). The possibility to use supernovae as “cosmic clocks” has first been recognised several decades ago by Wilson [319]. Indeed, with their high intrinsic brightness and associated timescales of only a few months, SN Ia are ideally suited for measurements of cosmological time dilation. The first measurement of this effect was carried out by Leibundgut et al. [171] on the light curve of SN 1995K ($z = 0.479$), whose time axis had to be diluted by the $(1+z)$ factor in order to match the light-curve shape of the local events. This result was extended to a total of 42 SN Ia light curves by Goldhaber et al. [99], and confirmed at the 18σ level.

These results confirm the cosmological nature of extragalactic redshifts, and rule out

alternative explanations, such as Zwicky’s “tired light” theory¹, or theories in which the mass of elementary particles evolve with redshift (known as “variable-mass” theories; see, e.g., [206]). In the first case, no time dilation is predicted, which is ruled by the $(1+z)$ factor required to “stretch” the SN Ia light curves. In the second, the number of coincidences required to mimic the $(1+z)$ dilation factor makes this theory dubious, although Narlikar and Arp [207] argue that the increased light-curve width can be explained with such a theory.

The problem in using the light curves of SN Ia to test for the expected $(1+z)$ time dilation is that this effect is degenerate with the intrinsic width of the light curve, which varies by factors of $\sim 0.6 - 1.5$ about the “normal” width [99]. SN Ia *spectra*, on the other hand, are not subject to these uncertainties, and are thus in principle better suited for such a test.

As seen in Chap. 2, the spectra of spectroscopically “normal” SN Ia evolve very rapidly (and uniformly) around maximum light (see, e.g., [75]). This property was used by Riess et al. [245] to determine the phase of SN Ia based on their spectra *alone*. This way, they were able to confirm the $(1+z)$ dilation factor based on two spectra of SN 1996bj ($z = 0.574$) separated by 10.05 days in the observer frame, and by 3.35 ± 3.2 days in the SN Ia rest frame. These results are inconsistent with the null hypothesis of no time dilation at the 96.4% confidence level. More recently, Foley et al. [84] reached the same conclusion using three epochs of SN 1997ex ($z = 0.361$), excluding the null hypothesis with 99.0% confidence. These results also definitely rule out the variable-mass theory, as the latter would require a change in the spectral evolution of SN Ia with redshift, which is not observed (see also Chap. 5).

Note that one does not necessarily need spectra of high- z SN Ia at multiple epochs to test for time dilation. With a well-sampled light curve and a single SN Ia spectrum, one can determine the time elapsed since the date of, e.g., B -band maximum, which is not affected by the $(1+z)$ stretching. One could in principle also use the date of explosion, though this is poorly constrained using the currently available high- z light-curve data.

In this Chapter, we present a method to determine the phase of a SN Ia spectrum, using the cross-correlation algorithm presented in Chap. 4 (SNID; Blondin et al., in prep), along with an error model used to determine the associated statistical and systematic error (Sect. 6.2). In Sect. 6.3, we present the result of spectral phase measurements carried out on 29 high-redshift ($0.20 \leq z \leq 0.64$) SN Ia spectra with phases $-11 \lesssim t \lesssim +18$ d, taken from Matheson et al. [187] (Appendix A). A conclusion and discussion of possible improvements to the spectral phase determination follow in Sect. 6.4.

¹In the tired light theory, photons lose energy as they travel, causing their wavelengths to lengthen according to $d\lambda/dr = (H_0/c)\lambda$, which in turn leads to Hubble’s law.

6.2 Determining the phase of a SN Ia *via* cross-correlation

Preliminary test on local SN Ia spectra

To check the feasibility of determining the phase of a SN Ia spectrum using SNID, we run a first test on the 136 SN Ia spectra that form the spectral database of spectroscopically “normal” SN Ia (see Table 4.1, p. 103), with phases $-15 \leq t \leq +30$ d, in days from B -band maximum. The test is fairly basic: we draw a spectrum from the database and run it through SNID. To avoid auto-correlations, or correlations with spectra corresponding to the same supernova, we temporarily remove these spectra from the database prior to the cross-correlation. We then compare the phase of the best-fit database spectrum (i.e., the one corresponding to the highest “rlap” value – see Chap. 4, Sect. 4.2.2) with the actual phase of the input spectrum (determined from the light curve). We repeat this process for all 136 database spectra, and show the results in Fig. 6.1 (*upper panel*). The phase determined *via* cross-correlations using SNID (t_{SNID}) is in good agreement with the actual light-curve phase (t_{LC}), with a dispersion $\sigma_{\text{phase}} = 3.2$ d about the one-to-one correspondence (*dashed line*). This confirms that one can determine a reliable phase for a spectroscopically “normal” SN Ia from the spectrum alone, and that SNID is well suited to do this with reasonable accuracy. Including the spectroscopically “peculiar” SN Ia (SN 1986G, 1991T, 1991bg, 1997br, 1997cn, 1999by – see Table 4.1, p. 103) increases the dispersion to 5.4 d, and illustrates the difficulty to determine the phase for such events based on the spectra alone. Note the discretisation of the SNID phases apparent in the results of Fig. 6.1.

Note that the 3.2 d dispersion quoted here is almost twice that quoted in Riess et al. [245], who perform a similar test using their “spectral feature age” (SFA) algorithm, and find a 1.7 d dispersion for 100 SN Ia spectra, most of which have been included in the SNID database. Part of the reason for this discrepancy is that Riess et al. [245] only remove the input spectrum from the database before running their SFA code, rather than all the spectra corresponding to the input supernova. Thus, if for instance SN 1995D at +4 d is the input spectrum, then the spectra of SN 1995D at +3 d and +5 d are not temporarily removed from the database, heavily biasing the test results to higher accuracy. Using the same (erroneous, in our view) approach, we find the dispersion is reduced to ~ 2 d, in better agreement with the results of Riess et al. [245]. Remaining differences can be attributed to the algorithm used: SNID runs a standard cross-correlation on the whole spectrum, while the SFA algorithm performs a χ^2 analysis on eight different spectral “features” in the range 3800–6800 Å.

The phase residuals ($t_{\text{SNID}} - t_{\text{LC}}$) plotted in the lower panel of Fig. 6.1 reveal a bias to higher phases for $t_{\text{LC}} \lesssim +0$ d. This is a direct impact of the phase distribution of the SN Ia templates used by SNID (see Fig. 4.1, p. 104), with the relative overabundance of templates around maximum causes an “attractor” solution at these phases. Similarly, we expect a bias to lower phases for $t_{\text{LC}} \gtrsim +10$ d, which is not observed. The slower fall-off of the SN Ia distribution at $t_{\text{LC}} \gtrsim +10$ d with respect to $t_{\text{LC}} \lesssim +0$ d in part explains this difference, although the variation of the relative strengths of spectral features with SN

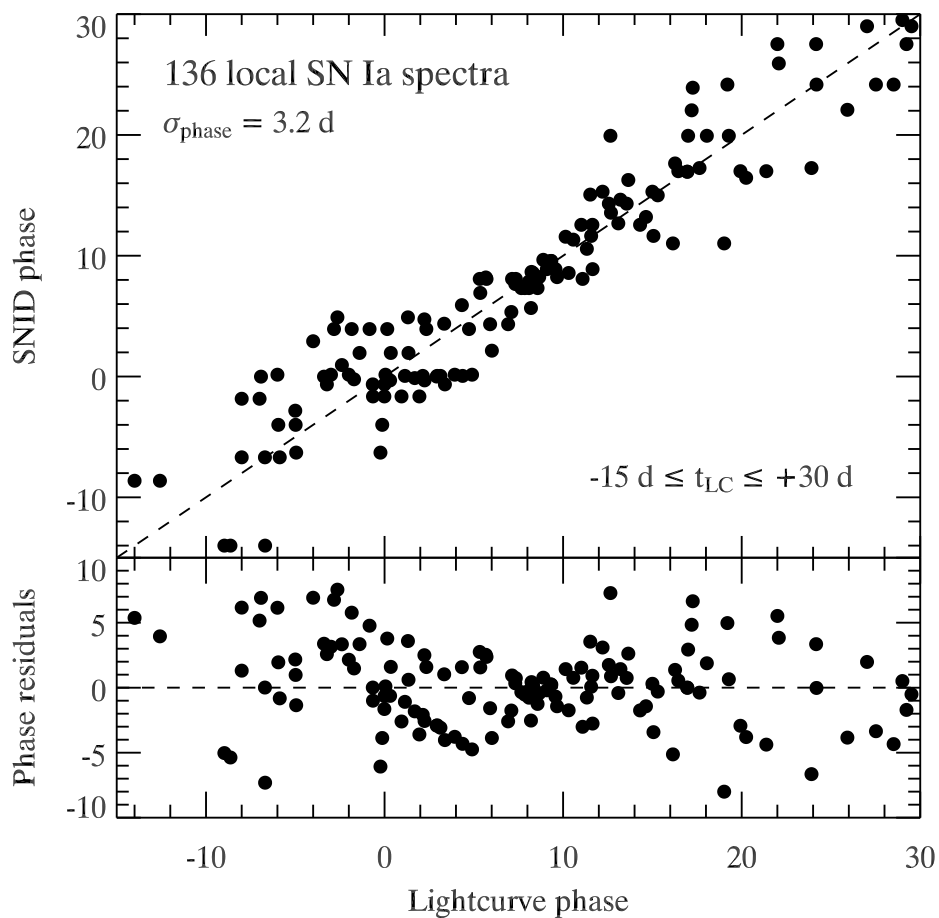


Figure 6.1: **Upper panel:** Comparison of phases as determined by cross-correlations using SNID (t_{SNID}) and from the light curve (t_{LC}). The dispersion about the one-to-one correspondence is $\sigma_{\text{phase}} = 3.2 \text{ d}$. **Lower panel:** Phase residuals *vs.* t_{LC} .

phase could cause this lower degeneracy at later phases.

There is another issue with the results of Fig. 6.1, also partially related to the phase distribution of templates. Since the various supernovae in the database have a different associated number of spectral templates (which in turn have a different distribution in phase), we will be removing a different number of templates from the database for each input spectrum, as well as modify their phase distribution. The impact will be significant for input spectra corresponding to supernovae with a good coverage in phase (e.g., SN 1994D has 22 associated spectral templates – see Table 4.1, p. 103). One would need a sufficient number of local SN Ia spectral templates for a database with a uniform distribution in phase to be elaborated, so as to quantify this effect. This should soon be possible with the advent of large samples of local SN Ia with associated light curves (CfA sample, Matheson et al., in prep, Jha et al., in prep; LOSS sample, Li et al., in prep).

For the high- z SN Ia spectra, we first determine the phase by running the spectrum through SNID, and calculating the mean phase of all templates for which $\text{rlap} > 5$ (see Chap. 4). A further requirement is that the redshift determined by SNID using a given template must not be off the true redshift of the input spectrum by more than 0.01 (i.e. $dz \leq 0.01$) – the typical 1σ error associated with correlation redshifts (Sect. 4.2.3, 114). We also calculate the mean rlap value of all correlations satisfying $\text{rlap} > 5$. The error on the phase determined this way is evaluated using the model described below.

Error model

It is difficult to associate a meaningful error to the phase estimates based on supernova spectra, as it is difficult to disentangle errors due to the phase distribution of the spectral templates, the variation of the relative strength of spectral features with phase, and its intrinsic dispersion at a given phase. The points in Fig. 6.1 have no associated error bars, and the two previous studies on SFA [245, 84] quote the error in their measurements as the dispersion about the one-to-one correspondence of SFA and light-curve phases, over the entire phase range ($-10 \leq t \leq +30$ d). These errors will only be an approximation of the “true” uncertainty in the measurement, and will be phase dependent. As pointed out by Riess et al. [245], our spectral templates are not a function of age, but are merely labeled by age. We do not know *a priori* what a SN Ia at a given phase is “supposed” to look like, and have many parameters affecting the result.

The error model presented in this section, though different from the one presented by Riess et al. [245], bares the same caveats. However, we are able to assign a systematic error to our measurements, in addition to the statistical error associated with the cross-correlation algorithm. Nevertheless, we will see in the next section that our error model tends to *overestimate* the error in the phase.

All the high- z spectra used in this Chapter to determine their phase are noisier than the local templates in the SNID database. At different redshifts, the sky noise will affect a different rest-frame bandpass of the spectrum, whose rest-frame optical wavelength range will also be restricted with respect to the local spectra. For each input high- z spectrum, we determine a noise spectrum, defined as the difference between the input spectrum and

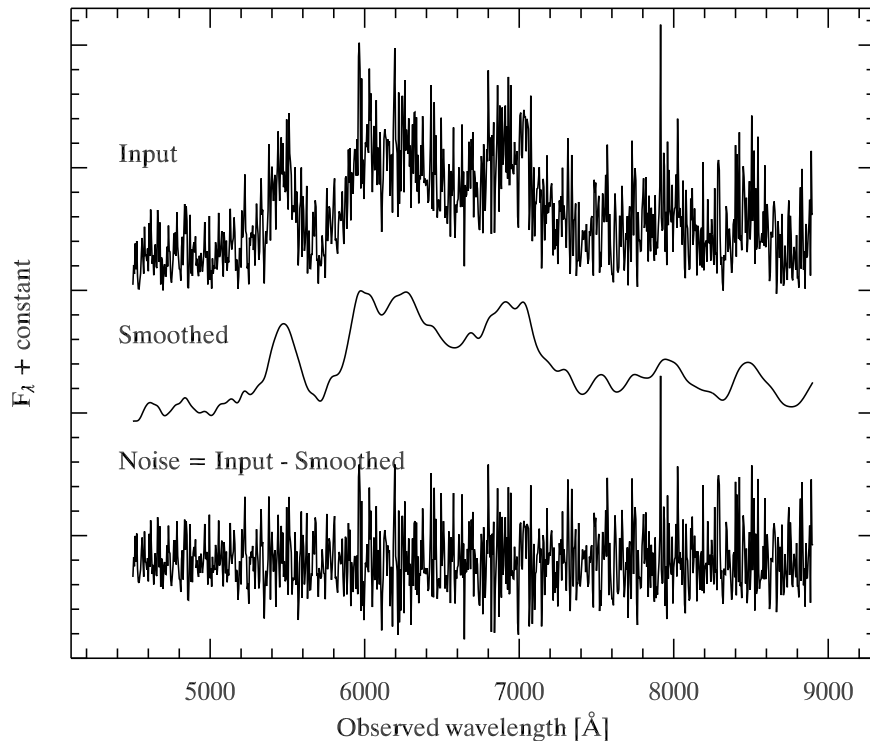


Figure 6.2: *From top to bottom:* Input spectrum, smoothed spectrum (smoothing factor $d\lambda/\lambda = 0.005$), and noise spectrum (defined as the difference between the input and smoothed spectra) for SN 2003jo at $z = 0.524$.

a smoothed version using the algorithm presented in Chap. 5 (p. 136), with a smoothing factor $d\lambda/\lambda = 0.005$. An example of such a noise spectrum for SN 2003jo ($z = 0.524$) is shown in Fig. 6.2.

We then fix the *observed* wavelength range to use for the correlation analysis, and in particular discard regions of the spectra greatly affected by sky background ($\lambda \gtrsim 9000 \text{ \AA}$). We then perform the test presented previously (see Fig. 6.1) using the local database spectra only. The difference here is that the wavelength axis of each database spectrum is scaled to match the redshift of the input spectrum, and trimmed to match the common wavelength coverage. The noise spectrum is then added to each database spectrum before running through SNID.

The rlap value for each correlation satisfying $dz \leq 0.01$ is plotted against the phase residual (between the light-curve phase – which is known for all the database spectra – and the phase of each database spectrum) in Fig. 6.3, in the case of SN 2003jo. For N database spectra, the maximum number of correlations satisfying this criterion is simply $N^2 = 18496$ for 136 database spectra. The statistical error (σ_{stat}) in the phase is *defined* as the standard deviation of the phase residuals in the integer rlap interval of size one which includes the mean rlap value of the high- z correlation. In the case of SN 2003jo, the

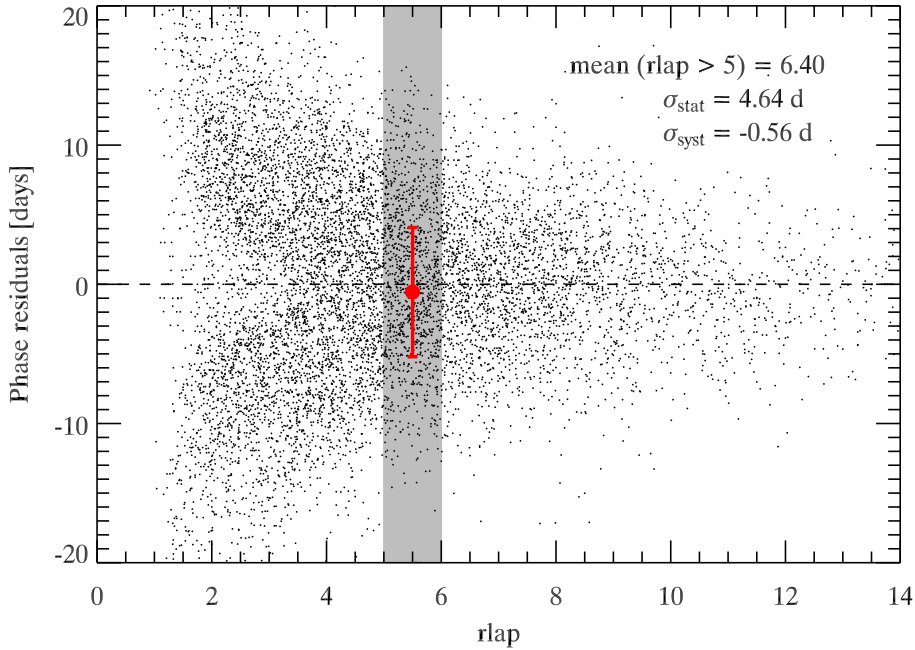


Figure 6.3: Phase residuals plotted against the rlap value for correlations satisfying $dz \leq 0.01$. The input spectrum was SN 2003jo ($z = 0.524$), for which the mean rlap value is 5.42. The statistical error is thus computed as the standard deviation of phase residuals in the rlap interval [5,6] (*grey shaded area*), which in this case is $\sigma_{\text{stat}} = 4.64$ d. The systematic error is given by the mean phase residual in the same rlap interval, giving $\sigma_{\text{syst}} = -0.56$ d.

mean rlap value is 5.42, and so the statistical error is calculated as the standard deviation of phase residuals in the rlap interval [5,6] (see the grey shaded area in Fig. 6.3), giving $\sigma_{\text{stat}} = 4.64$ d. The systematic error is given by the mean phase residual in the same rlap interval; in this case, $\sigma_{\text{syst}} = -0.56$ d. The final spectral age is calculated according to:

$$t_{\text{SNID}} = \bar{t} - \sigma_{\text{syst}} \pm \sigma_{\text{stat}}, \quad (6.1)$$

where \bar{t} is the mean phase of all templates for which $\text{rlap} > 5$ and $dz \leq 0.01$, in the initial run of the input high- z spectrum through SNID. For SN 2003jo, $\bar{t} = +2.83$ d, and so $t_{\text{SNID}} = (2.83 + 0.56) \pm 4.64 = 3.39 \pm 4.64$ d.

6.3 Testing for time dilation in high- z SN Ia spectra

6.3.1 Spectral phases in high- z SN Ia

We were able to determine the spectral phase for 29 high- z SN Ia spectra from Matheson et al. [187] (Appendix A). The results are given at the end of this Chapter in Table 6.1.

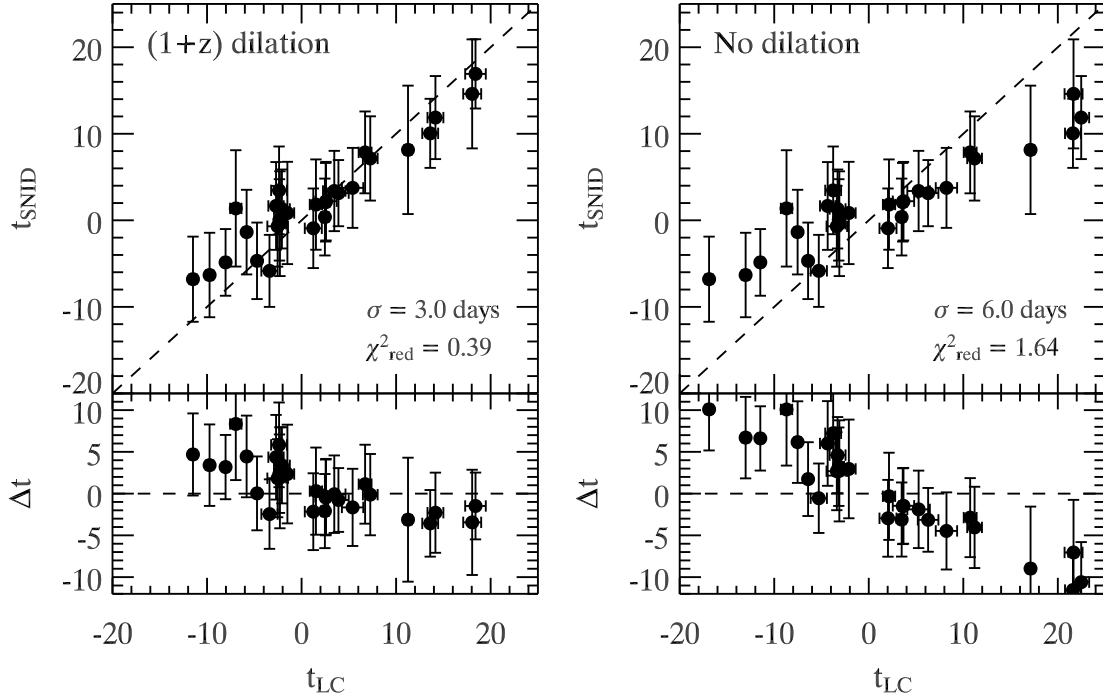


Figure 6.4: Spectral phase *vs.* light-curve phase, where t_{LC} has been corrected for the $(1+z)$ dilation factor (*left*), and when no correction has been applied (*right*).

We show the results of comparing the spectral phase with the light-curve phase in Fig. 6.4. The left panel shows t_{SNID} plotted against the light-curve phase t_{LC} (as determined from the date of rest-frame B -band maximum – see column (3) in Table 6.1), which has been corrected for the expected $(1+z)$ dilation factor. The fit is satisfactory, with a dispersion about the one-to-one correspondence (*dashed line*) of $\sigma \approx 3.0$ d, in good agreement with the accuracy obtained in our preliminary test on the local SN Ia ($\sigma_{\text{phase}} \approx 3.2$ d; see Fig. 6.1). The lower panel of this plot shows the residuals $\Delta t = t_{\text{SNID}} - t_{\text{LC}}$ *vs.* t_{LC} , revealing a bias to higher phases for $t_{\text{LC}} \lesssim -5$ d, and to lower phases for $t_{\text{LC}} \gtrsim +10$ d, primarily due to the phase distribution of the database spectra (see previous section). The reduced χ^2 is less than unity ($\chi_{\text{red}}^2 = 0.39$), showing that we are *overestimating* our errors with the model we use. To obtain $\chi_{\text{red}}^2 \approx 1$, we need to multiply our error bars by ~ 0.5 .

The right panel of Fig. 6.4 shows t_{SNID} plotted *vs.* the light-curve phase, *uncorrected for time dilation*. The dispersion blows up by a factor two, from 3.0 d to 6.0 d, and the residuals in the lower panel increase as we move away from $t_{\text{LC}} = 0$, as expected from a time-dilation effect.

The spectral phases plotted in Fig. 6.4 have been corrected for the systematic error σ_{sys} whose determination was presented in the previous section. One could object that our measurements are affected by a bias in our determination of the systematic error, due to the phase distribution of our database spectra. In Fig. 6.5 we show the variation of the

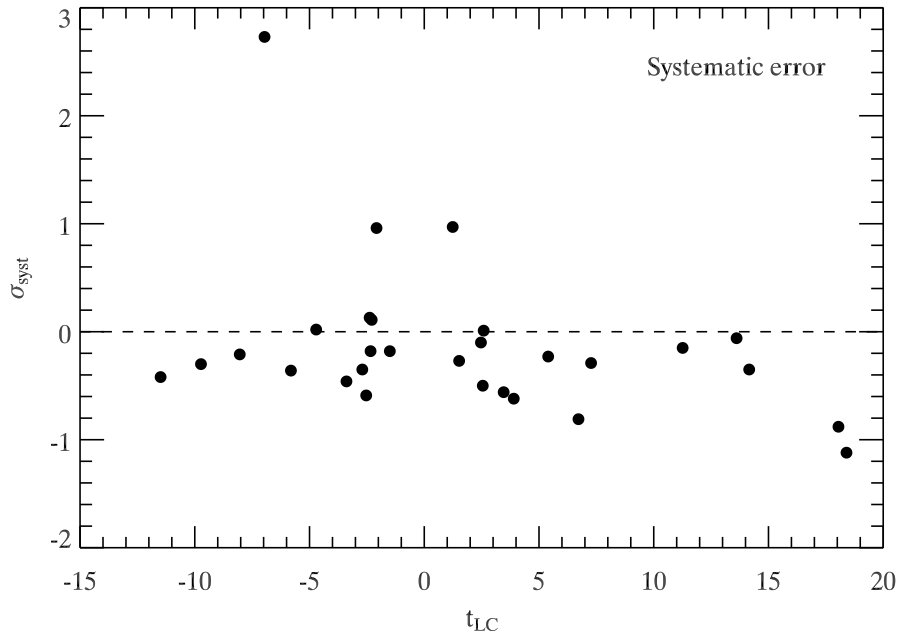


Figure 6.5: Variation of the systematic error with phase. Most of the values for σ_{syst} are in the range $-1 \lesssim \sigma_{\text{syst}} \lesssim 0$, and our results are not due to a bias in our systematic error correction.

systematic error with the light-curve phase t_{LC} (corrected for the $(1+z)$ dilation factor). There is no systematic variation in σ_{syst} with t_{LC} . Most of the values for σ_{syst} are in the range $-1 \lesssim \sigma_{\text{syst}} \lesssim 0$, and so the applied correction (equal to $-\sigma_{\text{syst}}$) is simply a uniform shift of t_{SNID} by no more than $\sim +1$ d, and does not affect the slope of the t_{SNID} vs. t_{LC} correlation in the left panel of Fig. 6.4. Bypassing the correction for σ_{syst} only slightly increases the dispersion about the one-to-one correspondence, from 3.0 d to 3.4 d. If t_{LC} is not corrected for time dilation, then this dispersion also increase, from 6.0 d to 6.4 d. The results of Fig. 6.4 are thus not due to a bias in our systematic error correction. Note, however, that the results of Fig. 6.5 suggests that we are systematically underestimating the phase, at all phases in the (rest-frame) range $-15 \lesssim t \lesssim +30$ d. This is different to the bias present in the residual plots of Fig. 6.1 & 6.4, and could point to a secondary effect, not taken into account in our systematic error determination.

6.3.2 Determining the age factor

The results of Fig. 6.4 show that we can successfully estimate the phase of a high-redshift SN Ia based on its spectrum alone, if we account for the $(1+z)$ time dilation effect. However, we have no real measure of the magnitude of the dilation present in Fig. 6.4, since the SN Ia span a large range of redshifts ($0.20 \leq z \leq 0.64$), and the $(1+z)$ correction will be different for each individual point. This is also the case for supernovae for which

we have spectra at different epochs (see Table 6.1). Despite being at the same redshift, the $(1+z)$ dilation will have a stronger effect for spectra that are more separated in phase from the time of B -band maximum (since this is our reference point). We present spectral phase determinations on three epochs of SN 2002iy ($z = 0.587$) in Sect. 6.3.3.

To measure the time dilation present in our spectroscopic data in absolute terms, we need to transform all the data to a common reference redshift z_{ref} , and see whether we retrieve the $(1+z_{\text{ref}})^{-1}$ slope in the plot of t_{SNID} vs. t_{LC} . We choose this reference redshift to be the median redshift of the high- z spectra, $\tilde{z} = 0.417$, so as to minimize the magnitude of the correction to apply to each light curve phase (as well as have equal blueshift and redshift corrections). Supposing t_{LC} has not been corrected for time dilation, we transform the light curve phases according to:

$$\begin{aligned} t_{\text{LC}} &\longrightarrow t_{\text{LC}}(z_{\text{med}}) = t_{\text{LC}} \times [1 + (z - \tilde{z})]^{-1} && \text{for } z \geq \tilde{z} \\ t_{\text{LC}} &\longrightarrow t_{\text{LC}}(z_{\text{med}}) = t_{\text{LC}} \times [1 + (\tilde{z} - z)] && \text{for } z \leq \tilde{z}, \end{aligned} \quad (6.2)$$

to transform all the data to $z = \tilde{z}$. The results are displayed in Fig. 6.6 (*upper panel*). The slope of the best-fit line to the graph of t_{SNID} vs. $t_{\text{LC}}(z_{\text{med}})$, also called the ‘‘age factor’’ by Foley et al. [84], corresponds to $(1+z) = 1.842 \pm 0.268$. This is $\sim 1.6\sigma$ off the expected 1.417 factor. However, we point out that similar results are often quoted (see [245, 84]) not in terms of consistency with time dilation but rather in terms of *inconsistency* with no dilation. Playing the same game, our results are inconsistent with the null hypothesis (i.e. a unity age factor) at the $\sim 3.14\sigma$ level ($> 99.8\%$ confidence).

Nevertheless, our results are not satisfactory, as revealed by the plot of t_{SNID} residuals (with respect to the expected time dilation) in Fig. 6.6 (*bottom panel*). Here again, the phase distribution of our database spectra introduces a bias to higher phases for $t_{\text{LC}}(z_{\text{med}}) \lesssim -10$ d, and a less pronounced bias to lower phases for $t_{\text{LC}}(z_{\text{med}}) \gtrsim -10$ d. The resulting trend causes a shallower slope of the best-fit line, hence a higher age factor.

6.3.3 Time dilation from multi-epoch spectra of SN 2002iy at $z = 0.587$

There are nine high- z SN Ia in our sample for which we have multi-epoch spectra, sufficiently separated in phase for a measurement of time dilation on a single supernova to be possible (see Table 6.1). Unfortunately, for only one of these SN Ia (SN 2002iy at $z = 0.587$) were we able to determine a reliable phase for at least two spectra. The three spectra of SN 2002iy correspond to rest-frame (i.e. corrected for the $(1+z)$ factor) light-curve phases -2.08 d, $+13.61$ d, and $+14.16$ d (in days from B -band maximum). We plot these three spectra, alongside local templates with similar rest-frame phases drawn from our database, in Fig. 6.7. Despite their low signal-to-noise ratio, the spectra reproduce the spectral evolution expected from local SN Ia (here SN 1998bu, 1994ae, and 1972E).

The measured spectral phases for the SN 2002iy spectra are (corrected for the systematic error, σ_{syst}): $+1.31 \pm 4.56$, $+10.05 \pm 3.99$, and $+11.87 \pm 4.80$, respectively (see Table 6.1). We plot these spectral phases vs. the time from B -band maximum ($\text{MJD}_{\text{max}} = 52592.75$) in

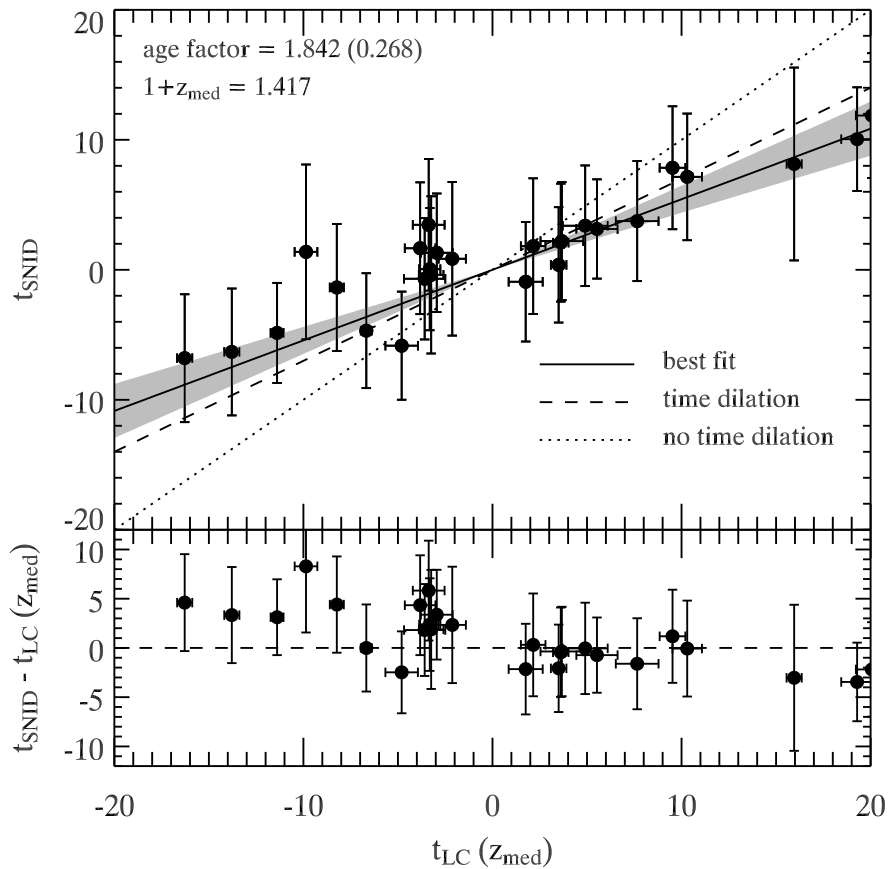


Figure 6.6: **Upper panel:** Plot of t_{SNID} vs. the light-curve phase corrected to $\tilde{z} = 0.417$, $t_{LC}(z_{med})$. The dashed line is the expected age factor (corresponding to a slope of $1/1.417$), whilst the solid line is the best fit, fixed at the origin. The grey area corresponds to the 1σ error in the slope. The best-fit line corresponds to an age factor of 1.842 ± 0.268 , i.e. $\sim 1.6\sigma$ off the expected value. The dotted line is the null hypothesis of no dilation (unity slope). **Lower panel:** Spectral phase residuals with respect to the expected time dilation, revealing the bias to higher[lower] phases for $t_{LC}(z_{med}) \lesssim -10$ d [$t_{LC}(z_{med}) \gtrsim +10$ d].

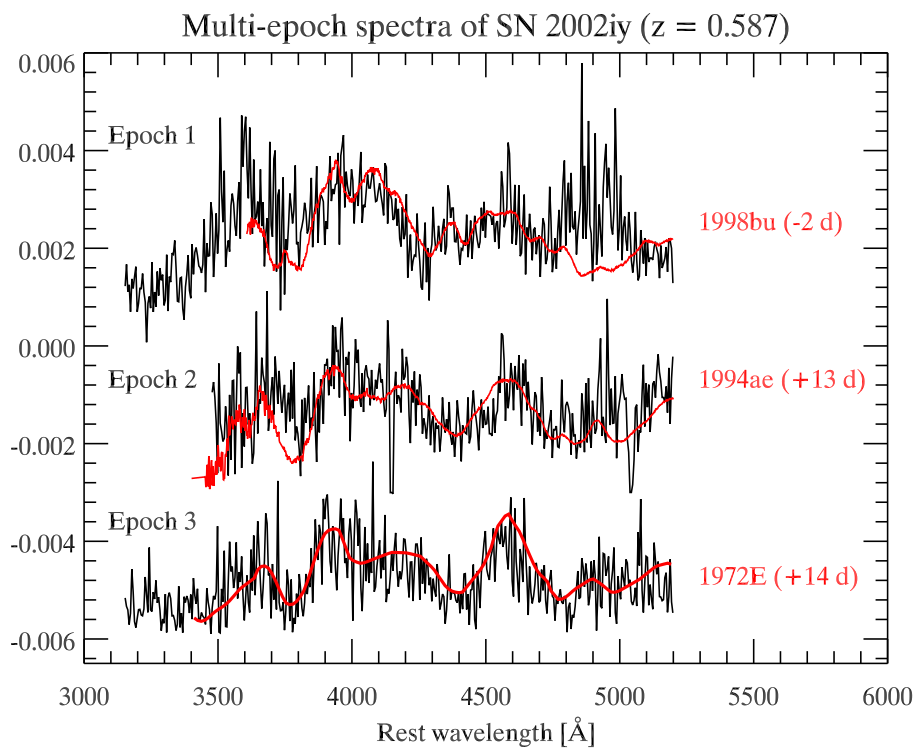


Figure 6.7: Multi-epoch spectra of SN 2002iy at $z = 0.587$, plotted in increasing phase from top to bottom. Overplotted in red are local template spectra at similar rest-frame phases (in days from B -band maximum).

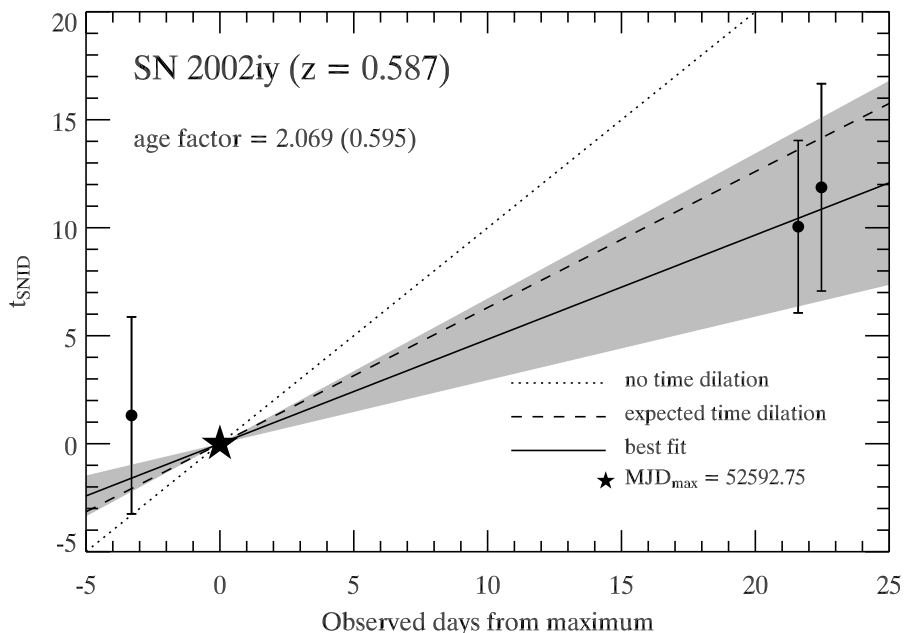


Figure 6.8: Age factor for SN 2002iy at $z = 0.587$. The dashed line is the expected age factor (corresponding to a slope of $1/1.587$), whilst the solid line is the best fit, fixed at the origin (*black star*). The grey area correspond to the 1σ error in the slope. The best-fit line corresponds to an age factor of 2.069 ± 0.595 , i.e. $\sim 0.8\sigma$ off the expected value. The dotted line is the null hypothesis of no dilation (unity slope).

Fig. 6.8, so as to compare the measured age factor with the expected one of 1.587 from time dilation. Again, we evaluate the best-fit line which passes through the origin (i.e. MJD_{max} , our reference point), and find the corresponding age factor to be 2.069 ± 0.595 . This is in better agreement with the expected age factor of 1.587 (“only” $\sim 0.8\sigma$ off; *dashed line*), though the error on the fit (*grey shaded area*) is large. The results of Riess et al. [245] and Foley et al. [84] were off by 0.95σ and 1.03σ , respectively. The data are inconsistent with the null hypothesis (*dotted line*) at the $\sim 1.8\sigma$ level, or $\sim 93\%$ confidence.

6.4 Conclusion

We have presented preliminary results on time-dilation measurements in 29 high-redshift Type Ia supernova spectra, including three epochs of the same SN Ia (SN 2002iy at $z = 0.587$). The results are inconsistent with the null hypothesis of no time dilation at a high confidence level ($> 90\%$), and are within $\sim 1\sigma$ of the $(1+z)$ value expected from the universal expansion. Thus, we rule out alternative explanations for the measured dilation, such as variable-mass theories, which require a large amount of fine tuning to reproduce this effect.

However, the errors in the age factors are large, and our measurements reveal a bias which we associate primarily with the phase distribution of our templates, although we have not thoroughly studied the impact of this effect on our results. To do so, one would need a larger database of local SN Ia spectra, well sampled in phase (between ~ -10 d and $\sim +30$ d from maximum), and see the impact of varying the phase distribution of the template spectra on the recovered spectral age. Also, a uniform spectral database would enable the study of (i) the intrinsic dispersion of SN Ia spectral features at a given phase and (ii) the variation of this dispersion with phase. Understanding both these effects will greatly enhance the ability to determine the phase of a SN Ia based on its spectrum alone.

The spectral phases are found to be accurate to within ~ 3 d (1σ) from the rest frame light-curve phase. The fact that we are able to determine the phase of a high- z SN Ia spectrum *via* cross-correlations with a database of local SN Ia spectral templates further suggests that there is no large evolutionary bias affecting SN Ia at high redshifts.

Table 6.1: Spectral feature ages and time dilation

SN (1)	z (2)	MJD _{max} (3)	MJD _{obs} (4)	$t_{\text{LC}}/(1+z)$ (5)	t_{SNID} (6)	σ_{stat} (7)	$-\sigma_{\text{sys}}$ (8)
2002ja	0.33	52585.42 (1.97)	52587.33	+1.44 (1.48)
2002jb	0.25	52596.01 (0.67)	52587.31	-6.96 (0.60)	+4.11	6.72	-2.73
2003ji	0.21	52921.14 (1.79)	52944.23	+19.08 (1.74)
2003jj	0.583	52946.83 (1.33)	52943.07	-2.38 (0.84)	+3.59	5.07	+0.13
2003jl	0.429	52931.72 (0.66)	52943.34	+8.13 (0.46)	+4.61
2003jm	0.522	52933.97 (1.72)	52942.19	+5.40 (1.13)	+3.52	4.62	+0.23
2003jn	0.33	52937.03 (0.59)	52941.29	+3.20 (0.45)
2003jo	0.524	52935.81 (1.81)	52941.09	+3.46 (1.19)	+2.83	4.64	+0.56
2003jq	0.16	52935.25 (0.36)	52936.21	+0.83 (0.31)	+18.40
2003jr	0.340	52920.76 (1.44)	52944.18	+17.48 (1.08)
2003jt	0.45	52936.84 (1.03)	52941.32	+3.09 (0.71)	-6.90
2003jv	0.405	52942.48 (1.01)	52940.37	-1.50 (0.72)	+0.67	5.91	+0.18
2003jw	0.296	52949.85 (0.48)	52942.32	-5.81 (0.37)	-1.72	4.89	+0.36
2003jy	0.339	52956.13 (0.53)	52943.10	-9.73 (0.40)	-6.62	4.88	+0.30
2003kk	0.164	52966.29 (0.39)	52962.11	-3.59 (0.34)
2003kn	0.244	52974.01 (0.46)	52965.08	-7.18 (0.37)
2003ko	0.360	52968.25 (0.88)	52965.13	-2.29 (0.65)	-0.28	6.05	-0.11
2003kp	0.64	52963.14 (1.48)	52965.18	+1.24 (0.90)	+0.05	4.60	-0.97
2003kq	0.61	52969.64 (1.31)	52965.29	-2.70 (0.81)	+1.31	5.07	+0.35
2003kr	0.427	52976.71 (0.48)	52965.23	-8.04 (0.34)	-5.07	3.85	+0.21
2003kt	0.61	52959.82 (1.75)	52966.10	+3.90 (1.09)	+2.52	3.82	+0.62
2003le	0.56	52995.50 (1.56)	52993.23	-1.46 (1.00)
2003lh	0.54	52985.48 (1.03)	52994.31	+5.73 (0.68)
2003li	0.544	52984.95 (1.23)	52993.42	+5.49 (0.80)
2003lj	0.417	52989.60 (1.60)	52993.27	+2.59 (1.13)	+2.22	4.54	-0.01
2003ll	0.596	52983.71 (1.09)	52994.44	+6.72 (0.68)	+7.04	4.73	+0.81
2003lm	0.408	52992.14 (0.91)	52994.28	+1.52 (0.65)	+1.55	5.22	+0.27
2003ln	0.63	52987.80 (1.23)	52994.25	+3.96 (0.76)
Multi-epoch data							
2002jq	0.49	52603.47 (0.02)	52584.29	-12.87 (0.26)
			52612.27	+5.91 (0.12)
2002iy	0.587	52592.75 (1.34)	52584.39	-5.27 (0.84)
			52589.45	-2.08 (0.84)	+2.27	4.56	-0.96
			52614.35	+13.61 (0.84)	+9.99	3.99	+0.06
			52615.22	+14.16 (0.84)	+11.52	4.80	+0.35
2002iz	0.428	52587.80 (1.56)	52584.45	-2.35 (1.09)	-2.15
			52614.07	+18.40 (1.09)	+15.80	4.00	+1.12
2002jc	0.52	52596.27 (0.52)	52587.45	-5.80 (0.36)

			52613.39	+11.26 (0.40)	+7.99	7.42	+0.15
2002js	0.54	52600.21 (1.19)	52589.57	-6.91 (0.78)
			52611.41	+7.27 (0.78)	+6.86	4.87	+0.29
2002jd	0.32	52593.29 (0.56)	52589.45	-2.91 (0.43)
			52614.07	+15.74 (0.65)
			52617.27	+18.17 (0.71)
2002jt	0.56	52615.42 (1.34)	52610.13	-3.39 (0.86)	-6.30	4.16	+0.46
			52615.29	-0.08 (0.86)
2002jw	0.357	52618.35 (0.76)	52615.18	-2.34 (0.56)	-0.13	4.70	+0.18
			52644.37	+19.17 (0.56)
2003ju	0.20	52948.44 (0.37)	52939.06	-7.82 (0.50)
			52970.10	+18.05 (0.95)	+13.73	6.30	+0.88
2003js	0.363	52948.38 (0.40)	52941.96	-4.71 (0.29)	-4.66	4.42	-0.02
			52966.21	+13.08 (0.30)
2003kl	0.335	52965.52 (1.46)	52962.14	-2.53 (1.09)	-1.28	4.67	+0.59
			52965.11	-0.31 (1.09)
2003km	0.47	52981.10 (0.46)	52963.21	-12.17 (0.41)
			52964.21	-11.49 (0.40)	-7.22	4.92	+0.42
2003lf	0.41	52990.69 (0.57)	52994.17	+2.47 (0.41)	+0.28	4.44	+0.10
			52994.29	+2.55 (0.41)	+1.59	4.54	+0.50

*The horn, the horn, the lusty horn
Is not a thing to laugh to scorn.
William Shakespeare (As You Like It, Act IV, scene 2)*

Chapter 7

Conclusion

Are distant Type Ia supernovae different from nearby ones?

That is the question which has motivated the research presented in this thesis. The results presented in Chap. 4-6 suggest otherwise: SN Ia have not evolved significantly between redshift $z \lesssim 0.8$ and today, thereby justifying the extrapolation to higher redshifts of the empirical calibration method used to determine distances to the local ($z \lesssim 0.01$) events.

In what follows we briefly summarize the main results of this thesis:

1. We have developed a novel method to extract the spectrum of a supernova from that of the contaminating background of its host galaxy (Chap 3; see [27]). The algorithm is based on a two-channel iterative technique employing the Richardson-Lucy restoration method. This technique has been successfully applied to SN Ia spectra taken with the ESO *Very Large Telescope*, published by Matheson et al. [187] (Appendix A) and displayed at the end of Chap. 2 in Figs. 2.19-2.21 (pp. 65-67). This alternative approach to spectral data reduction is proved useful for quantitative analyses of supernova spectra, and is gaining interest amongst SN Ia researchers (members of both the Supernova Cosmology Project and the Supernova Legacy Survey are currently using this method). It is becoming the standard for the extraction of long-slit SN Ia spectra in the ESSENCE project.
2. We have presented a cross-correlation technique, based on the algorithm of Tonry and Davis [290], to determine the redshift of a SN Ia spectrum without recourse to that determined using narrow lines in the spectrum of the host galaxy (Chap. 4). By comparing the supernova and galaxy redshifts, we show that the cross-correlation redshift is accurate to $\sigma_z \approx 0.01$ (see Fig. 4.12, p. 126). With the improvements discussed at the end of Chap. 4, this technique should yield more accurate (although less precise) redshifts than those obtained from the (assumed) host galaxy, and enable a uniform determination of SN Ia redshifts in ongoing large surveys. Accurate redshifts are fundamental to the elaboration of a Hubble diagram, and in turn to the inference of cosmological parameters.

3. Using the CMFGEN model atmosphere code of Hillier and Miller [118], and adapted to supernova conditions (homologous velocity field, power-law radial density profile) by Dessart and Hillier [66, 65], we illustrate the formation of spectral lines in SN Ia outflows (Chap. 5; see [26]). In particular, we have shown the resulting P-Cygni line profile shapes (characterised by blueshifted absorption and symmetric emission about line center) to have emission peaks that are systematically blueshifted with respect to the rest wavelength of the transition. We attribute this effect, explained here for the first time in the context of SN Ia, to the steep radial density profile, confining all line-formation mechanisms to the innermost part of the SN Ia ejecta. Furthermore, we explain the relationship between the velocity at maximum absorption (v_{abs}) and the velocity of the continuum photosphere (v_{phot}), when the continuum is optically thick (i.e. during the earlier phases). We show that v_{abs} can *underestimate* v_{phot} for the weakest (optically thinner) lines.
4. In this same chapter, we present a census of velocity measurements in local and high-redshift SN Ia carried out on several lines characteristic of SN Ia spectra (Ca II $\lambda 3945$, Si II $\lambda 6355$, and S II $\lambda \lambda 5454, 5640$). Using the velocities associated with the location of maximum absorption (“absorption velocity”, v_{abs}) and peak emission (“emission-peak” velocity, v_{peak}), we show that the line-profile morphologies in nearby and distant SN Ia are similar, thereby providing quantitative evidence against evolutionary effects affecting the SN Ia sample at high redshifts.
5. Again in Chap. 5, we show that v_{abs} for the weak S II $\lambda \lambda 5454, 5640$ lines, and v_{peak} for S II $\lambda 5454$, can be used to identify fast-declining (in luminosity) SN Ia, which are also subluminous, provided the phase of the SN Ia is known. This new diagnostic tool can be proved useful when seeking an independent confirmation of the subluminous nature of a SN Ia event, in addition to the (calibrated) light curve.
6. Finally, in Chap. 6, we use the cross-correlation algorithm presented in Chap. 4 to show that the phase of a SN Ia can be determined to a reasonable accuracy ($\sigma \sim 3$ d) based on the spectrum *alone*, for both the local and high-redshift events. By comparing the (rest-frame) spectral phase for a sample of 29 high- z ($0.20 \leq z \leq 0.64$) SN Ia with the *observed* phases determined using their light curve, we are able to check for the $(1+z)$ cosmological time-dilation factor expected in an expanding universe. Our (preliminary) results are inconsistent with the null hypothesis of no time dilation at a high confidence level ($> 90\%$), though are off by $\sim 1.6\sigma$ from the expected $(1+z)$ factor. Using the spectra of a high-redshift SN Ia ($z = 0.587$) taken at three different epochs, we are able to improve the agreement slightly, though are still off by $\sim 0.8\sigma$. These results represent a slight improvement over previously published work [245, 84], although call for improvement. The public release of large databases of local SN Ia data (photometric and spectroscopic) will help to better evaluate systematic errors affecting the spectral phase determinations.

It is no exaggeration to say that cosmology drives the field of Type Ia supernova research, and it is customary to devote a section to “cosmological implications” of one’s

results in publications on SN Ia. However, SN Ia are astrophysical events interesting in their own right, and their modeling requires the use of hydrodynamical and radiative transfer computations at the forefront of numerical simulation. Moreover, recent observational evidence from polarization measurements for aspherical SN Ia explosions [304] has set new challenges for modellers working in the field.

Cosmology with SN Ia has a bright future: a space-based mission, the Joint Dark Energy Mission (JDEM¹), has been devised to determine the expansion history of the universe out to $z \sim 2$ using observations of thousands of SN Ia. This will set tight constraints on the equation-of-state parameter of the “Dark Energy”, and hence on the nature of this mysterious form of energy that was found, less than a decade ago [244, 226], to constitute no less than $\sim 70\%$ of the universe’s total energy density.

This thesis can serve to reassure observational cosmologists who use SN Ia as cosmological distance indicators, and as a motivation to theorists in pursuing their efforts to pin down the mechanisms by which a White Dwarf star explodes, and identify the progenitors of Type Ia supernovae. Only through a *physical* understanding of these events will we be able to make progress in the assessment of systematic effects biasing the cosmological results derived from observations of SN Ia. Despite the precision cosmology with SN Ia promised by the JDEM, the lack of physical basis to the empirical relation used to calibrate their light curves (and hence determine the luminosity distance to these objects) remains an embarrassing fact, that will only be resolved *via* a careful study of *nearby* SN Ia (e.g., the European Research Training Network on SN Ia explosions²).

In any case, the cosmological implications of observations of Type Ia supernovae are significant and affect cosmologists and particle physicists alike. However exciting these results may be, they point to an embarrassing gap in our current understanding of fundamental physics. To the dark matter which makes up $\sim 80\%$ of the matter energy density we must add another “dark” component with negative pressure that makes up $\sim 2/3$ of the total energy density of the universe. Thus we are left with a “concordance” universe for which 95% of the energy content is unaccounted for. As said by Sir Arthur Eddington (originally a comment on Heisenberg’s uncertainty principle): *Something unknown is doing we don’t know what.*

¹The Joint Dark Energy Mission is a proposal to construct a wide-field telescope in space to discover and follow-up thousands of SN Ia out to $z \sim 2$, planned for launch in ~ 2015 ; it is the result of a collaboration between the National Aeronautics and Space Administration (NASA) and the Department of Energy (DOE). Candidates for JDEM include Destiny (<http://destiny.asu.edu/>) and SNAP (<http://snap.lbl.gov/>)

²RTN – The physics of Type Ia supernova explosions; <http://www.mpa-garching.mpg.de/~rtn/>

Existence precedes and rules essence.

Jean-Paul Sartre

Appendix A

Spectroscopy of high-redshift supernovae from the ESSENCE project: the first 2 years

Thomas Matheson, Stéphane Blondin, Ryan J. Foley, Ryan Chornock, Alexei V. Filippenko, Bruno Leibundgut, R. Chris Smith, Jesper Sollerman, Jason Spyromilio, Robert P. Kirshner, Alejandro Clocchiatti, Claudio Aguilera, Brian Barris, Andrew C. Becker, Peter Challis, Ricardo Covarrubias, Peter Garnavich, Malcolm Hicken, Saurabh Jha, Kevin Krisciunas, Weidong Li, Anthony Miceli, Gajus Miknaitis, Jose Luis Prieto, Armin Rest, Adam G. Riess, Maria Elena Salvo, Brian P. Schmidt, Christopher W. Stubbs, Nicholas B. Suntzeff, and John L. Tonry

The Astronomical Journal, **431**, 757 (2005)

Abstract: We present the results of spectroscopic observations of targets discovered during the first two years of the ESSENCE project. The goal of ESSENCE is to use a sample of ~ 200 Type Ia supernovae (SN Ia) at moderate redshifts ($0.2 \lesssim z \lesssim 0.8$) to place constraints on the equation of state of the Universe. Spectroscopy not only provides the redshifts of the objects, but also confirms that some of the discoveries are indeed SN Ia. This confirmation is critical to the project, as techniques developed to determine luminosity distances to SN Ia depend upon the knowledge that the objects at high redshift have the same properties as the ones at low redshift. We describe the methods of target selection and prioritization, the telescopes and detectors, and the software used to identify objects. The redshifts deduced from spectral matching of high-redshift SN Ia with low-redshift SN Ia are consistent with those determined from host-galaxy spectra. We show that the high-redshift SN Ia match well with low-redshift templates. We include all spectra obtained by the ESSENCE project, including 52 SN Ia, 5 core-collapse SN, 12 active galactic nuclei, 19 galaxies, 4 possibly variable stars, and 16 objects with uncertain identifications.

A.1 Introduction

The revolution wrought in modern cosmology using luminosity distances of Type Ia supernovae (see [76, 78] for recent reviews, and [270, 244, 226, 250, 152, 291, 14, 252]) relies upon the fact that the objects so employed are, in fact, SN of Type Ia (SN Ia). Although the light-curve shape alone is useful (e.g., [14]), the only way to be sure of the true nature of an object as a SN Ia is through spectroscopy. The calculation of luminosity distances depends upon the high-redshift objects being SN Ia so that low-redshift calibration methods can be employed. The classification scheme for SN is based upon their optical spectra, generally near maximum brightness (see [75] for a review of SN types), so rest-wavelength optical spectroscopy is necessary to properly identify SN Ia at high redshifts. Despite this significance, relatively little attention has been paid to the spectroscopy of the high-redshift SN Ia, with some notable exceptions [57]. Other publications that include high-redshift SN Ia spectra include [270, 244, 225, 172, 291, 14, 252, 27, 179].

In addition to providing evidence for the acceleration of the expansion of the Universe, it was recognized at an early stage that high-redshift SN Ia could put constraints on the equation of state of the Universe [96], parameterized as $w = P/(\rho c^2)$, the ratio of the dark energy's pressure to its density. To further explore this, the ESSENCE (Equation of State: SuperNovae trace Cosmic Expansion) project was begun. The ESSENCE project is a five-year ground-based SN survey designed to place constraints on the equation-of-state parameter for the Universe using ~ 200 SN Ia over a redshift range of $0.2 \lesssim z \lesssim 0.8$ (see [201]; Smith et al., in prep, for a more extensive discussion of the goals and implementation of the ESSENCE project).

Spectroscopic identification of optical transients is a major component of the ESSENCE project. In addition to confirming some targets as SN Ia, the spectroscopy provides redshifts, allowing the derived luminosity distances to be compared with a given cosmological model. So many targets are discovered during the ESSENCE survey that a large amount of telescope time on 6.5 m to 10 m telescopes is required. In the first two years of the program, we were fortunate enough to have been awarded over 60 nights at large-aperture telescopes. Even with this much time, though, our resources were insufficient to spectroscopically identify all of the potentially useful candidates. This remains the most significant limiting factor in achieving the ESSENCE goal of finding, identifying, and following the desired number of SN Ia with the appropriate redshift distribution.

Nonetheless, spectroscopic observations of ESSENCE targets in the time available have been successful, with almost fifty SN Ia clearly identified, and several more characterized as likely SN Ia. Other identifications include core-collapse SN, active galactic nuclei (AGNs), and galaxies. The galaxy spectra may still include an unidentified SN component, and efforts are underway to isolate it through principal component analysis and template subtraction (Foley et al., in prep).

This paper will describe the results of the spectroscopic component of the first two years of the ESSENCE program. During the campaign, spectroscopically confirmed SN were announced in International Astronomical Union Circulars [276, 50, 62, 61, 51, 116]. Year One refers to our 2002 Sep.-Dec. campaign; Year Two was our 2003 Sep.-Dec. campaign.

In Section A.2, we describe the process of target selection and prioritization. Section A.3 describes the technical aspects of the observations. We discuss target identification in Section A.4. The summary of results in terms of types of objects and success rates is given in Section A.5. In addition, we present in Section A.5 all of the spectra obtained, including those of the SN Ia (compared with low-redshift templates), core-collapse SN, AGNs, galaxies, stars, and objects that remain unidentified.

A.2 Target Selection

The ESSENCE survey uses the Blanco 4 m telescope at CTIO with the MOSAIC wide-field CCD camera to detect many kinds of optical transients (Smith et al., in prep). Solar-system objects, such as Kuiper Belt Objects and asteroids, are identified through their obvious parallax in our multiple observations. Known AGNs and variable stars can also be eliminated from the possible SN Ia list. The remaining transients are all potentially SN. They are also faint, requiring large-aperture telescopes to obtain spectra of the quality necessary to securely classify the object. Exposure times on 8-10 m telescopes are typically about half an hour, but can be as long as two hours. Such telescope time is difficult to obtain in quantity, so not all of the detected transients can be examined spectroscopically. We apply several criteria to prioritize target selection for spectroscopic observation.

The first step in sorting targets is based upon the spectroscopic resources available. The equatorial fields used for the ESSENCE program are accessible from most major astronomical sites, so the main concern with matching targets to spectroscopic telescopes is the aperture size of the telescope. The ESSENCE targets are generally in the range $18 \lesssim m_R \lesssim 24$ mag. When 8-10 m telescopes are unavailable, the fainter targets become lower in priority. The limit for low-dispersion spectroscopy to identify SN with the 6.5 m telescopes is $m_R \approx 22-23$ mag, although this will vary with weather conditions and seeing. If the full range of telescopes is available, then targets are prioritized by magnitude for observation at a given telescope. The longitudinal distribution of spectroscopic resources can be important if confirmation of a high-priority target is made during a night when multiple spectroscopic resources are available. By the time a target is confirmed, the fields may have set for telescopes in Chile, while they are still accessible from Hawaii. This requires active, real-time collaboration between the group finding SN candidates and those running the spectroscopic observations.

One advantage of the ESSENCE program is that fields are imaged in multiple filters, allowing for discrimination of targets by color. Tonry et al. [291] present a table of expected SN Ia peak magnitudes as a function of redshift; see also [235, 91, 253, 284], and Smith et al. (in prep) for discussions of color selection for SN candidates. Given apparent R -band and I -band magnitudes, one can calculate the $R - I$ color and compare that with an expected color for those magnitudes. The cadence of the ESSENCE program (returning to the same field every four days) will likely catch SN at early phases (i.e., before maximum brightness). Early core-collapse SN are bluer than SN Ia, as are AGNs. For example, when selecting for higher-redshift targets, objects with $R - I \lesssim 0.2$ mag were considered

unlikely to be SN Ia, while objects with $R - I \gtrsim 0.4$ mag were made high priority for spectroscopic observation. The exact values of $R - I$ used for selection depended on the observed R -band magnitude. This method was used more consistently in the last month of Year Two, reducing the fraction of spectroscopic targets that were identified as AGNs from $\sim 10\%$ over the lifetime of the project to $\sim 5\%$ during that month.

The cadence of the ESSENCE program is designed to catch SN early. At the start of an observing campaign or after periods of bad weather, though, we may have missed SN during their rise to maximum brightness and only caught them while they are declining from maximum. If a target is brightening, then it is a higher priority than one that is not. This prioritization by phase of the SN became even more important when our *Hubble Space Telescope* (*HST*) program to observe some of the ESSENCE SN Ia was active (see [156]). The response time of *HST* for a new target, even if the rough position on the sky is known from our chosen search fields, is still on the order of several days. To ensure that *HST* was not generally looking at SN Ia after maximum brightness, we would emphasize targets for spectroscopic identification that appeared to be at an early epoch. In addition, we chose fainter objects, as higher-redshift SN Ia were a prime motivation for *HST* photometry. The *HST* observations, while still formally targets of opportunity, were prescheduled for specific ESSENCE search fields, so new targets in those particular fields were given the highest priority.

The position of the SN in the host galaxy also influences the priority for observation. An optical transient located at the core of a galaxy is often an AGN, rather than an SN. The color selection described above is a less-biased predictor. In addition, even if the object is an SN, the signal of the SN itself is diluted by the light of the galaxy, making proper identification difficult. Objects that are well separated from the host galaxy are given a higher priority. Being too far from the galaxy can, however, present another problem—the difficulty in obtaining a spectrum of the host in addition to the SN. Without a high signal-to-noise ratio (S/N) spectrum of the host, there is no precise measure of the redshift. This is especially true if the host galaxy cannot be included in the slit with the target, either to orient the slit at the parallactic angle [74] or as a result of other observational constraints. In addition, host galaxies can be faint, so the large luminosity contrast with the SN makes detection of the host problematic (the so-called “hostless” SN), although we did not reject any candidates solely for this reason. The best compromise is to have an object well separated from the host, but with the host still in the spectrograph slit. Without narrow-line features from the host (either emission or absorption lines), the redshift can be difficult to determine. This lack of a host-galaxy spectrum became less of a concern, though, as we found that the SN spectrum itself is a relatively accurate, if less precise, measure of the redshift (see discussion below). The light curve alone can be used to estimate distances in a redshift-independent way [14], but only with a well-sampled and accurate light curve.

The target selection process is complex and dynamic. Biases are introduced by some of the steps; for example, SN candidates near the centers of galaxies are less likely to be observed. Since the goal is to optimize the spectroscopic telescope time to identify SN Ia in a specific redshift range, we have chosen these selection processes as our best compromise. The biases introduced, though, may make the identified sample of SN Ia problematic for

uses in statistical studies of the nature of SN Ia at high redshift.

A.3 Observations

Spectroscopic observations of ESSENCE targets were obtained at a wide variety of telescopes: the Keck I and II 10 m telescopes, the VLT 8 m telescopes, the Gemini North and South 8 m telescopes, the Magellan Baade and Clay 6.5 m telescopes, the MMT 6.5 m telescope, and the Tillinghast 1.5 m telescope at the F. L. Whipple Observatory (FLWO). The spectrographs used were LRIS [216] with Keck I, ESI [274] with Keck II, FORS1 with VLT [5], GMOS [127] at Gemini (North and South), IMACS [68] with Baade, LDSS2 [204] with Clay, the Blue Channel [271] at MMT, and FAST [72] at FLWO. Nod-and-shuffle techniques [98] were used with GMOS (North and South) and IMACS to improve sky subtraction in the red portion of the spectrum.

Standard CCD processing and spectrum extraction were accomplished with IRAF¹⁷. Most of the data were extracted using the optimal algorithm of Horne [129]; for the VLT data, an alternative extraction method based upon Richardson-Lucy restoration [27] was employed. Low-order polynomial fits to calibration-lamp spectra were used to establish the wavelength scale. Small adjustments derived from night-sky lines in the object frames were applied. We employed IRAF and our own IDL routines to flux calibrate the data and, in most cases, to remove telluric lines using the well-exposed continua of the spectrophotometric standards [302, 188].

A.4 Target Identification

Once a calibrated spectrum is available, the next step is to properly classify the object. For brighter objects yielding high S/N spectra, an SN is often easy to distinguish and classify. Most of the ESSENCE targets are faint enough to be difficult objects even for large-aperture telescopes. The resulting noisy spectra can be confusing. Even for well-exposed spectra, though, exact classification can occasionally still be challenging.

For SN, the classification scheme is based upon the optical spectrum, usually near maximum brightness [75]. Type II SN are distinguished by the presence of hydrogen lines. The Type I SN lack hydrogen, and are further subdivided by the presence or absence of other features. The hallmark of SN Ia is a strong Si II $\lambda 6355$ absorption feature. Near maximum brightness, this absorption is blueshifted by $\sim 10,000$ km s⁻¹ and appears near 6150 Å. In SN Ib, this line is not as strong, and the optical helium series dominates the spectrum, especially ~ 1 month past maximum brightness. The SN Ic lack all these identifying lines.

At high redshift, the Si II $\lambda 6355$ feature is at wavelengths inaccessible to optical spectrographs, so the identification relies upon the pattern of features in the rest-frame ultraviolet

¹⁷IRAF is distributed by the National Optical Astronomy Observatory, which is operated by AURA under cooperative agreement with the NSF.

(UV) and blue-optical wavelengths. The Ca II H&K $\lambda\lambda 3934, 3968$ doublet is a distinctive feature in SN Ia, but it is also present in SN Ib/c, so the overall pattern is important for a clear identification as a SN Ia. Other important features to identify SN Ia include Si II $\lambda 4130$, Mg II $\lambda 4481$, Fe II $\lambda 4555$, Si III $\lambda 4560$, S II $\lambda 4816$, and Si II $\lambda 5051$ (see, e.g., [136, 149, 197, 57]).

The first stage of classification is done by eye. Drawing upon the extensive experience of the spectroscopic observers associated with ESSENCE, we can provide a solid evaluation of the spectrum. Objects such as AGNs and normal galaxies are fairly easy to distinguish. The SN Ia are also often clear, but some fraction of the data will require more extensive analysis. The first step is simply to make certain that the collective expertise is used, rather than just the individual at the telescope. Spectroscopic data are widely disseminated via e-mail and through an internal web page, allowing rapid examination of any questionable spectrum by the entire collaboration. Broad discussion often leads to a consensus.

In addition to the traditional by-eye approach, we employ automated comparisons. If the object is likely to be a SN Ia, and if the S/N is sufficiently high and the rest-wavelength coverage appropriate, we can use a spectral-feature aging routine [245] that compares specific components of the SN Ia spectrum with a library of SN Ia spectra at known phases. This can pin down the epoch of a SN Ia to within a few days. This program, though, is limited to normal SN Ia (i.e., not spectroscopically peculiar objects, which are often overluminous or underluminous). In addition, it does not identify objects that do not match the Type Ia SN spectra in the library.

For a more general identification routine, we use an algorithm called SuperNova IDentification (SNID; Blondin et al., in prep). This program takes the input spectrum and compares it against a library of objects of many types. The templates include SN Ia of various luminosity classes and at a range of ages, core-collapse SN, and galaxies. The offset in wavelength caused by redshift is a free parameter, so the output includes an estimate of the redshift of the object.

The SNID routine is based on the cross-correlation techniques described by Tonry and Davis [290]. The input spectrum and the template spectra are binned onto a common logarithmic wavelength scale, such that a redshift corresponds to a uniform shift in $\ln \lambda$. The pseudo-continua are removed with a spline fit that effectively discards all color information, so the comparison only considers the relative shape of the spectral features. A bandpass filter is applied to the spectra to remove low-frequency residuals left over from the pseudo-continuum subtraction and high-frequency noise components. The input spectrum is cross-correlated with each of the template spectra in Fourier space, and a fourth-order polynomial is fit to the highest peak in the resulting cross-correlation function. The center of this fit corresponds to the shift (δ) in $\ln \lambda$ between the input spectrum and the zero-redshift template, and hence to the redshift of the input spectrum. After this initial identification of the redshift, portions of the template and supernova spectra that do not overlap at this redshift are masked out and the cross-correlation process is repeated. Again, in this refined correlation, a fourth-order polynomial is fit to the highest peak in the resulting cross-correlation function. The ratio of the peak height h to the antisymmetric part of the correlation function about $\ln \lambda = \delta$ gives the error associated with the output

SNID redshift:

$$r = \frac{h}{2\sigma_{\text{anti}}}, \quad (\text{A.1})$$

where σ_{anti} is the root-mean-square (rms) of the antisymmetric part of the cross-correlation function; this is normalized such that $h = 1$ at zero lag for a perfect spectrum-template match. Thus, r will be small ($\sim 1 - 2$) for a non-significant correlation peak, and large (≥ 5) for a good correlation, as h will be a significant fraction of 1 and σ_{anti} will be small. The above r -value is further weighted by the overlap (“*lap*”) in $\ln \lambda$ space between the input spectrum and a given template. For a typical wavelength range of our optical spectra, say $4000 \leq \lambda \leq 9000 \text{ \AA}$, the maximum value of this overlap is $lap_{\text{max}} = \ln(9000/4000) \approx 0.8$. We thus consider a redshift output by SNID as “good” when

$$r \times lap \geq 5, \quad (\text{A.2})$$

and “poor” otherwise. The error in the redshift found by SNID is taken to be the standard deviation of the template redshifts with the five highest $r \times lap$ values. The phase of the input spectrum is assumed equal to that of the best-fit template, i.e., the one with the biggest $r \times lap$ value. Clearly a more thorough error analysis is needed to investigate the true statistical significance of the $r \times lap$ parameter; this will be done by Blondin et al. (in prep). For a subset of the objects ($\lesssim 10\%$), the SNID comparison is not optimal. This may be the result of contamination by host-galaxy light, the lack of a matching template in the SNID library, or poor S/N of the spectrum in question. All SNID comparisons are checked by eye for a qualitative judgment of the goodness of fit.

The redshift of the object can also be directly determined from the spectrum itself if narrow emission or absorption lines associated with the host galaxy are present. Occasionally, observations are set up to include the host galaxy in the spectrograph slit specifically for the purpose of obtaining a redshift. If there is a strong enough signal of a galaxy spectrum, but no clearly identifiable narrow emission or absorption lines, cross-correlation with an absorption template could be used. For the spectra that had narrow emission or absorption lines (or were cross-correlated with a template), we report the redshift to three significant digits. If the redshift determination is based solely on a comparison of the SN spectrum to a low-redshift analog, the redshift is less certain, and we only report the value to two significant digits. The uncertainty of 0.01 in redshift is fully vindicated by the results in Figure A.1.

For the objects with a more precise redshift derived from the host galaxy, we can compare the galactic redshift with the value of the redshift estimated by SNID. Figure A.1 shows that the SNID redshifts agree well with the galaxy redshifts. Tests with template spectra that have unusual line shapes or high-velocity features indicate that the derived redshift is not affected significantly, but we do include possible effects of these spectroscopic features in the errors of the derived redshifts. Thus, for objects without precise redshifts from host-galaxy spectra, the SNID redshifts can be used as reliable substitutes. In cases where SNID preferred a SN redshift significantly different from the host-galaxy redshift,

we classified the SN by forcing its redshift to equal that of the host galaxy. The only object where this was necessary is b004 (see below).

A.5 Results

The results of our spectroscopic observations during the first two years of the ESSENCE program are summarized in Table A.1. There are 46 SN Ia (and 6 additional likely SN Ia), along with 5 core-collapse SN. Note also that there were 54 transients in the first two years that were not observed spectroscopically, so the yield of SN Ia is 52 out of 120 objects. Through the target selection methods described in Section A.2, we were able to prioritize the more likely candidates, but many of these were not observed simply because of the lack of sufficient spectroscopic resources. This became more of an issue toward the end of Year Two, when good weather and increasingly efficient detection algorithms increased the number of transients discovered.

The goal of the ESSENCE project is to find ~ 200 SN Ia over the redshift range $0.2 \lesssim z \lesssim 0.8$. In Figure A.2, we show the actual distribution in redshift of the SN Ia from the ESSENCE project that are spectroscopically confirmed. There are SN over most of the targeted redshift range, although there are relatively fewer at the high end ($z \gtrsim 0.6$). A significant fraction of the signal of w is accessible at $z \approx 0.5$ [201], but a goal for the last three years of the program is to ensure that the SN Ia observed spectroscopically are distributed optimally over our targeted redshift range. This highlights the importance of the 8-10 m telescopes such as Gemini, the VLT, and Keck that are critical to spectroscopy of the faint objects at the high-redshift end of our range.

Both SNID and the spectral-feature aging method described in Section A.4 give an indication of the age of the SN Ia. Light curves will provide a more precise measure of the age of the SN at the time of the spectroscopy, but an estimate of the epoch of the spectrum to within a few days is possible from the spectral features alone. Figure A.3 shows the distribution in age (relative to maximum brightness) at the time of spectroscopy (not discovery, as spectra are often taken up to several days after discovery). In the 15 cases¹⁸ where we have spectra of the same SN Ia at multiple epochs, the relative ages are consistent with the times of the spectroscopic exposures (also considering the effects of cosmological time dilation and probable errors of the fits of $\sim \pm 3$ days). There is one exception to this consistency (b027), but at later epochs when the uncertainty in the estimated spectroscopic age increases as a result of slower spectral evolution.

Table A.2 gives all ESSENCE targets that were selected for spectroscopic identification. The results for these first two years include 52 SN Ia or likely SN Ia (Figures 4-10), 4 SN II (Figure A.11), 1 SN Ib/c (Figure A.11), 12 AGNs (Figures 12 and 13), 4 possibly variable stellar objects (Figure A.14), 19 galaxies (Figures 15 and 16), and 16 objects of unknown classification (Figures 17 and 18). There were 10 objects for which we pointed the telescope

¹⁸These are b008, b010, b013, b020, b022, b023, b027, c003, c012, c015, d086, d093, e029, e108, and f076.

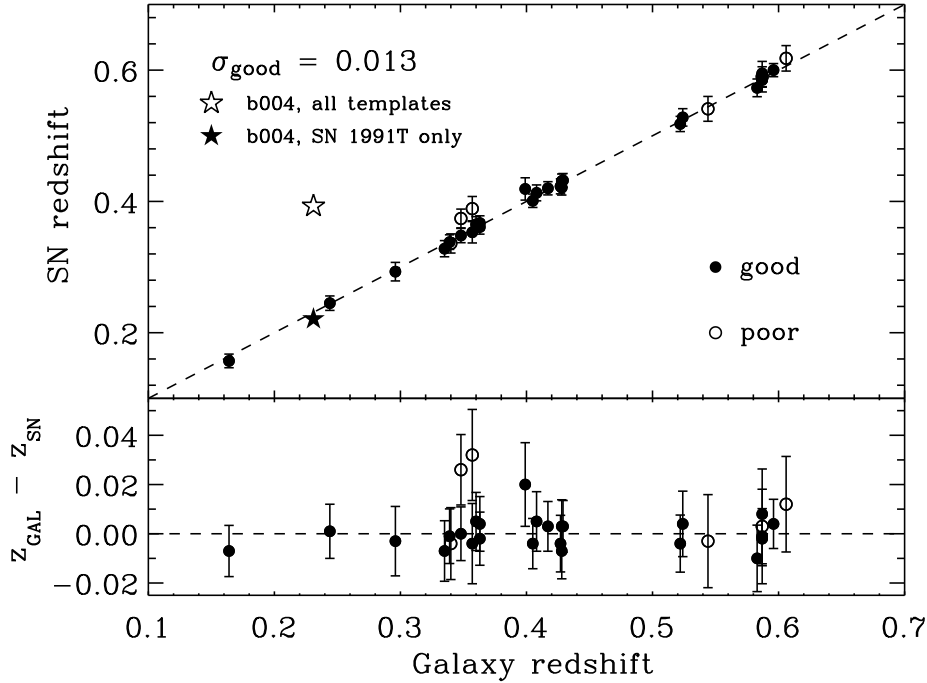


Figure A.1: Comparison of redshifts as determined by SNID and from narrow emission or absorption lines in the host-galaxy spectrum. Grades for the fits in SNID are described in the text and the good fits (*solid circles*) are shown as well as the poor fits (*open circles*). The dispersion around one-to-one correspondence of the redshifts for the good data is excellent, with $\sigma = 0.013$. Errors include 0.01 in z added in quadrature to account for potential effects on the cross-correlation related to unusual velocity features in the spectra. There is one outlier (b004) for which the redshift determination using SNID is highly degenerate, as it is likely to be a peculiar SN Ia (see text); we do not show b004 in the residual plot for the sake of clarity. Note that the mean residual is $\sim 10^{-4} \ll \sigma_{\text{good}}$, which shows that there are no systematic effects associated with the use of SNID in determining the SN redshift.

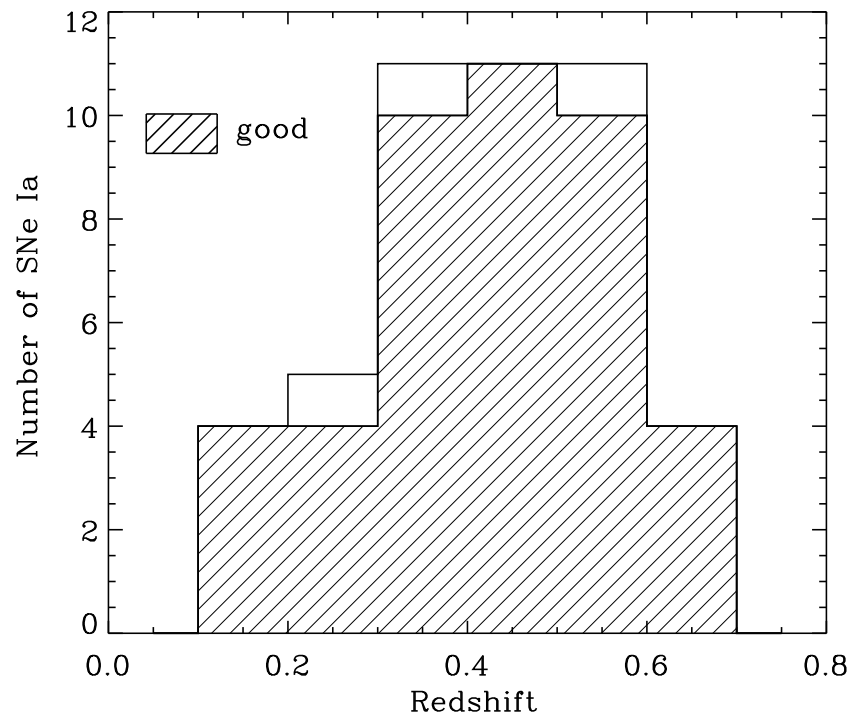


Figure A.2: Redshift distribution of definite, spectroscopically identified SN Ia from the first two years of the ESSENCE project. The SN for which the SNID fit is good (see text) are indicated by the cross-hatched area, while those that were poor fits are indicated by the blank spaces.

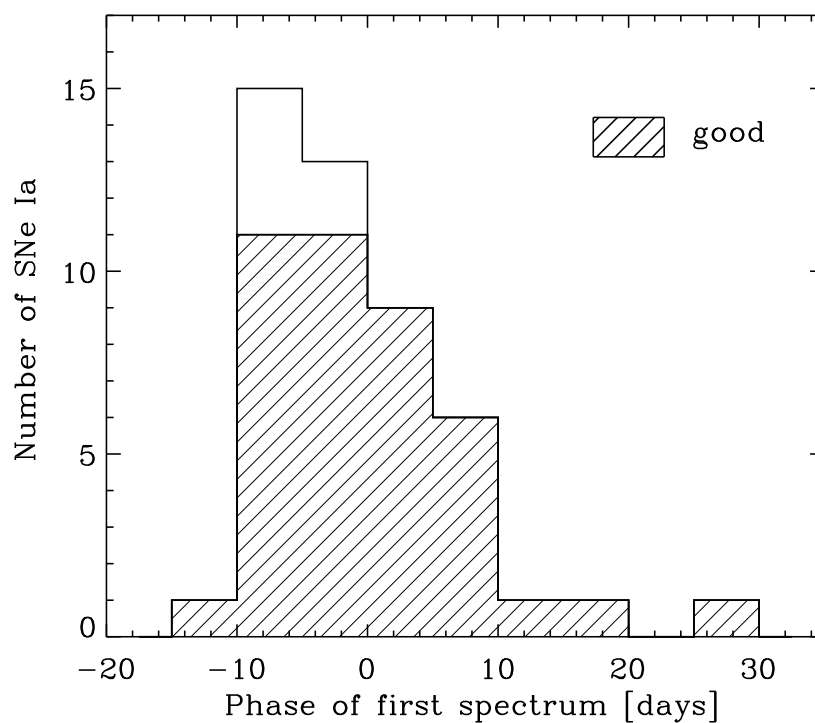


Figure A.3: Age distribution (relative to maximum brightness) of definite, spectroscopically identified SN Ia from the first two years of the ESSENCE project. Ages are determined from spectroscopic features alone. The SN for which the SNID fit is good (see text) are indicated by the cross-hatched area, while those that were poor fits are indicated by the blank spaces. For objects with multiple epochs of spectroscopy, this figure only reflects the first spectrum.

at the target and did not get a spectrum, either because of poor sky conditions or the target was actually a solar-system object and had moved out of the field.

No attempt has been made to remove host-galaxy contamination for any object presented in Figures 4-11. The amount of galaxy light is significant for some objects (e.g., f221 in Figure 8). In addition, no extinction corrections have been applied, either for Galactic reddening or extinction in the host galaxy. Given the Galactic latitudes of the ESSENCE fields (Smith et al., in prep) and our preference for targets well separated from the host galaxy, the effects of extinction are likely to be minimal (Blondin et al., in prep; Foley et al., in prep).

For each SN Ia in Figures 4-10, the best match low-redshift comparison spectrum as determined using SNID is included (the low-redshift SN is listed in Table A.2). In general, the high-redshift SN Ia look very similar to those at low redshift, implying that there are no significant evolutionary effects. Future papers will deal in much greater detail with the comparison with low-redshift SN Ia, as well as removal of host-galaxy contamination and the effects of extinction ([26]; Foley et al., in prep).

While most of the high-redshift SN Ia appear to be normal, there are some examples of peculiar SN Ia. Both b004 (SN 2002iv; Figure 4) and d083 (SN 2003jn; Figure 5) show strong similarities with SN 1991T, an overluminous Type Ia SN [81, 232]. Given the high rate of peculiar SN Ia at low redshift [176], we would expect to find such objects in a high-redshift sample.

We note that in Figures 4-10, there are several examples of high-redshift SN Ia from the ESSENCE sample for which the low-redshift template appears to be a poor match. Examples include d086 (2003-10-27), b008 (2002-11-06), e149, and b022 (2002-12-05). The most likely explanation for this is that the templates included in SNID do not cover the complete range of possibilities, although problems with the spectrum (e.g., poor S/N or sky subtraction) may also play a role. Rather than perform a non-objective search for the best match, we leave these as examples of the current limitations of SNID. We plan to expand the SNID templates to eliminate such occurrences in the future.

Two unusual cases in the sample of SN Ia spectra are e315 (SN 2003ku) and b004 (SN 2002iv). They are the only SN for which the redshift determination in SNID was ambiguous. For e315, if we assume that it is a SN Ia, then the best-fit redshift is 0.79, but a fit at a redshift of 0.41 is only marginally worse. All other SN Ia spectra in the ESSENCE sample had redshifts determined by SNID that were unambiguous. If we rely on the spectrum alone, the SNID result of $z = 0.79$ is what we would choose, and so we report it in this paper. Analysis presented by Krisciunas et al. [156] shows that neither of the redshifts suggested by SNID gives a very satisfactory fit to the photometry. In the case of b004, the SNID result is $z = 0.39$, while the fit when $z = 0.231$, known from galaxy features, is almost as good. As b004 is similar to SN 1991T (see above), the lack of good templates in SNID may be the source of this discrepancy. Correlation of b004 with SN 1991T templates yields a redshift of $z = 0.22$, close to the value derived from the host galaxy. This highlights some of the perils of identifying optical transients with low S/N spectra. Sometimes the spectrum alone is not enough; a consideration of all the information (spectrum, light curve, host galaxy, etc.) is necessary to draw the appropriate

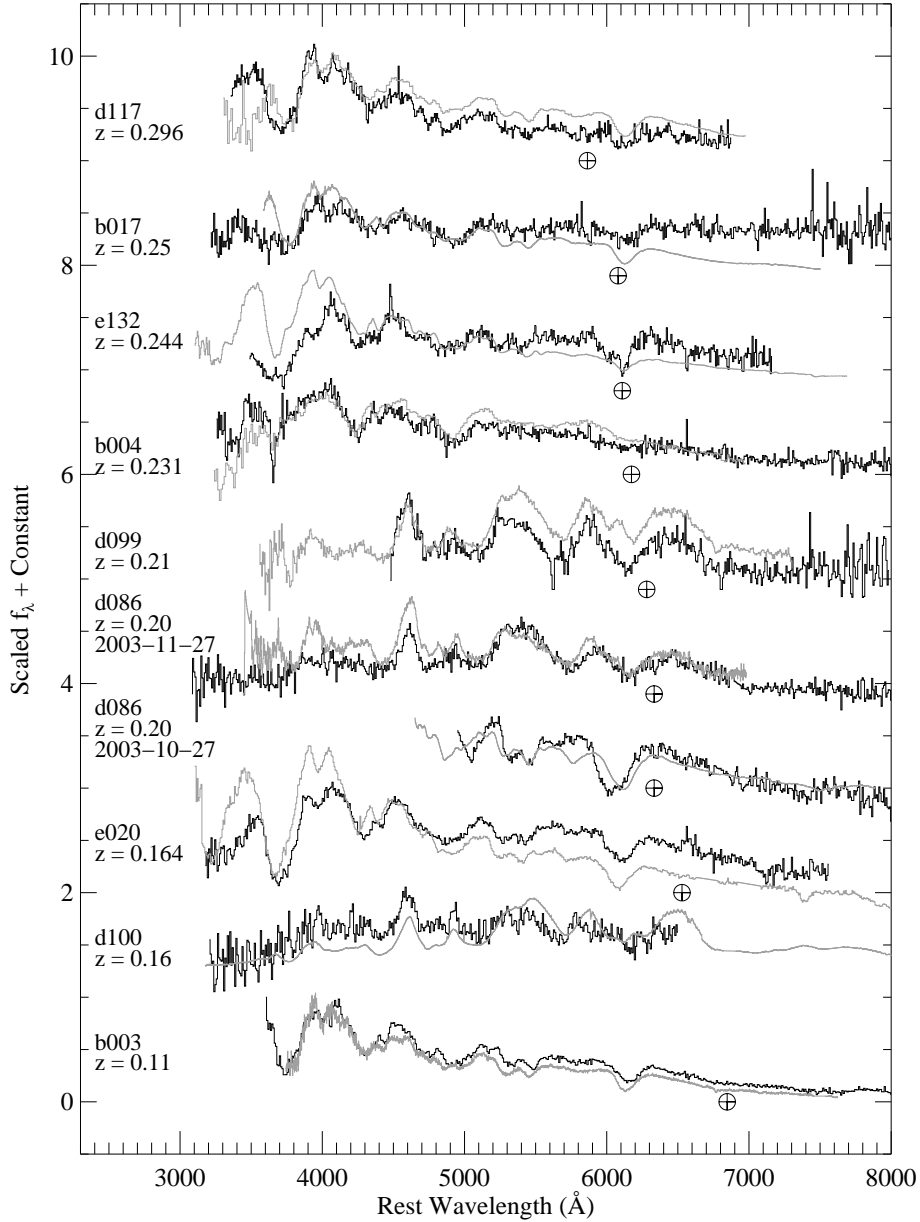


Figure A.4: Rest-wavelength spectra of SN Ia (or likely SN Ia) from the first two years of the ESSENCE project in order of increasing redshift. Each ESSENCE SN (*black line*) is overplotted by a low-redshift SN Ia (*gray line*) for comparison. The low-redshift SN Ia used for comparison is listed in Table A.2. In addition, each spectrum is labeled with the ESSENCE identification number and the deduced redshift. Spectra of the uncertain SN Ia are indicated with an asterisk (*). The deredshifted location of the A-band atmospheric absorption feature is indicated with a telluric symbol. We usually, but not always, were able to remove this feature through division by the spectrum of a featureless standard star. The flux scale is f_λ with arbitrary additive offsets between the spectra.

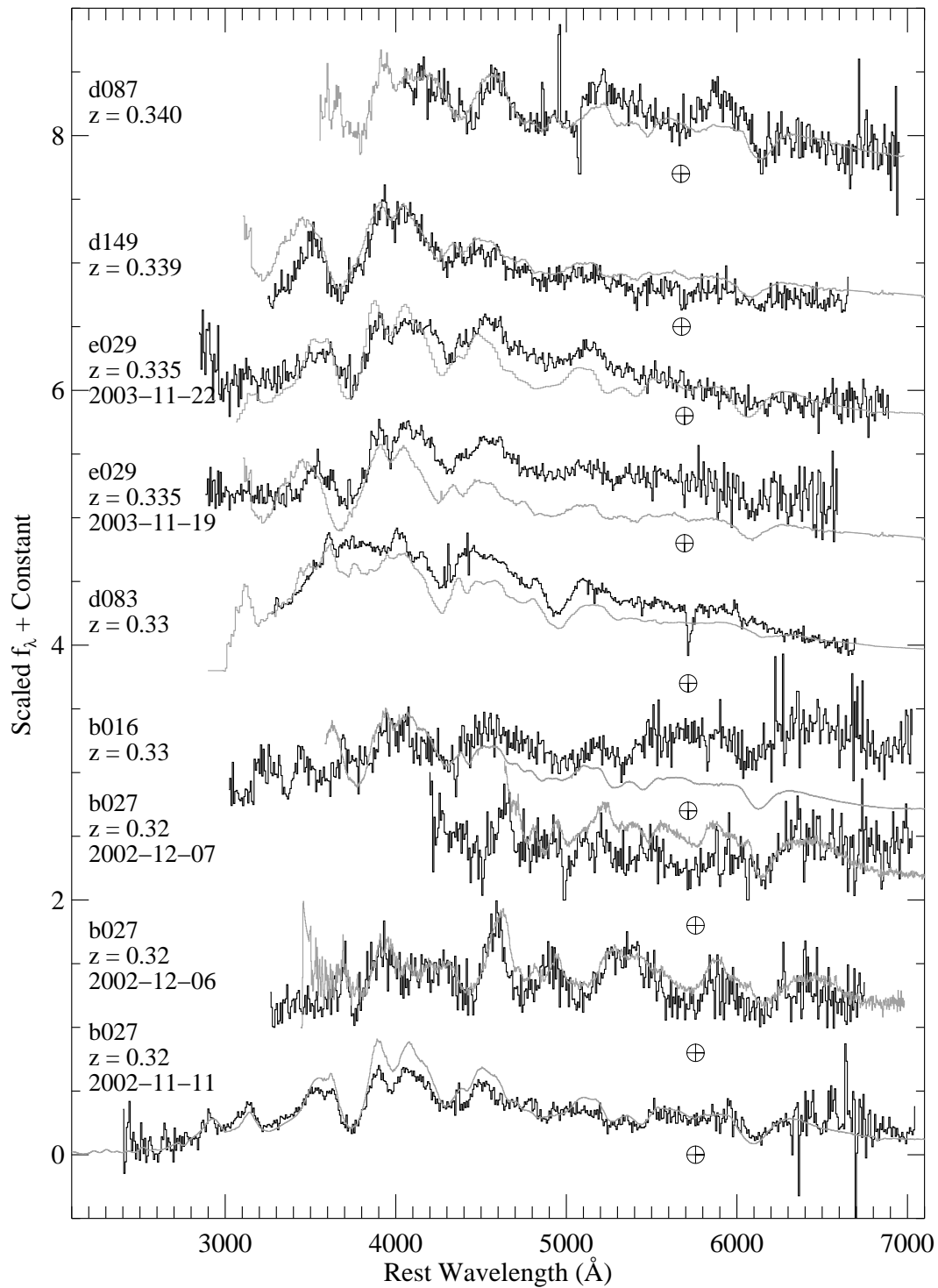


Figure A.5: Rest-wavelength spectra of ESSENCE SN Ia as in Figure 4.

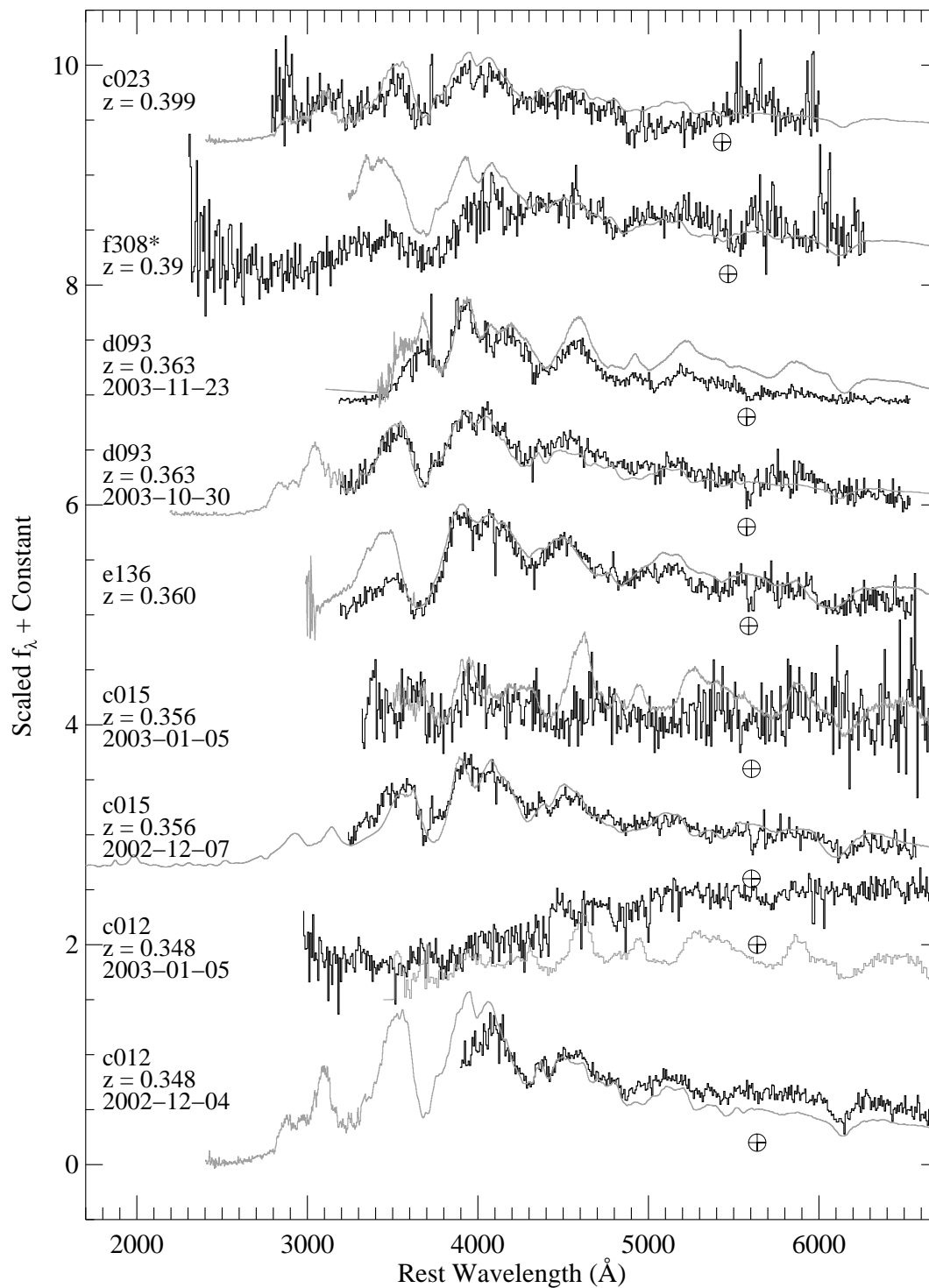


Figure A.6: Rest-wavelength spectra of ESSENCE SN Ia as in Figure 4. The 2003-01-03 spectrum of c012 is a weighted average of the Clay and GMOS spectra.

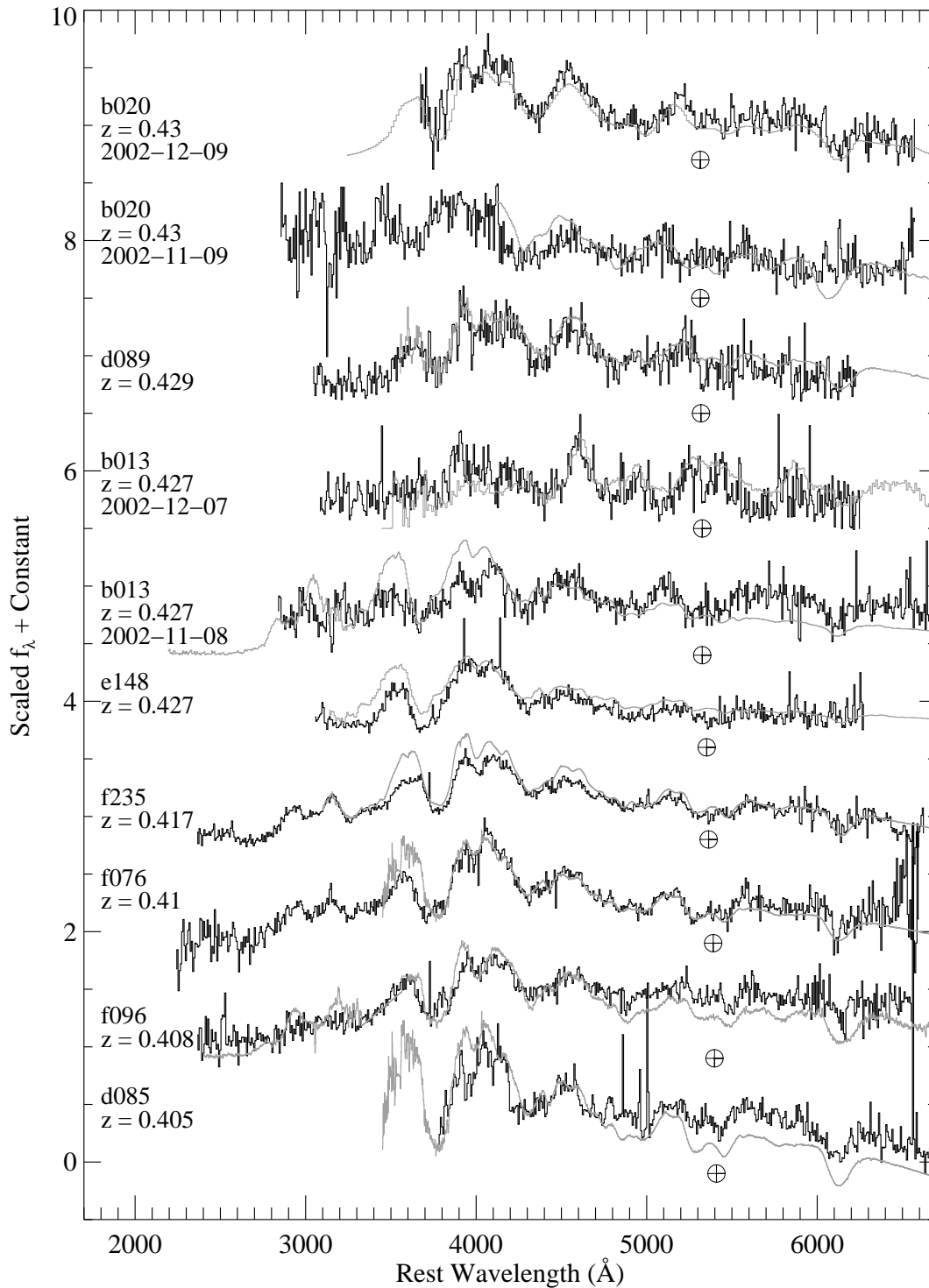


Figure A.7: Rest-wavelength spectra of ESSENCE SN Ia as in Figure 4. The spectrum of f076 is a weighted average of the MMT and KI/LRIS spectra.

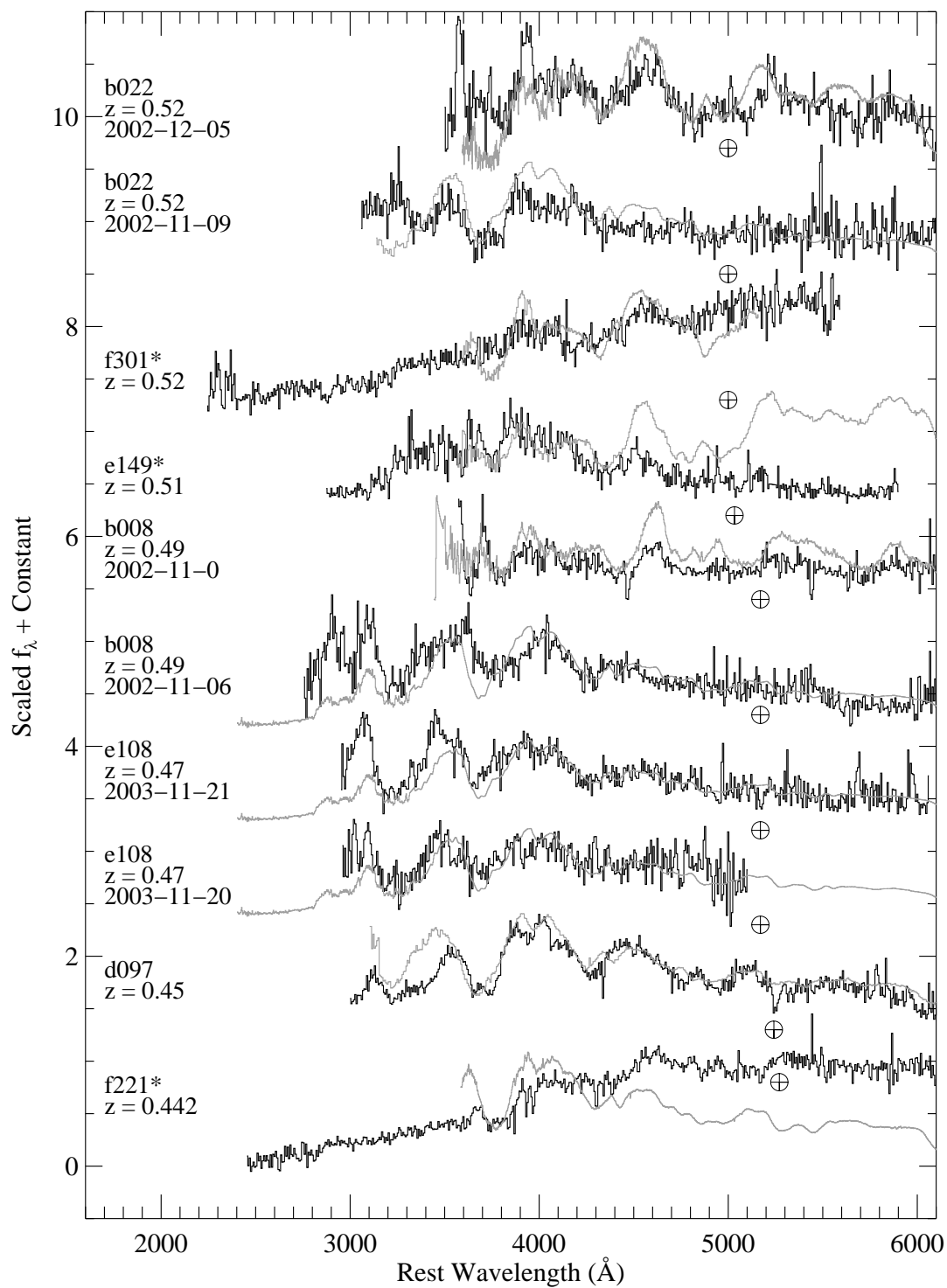


Figure A.8: Rest-wavelength spectra of ESSENCE SN Ia as in Figure 4.

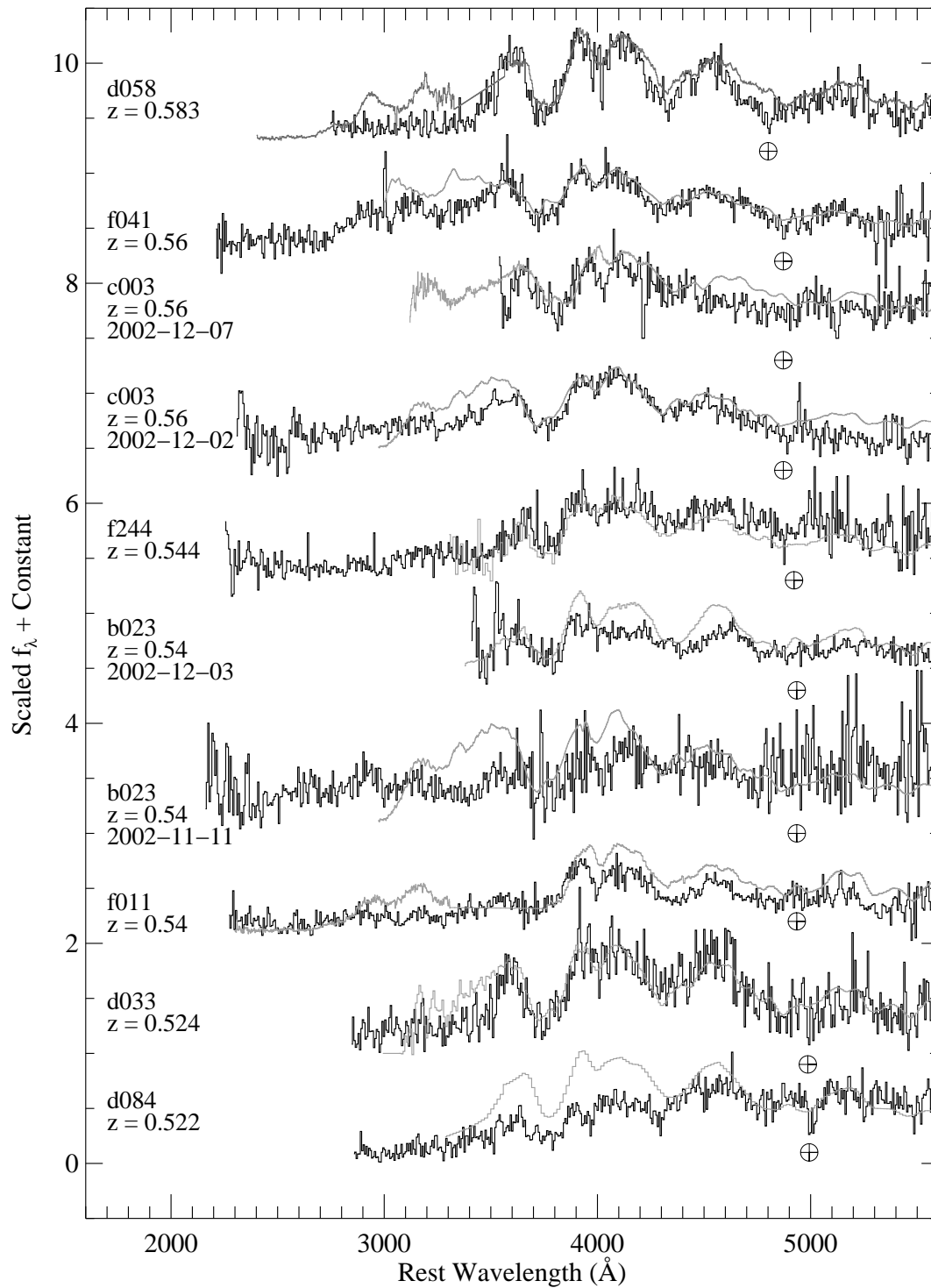


Figure A.9: Rest-wavelength spectra of ESSENCE SN Ia as in Figure 4.

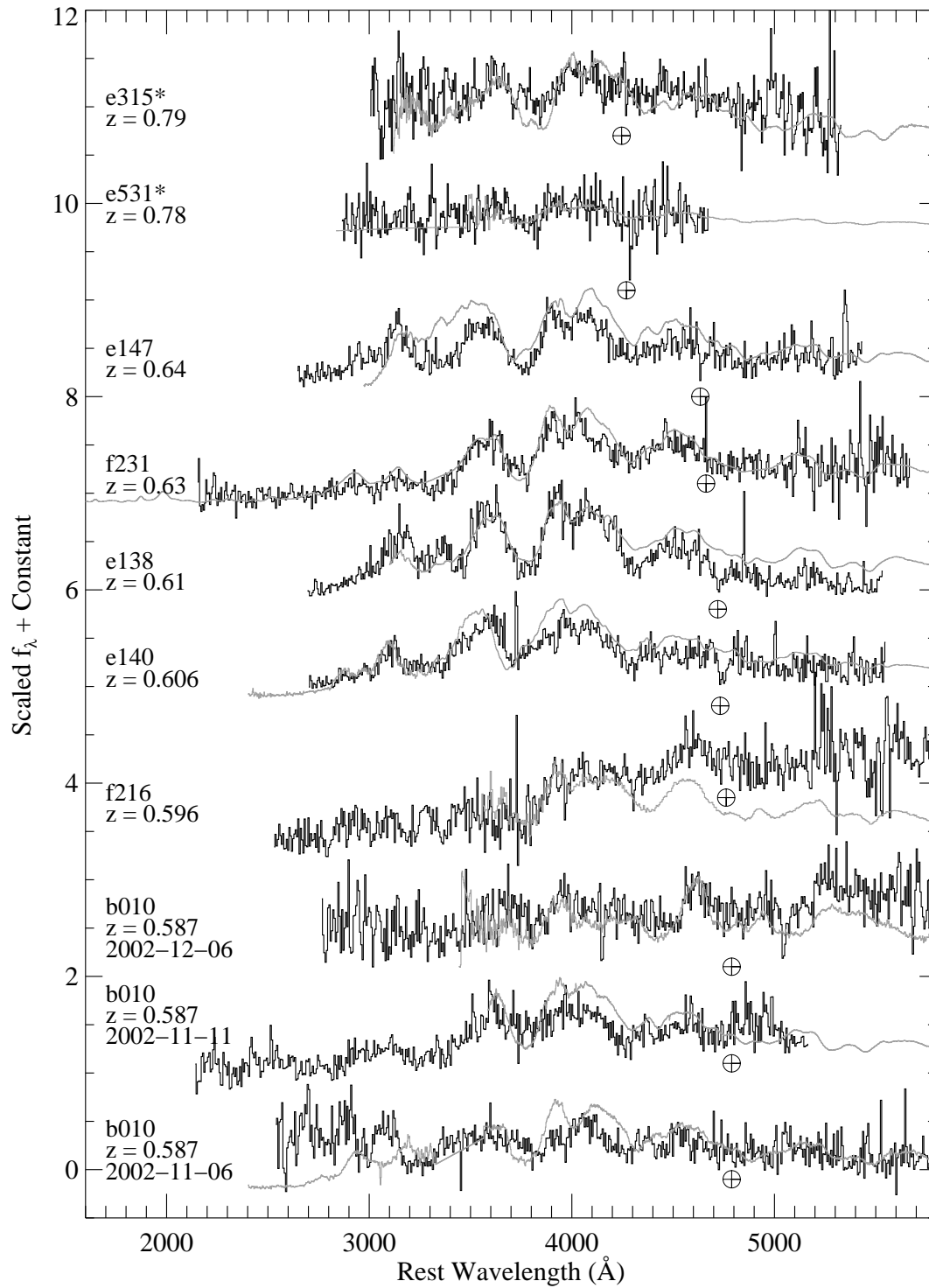


Figure A.10: Rest-wavelength spectra of ESSENCE SN Ia as in Figure 4. The GMOS and VLT spectra of b010 have been combined.

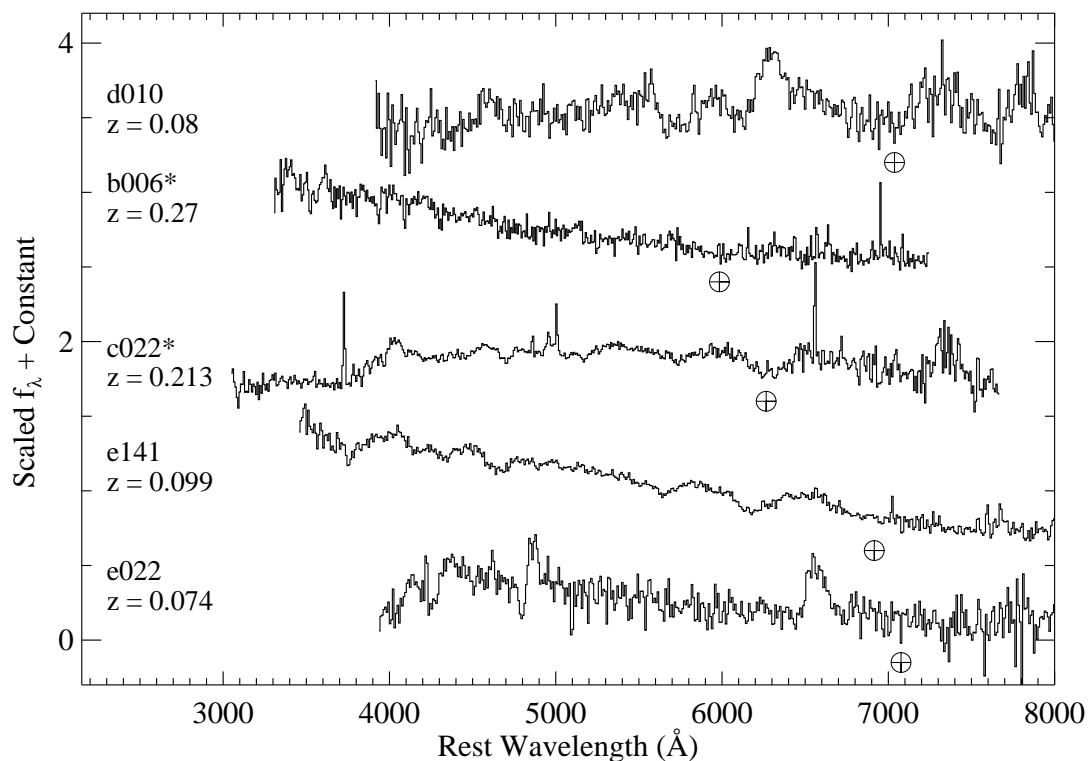


Figure A.11: Spectra of SN II and one SN Ib/c from the first two years of the ESSENCE project. Each spectrum is labeled with the ESSENCE identification number and the deduced redshift. Spectra of uncertain SN II are indicated with an asterisk (*). The deredshifted location of the A-band atmospheric absorption feature is indicated with a telluric symbol. We usually, but not always, were able to remove this feature through division by the spectrum of a featureless standard star. The flux scale is f_λ with arbitrary additive offsets between the spectra. The SN Ib/c is d010 = SN 2003jp.

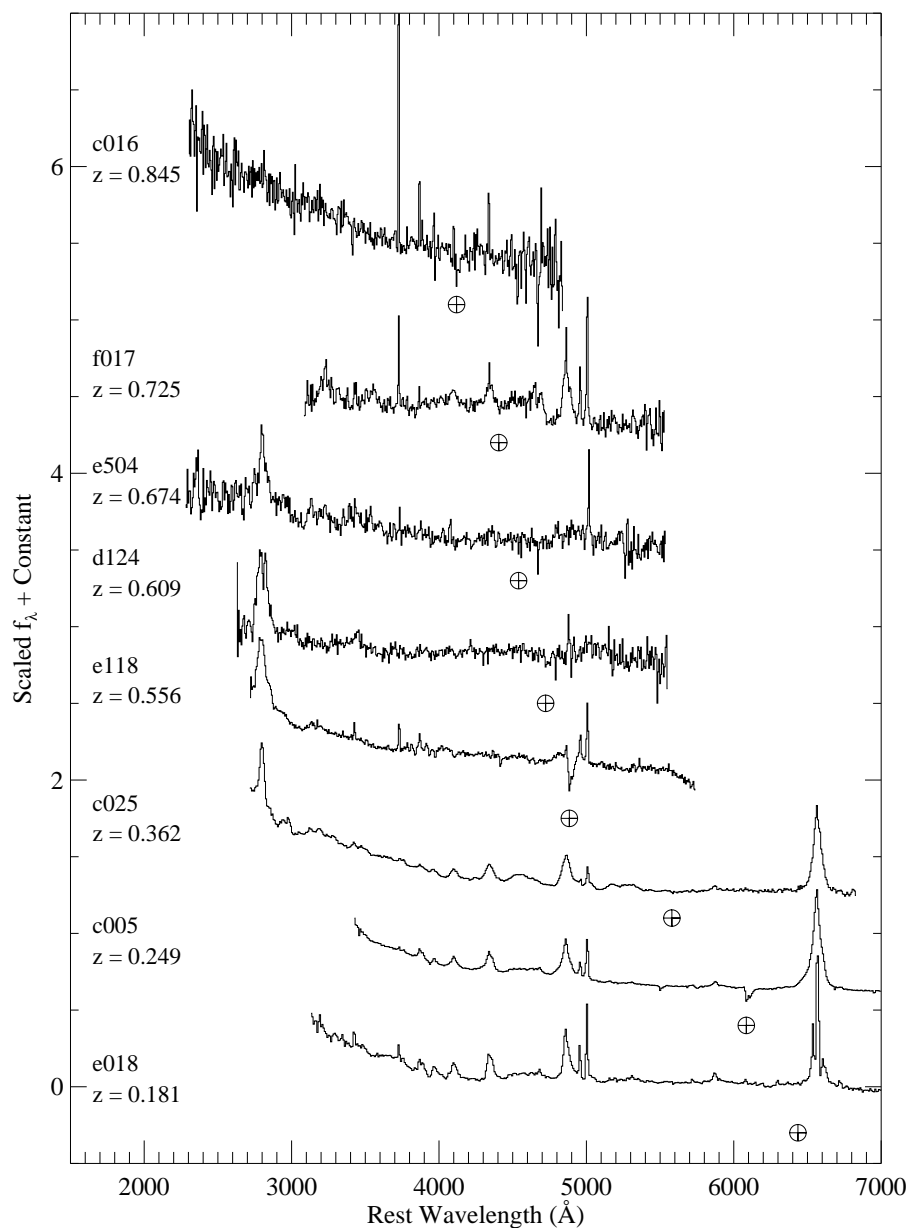


Figure A.12: Spectra of AGNs from the first two years of the ESSENCE project. Each spectrum is labeled with the ESSENCE identification number and the deduced redshift. The deredshifted location of the A-band atmospheric absorption feature is indicated with a telluric symbol. We usually, but not always, were able to remove this feature through division by the spectrum of a featureless standard star. The flux scale is f_λ with arbitrary additive offsets between the spectra.

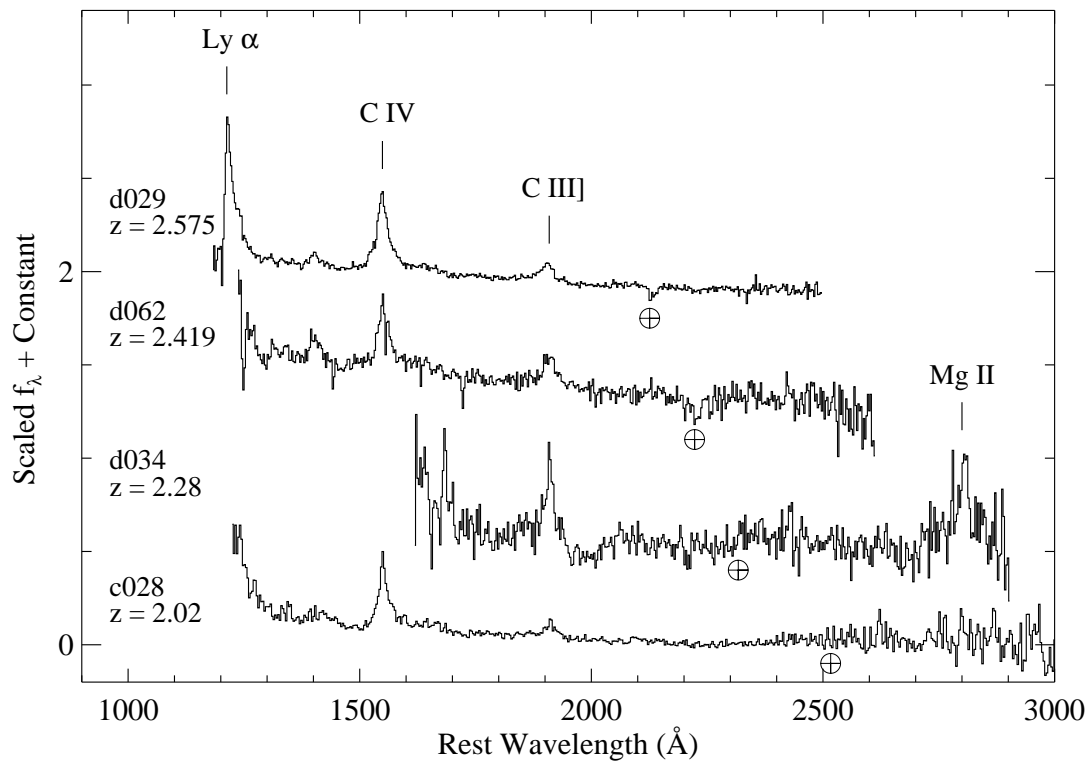


Figure A.13: Spectra of AGNs from the first two years of the ESSENCE project, as in Figure 12.

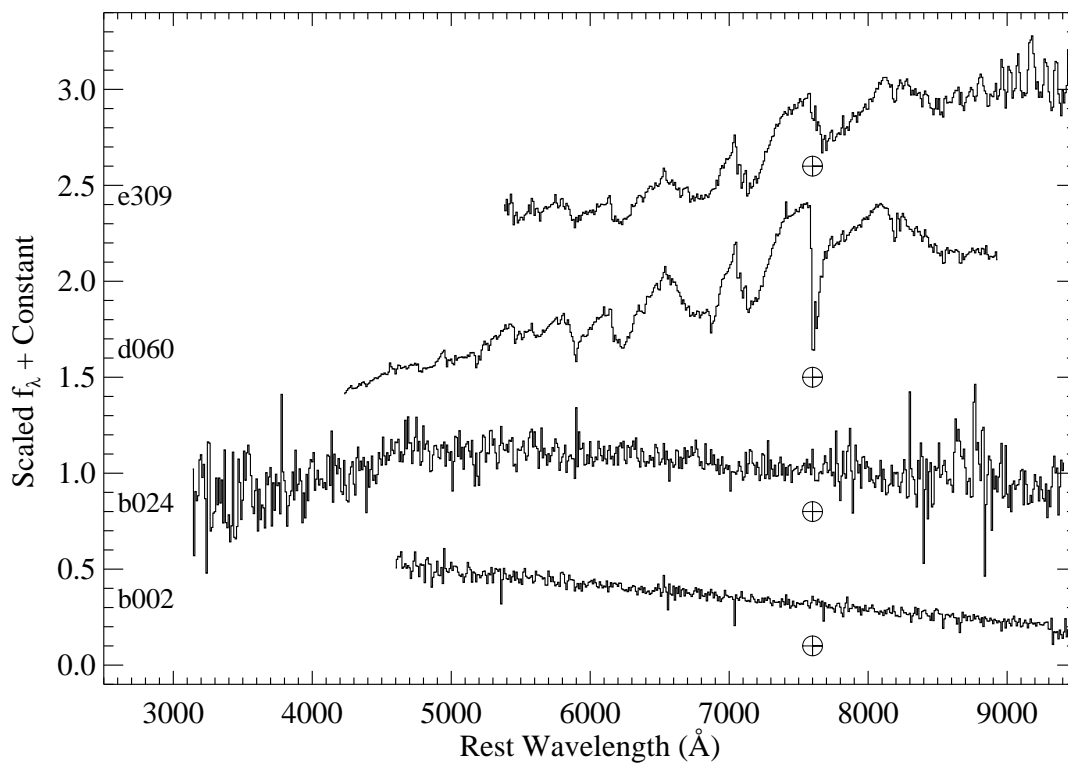


Figure A.14: Spectra of four stars from the first two years of the ESSENCE project. Each spectrum is labeled with the ESSENCE identification number. The location of the A-band atmospheric absorption feature is indicated with a telluric symbol. We usually, but not always, were able to remove this feature through division by the spectrum of a featureless standard star. The flux scale is f_λ with arbitrary additive offsets between the spectra.

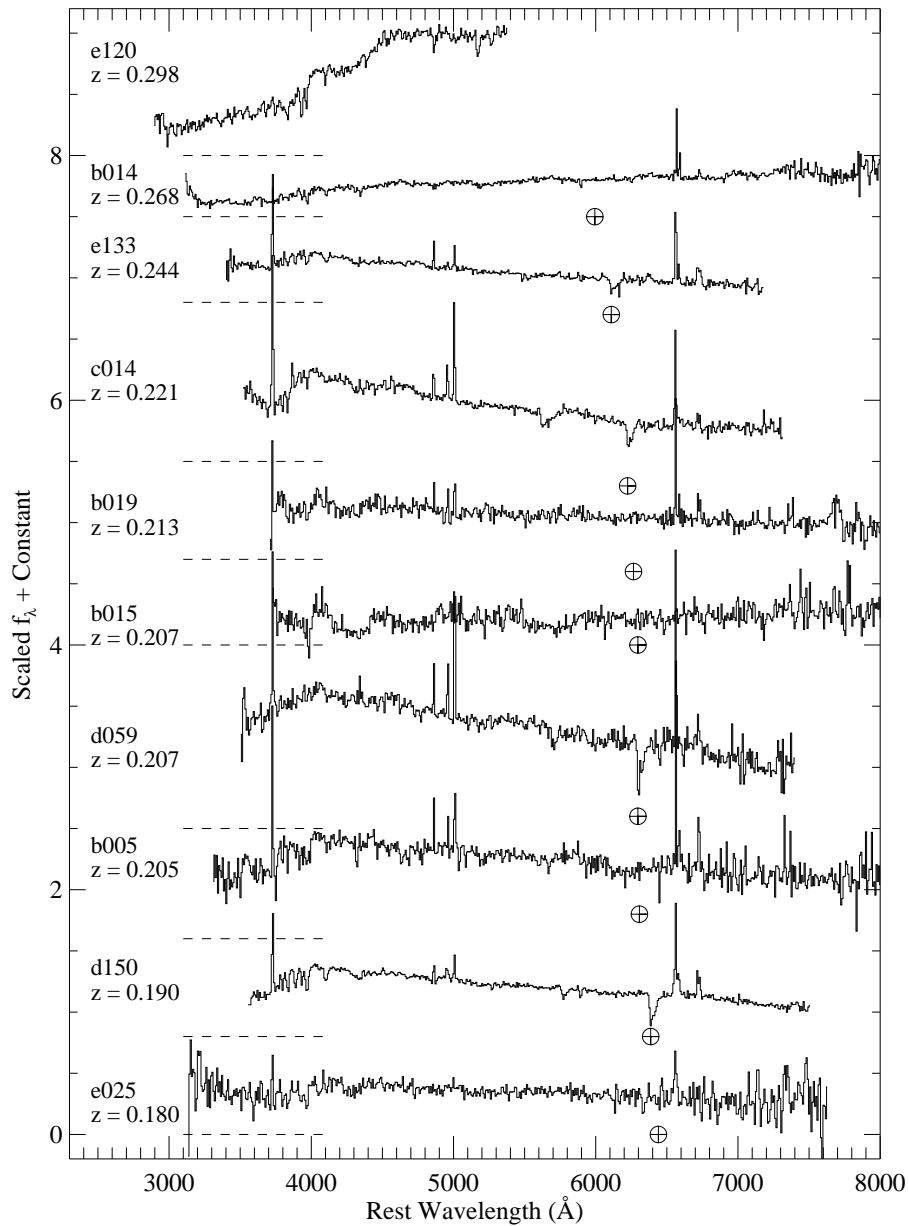


Figure A.15: Spectra of galaxies from the first two years of the ESSENCE project. Each spectrum is labeled with the ESSENCE identification number and the deduced redshift. The deredshifted location of the A-band atmospheric absorption feature is indicated with a telluric symbol. We usually, but not always, were able to remove this feature through division by the spectrum of a featureless standard star. The flux scale is f_λ with arbitrary additive offsets between the spectra. The zero-point of the flux scale for each spectrum is indicated (*dashed line*). For b005, the KII/ESI and MMT spectra have been combined. For c014, the VLT and GMOS spectra have been combined.

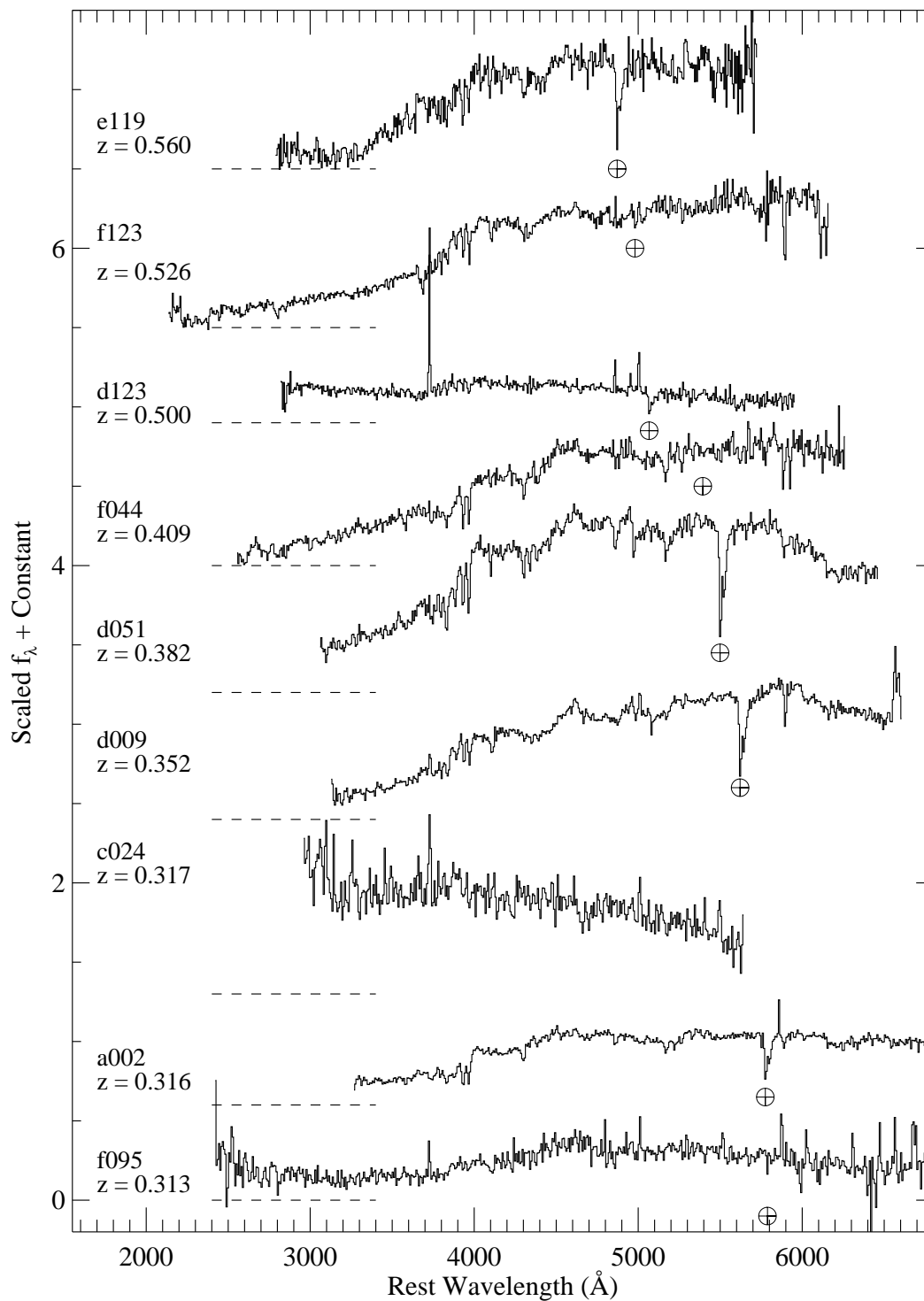


Figure A.16: Spectra of galaxies from the first two years of the ESSENCE project, as in Figure 15. For d009, the two VLT spectra have been combined.

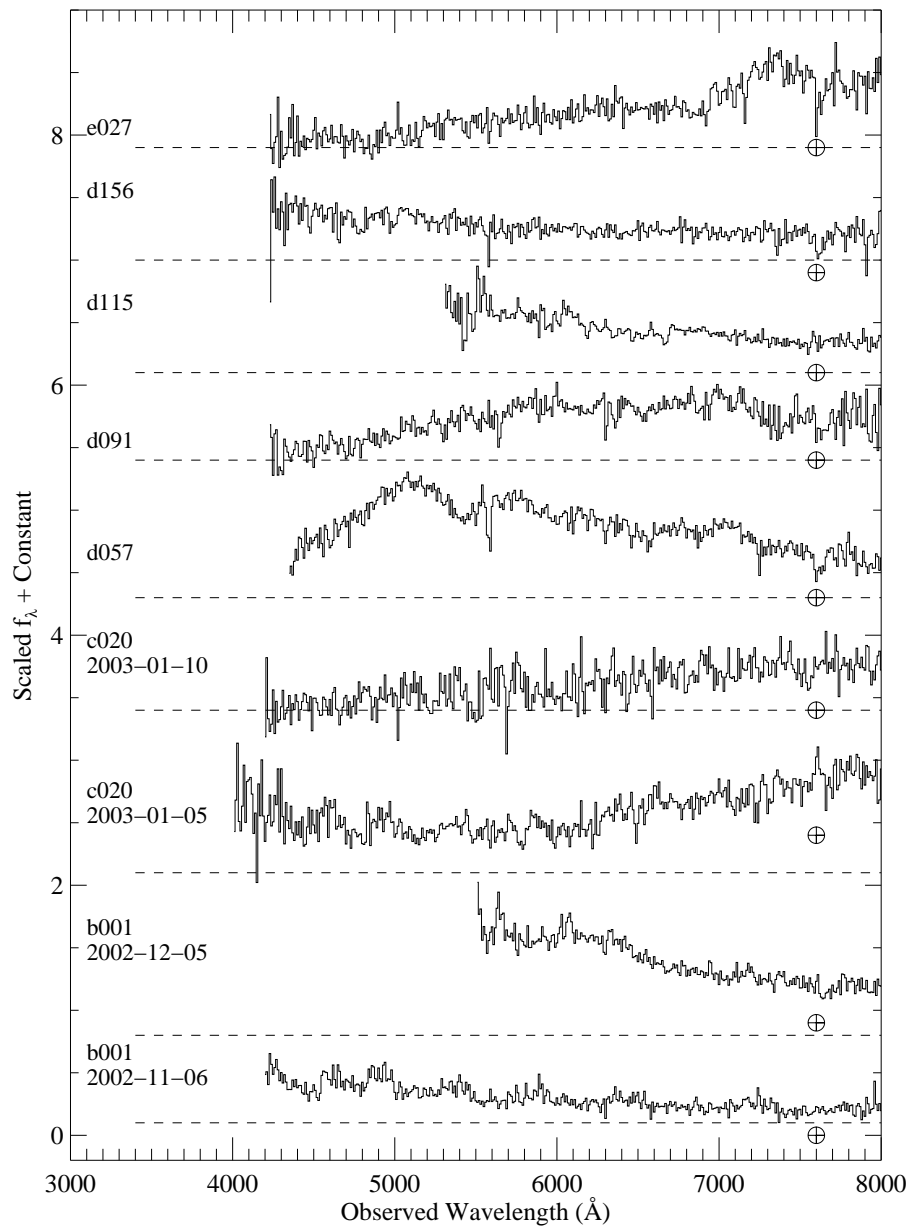


Figure A.17: Spectra of objects whose classification is uncertain from the first two years of the ESSENCE project. Each spectrum is labeled with the ESSENCE identification number. The location of the A-band atmospheric absorption feature is indicated with a telluric symbol. We usually, but not always, were able to remove this feature through division by the spectrum of a featureless standard star. The flux scale is f_λ with arbitrary additive offsets between the spectra. The zero-point of the flux scale for each spectrum is indicated (*dashed line*).

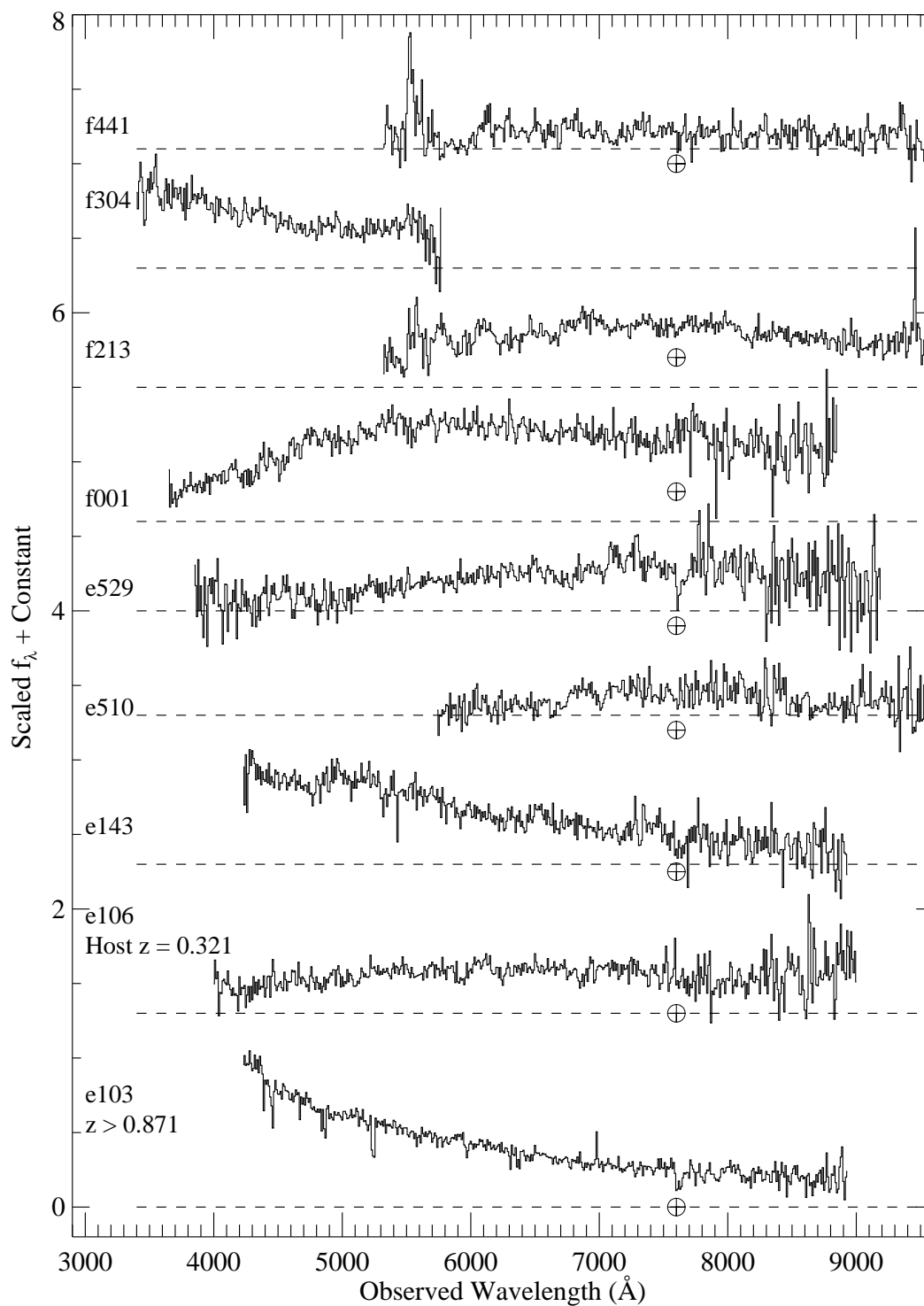


Figure A.18: Spectra of objects whose classification is uncertain from the first two years of the ESSENCE project, as in Figure 17.

conclusion.

In Figure 11, we show only spectra of objects that can be definitively identified as core-collapse SN. It is likely that some of the objects that we classify as unknown (Figures 17 and 18) are also core-collapse events. Early spectra of core-collapse SN often show featureless blue continua, but such a spectrum could result from some other kind of object, such as an AGN. Without a redshift or identifiable line features, we could not arbitrarily classify all objects with blue continua as core-collapse SN. There are fewer core-collapse events overall (compared to SN Ia) as a result of the color selection described above (avoiding relatively blue objects) and the fact that the ESSENCE survey is magnitude limited, discriminating against the intrinsically fainter core-collapse SN.

Among the unknown spectra (Figures 17 and 18), there are three spectra that require some discussion. For e106, the redshift is known because the host galaxy was also observed. The emission line appearing at the observed wavelength of 9457 Å in f213 is real. If this is H α then $z = 0.44$; if it is [O III] λ 5007, then $z = 0.89$. There is an apparent doublet absorption line in e103 at an observed wavelength of 5240 Å. We interpret this as Mg II λ 2800 at a redshift of 0.871, implying that this object has a redshift at least that high. It is likely to be a high-redshift AGN, but we do not have enough information to move it out of the category of unknown objects.

A.6 Conclusions

We have presented optical spectroscopy of the targets selected for follow-up observations from the first two years of the ESSENCE project. As the target selection process has improved, we have increased our yield of SN Ia that are needed for the primary purpose of the ESSENCE project—measuring luminosity distances to ~ 200 SN Ia over the redshift range ($0.2 \lesssim z \lesssim 0.8$). The SN Ia show strong similarities with low-redshift SN Ia, implying that there are no significant evolutionary changes in the nature of Type Ia SN and that our methods for identifying objects have been successful. This is also shown by the concordance of redshifts derived from SN spectra and those found from the host galaxy itself. Over the next three years, ESSENCE will continue to discover high-redshift SN Ia. With enough spectroscopic telescope time, we plan to be even more successful in correctly identifying Type Ia SN than we have been during the first two years.

We would like to thank the staffs of the Paranal, Gemini, Keck, Las Campanas, MMT, F. L. Whipple, and Cerro Tololo Inter-American Observatories for their extensive assistance and support during this project. We would also like to thank Warren Brown and Craig Heinke for assistance with the MMT observations. This work is supported primarily by NSF grants AST-0206329 and AST-0443378. In addition, A.V.F. is grateful for the support of NSF grant AST-0307894, and for a Miller Research Professorship at UC Berkeley during which part of this work was completed. C.W.S thanks the McDonnell Foundation and Harvard University for their support. A.C. acknowledges the support of CONICYT (Chile) through FONDECYT grants 1000524 and 7000524.

Table A.1: ESSENCE spectroscopy results: the first two years

Type ^a	Year 1	Year 2	Total
Ia	15	31	46
Ia?	0	6	6
II	2	2	4
Ib/c	0	1	1
AGN	4	8	12
Gal	7	12	19
star	2	2	4
N.S.	5	5	10
Unk.	2	14	16
N.A.	13	43	54
Total	50	124	174

(a) Our best guess as to classification of the object. Ia? indicates a lack of certainty in the identification as a SN Ia. N.S. indicates that the telescope was pointed to the object, but no spectrum was obtained or the exposure contained essentially no signal. Unk. represents objects for which we have spectra, but are uncertain as to their classification. N.A. indicates that a transient was found in the ESSENCE search, but no attempt to take a spectrum was made, either because it was a poor target or there were not enough spectroscopic resources available.

A. Spectroscopy of high-redshift supernovae from the ESSENCE project: the first 2 years

232

Table A.2: ESSENCE spectroscopic targets: the first two years

ESSENCE ID ^a	IAUC ID ^b	UT Date ^c	Telescope	Type ^d	z^e (Gal)	z^f (SNID)	Epoch ^g (SNID)	Template ^h	Grade ⁱ	Disc. ^j Mag.	Exp. (s)
a002.wxc1.04	...	2002-12-06.03	VLT	Gal	0.316	900
b001.wxcl.14	...	2002-11-06.27	KII/ESI	Unk	23.6	1600
b001.wxcl.14	...	2002-11-11.32	KI/LRIS	Unk	23.6	1800
b001.wxcl.14	...	2002-12-05.26	GMOS	Unk	23.6	2x1800
b002.wxhl.01	...	2002-11-01.44	KII/ESI	star	900
b003.wxhl.14	2002iu	2002-11-01.43	KII/ESI	Ia	...	0.11	2	94S	good	18.9	600
b004.wxft.06	2002iv	2002-11-02.45	KII/ESI	Ia	0.231	0.39	-4	95ac	good	20.9	1200
b005.wxdl.11	2002iw	2002-11-03.16	MMT	Gal	0.205	21.8	3x1800
b005.wxdl.11	2002iw	2002-11-06.32	KII/ESI	Gal	0.205	21.8	1800
b006.wxbl.16	2002ix	2002-11-03.10	MMT	N.S.	22.2	...
b006.wxbl.16	2002ix	2002-11-06.24	KII/ESI	II?	22.2	1800
b008.wxcl.05	2002jq	2002-11-06.29	KII/ESI	Ia	...	0.49	-8	90N	good	21.9	1800
b008.wxcl.05	2002jq	2002-12-04.27	GMOS	Ia	...	0.49	+13	89B	good	21.9	4x1800
b010.wxv2.07	2002iy	2002-11-06.39	KII/ESI	Ia	...	0.59	-1	92A	poor	21.3	1800
b010.wxv2.07	2002iy	2002-11-11.45	KI/LRIS	Ia	...	0.59	+2	94ae	good	21.3	1800
b010.wxv2.07	2002iy	2002-12-06.35	GMOS	Ia	...	0.59	+13	89B	good	21.3	5x1800
b010.wxv2.07	2002iy	2002-12-07.22	VLT	Ia	0.587	0.59	+17	95al	good	21.3	2x1800
b013.wxv2.10	2002iz	2002-11-06.45	KII/ESI	Ia	0.427	0.42	-6	90N	good	22.1	1800
b013.wxv2.10	2002iz	2002-12-06.07	VLT	Ia	0.428	0.43	+14	89B	good	22.1	1800
b014.wxv2.15	...	2002-11-06.41	KII/ESI	Gal	0.268	22.8	1800
b015.wcx1.09	...	2002-11-06.34	KII/ESI	Gal	0.207	1800
b016.wxbl.15	2002ja	2002-11-09.33	KII/ESI	Ia	...	0.33	+2	94ae	good	22.2	1200
b017.wxbl.06	2002jb	2002-11-09.31	KII/ESI	Ia	...	0.25	+2	94ae	good	21.4	1200
b019.wxdl.04	...	2002-11-09.35	KII/ESI	Gal	0.213	22.2	1200
b020.wye2.01	2002jr	2002-11-09.42	KII/ESI	Ia	...	0.43	-9	91M	poor	22.7	1800
b020.wye2.01	2002jr	2002-12-09.39	GMOS	Ia	...	0.43	+7	72E	good	22.7	2x1800
b022.wyc3.03	2002jc	2002-11-09.45	KII/ESI	Ia	...	0.52	-7	90N	poor	23.1	1800
b022.wyc3.03	2002jc	2002-12-05.39	GMOS	Ia	...	0.52	+4	96Z	good	23.1	4x1800
b023.wxu2.09	2002js	2002-11-11.57	KI/LRIS	Ia	...	0.54	-7	89B	poor	22.9	2100
b023.wxu2.09	2002js	2002-12-03.41	GMOS	Ia	...	0.54	+6	92A	good	22.9	4x1800
b024.wxc1.16	...	2002-11-11.27	KI/LRIS	VStar	21.5	1800
b025.wxa1.05	...	2002-11-11.29	KI/LRIS	N.S.	22.2	1800
b026.wxl1.05	...	2002-11-11	KI/LRIS	N.S.	22.2	...
b027.wxm1.16	2002jd	2002-11-11.45	KI/LRIS	Ia	...	0.32	+0	81B	good	22.0	3600,1800 ^k
b027.wxm1.16	2002jd	2002-12-06.07	VLT	Ia	...	0.32	+13	89B	good	22.0	1800
b027.wxm1.16	2002jd	2002-12-09.27	GMOS	Ia	...	0.32	+12	92G	poor	22.0	4x1800
c002.wxp1.14	...	2002-12-01	Clay	N.S.	22.4	...
c002.wxp1.14	...	2002-12-03	GMOS	N.S.	22.4	...
c003.wxhl.15	2002jt	2002-12-02.13	Clay	Ia	...	0.56	-7	89B	good	22.6	2x1800
c003.wxhl.15	2002jt	2002-12-07.29	GMOS	Ia	...	0.56	+0	94S	poor	22.6	3x1800
c005.wxbl.10	...	2002-12-06.05	VLT	AGN	0.249	900
c012.wxu2.16 ^l	2002ju	2002-12-03.15	Clay	Ia	0.348	0.35	-8	90N	good	21.6	2x1800
c012.wxu2.16 ^l	2002ju	2002-12-04.43	GMOS	Ia	0.348	0.35	-8	90N	good	21.6	3x1200

c012.wxu2_16	2002ju	2003-01-05.33	KII/ESI	Ia	0.348	0.35	+14	89B	poor	21.6	1800
c013.wxm1_13	...	2002-12-05	GMOS	N.S.
c014.wyb3_03	2002jv	2002-12-07.12	VLT	Gal	0.221	22.6	2x1800
c014.wyb3_03	2002jv	2003-01-04.28	GMOS	Gal	0.221	22.6	4x1800
c015.wxv2_02	2002jw	2002-12-07.18	VLT	Ia	0.357	0.35	+0	81B	good	22.8	2x1800
c015.wxv2_02	2002jw	2003-01-05.37	KII/ESI	Ia	0.356	0.38	+12	89B	poor	22.8	2400
c016.wxm1_04	...	2002-12-07.07	VLT	AGN	0.845	23.5	2x1800
c020.wxt2_15	...	2003-01-05.30	KII/ESI	Unk	0.650	23.3	2x900
c020.wxt2_15	...	2003-01-10.11	VLT	Unk	23.3	2x1800
c022.wxu2_15	...	2003-01-04.09	Clay	II?	0.213	2x1200
c023.wxm1_15	...	2003-01-03.07	Clay	Ia	0.399	0.42	-8	90N	poor	...	2x1200
c024.wxv2_05	...	2003-01-03.12	Clay	Gal	0.317	1800
c028.wxu2_16	...	2003-01-04.05	Clay	AGN	0.362	600
d009.waa6_16 ^m	...	2003-01-04.13	Clay	AGN	2.02	1800
d106.waa6_16 ^m	...	2003-10-29.11	VLT	Gal	0.352	1800
d010.waa6_16	2003jp	2003-10-31.01	VLT	Gal	0.353	1800
d029.waa6_13	...	2003-10-30.03	VLT	Ib/c	...	0.08	+35	87M ⁿ	poor	21.6	2x1800
d033.waa6_10	2003jo	2003-10-29.03	VLT	AGN	2.575	21.6	2x1800
d033.waa6_10	2003jo	2003-10-29.09	VLT	Ia	0.524	0.53	-1	89B	good	20.9	2x1800
d034.waa7_10	...	2003-11-23.05	VLT	N.S.	0.524	20.9	2x1800
d051.wcc8_2	...	2003-10-28.29	GMOS	AGN	2.28	21.4	2x1200
d057.wbb6_3	2003jk	2003-10-30.22	VLT	Gal	0.382	1800
d058.wbb6_3	2003jj	2003-10-30.15	VLT	Unk	20.9	2x1800
d059.wcc5_3	...	2003-10-31.07	VLT	Ia	0.583	0.58	-1	92A	good	23.1	2x1800
d060.wcc7_3	...	2003-10-29.17	VLT	Gal	0.207	19.2	2x1800
d062.wcc9_3	...	2003-10-30.35	VLT	M-star	1800
d083.wdd9_12	2003jn	2003-10-29.26	VLT	AGN	2.42	20.3	1800
d084.wdd9_11	2003jm	2003-10-29.29	VLT	Ia	...	0.33	-1	91T	good	20.8	1800
d085.waa5_16	2003jv	2003-10-30.19	VLT	Ia	0.522	0.52	+8	72E	good	22.9	1800
d086.waa5_3	2003ju	2003-10-28.37	GMOS	Ia	0.405	0.41	+3	94ae	good	22.2	3x1200
d086.waa5_3	2003ju	2003-10-27.06	GMOS	Ia	...	0.20	-7	89B	poor	21.6	3x600
d087.wbb5_4	2003jr	2003-11-27.10	Baade	Ia	...	0.20	+13	89B	good	21.6	3x1800
d089.wdd6_8	2003jl	2003-11-01.18	GMOS	Ia	0.340	0.34	+6	95E	good	21.9	3x600
d091.wcc1_2	...	2003-10-31.34	VLT	Ia	0.429	0.43	+6	95E	good	22.4	1800
d093.wdd5_3 ^o	2003js	2003-10-29.22	VLT	Unk	2x1800
e142.wdd5_3 ^o	2003js	2003-10-29.96	VLT	Ia	0.363	0.36	-6	90N	good	22.0	923+600
d097.wdd5_10	2003jt	2003-11-23.21	VLT	Ia	0.363	0.36	+12	95D	good	22.0	3x1200
d099.wcc2_16	2003jt	2003-10-29.32	VLT	Ia	...	0.45	-5	90O	good	22.0	1800
d100.waa7_16	2003jq	2003-11-01.23	GMOS	Ia	...	0.21	+17	95bd	good	20.9	3x600
d115.wbb6_11	...	2003-10-24.21	FLWO	Ia	...	0.16	+26	95al	good	19.8	2x1800
d117.wdd8_16	2003jw	2003-10-28.43	GMOS	Unk	20.2	1200
d123.wcc9_16	...	2003-10-30.32	VLT	Ia	0.296	0.29	-1	95E	good	22.6	1800
d124.wcc9_15	...	2003-10-30.27	VLT	Gal	0.500
d149.wcc4_11	2003jy	2003-10-31.26	VLT	AGN	0.609	20.5	1800
d150.wcc1_12	...	2003-10-31.10	VLT	Ia	0.339	0.34	-5	90O	good	22.7	1800
d156.wcc2_4	2003jx	2003-10-31.31	VLT	Gal	0.190
e018.wbb7_2	...	2003-10-31.15	VLT	Unk	2x1800
e018.wbb7_2	...	2003-11-19.05	Clay	AGN	0.181	18.6	600

A. Spectroscopy of high-redshift supernovae from the ESSENCE project: the first 2 years

e020.waa6_9	2003kk	2003-11-19.11	Clay	Ia	0.164	0.16	-5	900	good	20.3	3x300
e022.wbb7_12	2003kj	2003-11-22.03	VLT	II	0.074	22.3	1800+900
e025.wdd3_15	...	2003-11-19.21	Clay	Gal	0.180	3x1200
e027.wcc7_16	...	2003-11-21.16	VLT	Unk	3x1200
e029.wbb3_15 ^P	2003kl	2003-11-19.14	Clay	Ia	0.335	0.33	-5	900	good	22.5	3x600
e121.wbb3_15 ^P	2003kl	2003-11-22.11	Clay	Ia	0.335	0.33	-1	81B	good	21.0	3x1200
e103.wbb9_2	...	2003-11-21.05	VLT	Unk	0.871	1800
e106.wbb6_11	...	2003-11-20.14	Clay	Unk	0.321	19.4	3x1200
e108.wdd8_4	2003km	2003-11-20.21	Clay	Ia	...	0.47	-8	90N	good	21.8	3x1200
e108.wdd8_4	2003km	2003-11-21.21	VLT	Ia	...	0.47	-8	90N	good	21.8	2x1800
e118.waa5_11	...	2003-11-22.03	VLT	AGN	0.556	2x1200
e119.wbb1_7	...	2003-11-23.19	VLT	Gal	0.560	1800
e120.waa5_9	...	2003-11-22.05	Clay	Gal	0.298	1200
e132.wcc1_7	2003kn	2003-11-22.08	VLT	Ia	0.244	0.24	-6	90N	good	21.3	2x1800
e133.wcc1_7	...	2003-11-22.08	VLT	Gal	0.244	2x1800
e136.wcc1_12	2003ko	2003-11-22.13	VLT	Ia	0.360	0.36	-11	94D	good	21.7	2x1800
e138.wdd4_1	2003kt	2003-11-23.10	VLT	Ia	...	0.61	+5	95D	good	22.8	3x1200
e140.wdd5_15	2003kq	2003-11-22.29	VLT	Ia	0.606	0.62	-8	90N	good	22.6	3x1200
e141.wdd7_2	...	2003-11-22.16	Clay	II	0.099	2x1200
e143.wdd7_3	...	2003-11-23.15	VLT	Unk	2x1200
e147.wdd5_9	2003kp	2003-11-22.18	VLT	Ia	...	0.64	-7	89B	good	22.1	2x1800
e148.wdd5_10	2003kr	2003-11-22.23	VLT	Ia	0.427	0.42	-7	90N	good	22.0	3x1200
e149.wdd5_10	2003ks	2003-11-23.28	VLT	Ia?	...	0.51	+12	95bd	poor	22.2	3x1200
e309.waa9_14	...	2003-11-23.32	GMOS	M-star	3x1200
e315.wbb9_3	2003ku	2003-11-24.31	GMOS	Ia?	...	0.79	+0	94S	poor	22.9	3x1200
e418.wcc2_8	...	2003-11-27	Baade	N.S.
e501.waa1_1	...	2003-11-28	Baade	N.S.
e504.waa3_4	...	2003-11-29.05	Baade	AGN	0.674	23.2	3x1800
e510.waa1_13	...	2003-11-29.08	GMOS	Unk	23.0	1800
e528.wcc5_3	...	2003-11-28	Baade	N.S.	23.4	...
e529.wcc5_3	...	2003-11-29.10	Clay	Unk	23.8	3x1800
e531.wcc1_4	2003kv	2003-11-29.14	Baade	Ia?	...	0.78	-3	95E	poor	23.4	3x1800
f001.wbb7_1	2003lg	2003-12-19.17	MMT	Unk	22.5	3x1800
f011.wcc7_12	2003lh	2003-12-21.31	KI/LRIS	Ia	...	0.54	+4	90N	good	22.7	1500
f017.wbb9_10	...	2003-12-20.33	GMOS	AGN	0.725	22.7	3x1200
f041.wbb6_8	2003le	2003-12-20.23	KI/LRIS	Ia	...	0.56	-4	94D	good	22.7	2x1200
f044.wbb8_8	...	2003-12-21.10	MMT	Gal	0.409	3x1800
f076.wbb9_01	2003lf	2003-12-21.29	KI/LRIS	Ia	...	0.41	+3	94ae	good	22.1	900
f076.wbb9_1	2003lf	2003-12-21.17	MMT	Ia	...	0.41	+4	95D	good	22.1	3x900
f095.wcc2_8	...	2003-12-20.31	KI/LRIS	Gal	0.313	21.6	3x1200
f096.waa3_3	2003ln	2003-12-21.28	KI/LRIS	Ia	0.408	0.41	-1	92A	good	22.5	1500
f116.wbb1_7	...	2003-12-20	KI/LRIS	N.S.	21.6	...
f123.wcc1_7	...	2003-12-21.34	KI/LRIS	Gal	0.526	21.6	2x1200
f213.wbb4_12	...	2003-12-19.34	GMOS	Unk	2x1200
f216.wdd4_15	2003ll	2003-12-21.44	KI/LRIS	Ia	0.596	0.60	+5	95E	good	21.6	1800
f221.wcc4_14	2003lk	2003-12-21.36	KI/LRIS	Ia?	0.442	0.45	+2	94ae	poor	22.8	1500
f231.waa1_13	2003ln	2003-12-21.25	KI/LRIS	Ia	...	0.63	+0	81B	good	22.9	1500
f235.wbb5_13	2003lj	2003-12-20.27	KI/LRIS	Ia	0.417	0.42	+5	95D	good	22.1	2x1200

f244.wd3.8	2003li	2003-12-20.42	KI/LRIS	Ia	0.544	0.54	-1	95E	poor	22.8	2x1800
f301.wd6_1	...	2003-12-21.42	KI/LRIS	Ia?	...	0.52	-3	86G	good	21.6	1500
f304.wd6_2	...	2003-12-21.39	KI/LRIS	Unk	21.6	1800
f308.wd6_10	...	2003-12-20.37	KI/LRIS	Ia?	...	0.39	-7	94D	good	21.6	3x1800
f441.wbb6_7	...	2003-12-23.25	GMOS	Unk	3x1200

^a ESSENCE internal identification. The first letter indicates the month in the observing season. This is followed by a sequential number as targets are discovered. The remaining letters and numbers show the specific ESSENCE field where the object was located (Smith et al., in prep).

^b Note that not all objects judged to be SN have official International Astronomical Union (IAU) names.

^c The UT date at the midpoint of the observation(s).

^d Our best guess as to classification of the object. Ia? indicates a lack of certainty in the identification as a SN Ia. II? indicates a lack of certainty in the identification as a SN II. Objects marked Unk are unknown. N.S. indicates that the telescope was pointed to the object, but no exposure was taken or the exposure contained no signal.

^e Redshift measured from narrow emission or absorption lines from the host galaxy.

^f Redshift measured from the SN spectrum by SNID.

^g Age of the SN relative to maximum brightness based upon comparisons with SNID templates.

^h Template spectrum in SNID that provides the best match to the observed spectrum.

ⁱ The "good" SNID fits correspond to $r \times lap \geq 5$ (see description in text).

^j Magnitude at discovery, not at time of spectroscopy.

^k As a result of problems with the LRIS spectrograph, b027 was observed for 1800 s on the blue side only, followed by a gap of a little over half an hour, then observed for 1800 s with both the blue and red sides. The time of observation listed is halfway between the midpoints of the two observations.

^l The SNID analysis was performed on the weighted combination of the GMOS and Clay spectra.

^m Objects d009 and d106 are the same, inadvertently assigned two different internal identifications.

ⁿ SN 1987M is of Type Ic [79].

^o Objects d093 and e142 are the same, inadvertently assigned two different internal identifications.

^p Objects e029 and e121 are the same, inadvertently assigned two different internal identifications.

Bibliography

- [1] Abbott, D. C. and P. S. Conti (1987). Wolf-Rayet stars. *ARA&A* **25**, 113–150.
- [2] Aguirre, A. (1999a). Intergalactic Dust and Observations of Type IA Supernovae. *ApJ* **525**, 583–593.
- [3] Aguirre, A. N. (1999b). Dust versus Cosmic Acceleration. *ApJ* **512**, L19–L22.
- [4] Aldering, G., R. Knop, and P. Nugent (2000). The Rise Times of High- and Low-Redshift Type IA Supernovae Are Consistent. *AJ* **119**, 2110–2117.
- [5] Appenzeller, I., K. Fricke, W. Furtig, W. Gassler, R. Hafner, R. Harkl, H.-J. Hess, W. Hummel, P. Jurgens, R.-P. Kudritzki, K.-H. Mantel, W. Meisl, B. Muschielok, H. Nicklas, G. Rupprecht, W. Seifert, O. Stahl, T. Szeifert, and K. Tarantik (1998). Successful commissioning of FORS1 - the First Optical Instrument on the VLT. *The Messenger* **94**, 1–6.
- [6] Arnett, W. D. (1982). Type I supernovae. I - Analytic solutions for the early part of the light curve. *ApJ* **253**, 785–797.
- [7] Arnett, W. D., D. Branch, and J. C. Wheeler (1985). Hubble's constant and exploding carbon-oxygen white dwarf models for Type I supernovae. *Nature* **314**, 337–+.
- [8] Avila, G., G. Rupprecht, and J. M. Beckers (1997). Atmospheric dispersion correction for the FORS Focal Reducers at the ESO VLT. In *Proc. SPIE Vol. 2871, p. 1135-1143, Optical Telescopes of Today and Tomorrow, Arne L. Ardeberg; Ed.*, pp. 1135–1143.
- [9] Baade, W. and F. Zwicky (1934). Cosmic Rays from Super-novae. *Proceedings of the National Academy of Science* **20**, 259–263.
- [10] Barbon, R., S. Benetti, L. Rosino, E. Cappellaro, and M. Turatto (1990). Type IA supernova 1989B in NGC 3627. *A&A* **237**, 79–90.
- [11] Baron, E., P. H. Hauschildt, P. Nugent, and D. Branch (1996). Non-local thermodynamic equilibrium effects in modelling of supernovae near maximum light. *MNRAS* **283**, 297–315.

- [12] Baron, E., E. J. Lentz, and P. H. Hauschildt (2003). Detectability of Mixed Unburnt C+O in Type Ia Supernova Spectra. *ApJ* **588**, L29–L32.
- [13] Barris, B. J. and J. L. Tonry (2004). Redshift-independent Distances to Type Ia Supernovae. *ApJ* **613**, L21–L24.
- [14] Barris, B. J., J. L. Tonry, S. Blondin, P. Challis, R. Chornock, A. Clocchiatti, A. V. Filippenko, P. Garnavich, S. T. Holland, S. Jha, R. P. Kirshner, K. Krisciunas, B. Leibundgut, W. Li, T. Matheson, G. Miknaitis, A. G. Riess, B. P. Schmidt, R. C. Smith, J. Sollerman, J. Spyromilio, C. W. Stubbs, N. B. Suntzeff, H. Aussel, K. C. Chambers, M. S. Connelley, D. Donovan, J. P. Henry, N. Kaiser, M. C. Liu, E. L. Martín, and R. J. Wainscoat (2004). Twenty-Three High-Redshift Supernovae from the Institute for Astronomy Deep Survey: Doubling the Supernova Sample at $z > 0.7$. *ApJ* **602**, 571–594.
- [15] Barrow, J. D. (1999). Cosmologies with varying light speed. *Phys. Rev. D* **59**(4), 043515–+.
- [16] Beals, C. S. (1950). The Atmospheres of the Early Type Stars (with Plates XVII to IX). *JRASC* **44**, 221–+.
- [17] Benetti, S., E. Cappellaro, P. A. Mazzali, M. Turatto, G. Altavilla, F. Bufano, N. Elias-Rosa, R. Kotak, G. Pignata, M. Salvo, and V. Stanishev (2005). The Diversity of Type Ia Supernovae: Evidence for Systematics? *ApJ* **623**, 1011–1016.
- [18] Benetti, S., P. Meikle, M. Stehle, G. Altavilla, S. Desidera, G. Folatelli, A. Goobar, S. Mattila, J. Mendez, H. Navasardyan, A. Pastorello, F. Patat, M. Riello, P. Ruiz-Lapuente, D. Tsvetkov, M. Turatto, P. Mazzali, and W. Hillebrandt (2004). Supernova 2002bo: inadequacy of the single parameter description. *MNRAS* **348**, 261–278.
- [19] Benítez, N., A. Riess, P. Nugent, M. Dickinson, R. Chornock, and A. V. Filippenko (2002). The Magnification of SN 1997ff, the Farthest Known Supernova. *ApJ* **577**, L1–L4.
- [20] Bennett, C. L., M. Halpern, G. Hinshaw, N. Jarosik, A. Kogut, M. Limon, S. S. Meyer, L. Page, D. N. Spergel, G. S. Tucker, E. Wollack, E. L. Wright, C. Barnes, M. R. Greason, R. S. Hill, E. Komatsu, M. R. Nolta, N. Odegard, H. V. Peiris, L. Verde, and J. L. Weiland (2003). First-Year Wilkinson Microwave Anisotropy Probe (WMAP) Observations: Preliminary Maps and Basic Results. *ApJS* **148**, 1–27.
- [21] Bertola, F. (1964). The Supernovae in NGC 1073 and NGC 1058. *Annales d’Astrophysique* **27**, 319–+.
- [22] Blakeslee, J. P., Z. I. Tsvetanov, A. G. Riess, H. C. Ford, G. D. Illingworth, D. Magee, J. L. Tonry, N. Benítez, M. Clampin, G. F. Hartig, G. R. Meurer, M. Sirianni, D. R. Ardila, F. Bartko, R. Bouwens, T. Broadhurst, N. Cross, P. D. Feldman, M. Franx,

- D. A. Golimowski, C. Gronwall, R. Kimble, J. Krist, A. R. Martel, F. Menanteau, G. Miley, M. Postman, P. Rosati, W. Sparks, L.-G. Strolger, H. D. Tran, R. L. White, and W. Zheng (2003). Discovery of Two Distant Type Ia Supernovae in the Hubble Deep Field-North with the Advanced Camera for Surveys. *ApJ* **589**, 693–703.
- [23] Blandford, R. D. and R. Narayan (1992). Cosmological applications of gravitational lensing. *ARA&A* **30**, 311–358.
- [24] Blinnikov, S. I. (1996). The opacity of an expanding medium. *Astronomy Letters* **22**, 79–84.
- [25] Blondin, S. (2003). Spectroscopy of High-Redshift Type Ia Supernovae - December 2002 VLT Observations As Part of the ESSENCE Program. *Master Thesis*.
- [26] Blondin, S., L. Dessart, B. Leibundgut, D. Branch, P. Höflich, J. L. Tonry, T. Matheson, R. J. Foley, R. Chornock, A. V. Filippenko, J. Sollerman, J. Spyromilio, R. P. Kirshner, C. A. Wood-Vasey, W. M., C. Aguilera, B. Barris, A. C. Becker, P. Challis, R. Covarrubias, T. Davis, P. Garnavich, M. Hicken, S. Jha, K. Krisciunas, W. Li, A. Miceli, G. Miknaitis, G. Pignata, J. L. Prieto, A. Rest, A. G. Riess, M. E. Salvo, B. P. Schmidt, R. C. Smith, C. W. Stubbs, and N. B. Suntzeff (2005). Using line profiles to test the fraternity of Type Ia supernovae at high and low redshifts. *AJ*, *accepted (astro-ph/0510089)*.
- [27] Blondin, S., J. R. Walsh, B. Leibundgut, and G. Sainton (2005). Extracting clean supernova spectra. Towards a quantitative analysis of high-redshift Type Ia supernova spectra. *A&A* **431**, 757–771.
- [28] Bolte, M., L. Saddlemyer, C. Mendes de Oliveira, and P. Hodder (1989). Optical spectra near maximum light of the type IA supernova 1989B. *PASP* **101**, 921–924.
- [29] Branch, D. (1977). Type I supernovae and the value of the Hubble constant. *MNRAS* **179**, 401–408.
- [30] Branch, D. (1980). Synthetic Spectra of Supernovae. In *AIP Conf. Proc. 63: Supernovae Spectra*, pp. 39–+.
- [31] Branch, D. (1992). The Hubble constant from nickel radioactivity in type IA supernovae. *ApJ* **392**, 35–40.
- [32] Branch, D. (1998). Type IA Supernovae and the Hubble Constant. *ARA&A* **36**, 17–56.
- [33] Branch, D., E. Baron, N. Hall, M. Melakayil, and J. Parrent (2005). Comparative Direct Analysis of Type Ia Supernova Spectra. I. SN 1994D. *PASP* **117**, 545–552.

- [34] Branch, D., R. Buta, S. W. Falk, M. L. McCall, A. Uomoto, J. C. Wheeler, B. J. Wills, and P. G. Sutherland (1982). Interpretation of the maximum light spectrum of a Type I supernova. *ApJ* **252**, L61–L64.
- [35] Branch, D., A. Fisher, and P. Nugent (1993). On the relative frequencies of spectroscopically normal and peculiar type IA supernovae. *AJ* **106**, 2383–2391.
- [36] Branch, D., P. Garnavich, T. Matheson, E. Baron, R. C. Thomas, K. Hatano, P. Chailis, S. Jha, and R. P. Kirshner (2003). Optical Spectra of the Type Ia Supernova 1998aq. *AJ* **126**, 1489–1498.
- [37] Branch, D., C. H. Lacy, M. L. McCall, P. G. Sutherland, A. Uomoto, J. C. Wheeler, and B. J. Wills (1983). The Type I supernova 1981b in NGC 4536 - The first 100 days. *ApJ* **270**, 123–125.
- [38] Branch, D., M. Livio, L. R. Yungelson, F. R. Boffi, and E. Baron (1995). In Search of the Progenitors of Type IA Supernovae. *PASP* **107**, 1019–+.
- [39] Branch, D., W. Romanishin, and E. Baron (1996). Statistical Connections between the Properties of Type IA Supernovae and the B-V Colors of Their Parent Galaxies, and the Value of H_0 : Erratum. *ApJ* **467**, 473–+.
- [40] Branch, D. and G. A. Tammann (1992). Type IA supernovae as standard candles. *ARA&A* **30**, 359–389.
- [41] Bucher, M. and D. Spergel (1999). Is the dark matter a solid? *Phys. Rev. D* **60**(4), 043505–+.
- [42] C el erier, M.-N. (2000). Do we really see a cosmological constant in the supernovae data? *A&A* **353**, 63–71.
- [43] Caldwell, R. R., M. Kamionkowski, and N. N. Weinberg (2003). Phantom Energy: Dark Energy with $w < -1$ Causes a Cosmic Doomsday. *Physical Review Letters* **91**(7), 071301–+.
- [44] Cappellaro, E., M. Turatto, D. Y. Tsvetkov, O. S. Bartunov, C. Pollas, R. Evans, and M. Hamuy (1997). The rate of supernovae from the combined sample of five searches. *A&A* **322**, 431–441.
- [45] Carroll, S. M. (2001). The Cosmological Constant. *Living Reviews in Relativity* **4**, 1–+.
- [46] Carroll, S. M., W. H. Press, and E. L. Turner (1992). The cosmological constant. *ARA&A* **30**, 499–542.
- [47] Cassisi, S., I. J. Iben, and A. Tornambe (1998). Hydrogen-accreting Carbon-Oxygen White Dwarfs. *ApJ* **496**, 376–+.

- [48] Castor, J. I. (1970). Spectral line formation in Wolf-rayet envelopes. *MNRAS* **149**, 111–+.
- [49] Castor, J. I., D. C. Abbott, and R. I. Klein (1975). Radiation-driven winds in Of stars. *ApJ* **195**, 157–174.
- [50] Challis, P. (2002). Supernovae 2002jq-2002jx. *IAU Circ.* **8034**, 2–+.
- [51] Challis, P. (2003). Supernovae 2003kj-2003kv. *IAU Circ.* **8251**, 1–+.
- [52] Chand, H., P. Petitjean, R. Srianand, and B. Aracil (2005). Probing the time-variation of the fine-structure constant: Results based on Si IV doublets from a UVES sample. *A&A* **430**, 47–58.
- [53] Chandrasekhar, S. (1931a). The highly collapsed configurations of a stellar mass. *MNRAS* **91**, 456–+.
- [54] Chandrasekhar, S. (1931b). The Maximum Mass of Ideal White Dwarfs. *ApJ* **74**, 81–+.
- [55] Clements, D. L., D. Farrah, M. Rowan-Robinson, J. Afonso, R. Priddey, and M. Fox (2005). Cold dust in (some) high-z supernova host galaxies. *MNRAS* **363**, 229–235.
- [56] Clocchiatti, A., M. M. Phillips, N. B. Suntzeff, M. DellaValle, E. Cappellaro, M. Turatto, M. Hamuy, R. Avilés, M. Navarrete, C. Smith, E. P. Rubenstein, R. Covarrubias, P. B. Stetson, J. Maza, A. G. Riess, and C. Zanin (2000). The Luminous Type IC Supernova 1992AR at $z=0.145$. *ApJ* **529**, 661–674.
- [57] Coil, A. L., T. Matheson, A. V. Filippenko, D. C. Leonard, J. Tonry, A. G. Riess, P. Challis, A. Clocchiatti, P. M. Garnavich, C. J. Hogan, S. Jha, R. P. Kirshner, B. Leibundgut, M. M. Phillips, B. P. Schmidt, R. A. Schommer, R. C. Smith, A. M. Soderberg, J. Spyromilio, C. Stubbs, N. B. Suntzeff, and P. Woudt (2000). Optical Spectra of Type IA Supernovae at $Z=0.46$ and $Z=1.2$. *ApJ* **544**, L111–L114.
- [58] Colgate, S. A. and C. McKee (1969). Early Supernova Luminosity. *ApJ* **157**, 623–+.
- [59] Colless, M. (1999). First results from the 2dF Galaxy Redshift Survey. *Royal Society of London Philosophical Transactions Series A* **357**, 105–+.
- [60] Contardo, G., B. Leibundgut, and W. D. Vacca (2000). Epochs of maximum light and bolometric light curves of type Ia supernovae. *A&A* **359**, 876–886.
- [61] Covarrubias, R. (2003). Supernovae 2003jv, 2003jw, 2003jx, and 2003jy. *IAU Circ.* **8238**, 1–+.
- [62] Covarrubias, R., A. Alda, J. L. Prieto, P. Berlind, S. Blondin, B. Leibundgut, and T. Matheson (2003). Supernovae 2003ji-2003ju. *IAU Circ.* **8237**, 2–+.

- [63] de Lapparent, V., M. J. Geller, and J. P. Huchra (1988). The mean density and two-point correlation function for the CfA redshift survey slices. *ApJ* **332**, 44–56.
- [64] de Vaucouleurs, G. (1959). *Handbuch der Physik* **53**, 275.
- [65] Dessart, L. and D. J. Hillier (2005a). Distance determinations using type II supernovae and the expanding photosphere method. *A&A* **439**, 671–685.
- [66] Dessart, L. and D. J. Hillier (2005b). Quantitative spectroscopy of photospheric-phase type II supernovae. *A&A* **437**, 667–685.
- [67] Drenkhahn, G. and T. Richtler (1999). SN 1994D in NGC 4526: a normally bright type IA supernova. *A&A* **349**, 877–886.
- [68] Dressler, A. (2004). *A User's Manual for IMACS*.
- [69] Efstathiou, G., S. L. Bridle, A. N. Lasenby, M. P. Hobson, and R. S. Ellis (1999). Constraints on Ω_{Λ} and Ω_m from distant Type IA supernovae and cosmic microwave background anisotropies. *MNRAS* **303**, L47–L52.
- [70] Einstein, A. (1917). Kosmologische Betrachtungen zur allgemeinen Relativitätstheorie. *Sitzungsber. Königl. Preuss. Akad. Wiss. (Berlin)*.
- [71] Elias, J. H., J. A. Frogel, J. A. Hackwell, and S. E. Persson (1981). Infrared light curves of Type I supernovae. *ApJ* **251**, L13–L16.
- [72] Fabricant, D., P. Cheimets, N. Caldwell, and J. Geary (1998). The FAST Spectrograph for the Tillinghast Telescope. *PASP* **110**, 79–85.
- [73] Falco, E. E., C. D. Impey, C. S. Kochanek, J. Lehár, B. A. McLeod, H.-W. Rix, C. R. Keeton, J. A. Muñoz, and C. Y. Peng (1999). Dust and Extinction Curves in Galaxies with $z > 0$: The Interstellar Medium of Gravitational Lens Galaxies. *ApJ* **523**, 617–632.
- [74] Filippenko, A. V. (1982). The importance of atmospheric differential refraction in spectrophotometry. *PASP* **94**, 715–721.
- [75] Filippenko, A. V. (1997). Optical Spectra of Supernovae. *ARA&A* **35**, 309–355.
- [76] Filippenko, A. V. (2004). Evidence from Type Ia Supernovae for an Accelerating Universe and Dark Energy. In *Measuring and Modeling the Universe*, pp. 270–+.
- [77] Filippenko, A. V. (2005a). . In *White Dwarfs: Probes of Galactic Structure and Cosmology*, ed. E. M. Sion, H. L. Shipman, and S. Vennes (Dordrecht: Kluwer); in press (*astro-ph/0410609*).
- [78] Filippenko, A. V. (2005b). Supernovae and Their Massive Star Progenitors. In *Astronomical Society of the Pacific Conference Series*, pp. 34–+.

- [79] Filippenko, A. V., A. C. Porter, and W. L. W. Sargent (1990). The type IC (helium-poor Ib) supernova 1987M - Transition to the supernebular phase. *AJ* **100**, 1575–1587.
- [80] Filippenko, A. V., M. W. Richmond, D. Branch, M. Gaskell, W. Herbst, C. H. Ford, R. R. Treffers, T. Matheson, L. C. Ho, A. Dey, W. L. W. Sargent, T. A. Small, and W. J. M. van Breugel (1992). The subluminous, spectroscopically peculiar type IA supernova 1991bg in the elliptical galaxy NGC 4374. *AJ* **104**, 1543–1556.
- [81] Filippenko, A. V., M. W. Richmond, T. Matheson, J. C. Shields, E. M. Burbidge, R. D. Cohen, M. Dickinson, M. A. Malkan, B. Nelson, J. Pietz, D. Schlegel, P. Schmeer, H. Spinrad, C. C. Steidel, H. D. Tran, and W. Wren (1992). The peculiar Type IA SN 1991T - Detonation of a white dwarf? *ApJ* **384**, L15–L18.
- [82] Fisher, A., D. Branch, K. Hatano, and E. Baron (1999). On the spectrum and nature of the peculiar Type IA supernova 1991T. *MNRAS* **304**, 67–74.
- [83] Fisher, A., D. Branch, P. Nugent, and E. Baron (1997). Evidence for a High-velocity Carbon-rich Layer in the Type IA SN 1990N. *ApJ* **481**, L89+.
- [84] Foley, R. J., A. V. Filippenko, D. C. Leonard, A. G. Riess, P. Nugent, and S. Perlmutter (2005). A Definitive Measurement of Time Dilation in the Spectral Evolution of the Moderate-Redshift Type Ia Supernova 1997ex. *ApJ* **626**, L11–L14.
- [85] Freedman, W. L., B. F. Madore, B. K. Gibson, L. Ferrarese, D. D. Kelson, S. Sakai, J. R. Mould, R. C. Kennicutt, H. C. Ford, J. A. Graham, J. P. Huchra, S. M. G. Hughes, G. D. Illingworth, L. M. Macri, and P. B. Stetson (2001). Final Results from the Hubble Space Telescope Key Project to Measure the Hubble Constant. *ApJ* **553**, 47–72.
- [86] Freeman, K. C. (1970). On the Disks of Spiral and so Galaxies. *ApJ* **160**, 811–+.
- [87] Fried, D. L. (1965). Statistics of a Geometric Representation of Wavefront Distortion. *Optical Society of America Journal* **55**, 1427–1435.
- [88] Fried, D. L. (1975). Differential Angle of Arrival: Theory, Evaluation and Measurement Feasibility. *Radio Science* **10**, 71–76.
- [89] Friedmann, A. (1922). Über die Krümmung des Raumes. *Z. Phys.* **10**, 377–+.
- [90] Frogel, J. A., B. Gregory, K. Kawara, D. Laney, M. M. Phillips, D. Terndrup, F. Vrba, and A. E. Whitford (1987). Infrared photometry and spectroscopy of supernova 1986g in NGC 5128-Centaurus A. *ApJ* **315**, L129–L134.
- [91] Gal-Yam, A., D. Poznanski, D. Maoz, A. V. Filippenko, and R. J. Foley (2004). Photometric Identification of Young Stripped-Core Supernovae. *PASP* **116**, 597–603.
- [92] Gallagher, J., P. Garnavich, P. Berlind, S. Jha, P. Challis, and R. P. Kirshner (2004). Spectroscopic Properties of Type Ia Supernova Host Galaxies. *American Astronomical Society Meeting Abstracts* **205**, –+.

- [93] Gamow, G. (1970). *My world line: an informal autobiography*. New York, NY: Viking Press, 1970.
- [94] Garavini, G., G. Folatelli, A. Goobar, S. Nobili, G. Aldering, A. Amadon, R. Amanullah, P. Astier, C. Balland, G. Blanc, M. S. Burns, A. Conley, T. Dahlén, S. E. Deustua, R. Ellis, S. Fabbro, X. Fan, B. Frye, E. L. Gates, R. Gibbons, G. Goldhaber, B. Goldman, D. E. Groom, J. Haissinski, D. Hardin, I. M. Hook, D. A. Howell, D. Kasen, S. Kent, A. G. Kim, R. A. Knop, B. C. Lee, C. Lidman, J. Mendez, G. J. Miller, M. Moniez, A. Mourão, H. Newberg, P. E. Nugent, R. Pain, O. Perdureau, S. Perlmutter, V. Prasad, R. Quimby, J. Raux, N. Regnault, J. Rich, G. T. Richards, P. Ruiz-Lapuente, G. Sainton, B. E. Schaefer, K. Schahmaneche, E. Smith, A. L. Spadafora, V. Stanishev, N. A. Walton, L. Wang, and W. M. Wood-Vasey (2004). Spectroscopic Observations and Analysis of the Peculiar SN 1999aa. *AJ* **128**, 387–404.
- [95] Garnavich, P. M., A. Z. Bonanos, K. Krisciunas, S. Jha, R. P. Kirshner, E. M. Schlegel, P. Challis, L. M. Macri, K. Hatano, D. Branch, G. D. Bothun, and W. L. Freedman (2004). The Luminosity of SN 1999by in NGC 2841 and the Nature of “Peculiar” Type Ia Supernovae. *ApJ* **613**, 1120–1132.
- [96] Garnavich, P. M., S. Jha, P. Challis, A. Clocchiatti, A. Diercks, A. V. Filippenko, R. L. Gilliland, C. J. Hogan, R. P. Kirshner, B. Leibundgut, M. M. Phillips, D. Reiss, A. G. Riess, B. P. Schmidt, R. A. Schommer, R. C. Smith, J. Spyromilio, C. Stubbs, N. B. Suntzeff, J. Tonry, and S. M. Carroll (1998). Supernova Limits on the Cosmic Equation of State. *ApJ* **509**, 74–79.
- [97] Gerardy, C. L., P. Höflich, R. A. Fesen, G. H. Marion, K. Nomoto, R. Quimby, B. E. Schaefer, L. Wang, and J. C. Wheeler (2004). SN 2003du: Signatures of the Circumstellar Environment in a Normal Type Ia Supernova? *ApJ* **607**, 391–405.
- [98] Glazebrook, K. and J. Bland-Hawthorn (2001). Microslit Nod-Shuffle Spectroscopy: A Technique for Achieving Very High Densities of Spectra. *PASP* **113**, 197–214.
- [99] Goldhaber, G., D. E. Groom, A. Kim, G. Aldering, P. Astier, A. Conley, S. E. Deustua, R. Ellis, S. Fabbro, A. S. Fruchter, A. Goobar, I. Hook, M. Irwin, M. Kim, R. A. Knop, C. Lidman, R. McMahon, P. E. Nugent, R. Pain, N. Panagia, C. R. Pennypacker, S. Perlmutter, P. Ruiz-Lapuente, B. Schaefer, N. A. Walton, and T. York (2001). Timescale Stretch Parameterization of Type Ia Supernova B-Band Light Curves. *ApJ* **558**, 359–368.
- [100] Gomez, G., R. Lopez, and F. Sanchez (1996). The Canaris Type IA Supernovae Archive (I). *AJ* **112**, 2094–+.
- [101] Goobar, A., L. Bergström, and E. Mörtzell (2002). Measuring the properties of extragalactic dust and implications for the Hubble diagram. *A&A* **384**, 1–10.

- [102] Gutierrez, J., E. Garcia-Berro, I. J. Iben, J. Isern, J. Labay, and R. Canal (1996). The Final Evolution of ONeMg Electron-Degenerate Cores. *ApJ* **459**, 701–+.
- [103] Hamuy, M., J. Maza, P. A. Pinto, M. M. Phillips, N. B. Suntzeff, R. D. Blum, K. A. G. Olsen, D. J. Pinfield, V. D. Ivanov, T. Augusteijn, S. Brilliant, M. Chadid, J.-G. Cuby, V. Doublier, O. R. Hainaut, E. Le Floc’h, C. Lidman, M. G. Petr-Gotzens, E. Pompei, and L. Vanzì (2002a). Optical and Infrared Spectroscopy of SN 1999ee and SN 1999ex. *AJ* **124**, 417–429.
- [104] Hamuy, M., J. Maza, P. A. Pinto, M. M. Phillips, N. B. Suntzeff, R. D. Blum, K. A. G. Olsen, D. J. Pinfield, V. D. Ivanov, T. Augusteijn, S. Brilliant, M. Chadid, J.-G. Cuby, V. Doublier, O. R. Hainaut, E. Le Floc’h, C. Lidman, M. G. Petr-Gotzens, E. Pompei, and L. Vanzì (2002b). Erratum: “Optical and Infrared Spectroscopy of SN 1999ee and SN 1999ex” [[bib_query?2002AJ....124..417H](#)]. *Astron. J.* **124**, 417 (2002);/A]. *AJ* **124**, 2339–2340.
- [105] Hamuy, M., M. M. Phillips, N. B. Suntzeff, J. Maza, L. E. González, M. Roth, K. Krisciunas, N. Morrell, E. M. Green, S. E. Persson, and P. J. McCarthy (2003). An asymptotic-giant-branch star in the progenitor system of a type Ia supernova. *Nature* **424**, 651–654.
- [106] Hamuy, M., M. M. Phillips, N. B. Suntzeff, R. A. Schommer, J. Maza, A. R. Antezan, M. Wischnjewsky, G. Valladares, C. Muenza, L. E. Gonzales, R. Aviles, L. A. Wells, R. C. Smith, M. Navarrete, R. Covarrubias, G. M. Williger, A. R. Walker, A. C. Layden, J. H. Elias, J. A. Baldwin, M. Hernandez, H. Tirado, P. Ugarte, R. Elston, N. Saavedra, F. Barrientos, E. Costa, P. Lira, M. T. Ruiz, C. Anguita, X. Gomez, P. Ortiz, M. della Valle, J. Danziger, J. Storm, Y.-C. Kim, C. Bailyn, E. P. Rubenstein, D. Tucker, S. Cersosimo, R. A. Mendez, L. Siciliano, W. Sherry, B. Chaboyer, R. A. Koopmann, D. Geisler, A. Sarajedini, A. Dey, N. Tyson, R. M. Rich, R. Gal, R. Lamontagne, N. Caldwell, P. Guhathakurta, A. C. Phillips, P. Szkody, C. Prosser, L. C. Ho, R. McMahan, G. Baggley, K.-P. Cheng, R. Havlen, K. Wakamatsu, K. Janes, M. Malkan, F. Baganoff, P. Seitzer, M. Shara, C. Sturch, J. Hesser, A. N. P. Hartig, J. Hughes, D. Welch, T. B. Williams, H. Ferguson, P. J. Francis, L. French, M. Bolte, J. Roth, S. Odewahn, S. Howell, and W. Krzeminski (1996). BVRI Light Curves for 29 Type IA Supernovae. *AJ* **112**, 2408–+.
- [107] Hamuy, M., M. M. Phillips, N. B. Suntzeff, R. A. Schommer, J. Maza, and R. Aviles (1996a). The Absolute Luminosities of the Calan/Tololo Type IA Supernovae. *AJ* **112**, 2391–+.
- [108] Hamuy, M., M. M. Phillips, N. B. Suntzeff, R. A. Schommer, J. Maza, and R. Aviles (1996b). The Hubble Diagram of the Calan/Tololo Type IA Supernovae and the Value of H_0 . *AJ* **112**, 2398–+.
- [109] Hamuy, M., N. B. Suntzeff, S. R. Heathcote, A. R. Walker, P. Gigoux, and M. M. Phillips (1994). Southern spectrophotometric standards, 2. *PASP* **106**, 566–589.

- [110] Hamuy, M., S. C. Trager, P. A. Pinto, M. M. Phillips, R. A. Schommer, V. Ivanov, and N. B. Suntzeff (2000). A Search for Environmental Effects on Type IA Supernovae. *AJ* **120**, 1479–1486.
- [111] Harkness, R. P., J. C. Wheeler, B. Margon, R. A. Downes, R. P. Kirshner, A. Uomoto, E. S. Barker, A. L. Cochran, H. L. Dinerstein, D. R. Garnett, and R. M. Levreault (1987). The early spectral phase of type Ib supernovae - Evidence for helium. *ApJ* **317**, 355–367.
- [112] Hatano, K., D. Branch, A. Fisher, E. Baron, and A. V. Filippenko (1999). On the High-Velocity Ejecta of the Type IA Supernova SN 1994D. *ApJ* **525**, 881–885.
- [113] Hawking, S. W. and G. F. R. Ellis (1973). *The large scale structure of space-time*. Cambridge Monographs on Mathematical Physics, London: Cambridge University Press, 1973.
- [114] Herald, J. E., D. J. Hillier, and R. E. Schulte-Ladbeck (2001). Tailored Analyses of the WN 8 Stars WR 40 and WR 16. *ApJ* **548**, 932–952.
- [115] Hernandez, M., W. P. S. Meikle, A. Aparicio, C. R. Benn, M. R. Burleigh, A. C. Chrysostomou, A. J. L. Fernandes, T. R. Geballe, P. L. Hammersley, J. Iglesias-Paramo, D. J. James, P. A. James, S. N. Kemp, T. A. Lister, D. Martinez-Delgado, A. Oscoz, D. L. Pollacco, M. Rozas, S. J. Smartt, P. Sorensen, R. A. Swaters, J. H. Telting, W. D. Vacca, N. A. Walton, and M. R. Zapatero-Osorio (2000). An early-time infrared and optical study of the Type Ia Supernova 1998bu in M96. *MNRAS* **319**, 223–234.
- [116] Hicken, M. (2004). Supernovae 2003le-2003ln. *IAU Circ.* **8261**, 1–+.
- [117] Hillebrandt, W. and J. C. Niemeyer (2000). Type IA Supernova Explosion Models. *ARA&A* **38**, 191–230.
- [118] Hillier, D. J. and D. L. Miller (1998). The Treatment of Non-LTE Line Blanketing in Spherically Expanding Outflows. *ApJ* **496**, 407–+.
- [119] Höflich, P. (1995). Analysis of the type IA supernova SN 1994D. *ApJ* **443**, 89–108.
- [120] Höflich, P., C. Gerardy, E. Linder, and et al. (2003). Models for Type Ia Supernovae and Cosmology. *LNP Vol. 635: Stellar Candles for the Extragalactic Distance Scale* **635**, 203–227.
- [121] Höflich, P., C. L. Gerardy, R. A. Fesen, and S. Sakai (2002). Infrared Spectra of the Subluminous Type Ia Supernova SN 1999by. *ApJ* **568**, 791–806.
- [122] Höflich, P. and A. Khokhlov (1996). Explosion Models for Type IA Supernovae: A Comparison with Observed Light Curves, Distances, H 0, and Q 0. *ApJ* **457**, 500–+.
- [123] Höflich, P., A. Khokhlov, J. C. Wheeler, M. M. Phillips, N. B. Suntzeff, and M. Hamuy (1996). Maximum Brightness and Postmaximum Decline of Light Curves of Type IA Supernovae: A Comparison of Theory and Observations. *ApJ* **472**, L81+.

- [124] Höflich, P., E. Müller, and A. Khokhlov (1993). Light curve models for type IA supernovae - Physical assumptions, their influence and validity. *A&A* **268**, 570–590.
- [125] Höflich, P., J. C. Wheeler, and F. K. Thielemann (1998). Type IA Supernovae: Influence of the Initial Composition on the Nucleosynthesis, Light Curves, and Spectra and Consequences for the Determination of Omega M and Lambda. *ApJ* **495**, 617–+.
- [126] Homeier, N. L. (2005). The Effect of Type Ibc Contamination in Cosmological Supernova Samples. *ApJ* **620**, 12–20.
- [127] Hook, I., J. R. Allington-Smith, S. M. Beard, D. Crampton, R. L. Davies, C. G. Dickson, A. W. Ebbers, J. M. Fletcher, I. Jorgensen, I. Jean, S. Juneau, R. G. Murowinski, R. Nolan, K. Laidlaw, B. Leckie, G. E. Marshall, T. Purkins, I. M. Richardson, S. C. Roberts, D. A. Simons, M. J. Smith, J. R. Stilburn, K. Szeto, C. Tierney, R. J. Wolff, and R. Wooff (2003). Gemini-north multiobject spectrograph integration, test, and commissioning. In *Instrument Design and Performance for Optical/Infrared Ground-based Telescopes. Edited by Iye, Masanori; Moorwood, Alan F. M. Proceedings of the SPIE, Volume 4841, pp. 1645-1656 (2003).*, pp. 1645–1656.
- [128] Hook, R. N. and L. B. Lucy (1994). Image Restorations of High Photometric Quality. II. Examples. In *The Restoration of HST Images and Spectra - II*, pp. 86–+.
- [129] Horne, K. (1986). An optimal extraction algorithm for CCD spectroscopy. *PASP* **98**, 609–617.
- [130] Howell, D. A., P. Höflich, L. Wang, and J. C. Wheeler (2001). Evidence for Asphericity in a Subluminous Type Ia Supernova: Spectropolarimetry of SN 1999by. *ApJ* **556**, 302–321.
- [131] Hoyle, F. and W. A. Fowler (1960). Nucleosynthesis in Supernovae. *ApJ* **132**, 565–+.
- [132] Hubble, E. (1929). A Relation between Distance and Radial Velocity among Extra-Galactic Nebulae. *Proceedings of the National Academy of Science* **15**, 168–173.
- [133] Iben, I. and A. V. Tutukov (1984). The evolution of low-mass close binaries influenced by the radiation of gravitational waves and by a magnetic stellar wind. *ApJ* **284**, 719–744.
- [134] Iben, I. J. (1991). Single and binary star evolution. *ApJS* **76**, 55–114.
- [135] Jeffery, D. J. and D. Branch (1990). Analysis of Supernova Spectra. In *Supernovae, Jerusalem Winter School for Theoretical Physics*, pp. 149–+.
- [136] Jeffery, D. J., B. Leibundgut, R. P. Kirshner, S. Benetti, D. Branch, and G. Sonneborn (1992). Analysis of the photospheric epoch spectra of type Ia supernovae SN 1990N and SN 1991T. *ApJ* **397**, 304–328.

- [137] Jha, S. (2002). Exploding stars, near and far. *Ph.D. Thesis*.
- [138] Jha, S., P. M. Garnavich, R. P. Kirshner, P. Challis, A. M. Soderberg, L. M. Macri, J. P. Huchra, P. Barmby, E. J. Barton, P. Berlind, W. R. Brown, N. Caldwell, M. L. Calkins, S. J. Kannappan, D. M. Koranyi, M. A. Pahre, K. J. Rines, K. Z. Stanek, R. P. Stefanik, A. H. Szentgyorgyi, P. Väisänen, Z. Wang, J. M. Zajac, A. G. Riess, A. V. Filippenko, W. Li, M. Modjaz, R. R. Treffers, C. W. Hergenrother, E. K. Grebel, P. Seitzer, G. H. Jacoby, P. J. Benson, A. Rizvi, L. A. Marschall, J. D. Goldader, M. Beasley, W. D. Vacca, B. Leibundgut, J. Spyromilio, B. P. Schmidt, and P. R. Wood (1999). The Type IA Supernova 1998BU in M96 and the Hubble Constant. *ApJS* **125**, 73–97.
- [139] Jones, D. H., W. Saunders, M. Colless, M. A. Read, Q. A. Parker, F. G. Watson, L. A. Campbell, D. Burkey, T. Mauch, L. Moore, M. Hartley, P. Cass, D. James, K. Russell, K. Fiegert, J. Dawe, J. Huchra, T. Jarrett, O. Lahav, J. Lucey, G. A. Mamon, D. Proust, E. M. Sadler, and K. Wakamatsu (2004). The 6dF Galaxy Survey: samples, observational techniques and the first data release. *MNRAS* **355**, 747–763.
- [140] Karp, A. H., G. Lasher, K. L. Chan, and E. E. Salpeter (1977). The opacity of expanding media - The effect of spectral lines. *ApJ* **214**, 161–178.
- [141] Kasen, D., D. Branch, E. Baron, and D. Jeffery (2002). A Complete Analytic Inversion of Supernova Lines in the Sobolev Approximation. *ApJ* **565**, 380–384.
- [142] Kasen, D., P. Nugent, L. Wang, D. A. Howell, J. C. Wheeler, P. Höflich, D. Baade, E. Baron, and P. H. Hauschildt (2003). Analysis of the Flux and Polarization Spectra of the Type Ia Supernova SN 2001el: Exploring the Geometry of the High-Velocity Ejecta. *ApJ* **593**, 788–808.
- [143] Kennicutt, R. C. (1992). A spectrophotometric atlas of galaxies. *ApJS* **79**, 255–284.
- [144] Kent, S. M. (1985). CCD surface photometry of field Galaxies. II - Bulge/disk decompositions. *ApJS* **59**, 115–159.
- [145] Khokhlov, A., E. Müller, and P. Höflich (1993). Light curves of Type IA supernova models with different explosion mechanisms. *A&A* **270**, 223–248.
- [146] Khokhlov, A. M. (1991). Delayed detonation model for type IA supernovae. *A&A* **245**, 114–128.
- [147] King, D. L., G. Vladilo, K. Lipman, K. S. de Boer, M. Centurion, P. Moritz, and N. A. Walton (1995). NGC 4526 gas, high velocity clouds, and Galactic halo gas: the interstellar medium towards SN 1994D. *A&A* **300**, 881–+.
- [148] Kirshner, R. P. (2002). *The extravagant universe : exploding stars, dark energy and the accelerating cosmos*. The extravagant universe : exploding stars, dark energy and

- the accelerating cosmos / Robert P. Kirshner. Princeton, N.J. : Princeton University Press, c2002.
- [149] Kirshner, R. P., D. J. Jeffery, B. Leibundgut, P. M. Challis, G. Sonneborn, M. M. Phillips, N. B. Suntzeff, R. C. Smith, P. F. Winkler, C. Winge, M. Hamuy, D. A. Hunter, K. C. Roth, J. C. Blades, D. Branch, R. A. Chevalier, C. Fransson, N. Panagia, R. V. Wagoner, J. C. Wheeler, and R. P. Harkness (1993). SN 1992A: Ultraviolet and Optical Studies Based on HST, IUE, and CTIO Observations. *ApJ* **415**, 589–+.
- [150] Kirshner, R. P. and J. Kwan (1974). Distances to extragalactic supernovae. *ApJ* **193**, 27–36.
- [151] Kirshner, R. P., J. B. Oke, M. V. Penston, and L. Searle (1973). The spectra of SN. *ApJ* **185**, 303–+.
- [152] Knop, R. A., G. Aldering, R. Amanullah, P. Astier, G. Blanc, M. S. Burns, A. Conley, S. E. Deustua, M. Doi, R. Ellis, S. Fabbro, G. Folatelli, A. S. Fruchter, G. Garavini, S. Garmond, K. Garton, R. Gibbons, G. Goldhaber, A. Goobar, D. E. Groom, D. Hardin, I. Hook, D. A. Howell, A. G. Kim, B. C. Lee, C. Lidman, J. Mendez, S. Nobili, P. E. Nugent, R. Pain, N. Panagia, C. R. Pennypacker, S. Perlmutter, R. Quimby, J. Raux, N. Regnault, P. Ruiz-Lapuente, G. Sainton, B. Schaefer, K. Schahmanche, E. Smith, A. L. Spadafora, V. Stanishev, M. Sullivan, N. A. Walton, L. Wang, W. M. Wood-Vasey, and N. Yasuda (2003). New Constraints on Ω_M , Ω_Λ , and w from an Independent Set of 11 High-Redshift Supernovae Observed with the Hubble Space Telescope. *ApJ* **598**, 102–137.
- [153] Kobayashi, C., T. Tsujimoto, K. Nomoto, I. Hachisu, and M. Kato (1998). Low-Metallicity Inhibition of Type IA Supernovae and Galactic and Cosmic Chemical Evolution. *ApJ* **503**, L155+.
- [154] Koen, C., J. A. Orosz, and R. A. Wade (1998). KPD 0422+5421: a new short-period subdwarf B/white dwarf binary. *MNRAS* **300**, 695–704.
- [155] Kozma, C., C. Fransson, W. Hillebrandt, C. Travaglio, J. Sollerman, M. Reinecke, F. K. Röpkke, and J. Spyromilio (2005). Three-dimensional modeling of type Ia supernovae - The power of late time spectra. *A&A* **437**, 983–995.
- [156] Krisciunas, K., P. Garnavich, P. Challis, J. L. Prieto, A. G. Riess, B. Barris, C. Aguilera, A. C. Becker, S. Blondin, R. Chornock, A. Clocchiatti, R. Covarrubias, A. V. Filippenko, R. J. Foley, M. Hicken, S. Jha, R. P. Kirshner, B. Leibundgut, W. Li, T. Matheson, A. Miceli, G. Miknaitis, A. Rest, M. E. Salvo, B. P. Schmidt, R. C. Smith, J. Sollerman, J. Spyromilio, C. W. Stubbs, N. B. Suntzeff, J. L. Tonry, and W. M. Wood-Vasey (2005). Hubble Space Telescope Observations of Nine High-Redshift ESSENCE Supernovae. *AJ*, *in press*.

- [157] Krisciunas, K., N. C. Hastings, K. Loomis, R. McMillan, A. Rest, A. G. Riess, and C. Stubbs (2000). Uniformity of (V-Near-Infrared) Color Evolution of Type Ia Supernovae and Implications for Host Galaxy Extinction Determination. *ApJ* **539**, 658–674.
- [158] Krisciunas, K., M. M. Phillips, and N. B. Suntzeff (2004). Hubble Diagrams of Type Ia Supernovae in the Near-Infrared. *ApJ* **602**, L81–L84.
- [159] Krisciunas, K., N. B. Suntzeff, M. M. Phillips, P. Candia, J. L. Prieto, R. Antezana, R. Chassagne, H. Chen, M. Dickinson, P. R. Eisenhardt, J. Espinoza, P. M. Garnavich, D. González, T. E. Harrison, M. Hamuy, V. D. Ivanov, W. Krzemiński, C. Kulesa, P. McCarthy, A. Moro-Martín, C. Muena, A. Noriega-Crespo, S. E. Persson, P. A. Pinto, M. Roth, E. P. Rubenstein, S. A. Stanford, G. S. Stringfellow, A. Zapata, A. Porter, and M. Wischnjewsky (2004). Optical and Infrared Photometry of the Type Ia Supernovae 1991T, 1991bg, 1999ek, 2001bt, 2001cn, 2001cz, and 2002bo. *AJ* **128**, 3034–3052.
- [160] Kulkarni, S. R., D. A. Frail, M. H. Wieringa, R. D. Ekers, E. M. Sadler, R. M. Wark, J. L. Higdon, E. S. Phinney, and J. S. Bloom (1998). Radio emission from the unusual supernova 1998bw and its association with the gamma-ray burst of 25 April 1998. *Nature* **395**, 663–669.
- [161] Kurucz, R. (1993). Atomic data for opacity calculations. *Atomic data for opacity calculations. Kurucz CD-ROM No. 1. Cambridge, Mass.: Smithsonian Astrophysical Observatory, 1993. 1.*
- [162] Kurucz, R. L. and B. Bell (1995). *Atomic line list*. Kurucz CD-ROM, Cambridge, MA: Smithsonian Astrophysical Observatory, —c1995, April 15, 1995.
- [163] Leavitt, H. S. and E. C. Pickering (1912). Periods of 25 Variable Stars in the Small Magellanic Cloud. *Harvard College Observatory Circular* **173**, 1–3.
- [164] Leibundgut, B. (2000). Type Ia Supernovae. *A&A Rev.* **10**, 179–209.
- [165] Leibundgut, B. (2001). Cosmological Implications from Observations of Type Ia Supernovae. *ARA&A* **39**, 67–98.
- [166] Leibundgut, B. (2004). Are Type Ia Supernovae Standard Candles? *Ap&SS* **290**, 29–41.
- [167] Leibundgut, B. and S. Blondin (2004). Evidence for Dark Energy from Type Ia Supernovae. In *8th International Workshop on Topics in Astroparticle and Underground Physics (TAUP)*.
- [168] Leibundgut, B., R. P. Kirshner, A. V. Filippenko, J. C. Shields, C. B. Foltz, M. M. Phillips, and G. Sonneborn (1991). Premaximum observations of the type IA SN 1990N. *ApJ* **371**, L23–L26.

- [169] Leibundgut, B., R. P. Kirshner, M. M. Phillips, L. A. Wells, N. B. Suntzeff, M. Hamuy, R. A. Schommer, A. R. Walker, L. Gonzalez, P. Ugarte, R. E. Williams, G. Williger, M. Gomez, R. Marzke, B. P. Schmidt, B. Whitney, N. Coldwell, J. Peters, F. H. Chaffee, C. B. Foltz, D. Rehner, L. Siciliano, T. G. Barnes, K.-P. Cheng, P. M. N. Hintzen, Y.-C. Kim, J. Maza, J. W. Parker, A. C. Porter, P. C. Schmidtke, and G. Sonneborn (1993). SN 1991bg - A type IA supernova with a difference. *AJ* **105**, 301–313.
- [170] Leibundgut, B. and P. A. Pinto (1992). A distance-independent calibration of the luminosity of type IA supernovae and the Hubble constant. *ApJ* **401**, 49–59.
- [171] Leibundgut, B., R. Schommer, M. Phillips, A. Riess, B. Schmidt, J. Spyromilio, J. Walsh, N. Suntzeff, M. Hamuy, J. Maza, R. P. Kirshner, P. Challis, P. Garnavich, R. C. Smith, A. Dressler, and R. Ciardullo (1996). Time Dilation in the Light Curve of the Distant Type IA Supernova SN 1995K. *ApJ* **466**, L21+.
- [172] Leibundgut, B. and J. Sollerman (2001). A cosmological surprise: the universe accelerates. *Europhysics News* **32**, 121–+.
- [173] Lentz, E. J., E. Baron, D. Branch, P. H. Hauschildt, and P. E. Nugent (2000). Metallicity Effects in Non-LTE Model Atmospheres of Type IA Supernovae. *ApJ* **530**, 966–976.
- [174] Li, W., A. V. Filippenko, R. Chornock, E. Berger, P. Berlind, M. L. Calkins, P. Challis, C. Fassnacht, S. Jha, R. P. Kirshner, T. Matheson, W. L. W. Sargent, R. A. Simcoe, G. H. Smith, and G. Squires (2003). SN 2002cx: The Most Peculiar Known Type Ia Supernova. *PASP* **115**, 453–473.
- [175] Li, W., A. V. Filippenko, E. Gates, R. Chornock, A. Gal-Yam, E. O. Ofek, D. C. Leonard, M. Modjaz, R. M. Rich, A. G. Riess, and R. R. Treffers (2001). The Unique Type Ia Supernova 2000cx in NGC 524. *PASP* **113**, 1178–1204.
- [176] Li, W., A. V. Filippenko, R. R. Treffers, A. G. Riess, J. Hu, and Y. Qiu (2001). A High Intrinsic Peculiarity Rate among Type IA Supernovae. *ApJ* **546**, 734–743.
- [177] Li, W. D., Y. L. Qiu, Q. Y. Qiao, X. H. Zhu, J. Y. Hu, M. W. Richmond, A. V. Filippenko, R. R. Treffers, C. Y. Peng, and D. C. Leonard (1999). The Type IA Supernova 1997BR in ESO 576-G40. *AJ* **117**, 2709–2724.
- [178] Lidman, C. (2004). Observing distant type Ia supernovae with the ESO VLT. *The Messenger* **118**, 24–30.
- [179] Lidman, C., D. A. Howell, G. Folatelli, G. Garavini, S. Nobili, G. Aldering, R. Amanullah, P. Antilogus, P. Astier, G. Blanc, M. S. Burns, A. Conley, S. E. Deustua, M. Doi, R. Ellis, S. Fabbro, V. Fadeyev, R. Gibbons, G. Goldhaber, A. Goobar, D. E. Groom, I. Hook, N. Kashikawa, A. G. Kim, R. A. Knop, B. C. Lee, J. Mendez, T. Morokuma,

- K. Motohara, P. E. Nugent, R. Pain, S. Perlmutter, V. Prasad, R. Quimby, J. Raux, N. Regnault, P. Ruiz-Lapuente, G. Sainton, B. E. Schaefer, K. Schahmaneche, E. Smith, A. L. Spadafora, V. Stanishev, N. A. Walton, L. Wang, W. M. Wood-Vasey, and N. Yasuda (The Supernova Cosmology Project) (2005). Spectroscopic confirmation of high-redshift supernovae with the ESO VLT. *A&A* **430**, 843–851.
- [180] Livio, M. (2000). The Progenitors of Type Ia Supernovae. In *Type Ia Supernovae, Theory and Cosmology*. Edited by J. C. Niemeyer and J. W. Truran. Published by Cambridge University Press, 2000., p.33, pp. 33–+.
- [181] Livio, M. and A. G. Riess (2003). Have the Elusive Progenitors of Type Ia Supernovae Been Discovered? *ApJ* **594**, L93–L94.
- [182] Livne, E. and D. Arnett (1995). Explosions of Sub-Chandrasekhar Mass White Dwarfs in Two Dimensions. *ApJ* **452**, 62–+.
- [183] Lucy, L. B. (1974). An iterative technique for the rectification of observed distributions. *AJ* **79**, 745–+.
- [184] Lucy, L. B. (1994). Image Restorations of High Photometric Quality. In *The Restoration of HST Images and Spectra - II*, pp. 79–+.
- [185] Lucy, L. B. and J. R. Walsh (2003). Iterative Techniques for the Decomposition of Long-Slit Spectra. *AJ* **125**, 2266–2275.
- [186] Mather, J. C., E. S. Cheng, R. E. Eplee, R. B. Isaacman, S. S. Meyer, R. A. Shafer, R. Weiss, E. L. Wright, C. L. Bennett, N. W. Boggess, E. Dwek, S. Gulkis, M. G. Hauser, M. Janssen, T. Kelsall, P. M. Lubin, S. H. Moseley, T. L. Murdock, R. F. Silverberg, G. F. Smoot, and D. T. Wilkinson (1990). A preliminary measurement of the cosmic microwave background spectrum by the Cosmic Background Explorer (COBE) satellite. *ApJ* **354**, L37–L40.
- [187] Matheson, T., S. Blondin, R. J. Foley, R. Chornock, A. V. Filippenko, B. Leibundgut, R. C. Smith, J. Sollerman, J. Spyromilio, R. P. Kirshner, A. Clocchiatti, C. Aguilera, B. Barris, A. C. Becker, P. Challis, R. Covarrubias, P. Garnavich, M. Hicken, S. Jha, K. Krisciunas, W. Li, A. Miceli, G. Miknaitis, J. L. Prieto, A. Rest, A. G. Riess, M. E. Salvo, B. P. Schmidt, C. W. Stubbs, N. B. Suntzeff, and J. L. Tonry (2005). Spectroscopy of High-Redshift Supernovae from the ESSENCE Project: The First 2 Years. *AJ* **129**, 2352–2375.
- [188] Matheson, T., A. V. Filippenko, L. C. Ho, A. J. Barth, and D. C. Leonard (2000). Detailed Analysis of Early to Late-Time Spectra of Supernova 1993J. *AJ* **120**, 1499–1515.
- [189] Mattila, S., P. Lundqvist, J. Sollerman, C. Kozma, E. Baron, C. Fransson, B. Leibundgut, and K. Nomoto (2005). Early and late time VLT spectroscopy of SN 2001el - progenitor constraints for a type Ia supernova. *A&A*, submitted (*astro-ph/0501433*).

- [190] Maxted, P. F. L. and T. R. Marsh (1999). The fraction of double degenerates among DA white dwarfs. *MNRAS* **307**, 122–132.
- [191] Mazzali, P. A. (2001). On the presence of silicon and carbon in the pre-maximum spectrum of the Type Ia SN 1990N. *MNRAS* **321**, 341–346.
- [192] Mazzali, P. A., S. Benetti, G. Altavilla, G. Blanc, E. Cappellaro, N. Elias-Rosa, G. Garavini, A. Goobar, A. Harutyunyan, R. Kotak, B. Leibundgut, P. Lundqvist, S. Mattila, J. Mendez, S. Nobili, R. Pain, A. Pastorello, F. Patat, G. Pignata, P. Podsiadlowski, P. Ruiz-Lapuente, M. Salvo, B. P. Schmidt, J. Sollerman, V. Stanishev, M. Stehle, C. Tout, M. Turatto, and W. Hillebrandt (2005). High-Velocity Features: A Ubiquitous Property of Type Ia Supernovae. *ApJ* **623**, L37–L40.
- [193] Mazzali, P. A., S. Benetti, M. Stehle, D. Branch, J. Deng, K. Maeda, K. Nomoto, and M. Hamuy (2005). High-velocity features in the spectra of the Type Ia supernova SN 1999ee: a property of the explosion or evidence of circumstellar interaction? *MNRAS* **357**, 200–206.
- [194] Mazzali, P. A., E. Cappellaro, I. J. Danziger, M. Turatto, and S. Benetti (1998). Nebular Velocities in Type IA Supernovae and Their Relationship to Light Curves. *ApJ* **499**, L49+.
- [195] Mazzali, P. A., N. Chugai, M. Turatto, L. B. Lucy, I. J. Danziger, E. Cappellaro, M. della Valle, and S. Benetti (1997). The properties of the peculiar type IA supernova 1991bg - II. The amount of ^{56}Ni and the total ejecta mass determined from spectrum synthesis and energetics considerations. *MNRAS* **284**, 151–171.
- [196] Mazzali, P. A., I. J. Danziger, and M. Turatto (1995). A study of the properties of the peculiar SN IA 1991T through models of its evolving early-time spectrum. *A&A* **297**, 509+.
- [197] Mazzali, P. A., L. B. Lucy, I. J. Danziger, C. Gouiffes, E. Cappellaro, and M. Turatto (1993). Models for the early-time spectral evolution of the 'standard' type IA supernova 1990 N. *A&A* **269**, 423–445.
- [198] McElroy, D. B. (1995). A Catalog of Stellar Velocity Dispersions. II. 1994 Update. *ApJS* **100**, 105+.
- [199] Meikle, W. P. S., R. J. Cumming, T. R. Geballe, J. R. Lewis, N. A. Walton, M. Balcells, A. Cimatti, S. M. Croom, V. S. Dhillon, F. Economou, C. R. Jenkins, J. H. Knapen, V. S. Meadows, P. W. Morris, I. Perez-Fournon, T. Shanks, L. J. Smith, N. R. Tanvir, S. Veilleux, J. Vilchez, J. V. Wall, and J. R. Lucey (1996). An early-time infrared and optical study of the Type IA supernovae SN 1994D and 1991T. *MNRAS* **281**, 263–280.
- [200] Mihalas, D. (1978). *Stellar atmospheres /2nd edition/*. San Francisco, W. H. Freeman and Co., 1978. 650 p.

- [201] Miknaitis, G., J. L. Tonry, P. Garnavich, C. W. Stubbs, R. C. Smith, N. B. Suntzeff, C. Aguilera, A. C. Becker, S. Blondin, P. Challis, R. Chornock, A. Clocchiatti, R. Covarrubias, A. V. Filippenko, R. J. Foley, M. Hicken, S. Jha, R. P. Kirshner, K. Krisciunas, B. Leibundgut, W. Li, T. Matheson, A. Miceli, J. L. Prieto, A. Rest, A. G. Riess, M. E. Salvo, B. P. Schmidt, J. Sollerman, and J. Spyromilio (2005). The ESSENCE Project: A Supernova Survey Optimized to Constrain the Equation of State of the Cosmic Dark Energy. *AJ*, *submitted*.
- [202] Minkowski, R. (1939). The Spectra of the Supernovae in IC 4182 and in NGC 1003. *ApJ* **89**, 156–+.
- [203] Minkowski, R. (1941). Spectra of Supernovae. *PASP* **53**, 224–+.
- [204] Mulchaey, J. (2001). *LDSS-2 User's Guide*.
- [205] Napiwotzki, R., D. Koester, G. Nelemans, L. Yungelson, N. Christlieb, A. Renzini, D. Reimers, H. Drechsel, and B. Leibundgut (2002). Binaries discovered by the SPY project. II. HE 1414-0848: A double degenerate with a mass close to the Chandrasekhar limit. *A&A* **386**, 957–963.
- [206] Narlikar, J. and H. Arp (1993). Flat spacetime cosmology - A unified framework for extragalactic redshifts. *ApJ* **405**, 51–56.
- [207] Narlikar, J. V. and H. C. Arp (1997). Time Dilation in the Supernova Light Curve and the Variable Mass Hypothesis. *ApJ* **482**, L119+.
- [208] Nomoto, K. (1982). Accreting white dwarf models for type I supernovae. I - Presupernova evolution and triggering mechanisms. *ApJ* **253**, 798–810.
- [209] Nomoto, K. and Y. Kondo (1991). Conditions for accretion-induced collapse of white dwarfs. *ApJ* **367**, L19–L22.
- [210] Nomoto, K. and D. Sugimoto (1977). Rejuvenation of Helium White Dwarfs by Mass Accretion. *PASJ* **29**, 765–780.
- [211] Nomoto, K., F.-K. Thielemann, and K. Yokoi (1984). Accreting white dwarf models of Type I supernovae. III - Carbon deflagration supernovae. *ApJ* **286**, 644–658.
- [212] Nomoto, K., H. Umeda, C. Kobayashi, I. Hachisu, M. Kato, and T. Tsujimoto (2000). Type Ia supernovae: Progenitors and evolution with redshift. In *American Institute of Physics Conference Series*, pp. 35–52.
- [213] Nørgaard-Nielsen, H. U., L. Hansen, H. E. Jorgensen, A. Aragon Salamanca, and R. S. Ellis (1989). The discovery of a type IA supernova at a redshift of 0.31. *Nature* **339**, 523–525.

- [214] Nugent, P., A. Kim, and S. Perlmutter (2002). K-Corrections and Extinction Corrections for Type Ia Supernovae. *PASP* **114**, 803–819.
- [215] Nugent, P., M. Phillips, E. Baron, D. Branch, and P. Hauschildt (1995). Evidence for a Spectroscopic Sequence among Type Ia Supernovae. *ApJ* **455**, L147+.
- [216] Oke, J. B., J. G. Cohen, M. Carr, J. Cromer, A. Dingizian, F. H. Harris, S. Labrecque, R. Lucinio, W. Schaal, H. Epps, and J. Miller (1995). The Keck Low-Resolution Imaging Spectrometer. *PASP* **107**, 375+.
- [217] Pain, R. and SNLS Collaboration (2002). The Supernova program of the Canada-France-Hawaii-Telescope Legacy Survey. *Bulletin of the American Astronomical Society* **34**, 1169+.
- [218] Parodi, B. R., A. Saha, A. Sandage, and G. A. Tammann (2000). Supernova Type Ia Luminosities, Their Dependence on Second Parameters, and the Value of H_0 . *ApJ* **540**, 634–651.
- [219] Patat, F. (2003). UBVRI night sky brightness during sunspot maximum at ESO-Paranal. *A&A* **400**, 1183–1198.
- [220] Patat, F., S. Benetti, E. Cappellaro, I. J. Danziger, M. della Valle, P. A. Mazzali, and M. Turatto (1996). The type IA supernova 1994D in NGC 4526: the early phases. *MNRAS* **278**, 111–124.
- [221] Patat, F., E. Cappellaro, J. Danziger, P. A. Mazzali, J. Sollerman, T. Augusteijn, J. Brewer, V. Doublier, J. F. Gonzalez, O. Hainaut, C. Lidman, B. Leibundgut, K. Nomoto, T. Nakamura, J. Spyromilio, L. Rizzi, M. Turatto, J. Walsh, T. J. Galama, J. van Paradijs, C. Kouveliotou, P. M. Vreeswijk, F. Frontera, N. Masetti, E. Palazzi, and E. Pian (2001). The Metamorphosis of SN 1998bw. *ApJ* **555**, 900–917.
- [222] Pauldrach, A. W. A., M. Duschinger, P. A. Mazzali, J. Puls, M. Lennon, and D. L. Miller (1996). NLTE models for synthetic spectra of type IA supernovae. The influence of line blocking. *A&A* **312**, 525–538.
- [223] Peebles, P. J. E. and B. Ratra (1988). Cosmology with a time-variable cosmological 'constant'. *ApJ* **325**, L17–L20.
- [224] Percival, W. J., C. M. Baugh, J. Bland-Hawthorn, T. Bridges, R. Cannon, S. Cole, M. Colless, C. Collins, W. Couch, G. Dalton, R. De Propris, S. P. Driver, G. Efstathiou, R. S. Ellis, C. S. Frenk, K. Glazebrook, C. Jackson, O. Lahav, I. Lewis, S. Lumsden, S. Maddox, S. Moody, P. Norberg, J. A. Peacock, B. A. Peterson, W. Sutherland, and K. Taylor (2001). The 2dF Galaxy Redshift Survey: the power spectrum and the matter content of the Universe. *MNRAS* **327**, 1297–1306.

- [225] Perlmutter, S., G. Aldering, M. della Valle, S. Deustua, R. S. Ellis, S. Fabbro, A. Fruchter, G. Goldhaber, D. E. Groom, I. M. Hook, A. G. Kim, M. Y. Kim, R. A. Knop, C. Lidman, R. G. McMahon, P. Nugent, R. Pain, N. Panagia, C. R. Pennypacker, P. Ruiz-Lapuente, B. Schaefer, and N. Walton (1998). Discovery of a supernova explosion at half the age of the universe. *Nature* **391**, 51–+.
- [226] Perlmutter, S., G. Aldering, G. Goldhaber, R. A. Knop, P. Nugent, P. G. Castro, S. Deustua, S. Fabbro, A. Goobar, D. E. Groom, I. M. Hook, A. G. Kim, M. Y. Kim, J. C. Lee, N. J. Nunes, R. Pain, C. R. Pennypacker, R. Quimby, C. Lidman, R. S. Ellis, M. Irwin, R. G. McMahon, P. Ruiz-Lapuente, N. Walton, B. Schaefer, B. J. Boyle, A. V. Filippenko, T. Matheson, A. S. Fruchter, N. Panagia, H. J. M. Newberg, W. J. Couch, and The Supernova Cosmology Project (1999). Measurements of Omega and Lambda from 42 High-Redshift Supernovae. *ApJ* **517**, 565–586.
- [227] Perlmutter, S., S. Gabi, G. Goldhaber, A. Goobar, D. E. Groom, I. M. Hook, A. G. Kim, M. Y. Kim, J. C. Lee, R. Pain, C. R. Pennypacker, I. A. Small, R. S. Ellis, R. G. McMahon, B. J. Boyle, P. S. Bunclark, D. Carter, M. J. Irwin, K. Glazebrook, H. J. M. Newberg, A. V. Filippenko, T. Matheson, M. Dopita, W. J. Couch, and The Supernova Cosmology Project (1997). Measurements of the Cosmological Parameters Omega and Lambda from the First Seven Supernovae at $Z \geq 0.35$. *ApJ* **483**, 565–+.
- [228] Perlmutter, S., C. R. Pennypacker, G. Goldhaber, A. Goobar, R. A. Muller, H. J. M. Newberg, J. Desai, A. G. Kim, M. Y. Kim, I. A. Small, B. J. Boyle, C. S. Crawford, R. G. McMahon, P. S. Bunclark, D. Carter, M. J. Irwin, R. J. Terlevich, R. S. Ellis, K. Glazebrook, W. J. Couch, J. R. Mould, T. A. Small, and R. G. Abraham (1995). A supernova at $Z = 0.458$ and implications for measuring the cosmological deceleration. *ApJ* **440**, L41–L44.
- [229] Phillips, M. M. (1993). The absolute magnitudes of Type IA supernovae. *ApJ* **413**, L105–L108.
- [230] Phillips, M. M., P. Lira, N. B. Suntzeff, R. A. Schommer, M. Hamuy, and J. Maza (1999). The Reddening-Free Decline Rate Versus Luminosity Relationship for Type IA Supernovae. *AJ* **118**, 1766–1776.
- [231] Phillips, M. M., A. C. Phillips, S. R. Heathcote, V. M. Blanco, D. Geisler, D. Hamilton, N. B. Suntzeff, F. J. Jablonski, J. E. Steiner, A. P. Cowley, P. Schmidtke, S. Wyckoff, J. B. Hutchings, J. Tonry, M. A. Strauss, J. R. Thorstensen, W. Honey, J. Maza, M. T. Ruiz, A. U. Landolt, A. Uomoto, R. M. Rich, J. E. Grindlay, H. Cohn, H. A. Smith, J. H. Lutz, R. J. Lavery, and A. Saha (1987). The type 1a supernova 1986G in NGC 5128 - Optical photometry and spectra. *PASP* **99**, 592–605.
- [232] Phillips, M. M., L. A. Wells, N. B. Suntzeff, M. Hamuy, B. Leibundgut, R. P. Kirshner, and C. B. Foltz (1992). SN 1991T - Further evidence of the heterogeneous nature of type IA supernovae. *AJ* **103**, 1632–1637.

- [233] Pinto, P. A. and R. G. Eastman (2000a). The Physics of Type IA Supernova Light Curves. I. Analytic Results and Time Dependence. *ApJ* **530**, 744–756.
- [234] Pinto, P. A. and R. G. Eastman (2000b). The Physics of Type IA Supernova Light Curves. II. Opacity and Diffusion. *ApJ* **530**, 757–776.
- [235] Poznanski, D., A. Gal-Yam, D. Maoz, A. V. Filippenko, D. C. Leonard, and T. Matheson (2002). Not Color-Blind: Using Multiband Photometry to Classify Supernovae. *PASP* **114**, 833–845.
- [236] Prieto, J. L., A. Rest, and N. B. Suntzeff (2005). A New Method to Calibrate the Magnitudes of Type Ia Supernovae at Maximum Light. In *ASP Conf. Ser. 339: Observing Dark Energy*, pp. 69–+.
- [237] Prinja, R. K., M. J. Barlow, and I. D. Howarth (1990). Terminal velocities for a large sample of O stars, B supergiants, and Wolf-Rayet stars. *ApJ* **361**, 607–620.
- [238] Pritchett, C. J. (2004). SNLS – the Supernova Legacy Survey. *astro-ph/0406242*.
- [239] Pych, W. (2004). A Fast Algorithm for Cosmic-Ray Removal from Single Images. *PASP* **116**, 148–153.
- [240] Röpke, F. K. and W. Hillebrandt (2004). The case against the progenitor’s carbon-to-oxygen ratio as a source of peak luminosity variations in type Ia supernovae. *A&A* **420**, L1–L4.
- [241] Ratnatunga, K. U., R. E. Griffiths, and E. J. Ostrander (1999). Disk and Bulge Morphology of WFPC2 Galaxies: The HUBBLE SPACE TELESCOPE Medium Deep Survey. *AJ* **118**, 86–107.
- [242] Renzini, A. (1996). Searching for Type IA Supernova Progenitors. In *IAU Colloq. 145: Supernovae and Supernova Remnants*, pp. 77–+.
- [243] Richardson, W. H. (1972). Bayesian-based iterative method of image restoration. *Optical Society of America Journal* **62**, 55–59.
- [244] Riess, A. G., A. V. Filippenko, P. Challis, A. Clocchiatti, A. Diercks, P. M. Garnavich, R. L. Gilliland, C. J. Hogan, S. Jha, R. P. Kirshner, B. Leibundgut, M. M. Phillips, D. Reiss, B. P. Schmidt, R. A. Schommer, R. C. Smith, J. Spyromilio, C. Stubbs, N. B. Suntzeff, and J. Tonry (1998). Observational Evidence from Supernovae for an Accelerating Universe and a Cosmological Constant. *AJ* **116**, 1009–1038.
- [245] Riess, A. G., A. V. Filippenko, D. C. Leonard, B. P. Schmidt, N. Suntzeff, M. M. Phillips, R. Schommer, A. Clocchiatti, R. P. Kirshner, P. Garnavich, P. Challis, B. Leibundgut, J. Spyromilio, and R. C. Smith (1997). Time Dilation from Spectral Feature Age Measurements of Type IA Supernovae. *AJ* **114**, 722–729.

- [246] Riess, A. G., A. V. Filippenko, W. Li, R. R. Treffers, B. P. Schmidt, Y. Qiu, J. Hu, M. Armstrong, C. Faranda, E. Thouvenot, and C. Buil (1999). The Rise Time of Nearby Type IA Supernovae. *AJ* **118**, 2675–2688.
- [247] Riess, A. G., R. P. Kirshner, B. P. Schmidt, S. Jha, P. Challis, P. M. Garnavich, A. A. Esin, C. Carpenter, R. Grashius, R. E. Schild, P. L. Berlind, J. P. Huchra, C. F. Prosser, E. E. Falco, P. J. Benson, C. Briceño, W. R. Brown, N. Caldwell, I. P. dell’Antonio, A. V. Filippenko, A. A. Goodman, N. A. Grogin, T. Groner, J. P. Hughes, P. J. Green, R. A. Jansen, J. T. Kleyana, J. X. Luu, L. M. Macri, B. A. McLeod, K. K. McLeod, B. R. McNamara, B. McLean, A. A. E. Milone, J. J. Mohr, D. Moraru, C. Peng, J. Peters, A. H. Prestwich, K. Z. Stanek, A. Szentgyorgyi, and P. Zhao (1999). BVRI Light Curves for 22 Type IA Supernovae. *AJ* **117**, 707–724.
- [248] Riess, A. G., W. Li, P. B. Stetson, A. V. Filippenko, S. Jha, R. P. Kirshner, P. M. Challis, P. M. Garnavich, and R. Chornock (2005). Cepheid Calibrations from the Hubble Space Telescope of the Luminosity of Two Recent Type Ia Supernovae and a Redetermination of the Hubble Constant. *ApJ* **627**, 579–607.
- [249] Riess, A. G., P. Nugent, A. V. Filippenko, R. P. Kirshner, and S. Perlmutter (1998). Snapshot Distances to Type IA Supernovae: All in “One” Night’s Work. *ApJ* **504**, 935–+.
- [250] Riess, A. G., P. E. Nugent, R. L. Gilliland, B. P. Schmidt, J. Tonry, M. Dickinson, R. I. Thompson, T. Budavári, S. Casertano, A. S. Evans, A. V. Filippenko, M. Livio, D. B. Sanders, A. E. Shapley, H. Spinrad, C. C. Steidel, D. Stern, J. Surace, and S. Veilleux (2001). The Farthest Known Supernova: Support for an Accelerating Universe and a Glimpse of the Epoch of Deceleration. *ApJ* **560**, 49–71.
- [251] Riess, A. G., W. H. Press, and R. P. Kirshner (1996). A Precise Distance Indicator: Type IA Supernova Multicolor Light-Curve Shapes. *ApJ* **473**, 88–+.
- [252] Riess, A. G., L. Strolger, J. Tonry, S. Casertano, H. C. Ferguson, B. Mobasher, P. Challis, A. V. Filippenko, S. Jha, W. Li, R. Chornock, R. P. Kirshner, B. Leibundgut, M. Dickinson, M. Livio, M. Giavalisco, C. C. Steidel, T. Benítez, and Z. Tsvetanov (2004). Type Ia Supernova Discoveries at $z > 1$ from the Hubble Space Telescope: Evidence for Past Deceleration and Constraints on Dark Energy Evolution. *ApJ* **607**, 665–687.
- [253] Riess, A. G., L. Strolger, J. Tonry, Z. Tsvetanov, S. Casertano, H. C. Ferguson, B. Mobasher, P. Challis, N. Panagia, A. V. Filippenko, W. Li, R. Chornock, R. P. Kirshner, B. Leibundgut, M. Dickinson, A. Koekemoer, N. A. Grogin, and M. Giavalisco (2004). Identification of Type Ia Supernovae at Redshift 1.3 and Beyond with the Advanced Camera for Surveys on the Hubble Space Telescope. *ApJ* **600**, L163–L166.
- [254] Robertson, H. P. (1935). Kinematics and World-Structure. *ApJ* **82**, 284–+.

- [255] Robertson, H. P. (1936). Kinematics and World-Structure II. *ApJ* **83**, 187–+.
- [256] Ruiz-Lapuente, P., E. Cappellaro, M. Turatto, C. Gouiffes, I. J. Danziger, M. della Valle, and L. B. Lucy (1992). Modeling the iron-dominated spectra of the type IA supernova SN 1991T at premaximum. *ApJ* **387**, L33–L36.
- [257] Rybicki, G. B. and D. G. Hummer (1978). A generalization of the Sobolev method for flows with nonlocal radiative coupling. *ApJ* **219**, 654–675.
- [258] Sadakane, K., T. Yokoo, J.-I. Arimoto, K. Matsumoto, S. Honda, K. Tanabe, K.-I. Wakamatsu, M. Nishida, M. Yoshida, and M. Takada-Hidai (1996). Type-Ia Supernova SN 1995D in NGC 2962: Optical V, R, and I Band Photometry and Spectra. *PASJ* **48**, 51–57.
- [259] Saha, A., A. Sandage, L. Labhardt, G. A. Tammann, F. D. Macchetto, and N. Panagia (1997). Cepheid Calibration of the Peak Brightness of Type IA Supernovae. VIII. SN 1990N in NGC 4639. *ApJ* **486**, 1–+.
- [260] Saha, A., A. Sandage, G. A. Tammann, A. E. Dolphin, J. Christensen, N. Panagia, and F. D. Macchetto (2001). Cepheid Calibration of the Peak Brightness of Type Ia Supernovae. XI. SN 1998aq in NGC 3982. *ApJ* **562**, 314–336.
- [261] Sainton, G. (2004). *Spectroscopie des supernovæ à grand décalage vers le rouge* ($0.3 \leq z \leq 1.2$). Ph. D. thesis, Université Lyon I, N° ordre: 131-2004.
- [262] Saio, H. and K. Nomoto (1998). Inward Propagation of Nuclear-burning Shells in Merging C-O and He White Dwarfs. *ApJ* **500**, 388–+.
- [263] Salvo, M. E., E. Cappellaro, P. A. Mazzali, S. Benetti, I. J. Danziger, F. Patat, and M. Turatto (2001). The template type Ia supernova 1996X. *MNRAS* **321**, 254–268.
- [264] Sandrock, S., R. Amestica, P. Duhoux, J. Navarrete, and M. S. Sarazin (2000). VLT astronomical site monitor: control, automation, and data flow. In *Proc. SPIE Vol. 4009, p. 338-349, Advanced Telescope and Instrumentation Control Software, Hilton Lewis; Ed.*, pp. 338–349.
- [265] Sarazin, M. and F. Roddier (1990). The ESO differential image motion monitor. *A&A* **227**, 294–300.
- [266] Saunders, W., R. Cannon, and W. J. Sutherland (2004). Improvements to *runz*. *Anglo-Australian Observatory Newsletter*, 16–17.
- [267] Schaefer, B. E. (1998). The Peak Brightness of SN 1974G in NGC 4414 and the Hubble Constant. *ApJ* **509**, 80–84.
- [268] Schlegel, D. J., D. P. Finkbeiner, and M. Davis (1998). Maps of Dust Infrared Emission for Use in Estimation of Reddening and Cosmic Microwave Background Radiation Foregrounds. *ApJ* **500**, 525–+.

- [269] Schlegel, E. M. (1990). A new subclass of Type II supernovae? *MNRAS* **244**, 269–271.
- [270] Schmidt, B. P., N. B. Suntzeff, M. M. Phillips, R. A. Schommer, A. Clocchiatti, R. P. Kirshner, P. Garnavich, P. Challis, B. Leibundgut, J. Spyromilio, A. G. Riess, A. V. Filippenko, M. Hamuy, R. C. Smith, C. Hogan, C. Stubbs, A. Diercks, D. Reiss, R. Gilliland, J. Tonry, J. Maza, A. Dressler, J. Walsh, and R. Ciardullo (1998). The High-Z Supernova Search: Measuring Cosmic Deceleration and Global Curvature of the Universe Using Type IA Supernovae. *ApJ* **507**, 46–63.
- [271] Schmidt, G. D., R. J. Weymann, and C. B. Foltz (1989). A moderate-resolution, high-throughput CCD channel for the Multiple Mirror Telescope spectrograph. *PASP* **101**, 713–724.
- [272] Schroeder, D. J. (1987). *Astronomical Optics*. San Diego: Academic Press, 1987.
- [273] Shapiro, S. L. and S. A. Teukolsky (1983). *Black holes, white dwarfs, and neutron stars: The physics of compact objects*. Research supported by the National Science Foundation. New York, Wiley-Interscience, 1983, 663 p.
- [274] Sheinis, A. I., M. Bolte, H. W. Epps, R. I. Kibrick, J. S. Miller, M. V. Radovan, B. C. Bigelow, and B. M. Sutin (2002). ESI, a New Keck Observatory Echellette Spectrograph and Imager. *PASP* **114**, 851–865.
- [275] Sil’chenko, O. K., A. V. Zasov, A. N. Burenkov, and J. Boulesteix (1997). A ring-like zone of strong radial gas motions in the disk of NGC 6181. *A&AS* **121**, 1–9.
- [276] Smith, R. C., N. Suntzeff, C. Stubbs, C. Aguilera, B. Barris, A. Becker, P. Challis, R. Chornock, A. Clocchiatti, R. Covarrubias, A. V. Filippenko, P. Garnavich, S. T. Holland, S. Jha, R. Kirshner, K. Krisciunas, B. Leibundgut, W. Li, T. Matheson, A. Miceli, G. Miknaitis, A. Rest, A. Riess, B. Schmidt, J. Sollerman, J. Spyromilio, J. Tonry, S. Nikolaev, and M. Hamuy (2002). Supernovae 2002iu-2002je. *IAU Circ.* **8021**, 1–+.
- [277] Sobolev, V. V. (1960). *Moving envelopes of stars*. Cambridge: Harvard University Press, 1960.
- [278] Spergel, D. N., L. Verde, H. V. Peiris, E. Komatsu, M. R.olta, C. L. Bennett, M. Halpern, G. Hinshaw, N. Jarosik, A. Kogut, M. Limon, S. S. Meyer, L. Page, G. S. Tucker, J. L. Weiland, E. Wollack, and E. L. Wright (2003). First-Year Wilkinson Microwave Anisotropy Probe (WMAP) Observations: Determination of Cosmological Parameters. *ApJS* **148**, 175–194.
- [279] Spyromilio, J., P. A. Pinto, and R. G. Eastman (1994). On the Origin of the 1.2-MICRON Feature in Type-Ia Supernova Spectra. *MNRAS* **266**, L17+.
- [280] Stehle, M., P. A. Mazzali, S. Benetti, and W. Hillebrandt (2005). Abundance stratification in Type Ia supernovae - I. The case of SN 2002bo. *MNRAS* **360**, 1231–1243.

- [281] Stritzinger, M. (2005). *Supernovae of the Type Ia: Bolometric properties and new tools for photometric techniques*. Ph. D. thesis, Technische Universität München.
- [282] Stritzinger, M., M. Hamuy, N. B. Suntzeff, R. C. Smith, M. M. Phillips, J. Maza, L.-G. Strolger, R. Antezana, L. González, M. Wischnjewsky, P. Candia, J. Espinoza, D. González, C. Stubbs, A. C. Becker, E. P. Rubenstein, and G. Galaz (2002). Optical Photometry of the Type Ia Supernova 1999ee and the Type Ib/c Supernova 1999ex in IC 5179. *AJ* **124**, 2100–2117.
- [283] Stritzinger, M. and B. Leibundgut (2005). Lower limits on the Hubble constant from models of type Ia supernovae. *A&A* **431**, 423–431.
- [284] Strolger, L., A. G. Riess, T. Dahlen, N. Panagia, P. Challis, J. Tonry, A. V. Filippenko, and R. Chornock (2004). The Hubble Higher-Z Supernova Search: Supernovae to $z=1.6$ and Constraints on Type Ia Progenitor Models. *ApJ*, in press.
- [285] Sullivan, M., R. S. Ellis, G. Aldering, R. Amanullah, P. Astier, G. Blanc, M. S. Burns, A. Conley, S. E. Deustua, M. Doi, S. Fabbro, G. Folatelli, A. S. Fruchter, G. Garavini, R. Gibbons, G. Goldhaber, A. Goobar, D. E. Groom, D. Hardin, I. Hook, D. A. Howell, M. Irwin, A. G. Kim, R. A. Knop, C. Lidman, R. McMahon, J. Mendez, S. Nobili, P. E. Nugent, R. Pain, N. Panagia, C. R. Pennypacker, S. Perlmutter, R. Quimby, J. Raux, N. Regnault, P. Ruiz-Lapuente, B. Schaefer, K. Schahmaneche, A. L. Spadafora, N. A. Walton, L. Wang, W. M. Wood-Vasey, and N. Yasuda (2003). The Hubble diagram of type Ia supernovae as a function of host galaxy morphology. *MNRAS* **340**, 1057–1075.
- [286] Suntzeff, N. B. (1996). Observations of Type IA Supernovae. In *IAU Colloq. 145: Supernovae and Supernova Remnants*, pp. 41–+.
- [287] Suntzeff, N. B. (2003). Optical, Infrared, and Bolometric Light Curves of Type Ia Supernovae. In *From Twilight to Highlight: The Physics of Supernovae*, pp. 183–+.
- [288] Swartz, D. A., A. Clocchiatti, R. Benjamin, D. F. Lester, and J. C. Wheeler (1993). Supernova 1993J as a spectroscopic link between type II and type Ib supernovae. *Nature* **365**, 232–234.
- [289] Thomas, R. C., D. Branch, E. Baron, K. Nomoto, W. Li, and A. V. Filippenko (2004). On the Geometry of the High-Velocity Ejecta of the Peculiar Type Ia Supernova 2000cx. *ApJ* **601**, 1019–1030.
- [290] Tonry, J. and M. Davis (1979). A survey of galaxy redshifts. I - Data reduction techniques. *AJ* **84**, 1511–1525.
- [291] Tonry, J. L., B. P. Schmidt, B. Barris, P. Candia, P. Challis, A. Clocchiatti, A. L. Coil, A. V. Filippenko, P. Garnavich, C. Hogan, S. T. Holland, S. Jha, R. P. Kirshner, K. Krisciunas, B. Leibundgut, W. Li, T. Matheson, M. M. Phillips, A. G. Riess, R. Schommer, R. C. Smith, J. Sollerman, J. Spyromilio, C. W. Stubbs, and N. B. Suntzeff (2003). Cosmological Results from High-z Supernovae. *ApJ* **594**, 1–24.

- [292] Tsvetanov, Z., J. Blakeslee, H. Ford, D. Magee, G. Illingworth, and A. Riess (2002). Supernova 2002dd. *IAU Circ.* **7912**, 1–+.
- [293] Turatto, M. (2003). Classification of Supernovae. *LNP Vol. 598: Supernovae and Gamma-Ray Bursters* **598**, 21–36.
- [294] Turatto, M., S. Benetti, E. Cappellaro, I. J. Danziger, M. della Valle, C. Gouiffes, P. A. Mazzali, and F. Patat (1996). The properties of the peculiar type IA supernova 1991bg. I. Analysis and discussion of two years of observations. *MNRAS* **283**, 1–17.
- [295] Turatto, M., A. Piemonte, S. Benetti, E. Cappellaro, P. A. Mazzali, I. J. Danziger, and F. Patat (1998). A New Faint Type IA Supernova: SN 1997CN in NGC 5490. *AJ* **116**, 2431–2437.
- [296] Umeda, H., K. Nomoto, C. Kobayashi, I. Hachisu, and M. Kato (1999). The Origin of the Diversity of Type IA Supernovae and the Environmental Effects. *ApJ* **522**, L43–L47.
- [297] van den Heuvel, E. P. J., D. Bhattacharya, K. Nomoto, and S. A. Rappaport (1992). Accreting white dwarf models for CAL 83, CAL 87 and other ultrasoft X-ray sources in the LMC. *A&A* **262**, 97–105.
- [298] Vandenberg, D. A., P. B. Stetson, and M. Bolte (1996). The Age of the Galactic Globular Cluster System. *ARA&A* **34**, 461–510.
- [299] Vilenkin, A. (1984). String-dominated universe. *Physical Review Letters* **53**, 1016–1018.
- [300] Vinkó, J., L. L. Kiss, B. Csák, G. Fűrész, R. Szabó, J. R. Thomson, and S. W. Mochnecki (2001). The Peculiar Type Ia Supernova 1999by: Spectroscopy at Early Epochs. *AJ* **121**, 3127–3132.
- [301] Vinkó, J., L. L. Kiss, J. Thomson, G. Fűrész, W. Lu, G. Kaszás, and Z. Balog (1999). Early-time spectroscopic observations of SN 1998aq in NGC 3982. *A&A* **345**, 592–596.
- [302] Wade, R. A. and K. Horne (1988). The radial velocity curve and peculiar TiO distribution of the red secondary star in Z Chamaeleontis. *ApJ* **324**, 411–430.
- [303] Walker, A. G. (1936). . In *Proceedings of the London Mathematical Society*, pp. 90–+.
- [304] Wang, L., D. Baade, P. Höflich, A. Khokhlov, J. C. Wheeler, D. Kasen, P. E. Nugent, S. Perlmutter, C. Fransson, and P. Lundqvist (2003). Spectropolarimetry of SN 2001el in NGC 1448: Asphericity of a Normal Type Ia Supernova. *ApJ* **591**, 1110–1128.
- [305] Wang, L., J. C. Wheeler, and P. Höflich (1997). Polarimetry of the Type IA Supernova SN 1996X. *ApJ* **476**, L27+.

- [306] Webb, J. K., V. V. Flambaum, C. W. Churchill, M. J. Drinkwater, and J. D. Barrow (1999). Search for Time Variation of the Fine Structure Constant. *Physical Review Letters* **82**, 884–887.
- [307] Webbink, R. F. (1984). Double white dwarfs as progenitors of R Coronae Borealis stars and Type I supernovae. *ApJ* **277**, 355–360.
- [308] Weinberg, S. (1972). *Gravitation and cosmology: Principles and applications of the general theory of relativity*. New York: Wiley, —c1972.
- [309] Weinberg, S. (1987). Anthropic bound on the cosmological constant. *Physical Review Letters* **59**, 2607–2610.
- [310] Weinberg, S. (1989). The cosmological constant problem. *Reviews of Modern Physics* **61**, 1–23.
- [311] Weiss, N. (1987). Possible origins of a small, nonzero cosmological constant. *Physics Letters B* **197**, 42–44.
- [312] Wells, L. A. and M. G. Lee (1995). Erratum: The Type IA Supernova 1989B in NGC 3627 (M66). *AJ* **110**, 1440–+.
- [313] Wells, L. A., M. M. Phillips, B. Suntzeff, S. R. Heathcote, M. Hamuy, M. Navarrete, M. Fernandez, W. G. Weller, R. A. Schommer, R. P. Kirshner, B. Leibundgut, S. P. Willner, S. P. Peletier, E. M. Schlegel, J. C. Wheeler, R. P. Harkness, D. J. Bell, J. M. Matthews, A. V. Filippenko, J. C. Shields, M. W. Richmond, D. Jewitt, J. Luu, H. D. Tran, P. N. Appleton, E. I. Robson, J. A. Tyson, P. Guhathakurta, J. A. Eder, H. E. Bond, M. Potter, S. Veilleux, A. C. Porter, R. M. Humphreys, K. A. Janes, T. B. Williams, E. Costa, M. T. Ruiz, J. T. Lee, J. H. Lutz, R. M. Rich, P. F. Winkler, and N. D. Tyson (1994). The Type IA supernova 1989B in NGC 3627 (M66). *AJ* **108**, 2233–2250.
- [314] Wetterich, C. (1988). Cosmology and the fate of dilatation symmetry. *Nuclear Physics B* **302**, 668–696.
- [315] Wheeler, J. C. and R. P. Harkness (1990). Type I supernovae. *Reports of Progress in Physics* **53**, 1467–1557.
- [316] Wheeler, J. C., T. Piran, and S. Weinberg (Eds.) (1990). *Jerusalem Winter School for Theoretical Physics. Supernovae. Volume 6, Jerusalem, Dec. 28, 1988- Jan. 5, 1989*.
- [317] Whelan, J. and I. J. Iben (1973). Binaries and Supernovae of Type I. *ApJ* **186**, 1007–1014.
- [318] Williams, B. F., C. J. Hogan, B. Barris, P. Candia, P. Challis, A. Clocchiatti, A. L. Coil, A. V. Filippenko, P. Garnavich, R. P. Kirshner, S. T. Holland, S. Jha, K. Krisciunas, B. Leibundgut, W. Li, T. Matheson, J. Maza, M. M. Phillips, A. G. Riess, B. P.

- Schmidt, R. A. Schommer, R. C. Smith, J. Sollerman, J. Spyromilio, C. Stubbs, N. B. Suntzeff, and J. L. Tonry (2003). Imaging and Demography of the Host Galaxies of High-Redshift Type Ia Supernovae. *AJ* **126**, 2608–2621.
- [319] Wilson, O. C. (1939). Possible Applications of Supernovae to the Study of the Nebular Red Shifts. *ApJ* **90**, 634–+.
- [320] Woosley, S. E., R. E. Taam, and T. A. Weaver (1986). Models for Type I supernova. I - Detonations in white dwarfs. *ApJ* **301**, 601–623.
- [321] Woosley, S. E. and T. A. Weaver (1986). The physics of supernova explosions. *ARA&A* **24**, 205–253.
- [322] Woosley, S. E. and T. A. Weaver (1994). Sub-Chandrasekhar mass models for Type IA supernovae. *ApJ* **423**, 371–379.
- [323] Zel'dovich, Y. B. (1968). The cosmological constant and the theory of elementary particles. *Sov. Phys. Usp.* **11**, 381–393.
- [324] Zwicky, F. (1965). *Supernovae*, pp. 367–424. *Stellar Structure - Stars and Stellar Systems: Compendium of Astronomy and Astrophysics, Vol. VIII*, edited by Lawrence H. Aller and Dean B. McLaughlin. University of Chicago Press, 1965., p.367-424.

Acknowledgements

First and foremost, I would like to express my deepest thanks to my thesis supervisor at ESO, Bruno Leibundgut, for a successful introduction to the world of research, and for giving me the motivation to continue this exciting career. Bruno offered the right kind of support to get me going on my thesis, whilst leaving me enough independence to lead my own research projects.

Thanks to Bruno I was able to enjoy yearly observing trips to Chile, where I met most of the ESSENCE team members, whom I also thank for the good times spent on the other side of the Atlantic. Thanks to the Cerro-Tololo Inter-American Observatory for its hospitality. The ESSENCE project was a great way for me to have access to supernova spectroscopic data, which in turn enabled me to write the important paper which constitutes Chapter 5 of this thesis.

Also through ESSENCE was I able to meet the charismatic astronomer Robert Kirshner; thanks to him for his trust in offering me a post-doctoral position at the CfA, thereby enabling me to further my research career in this field. I look forward to moving to Cambridge, MA, at the end of this year.

The first refereed publication constitutes a landmark in one's scientific career; thanks again to Jeremy Walsh, Bruno Leibundgut, and Grégory Sainton, for being such great first-time co-authors! Their efforts are best seen in Chapter 3 of this thesis.

Chapter 5 would not have been quite the same without the frantic support of my good friend Luc Dessart, to whom I also owe invaluable discussions on radiative transfer in stellar atmospheres. I value his scientific judgement and integrity, and look forward to collaborating with him on supernova spectra in the near future.

David Branch, Peter Höflich, and Nando Patat, I value your pedagogical insights into supernova spectroscopy, and also look forward to future collaborations.

This Ph. D. would not have been possible without the financial support of the European Southern Observatory, *via* a studentship from the International Max Planck Research School (IMPRS) on Astrophysics at the University of Munich.

Last, thanks in advance to the members of my thesis committee for their time spent in reading this thesis.

I dedicate this thesis to my daughter Lea, should she one day have the will to read this manuscript, and to her mother, Mariola, for being so supportive during the few months this thesis was written in.

Garching bei München, 7th August 2005.

Curriculum Vitae

Stéphane Blondin

European Southern Observatory (ESO)
Karl-Schwarzschild-Strasse 2
D-85748 Garching bei München
Germany

Born 26th May 1980
French nationality
Married, one child

Phone: +49 (0) 89 320 06 554
E-mail: sblondin@eso.org
Homepage: <http://www.eso.org/~sblondin/>

EDUCATION

- 2005-** POSTDOCTORAL FELLOWSHIP
Harvard-Smithsonian Center for Astrophysics, Optical and Infrared
Astronomy Division
- 2002-2005** PHD IN ASTRONOMY
European Southern Observatory, Ludwig-Maximilians-Universität
München
“Optical Spectra of Thermonuclear Supernovae in the Local and
Distant Universe”
▷ *Supervisor: Dr. Bruno Leibundgut (ESO)*
- 1998-2002** MASTER OF PHYSICS
University of Southampton (UK)
▷ *First class honours*
- 1997** FRENCH BACCALAURÉAT SCIENTIFIQUE
Lycée International de Saint Germain en Laye (France)
▷ *Mathematics option*

 RESEARCH INTERESTS

Cosmology	Cosmology with Type Ia supernovae, Dark Energy
Supernovae	Spectra of supernovae, theory and observation
Algorithms	Spectral restoration and cross-correlation tools

 AWARDS

2002-2005	ESO-IMPRS PhD studentship
2002	University of Southampton Physics and Astronomy Departmental Prize
2001	University of Southampton Physics and Astronomy Departmental Prize

 OBSERVING EXPERIENCE

Observing programmes	<ul style="list-style-type: none"> ▷ PI on ESO programme 073.A-0642, <i>Host Galaxies of High-Redshift Type Ia Supernovae</i> ▷ Co-I on ESO large programme 170.A-0519, <i>The ω Project: Measuring the Equation of State of the Universe</i>
Optical observations	<ul style="list-style-type: none"> VLT+FORs1/2, imaging & spectroscopy GEMINI N&S+GMOS, spectroscopy MAGELLAN+LDSS2, spectroscopy

 COMPUTER KNOWLEDGE

Programming	IDL, Fortran, C, shell
Astronomy	IRAF & Pyraf
OS	UNIX & Linux, Mac OS-X, Windows

 LANGUAGES

French	mother tongue
English	perfectly bilingual
Spanish	excellent oral and written comprehension
German	good oral and written comprehension

REFERENCES

Dr. Bruno Leibundgut (ESO)

Karl-Schwarzschild-Strasse 2, D-85748 Garching bei München, Germany
e-mail: bleibund@eso.org; Phone: +49 (0) 89 320 06 295

Dr. Jeremy Walsh (ESO/ST-ECF)

Karl-Schwarzschild-Strasse 2, D-85748 Garching bei München, Germany
e-mail: jwalsh@eso.org; Phone: +49 (0) 89 320 06 248

Dr. Brian P. Schmidt (RSAA)

via Cotter Rd, Weston Creek, ACT 2611, Australia
e-mail: brian@mso.anu.edu.au; Phone: +61 (0) 2 6125 8042

REFEREED PUBLICATIONS

2005

▷ *The ESSENCE Project: A Supernova Survey Optimized to Constrain the Equation of State of the Cosmic Dark Energy*
Miknaitis, G., et al. 2005, in prep.

▷ *Using line profiles to test the fraternity of Type Ia supernovae at high and low redshifts*

Blondin, S., et al. 2005, accepted for publication in The Astronomical Journal (astro-ph/0510089)

▷ *Hubble Space Telescope Observations of Nine High-Redshift ESSENCE Supernovae*

Krisciunas, K., et al. 2005, submitted to The Astronomical Journal

▷ *Spectroscopy of High-Redshift Supernovae from the ESSENCE Project: The First 2 Years*

Matheson, T., et al. 2005, The Astronomical Journal, **129**, 2352

▷ *Extracting clean supernova spectra. Towards a quantitative analysis of high-redshift Type Ia supernova spectra*

Blondin, S., Walsh, J. R., Leibundgut, B., & Sainton, G. 2005, Astronomy & Astrophysics, **431**, 757

2004

▷ *The Hubble Higher z Supernova Search: Supernovae to $z \sim 1.6$ and Constraints on Type Ia Progenitor Models*

Strolger, L. -G., et al. 2004, The Astrophysical Journal, **613**, 200

▷ *Twenty-Three High-Redshift Supernovae from the Institute for Astronomy Deep Survey: Doubling the Supernova Sample at $z > 0.7$*

Barris, B. J., et al. 2004, The Astrophysical Journal, **602**, 571

NON-REFEREED PUBLICATIONS

2003

▷ *Spectroscopy of High-Redshift Type Ia Supernovae – December 2002 VLT observations as part of the ESSENCE program*

Blondin, S. 2003, Diploma Thesis, Ludwig-Maximilians-Universität München

▷ *Evidence for dark energy from Type Ia supernovae*

Leibundgut, B. & **Blondin, S.** 2003, Proceedings of the 8th International Workshop on Topics in Astroparticle and Underground Physics (TAUP), University of Washington, Seattle, September 2003

▷ *Spectroscopy of High-Redshift Type Ia Supernovae – Impacts on Cosmology*

Blondin, S. 2003, Proceedings of the Laboratoire d’Astrophysique de Marseille (LAM) IVth International Cosmology Conference, June 2003